U.S. DEPARTMENT OF
ENERGY

Office of
ENERGY EFFICIENCY &
RENEWABLE ENERGY

Electrification

2018 Annual Progress Report

Vehicle Technologies Office

(This page intentionally left blank)

Disclaimer

This report was prepared as an account of work sponsored by an agency of the United States government. Neither the United States government nor any agency thereof, nor any of their employees, makes any warranty, express or implied, or assumes any legal liability or responsibility for the accuracy, completeness, or usefulness of any information, apparatus, product, or process disclosed or represents that its use would not infringe privately owned rights. Reference herein to any specific commercial product, process, or service by trade name, trademark, manufacturer, or otherwise does not necessarily constitute or imply its endorsement, recommendation, or favoring by the United States government or any agency thereof. The views and opinions of authors expressed herein do not necessarily state or reflect those of the United States government or any agency thereof.

Acronyms

AC	Alternating Current
ACC	Adaptive Cruise Control
accel	Acceleration
ACS	Advanced Combustion Systems
ACSforEVER	Advanced Climate Systems for EV Extended Range
AER	All-electric range
AFV	Alternative Fuel Vehicle
AMI	Advanced Metering Infrastructure
AMT	Automated Mechanical Transmission
ANL	Argonne National Laboratory
ANN	Artificial Neural Network
AOI	Areas of Interest
APEC	Asia Pacific Economic Council
APRF	Advanced Powertrain Research Facility
APT	Pressure Sensor
ASD	Aftermarket Safety Device
AVTA	Advanced Vehicle Testing Activity
AVTE	Advanced Vehicle Testing and Evaluation
BaSce	Baseline and Scenario
Batt	Battery
BEB	Battery Next-Generation Electric Transit Bus
BEC	Bussed Electrical Center
BEMS	Building Energy Management System
BET	Battery Electric Truck
BEV	Battery Electric Vehicle
BMW	Bayerische Motoren Werke AG
BSFC	Brake Specific Fuel Consumption
BTE	Brake Thermal Efficiency
CAC	Charge Air Cooler
CACC	Cooperative Adaptive Cruise Control
CAE	Computer-Aided Engineering
CAFE	Corporate Average Fuel Economy
CAN	Controller Area Network
CAV	Connected and automated vehicles
CARB	California Air Resources Board
CBD	Central Business District
CCS	Combined Charging System
CW, CCW	Clockwise, Counter Clockwise
CD	Charge-Depleting
CERV	Conference on Electric Roads and Vehicles

CFD	Computational Fluid Dynamics
CFDC	Commercial Fleet Data Center
CFL	Combined Fluid Loop
CH4	Methane
CHTS	California Household Travel Survey
CIP	Common Integration Platform
Cm3	Cubic
CNG	Compressed Natural Gas
CO	Carbon monoxide
CO2	Carbon Dioxide
COMM	Commuter
Conv	Conventional Vehicle
COP	Coefficient of Performance
CRADA	Cooperative Research and Development Agreement
CS	Charge Sustaining
Cs	Cold start
CV	Conventional vehicle
D3	Downloadable Dynamometer Database
DC	Direct current
DCFC	Direct Current Fast Charge
DCT	Dual-clutch transmission
decel	Deceleration
DER	Distributed energy resource
DFGM	Digital Flux Gate Magnetometer
DFMEA	Design of Failure Modes Analysis
DGE	Diesel Gallon Equivalent
DOE	U.S. Department of Energy
DOHC	Dual overhead cam
DS	Down speeding
DSM	Distributed Security Module
DSM	Diagnostic Security Module
DSP	Digital Signal Processor
DSRC	Dedicated Short Range Communications
dt	Change in time
dv	Change in velocity
Dyno	Dynamometer
EAVS	Electrically Assisted Variable Speed Supercharger
EC	European Commission
EDV	Electric Drive Vehicle
EDT	Electric Drive Technologies
EDX	Energy dispersive x-ray spectroscopy
EERE	Energy Efficiency and Renewable Energy
EGR	Exhaust Gas Recirculation

EG/W	Ethylene glycol/water
EOL	End of life
EPA	Environmental Protection Agency
ePATHS	Electrical PCM Assisted Thermal Heating System
EREV	Extended-Range Electric Vehicles
ESIF	Energy Systems Integration Facility
ESS	Energy Storage System
ETT	Electric Transportation Technologies
E-TREE	Electric Truck with Range Extending Engine
EUMD	End-Use Measurement Device
EV	Electric Vehicle
EV2G	Electric Vehicle-to-Grid
EVSE	Electric Vehicle Service Equipment
EXV	Electronic Expansion Valve
$\bar{F}$	Force
FASTSim	Future Automotive Systems Technology Simulator
FC	Fuel cell
FC	Fast charge
FCons	Fuel consumption
FCTO	Fuel Cell Technologies Office
FE	Fuel Economy
FEA	Finite Element Analysis
FEX	Front-end Heat Exchanger
FHWA	Federal Highway Administration
FLNA	Frito-Lay North America
FM	Friction Modifier
FMEP	Friction Mean Effective Pressure
FOA	Funding Opportunity Announcement
FTIR	Fourier transform infrared spectroscopy
FTP	Federal Test Procedure
FWD	Four wheel drive
FY	Fiscal year
$\bar{g}$	gram
GB	Gigabyte
GCEDV	Grid Connected Electrical Drive Vehicles
GEM	Gas Emissions Model
GHG	Greenhouse Gas
GITT	Grid Interaction Tech Team
GMLC	Grid Modernization Lab Consortium
GnPs	graphene nanoplatelets
GO	Graphene Oxide
GPRA	Government Performance and Results Act
GPS	Global Positioning System

GREET	Greenhouse gases, Regulated Emissions, and Energy use in Transportation
GSF1	Generic Speed Form 1
GSU	Grid side unit
GUI	Graphic User Interface
GVW	Gross Vehicle Weight
h-APU	hybrid Auxiliary Power Unit
HATCI	Hyundai America Technical Center, Inc.
HC	Unburned hydrocarbons
HD	Heavy Duty
HEV	Hybrid-Electric Vehicle
H-GAC	Houston-Galveston Area Council
HHDDT	Heavy Heavy-Duty Diesel Truck
HHV	Hydraulic Hybrid Vehicle
HIL	Hardware-In-the-Loop
HP	Heat Pump
Hp	Horsepower
HTML	HyperText Markup Language
HV	High Voltage
HVAC	Heating Ventilating and Air Conditioning
HWFET	Highway Fuel Economy Test
HPMS	Highway Performance Monitoring System
HVTB	High Voltage Traction Battery
HWY	Highway Program or Highway Fuel Economy Test Cycle
HPC	High Performance Computing
HTR	Heater
Hz	Hertz
I	Inertia
IC	Internal Combustion
ICD	Interim Component Durability
ICDV	Internal Combustion Drive Vehicles
ICE	Internal Combustion Engine
ICTF	Intermodal Container Transfer Facility
ICU	Inverter-Charger Unit
IEB	Information Exchange Bus
IEC	International Electrotechnical Commission
IGBT	Insulated Gate Bipolar Transistors
IHX	Internal Heat Exchanger
INL	Idaho National Laboratory
INTEGRATE	Integrated Network Testbed for Energy Grid Research and Technology
IOT	Internet of Things
IR	Infrared Radiation
ISO	International Organization for Standardization
ITS	Intelligent Transportation Systems

JIT	Just-in-Time
kg	Kilogram
km	Kilometer
kW	Kilowatt
kWh	Kilowatt hour
L	litre
L1	Level 1 benchmark
L2	Level 2 benchmark
Lbf	Pounds force
LCC	Liquid-Cooled Condenser
LD	Light-duty
LH	line haul
Li	Lithium
LIB	Lithium ion battery
LLNL	Lawrence Livermore National Laboratory
LNG	Liquified natural gas
LTC	Lockport Technical Center
LV	Leading Vehicle
M	Mass
MBSE	Model Based System Engineering
MD	Medium Duty
mpg	Miles per gallon
MMTCE	Million Metric Tons of Carbon Equivalent
MIIT	Ministry of Industry and Information Technology
mi	Mile
MJ	Megajoules
MOSFET	Metal-Oxide Semiconductor Field-Effect Transistor
mph	Miles per hour
MPGe,	Miles per gallon equivalent, Miles per gallon gasoline equivalent
MTDC	Medium Truck Duty Cycle
MOVES	Motor Vehicle Emission Simulator
MRF	Moving Reference Frame
MURECP	Medium-Duty Urban Range Extended Connected Powertrain
MY	Model year
M2	Meters squared
NACFE	North American Council for Freight Efficiency
NDA	Non-Disclosure Agreement
NETL	National Energy Technology Laboratory
NHTS	National Household Travel Survey
NHTSA	National Highway Transportation Safety Administration

NM	Newton meters
NOx	Nitrogen oxides
NR	Natural Rubber
NRE	Non Recurring Engineering
NREL	National Renewable Energy Laboratory
NRT	National Retail Trucking
NVH	Noise, vibration, and harshness
NVUSD	Napa Valley Unified School District
NYSERDA	New York State Energy Research Development Authority
OBC	On-board charger
OCBC	Orange County Bus Cycle
OEM	Original Equipment Manufacturer
OneSAF	One Semi-Automated Forces
ORNL	Oak Ridge National Laboratories
P	Active Power
PC	Polycarbonate
PCM	Phase-Change Material
PCU	Power Control Unit
PCU	Powertrain Control Unit
PEEM	Power Electronics and Electric Motor
PFC	Power factor correction
PFI	Port fuel injection
PGW	Pittsburgh Glass Works
PHEV	Plug-in Hybrid Electric Vehicle
PHEV##	Plug-in hybrid electric vehicle with ## miles of all-electric range
PI	Principal Investigator
PM	Permanent Magnet
PM	Particulate Matter
ppm	Parts per Million
PTC	Positive Temperature Coefficient (Electric Heater)
PTO	Power Take-Off
PVP	Polyvinylpyrrolidone
PWWMD	Public Works and Waste Management Department
λ	Power Factor
φ	Power Angle
Q	Reactive power
QA	Quality assurance
QC	Quality control
R2	Coefficient of Determination
R/D	Receiver / Dryer
REV	New York State's Reforming the Energy Vision Initiative

REx	Range Extending Engine
rGO	reduced graphene oxide
RH	Relative Humidity
RMS	Root Mean Square
ROL	Ring-On-Liner
rpm	Revolutions Per Minute
RSU	Road Side Unit
RWDC	Real-World Drive-Cycle
$\bar{S}$	Apparent power
SAE	Society of Automotive Engineers
SBR	Styrene-Butadiene Rubber
SC03	SC03 Supplemental Federal Test Procedure
SCAG	Southern California Association of Governments
SCAQMD	South Coast Air Quality Management District
SCIG	Southern California International Gateway
SCR	Silicon Controlled Rectifier
SCR	Selective Catalytic Reduction
SDO	Standards Definition Organizations
SI	Système International d'Unités
SI	Gasoline Spark Ignition
SNR	Sensor
SOC	State of Charge
SPL	Sound Pressure Level
SR	Speed Ratio
SS	Steady State
SPaT	Signal Phase and Timing
StAR	Storage-Assisted Recharging
$\overline{T}$	Torque
TA	Technical Area
TA	Torque Assist
TC	Thermocouple
TE	Thermoelectric
TE	Transmission Error
TES	Thermal Energy Storage
TGA	thermogravimetric analysis
THC	Total hydrocarbon emissions
TIM	Thermal Interface Materials
TLRP	Thermal Load Reduction Package
TN	Testing Network
TOU	Time-Of-Use
TSDC	Transportation Secure Data Center
TSI	Turbocharged stratified injection
TUSD	Torrance Unified School District

TXVs	Thermal Expansion Valves
U.S. DRIVE	U.S. Driving Research and Innovation for Vehicle Efficiency and Energy Sustainability
UA	Transfer Coefficient
UC	Ultra-capacitor
UCR	University of California, Riverside
UDDS	Urban Dynamometer Driving Schedule
UN ECE	United Nations Economic Council for Europe
UPS	United Parcel Service
URL	Uniform Resource Locator
US06	Environmental Protection Agency US06 or Supplemental Federal Test Procedure
USABC	United States Advanced Battery Consortium
USCAR	U.S. Council for Automotive Research
Util	Battery capacity utilization
V	Voltage
V2G	Vehicle-to-Grid
VAr	Volt-Amp-reactive
VGI	Vehicle-Grid Integration
VGT	Variable Geometry Turbocharger
VIP	Vacuum Insulated Panels
VMT	Vehicle Miles Traveled
VS	Vehicle Systems
VSATT	Vehicle Systems Analysis Technical Team
VSI	Vehicle Systems Integration
VSST	Vehicle Systems Simulation and Testing
VTCab	Vehicle Thermal Cab Simulator
VTIF	Vehicle Testing and Integration Facility
VTO	Vehicle Technologies Office
dw	Change in Angle W
WCC	Water Cooled Condenser
WEC	World Endurance Championship
WEG	Water/Ethylene Glycol
Wh	Watt hour
WHR	Waste Heat Recovery
WPT	Wireless Power Transfer
WTW	Well-to-Wheels
XPS	x-ray photoelectron spectroscopy
ZECT	Zero-emissions cargo transport

Executive Summary

During fiscal year 2018 (FY 2018), the U.S. Department of Energy (DOE) Vehicle Technologies Office (VTO) funded early stage research & development (R&D) projects that address batteries and electrification of the U.S. transportation sector. The VTO Electrification Sub-Program is composed of Electric Drive Technologies, and Grid Integration activities. The Electric Drive Technologies group conducts R&D projects that advance electric motors and power electronics technologies. The Grid and Charging Infrastructure group conducts R&D projects that advance grid modernization and electric vehicle charging technologies. This document presents a brief overview of the Electrification Sub-Program and progress reports for its R&D projects. Each of the progress reports provide a project overview and highlights of the technical results that were accomplished in FY 2018.

Table of Contents

Vehicle Technologies Office Overview **1**
Organization Chart 1

Electric Drive Technologies Overview **2**
Introduction 2
Goals and Objectives 2
Program Design and Execution 2
Electric Drive Technologies Lab Consortium 3
Research Highlights 3

Grid and Infrastructure Program Overview **7**
Introduction 7
Goals and Objectives 7
State of the Art 8
Research Highlights 10

I. Electric Drive Technologies Research **14**
I.1 Advanced HPC Multiphysics Modeling of Motors and Materials (ORNL) 14
I.2 Advanced Multiphysics Integration and Designs (ORNL) 24
I.3 Drivetrain Performance Improvement Techniques (ORNL) 35
I.4 High-Silicon Laminates for Electric Motors (ORNL) 45
I.5 Innovative Chargers and Converters (ORNL) 49
I.6 Materials for Advanced Packaging (ORNL) 59
I.7 Non-Rare-Earth Electric Motors (ORNL) 63
I.8 Ultra-Conducting Copper (ORNL) 73
I.9 Development of Radically Enhanced alnico Magnets (DREaM) for Traction Drive Motors (Ames Laboratory) 83
I.10 Performance and Reliability of Bonded Interfaces for High-Temperature Packaging Insert Section Heading (NREL) 90
I.11 Power Electronics Thermal Management (NREL) 99
I.12 Electric Motor Thermal Management Research (NREL) 109

II. Electric Drive Technologies Development **119**
II.1 Dual Phase Soft Magnetic Laminates for Low-cost, Non/Reduced-Rare-Earth Containing Electrical Machines (GE) 119
II.2 Cost Effective 6.5% Silicon Steel Laminate for Electric Machines (Iowa State University) 125
II.3 Highly Integrated Wide Bandgap Power Module for Next Generation Plug-In Vehicles (General Motors) 133
II.4 High Speed Hybrid Reluctance Motor Utilizing Anisotropic Materials (General Motors) 141
II.5 Assessing Class 3-8 HEV and EV Vehicles Operating on North American Roads and Their Supply Chain for Drive-Train Motors, Inverters, Converters and Batteries (Synthesis Partners, LLC) 149
II.6 Wound Field and Hybrid Synchronous Machines for EV Traction with Brushless Capacitive Rotor Field Excitation (Illinois Institute of Technology) 159

II.7 Development and Demonstration of Medium-Heavy Duty PHEV Work Trucks (Odyne Systems LLC) 168
II.8 V2G Electric School Bus Commercialization Project (Blue Bird Corporation) 174

III. Grid and Infrastructure: Industry Awards 180
III.1 Zero Emission Drayage Trucks Demonstration - ZECT I (SCAQMD) 180
III.2 Zero-Emission Delivery Vehicles Deployment Project (Houston-Galveston Area Council).... 186
III.3 San Pedro Bay Ports Hybrid & Fuel Cell Electric Vehicle Project –ZECT 2 (SCAQMD) 191
III.4 Medium-Duty Urban Range Extended Connected Powertrain (MURECP), (Robert Bosch LLC) 201
III.5 Cummins Electric Truck with Range-Extending Engine (ETREE) (Cummins, Inc.) 207
III.6 Medium Duty Vehicle Powertrain Electrification and Demonstration (McLaren Engineering) 211
III.7 Bidirectional Wireless Power Flow for Medium-Duty Vehicle-to-Grid Connectivity (CALSTART) 216
III.8 Comprehensive Assessment of On-and Off-Board Vehicle-to-Grid Technology Performance and Impacts on Battery and the Grid (Electric Power Research Institute (EPRI)) [DE-EE0007792] 223

IV. Grid and Infrastructure: Grid Modernization 231
IV.1 Vehicle to Grid Integration Pathway (ANL, INL, LBNL, NREL, PNNL) 231
IV.2 GM0085 Systems Research for Standards and Interoperability 238
IV.3 Diagnostic Security Modules for Electric Vehicle to Building Integration (GMLC) [Category 2 GMLC 0163] 241
IV.4 Testing Network and Open Library 245
IV.5 GMLC 1.4.2 – Definitions, Standards and Test Procedures for Grid Services from Devices (PNNL, with ANL, INL, LBNL, LANL, NREL, ORNL, SNL) 251

V. Grid and Infrastructure: Fast Charging Enabling Technologies 258
V.1 Demand Charge Mitigation Technologies 258
V.2 Fast Charging: Grid Impacts and Cybersecurity (INL) 263
V.3 Extreme Fast Charging – High Power Wireless Power Transfer 267
V.4 Interoperability, Grid Integration and Fast Charging (ANL) 274

List of Figures

Figure I.1.1 Typical B-H curve material model used for magnetic simulations; (Right) more realistic B-H material model showing both major and minor hysteresis loops that impact motor efficiency. 16

Figure I.1.2 Synchronous reluctance machine model created using OeRSTED's internal nonlinear geometric constraint solver with a total of 21 geometric parameters. 17

Figure I.1.3 Copy of the synchronous reluctance machined modeled in OeRSTED reconstructed in commercial software package showing the dimensioned angular, radial, and distance constraints. 18

Figure I.1.4 Torque calculation comparison between OeRSTED and a commercially available software package using (left) linear magnetic properties and (right) nonlinear magnetic properties; the salient pole rotor structure was chosen because of its difficulty (from a numerical accuracy point of view) due to the large amount of torque ripple. 18

Figure I.1.5 Flux density comparison of a synchronous reluctance machine simulated in OeRSTED and a commercially available finite element analysis software; good agreement is obtained even at high flux density. 19

Figure I.1.6 Diagram of work distribution for motor optimization on an HPC system; each node simulates one candidate design; each core works on a current vector; the rotor position is advanced once all the current vectors for the active rotor position are analyzed; the results are combined to calculate the entire motor efficiency map. 20

Figure I.1.7 Schematic description of the asynchronous fully-informed particle swarm method: 1) queen sends task to worker, 2) worker performs computation, 3) worker sends data to queen, 4) queen updates swarm status. 21

Figure I.1.8 (Left) Normalized second quadrant magnetization characteristic of an AlNiCo permanent magnet showing nonlinear recoil lines; (Right) Everett function associated with a Preisach model of an AlNiCo permanent magnet identified from a set of permanent magnet hysteresis loops; 22

Figure I.1.9 (Left) AlNiCo magnet in a uniform applied field demonstrating nonuniform demagnetization due to a combination of high second—quadrant differential permeability and boundary effects. (Right) Central AlNiCo magnet in a nine-magnet array demonstrating improved uniformity in the demagnetization field, especially in the body of the magnet. Gaps between the magnets necessary for sensors are the main cause of nonuniformity at the surfaces of the magnet. 23

Figure I.2.1 Illustration of a conventional power module cross section. 25

Figure I.2.2 (Left) Structure of the base plate with copper encapsulant for in-plane and through-plane thermal conductivity and specific gravity analysis. (Right) In-plane and through-plane thermal conductivity and specific gravity of the base plate with respect to TPG ratio. 26

Figure I.2.3 Structure of the encapsulated TPG used in this study and manufactured bare copper and encapsulated TPG-based samples. 27

Figure I.2.4 The experimental setup with four-resistor assembly. 27

Figure I.2.5 Observed reduction in simulation and experiments with 15 W power dissipation across each resistor's in-case temperature and thermal resistance when copper is replaced with a TPG-embedded substrate. 28

Figure I.2.6 Conventional DBC solution cross section. 28

Figure I.2.7 Proposed IMS solution with TPG insert and the cross section. 29

Figure I.2.8 Design of the IMS with TPG insert. 29

Figure I.2.9 ANSYS steady state thermal simulation results. 29

Figure I.2.10 Chip-to-chip and board-to-board interconnect examples with quilt packaging [4]. 29

Figure I.2.11 Vertical SiC MOSFET structure with quilt interconnects. 30

Figure I.2.12 Quilt-based interconnect nodules on Si substrate and test data for current capability. 30

Figure I.2.13 Block diagram of the proposed system. 31

Figure I.2.14 Single-turn near-field coupled system and mutual inductance for two coils of 10 mm radius. 32

Figure I.2.15 Quality factor and efficiency of the design coil with respect to operating frequency. 32

Figure I.2.16 Active clamp flyback converter and main waveforms under steady-state operation with simulation- and time-domain-based analytical modeling. 32

Figure I.3.1 (a) Approximation of typical SiC MOSFET reverse conduction characteristics for loss modeling, (b) Inverter phase current. 36

Figure I.3.2 (a) Traction drive system and (b) two-phase modulation signals. 37

Figure I.3.3 Losses for switches and diodes in a SiC MOSFET phase-leg use the switching timing-based generic inverter loss computation method. 38

Figure I.3.4 (a) Experimental inverter operating waveforms under two-phase modulation. From top, v_{bn}, v_{cn}, 500V/div; i_a, i_b, 50A/div. (b) Measured and computed inverter efficiency vs. power. 39

Figure I.3.5 (a,b,c) Modeled conduction loss reduction using MOSFET reverse conduction by sweeping through current, modulation index, and power factor. (d) Minimum and maximum total inverter loss reduction. 39

Figure I.3.6 (a,b,c) Simulated switching loss reduction using two-phase modulation by sweeping through current, modulation index, and power factor. (d) Minimum and maximum inverter switching loss reduction vs. current. 40

Figure I.3.7 Torque, voltage, current, power, and power factor profiles under maximum torque per amp control for a 2016 BMW i3 motor (a) and 2007 Camry motor (b). 41

Figure I.3.8 Total loss reduction vs. speed for the maximum torque envelop for 2007 Camry and 2016 BMW i3 motors. 41

Figure I.3.9 Simulated inverter loss reduction (a) and efficiency (b) maps for the 2016 BMW i3 motor. 42

Figure I.3.10 Simulated inverter loss reduction (a) and efficiency (b) maps for the 2007 Camry motor. 43

Figure I.4.1 Fe-6.5Si-X steel thermomechanically processed and rolled at room temperature to a final thickness of 0.35 mm with no significant edge cracking 47

Figure I.4.2 Formation energies (energy per atom, and total energies with respect to bulk phases and atomic phases) and volumes of $Fe_4M_2Si_2$. 48

Figure I.5.1 Schematic of the proposed novel integrated wireless EV charging architecture 50

Figure I.5.2 FEA model and prototype of the optimized 11 kW DD coil. 51

Figure I.5.3 FEA simulation results indicating compliance with the International Commission on Non-Ionizing Radiation Protection. 51

Figure I.5.4 Circuit model of primary side leadless chip carrier and secondary side series tuned wireless EV charging system to analyze sensitivity to variation in coupling coefficient and load resistance. 52

Figure I.5.5 Variation of magnitude and phase of input impedance and input current, as a function of frequency for different load resistances for the designed 11 kW integrated wireless EV charging system. 52

Figure I.5.6 Variation of magnitude and phase primary coil current, voltage and current gain and the output power as a function of frequency for different load resistances for the designed 11 kW integrated wireless EV charging system. 53

Figure I.5.7 Variation of magnitude and phase of input impedance and input current, as a function of frequency for coupling coefficients for the 11 kW integrated wireless EV charging system. 54

Figure I.5.8 Variation of magnitude and phase primary coil current, voltage and current gain, and output power as a function of frequency for different coupling coefficients for the 11 kW integrated wireless EV charging system. 55

Figure I.5.9 Zin as a function of frequency at different load levels: (a) MATLAB model analysis and (b) experimental measurement from frequency response analyzer. 55

Figure I.5.10 ϕZin as a function of frequency at different load levels: (a) MATLAB model analysis and (b) experimental measurement from frequency response analyzer. 56

Figure I.5.11 Primary coil and the secondary side components of the integrated wireless EV charging system (laboratory prototype). 56

Figure I.5.12 The efficiencies of different stages of the integrated wireless EV charging system and primary side inverter voltage and current and secondary side rectifier input voltage and current of the charging system operating at 12 kW (BMW motor is not connected). 57

Figure I.5.13 The efficiencies of different stages of the integrated wireless EV charging system operating at 12 kW (BMW motor is connected to traction inverter). The efficiency of the rectifier includes the losses in the motor. 57

Figure I.7.1 Integration concept of a rotary transformer inside a wound rotor synchronous motor. 65

Figure I.7.2 Proposed rotary transformer topology. 65

Figure I.7.3 Attributes and size of the proposed vs. conventional rotary transformers for 10 kW output power. 65

Figure I.7.4 Final optimized design: geometry, dimensions, and performance. 66

Figure I.7.5 Mechanical stress and total displacement in rotor at 20,000 rpm (25% margin from top speed of 16,000 rpm). 67

Figure I.7.6 Proof-of-concept prototype test bench design. 67

Figure I.7.7 Assembled rotary transformer prototypes. 67

Figure I.7.8 Inductances of rotary transformer prototypes. 68

Figure I.7.9 The 10.7 kW power transfer test results. 68

Figure I.7.10 Conductivity of ultra-conductive copper vs. reference copper. 69

Figure I.7.11 Size and weight comparison for ultra-conductive copper vs. copper winding 100 kW traction motor designs. 69

Figure I.7.12 Comparison of AlNiCo motor and BMW i3 motor. 70

Figure I.7.13 Feasibility of the AlNiCo design under worst demagnetization scenario. 70

Figure I.7.14 Torque and demagnetization resistance comparison with BMW i3. 71

Figure I.8.1 Schematic illustration of the process flow for producing Cu-CNT-Cu multilayer composite tapes. 75

Figure I.8.2 Scanning electron microscopy images displaying the surface microstructure of CNT-coated Cu tapes using dispersions incorporating DMF, NMP, and MEK. 76

Figure I.8.3 Comparison of TGA results for mass loss versus temperature for AC and AQ. The inset shows the normalized data to 100°C. 77

Figure I.8.4 Typical Raman spectra and scanning electron microscopy images of SWCNT and MWCNT coated Cu tapes. 77

Figure I.8.5 Classical molecular dynamics simulations using Lennard-Jones pairwise potential describing Cu-Cu, C-C, Cu-C atomic interactions. 78

Figure I.8.6 Scanning electron microscopy images displaying the evolution of the surface microstructures of Cu/CNT/Cu tapes. Surface morphology of 50 nm (top panels), 150 nm (middle panels), and 450 nm (bottom panels) thick Cu-coated CNT/Cu tapes before and after heat treatments at 400 and 900°C. High-temperature annealing data for the 50 nm coating are not shown because the sample did not show uniform coverage at lower processing temperatures. 79

Figure I.8.7 Z-contrast transmission electron microscopy images of a Cu/CNT/Cu sample, where the Cu overlayer thickness is ~ 300 nm, illustrating the porous nature of the Cu film throughout its thickness. 80

Figure I.8.8 Electrical performance of several Cu/CNT/Cu tapes as a function of temperature ranging from 0 to 120°C. Data for the reference uncoated Cu tape are also included for comparison. 80

Figure I.9.1 Demagnetization Curves of Ames Processed Samples and Arnold Magnetics alnico 8B. 86

Figure I.9.2 TRS testing for Ames Laboratory Alnico at 150 °C, 25 C, and -40 °C to simulate the temperatures that a PM motor could experience while in service. 87

Figure I.9.3 The 3D reconstruction (volume of 1176 nm x 985 nm x 706 nm) showing that interconnected (α1)Fe-Co-rich phase is rare but does occur in this section of a grain that was well aligned to the magnetic field during magnetic annealing. b) TEM image of a similar region, but representative of a 2D transverse section of a grain that was well-aligned to the magnetic field. 88

Figure I.10.1 Double-lap sample configuration for mechanical characterization 92

Figure I.10.2 Sintering profile of nano silver (left) and hybrid silver (right) 92

Figure I.10.3 C-SAM images of double-lap samples synthesized at NREL with nano silver (left) and at VT with hybrid silver (right). Dark/grey regions indicate a bonded interface whereas white spots/patches denote voids or other discontinuities 92

Figure I.10.4 Sintering profile of pressure-assisted round samples with hybrid silver 93

Figure I.10.5 Load – displacement graph 94

Figure I.10.6 Shear stress values of nano-silver. These samples were synthesized at NREL using pressureless sintering 95

Figure I.10.7 Shear stress values of hybrid silver made using pressureless sintering (left); impact of sintering pressure on the shear stress values (right) 95

Figure I.10.8 C-SAM images of pressureless samples from copper side (left) and Invar side (right); 22 mm (top), 16 mm (center), and 10 mm (bottom). 96

Figure I.10.9 Strain energy density results of round coupons 97

Figure I.11.1 Specific thermal resistance versus the HTC for three cooling configurations (left) and an image of the 2015 BMWi3 power module used for the thermal analysis (right). 101

Figure I.11.2 Planar package, dielectric cooling concept 101

Figure I.11.3 Cross-sectional views of the three-dimensional slot (left) and circular (right) jet models used for the CFD simulations. 102

Figure I.11.4 Junction-to-coolant thermal resistance versus pumping power for the circular and slot jet configurations. Results for the 1- and 3-mm characteristic jet dimension are shown..... 103

Figure I.11.5 Sectional views of the 1- (left) and 3- (middle) mm finned cases. The top view schematic is shown on the right..... 103

Figure I.11.6 Junction-to-coolant thermal resistance versus the jet velocity for the two-finned cases and the baseline (no fin) case. 104

Figure I.11.7 CFD-computed temperatures for the 2.5-mm-tall fins configuration and jet velocity of 0.5 m/s (left). The fluid streamlines are shown as black lines. A schematic of a conceptual inverter with cooling system consisting of 24 devices predicted to enable reaching the 100-kW/L power density target (right). 105

Figure I.11.8 FE model used to determine the HTC cooling requirements for cooling the electrical interconnect..... 106

Figure I.11.9 FE-computed interconnect maximum top-surface temperatures versus the applied interconnect HTCs, interconnect distance from MOSFET, and interconnect height. 106

Figure I.11.10 CFD-computed electrical interconnect temperatures and relevant model dimensions (left). Interconnect average heat transfer coefficient versus the dielectric fluid velocity (right). 107

Figure I.12.1 Illustration of thermal management impact on motor operation to increase continuous power operating limits (left). Heat must pass through several layers within the motor to be extracted through active cooling such as through a cooling jacket or jet impingement cooling with oil such as ATF (right). 110

Figure I.12.2 Jet impingement experimental setup and experimental factors. 111

Figure I.12.3 Orifice jet center impingement (left). Orifice jet edge impingement (right) 111

Figure I.12.4 Orthotropic thermal property orientation for machine laminations. Through-stack conductivity is along the z-axis, and in-plane thermal conductivity is along the x-y plane. 111

Figure I.12.5 Schematic (left) and photo (right) of the steady-state setup for measuring orthotropic thermal conductivity values 112

Figure I.12.6 ATF impingement heat transfer coefficient as function of jet velocity, target surface temperature, and impingement location for 50°C fluid temperature (left) and 70°C fluid temperature (right) 113

Figure I.12.7 Sample jet impingement CFD results showing temperature profile (left) and fluid volume fractions (right). 114

Figure I.12.8 Sample comparison of the heat transfer coefficients predicted by the model and the experimental results. 114

Figure I.12.9 Photo and height map of ridged and smooth surfaces 115

Figure I.12.10 Interlamination thermal contact resistances shown with averages of smooth samples and samples with a ridged pattern on one side. 115

Figure I.12.11 Results predicted by the model compared to experimental data for contact resistance. 116

Figure II.1.1 Illustration of the dual phase structure in a laminate used to manufacture a SynRel machine. ... 120

Figure II.1.2 Manufacturing sequence for prototypes containing dual phase magnetic laminates. 121

Figure II.1.3 Measured performance of a sub-scale dual phase synchronous reluctance prototype compared with predicted performance by design. The prototype with a rotor manufactured from 0.010” thick Dual Phase

sheet is measured to have at least 30% higher power and torque output than a synchronous reluctance motor with its rotor made of grade HF10 Silicon Steel by the same design. 122

Figure II.1.4 Subscale prototype motor on a dynameter test stand. 122

Figure II.2.1 Magnetization vs. applied field hysteresis loops of the feedstock powder (red) and the bulk magnet fabricated using the newly developed CIP process (green). The energy products of the feedstock powder and the bulk magnet are 12 MGOe and 8 MGOe, respectively. 128

Figure II.2.2 Flakes of Fe-6.5wt%Si prepared by melt spun method. The flakes on the right are spread out to show their dimensions. Flake dimensions are uniform in length (2 mm), but the width varies due to an undulating melt pool. 128

Figure II.2.3 SEM images of the ribbons prepared at 5 m/s and 10 m/s; and TEM images of the ribbons prepared at 1 m/s and 30 m/s. 129

Figure II.2.4 A 50 mm OD ring sample consolidated from melt-spun 6.5% Si steel flakes. 129

Figure II.2.5 Target performance metrics for torque and power as function of speed 130

Figure II.2.6 Picture of the prototype rotor (left) and stator (right), both using 0.1 mm 6.5%Si steel purchased from JFE. 131

Figure II.3.1 Manufactured prototype of the power module: (a) module picture (b) electrical schematic. Work performed by General Motors Subrecipient, Virginia Polytechnic Institute and State University, CPES 134

Figure II.3.2 Static characteristic of designed power module: (a) switch resistance (b) output characteristic . 135

Figure II.3.3 Static characteristic of designed power module for different Vgs voltages: (a) switch resistance (b) output characteristic 135

Figure II.3.4 Switch on state resistance for different temperatures 135

Figure II.3.5 Output characteristic of internal body diode: (a) room temperature (b) hot temperatures 136

Figure II.3.6 Hardware set-up for double pulse testing 136

Figure II.3.7 Representative switching waveform during switching transients: (a) turn-on (b) turn-off 137

Figure II.3.8 Power module switching losses: (a) turn on losses (blue) (b) turn off losses (orange) (c) total switching losses (gray) 137

Figure II.3.9 DC measurement error of R_{dson} estimation 139

Figure II.4.1 Variant 1 2D lamination design, left. Torque-speed and power-speed curves, right. 143

Figure II.4.2 Variant 2 2D lamination design, left. Torque-speed curve, middle. Power-speed curve, right. .. 144

Figure II.4.3 Variant 2, 2D lamination design, left. Torque-speed and power-speed curves with comparison to baseline Al design, right. 144

Figure II.4.4 Variant 1, stator, left. Variant 3 stator in fixture, right. 145

Figure II.4.5 Variant 2, left, and Variant 3, right, power loss due to slot tooth width decrease 145

Figure II.4.6 Predicted demagnetization compared to experimental results, left. Field measurement of sequential demagnetization tests along the motor axis, right. 146

Figure II.4.7 First Tensile Test Setup. 147

Figure II.4.8 Comparison of stress-strain curves of three candidate materials. 147

Figure II.4.9 Comparison of ultimate tensile strength and 0.2% yield for three candidate materials. 148

Figure II.4.10 Comparison of uniform plastic strain and total elongation for three candidate materials 148

Figure II.5.1 Sources Accessed and Selected Outcomes 151

Figure II.5.2 Relevant Class 3-8 vehicle classifications, determined by the gross vehicle weight rating (GVWR) of the vehicle 151

Figure II.5.3 Estimated Number of Class 3-8 HEV and EV Trucks, By Supplier, In Operation in NA in 2018. 153

Figure II.5.4 Estimated Number of Class 3-8 HEV or EV Buses, By Supplier, in Operation in NA in 2018.. 154

Figure II.5.5 Estimated Number of Class 3-8 Up-fitted HEV or EVs, By Supplier, In Operation in NA in 2018. 155

Figure II.5.6 Frequency of expert source statements about gaps in the NA Class 3-8 HEV and EV supply chain, by main topic: 2013 to present 156

Figure II.6.1 Conceptual model of low cost wound field synchronous machine with die compressed fractional slot concentrated stator windings and rotor windings with low scrap segmented structure. Field power is transmitted using a brushless capacitive coupler manufactured from printed circuit boards 161

Figure II.6.2 Die for compression of rotor field winding coil (a), and representative compressed coil (b)..... 162

Figure II.6.3 Salient pole with die compressed field winding (a), and pole assembly slid into rotor yoke dovetail slot. 162

Figure II.6.4 Single Phase (left-a) and three phase (right-a) rotating capacitive PCBs (a), and single phase GaN inverter. 163

Figure II.6.5 Coupling and stray capacitances (a) and measured ESR (b) of single phase PCB CPC..... 163

Figure II.6.6 Open loop approximation error for different number of Taylor series terms as a function of switching frequency (a), and the discrete pole migration as a function of switching frequency for different number of Taylor series terms (b). 165

Figure II.6.7 Performance comparison of high and low switching frequency WFSM DB-DTFC at 4,000 RPM and 5 kHZ switching frequency. 166

Figure II.6.8 Electromagnetic optimization Pareto fronts of 12 slot 10 pole star-delta designs for two different current density ratios at 4,000 RPM. Down-selected designs from original simulations are solid dots. Corresponding designs re-simulated at the opposite current density are indicated by a diamond mark..... 166

Figure II.7.1 Odyne Powertrain Configuration 169

Figure II.7.2 Odyne Hybrid Architecture 170

Figure II.7.3 NREL fuel savings model 171

Figure II.7.4 Predicted fuel economy improvements 172

Figure II.7.5 Freightliner M2 test truck chassis 172

Figure II.7.6 Isometric view - Freightliner M2 model with hybrid components 173

Figure II.7.7 Plan view - Freightliner M2 model with hybrid components 173

Figure II.8.1 Left: Efficiency map of TM4 3000 motor + single gear ratio on the NREL School Bus Drive Cycle. * = motor operating point. Right: Efficiency map of UQMHD 250 + Eaton 2-speed transmission. * = 1st gear motor operating point. * = 2nd gear motor operating point. Both cases: loaded vehicle weight of 27,000 lbs. Per EDI's proprietary simulation platform. 176

Figure II.8.2 EDI's thermal management bench test unit. Note the three water pumps at the bottom of the unit. One will support battery heating/cooling and the other two will support drive system and bus heating/cooling. 177

Figure III.1.1 TransPower EDD trucks on display 182
Figure III.1.2 US hybrid battery electric truck 183
Figure III.1.3 TransPower PHET pulling its first trailer 184
Figure III.1.4 US Hybrid PHET pulling a container for TTSI 184
Figure III.2.1 The Workhorse E-100 electric delivery van 189
Figure III.3.1 BAE/Kenworth vehicle system 192
Figure III.3.2 TransPower fuel cell truck in foreground & CNG truck in background 192
Figure III.3.3 U.S. hybrid truck: design to fabrication 193
Figure III.3.4 BAE - CNG hybrid system architecture 193
Figure III.4.1 Target PHEV transmission design 202
Figure III.4.2 PHEV transmission model / first prototype 202
Figure III.4.3 Electro-hydraulic Power Steering (EHPS) Packaging and Bracket Design 203
Figure III.4.4 Thermal system design with VOSS thermally actuated control valve and five modes 204
Figure III.4.5 Complete Vehicle Network Diagram 204
Figure III.4.6 Powertrain dyno testing summary. 205
Figure III.4.7 Vehicle Packaging Study Report–completed by Morgan Olson 206
Figure III.5.1. ETREE powertrain test cell located at Cummins Technical Center, Columbus, Indiana 209
Figure III.5.2. ETREE alternate battery—drivers side enclosure (shown without cover) 209
Figure III.6.1 Hybrid system general layout 212
Figure III.6.2 Complete eAxle system 213
Figure III.6.3 eAxle Gearbox System Design Prototype on Oil Flow Testing Rig 213
Figure III.6.4 Vehicle, battery, axle & range extender systems exhibited at ACT Expo in Long Beach CA prior to final assembly of demonstrator. These are actual demonstrator subsystems. 214
Figure III.6.5 Oil lube flow testing of completed eAxle system 214
Figure III.7.1 System level diagram of the proposed architecture for the bidirectional wireless charging system. 218
Figure III.7.2 System resonant stage parameters. 219
Figure III.7.3 Coupling coils 3D design. 219
Figure III.7.4 Coils with 11” of nominal airgap. 219
Figure III.7.5 EM field distribution analysis of the coils. 219
Figure III.7.6 Grid interface inductor (1 of the 3) (a), primary-side (b), and secondary-side (c) resonant tuning inductors. 220
Figure III.7.7 Simulation results of the grid interface converter with charge mode (t<0.25s) and discharge mode (t>0.25s). 221
Figure III.7.8 Coupling factor sensitivity analysis. 221
Figure III.7.9 Load sensitivity analysis of the system. 221

Figure III.7.10 Charge-mode simulation waveforms. 222
Figure III.7.11 Discharge-mode simulation waveforms. 222
Figure III.8.1 Project Structural Overview of On-Vehicle AC and Off- Vehicle DC V2G 224
Figure III.8.2 Bi-directional Charging Inverter Installed into Chrysler Pacifica Van PHEVs 226
Figure III.8.3 EV Communications Controller (EVCC) Chrysler Pacifica Van PHEV 227
Figure III.8.4 UCSD Parking Lot Demonstration Site and Chrysler Pacifica Van PHEV and Honda Accord PHEV 227
Figure III.8.5 Demonstration site charging island (4 EVSEs, 75KVA transformer, 400A panel, transformer management system 227
Figure III.8.6 Transformer Management and Monitoring System (TMS) 227
Figure III.8.7 SPIN rack mounted unit for power controls and analytics algorithmic S/W integration and testing 228
Figure IV.1.1 GM0062 workplace charging project scope 231
Figure IV.1.2 GM0062 industry advisory board prioritized use cases 233
Figure IV.1.3 ANL demand response 233
Figure IV.1.4 PNNL demand charge mitigation EVSE / PEV control response 234
Figure IV.1.5. ANL preferential-based PEV charging demonstration with six PEVs 235
Figure IV.1.6. NREL control system campus net load during June 19th event 235
Figure IV.2.1 IEEE 34 node feeder. Bus A and bus B are marked in red. 239
Figure IV.2.2 Feeder Power when PEV charging is controlled and not controlled. 239
Figure IV.2.3 Voltage when PEV charging is controlled and not controlled for two nodes on the IEEE 34 node feeder. 240
Figure IV.3.1 DSM operator status in BEMS (Alpha System) 243
Figure IV.3.2 DCFC cyber manipulation results 243
Figure IV.4.1 GMLC 1.2.3 project organization and relation to gridPULSE. 247
Figure IV.4.2 Cover page for the gridPULSE Catalog of National Laboratory Testing Resources. 248
Figure IV.4.3 Open Library implementation, showing model categories (images at top) and entries (table at bottom). 249
Figure IV.4.4 gridPULSE.org website, showing links (top right) to About, Testing Resources, Open Library, and Contact Us. 250
Figure IV.5.1 Software architecture of services and device models 255
Figure V.1.1 Energy envelop of each device and aggregated energy envelop 259
Figure V.1.2 Structure of distributed control with hierarchy 260
Figure V.1.3 Tritium 50 kWh DC fast charger (left) and 40 kWh stationary ESS by Sharp (right) 260
Figure V.1.4 Plots of building load, clipping level, battery power, and battery energy 261
Figure V.1.5 DCFC demand charge mitigation with ESS 261
Figure V.1.6 Architecture of integrated control system for EVSE and ESS at NREL 262

Figure V.2.1 “Stop Charge” response of DCFC during a charge event 264
Figure V.2.2 DCFC power quality during malicious control event 265
Figure V.2.3 Power draw for potential future charging sites over several sample days. 266
Figure V.3.1 FEA simulation result of the DD coil pair designed for 100 kW operation with nominal airgap. 269
Figure V.3.2 High-power DD coil with 2 AWG Litz wire validated up to 120 kW. 269
Figure V.3.3 System level circuit diagram of the series-series tuned WPT system. 270
Figure V.3.4 The actual resonant stage. 270
Figure V.3.5 High-power inverter/rectifier used in primary and secondary-side power stages. 270
Figure V.3.6 Laboratory experimental setup of the 120 kW wireless power transfer system with the hardware integrations. 271
Figure V.3.7 Laboratory experimental setup of the 120 kW wireless power transfer system with the hardware integrations. 271
Figure V.3.8 Laboratory experimental setup of the 120 kW wireless power transfer system with the hardware integrations. 271
Figure V.3.9 Power analyzer test results with stage-by-stage power flow and efficiencies. 272
Figure V.3.10 Oscilloscope waveforms for inverter output and rectifier input on primary and secondary sides. 272
Figure V.3.11 Electric field emissions at 31.5” away from the center of the primary coil (14.06 V/m highest peak). 272
Figure V.3.12 Magnetic field emissions at 31.5” away from the center of the primary coil (21.64µT highest peak). 272
Figure V.4.1. FY 2018 DOE VTO/GMLC support activities 274
Figure V.4.2. Argonne Smart Energy Plaza Facility in Lowell, Illinois 278
Figure V.4.3. Basic connectivity of devices at the Smart Energy Plaza 278
Figure V.4.4 xFC sub-meter design 279
Figure V.4.5 SpEC2 module design 279
Figure V.4.6 SCA/DEVA beta design 279
Figure V.4.7 Two-way communication latency example 280
Figure V.4.8 Response time example – aggregated EVs 280

List of Tables

Table I.2.1 Typical Property Comparison of Heat Spreader Materials 26

Table I.2.2 Thermal Conductivity of Copper and TPG Embedded Copper 29

Table I.5.1 FEA Simulation and Measurement Results of Optimized 11 kW DD Coils 51

Table I.8.1 Comparison of the Properties of Single-Wall Cu vs. those of CNTs 74

Table I.8.2 Performance Comparison of WRSM Traction Motors with UCC against Baseline Conventional Copper. Inset: WRSM with Tape Windings in both Stator and Rotor 81

Table I.11.1 Estimated Volume for Components in a 100-kW Inverter 100

Table I.11.2 Properties for EC-140 and WEG. All Properties Taken at 100°C except where Noted. 102

Table I.12.1 Experimental Factors and Levels 111

Table II.1.1 Target vs. Calculated Performance of the Full-scale 55 kW Dual Phase Prototype 123

Table II.2.1 Processing Steps for Powder Fabrication and Consolidation 127

Table II.2.2 Comparison of Core Loss (400 Hz, 10 kOe) of the Ring Sample Consolidated using Melt-Spun Flake and the Thin Sheet Commercially Produced by JFE 129

Table II.2.3 Detailed Performance Specifications 130

Table II.3.1 Inverter Loss Breakdown for Different Operating Points 138

Table II.4.1 Summarizes the Motor Designs. The Designs Exceed the DoE Motor Year 2020 Power Density and Specific Power Targets. 143

Table II.4.2 Comparison of Properties from First Tensile Tests 147

Table II.5.1 Estimated Number of Class 3-8 HEV and EVs on the Road in North America in 2018 152

Table II.5.2 Estimated Number of Class 3-8 HEV and EVs Supplied Globally, Based on Information from Suppliers of Class 3-8 HEV and EV Drive Train Components, as of 2018. 152

Table II.6.1 Prototype Wound Field and Hybrid Excitation Synchronous Machine Target Metrics 160

Table II.6.2 Capacitive Coupler Qualitative Comparison 162

Table II.6.3 Single Phase CPC Bench Testing at 2 MHz 164

Table II.6.4 Single Phase CPC Bench Testing at 2 MHz and High Field Winding Resistance 164

Table II.7.1 Baseline Dynamometer Drive Cycle Results 171

Table II.7.2 Baseline Dynamometer Work Cycle Results 171

Table II.8.1 Motor Efficiency Modeling Results for the NREL Drive Cycle 176

Table II.8.2 Energy Efficiency Results for P1 from NREL's REFUEL Dynamometer (arithmetic deviations due to rounding) 178

Table III.1.1 2012 Zero Emission Cargo Transport Demonstration Portfolio 181

Table III.1.2 Average Daily Use – TransPower BETs 182

Table III.2.1 Project Vehicle Information 189

Table III.3.1 Hydrogenics Vehicle Systems Specifications 194

Table III.5.1 Summary of ETREE Powertrain Components 208

Table III.5.2 Summary of Technical Results for FY2018 210
Table III.7.1 Grid Interface Converter Design Parameters 218
Table III.7.2 Grid Interface Converter Design Parameters 218
Table III.7.3 Design Parameters of the Grid-Side and Primary and Secondary-Side Resonant Inductors 219
Table III.7.4 Design Parameters of the Grid-Side and Primary and Secondary-Side Resonant Inductors 220
Table III.8.1 Summary of Objectives, Accomplishments, Learnings and Future Scope for On-Vehicle V2G Development 229
Table IV.1.1 Test Bed / Control System Capabilities 236
Table-IV.1.2 Standards and Equipment Gaps Identified 237
Table IV.5.1 Device Class and Grid Services Responsibilities by Laboratory 253
Table V.3.1 100 kW DD Coil Design Parameters 268

Vehicle Technologies Office Overview

Vehicles move our national economy. Annually, vehicles transport 11 billion tons of freight[1] – more than $32 billion worth of goods each day[2] – and move people more than 3 trillion vehicle-miles.[3] Growing our national economy requires transportation and transportation requires energy. The transportation sector accounts for 70% of U.S. petroleum use. The United States imports 20% of the petroleum consumed – sending more than $15 billon per month[4] overseas for crude oil. The average U.S. household spends nearly one-sixth of its total family expenditures on transportation[5], making transportation the most expensive spending category after housing.

To strengthen national security, enable future economic growth, improve energy efficiency, and increase transportation energy affordability for Americans, the Vehicle Technologies Office (VTO) funds early-stage, high-risk research on innovative vehicle and transportation technologies. VTO leverages the unique capabilities and world-class expertise of the national laboratory system to develop innovations in electrification, including advanced battery technologies; advanced combustion engines and fuels, including co-optimized systems; advanced materials for lighter-weight vehicle structures; and energy efficient mobility systems.

VTO is uniquely positioned to address early-stage challenges due to strategic public-private research partnerships with industry (e.g., U.S. DRIVE, 21st Century Truck Partnership) that leverage relevant expertise. These partnerships prevent duplication of effort, focus DOE research on critical R&D barriers, and accelerate progress. VTO focuses on research that industry either does not have the technical capability to undertake on its own, usually due to a high degree of scientific or technical uncertainty, or it is too far from market realization to merit industry resources.

Organization Chart

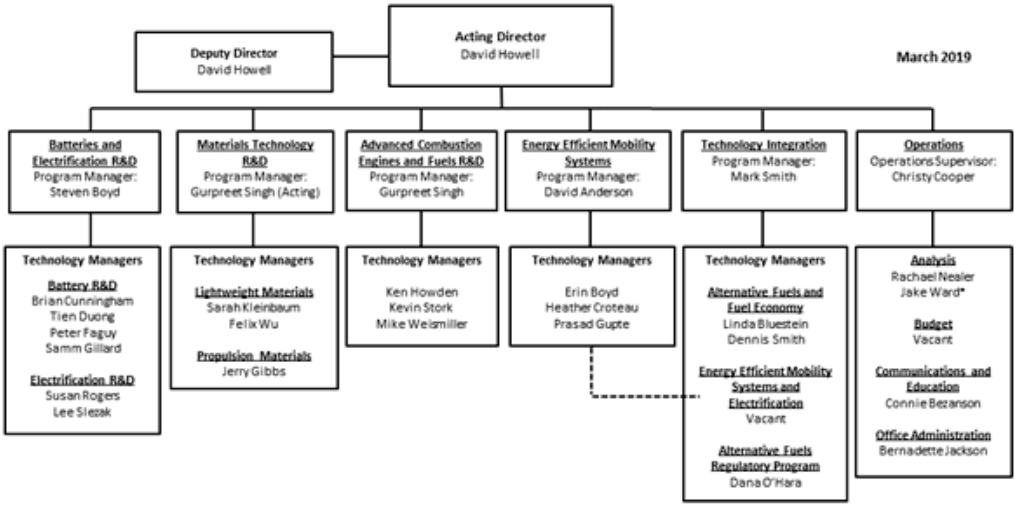

[1] Bureau of Transportation Statistics, DOT, 2016. Table 3-1 Weight and Value of Shipments by Transportation Mode https://www.bts.gov/archive/publications/transportation_statistics_annual_report/2016/tables/ch3/table3_1
[2] Ibid.
[3] Transportation Energy Data Book 37th Edition, ORNL, 2018. Table 3.8 Shares of Highway Vehicle-Miles Traveled by Vehicle Type, 1970-2016.
[4] EIA Monthly Energy Review https://www.eia.gov/totalenergy/data/monthly/pdf/mer.pdf
[5] Bureau of Labor Statistics, Consumer Expenditure Survey, 2017. Average annual expenditures and characteristics of all consumer units, 2013-2017. https://www.bls.gov/cex/2017/standard/multiyr.pdf

Electric Drive Technologies Overview

Introduction

The Electric Drive Technologies (EDT) subprogram's mission is to conduct early stage research and development on transportation electrification technologies that accelerate the development of cost-effective and compact electric traction drive systems that meet or exceed performance and reliability requirements of internal combustion engine (ICE)-based vehicles, thereby enabling electrification across all light-duty vehicle types.

Goals and Objectives

The goal of the EDT subprogram is to develop an electric traction drive system at a cost of $6/kW for a 100 kW peak system by 2025. In addition, the program has a 2025 power density target of 33 kW/L for a 100 kW peak system. While achieving these targets will require transformational technology changes to current materials and processes, it is essential for enabling widespread electrification across all light-duty vehicle platforms.

Program Design and Execution

The EDT subprogram provides support and guidance for many cutting-edge automotive technologies now under development. Researchers focus on developing revolutionary new power electronics (PE), electric motor (EM), and traction drive system (TDS) technologies that will leapfrog current on-the-road technologies. This will lead to lower cost and better efficiency in transforming battery energy to useful work. Research and development (R&D) is also aimed at achieving greater understanding of, and improvements in how the various components of tomorrow's automobiles will function as a unified system.

In supporting the development of advanced vehicle propulsion systems, the EDT program fosters the development of technologies that will significantly improve efficiency, costs, and fuel economy.

The EDT program directs early-stage research through a three-phase approach intended to

- Identify overall propulsion- and vehicle-related needs by analyzing programmatic goals and reviewing industry recommendations and requirements, and then develop and deliver the appropriate technical targets for systems, subsystems, and component R&D activities
- Develop, test, and validate individual subsystems and components, including EMs and PE
- Estimate how well the components and subsystems work together in a vehicle environment or as a complete propulsion system and whether the efficiency and performance targets at the vehicle level have been achieved.

The research performed under this program addresses the technical and cost barriers that currently inhibit the introduction of advanced propulsion technologies into hybrid electric vehicles (HEVs), plug-in HEVs, battery electric vehicles (BEVs), and fuel cell powered automobiles that meet the DOE goals.

A key element in making these advanced vehicles practical is providing an affordable electric TDS. This will require attaining weight, volume, efficiency, and cost targets for the PE and EM subsystems of the TDS. Areas of development include:

- Novel traction motor designs that result in increased power density and lower cost
- Inverter technologies that incorporate advanced wide bandgap (WBG) semiconductor devices to achieve higher efficiency while accommodating higher-temperature environments and delivering higher reliability

- Converter concepts that leverage higher-switching-frequency semiconductors, nanocomposite magnetics, higher-temperature capacitors, and novel packaging techniques that integrate more functionality into applications offering reduced size, weight, and cost
- New onboard battery charging electronics that build from advances in converter architectures for decreased cost and size
- More compact and higher-performing thermal controls achieved through novel thermal materials and innovative packaging technologies
- Integrated motor-inverter TDS architectures that optimize the technical strengths of the underlying PE and electric machine subsystems.

VTO competitively awards funding through funding opportunity announcement (FOA) selections, and projects are fully funded through the duration of the project in the year that the funding is awarded. The future direction for direct-funded work at the national laboratories is subject to change based on annual appropriations.

Electric Drive Technologies Lab Consortium

The multi-lab EDT Consortium will leverage U.S. research expertise and facilities at the national labs and universities to improve the power density of electric drives by 10X compared with the 2015 numbers while reducing the cost by 50% and doubling the lifetime miles within the next 5 years. The final objective of the consortium is to develop a 100 kW traction drive system that achieves a power density of 33 kW/L, has an operational life of 300,000 miles, and a cost of $6/kW. The system will be composed of a 100 kW/L inverter and a >20,000 rpm, 50 kW/L electric motor.

Research will be performed within the framework of a new research consortium consisting of a multi-disciplinary team that will plan, establish, conduct, and manage a portfolio of multi-lab and multi-university research efforts to advance the state-of-the-art in electric drive technologies.

The consortium is organized around three Keystone projects: (1) Power Electronics; (2) Electric Motors; and (3) Traction Drive System. The consortium will focus on early-stage research projects on advanced materials, high-density integration of dissimilar layers/materials, multifunctional subcomponents, and optimized and new thermal/electrical/magnetic architectures. New materials such as wide-bandgap semiconductors, soft magnetic materials, and ceramic dielectrics, merged using multi-objective co-optimization design techniques, will be utilized to achieve the program goals. Moreover, integration of components and subcomponents will further propel the research toward the goals of the consortium.

Consortium National Laboratory members include Ames Laboratory, The National Renewable Energy Laboratory (NREL), Oak Ridge National Laboratory (ORNL), and Sandia National Laboratory (SNL). University consortium partners include: North Carolina State University, The University of Arkansas, Virginia Polytechnic Institute, University of Wisconsin-Madison, Georgia Institute of Technology, University of California-Berkeley, Illinois Institute of Technology (IIT), Purdue University, The State University of New York (SUNY), and The Ohio State University.

Research Highlights

Novel integrated wireless EV charging architecture enables compact cost-effective wireless chargers

A wireless coil and a resonant capacitor are the only extra components needed to add wireless charging capability to any electric vehicle.

Electrified transportation is a viable alternative to fossil-fuel based transportation, which has detrimental effects on the environment and energy security. Cost-effective, convenient, and compact charging systems for battery electric vehicles (BEVs) are critical in accelerating the transition to electrified mobility. Although conventional conductive charging systems are cost-effective, they suffer from increased conductor weight as the charging power level increases and are inherently less suitable for automated charging, as they require the

user to physically plug-in the charger. This can be especially cumbersome in inclement weather conditions. Wireless charging of BEVs is a convenient alternative to plug-in or wired charging. Weight, volume, and cost of the on-board power electronic components of the wireless BEV charging system are the main challenges associated with increasing the appeal of wireless BEV charging systems.

The on-board components of a wireless BEV charging system include a vehicle side coil, resonant capacitor, high frequency rectifier (and the heat sink), and a filter capacitor. ORNL proposed an integrated wireless charger architecture, which utilizes the existing traction inverter and the DC link capacitor of the electric drive train as the secondary side rectifier of the wireless BEV charging system. This leads to increased power density, specific power, and reduced cost. An optimized interoperable double D coil pair was also designed and prototyped to facilitate in validation of the proposed integrated wireless charging architecture. The proposes integrated wireless BEV charging architecture aligns very well with the overall DOE/EDT goals that envisions ways to improve the power density and cost effectiveness of onboard components of BEVs.

ORNL developed an 11-kW integrated wireless charging system, which utilizes a 2016 BMW i3 traction inverter to be used as the secondary side rectifier of wireless BEV charging system. The effect of integrating the rectifier function into the traction inverter on the motor was also evaluated. The prototyped integrated wireless EV charging architecture was validated experimentally for 12-kW operation for a coil-t0-coil gap of 165.1 mm (6.5 inches). The dc-to-dc efficiency of the integrated wireless charging system without the motor connected was 91.8 % and with the motor connected was 88.96 %. One of the key observations is when the motor was connected to the traction inverter and operated as the rectifier for the integrated charger, the rotor showed no displacement and there were no signs of heating or chatter in the motor. This was evaluated for different starting positions of the rotor corresponding to different inductances as measured at the motor terminals (inverter was disconnected for inductance measurements). The worst-case measured loss of 340 W in the traction motor is a fraction of the rated capacity of the traction motor of 125 kW.

NREL develops new cooling technology to enable a 100 kW/L inverter

The innovative cooling concept is predicted to improve thermal performance (~50% thermal resistance reduction compared with 2014 Honda Accord Hybrid) and enable achieving the year 2025 power density target of 100 kW/L.

The DOE Roadmap proposes aggressive research targets to improve power electronics technology to enable the mass-market penetration of electric-drive vehicles. Achieving these aggressive targets will require a significant increase in power density (2025 EDT power density target: 100 kW/L) as compared with current, on-road technology. NREL has been working to develop innovative thermal management solutions to achieve this aggressive target.

NREL has developed—through thermal and computational fluid dynamics (CFD) modeling—a novel power electronics cooling concept that is predicted to enable achieving the 100 kW/L power density target. The cooling concept is unique (i.e., not used in automotive cooling systems) and is predicted to provide better thermal performance as compared with current automotive technology (~50% lower thermal resistance than the on -road technology). Submerged dielectric fluid jets impinging on highly-dense finned structures are used to cool a planar module via single-phase heat transfer. The planar module design eliminates layers to reduce package/conduction thermal resistance but requires the use of a dielectric fluid because the fluid is in direct contact with electrically active surfaces. The cooling concept and planar module design also eliminate the need for thermally conductive ceramics (e.g., silicon nitride) which are expensive and prone to thermomechanical failures, especially at high-temperature conditions (≥ 200°C). An added benefit of the cooling concept is the ability to directly cool the electrical interconnections which will decrease capacitor and gate driver temperatures and enable more compact packaging (high power density).

Thus far, EC-140 and Alpha 6 dielectric fluids have been used for the modeling design work. Both dielectric fluids have relatively high flash point temperatures, are safe (nontoxic, environmentally friendly), and have

good material compatibility. However, future work is planned to evaluate the use of automatic transmission fluid (ATF) as the dielectric coolant to decrease cost, allow for the use of an automotive-grade fluid, and enable integrating the power electronics with the electric motor.

Extensive CFD simulations have been performed to optimize the fin structures and to design the electrical interconnect cooling system. Future work is planned to model the effect of multiple dielectric fluid jets cooling multiple devices, evaluate the effect of high fluid viscosity at low-temperature conditions (-40°C temperature), and evaluate the use of ATF as the dielectric coolant. Once the design (via modeling) is complete, a prototype will be fabricated for experimental validation of the concept.

Open source modeling tool OeRSTED facilitates high throughput optimization of electric motors

The Oak Ridge Simulation Toolkit for Electromagnetic Devices (OeRSTED) will enable rapid design of electric motors (greater than 1000× speedup in efficiency map identification and multi-objective optimization compared to single core simulations) and support achieving the year 2025 power density targets of 50kW/L

Designing high power density, low cost electric motors with excellent reliability and long lifetimes requires optimizing drive systems to push the boundaries of feasibility. Because electric motors are geometrically complex multi-material systems, the amount of computational resources required to explore spaces consisting of dozens or even hundreds of design variables are staggering. Motor lifetime, reliability, and cost are strongly influenced by strict thermal and efficiency constraints and require precise magnetic material models to evaluate accurately within a simulation environment.

To meet the 2025 goals for electric motor, ORNL has begun the developing an open source high performance computing toolkit for electric motor modeling and optimization called OeRSTED; the Oak Ridge Toolkit for Electromagnetic Devices. The toolkit is scalable from workstations to the Department of Energy's (DOE) first-class high-performance computing (HPC) resources for high-throughput optimization of electric motors. Increasing throughput is achieved by developing analysis methods for quickly characterizing motor designs on single nodes/workstations and researching new and improved evolutionary optimization methods for simultaneous analysis of multiple designs.

Identifying the efficiency map for a single motor design is important for evaluating candidate design fitness. OeRSTED has been demonstrated to achieve 30× speedup in efficiency map identification on both a workstation and a single HPC node with 32 available cores. Additionally, a novel asynchronous particle swarm optimization method was developed and demonstrated to achieve linear scaling up to the number of simultaneous design evaluations, which was 40 in the largest demonstration. Combined, this represents more than a 1000× increase in optimization speed. Thus far, the speed increase has only been limited only by the amount of computational resources.

OeRSTED's standard analysis methods have been validated against existing commercial finite—element software. Advanced material models under development are driven by high—fidelity characterization methods. Material models, which would otherwise be too computationally expensive to implement within a finite element analysis framework, have been made feasible through the availability of advanced computing tools. Ultimate, these techniques will provide a step change in predicting phenomenon that are critical for electric motor reliability and cost such as demagnetization of permanent magnets.

Characterization and model for electric machine lamination materials and interfaces

Rigorous experimental characterization and model for electric machine lamination stack thermal resistance helps reduce design iterations in advanced motor designs.

Thermal models of electric motors such as finite element and computational fluid dynamics models are becoming increasingly sophisticated and utilized earlier in the design process. However, the modeling efforts are dependent on accurate material properties and data for material interfaces such as thermal interface resistance. The limited information in the open literature detailing the thermal properties of key materials

common in electric machines create challenges in simulating new or innovative motor designs. The lack of available literature, coupled with the strong interest from industry, led to this work to characterize and model the thermal contact resistance between machine laminations.

Silicon steel lamination materials are critical in the construction and operation of systems including inductors for power systems and electric motors. Thinner laminations decrease core losses within the lamination stack, but increase the number of contacts and consequently the thermal resistance within the stack. The increased number of contacts or interfaces between laminations impacts the effective thermal conductivity through the stack of laminations, influencing the temperature distribution within the motor assembly.

The thermal conductivity of the lamination stack is orthotropic. Thus, it was important to determine effective properties for both the in-plane (shown in Figure 1a as the x-y plane) and through-stack direction (shown in Figure 1a as the z direction). NREL developed a procedure to experimentally characterize layered materials, and the technique was applied to the silicon steel laminations. Data was measured for different lamination materials ranging in thickness from 0.178 mm to 0.47 mm and with different surface topologies. Using the experimental results, a model was developed that provided a good prediction for the interlamination contact resistance and the through-stack thermal conductivity. The work was recently published in the International Journal of Heat and Mass Transfer ("Experimental Characterization and Modeling of Thermal Resistance of Electric Machine Lamination Stacks," vol. 129, pp. 152–159, Feb. 2019) and is available online with hardcopies expected in February 2019.

These results fill a current need for material property data and models specific to electric machine design that currently does not exist in the public/open literature. The data and modeling approach is especially useful for simulating heat extraction axially through the lamination materials within the machine, which is particularly important for cooling rotors used in permanent-magnet machines.

Grid and Infrastructure Program Overview

Introduction

The Grid and Charging Infrastructure (G&I) program's mission is to conduct early stage research and development on transportation electrification technologies that enable reduced petroleum consumption by light, medium, and heavy duty vehicles. The program identifies and enables the role of vehicles in the future electrical grid.

Goals and Objectives

Program Goal: The G&I Program identifies systems pathways and conducts research to facilitate the development and harmonization of a robust, interoperable, and cyber secure, electric vehicle charging and grid infrastructure which incorporates advanced charging technologies, distributed energy resources, grid, and grid services.

The program achieves it goal by accomplishing the following objectives:

- **EV Grid Integration and Services:** Identify system requirements and research Grid to Vehicle power transfer and storage (V1G) and Vehicle to Grid power transfer (V2G) technologies that optimize vehicle charging efficiency, minimize systems disruptions, and facilitate integration of distributed energy resources
- **High Power Static / Dynamic Wireless Charging:** Conduct feasibility studies and technology research and development of high power static and dynamic wireless charging to enable additional consumer charging options and greater vehicle autonomy
- **EV / Electric Vehicle Service Equipment (EVSE) / Grid Interoperability & Control:** Research and develop technologies and tools to enable seamless interoperability (connectivity and communications) and control that maximize charging convenience and minimize impacts to the grid
- **Extreme Fast Charging (XFC):** Identify and assess system requirements and conduct research to enable extreme fast charging while minimizing impacts to the grid.
- **Cyber Security:** Address on-road vehicle and charging infrastructure related cyber security gaps.

Program Design and Execution

The G&I Program carries out its mission by focusing its R&D investments on early stage, medium and long-term technology projects that are unlikely to be pursued by industry alone, but have significant potential public benefit.

G&I R&D Functions:

- Perform R&D that focuses on defining requirements, designing, prototyping, and validating the enabling technologies that are needed. Document and share the results in public and industry forums where appropriate and feasible.
- Perform modeling and evaluation activities that provide objective, publicly available data to identify the most appropriate Federal investments and pathways for technology improvements and lessons learned for cost-effective future activities.
- Initiate outreach that provides technical assistance, tools, and resources to help stakeholders understand the technologies.

- Engage in research partnerships with industry to leverage technical expertise, prevent duplication, ensure public funding remains focused on the most critical barriers to technology commercialization, and accelerate progress. G&I will work collaboratively with its industry partners in the U.S. DRIVE Partnership (Grid Interaction Tech Team (GITT)) to analyze and identify technical R&D opportunities for passenger vehicles.
- Coordinate with other programs in EERE and across the DOE complex – National Laboratories, DOE's Office of Science, Office of Electricity Delivery and Energy Reliability (OE), and the Advanced Research Projects Agency-Energy (ARPA-E) to ensure the effective use of resources while avoiding duplication and facilitates the transfer of successful technologies across the research and development continuum. (i.e., Grid Modernization Initiative)
- Collaborate via strategic partnerships with end-users and other key stakeholders

The G&I program was established in January 2017. The program inherited many of its FY 2018 projects from VTO's Vehicle Systems program. In this r G&I projects have been assigned to Grid Modernization, Industry Awards, or Fast Charging Enabling Technologies sections of this Electrification Annual Progress Report (APR). The Grid Modernization section contains project reports that were awarded to members of the Grid Modernization Laboratory Consortium (GMLC). The Industry section describes projects that were awarded to commercial industry performers via DOE's Funding Opportunities Announcement (FOA) solicitation process. The Fast Charging Enabling Technologies projects were awarded to National Laboratories via direct funding agreements.

State of the Art

Electric Vehicle Charging

It is desirable to reduce EV refueling times to be competitive with conventional vehicle refueling times. The table below lists the refueling characteristics of several types of installed commercial EVSEs and a conventional gasoline fueling pump. The technologies employed in the EV charging stations are shown in the figure below.

Currently the most advanced Light Duty vehicle charging equipment is a proprietary system that can recharge the Tesla EV to 80% of battery capacity (and vehicle range capability) in approximately one-half hour of charging. This is accomplished by a charge rate of 140 KW.

The two open fast charging standards on the market today CCS and CHAdeMO were both originally designed to work at 400V. The Combined Charging System (CCS) was developed by seven carmakers and designed for charging up to 80KW at 400V. The standard is backed by major European and US OEMs and is positioned as the preferred option for a European network. CHAdeMO was an initiative of Japanese car companies and was originally designed to charge at up to 50KW at 400V.

The mid-term objective of XFC is to reduce LD charging time to approximately 10 minutes via a charge rate of approximately 350 to 400 KW. The long-term objective is to achieve charge rates of greater than 1 MW that will enable fast charging of both LD and Heavy Duty (HD) vehicles.

Table 1 Light Duty Conventional and Electric Vehicle Refueling Characteristics

Type of Refueling	Gasoline	Level 1 110V (~1.4kW)	Level 2 220V (~7.2kW)	DC Fast Charger (50kW)	Tesla SuperCharger (140kW)
Range per Charge Time	400 miles /5 mins	3-5 miles /60 mins	25 miles /60 mins	150 miles **/90 mins**	330 miles /60 mins
Time to Charge for 200 miles	<5 mins	**37 hours**	**8 hours**	**2 hours**	**25 mins**
Number of U.S. stations circa 2016	153,000	1,600	10,600	1,600	**705**

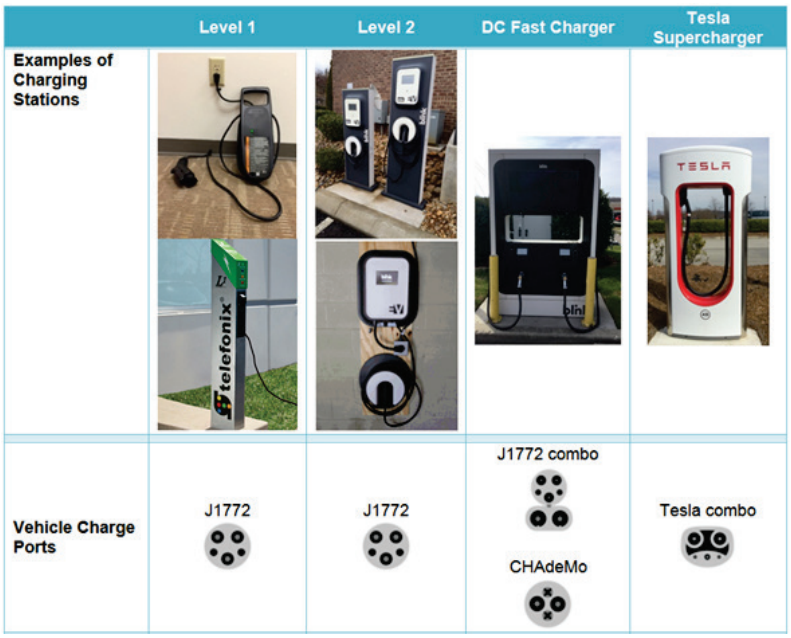

Figure 1 Examples of EV Charging Stations

Research Highlights

Accomplishments	Organization	Focus Area	Project Title
The Extreme Fast Charging (XFC) Wireless Power Transfer (WPT) project designed and prototyped an optimized DD electromagnetic coupling coil. A single phase state-of-the-art 1200 V SiC phase leg modules (CAS325M12HM2) based high efficiency inverter was designed, assembled and utilized to enable a high power stationary wireless charging system capable of transferring 120 kW. The resonant stage was analyzed based on the loosely coupled transformer model and the analyses agreed well with experimental measurements. The wireless charging system was tested at 120 kW and had a measured dc-to-dc efficiency of more than 97 % at nominal coil-to coil airgap	ORNL	Fast Charging Enabling Technologies	Extreme Fast Charging – High Power Wireless Power Transfer
As of September 2018, the ZECT1 project has completed eight of the eleven electric trucks funded under this project. NREL has received various data from these trucks including more than 34,000 miles of collective reported activity with drayage operators. The truck tests provided valuable data on performance and operational characteristics to help evaluate technical feasibility and viability of advanced technologies for drayage applications. Overall, the trucks that have completed demonstration have proven successful in demonstrating their feasibility in various drayage operations and handling daily loads and many routine schedules. The trucks have generated significant interest from trucking companies, which helps to promote and to accelerate market adoption of electric truck technologies in cargo transport operations	South Coast Air Quality Management District	Industry Awards	Zero Emission Drayage Trucks Demonstration (ZECT I)
The Bosch MURECP project developed an innovative PHEV powertrain for Medium Duty Vehicles, which can reduce fuel consumption by over 50% in charge sustaining mode when utilizing a multi-mode powersplit transmission with integrated electric motors. Utilizing the selected design for the target architecture from 2017 activities, the integration phase of the PHEV powertrain commenced. Supervisory control algorithms, battery management system, thermal energy management, and vehicle control strategy were integrated with the conventional powertrain controller and are now being further refined. The mechanical design and assembly of the hybrid drive system were completed along with the	Robert Bosch LLC	Industry Awards	Medium-Duty Urban Range Extended Connected Powertrain (MURECP)

manufacturing and delivery of two prototype transmissions			
The Electric Truck with Range Extending Engine (ETREE) project has selected and obtained the relevant powertrain components in order to meet the target objective of providing at least a 50% fuel consumption reduction across a wide range of class 6 pickup and delivery duty cycles. The ETREE program team has developed an EV powertrain and related systems to meet the project goals. The team has validated the powertrain in a powertrain test cell. While validating the test truck, the decision was made to develop an alternative robust battery, with a slightly greater energy capacity and therefore promise to exceed the initial fuel reduction goals. The alternative battery was successfully tested, off-vehicle.	Cummins	Industry Awards	Cummins Electric Truck with Range-Extending Engine (ETREE)
The CALSTART project made significant progress in developing systems for high power and high-efficiency wireless charging of an electric medium duty delivery trucks. Design activities were the system power conversion stages culminated in a successful design review meeting in May 2018. The team began building the hardware of all the system power conversion stages along with the control systems.	CALSTART	Industry Awards	Bidirectional Wireless Power Flow for Medium Duty Vehicle Grid Connectivity
The EPRI project evaluated grid DER management / integration use cases using V2G bidirectional power flow (charging and discharging) integrated with solar and stationary energy distributed resources in the AC (on-vehicle) and DC (off-vehicle) domains. Conclusions based on the resulting evaluations of the AC On-Vehicle V2G implementation and demonstration addressed (1) a requirement for utility adoption of J3072, (2) the design of a transformer management system for residential transformer and community aggregation application, (3) failure impacts of voltage and frequency transients on Transformer Management System and the vehicle charging systems.	EPRI	Industry Awards - Grid Modernization	Comprehensive Assessment of On- and Off-Board Vehicle-to-Grid Technology Performance and Impacts On Battery and the Grid [DE-EE0007792]
The Houston-Galveston area Zero Emission Delivery Vehicle project is producing a record of on-road experience and operational data, which will serve to accelerate the introduction and penetration of electric transportation technologies. To accomplish these goals, 18 zero-emission all-electric trucks manufactured by Workhorse have been deployed at UPS distribution facilities across the Houston region	Houston-Galveston Area Council	Industry Awards ZECT	Zero-Emission Delivery Vehicles Deployment Project

and are currently delivering packages as part of an ongoing two-year demonstration period.			
The first Fuel Cell truck developed by the project (FC1) has been in service at TTSI.As of September 2018 the truck had logged a total of 3731 km.	SCAQMD	Industry Awards ZECT	San Pedro Bay Ports Hybrid & Fuel Cell Electric Vehicle Project (ZECT 2)
The McLaren project specified a system using advanced modeling and simulation tools that will show the design parameters for an electrified vehicle powertrain system that will achieve the overall program objectives of 50% decrease in fossil fuel consumption on real world drive cycles. A novel eAxle system, energy storage & range extender systems have been built and tested for installation and final calibration in four demonstration vehicles.	McLaren Engineering division of Linamar	Industry Awards	Medium Duty Vehicle Powertrain Electrification and Demonstration
ANL produced more robust designs of Fast and Smart charging enabling technologies, i.e., sub-meters, second generation SpEC module and the Smart Charge Adaptor/Diagnostic Electric Vehicle Adaptor (SCA/DEVA), to prepare them for field testing in FY 2019	ANL	Fast Charging Enabling Technologies; EV / EVSE / Grid Interoperability & Control	Interoperability, Grid Integration and Fast Charging
NREL performed demand charge mitigation tests of a 50KW DC fast charger in conjunction with a stationary batter have been performed. A Nissan LEAF with CHAdeMO inlet was used. Results of the tests are shown in Figure I.1.5. The test results showed that the stationary ESS alleviates load by the DC fast charger by providing energy to grid and demonstrates that it performs well for demand charge mitigation.	NREL	Fast Charging Enabling Technologies	Demand Charge Mitigation Technologies
The Diagnostic Security Modules (DSM) for EV to Building project completed the implementation of the “generic” vehicle DSM algorithms for monitoring an EV. This includes basic vehicle fingerprinting and monitoring, and the reporting of generated alerts to the BEMS operator interface	INL	Grid Modernization - Cyber Security	Diagnostic Security Modules for Electric Vehicle to Building Integration (GMLC 0163)
The GMLC 1.4.2 Grid Services from Devices project has completed the specification of the general battery-equivalent interface for eight device models and is preparing to publish the models in the form of an open-source Python-based software library. The project is in the final stages of completing the grid services software that will be used for exercising the	GMLC - PNNL, with ANL, INL, LBNL, LANL, NREL, ORNL, SNL	Grid Modernization	GMLC 1.4.2 – Definitions, Standards and Test Procedures for Grid Services from Devices

models and provide insights into devices' abilities to respond to a range of prototypical grid services. The project has analyzed how existing appliance standards test procedures could be leveraged to provide equipment parameters useful for characterizing how well devices can supply grid services, and has developed plans for testing example devices from three device classes—electric vehicles, commercial refrigeration, and water heaters—to validate their device models.			
The Vehicle to Building Integration Pathway project (GM0062) project has made strong progress toward developing use cases for scalable systems and demonstrating at multiple laboratories affordable, communications and control platforms that are capable of controlling the charging of multiple PEVs.	GMLC -ANL, INL, LBNL, NREL, PNNL	Grid Modernization	Vehicle to Grid Integration Pathway

In this report the Grid and Infrastructure project reports have been grouped into the chapter categories of Industry Awards, Grid Modernization, and Fast Charging Enabling Technologies. Many of the projects address multiple programs objectives.

Questions regarding the Grid and Infrastructure Program can be directed to the Program Manager, Lee Slezak via email: Lee.Slezak@ee.doe.gov or telephone: (202) 586-2335

I. Electric Drive Technologies Research

I.1 Advanced HPC Multiphysics Modeling of Motors and Materials (ORNL)

Jason Pries, Principal Investigator
Oak Ridge National Laboratory
1 Bethel Valley Road
Oak Ridge, Tennessee 37831
E-mail: priesjl@ornl.gov

Susan Rogers, DOE Technology Development Manager
U.S. Department of Energy
E-mail: susan.rogers@ee.doe.gov

Start Date: October 1, 2017 End Date: September 30, 2018
Project Funding (FY18): $650,000 DOE share: $650,000 Non-DOE share: $0

Project Introduction

This project centers on the research and development of high-performance computing (HPC) tools and modeling techniques for high-accuracy modeling of magnetic materials. It will aid the optimization of electric motor designs using new materials like ultra-conducting copper, high-efficiency silicon steel, and reduced–rare earth and rare earth–free permanent magnet alloys to achieve the DOE ELT 2025 goals. ORNL's crosscutting expertise in motors, materials, and computation places its team in a uniquely qualified position to develop systems and modeling techniques to gain a fundamental understanding of the impact of materials on electric drive train performance.

Current electric motor models are limited by the assumption of lossless, homogenous material properties. Hysteresis is neglected in electrical steels and permanent magnets. Although eddy currents can be simulated to some extent, losses are generally not intrinsic to the simulation but are the result of post-processing the solution of a lossless model. Error on the order of 30% can be expected in the core loss calculation alone. Additionally, there is no accounting for manufacturing effects such as rolling direction, stamping, punching, laser cutting, or grain boundary diffusion in permanent magnets. Rolling direction creates anisotropies in the properties of both grain-oriented and non-oriented steel; the former are typically ignored.

Modeling deficits place pressure on an expensive prototyping stage to modify and validate a final design, which ultimately increases the required production time and cost of the motor. With experience, large manufacturers may develop their own internal heuristic "correction factors" to partially ameliorate this issue. However, this approach is process and scale specific and does not aid in improving ab initio predictions in novel circumstances.

In addition, computational algorithms have hidden assumptions, typically regarding the hardware on which they are run. Analysis techniques and algorithms have co-evolved over several decades to optimally solve a class of problems on a certain type of hardware. Simply porting one analysis/algorithm pair to a new set of hardware yields suboptimal results. The emerging paradigms of heterogeneous and general-purpose graphics processing unit (GPGPU) computing will require revisiting optimal solution methods.

This project aims to improve motor modeling fidelity by developing high-fidelity material models and integrating them within an HPC simulation platform. This will result in a unique capability to explore solutions to meet ELT power density and efficiency goals and reduce critical material usage in motors. A highly

accurate motor optimization tool able to fully utilize the most advanced present-day hardware - including DOE supercomputers - will reduce the design times and costs of both current and future technologies.

Objectives

The objective of this project is to develop tools and modeling techniques that will accelerate the adoption of novel electric motor designs offering high power density, specific power, efficiency, and reliability. Advanced HPC tools will be developed and implemented to yield unmatched motor modeling accuracy and complement new materials and processing developments. Fundamental research will be conducted to study the phenomena behind the magnetization and loss characteristics of soft magnetic materials in electric motors, details that are still not fully quantified or understood. For example, residual stresses or induced stresses incurred during manufacturing or motor operation have a considerable impact upon losses and magnetic permeability. Additionally, the impact of temperature, pulsed-width modulation excitation, and other factors impact the magnetic properties in a way that is not considered or modeled with conventional finite element analysis tools.

At present, state-of-the-art finite element solvers lack fidelity in certain areas that are critical for assessing performance, efficiency, and reliability over the broad range of operating conditions experienced in vehicle systems. These issues are typically solved either through overdesign margins that lead to a suboptimal component, or through extensive prototyping and evaluation cycles that must be repeated for new platforms. For example, both soft and hard magnetic exhibit hysteresis characteristics that impact losses and demagnetization. Losses determine the load placed on the vehicle cooling system and have a strong influence on insulation lifetime. The demagnetization process couples with thermal cycling over drive-cycle time scales and is exacerbated by local loss mechanisms, including minor hysteresis loops and eddy currents. The impacts of magnetic hysteresis are estimated using assumptions which do not represent the true material behavior.

A tightly integrated multiphysics/hysteresis simulation framework will allow more detailed investigations of these phenomena than does the current state of the art. These tools will enable improved electric machine designs through a deeper understanding of the fundamental material property issues in these complex systems. High-fidelity modeling tools are particularly important for motor designs that have weaker magnets with no or reduced heavy rare earth material content.

A step change in electric motor modeling accuracy can be achieved by devising ways to integrate high-fidelity hysteretic material characteristics into motor simulations to better predict core losses. A comparison of typical material field models with more realistic behavior is given in Figure I.1.1. As electric motors move to higher speeds to increase power density, the distribution of losses will migrate from conduction losses in the copper windings to hysteresis and eddy current losses in the motor core. Accurate determinations of core losses will be required to design high-efficiency, high-speed motors without highly expensive prototyping iterations. High-fidelity modeling tools will also help improve existing technology in operating regions where core losses significantly impact efficiency, such as cruising and regenerative breaking. These two regimes are important for extending range in urban settings. High-fidelity material modeling will also help reduce the use of critical rare earth permanent magnet materials by more accurately predicting local demagnetization behavior.

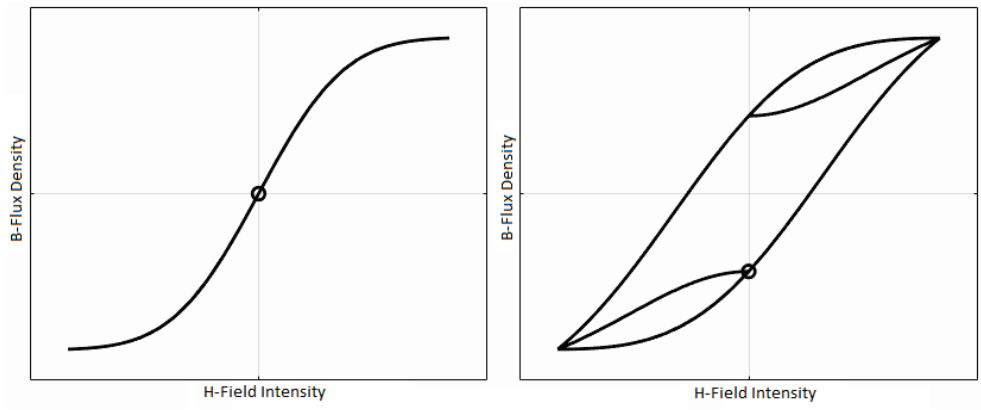

Figure I.1.1 Typical B-H curve material model used for magnetic simulations; (Right) more realistic B-H material model showing both major and minor hysteresis loops that impact motor efficiency.

As power density increases, heat removal will become an even more critical challenge. The optimal method of heat removal depends on both the magnitude and *distribution* of losses. Different strategies may be employed when core losses dominate conduction losses, and accurate prediction of the location of those losses will be important for determining the effectiveness of any cooling method. Heat buildup in the rotor due to core losses also impacts permanent magnet reliability. It is one of the most important factors driving the large coercivity requirements of permanent magnets in electric vehicle (EV) applications and leading to widespread use of rare earth materials in most on-the-road EVs.

Manufacturing effects also become more critical as power density is increased. The defect regions of punched, stamped, or laser-cut laminations are functions of the manufacturing method, independent of the size of the workpiece. The percentage of the overall lamination that is subject to these boundary effects increases with decreasing machine size. Hence, without any improvements to lamination processing techniques, accurately modeling these effects in the design stage will become more critical.

In addition to improved design confidence, taking full advantage of next-generation computing resources will enable shorter design cycles. Given enough computational power, genetic algorithms, artificial intelligence, and machine learning provide opportunities for unlimited diversity of design. These developments will enable closer matching of motor designs to target applications, improving system-level performance versus a middle-of-the-road approach that attempts to satisfy a wider swath of requirements. Experience leads to reduced uncertainty through the introduction of empirical design factors that are valid under limited circumstances. Unfortunately, such empirical knowledge is not available for novel and emerging motor technologies.

Approach

Our approach to achieving these objectives is to develop modeling and computational techniques and integrate them into an open source software project for electric machine optimization and design to meet current and future ELT goals. This project is called the Oak Ridge Simulation Toolkit for Electromagnetic Devices, or OeRSTED. OeRSTED is envisioned as being a one-of-a-kind, experiment-driven, open-source HPC software development project. The goal is to translate laboratory experimental characterization of materials into mathematical models, translate mathematical models into computational models, and integrate computational models into a useful, open source simulation and optimization framework. Phenomenological models will be developed and integrated in four stages:

1. Mathematical models and identification schemes are explored to describe experimental observations.
2. Material phenomena are characterized, generating large data sets for model identification and validation.
3. Algorithms are developed to translate mathematical models into efficient computational methods.

4. Phenomenological material models are integrated within the overall simulation framework

Additionally, OeRSTED will be constructed to take full advantage of current and future DOE supercomputing resources. The current generation of general-purpose GPU-based heterogeneous architectures provides a unique opportunity to employ artificial intelligence and machine learning to solve the challenges associated with ELT 2025 goals. A modular core codebase design using state-of-the art software engineering techniques will ensure adaptability to future changes in computing paradigms.

Results

Nonlinear Geometric Constraint Solver Implementation

One goal of the project is to enable motor optimization on HPC systems to support discovery of new motor topologies and utilization of new materials. Optimization of electric motors requires parameterized geometric models that can be sampled and numerically evaluated to determine estimated performance. One difficulty that quickly becomes apparent is that HPC systems require compiling code on a unique Linux operating system; this limits the use of existing commercial software for geometric modeling. Further, no open-source software exists for describing nonlinear geometric modeling constraints that are used in typical design workflows.

Our solution was to develop a modular, reusable nonlinear geometric constraint solver to drive our HPC motor optimization code. Figure I.1.2 shows a model of a synchronous reluctance machine created using OeRSTED's nonlinear geometric constraint solver. The model has a total of 21 geometric parameters. Figure I.1.3 shows the same model implemented in a commercial software package, along with dimensioned parameters. Many of the common types of dimensions and constraints available in packages like the commercial software are available in OeRSTED. These include specification of distances and angles between lines, radii and subtended angles of circular arcs, and tangencies between lines and circles. The internal geometric constraint solver in OeRSTED facilities HPC motor optimization and will make use of the code simpler for future partners.

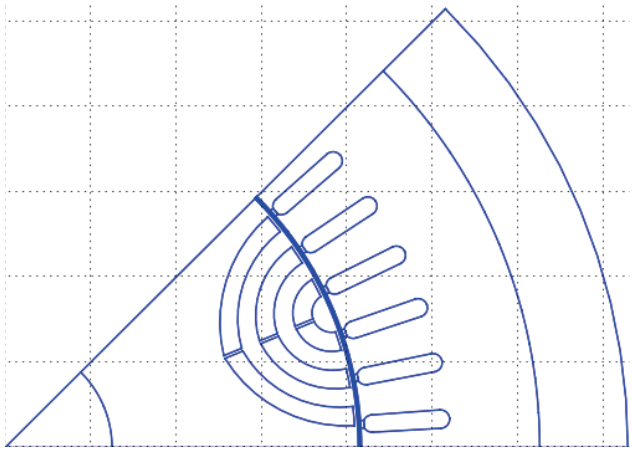

Figure I.1.2 Synchronous reluctance machine model created using OeRSTED's internal nonlinear geometric constraint solver with a total of 21 geometric parameters.

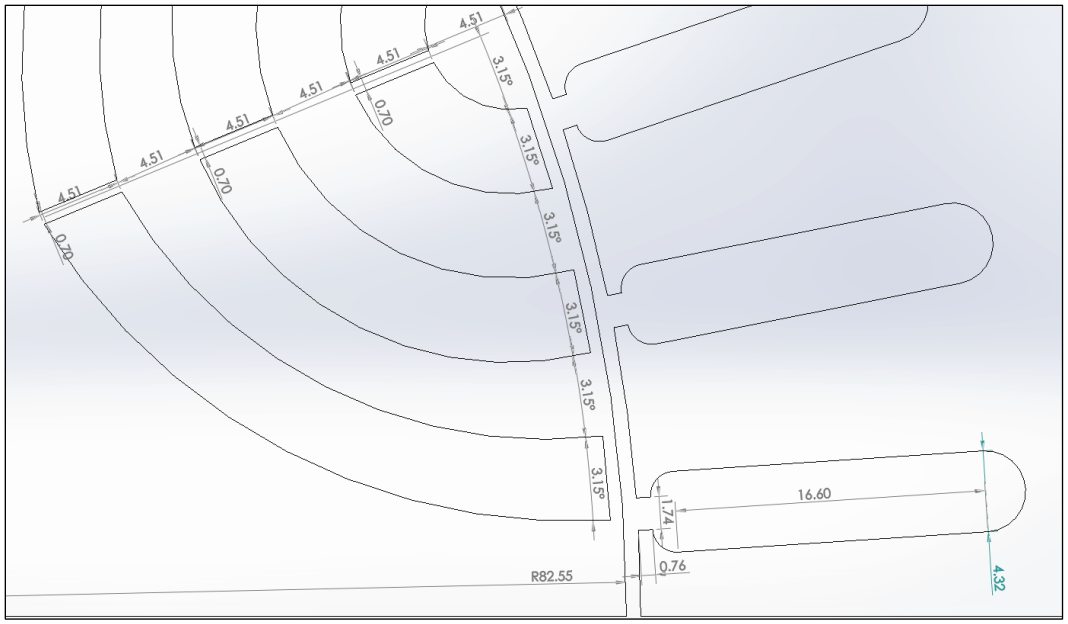

Figure I.1.3 Copy of the synchronous reluctance machined modeled in OeRSTED reconstructed in commercial software package showing the dimensioned angular, radial, and distance constraints.

2D Magnetostatic Solver Validation

Another goal of the project is to improve motor modeling fidelity. However, first a baseline must be set. The core codebase should be demonstrated to function correctly and achieve parity with commercial codes in terms of accuracy and computational speed. To this end, we implemented identical motor models in OeRSTED and a commercially available software package to validate the correctness of the core magnetic field simulation code.

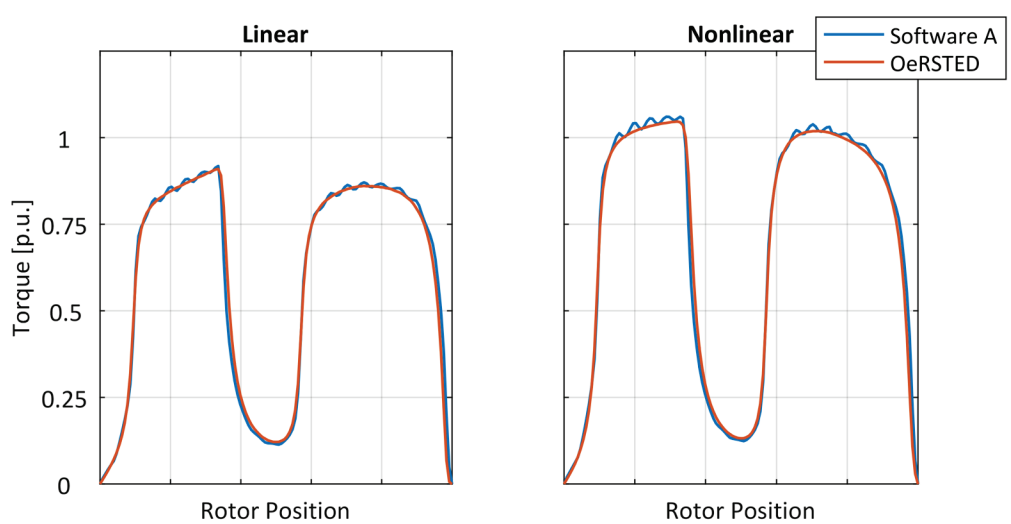

Figure I.1.4 Torque calculation comparison between OeRSTED and a commercially available software package using (left) linear magnetic properties and (right) nonlinear magnetic properties; the salient pole rotor structure was chosen because of its difficulty (from a numerical accuracy point of view) due to the large amount of torque ripple.

Figure I.1.4 shows a comparison of two different locked rotor torque calculations for a salient pole synchronous reluctance machine, one calculation with linear magnetic material properties and one with

nonlinear magnetic material properties. The salient pole structure was chosen because of the numerical difficulty posed by the large (and undesirable) torque ripple. Good agreement was obtained between the two software platforms. In fact, the commercial software exhibited some non-physical torque oscillations due to airgap discretization variations as the rotor position was changed. An improved torque calculation technique used in OeRSTED eliminated this artifact. Figure I.1.5 shows a comparison of the flux density of a simulated synchronous reluctance motors in a magnetically saturated condition. These plots also show good agreement and serve to validate the correctness of the core OeRSTED codebase.

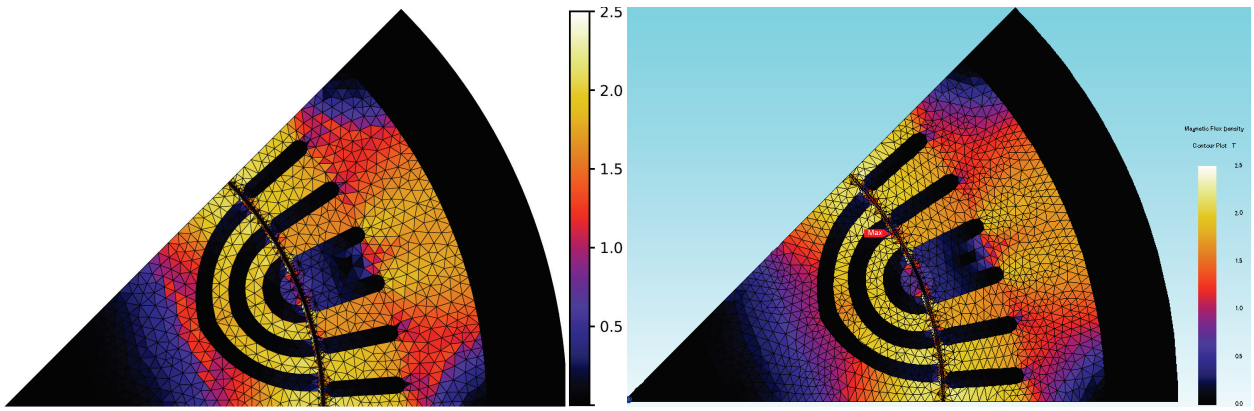

Figure I.1.5 Flux density comparison of a synchronous reluctance machine simulated in OeRSTED and a commercially available finite element analysis software; good agreement is obtained even at high flux density.

HPC Motor Efficiency Map Identification Routine Development

Having validated the basic functionality of our software, we set out to solve some of the computational issues associated with motor optimization. One big challenge is that robust motor optimization requires the identification of the entire motor efficiency map for each candidate design analyzed during the design process. Achieving maximal design throughput requires careful consideration of computational and memory resources at every level of the computation system, whether it be a workstation or an HPC system. To this end, we performed various computational experiments to determine the best work distribution strategy for motor optimization.

Figure I.1.6 shows a schematic representation of the optimal work distribution. At the highest level, the optimization problem has three dimensions that must be analyzed: candidate designs, rotor positions, and current vectors. Generally speaking, candidate design analysis represents the coarsest grain of work. Each design can be simulated independently with little data sharing. Therefore, candidate design analysis should be distributed among system nodes where communication speed is slowest.

For each candidate design, several rotor positions and current vectors must be analyzed to evaluate efficiency, torque ripple, field-weakening capability, and core losses over the full torque, power, and speed range. Since each rotor position requires a different mesh, simultaneous analysis of the current vectors for each rotor position is superior to simultaneous analysis of different rotor positions for a single current vector: In the former cases, only one mesh is required, and several operator matrices can be shared among processors. Reduced mesh and matrix storage requirements greatly reduce memory overhead.

Using this approach, we demonstrated effective linear scaling of individual candidate design efficiency map identification up to the number of cores per node. Specifically, greater than 30× speedup was demonstrated on both workstations and on Oak Ridge Leadership Computing Facility (OLCF) supercomputers. Linear scaling was also demonstrated when multiple candidate designs were analyzed simultaneously on OLCF computers up to the maximum number of nodes requested, which was 40 in our largest attempt. Combined, this represents a 1200× speedup versus a single core simulation.

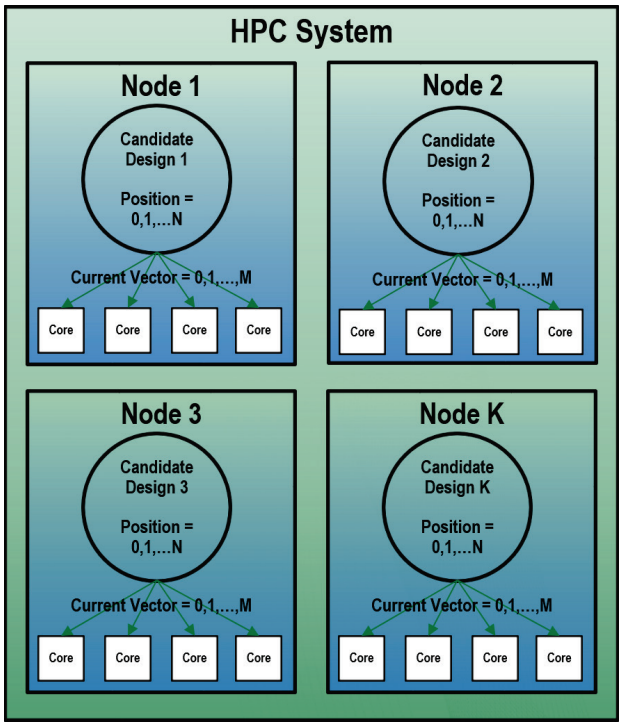

Figure I.1.6 Diagram of work distribution for motor optimization on an HPC system; each node simulates one candidate design; each core works on a current vector; the rotor position is advanced once all the current vectors for the active rotor position are analyzed; the results are combined to calculate the entire motor efficiency map.

Asynchronous Particle Swarm Optimization Algorithm Design

One challenge associated with exploring a large design space is that analyzing motors with different characteristics results in different computational costs. Larger motors and motors which are pushed further into magnetic saturation take longer to simulate than smaller, unsaturated motors. Most evolutionary optimization algorithms require synchronization of the population before the next iteration can begin. This causes an overall slowdown of the algorithm when different members of the population require different simulation times: The algorithm is only as fast as the slowest simulation.

In the standard fully informed particle swarm optimization method, particles talk directly to one another, communicating information on locations where they have experienced minimum/maximum values of the objective function. A modified particle swarm optimization algorithm was developed as part of the HPC motor design efforts. The workflow is demonstrated graphically in Figure I.1.7:

1. The queen sends a task to a worker.
2. The worker performs a complex computation.
3. The worker sends simulation results to the queen.
4. The queen updates the swarm status.

A key difference between standard methods is that, instead of direct communication, worker particles communicate asynchronously with a queen particle. Based on the swarm history, the queen assigns each worker a new task as the worker becomes free. Because the assignment occurs almost instantaneously compared with the time it takes for the worker to perform its task, there is effectively zero overhead due to synchronization requirements using this approach. An added benefit of this method is that the queen can assign

workers different objective functions, enabling true multi-objective optimization and pareto front identification.

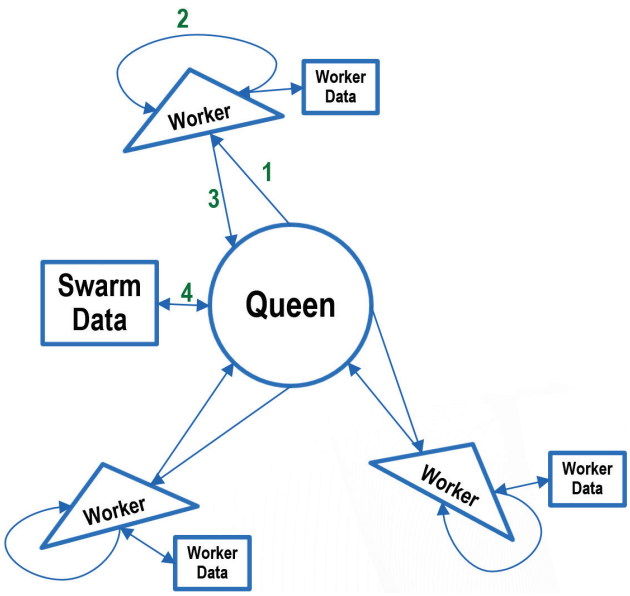

Figure I.1.7 Schematic description of the asynchronous fully-informed particle swarm method: 1) queen sends task to worker, 2) worker performs computation, 3) worker sends data to queen, 4) queen updates swarm status.

Permanent Magnet Demagnetization and Recoil Model Analysis

Investigating issues surrounding modeling of the demagnetization characteristics of permanent magnets is a key research objective of this project. Demagnetization is a particularly salient concern in moving to cheaper low-coercivity magnet materials such as aluminum-nickel-cobalt (AlNiCo); ferrites; and reduced rare earth neodymium-iron-boron (NdFeB). Ensuring robustness against demagnetization often means increasing design safety margins. This is especially true when state-of-the-art models are insufficient for predicting true demagnetization behavior [1]. Uncertainty reduces the achievable utility of rare-earth alternative motor designs. In the worst case, it may make alternative designs appear to be infeasible when they really are.

Previously, we demonstrated high-accuracy prediction of losses and resonant behavior of toroid inductors in simple LC circuits [2]. This approach used a circuit-coupled finite element model of the soft magnetic inductor along with a Preisach hysteresis model to capture the combined effect of hysteresis and eddy current losses. Our initial effort in this area was to validate that the Preisach model can be used to model hard-magnetic materials. We then examined the demagnetization and recoil predictions produced by this model and compared them with results from simpler approaches.

Figure I.1.8 shows the results of identifying a Preisach hysteresis model for an AlNiCo permanent magnet material developed at Ames Laboratory. The left plot shows the normalized second quadrant characteristics of the permanent magnet along with recoil characteristics after different demagnetizing fields were applied. The most striking aspect of this figure is the nonlinear recoil lines. Standard demagnetization models assume that the recoil lines are straight and associated with a fixed "recoil permeability." These predictions demonstrate that our proposed approach can capture much more complex behaviors than can standard modeling techniques. With further development, this approach will improve demagnetization predictions in motor simulations.

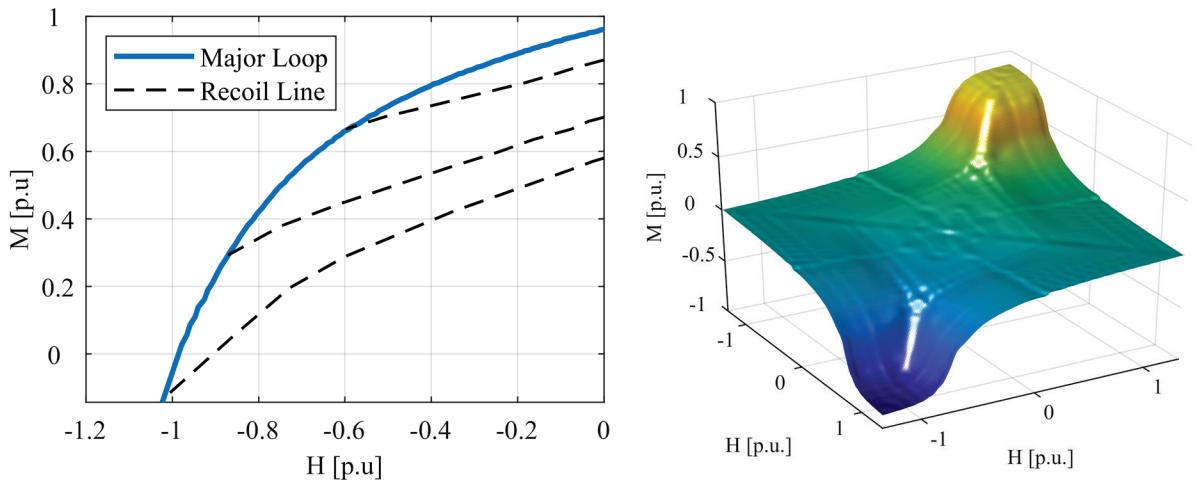

Figure I.1.8 (Left) Normalized second quadrant magnetization characteristic of an AlNiCo permanent magnet showing nonlinear recoil lines; (Right) Everett function associated with a Preisach model of an AlNiCo permanent magnet identified from a set of permanent magnet hysteresis loops;

Data provided courtesy of Ames Laboratory.

Permanent Magnet Demagnetization Analysis Apparatus Design

After verifying that the modeling technique can accurately capture single-axis permanent magnet demagnetization characteristics, we set out to design a magnet test fixture for identifying three-axis permanent magnet characteristics. Vector demagnetization characteristics are important for the most common type of electric motor (interior permanent magnet machines) because the demagnetization field usually has significant component perpendicular to the hard axis of the magnet. The large angle between the demagnetizing field and the magnet hard axis is due to the positioning of the magnet in the rotor. It has been shown that large errors in predicted demagnetization occur when the applied field is skewed relative to the magnet's hard axis [1]. However, only very limited data are available for off-axis permanent magnet characteristics.

During the design of the apparatus, we noticed a rather large nonuniformity in the simulated behavior around the knee of the magnetic characteristic (where the demagnetization occurs). This is a significant realization because standard methods for determining magnetic characteristics (using sense coils to determine average flux and magnetic circuit calculations to determine applied field) will yield significant errors in this critical region. The genesis of the problem is that magnets tend to undergo a sharp increase in differential permeability when they are being demagnetized. Boundary effects due to material discontinuities (i.e., between magnet and air) cause additional demagnetization at the edges.

Figure I.1.9 shows a comparison of a typical magnetization pattern near the knee of the magnetization characteristics for a typical experimental setup and contrasts it with a new approach that we have developed to ameliorate some of the nonuniformity. The image on the left is for a single magnet system, and the image on the right is the central magnet in a nine-magnet array that has nonuniformity reduced by a factor of 5. The array has gaps between the magnets to allow the placement of Hall effect sensors to measure the tangential magnetic field. The flux density will similarly be measured using a Hall effect sensor on the front surface of the magnet. The magnet array technique is effective because boundary effects are reduced when surfaces of similar properties are near each other due to the tangentially continuous nature of magnetic fields.

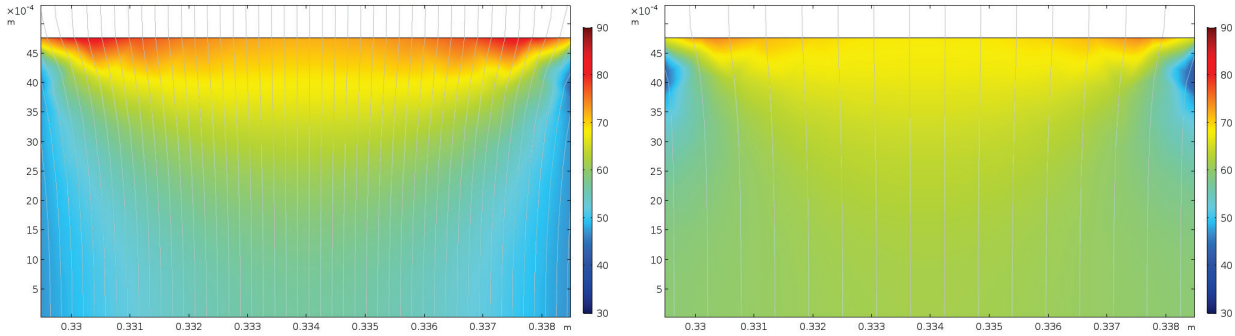

Figure I.1.9 (Left) AlNiCo magnet in a uniform applied field demonstrating nonuniform demagnetization due to a combination of high second—quadrant differential permeability and boundary effects. (Right) Central AlNiCo magnet in a nine-magnet array demonstrating improved uniformity in the demagnetization field, especially in the body of the magnet. Gaps between the magnets necessary for sensors are the main cause of nonuniformity at the surfaces of the magnet.

Conclusions

The project undertook the initial implementation of an HPC electric motor optimization codebase and began development of models and experimental systems for the examination of high-fidelity permanent magnet modeling techniques. Several core tools for motor design were developed and validated, including a nonlinear geometric constraint solver and magnetostatic finite-element solver. Optimization algorithms were developed to run on ORNL's supercomputers and demonstrated near ideal linear speedup compared with single core simulations. We successfully demonstrated that a unified modeling technique can capture key characteristics of both hard and soft magnetic materials in detail. Additionally, we designed a magnet testing fixture that will provide greater accuracy in determining the demagnetization characteristics of permanent magnets and aid in improving motor designs using reduced or rare-earth free permanent magnets with low coercivity.

Key Publications

1. Jason L. Pries, "Electric Motor Research at Oak Ridge National Laboratory: A Material Perspective." Lecture. January 10, 2018. Available at http://cmi.ameslab.gov/video/public/cmi-webinar-jason-pries-january-2018-part-1 (accessed October 2018).

References

1. Peng, Peng, Han Xiong, Julia Zhang, Wanfeng Li, Franco Leonardi, Chuanbing Rong, Michael W. Degner, Feng Liang, and Leyi Zhu, "Effects of External Field Orientation on Permanent Magnet Demagnetization," *IEEE Transactions on Industry Applications* 53(4) (2017), 3438–446. doi:10.1109/tia.2017.2686344.

2. Jason Pries, Lixin Tang, and Tim Burress, "Continuum Modeling of Inductor Hysteresis and Eddy Current Loss Effects in Resonant Circuits," 2017 IEEE Energy Conversion Congress and Exposition (ECCE), 2017. doi:10.1109/ecce.2017.8095814.

Acknowledgments

This work is supported by the DOE Office of Energy Efficiency and Renewable Energy, Vehicle Technologies Office, under contract number DE-AC05-00OR22725. The author wishes to thank project team members: Randy Wiles for assistance with the mechanical design of the magnetic fixture; Emre Gurpinar for discussions about and testing of magnetic components at high frequencies; researchers at Ames Laboratory, including Iver Anderson, Aaron Kassen, Matt Kramer, Emily Rink, Wei Tang, and Emma White for providing AlNiCo permanent magnet data and discussions on permanent magnet physics and manufacturing methods; the OLCF for providing core-hours on Eos and Titan through the Directors Discretion program, and Robert French for assistance in getting started using the OLCF resources.

I.2 Advanced Multiphysics Integration and Designs (ORNL)

Emre Gurpinar, Principal Investigator
Oak Ridge National Laboratory
1 Bethel Valley Road
Oak Ridge, Tennessee 37831
E-mail: gurpinare@ornl.gov

Susan Rogers, DOE Technology Development Manager
U.S. Department of Energy
E-mail: susan.rogers@ee.doe.gov

Start Date: October 1, 2017 End Date: September 30, 2018
Project Funding (FY18): $810,000 DOE share: $810,000 Non-DOE share: $0

Project Introduction

This project covers the multiphysics integration and design of next-generation wide-bandgap (WBG) power modules and associated components within a system. Various component challenges in a system were tackled such as substrates, interconnects, and gate driver circuitry to advance the system's power density and reduce its footprint.

Objectives

The overall objective of the project is to develop technologies for next-generation advanced integrated power electronic systems enabling high power density and reliability to achieve DOE ELT 2025 technical targets (100 kW/L, $2.7/kW, and 300,000 mile lifetime. Under the overall objective, two main streamlines have been identified: (1) power module design and (2) gate driver and auxiliary components. The power module design streamline will evaluate the feasibility of quilt packaging as an interconnect solution in power modules and evaluate the thermal performance and design challenges of an insulated metal substrate (IMS) with a thermal pyrolytic graphite insert as a substrate solution. The gate driver and auxiliary components streamline will investigate radio frequency (RF)-based solutions for ultra-compact isolated signal and power transfer and the development of low-profile, high-power-density, isolated compact DC/DC converter designs for a conventional gate drive supply.

Approach

The approach is to increase the power density and reliability of power electronics to meet DOE ELT 2025 targets (100 kW/L and 300,000 mile lifetime) by focusing on power electronic module and gate driver research.

Research will be conducted under the power module design streamline to investigate substrates for power electronic modules that allow increased power density and high reliability for WBG device–based power modules via (1) better coefficient of thermal expansion (CTE) matching between WBG devices and power module materials, (2) improved heat extraction, and (3) enhanced thermal and power cycling capability. Furthermore, interconnects with high power density will be evaluated and investigated for low-profile, high-current-density, reliable chip-to-chip and chip-to-package interconnects for power modules and auxiliary circuits (e.g., gate drivers). These will enable reduced parasitic inductance in the system for optimum switching performance, reduced power module size, and enhanced reliability by moving to wire bondless solutions.

Under gate driver research for WBG devices, novel architectures for combined signal and power transfer will be developed with advanced functionalities that will enable (1) high power density by minimizing auxiliary components, (2) integration of gate drive circuitry to WBG modules and advanced gate drive functionality for reduced electromagnetic interference (EMI), (3) short circuit protection, and (4) loss distribution.

In parallel with the effort to develop combined signal and power transfer in a small form factor, compact power and isolation transfer for conventional gate driver circuitry and auxiliary will be developed. The design and optimization will focus on low-profile, isolated, high-power-density DC/DC converters to enhance the overall power density of gate drivers for WBG devices via high-frequency operation to minimize passive components (e.g., isolation transformer). Soft switching for active switches will be utilized to maintain high efficiency, and optimized and controlled parasitic (e.g., coupling capacitance) will be a built-in design function.

Results

Insulated Metal Substrate with TPG Insert

An illustrative cross section of a conventional power module is presented in Figure I.2.1 with various components of the structure highlighted. The structure is made up of different materials, such as aluminum for bond wires and copper for electrical terminals, ceramic-based direct bonded copper (DBC) substrates, and so on. The multi-layer, multi-material–based structure has limited heat extraction capability. Furthermore, certain layers in the structure shown in Figure I.2.1 are subject to high mechanical stresses due to different CTEs between layers during power and environmental cycling of the module. These stresses lead to limited lifetimes and early failures caused by thermal stress [1].

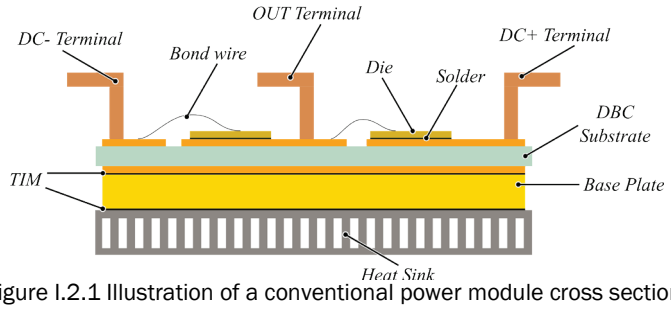

Figure I.2.1 Illustration of a conventional power module cross section.

Thermally annealed pyrolytic graphite (TPG) is an advanced thermal management material formed by well-aligned graphene planes that offer very high in-plane thermal conductivity. Graphene layers are processed through a high-temperature chemical vapor deposition process and heat treatment above 3000°C to form a well-aligned, oriented multi-layer graphite structure. TPG is a relatively soft material that can have low cross-plane thermal conductivity due to the weak van der Waals force between the graphene layers and the weak bonds between those layers. Furthermore, the inertness of graphite prevents it from joining to other metals or ceramics through regular plating, soldering, and brazing processes. For these reasons, the graphene is encapsulated in a metal to protect the relatively brittle material and make it available for attachment to other materials.

TPG provides up to four times higher in-plane thermal conductivity (>1500 W/m·K) at one-fourth the weight of copper, which is commonly used in thermal management of power modules. However, encapsulating the TPG in a metal case results in thermal conductivity higher than that of the metal encapsulant but lower than that of pure TPG material. The ratio of graphene to metal directly affects the thermal performance of the structure [2]. The typical encapsulation of TPG with a copper encapsulant, in which graphene layers are oriented for the optimal one-direction in-plane and through-plane thermal conductivity, is presented in Figure I.2.2. The thermal conductivity of the encapsulated TPG with copper encapsulant can be calculated by applying the material properties in Table I.2.1. The in-plane and through-plane thermal conductivity values of the encapsulant with respect to TPG ratio within the base plate are presented in Figure I.2.2. In this scenario, the TPG orientation provides high thermal conductivity in both in-plane and through-plane axes. It can be seen that above an 80% TPG ratio, the in-plane k is 3.2 times and the through-plane k is 2.4 times higher than the k of copper [3]. Moreover, the specific gravity of the structure can be reduced by 2.46 times, which will lead to a lighter structure with improved thermal conductivity. Finally, in such a system, although the thermal

conductivity and specific gravity of the structure are determined by the TPG ratio, as shown in Figure I.2.2, the CTE of the structure is determined by the CTE of the encapsulant material. With a high TPG ratio in the structure, due to decoupled thermal conductivity and CTE, an encapsulant material can be selected for optimal CTE matching between the layers of the module without compromising the thermal performance.

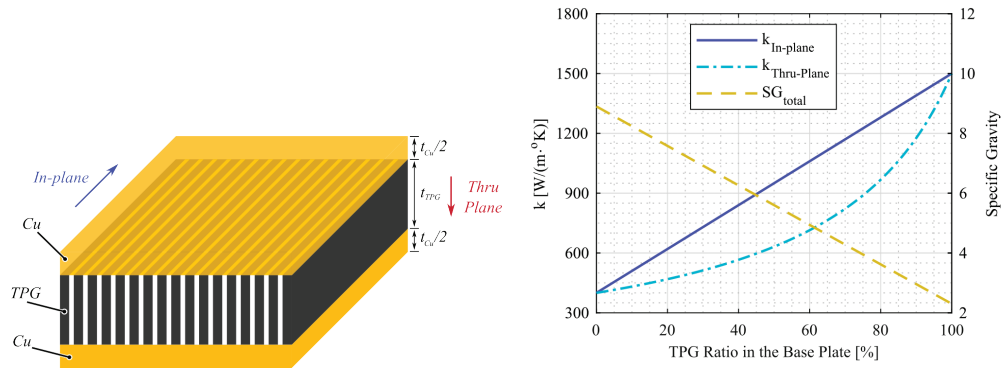

Figure I.2.2 (Left) Structure of the base plate with copper encapsulant for in-plane and through-plane thermal conductivity and specific gravity analysis. (Right) In-plane and through-plane thermal conductivity and specific gravity of the base plate with respect to TPG ratio.

Table I.2.1 Typical Property Comparison of Heat Spreader Materials

Material	In-plane TC [W/m·K]	Cross-plane TC [W/m·K]	In-plane CTE [ppm/°C]	Specific gravity	In-plane TC/ specific gravity
Aluminum	218	218	23	2.7	81
Copper	400	400	17	8.9	45
AlSiC-12	180	180	11	2.9	62
CuW	185	185	8.3	15.2	12
TPG	>1500	10	-1	2.3	650

For the simulation- and experiment-based verification of the thermal performance, a test setup was designed to represent multi-chip and single-chip power module scenarios in which encapsulated TPG or copper is used as the power module baseplate. The encapsulated TPG sample used in this case study is presented in Figure I.2.3. The sample is formed by the TPG core encapsulated in copper. The TPG core in the base plate is formed by four triangular tiles (*TPG 1–4*). The *TPG 1* and *TPG 3* tiles are aligned in the *in-plane 2* and *thru-plane* axes, and *TPG 2* and *TPG 4* tiles are aligned in the *in-plane 1* and *thru-plane* axes for optimal heat extraction from the center of the base plate. Based on the dimensions presented in Figure I.2.3, the TPG ratio in the through-plane axis is approximately 80%, which provides 1280 W/m·K of in-plane and 968 W/m·K of through-plane thermal conductivity. The manufactured bare copper and encapsulated TPG-based samples are presented in Figure I.2.3. The in-plane and through-plane thermal conductivity values of the encapsulated TPG-based sample is measured as 1250 W/m·K and is estimated as 950 W/m·K, respectively, which are well aligned with the theoretical results and show low contact resistance between layers. For the weight analysis of the sample, the side walls shown in Figure I.2.3 must be considered, and the total weight of the sample can be calculated based on the volume of the middle section, which is the equivalent of the structure shown in Figure I.2.2 and the specific gravity of TPG and Cu with 80% TPG ratio, which is 3.617. Based on the dimensions provided in Figure I.2.3 and specific gravity values, the weights of the encapsulated TPG and bare copper sample are calculated as 50.18 g and 94.5 g respectively. The measured weights of the encapsulated TPG and the bare copper sample are 49 g and 94.3 g, respectively, which are also well aligned with calculated values.

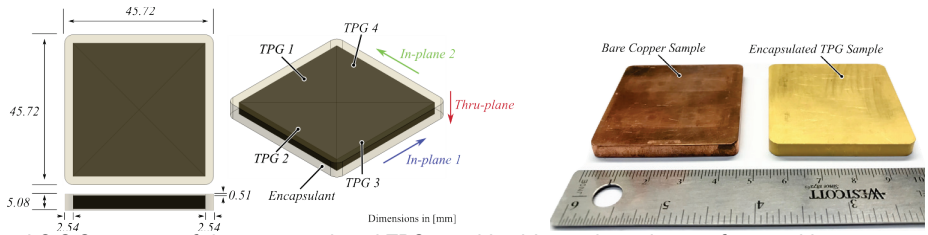

Figure I.2.3 Structure of the encapsulated TPG used in this study and manufactured bare copper and encapsulated TPG-based samples.

The setup to emulate the multi-chip and single-chip power module scenarios is presented in Figure I.2.4. The resistors with a TO-220 package are mounted on the base plate under test with thermal interface material (TIM) and with 5 W/m·K thermal conductivity between resistors and base plate, and base plate and cold plate. The cold plate temperature is controlled by a water–glycol mixture based liquid cooling system to evaluate the performance of different base plate materials under different temperature and loading conditions. In Figure I.2.4 four power resistors with 30 W continuous power rating at ambient temperature are distributed on the base plate. However, two different scenarios are considered in total for simulation- and experiment-based comparison: (1) four resistors distributed evenly on the base plate as shown in Figure I.2.4 and (2) a single resistor in the center of the base plate. In each scenario, a DC power supply is used to dissipate power across the mounted resistor or resistors. The power dissipated across the resistors increases as cold plate temperature changes from 0 to 60°C and until the case temperature of a single resistor reaches 100°C.

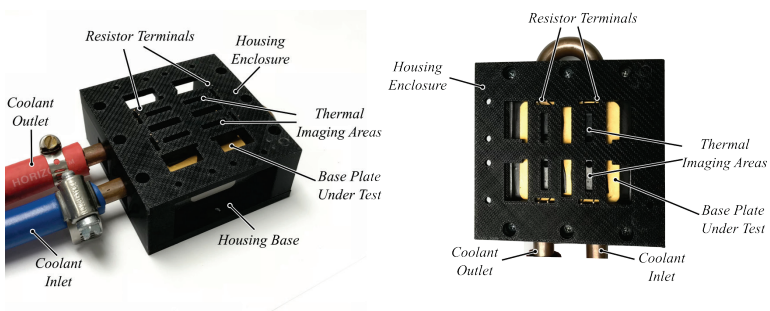

Figure I.2.4 The experimental setup with four-resistor assembly.

Compared with copper, the TPG base plate averaged a 3.104% lower thermal resistance for four resistors and 3.752% for one resistor in the experimental results. The SOLIDWORKS simulations reported an average thermal resistance decrease of 2.338% for four resistors and 3.797% for one resistor. The observed reductions in case temperature, occurring with 15 W power dissipation across each resistor, and in thermal resistance, occurring by replacing copper with the TPG embedded sample, are presented in Figure I.2.5. The case temperature reduction, and therefore thermal resistance reduction, over a wide range of coolant temperatures, is a positive trend and reiterates the superior properties of TPG over copper. The results showed that using a material with high TPG content could lead to more power dissipation with a centralized power source, rather than a spread-out orientation. The results of the simulations and experiments confirm that TPG provides better heat dissipation than copper while providing reduced weight. On average, the simulations reported a 3.0675% decrease in thermal resistance when changing from copper to the TPG. The experiment yielded an average of 3.428% decreased thermal resistance when comparing the two base plates.

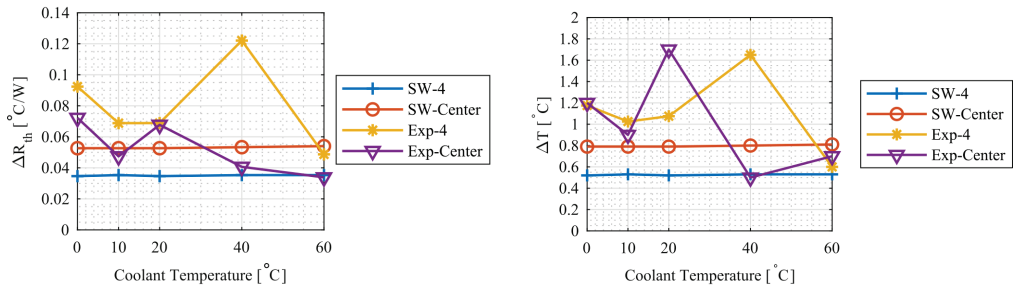

Figure I.2.5 Observed reduction in simulation and experiments with 15 W power dissipation across each resistor's in-case temperature and thermal resistance when copper is replaced with a TPG-embedded substrate.

As the performance of TPG over copper is verified with simulation- and experiment-based results, the next step is to use the performance of this material in a different section of the power module presented in Figure I.2.6 in an isolated substrate to replace the DBC substrate. Conventional DBC solutions are formed by using copper on two sides of a substrate with a ceramic material in between to provide excellent electrical isolation and adequate thermal conductivity. The typical structure of a DBC-based half-bridge module is presented in Figure I.2.6. On the other hand, TPG embedded IMS) can be a good alternative to DBCs, where TPG can overcome the limited thermal conductivity of the dielectric layer by spreading in the copper plane, thereby increasing the heat-spreading capability of conventional IMS solutions. A TPG embedded IMS substrate design based on this approach is presented in Figure I.2.7. In this design, two TPG tiles are placed underneath the SiC MOSFET dies to improve thermal conductivity in the *y* and *z* planes. The theoretical thermal conductivity calculations presented in Table I.2.2 show that TPG embedded copper can have approximately 2 times and 3 times higher thermal conductivity in the *z* and *y* planes respectively. To verify the thermal performance improvement with TPG embedded copper in IMS, test samples with the same footprint and electrical structure were designed with DBC (AlN core ceramic), IMS, and TPG embedded IMS. The design of the TPG embedded IMS is presented in Figure I.2.8. DBC, IMS and TPG embedded IMS are simulated with a thermal interface material (TIM) with 13 W/m·K thermal conductivity between the base of the structure and a constant temperature plane set at 65°C. Then the power dissipation across each SiC MOSFET is increased until the maximum hot spot on any die reaches 125°C. The results are presented in Figure I.2.9. Based on this analysis, each SiC MOSFET can dissipate up to 59 W, 42 W, and 52 Won DBC, IMS, and TPG embedded IMS, respectively, under the same operating conditions. The TPG improved the thermal dissipation capability of IMS up to 24% as a result of improved heat-spreading capability, making IMS a viable alternative to DBC substrates.

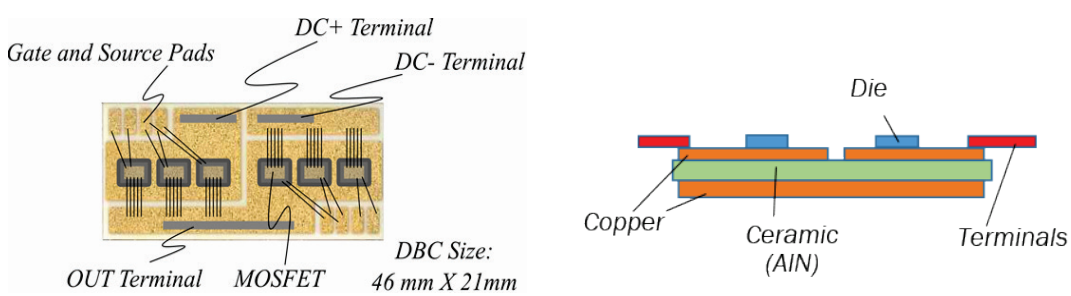

Figure I.2.6 Conventional DBC solution cross section.

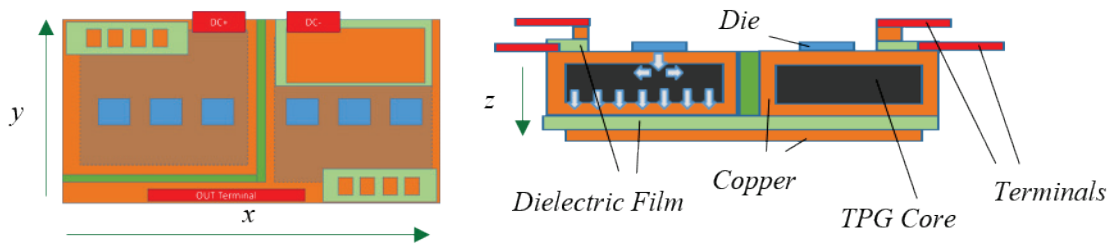

Figure I.2.7 Proposed IMS solution with TPG insert and the cross section.

Table I.2.2 Thermal Conductivity of Copper and TPG Embedded Copper

	Total thickness [mm]	TPG thickness [mm]	TC-in plane (*x*) [W/m·K]	TC-in plane (*y*) [W/m·K]	TC-in plane (*z*) [W/m·K]
Copper only	1.60	N/A	396	396	396
TMP-EX	1.60	1.1	131	1155	802

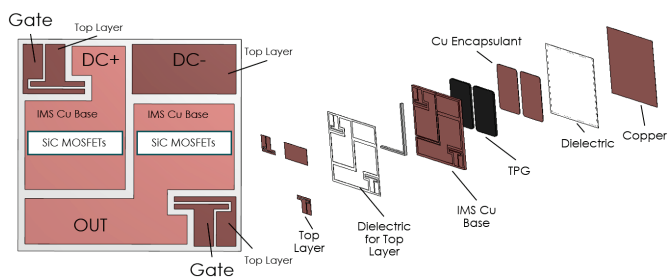

Figure I.2.8 Design of the IMS with TPG insert.

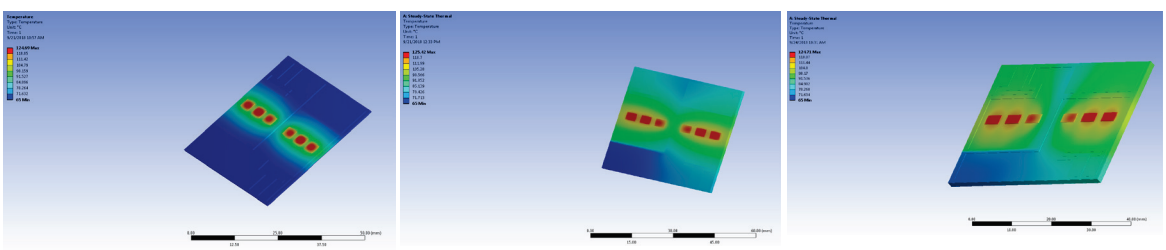

Figure I.2.9 ANSYS steady state thermal simulation results.

Quilt Interconnects

Quilt packaging is a chip-to-chip interconnect technology that incorporates conductive metal "nodules" on the sides of chips. These nodules, which are typically copper, can have widths varying from 5 to 500 µm, thicknesses from 20 to 50 µm, and possibly 10 µm nodule pitch with the standard manufacturing process [4]. Typical examples of quilt packaging in low-power, low-voltage chip-to-chip, and board-to-board interconnect solutions are presented in Figure I.2.10.

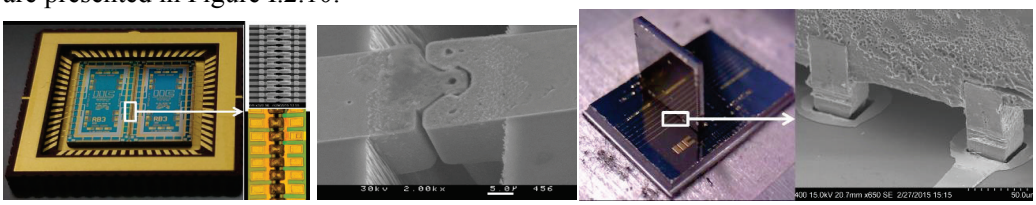

Figure I.2.10 Chip-to-chip and board-to-board interconnect examples with quilt packaging [4].

Increased power density, robust electrical and mechanical interconnects, reduced interconnect parasitics, and high-density 3-dimensional integration of gate drivers and auxiliary circuits are possible with such interconnects to reach the DOE ELT 2025 power density targets in WBG power modules. However, SiC MOSFETs are vertical devices, and the edges of the device, as shown in Figure I.2.11, must withstand the total blocking voltage of the device. High-voltage operation and edge terminations in vertical WBG devices must be considered for the application of quilt packaging in WBG power modules. Furthermore, the interconnect must have high current capability, as the target power for the next-generation traction system is 100 kW and above.

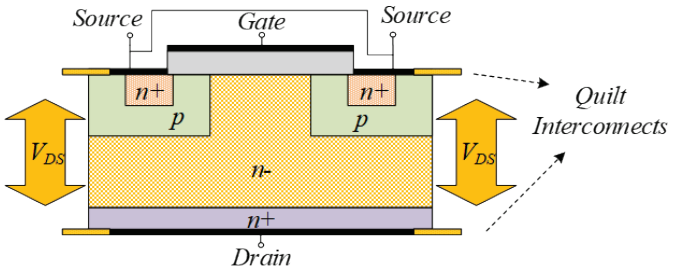

Figure I.2.11 Vertical SiC MOSFET structure with quilt interconnects.

Several quilt-based interconnect nodules on Si substrate without active power devices have been analyzed by Indiana IC for high current conduction capability. The nodules were subject to DC current, and results in Figure I.2.12 show potential for high current conditions. However, the current capability at different frequencies and the ambient temperature conditions need to be evaluated for power module applications.

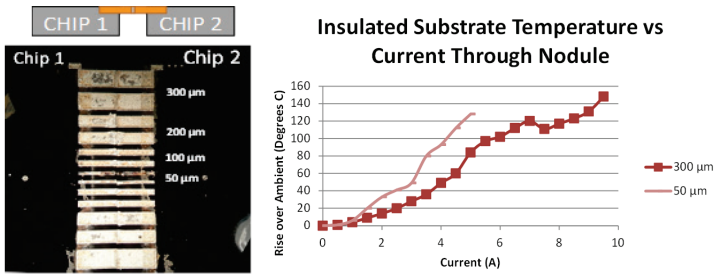

Figure I.2.12 Quilt-based interconnect nodules on Si substrate and test data for current capability.

Compact Signal and Power Transfer for Gate Drivers

Conventional gate drivers consist of discrete components and are not suitable for high-temperature operation. They are considered as the bottleneck components for high-power-density, low-profile power electronic converters with WBG devices. In addition, although the separation of the gate resistor for the power semiconductor device decouples optimization of turn-on and turn-off switching speeds independently, very low gate resistance values still cannot be used in conventional systems because of EMI, reliability, and safety concerns.

The block diagram of the system proposed in this work is presented in Figure I.2.13. The concept is based on transferring power, gate signal, and gate impedance data through a single, high-frequency waveform. At the logic stage, the reference signal, which contains the gate impedance and gate signal information, is multiplied with the high-frequency (>2.4 GHz) modulating signal via an amplitude modulation block. The output of the amplitude modulation circuit is a high-frequency AC signal, which can be transferred to the galvanically isolated side through the high-frequency signal isolator. Because of the high modulating frequency, the signal isolator can be very compact, and the resolution of the signal for gate impedance change can be high. With a 2.4 GHz modulating frequency, the period of the signal will be around 420 ps. With next-generation power semiconductor devices, the switching transitions will vary between 5 and 50 ns, which means that gate

impedance can be changed at least 10 times during a switching interval to optimize switching loss, EMI, and voltage overshoot.

At the isolated side of the high-frequency signal isolator are two parts: (1) the gate power supply and (2) the signal demodulation circuit. At the gate power supply stage, the signal will be rectified and smoothed with filtering components such as DC capacitors to provide the adequate gate-source voltage for turn-on and turn-off. This system includes high-frequency rectifiers with filtering components. The DC signal at the output of the circuit is used as the DC link voltage of the active gate driver. At the signal demodulation circuit, the signal will be rectified first and then filtered to extract the reference signal from the amplitude-modulated high-frequency signal. After reconstruction of the reference signal through signal rectification and filtering, the signal-level detector circuit uses the amplitude of the reference signal to extract the gate impedance and gate signal information.

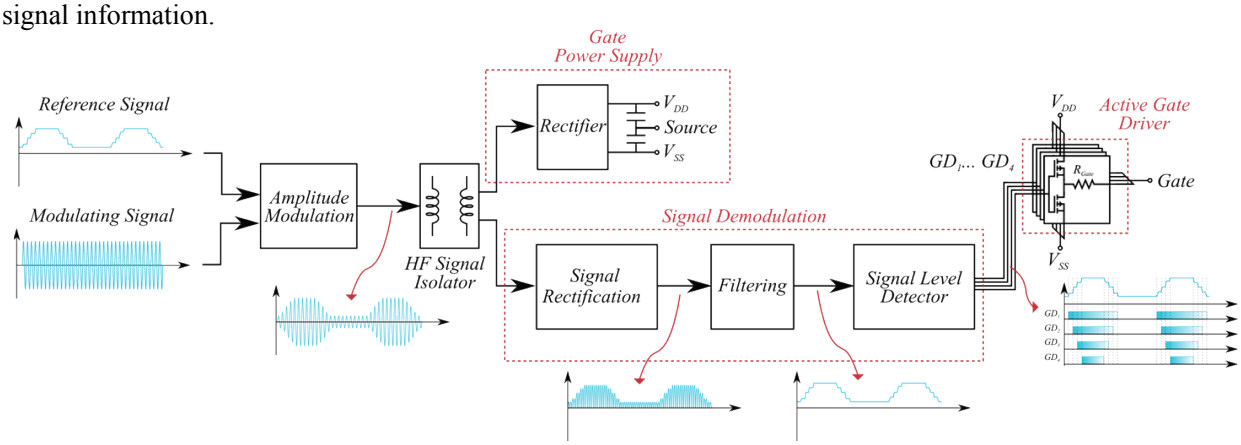

Figure I.2.13 Block diagram of the proposed system.

At the last stage of the system is an active gate driver circuit, which is formed of individual half-bridge inverters with the fixed resistor at the output, connected in parallel to control the gate impedance of the power semiconductor switch during switching transitions. The outputs of the parallel half-bridge inverters are connected after the resistor, and the common node is connected to the gate of the power semiconductor switch that needs to be controlled. The number of parallel inverters determines the step level between impedance values and can be as high as 10. The level of the extracted reference signal determines the number of half-bridge inverters that should be operated in parallel.

Based on this approach, a near-field inductive coupling system designed as the high-frequency signal isolator is presented in Figure I.2.14. The design is based on conventional printed circuit board techniques and is easily printable and low-profile. The design of the coil can be tailored for efficiency, frequency, isolation capacitance, and isolation rating. The near-field inductive coupling has naturally strong EMI immunity due to the close coupling between coils and coil filtering effects, and the coupling between coils is unaffected by most PCB substrates ($\mu r \approx 1$). The single-turn near-field coupled system and the illustration of single-turn coils on PCB are presented in Figure I.2.14. The loop circumference of the coil is set to 1/10th of the signal wavelength to ensure uniform current and strong magnetic field coupling. The quality factor and the efficiency of such an inductive coupler are presented in Figure I.2.15. The coil can achieve greater than 90% efficiency up to 4 GHz with a 0.57 mm coil radius and 0.044 pF estimated parasitic capacitance. Based on the analytical results, 2.8 GHz is selected as the operating frequency of the RF coupler.

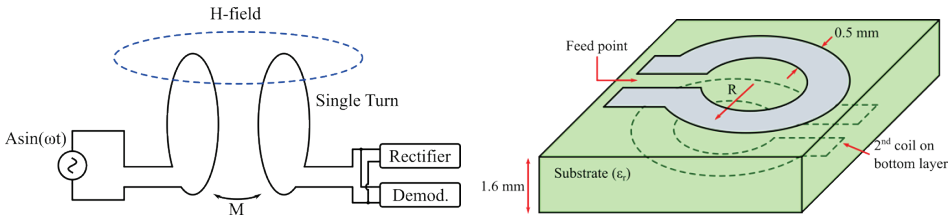

Figure I.2.14 Single-turn near-field coupled system and mutual inductance for two coils of 10 mm radius.

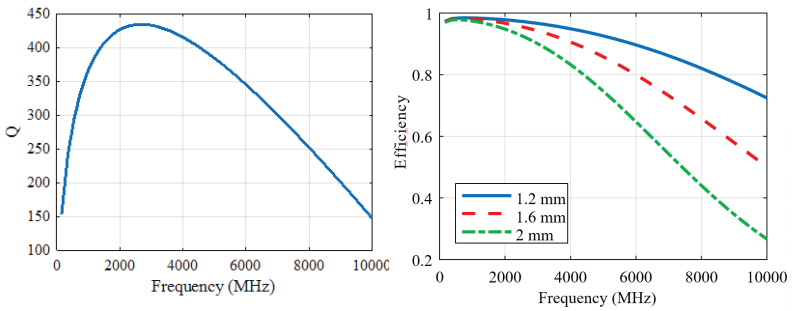

Figure I.2.15 Quality factor and efficiency of the design coil with respect to operating frequency.

Compact Isolated DC/DC Converter

According to the roadmap, the next-generation gate driver for WBG devices should be capable of supplying gate power to a 100 kW inverter with 50 kHz switching frequency. The gate voltage requirements are also defined as +20 V and −10 V. With the state-of-the-art 1.2 kV, 250 A SiC MOSFET power module in [5], the required gate power for an individual switch—which can process 100 kW output power at 50 kHz switching frequency—is approximately 1.5 W with 1.1 µC gate charge and 30 V gate voltage swing. However, the system is expected to be scaled up to 200 kW; therefore, the output power is selected as 3 W. Most of the solutions found in the literature have either low power density or high coupling capacitance, which makes them undesirable for next-generation automotive power electronics [6]. For this reason, Oak Ridge National Laboratory has set a target to design and demonstrate a 3 W DC/DC converter for gate driver applications with more than 90% efficiency, less than 1 pF isolation capacitance, and more than 5.5 kW/L power density.

The active-clamp–based flyback topology with resonant operation has been analyzed in detail in [7]. Although the methodology and the operation are correct, the design equations contain errors. In this work, the analysis in [7] is reviewed and analyzed. The converter schematic is presented in Figure I.2.16. The converter operates with fixed switching frequency and achieves zero voltage switching for active switches and zero current switching for the diode. This provides high-efficiency operation with minimal EMI at high-switching-frequency conditions.

The time-domain–based analytical modeling results, along with simulation results, are presented in Figure I.2.16. The analytical model matches well with the simulation results, which will be used for optimization and analysis of the design based on power density and efficiency targets.

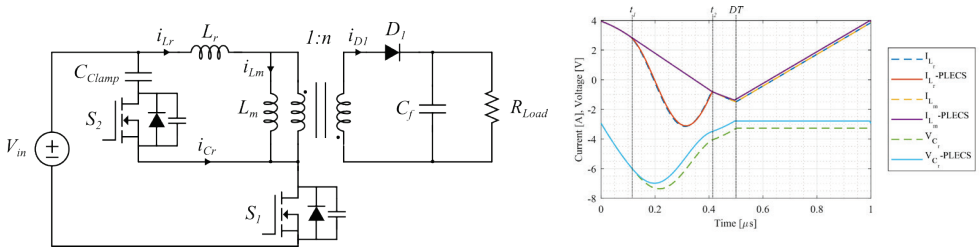

Figure I.2.16 Active clamp flyback converter and main waveforms under steady-state operation with simulation- and time-domain-based analytical modeling.

Conclusions

This report introduces new technologies for next-generation advanced integrated power electronic systems, enabling high power density and reliability to achieve DOE ELT 2025 technical targets (100 kW/L, $2.7/kW, and 300,000-mile lifetime).

TPG was evaluated as a heat spreader in power modules, and experiment- and simulation-based results show that up to 2.4 times reduction in thermal resistance and weight can be possible when bare copper is replaced with TPG embedded copper. The utilization of TPG in IMSs improves the thermal dissipation of IMS and makes it a strong competitor against DBC with higher design flexibility.

Quilt packaging is a promising concept for replacing the conventional wire bond interconnects in power modules by using copper nodules etched to the device edges. Preliminary current capability testing results and application results from low-power, low-voltage application domains show good performance; however, high-voltage and high-current capabilities must be evaluated to use it in WBG devices.

An RF-based solution for an ultra-compact isolated signal and power transfer concept is proposed, and preliminary design of the RF coupler is presented. The proposed architecture combines signal, gate impedance, and power transfer in a single isolator operated in a single PCB-based coil with controlled isolation capacitance and high efficiency.

Finally, a compact isolated DC/DC converter is designed and analytically modeled to achieve high power density in auxiliary circuitry for conventional gate drivers. The selected topology provides high switching frequency capability because of soft switching at the primary and secondary sides. Furthermore, the optimization of transformer size, system volume, and operating frequency is possible with the derived analytical model of the system.

Key Publications

1. Invention Disclosure 201704020, DOE S-138,684, "Amplitude Modulation Based High Frequency Gate Driver Circuit for Active Control of Power Semiconductor Devices," submitted November 2, 2017.

References

1. A. M. Aliyu and A. Castellazzi, "Prognostic System for Power Modules in Converter Systems Using Structure Function," IEEE Transactions on Power Electronics 33(1), 595–605 (January 2018).
2. W. Fan, A. Rape, and X. Liu, "How can millions of aligned graphene layers cool high power microelectronics?" International Symposium on Microelectronics, vol. 2014, no. 1, pp. 000 433–000 437, 2014. [Online]. Available: https://doi.org/10.4071/isom-WA26
3. Fan and X. Liu, Advancement in High Thermal Conductive Graphite for Microelectronic Packaging, ser. RF and Microwave Microelectronics Packaging II, K. Kuang and R. Sturdivant, Eds. Cham: Springer International Publishing, 2017. [Online]. Available: https://doi.org/10.1007/978-3-319-51697-4 10
4. Indiana IC, https://www.indianaic.com/
5. CREE, Cas325m12hm2 1.2 kV module, 2018 [Online]. Available at https://www.wolfspeed.com/media/downloads/967/CAS325M12HM2.pdf
6. B. Sun, R. Burgos, and D. Boroyevich, "2 W Gate Drive Power Supply Design with PCB-Embedded Transformer Substrate," in 2017 IEEE Applied Power Electronics Conference and Exposition (APEC), March 2017, pp. 197–204.
7. R. Perrin, N. Quentin, B. Allard, C. Martin, and M. Ali, "High-Temperature GaN Active-Clamp Flyback Converter with Resonant Operation Mode," IEEE Journal of Emerging and Selected Topics in Power Electronics 4(3), 1077–1085 (September 2016).

Acknowledgements

This work is supported by the DOE Office of Energy Efficiency and Renewable Energy, Vehicle Technologies Office, under contract number DE-AC05-00OR22725. The author wishes to thank project team members: Randy Wiles and Jordan Besnoff of ORNL for their contributions and Momentive, Henkel, and Indiana IC for industry collaboration.

I.3 Drivetrain Performance Improvement Techniques (ORNL)

Gui-Jia Su, Principal Investigator
Oak Ridge National Laboratory
1 Bethel Valley Road
Oak Ridge, Tennessee 37831
E-mail: sugj@ornl.gov

Susan Rogers, DOE Technology Development Manager
U.S. Department of Energy
E-mail: susan.rogers@ee.doe.gov

Start Date: October 1, 2017 End Date: September 30, 2018
Project Funding (FY18): $725,500 DOE share: $725,500 Non-DOE share: $0

Project Introduction

Traction drive inverters have low efficiency at light load conditions (<94%) and need to be increased to meet the DOE ELT 2025 targets [1]. Typical operating ranges that need improvement are (a) low speed: <2000 rpm, up to 200 Nm; and (b) high speed: <30 Nm, up to 10,000 rpm. While emerging wide-bandgap device–based inverters can significantly improve efficiency over existing inverters based on insulated-gate-bipolar-transistor (IGBTs), further improvements are needed to meet the DOE ELT 2025 targets.

In addition to their much lower conduction and switching losses compared with silicon IGBTs, silicon carbide (SiC) metal-oxide semiconductor field-effect transistors (MOSFETs) offer another opportunity to reduce inverter losses and increase efficiency. During freewheeling intervals with a positive voltage applied between the gate and the source, a SiC MOSFET will conduct current in the reverse direction with lower conduction losses than an antiparallel diode. On the other hand, a two-phase modulation scheme can reduce the inverter switching loss by up to 50% compared with three-phase modulation schemes. These two techniques can be combined to address concerns regarding efficiency at light load conditions.

Motor control strategies need to be optimized to maximize the efficiency of SiC inverters, because the inverter losses depend on the motor power factor and other operating conditions; these determine the loss distribution between the SiC MOSFETs and diodes and trade off the MOSFET switching loss with the conduction loss. Control schemes adaptive to the operating conditions can have a significant impact on the loss reduction capability of two-phase modulation schemes. Accurate loss models for SiC inverters are needed for tuning optimal motor control strategies. Moreover, loss models are needed that can be implemented efficiently in resource-constrained microprocesses for embedded control applications.

Inverter losses can be estimated using detailed device models or analytical equations derived from simplified equivalent circuit models. The former are usually used in circuit simulation and may not be suited for embedded control applications. This report summarizes the analytical loss equations developed in this project and modeling results for the 2016 BMW i3 motor and the 2007 Camry motor, which show significant reductions in inverter losses using two-phase modulation and SiC MOSFET reverse conduction for freewheeling intervals in both motoring and regeneration modes.

Objectives

The overall objectives of this project are

- Develop switching techniques and control strategies to improve electric traction drive system efficiency, especially at light load conditions, to meet the DOE ELT 2025 targets.
- Develop generic inverter loss computation software tools.

Specific objectives and tasks for FY 2018 are as follows:

- Identify state-of-the art pulse width modulation (PWM) switching schemes that can reduce inverter conduction and switching losses.
- Develop analytical methods for computing inverter conduction and switching losses for the selected switching schemes.
- Develop a switching timing-based generic inverter loss computation tool.
- Perform tests to validate the computation methods.
- Conduct a comprehensive simulation with real motor model and load conditions.

Approach

As mentioned in the introduction, a combination of SiC MOSFET reverse conduction and two-phase modulation was employed to address concerns regarding efficiency at light load conditions.

Reverse conduction exhibits two loss mechanisms. At low current, the MOSFET carries the current and presents a resistive loss mechanism. As the current increases and the voltage drop exceeds the diode threshold, the diode also carries a portion of the current, resulting in a diode-like loss mechanism. To accurately model the reverse conduction losses, these two loss mechanisms must be considered even within a fundamental cycle. A conducting MOSFET can be modeled as a resistor, and its average conduction loss can be computed from its rms current. On the other hand, a forward-conducting diode can be treated as a resistor and voltage source connected in series for conduction loss estimation. The diode loss calculation thus requires both the dc and rms values of the current. Figure I.3.1 (a) shows the reverse conduction characteristics of SiC MOSFETs. The reverse conduction can be modeled as a resistor when the voltage drop is below the diode threshold voltage, V_{dth}, and then as a resistor and a voltage source connected in series as in Eq. (1).

$$\begin{cases} V_{sd} = r_{sd1} I_{sd} & , \quad I_{sd} \le I_{SC} \\ V_{sd} = V_{sd0} + r_{sd2} I_{sd} & , \quad I_{sd} > I_{SC} \end{cases} \tag{1}$$

where r_{sd1} is the resistance of the MOSFET; r_{sd2} and V_{sd0} are the equivalent resistance and voltage source of the MOSFET and diode parallel circuit; I_{sc} is the current corresponding to the diode threshold voltage that separates the two loss mechanisms.

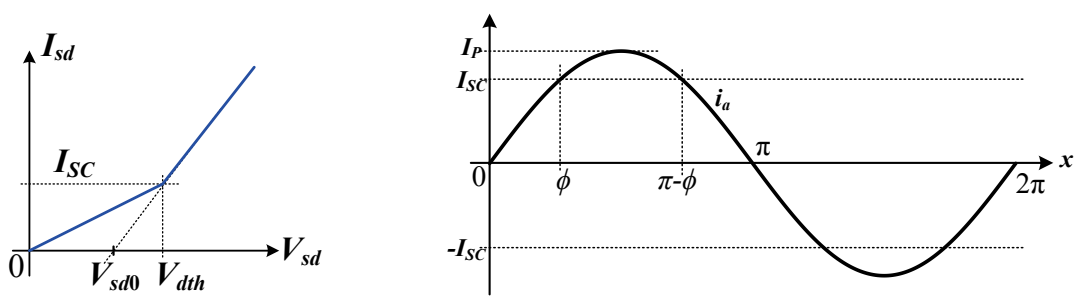

Figure I.3.1 (a) Approximation of typical SiC MOSFET reverse conduction characteristics for loss modeling, (b) Inverter phase current.

Assuming a sinusoidal inverter phase current i_a, the threshold current I_{sc} can be used to define the corresponding electrical angle ϕ in Figure I.3.1 (b) and Eq. (2), where I_p is the peak phase current. The threshold angle ϕ will be used in the derivation of equations for computing the reverse conduction losses.

$$\begin{cases} i_a = I_P \sin x \\ I_{SC} = I_P \sin \phi \end{cases} . \tag{2}$$

For a given reverse-conduction PWM duty, d_{fd}, determined by the chosen PWM scheme, the two reverse-conduction loss components, $P_{\mathrm{RCL_SW}}$ for the MOSFET only and $P_{\mathrm{RCL_FD}}$ for the MOSFET and diode together, can be computed by Eq. (3):

$$\begin{cases} P_{\mathrm{RCL_SW}} = \dfrac{r_{sd1} I_P^2}{2\pi}\{\int_0^{\phi} d_{fd}\sin^2 x dx + \int_{\pi-\phi}^{\pi} d_{fd}\sin^2 x dx\} \\ P_{\mathrm{RCL_FD}} = \dfrac{r_{sd2} I_P^2}{2\pi}\int_{\phi}^{\pi-\phi} d_{fd}\sin^2 x dx + \dfrac{V_{sd0} I_P}{2\pi}\int_{\phi}^{\pi-\phi} d_{fd}\sin x dx \end{cases} . \tag{3}$$

Figure I.3.2 shows a three-phase traction drive inverter (a) and its two-phase modulation signals (b). Under two-phase modulation, over each interval of 60 electrical degrees in every cycle, one of the SiC MOSFETs does not switch, thus eliminating the switching losses. At any given time, PWM is performed over two of the three phase-legs. The reverse conduction PWM duty for the two-phase modulation is expressed by Eq. (4).

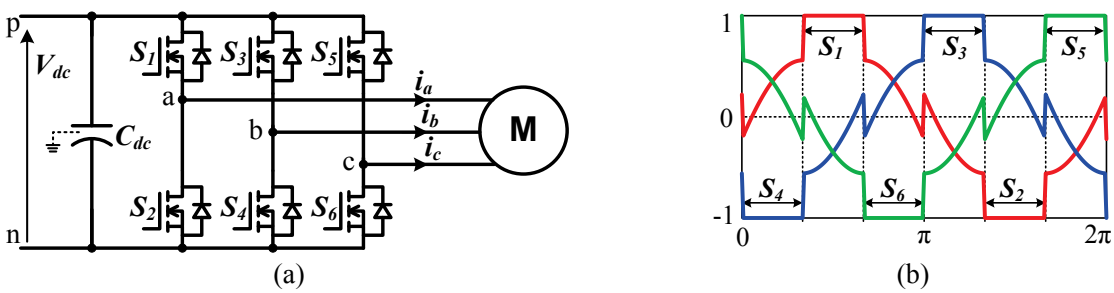

Figure I.3.2 (a) Traction drive system and (b) two-phase modulation signals.

$$d_{fd} = \begin{cases} 1-\frac{1}{2}m[\sin(x+\theta)-\sin(x+\theta-\frac{2}{3}\pi)] & 0 < x+\theta \le \frac{1}{3}\pi \\ 0 & \frac{1}{3}\pi < x+\theta \le \frac{2}{3}\pi \\ 1-\frac{1}{2}m[\sin(x+\theta)-\sin(x+\theta+\frac{2}{3}\pi)] & \frac{2}{3}\pi < x+\theta \le \pi \\ -\frac{1}{2}m[\sin(x+\theta)-\sin(x+\theta-\frac{2}{3}\pi)] & \pi < x+\theta \le \frac{4}{3}\pi \\ 1 & \frac{4}{3}\pi < x+\theta \le \frac{5}{3}\pi \\ -\frac{1}{2}m[\sin(x+\theta)-\sin(x+\theta+\frac{2}{3}\pi)] & \frac{5}{3}\pi < x+\theta \le 2\pi \end{cases} \tag{4}$$

Analytical equations for the reverse conduction loss components are derived separately for each of the cases determined by the relationship between the threshold angle ϕ and the power factor angle θ. These equations are quite complicated. Owing to space limitation, only equations for the case $\theta \le \pi/6$ and $\phi \le \theta$ are included below. The MOSFET-only conduction loss is expressed by Eq. (5) and the combined MOSFET and diode conduction loss by Eq. (6).

$$P_{\mathrm{RCL\text{-}SW}} = \frac{I_P^2 r_{\mathrm{sd1}}}{2\pi}\left(\frac{\phi}{2} - \frac{\sin 2\phi}{4} + m\cos\theta\left(\frac{3\cos\phi}{2} - \frac{\cos^3\phi}{2} - 1\right) + \sqrt{3}m\sin\theta\left(\frac{\cos^3\phi}{6} - \frac{\cos\phi}{2} + \frac{1}{3}\right)\right), \tag{5}$$

$$P_{\mathrm{RCL\text{-}FD2}} = \frac{I_P^2 r_{sd2}}{2\pi}\left(\begin{array}{l} \frac{\pi}{3} - \frac{\phi}{2} - \frac{\theta}{2} + \frac{\sin 2\phi}{4} + \frac{1}{2}\sin\left(2\theta - \frac{\pi}{3}\right) - \frac{m}{8} + \frac{\sqrt{3}m}{4}\sin\left(\phi + \theta - \frac{\pi}{3}\right) - \frac{\sqrt{3}m}{8}\sin\left(\phi - \theta + \frac{\pi}{3}\right) + \frac{\sqrt{3}m}{24}\cos\left(3\phi + \theta + \frac{\pi}{6}\right) \\ + \frac{\sqrt{3}m}{6}\cos^3\phi\cos\left(\theta + \frac{\pi}{6}\right) + \frac{3m\cos 2\theta}{8} - \frac{5\sqrt{3}m\sin 2\theta}{12} + \frac{\sqrt{3}m}{2}\cos\phi\sin\left(\theta - \frac{\pi}{3}\right) + \frac{m\cos^2\theta}{4} - \frac{\sqrt{3}m}{6}\sin^3\phi\sin\left(\theta + \frac{\pi}{6}\right) \end{array}\right). \tag{6}$$

The switching losses are proportional to the dc bus voltage, V_{dc}, and the output current, and can be calculated by

$$P_{SL_SW} = \frac{f_{sw} V_{dc} I_P}{\pi V_{dc_ref} I_{ref}} (E_{on_ref} + E_{off_ref})(1 - \frac{1}{2}\cos\theta), \quad (7)$$

where f_{sw} is the switching frequency; E_{on_ref} and E_{off_ref} are the turn-on and turn-off losses of the switch, respectively, at the reference dc bus voltage V_{ref} and output peak current I_{ref}.

A switching timing-based generic inverter loss computation method was also developed that can be applied to any PWM schemes without the need to derive loss equations. The steps are (1) find all the switching instants, (2) sum the conduction losses over each conduction interval, and (3) sum the switching losses at each switching instant. The generic inverter loss is shown in Figure I.3.3.

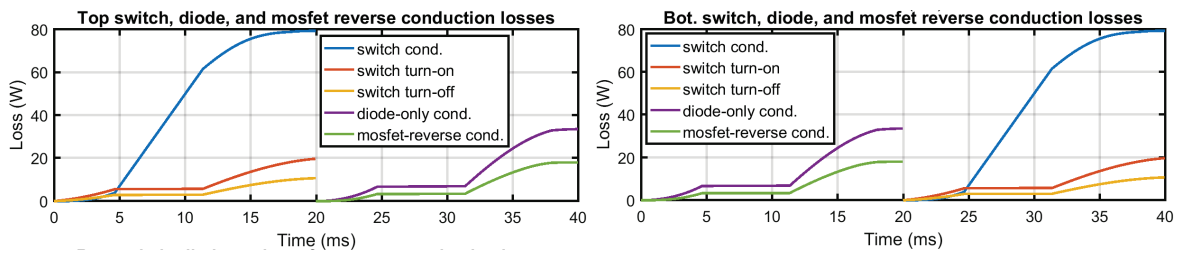

Figure I.3.3 Losses for switches and diodes in a SiC MOSFET phase-leg use the switching timing-based generic inverter loss computation method.

Results

To validate the SiC inverter loss models for two-phase modulation using SIC MOSFET reverse conduction, inverter loss tests were conducted using an inverter built in a previous project. Test results for a resistor load bank connected in series with a 0.45 mH inductor are given in Figure I.3.4, where (a) shows typical inverter operating waveforms of v_{bn}, v_{cn}, i_a and i_b and (b) shows measured and computed inverter efficiency vs. power. The 60° intervals of conduction only without switching can been seen clearly in the voltage waveforms. The test results indicate a small error range of ±0.16% between the measured and predicted inverter efficiency.

Modeling results are included here to illustrate the reduction of inverter conduction and switching losses by employing MOSFET reverse-conduction during freewheeling periods and the two-phase modulation scheme. An inverter using the Wolfspeed all-SiC module, CAS325M12HM2, rated at 1.2 kV and 3.7 mΩ, was modeled in the loss comparison. The parameters of the MOSFET on-resistance, diode internal on-resistance and voltage drop, and turn-on and turn-off losses were extracted from a Wolfspeed data sheet [2]. Conduction loss reduction using MOSFET reverse conduction over diode-only conduction was computed by sweeping through the inverter current from 50 A to 250 A, the PWM modulation index from 0.1 to 1, and the load power factor angle from 5 to 70 electrical degrees at an inverter dc bus voltage of 600 V and a switching frequency of 15 kHz. Figure I.3.5 plots the results for the peak currents of 50 A in (a), 150 A in (b), and 250 A in (c), and the minimum and maximum inverter conduction loss reduction vs. current in (d). The conduction loss reduction increased as load current decreased, with a maximum of 59.3% observed at 50 A.

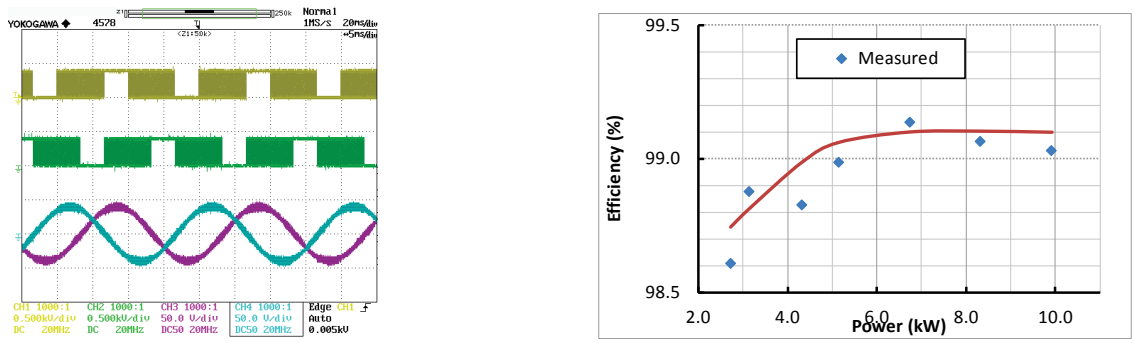

(a) (b)

Figure I.3.4 (a) Experimental inverter operating waveforms under two-phase modulation. From top, v_{bn}, v_{cn}, 500V/div; i_a, i_b, 50A/div. (b) Measured and computed inverter efficiency vs. power.

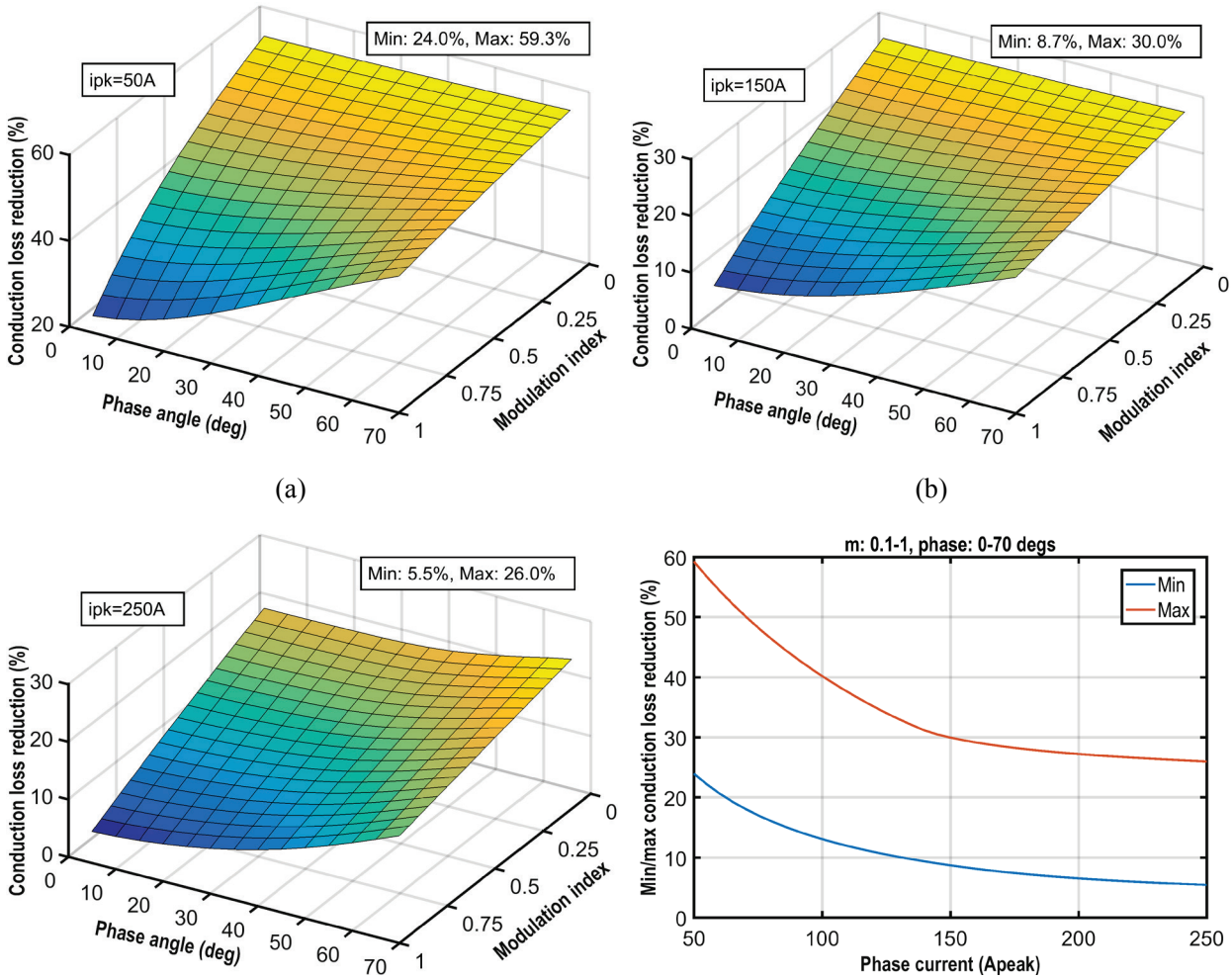

(a) (b) (c) (d)

Figure I.3.5 (a,b,c) Modeled conduction loss reduction using MOSFET reverse conduction by sweeping through current, modulation index, and power factor. (d) Minimum and maximum total inverter loss reduction.

Figure I.3.6 plots the inverter switching loss reduction for peak currents of 50 A in (a), 150 A in (b), and 250A in (c), and the minimum and maximum inverter switching loss reduction vs. current in (d). The switching loss

reduction depended significantly on the load power factor at a given load current. The range of reduction increased from 34.8–38.9% at 50 A to 36.8–45.2 % at 250 A.

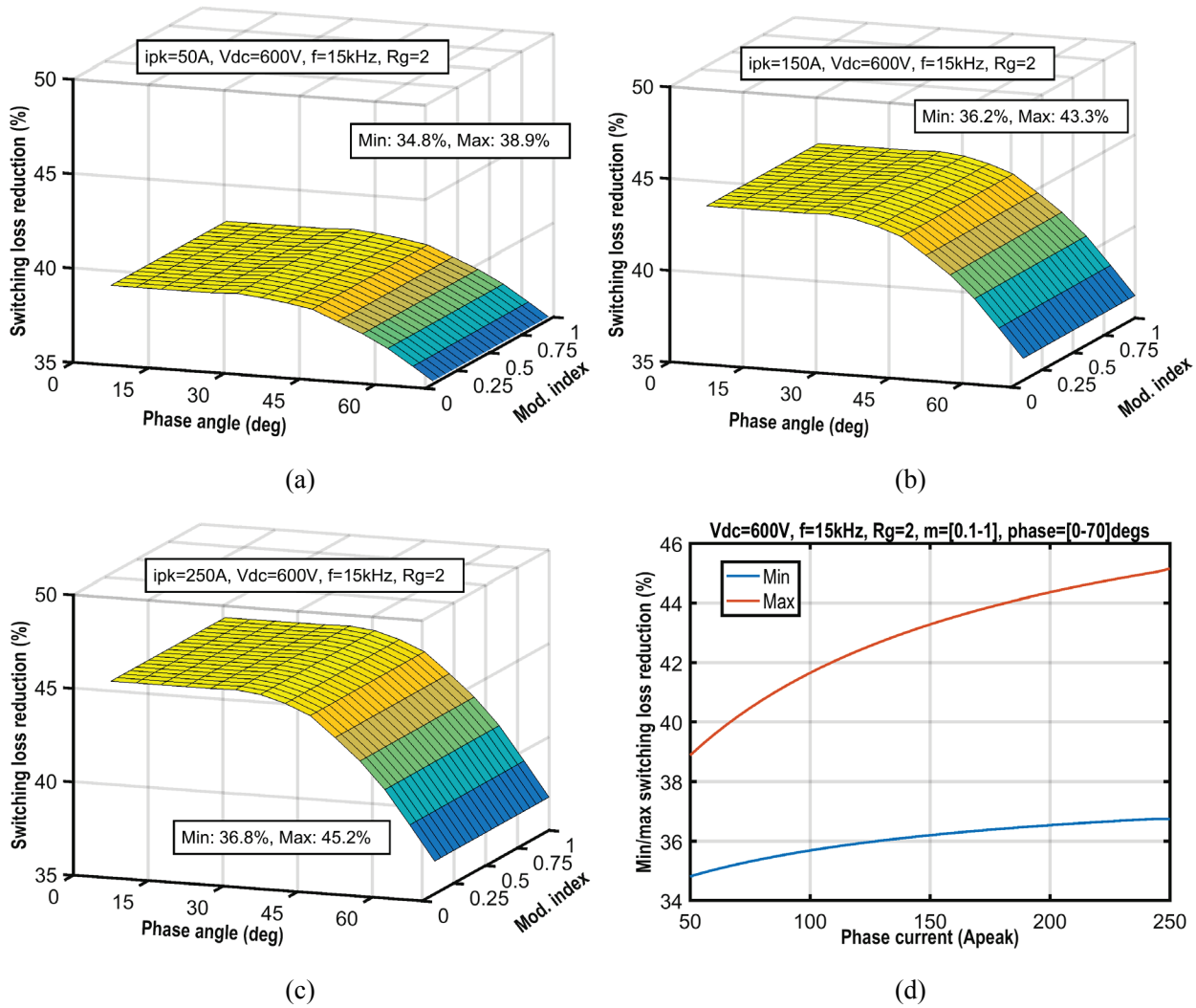

Figure I.3.6 (a,b,c) Simulated switching loss reduction using two-phase modulation by sweeping through current, modulation index, and power factor. (d) Minimum and maximum inverter switching loss reduction vs. current.

The impact of the switching schemes on SiC inverters for controlling the 2016 BMW i3 motor and 2007 Camry motor was then evaluated using the developed loss modeling methods. The inverter for the 2016 BMW i3 motor required two of the SiC modules in parallel for each phase and had a dc bus voltage of Vdc=355 V and a switching frequency of fsw=15 kHz. The inverter for the 2007 Camry motor required only one SiC module for each phase and had Vdc=650 V and fsw=15 kHz. Maximum torque per amp (MTPA) control models were developed for the two motors and implemented in MATLAB. Figure I.3.7 shows the torque, voltage, current, power, and power factor profiles under MTPA control for the 2016 BMW i3 motor in (a) and the 2007 Camry motor in (b). The profile data were fed to the inverter loss model, and total loss reductions were computed; they are plotted in Figure I.3.8. A higher loss reduction was observed for the 2007 Camry motor as a result of its higher dc bus voltage. Both motors had higher loss reductions at lower speeds.

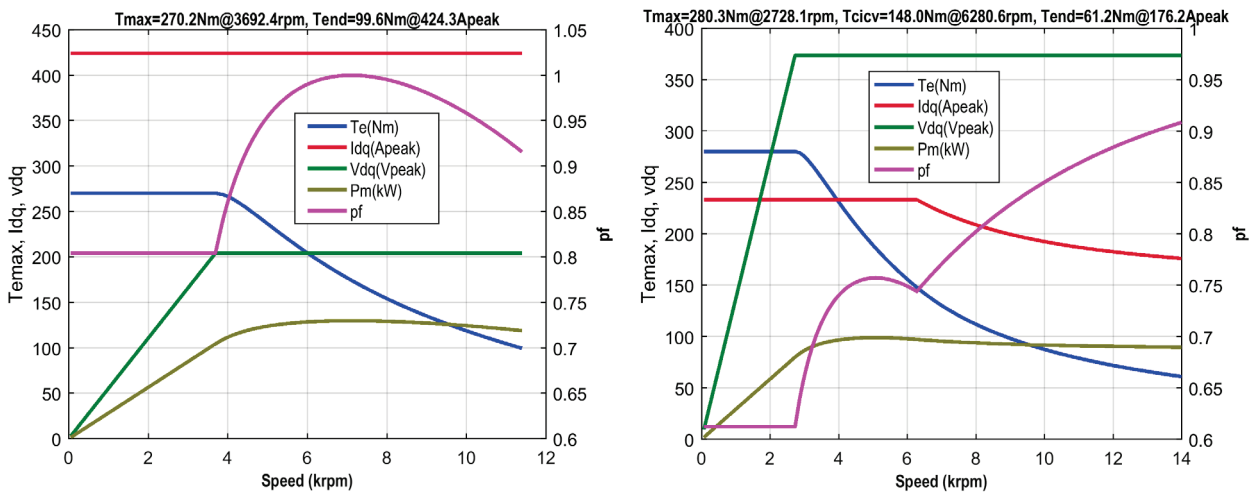

(a) (b)

Figure I.3.7 Torque, voltage, current, power, and power factor profiles under maximum torque per amp control for a 2016 BMW i3 motor (a) and 2007 Camry motor (b).

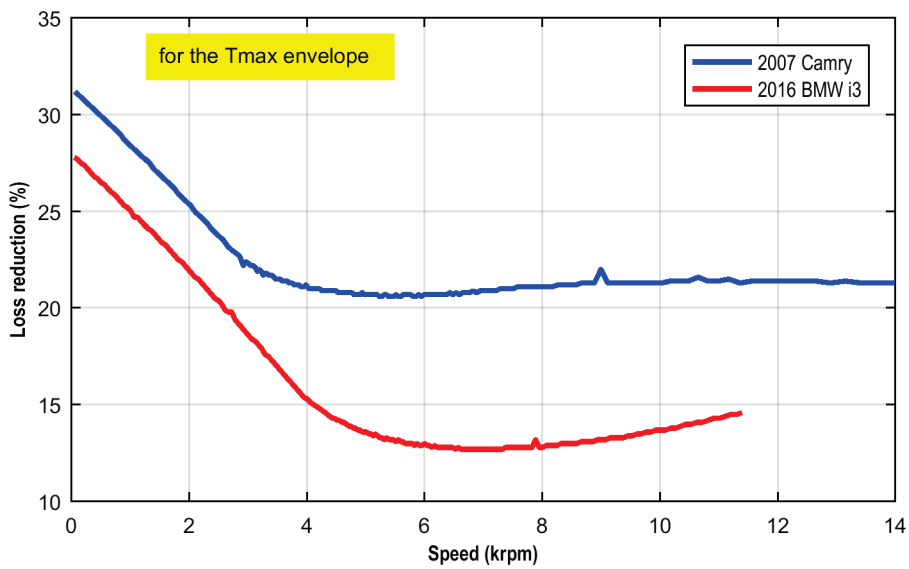

Figure I.3.8 Total loss reduction vs. speed for the maximum torque envelop for 2007 Camry and 2016 BMW i3 motors.

Figure I.3.9 plots a simulated inverter loss reduction map in (a) and an efficiency map in (b) for the 2016 BMW i3 motor for motoring and regeneration operations. The highest loss reduction region occurs at the low-speed end and at low torque in motoring mode, but at the mid-speed band and at low torque in regeneration mode. The switching scheme yielded higher reductions at any given speed and torque in regeneration mode than in motoring mode. The inverter efficiency was greater than 98% at 1700 rpm or above in both motoring and regeneration modes.

Figure I.3.10 plots a simulated inverter loss reduction map in (a) and an efficiency map in (b) for the 2007 Camry motor during motoring and regeneration operation. Again, the highest loss reduction region occurs at the low-speed and low-torque end in motoring mode, but at the mid-speed band and at low torque in regeneration mode. The switching scheme yielded higher reductions at any given speed and torque in regeneration mode than in motoring mode. The inverter efficiency was greater than 98% at 1800 rpm or above in both motoring and regeneration modes.

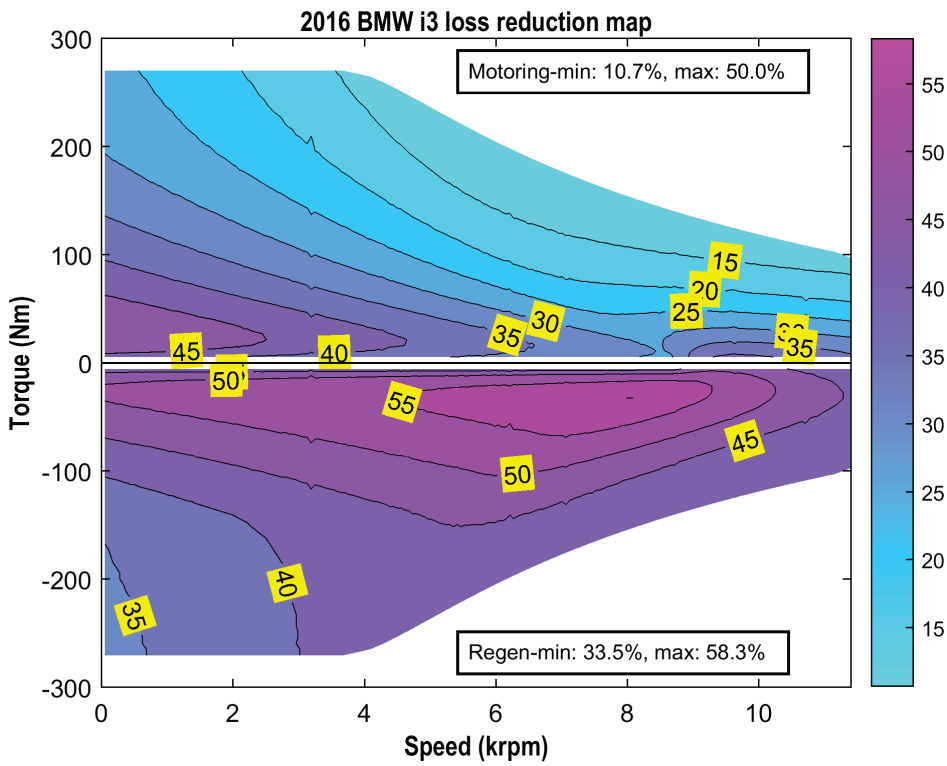

(a)

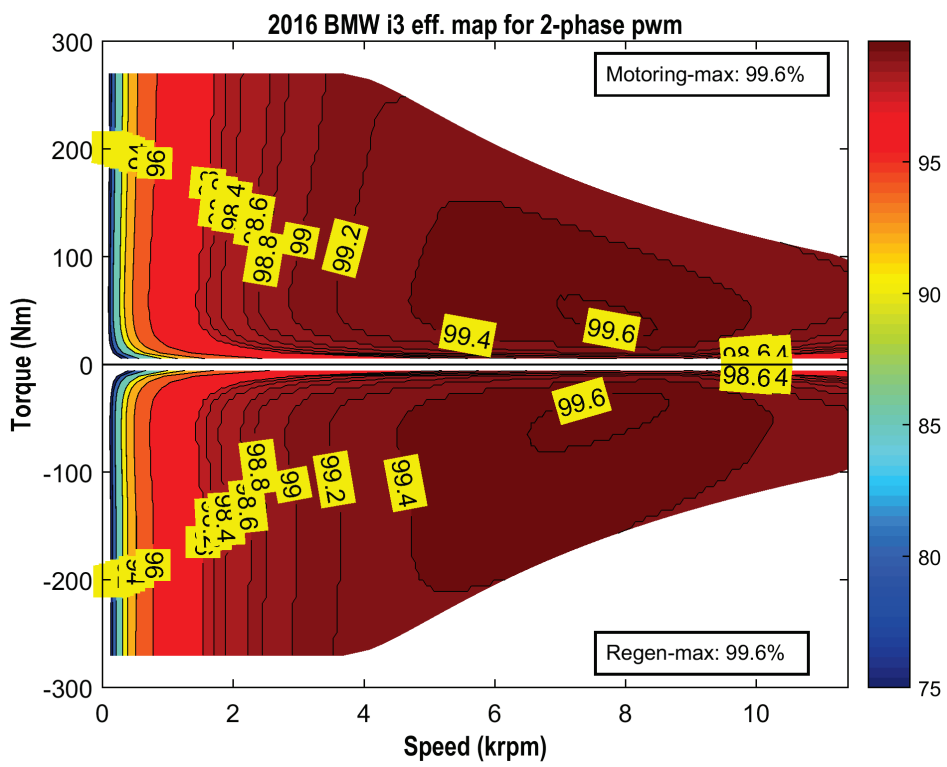

(b)

Figure I.3.9 Simulated inverter loss reduction (a) and efficiency (b) maps for the 2016 BMW i3 motor.

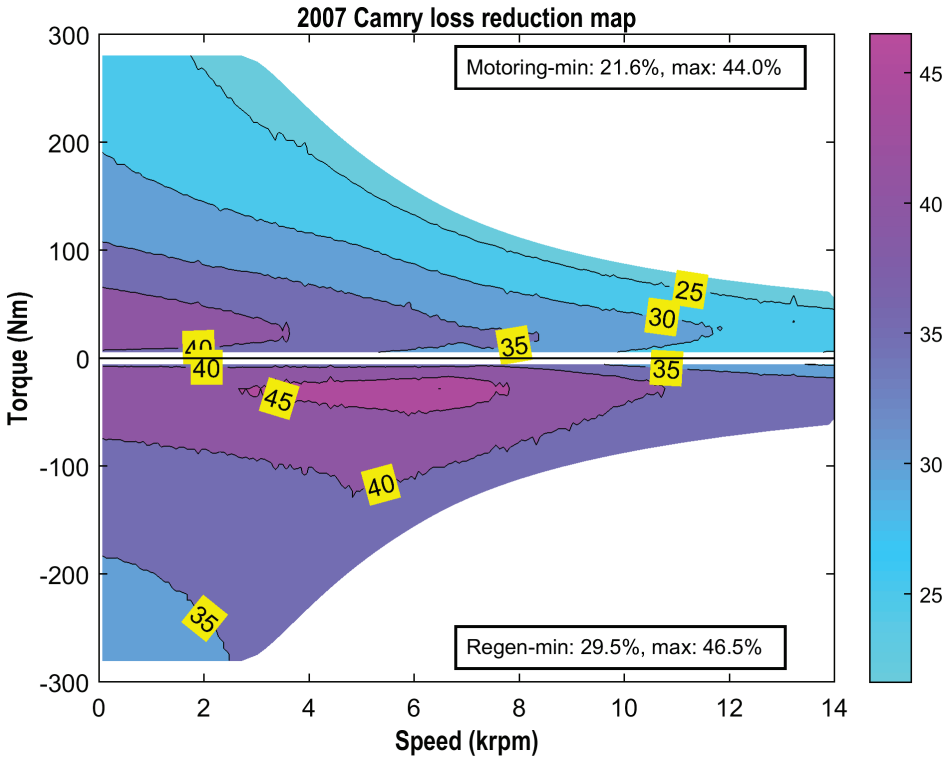

(a)

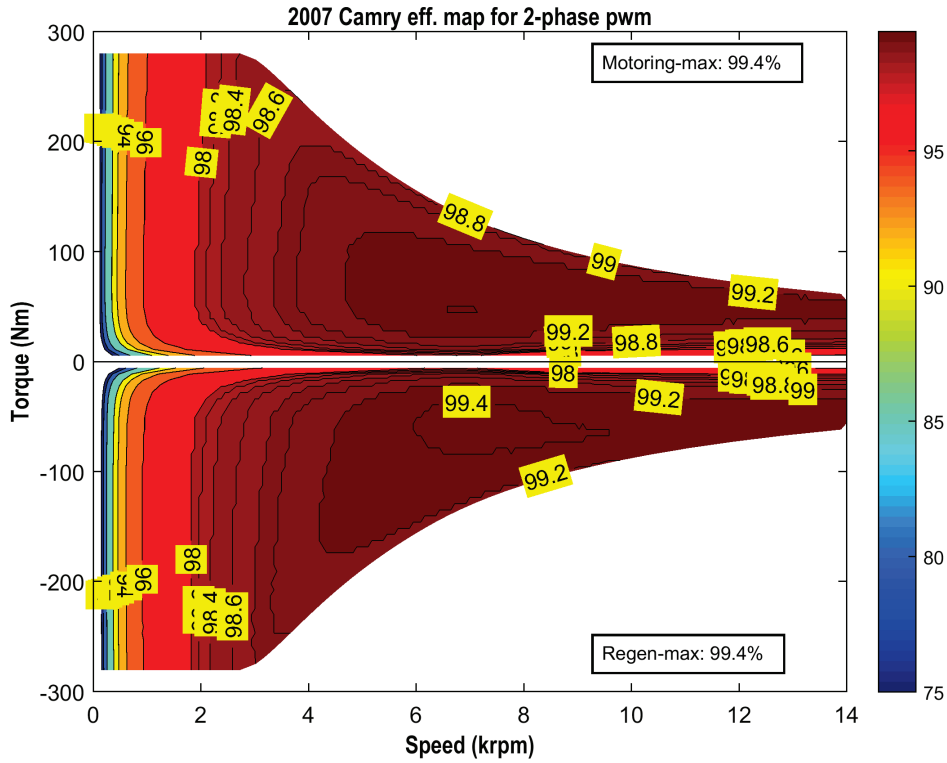

(b)

Figure I.3.10 Simulated inverter loss reduction (a) and efficiency (b) maps for the 2007 Camry motor.

Conclusions

A combination of two-phase modulation and SiC MOSFET reverse conduction was used to reduce inverter losses and improve electric traction drive system efficiency, especially at light load conditions. Modeling results for SiC MOSFET inverters for controlling the 2007 Camry motor and 2016 BMW i3 motor showed up to 98 % efficiency at light load conditions.

Analytical inverter loss models for two-phase modulation and MOSFET reverse conduction were derived and validated with experimental results. A switching timing-based generic inverter loss computation method also was developed that can be readily used for any PWM schemes and non-sinusoidal currents. Using the inverter loss models, traction drive loss simulation models for the 2007 Camry and 2016 BMW i3 motors showed a more than 40% loss reduction for the 2016 BMW i3 motor and more than 35% loss reduction for the 2007 Camry motor at light load conditions compared with typical three-phase modulation with diode-only conduction during freewheeling.

Future work should focus on developing optimal motor control methods that can fully use modulation schemes to maximize the reduction of losses.

Key Publications

1. G. J. Su. "Loss Modeling for SiC MOSFET Inverters." *IEEE 2018 Vehicle Power and Propulsion Conference (VPPC)*, August 27–30, 2018, Chicago, Illinois.

References

1. U.S. DRIVE Electrical and Electronics Technical Team Roadmap, 2017. Available at https://www.energy.gov/sites/prod/files/2017/11/f39/EESTT%20roadmap%202017-10-16%20Final.pdf Accessed October 2018.
2. Wolfspeed data sheet. https://www.wolfspeed.com/downloads/dl/file/id/967/product/204/cas325m12hm2.pdf

Acknowledgements

This work is supported by the DOE Office of Energy Efficiency and Renewable Energy, Vehicle Technologies Office, under contract number DE-AC05-00OR22725. The author wishes to thank project team members: Cliff White, Omer Onar, and Jason Pries.

I.4 High-Silicon Laminates for Electric Motors (ORNL)

Balasubramaniam Radhakrishnan, Principal Investigator
Oak Ridge National Laboratory
1 Bethel Valley Road
Oak Ridge, Tennessee 37831
E-mail: radhakrishnb@ornl.gov

Susan Rogers, DOE Technology Development Manager
U.S. Department of Energy
E-mail: susan.rogers@ee.doe.gov

Start Date: October 1, 2017 End Date: September 30, 2018
Project Funding (FY18): $320,000 DOE share: $320,000 Non-DOE share: $0

Project Introduction

Iron-silicon (Fe-Si) steels containing up to 6 weight (wt) % Si are very attractive, soft magnetic materials for motor applications. For high-frequency applications, such as in traction motors, the eddy current loss is significantly reduced by the high resistivity of the steel. However, steels containing more than 3 wt % Si are very brittle and cannot be thermomechanically processed into thin sheets like conventional Fe-Si steels that are 3 wt % Si. The only commercial process for making Fe-6Si steels is Si vapor deposition on a low-Si Fe-Si steel sheet followed by diffusion annealing, which results in an expensive steel that is not affordable for motor applications. It is therefore necessary to develop a novel alloying/thermal processing strategy for the production of a hot band that could be subsequently rolled at room temperature to a finished laminate thickness of about 0.5 mm. The development of such an approach is metallurgically very challenging because there are limited alloying options with the potential to eliminate or retard the ordering process responsible for room-temperature embrittlement without detrimentally impacting the soft magnetic properties of the Fe-Si binary alloy.

Objectives

- Identify critical material and process variables that influence the room-temperature formability of high-Si Fe-Si steel.
- Identify potential alloying additions to Fe-Si to promote bulk thermomechanical processing without significant loss of magnetic properties.

Approach

In previous years, we have tried two different approaches:

1. Introducing a warm-rolling step that imparts sufficient ductility to generate a high dislocation density to promote breakdown of the ordered structure, which could potentially render the steel more ductile at room temperature

2. Alloying the steel with different levels of boron and devising a high-temperature deformation and flash annealing strategy to achieve grain refinement in the steel.

The first approach was not successful—even though warm rolling indeed destroyed the ordering, the dislocation density was so high that it rendered the material brittle at room temperature. The second process was partially successful: the thickness was significantly reduced by optimizing the boron content and the flash annealing parameters; but extensive edge cracking limited the usefulness of the approach for producing sheets with good mechanical integrity. As part of the alloy optimization process, first-principles modeling was used to identify a ternary alloying addition that would effectively destabilize the ordering in the alloy. We

successfully identified an alloying element X that had a melting point close to that of the steel and that had a significant destabilizing effect on the ordering process.

During FY 2018, we cast the Fe-6Si-X alloy with different levels of X and optimized the hot rolling schedule and flash annealing parameters to achieve adequate grain refinement. The Fe-Si-X alloy also resulted in the precipitation of (Si, X) particles that had a beneficial effect on grain refinement by delaying the onset of recrystallization during flash annealing and by preventing the growth of recrystallized grains by pinning the grain boundaries.

Results

Thermomechanical Processing

The Fe- (6-6.5) Si alloys were typically cast as 1×1×3–4 in. long ingots. Ingots were homogenized and high-temperature rolling was performed to fabricate plates 0.25– 0.5 in. thick. When this work was initiated, no clear process path was identified in the literature to introduce sufficient dislocation density without causing dynamic recrystallization. While large thickness reductions at intermediate temperatures can achieve this effect, because of limitations related to the capacity of the small rolling mill, substantial reductions could not be achieved in a single pass at intermediate temperatures. This limitation can be overcome with the shear mill available at Oak Ridge National Laboratory (ORNL), which is currently being brought back into service.

One of the first achievements in this work was the development of a process to accumulate a significant dislocation density while avoiding dynamic recrystallization. The key to this process was to optimize the hot rolling temperature and perform consecutive rolling passes of the maximum thickness reduction (~ 25–30%) possible without reheating. Through trial-and-error, it was found that a maximum of four passes could be achieved without causing cracking of the plate. This process resulted in the introduction of substantial dislocation density without causing dynamic recrystallization within the material. Following this step, the effect of annealing on the microstructural evolution of the Fe-Si plates was evaluated. Again, through trial-and-error annealing experiments at different temperatures and times, an ideal microstructure for subsequent rolling was obtained. This combination of rolling processes combined with annealing conditions became the basis for comparing the effects of different alloying elements.

Effects of Alloying Element

The key to successful alloying element additions is the ability to achieve successful room-temperature rolling of the Fe-Si alloys. Based upon the experiments performed so far, no clear beneficial effects of boron have been observed on the room-temperature rolling capability. However, additions of a specific amount of X have shown beneficial effects toward achieving a room-temperature rolling capability; and an invention disclosure for alloying additions and process development will be submitted soon. Figure I.4.1 shows the effect of process parameters on the rolling characteristics of an Fe-6Si-X alloy. It shows the successful development of a 0.35 mm sheet through room-temperature rolling without the significant edge cracking that was seen previously for Fe-6Si-B steel.

Integrated Design of Laminate and Insulation

Figure I.4.1 Fe-6.5Si-X steel thermomechanically processed and rolled at room temperature to a final thickness of 0.35 mm with no significant edge cracking

In FY 2018, we also pursued an approach of integrating the optimization of the laminate sheet to achieve room-temperature formability, with the formation of an insulating coating on the steel surface that is required for the laminate application in a motor. We conducted detailed thermodynamic calculations to identify ternary and quaternary additions, X and Y, to an Fe-6Si binary alloy that would allow (1) precipitation of the Si initially to form a Si-lean matrix that can be easily processed to the final laminate thickness by room-temperature rolling; and (2) dissolution of Si-rich precipitates into the matrix and movement of dissolved Si to the surface, where it will combine with Y and possibly with the furnace atmosphere to form a stable thermal insulation. This approach is very similar to the approach used to produce Fe-3%Si steel during gross texture formation by secondary recrystallization. This approach will be further explored in FY 2019. In addition, we plan to perform isothermal rolling using the ORNL shear rolling mill that is expected to be fully commissioned by December 2018. Isothermal rolling will allow additional flexibility by eliminating the roll chilling that occurs in conventional rolling mills, which complicates the material behavior during rolling.

First Principles Modeling

In this subtask, we initiated an effort to explore ways to influence the thermodynamic stabilities of the Si B_2 phase using density functional theory (DFT) -based theoretical approaches. The DFT aspects of the calculations were performed using the Vienna Ab initio Simulation Package (VASP) and a particle swarm optimization–based algorithm was employed to further explore competing phases for a given composition. Specifically, we used our developed computational materials platform that combines materials database searching, first principles calculations, and global structure search algorithms. The key materials tuning parameters to enhance structural stabilities include metal dopants (M), $Fe_4M_2Si_2$, and/or metal doping ratio (x), M_xSi_{1-x}. For M_xSi_{1-x} systems, we considered several metallic elements. We focused on a high-dopant system as a model system, in which the metal dopant concentrations of most stable M-Si systems range between 0.3 and 0.75, depending on the metals. The volume changes per atom can be as high as ~87% in terms of x.

Figure I.4.2 summarizes the basic properties of $Fe_4M_2Si_2$ ternaries depending on the types of dopant metal M, where M=alkali metal, alkaline earth metal, transition metal, and charcogenide. Metal doping can greatly change the relative stabilities of ternaries and their volume changes; thus M is one of the key parameters to stabilize a Si B2-based phase. We will further employ global structure search algorithms to identify (meta)stable phases for a given M and x, which will enable systematic exploration of the key parameters for tuning structural stabilities and properties, and analysis of the characteristics of competing phases. Based on tight interaction with synthesis experiments, theoretical modeling will be further developed/modified to include key experimental parameters during the synthesis experiment.

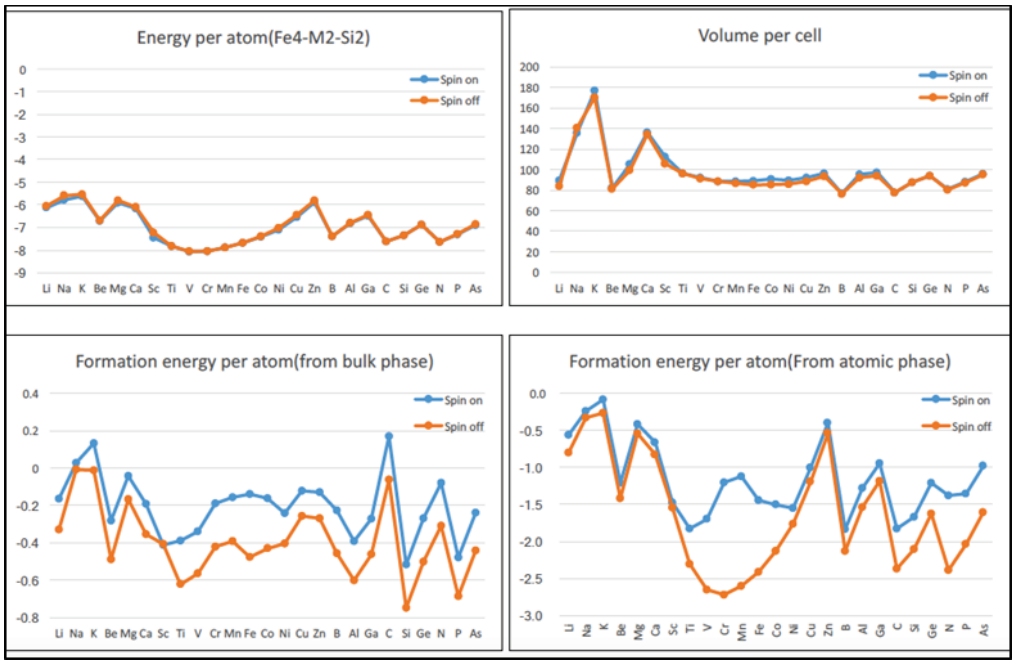

Figure I.4.2 Formation energies (energy per atom, and total energies with respect to bulk phases and atomic phases) and volumes of $Fe_4M_2Si_2$.

Conclusions

We identified an alloying strategy and a hot band processing approach to produce Fe-6Si-X steel that could be successfully rolled to a finish thickness of 0.35 mm by room-temperature rolling. The rolled material does not show significant edge cracking. We are also in the process of identifying quaternary additions to the steel that would allow us to design the laminate and the electrical insulation as an integrated product that could be manufactured through cold rolling followed by thermal annealing.

Key Publications

There will be no publications until intellectual property is filed and approved.

Acknowledgments

This work is supported by the DOE Office of Energy Efficiency and Renewable Energy, Vehicle Technologies Office, under contract number DE-AC05-00OR22725. The author wishes to thank project team members: Muralidharan Govindarajan (Materials Science and Technology Division, ORNL), who was responsible for the thermomechanical processing experiments, and Mina Yoon (Center for Nanophase Materials Sciences, ORNL), who performed the first principles modeling.

I.5 Innovative Chargers and Converters (ORNL)

Veda Prakash Galigekere, Principal Investigator
Oak Ridge National Laboratory
1 Bethel Valley Road
Oak Ridge, Tennessee 37831
E-mail: galigekerevn@ornl.gov

Susan Rogers, DOE Technology Development Manager
U.S. Department of Energy
E-mail: susan.rogers@ee.doe.gov

Start Date: October 1, 2017 End Date: September 30, 2018
Project Funding (FY18): $600,000 DOE share: $600,000 Non-DOE share: $0

Project Introduction

Transportation consumes approximately 1/3 of the overall energy consumption in the United States. Increased adoption of electric vehicles (EVs) is critical to offset the dependency on fossil fuel–based transportation and realize a more sustainable transportation ecosystem. Convenient recharging of onboard EV batteries is necessary to enhance the appeal to end users. Wireless EV charging via wireless power transfer (WPT) is an efficient, convenient alternative to conventional wired charging of EVs. Reducing the cost of the onboard components of a wireless EV charging system will make it more appealing for light duty vehicles and reducing their size (increasing the power density) will free space for higher-power wireless chargers to enable faster recharging via higher power levels. It is imperative to reduce the cost and size of wireless EV charging systems, specifically the onboard components.

The primary side, or offboard components, of a wireless EV charging system include a front-end or grid interface power electronics interface, a high-frequency (HF) inverter, a primary resonant network, and the primary or transmitter coil. The secondary, or onboard, components include a secondary or receiver coil, a secondary resonant network, an HF rectifier, and a filter capacitor at the terminals connecting to the battery. This project proposes a novel integrated wireless EV charging topology in which the onboard traction inverter and the DC link capacitor of the (electric) drive train (DT) are used as the secondary side rectifier and filter of the wireless charging system. Figure I.5.1 depicts the off-board and onboard components of the proposed integrated wireless EV charging architecture. The DC-DC converter interfacing the battery and the traction inverter is not present in many EV architectures, and its presence is not necessary for the proposed architecture to be rendered feasible. If the DT includes a boost converter, it can also be included in the wireless EV charging system if secondary side control is desirable.

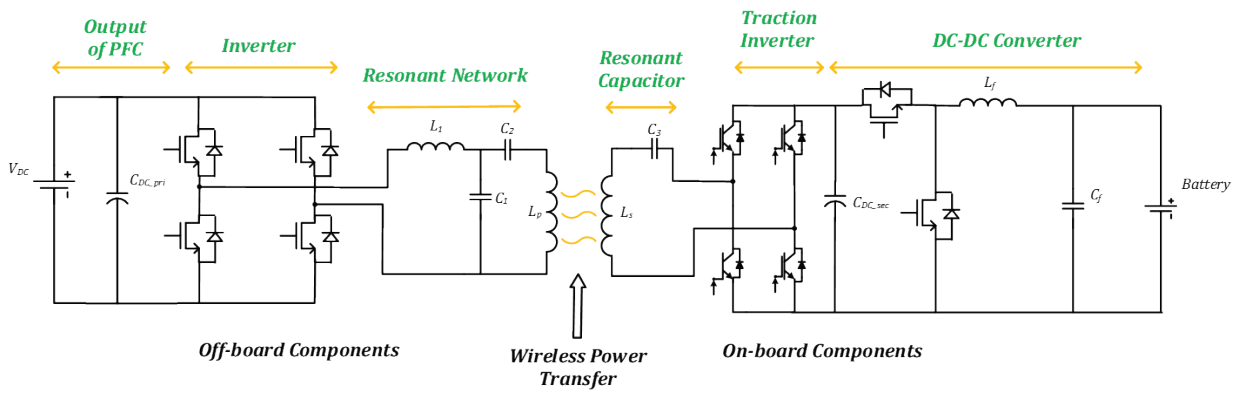

Figure I.5.1 Schematic of the proposed novel integrated wireless EV charging architecture.

The proposed architecture will be evaluated by designing an 11 kW integrated wireless EV charging system that uses the traction inverter and the DC link capacitor of a commercially available EV (2016 BMW i3) as a secondary side rectifier. The impact of the integrated charging architecture on the traction motor will also be evaluated.

Objectives

The overall objective is to develop and experimentally validate a proposed integrated wireless EV charging system that uses the high-voltage power electronics of the electric drive as the power electronics of the secondary side of the wireless EV charging system. Integrating the wireless charging system into the power electronics of the electric DT would improve the power density and cost to meet the DOE EETT 2025 power density and cost targets. The detailed objectives of the project are:

- Design, develop, and validate an optimized low-profile vehicle coil that can interoperate between SAE J2954 WPT power levels 1 and 3 (3.6–11 kW) and coil-to-coil distance categories Z_1 through Z_3.
- Develop and validate models to evaluate the sensitivity of the wireless charging system to variations in load power and coupling coefficient.
- Validate the proposed integrated wireless EV charging system by using a 2016 BMW i3 traction inverter as the secondary side power electronics for the wireless EV charging system.
- Evaluate the effects of the wireless charging system on the BMW i3 motor, and vice versa, for 11 kW operation.

Approach

The overall approach is to minimize the size and cost of the onboard components of an 11 kW wireless EV charging system. This will be achieved primarily by integrating a wireless charging system into the electric drive train to serve dual functionalities. The detailed approach to developing and validating an optimized integrated wireless EV charging system is summarized in the following sections.

Design and optimization of compact, interoperable vehicle coil - An optimized DD coil was designed to operate at the SAE J 2954–stipulated wireless power transfer (WPT) level 3, which is 11 kW at the Z height classification of Z_1 and Z_2 (3.93 to 8.26 in.). The coil was optimized by concurrent finite element analysis (FEA) simulation and circuit analysis of the WPT system based on a loosely coupled transformer model. Detailed circuit simulations were carried out on the Saber platform for the coil parameters corresponding to a coil-to-coil distance of 8 in., and the simulation results indicated feasibility.

Figure I.5.2 shows the FEA model and the prototype of the optimized DD coil. Commercial FEA software was used to simulate and design the optimized DD coil. The overall dimensions of the optimized vehicle coil are 381×482×25.4 mm, and it weighs 7.2 Kg. The prototype consists of eight turns of 6 AWG equivalent wire and Ferroxcube 3C95 ferrite tiles with a maximum magnetic field intensity of $B_{max} = 410$ mT at 100°C. Table

I.5.1 shows the FEA simulation and measurement results. Figure I.5.3 shows that the emissions from the designed coils are compliant with International Commission on Non-Ionizing Radiation Protection.

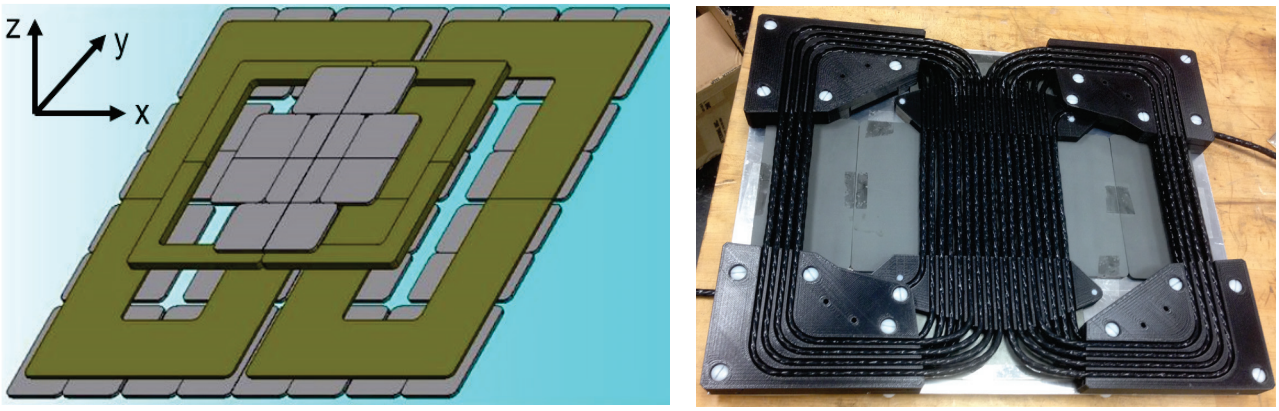

Figure I.5.2 FEA model and prototype of the optimized 11 kW DD coil.

Table I.5.1 FEA Simulation and Measurement Results of Optimized 11 kW DD Coils

	Simulated values			Measured values
Z distance (mm)	Primary coil inductance (μH)	Primary coil inductance (μH)	Coupling coefficient	Coupling coefficient k
100	82.86	84.21	0.302	0.251
125	81.20	81.62	0.239	0.210
150	80.14	79.88	0.190	0.170
175	79.56	78.88	0.151	0.138
210	79.35	79.22	0.121	0.107

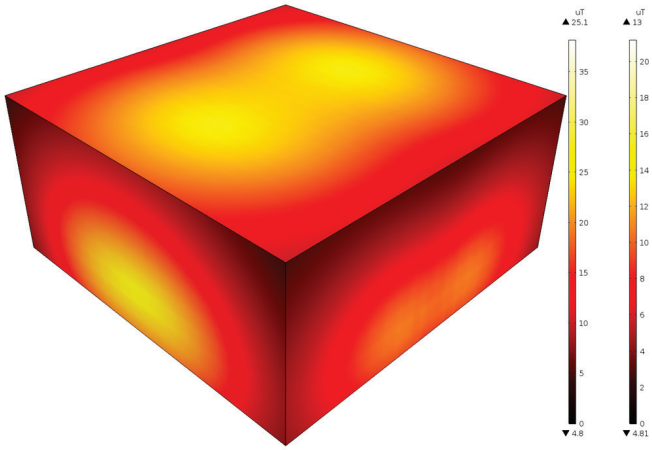

Figure I.5.3 FEA simulation results indicating compliance with the International Commission on Non-Ionizing Radiation Protection.

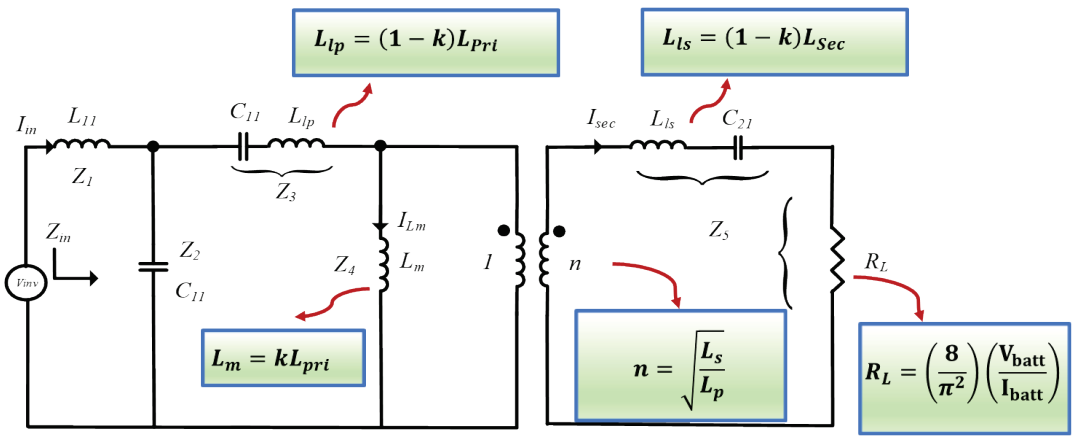

Figure I.5.4 Circuit model of primary side leadless chip carrier and secondary side series tuned wireless EV charging system to analyze sensitivity to variation in coupling coefficient and load resistance.

Resonant network modeling and sensitivity analysis – One of the key challenges in a WPT system with a small vehicle coil is to determine the effects of variation in the coupling coefficient and load power on the various parameters of the wireless charging system. A loosely coupled transformer model was used to derive circuit models to analyze the sensitivity to variation. Figure I.5.4 shows the circuit loosely coupled transformer model–based circuit model that can be used to perform sensitivity analyses. In the circuit model shown in Figure I.5.4, V_{inv} is the fundamental component of the inverter output voltage and $R_L$is the load resistance equivalent to the output power being transferred to the battery. L_m, L_{lp}, and $L_{ls}$are the magnetizing, primary leakage, and secondary leakage inductances, respectively. For the wirelss EV charging system, the circuit component voltages and currents can be obtained by performing linear circuit analysis.

- From Figure I.5.5 (a) and (c), it can be observed that the input impedance increases and the input current decreases as load resistance increases. This is because as the load resistance increases, the power transferred to the load decreases.

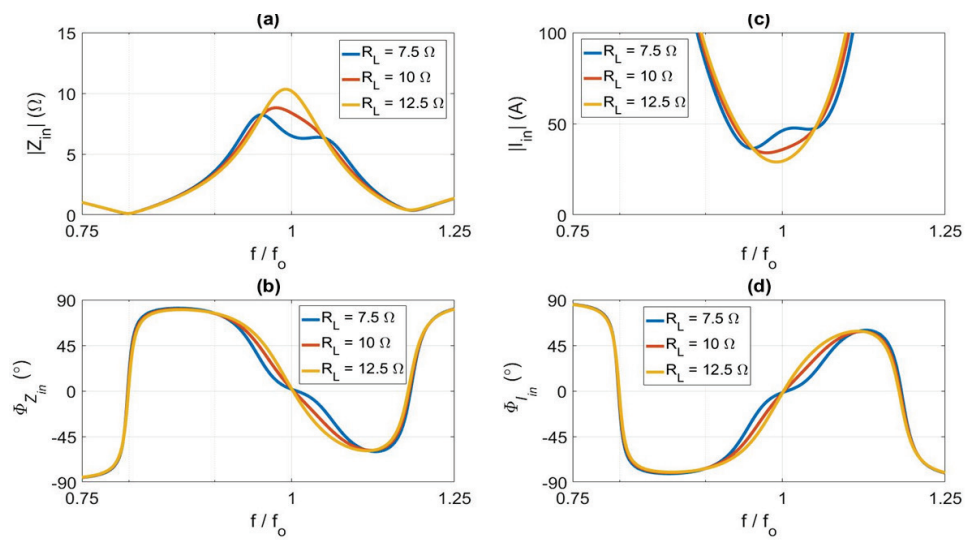

Figure I.5.5 Variation of magnitude and phase of input impedance and input current, as a function of frequency for different load resistances for the designed 11 kW integrated wireless EV charging system.

- Figure I.5.6 (a) shows that the primary coil current is constant independent of the load, and it remains almost flat around the resonant frequency. This is a positive feature, as any drift in the operating frequency will not affect the primary coil current.

- From Figure I.5.6 (b) and (d), it can be noted that the phase angles of the input impedance and the input current, respectively, are independent of the load and have almost a zero phase or unity power factor. There is a small phase angle by design to achieve zero voltage switching, which reduces the switching losses. It can also be observed that the phase angle does not cross zero in the immediate vicinity of the resonant frequency. This suggests that there is no concern of bifurcation (instability) around the resonant point.

- From Figure I.5.6 (c), it can be observed that voltage gain is constant at the resonant frequency and independent of the load resistor value. This is because a series-tuned secondary acts as a load-independent voltage source. The voltage gain is also noted to be flat around the resonant point, implying that any drift in resonant point will not lead to over-voltage conditions.

- From Figure I.5.6 (d), it can be inferred that as the load resistance increases, the output power decreases. This is because the output voltage is constant; as the resistance increases, the load current decreases, thereby reducing the output power. This can also be inferred from Figure I.5.6 (b), which shows that the current gain or the output current decreases as load resistance increases. Any drift in the operation frequency from the resonant frequency will lead to reduced output current, and the duty cycle of the inverter may have to be increased to compensate for it.

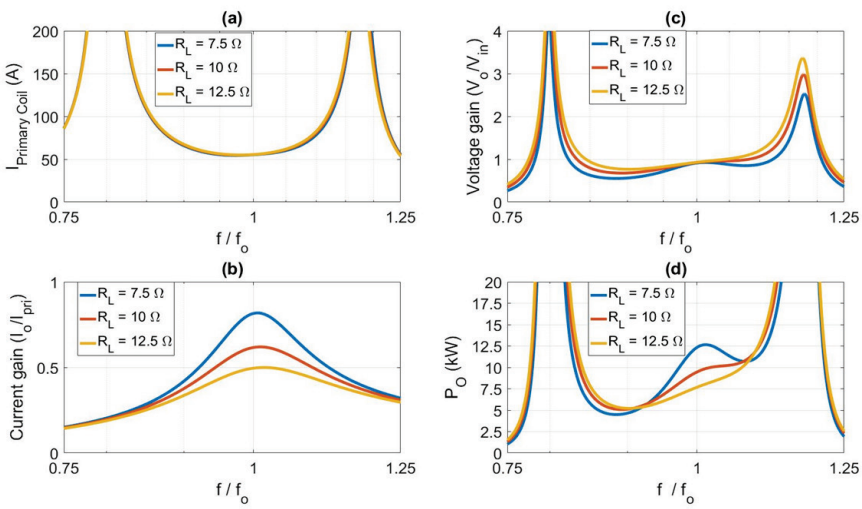

Figure I.5.6 Variation of magnitude and phase primary coil current, voltage and current gain and the output power as a function of frequency for different load resistances for the designed 11 kW integrated wireless EV charging system.

- From Figure I.5.7 (a) and (c) it can be observed that the input impedance increases and the input current decreases as the coupling coefficient decreases. This is because as the coupling coefficient decreases, the power transferred to the load decreases.
- From Figure I.5.7 (b) and (d), it can be noted that the phase angles of the input impedance and the input current, respectively, are independent of the coupling coefficient and have almost a zero phase or unity power factor. There is a small phase angle by design to achieve zero voltage switching, which reduces the switching losses.
- From Figure I.5.7 (b) and (d), it can be observed that the phase angle does not cross zero in the immediate vicinity of the resonant frequency. This suggests that there is no concern of bifurcation (instability) around the resonant point.

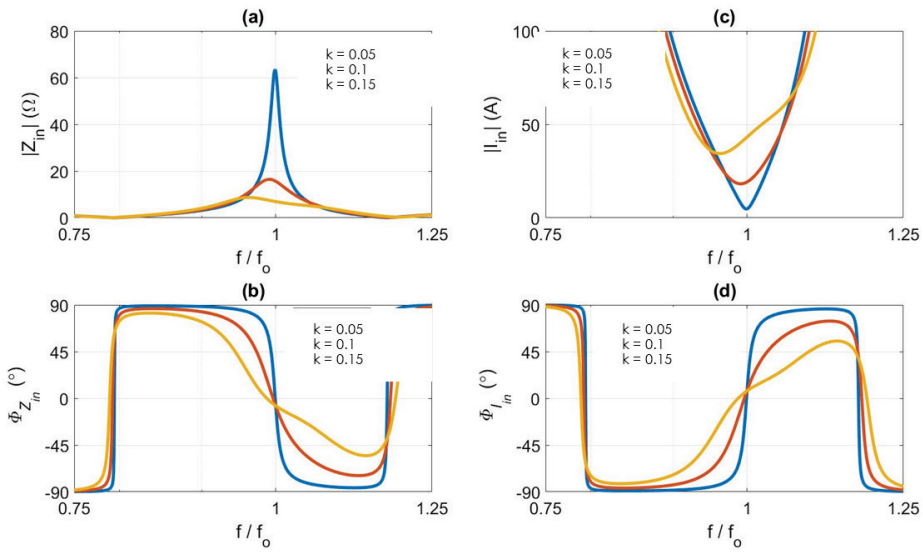

Figure I.5.7 Variation of magnitude and phase of input impedance and input current, as a function of frequency for coupling coefficients for the 11 kW integrated wireless EV charging system.

- Figure I.5.8 (a) shows that the primary coil current is constant independent of the coupling coefficient, and it remains almost flat around the resonant frequency. This is a positive feature, as any drift in the operating frequency will not affect the primary coil current, or the primary coil current is insensitive around the vicinity of the resonant frequency.

- From Figure I.5.8 (c), it can be observed that voltage gain increases as the coupling coefficient increases. Although the series-tuned secondary acts as a load-independent voltage source, an increase in the coupling coefficient will lead to a higher output voltage as the mutual inductance increases for a higher value of k. Note also that the output voltage is almost constant around the resonant frequency, especially for lower values of the coupling coefficient.

- From Figure I.5.8 (d), it can be inferred that as the coupling coefficient increases, the output power increases. This is because as the output voltage increases for a given load resistance, the load current increases, thereby increasing the output power. This can also be inferred from Figure I.5.4 (b), which shows that the current gain or the output current increases as the coupling coefficient increases. Any drift in the operation frequency from the resonant frequency will lead to reduced output current, and the duty cycle of the inverter may have to be increased to compensate for it. It can also be noted that for $k = 1.5$, the ouput power $P_o = 12.9$ kW; $k = 1.5$ corresponds to the coupling coefficient at a coil-to-coil distance of 6 in. or 203 mm.

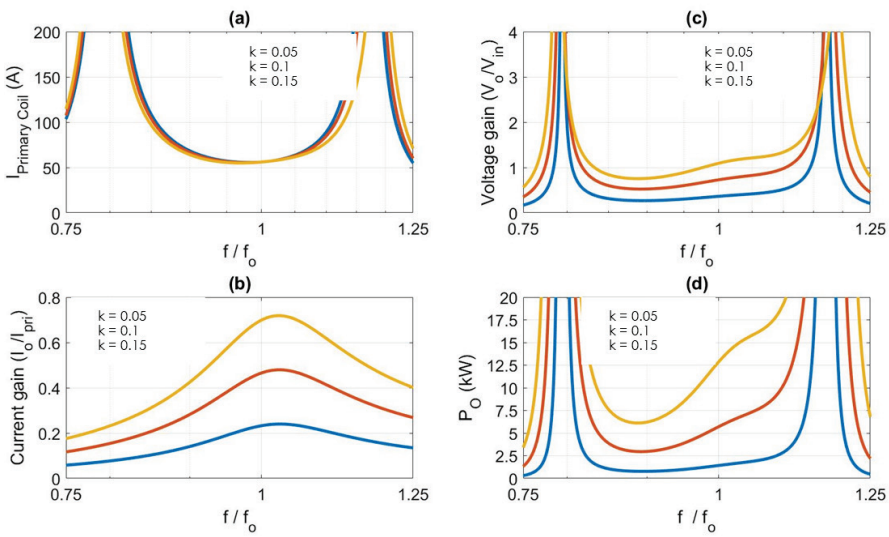

Figure I.5.8 Variation of magnitude and phase primary coil current, voltage and current gain, and output power as a function of frequency for different coupling coefficients for the 11 kW integrated wireless EV charging system.

Power electronics hardware design—For the primary side HF inverter, 1200 V/325 A CAS325M12HM2 silicon carbide (SiC) metal oxide semiconductor field-effect transistor (MOSFET) phase-leg power modules from Wolfspeed/CREE were used in an H-bridge arrangement with CGD15HB62LP gate drivers. Using SiC MOSFET power modules ensured efficient operation at the 85 kHz center operating frequency that complies with the SAE J2954 Recommended Practice. The control system of the inverter was implemented within a TMS320F28335PGFA digital signal processor module from Texas Instruments with a CAN link to adjust the operating parameters.

The proposed integrated wireless charger architecture was realized by incorporating the secondary side power electronics into the traction drive system of the BMW i3 in a laboratory setup. The output of the secondary coil and tuning capacitor (series tuned secondary) was directly connected to the AC output terminals of the BMW i3 inverter.

Results

The resonant network analyses were validated using a Venable 4400 frequency response analyzer. The coils and the resonant network were connected to an equivalent resistive load to obtain the characteristic behavior. The theoretically predicted and experimentally obtained magnitude and phase of the input impedance for the WPT system with a coil-to-coil gap of 165.1 mm (6.5 in.) are shown in Figure I.5.9 and Figure I.5.10, respectively.

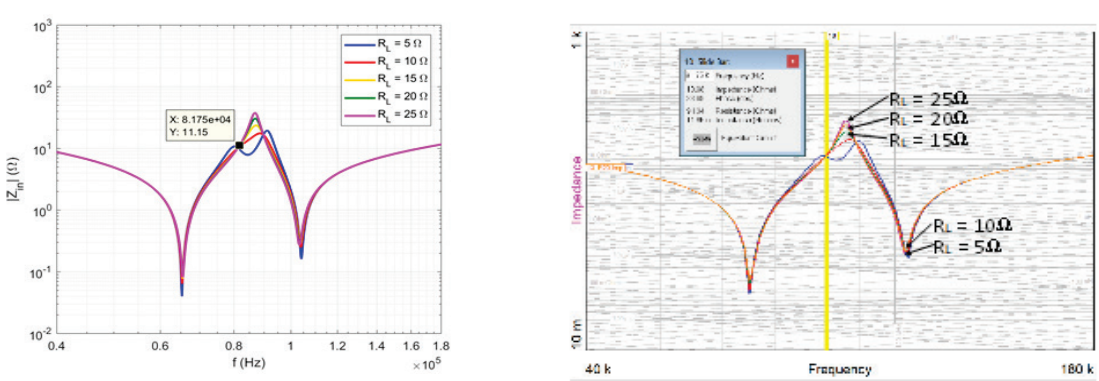

Figure I.5.9 $|Z_{in}|$ as a function of frequency at different load levels: (a) MATLAB model analysis and (b) experimental measurement from frequency response analyzer.

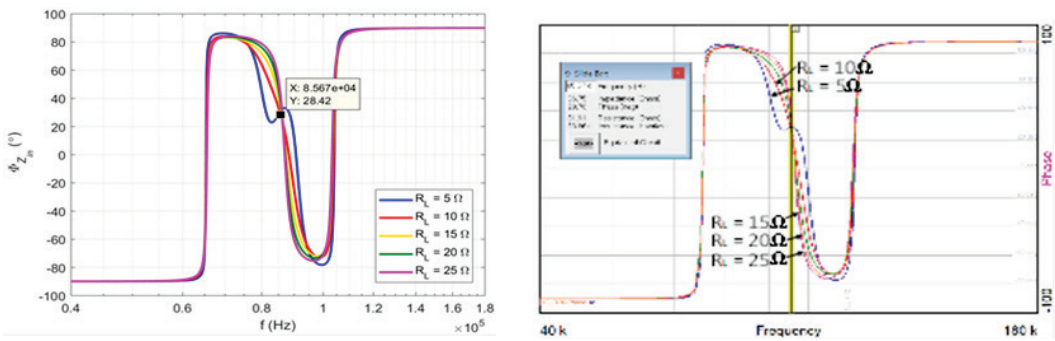

Figure I.5.10 $\phi_{Z_{in}}$ as a function of frequency at different load levels: (a) MATLAB model analysis and (b) experimental measurement from frequency response analyzer.

The wireless charging system was experimentally evaluated with and without the three-phase BMW motor connected to the AC output terminals to quantify the effect the rectifier mode of operation of the BMW traction inverter has on the motor and on the wireless charging system. The experimental setup is shown in Figure I.5.11. The primary side power electronics, and resonant network are not covered in Figure I.5.11, but it includes an SiC-based HF inverter and an LCC primary resonant network.

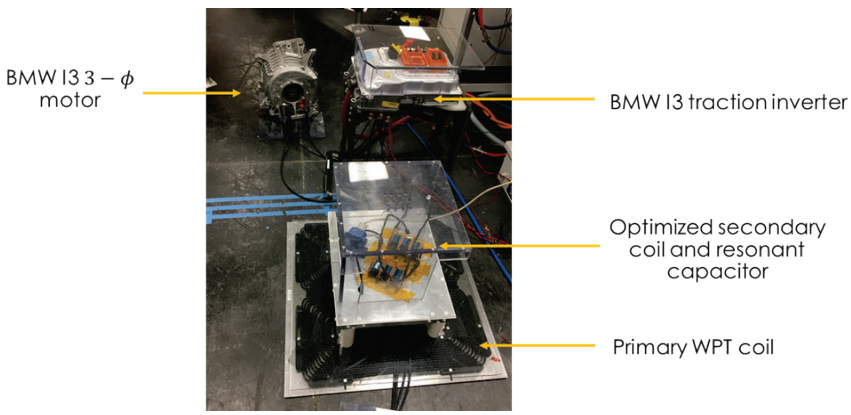

Figure I.5.11 Primary coil and the secondary side components of the integrated wireless EV charging system (laboratory prototype).

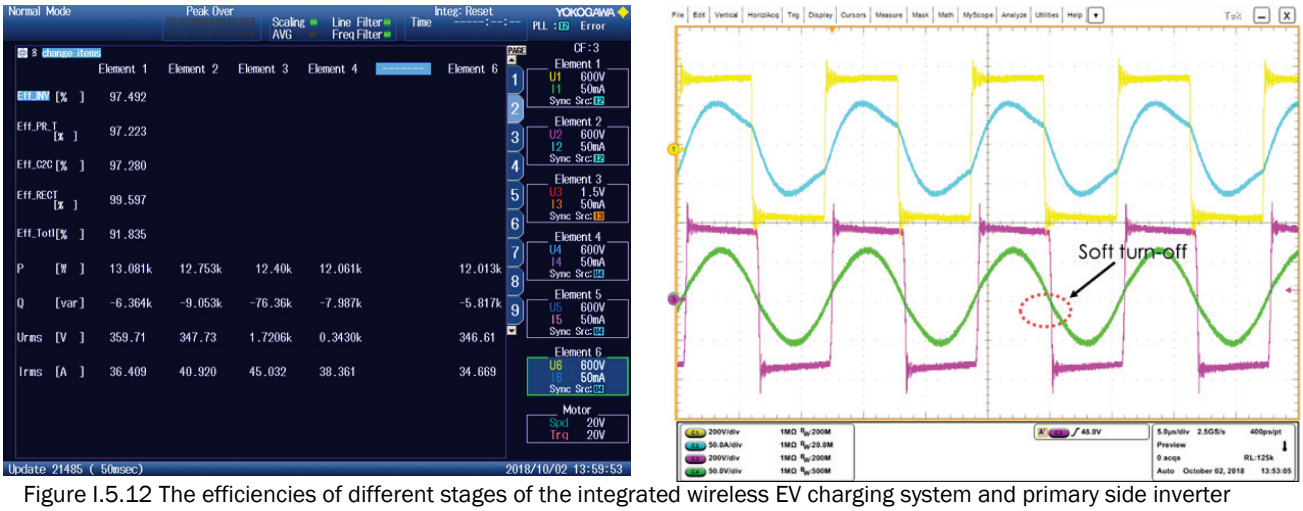

Figure I.5.12 The efficiencies of different stages of the integrated wireless EV charging system and primary side inverter voltage and current and secondary side rectifier input voltage and current of the charging system operating at 12 kW (BMW motor is not connected).

Figure I.5.13 The efficiencies of different stages of the integrated wireless EV charging system operating at 12 kW (BMW motor is connected to traction inverter). The efficiency of the rectifier includes the losses in the motor.

Conclusions

Linear circuit models to evaluate the sensitivity of the integrated wireless EV charging system was derived using the loosely coupled transformer. The derived models were validated using Venable 7400 frequency response analyzer. The predicted behavior agreed well with the measured results as shown in Figure I.5.10 and Figure I.5.11.

The functionality of the proposed integrated wireless EV charging architecture has been verified experimentally up to 12 kW with an optimized DD coil pair with a coil-to-coil gap of 165.1 mm (6.5 inches). The efficiency of the integrated wireless EV charging system with the 2016 BMW i3 traction inverter functioning (BMW i3 motor is not connected) as the secondary rectifier at 12 kW operation with a coil-to-coil gap of 165.1 mm (6.5 inches) was 91.83 % as shown in Figure I.5.12. The efficiency of the integrated wireless EV charging system with the 2016 BMW i3 traction inverter functioning as the secondary rectifier with the BMW I 3motor connected to the inverter at 12 kW operation with a coil-to-coil gap of 165.1 mm (6.5 inches) was 88.961 % as shown in Figure I.5.13. One of the key observations is when the BMW i3 $3-\phi$ motor was connected to the traction inverter and operated as the rectifier for the integrated charger, the rotor showed no

displacement and there were no signs of heating or chatter in the motor. This was evaluated for different starting potions of the rotor corresponding to different inductances as measured at the motor terminals (inverter was disconnected for inductance measurements). The worst-case measured loss of 340 W in the BMW traction motor is a fraction of the rated capacity of the traction motor of 125 kW.

Key Publications

1. V. P. Galigekere, O. Onar, J. Pries, S. Zou, Z. Wang and M. Chinthavali, "Sensitivity Analysis of Primary-Side LCC and Secondary-Side Series Compensated Wireless Charging System," *2018 IEEE Transportation Electrification Conference and Expo (ITEC)*, Long Beach, CA, 2018, pp. 885-891. doi: 10.1109/ITEC.2018.8450163
2. Veda Galigekere, Omer Onar, Et,. Al,. "Modeling, Design, and Experimental Verification of a WPT Level-3 Wireless Charger with Compact Secondary Coupler", Accepted for presentation at Applied Power Electronics Conference 2019.

References

1. https://www.eia.gov/energyexplained/?page=us_energy_home
2. https://www.energy.gov/sites/prod/files/2017/11/f39/EETT%20Roadmap%2010-27-17.pdf

I.6 Materials for Advanced Packaging (ORNL)

Andrew Wereszczak, Principal Investigator
Oak Ridge National Laboratory
1 Bethel Valley Road
Oak Ridge, Tennessee 37831
E-mail: wereszczakaa@ornl.gov

Susan Rogers, DOE Technology Development Manager
U.S. Department of Energy
E-mail: susan.rogers@ee.doe.gov

Start Date: October 1, 2017 End Date: September 30, 2018
Project Funding (FY18): $75,000 DOE share: $75,000 Non-DOE share: $0

Project Introduction

For power electronic (PE) devices, the potential use of sintered-silver (Ag) interconnection technology has several advantages over conventionally used solder-based interconnection technology (e.g., better electrical and thermal conductivities, higher temperature capability, microstructural equilibrium, better reliability, and RoHS compliance). But its adoption has been sluggish because it is a relatively new technology, its processing is sufficiently different from conventional solder processing, and the PE community is relatively conservative when it comes to using new processing technologies. This effort seeks to hasten the more confident adoption of sintered-Ag by developing more economical ways to process it without compromise to overall mechanical reliability.

Objectives

Advanced sintered-Ag interconnect technology to enable a 200°C-capable, low-cost, and reliable electronic package with at least a 15-year life. This is relevant because contemporary PE devices cannot operate at 200°C because most conventional interconnect materials (solders) are in nonequilibrium above 150°C.

Approach

- Advance the processing and mechanical reliability of sintered-Ag for PE devices.
- Promote using common reflow oven technology for pressurelessly sintering Ag interconnects.
- Ultimately promote 200°C PE device operation.
- Interact with academia and material suppliers for project support.
- Disseminate results and interpretations to the open literature.

Results

Contact Drying of Sintered-Silver Interconnects

Drying, a crucial pre-sintering step for sinterable-Ag interconnect processing, can be done via open-face contact heating, as shown in this study. Such contact heating or contact drying is advocated for several reasons. Contact drying enables good paste-wetting with both mated surfaces, the avoidance of pressure assistance during later sintering, large-area bonding, a decrease in overall processing time, efficient and complete removal of paste solvents, and minimization of the number of printing defects. It also can be implemented in mass production of PE devices having sintered-Ag interconnects. The combination of contact drying attributes is arguably more attractive than those of presently prescribed (noncontact) drying methods used for sinterable-Ag interconnects.

Strong interconnects resulted from sintered-Ag interconnects processed using open-face contact drying. The use of contact drying followed by pressureless sintering resulted in good shear failure resistance, and it

produced equivalent microstructures in the sintered-Ag interconnect layer (and presumably equivalent electrical, thermal, and elastic responses).

Details are provided in A. A. Wereszczak, M. C. Modugno, B. R. Chen, and W. M. Carty, "Contact Drying of Printed Sinterable-Silver Paste," *IEEE Transactions on Components, Packaging and Manufacturing Technology* 7, 2079–86 (2017). doi: 10.1109/TCPMT.2017.2752140.

Reflow Oven Processing of Sintered-Silver Interconnects

High shear strengths (greater than 40 MPa) of pressureless sintered-Ag interconnects were produced using conventional reflow oven technology in ambient air. This was enabled through the use of contact drying of the wet, printed Ag paste before it was sintered. The combination of contact drying and reflow oven sintering yielded a desirable narrow distribution of sintered-Ag interconnect shear strengths, as illustrated by a relatively high Weibull modulus and low standard deviation.

The successful adaptation of using a standard reflow oven for fabricating pressureless sintered-Ag interconnects shows that a commonly available mass production technology can be used to consistently fabricate sintered-Ag interconnects with high strength. Additionally, reflow oven sintering enabled continuous production, unlike batch-limiting sintering production using a static convective oven.

Details are provided in A. A. Wereszczak, B. R. Chen, and B. A. Oistad, "Reflow-Oven-Processing of Pressureless Sintered-Silver Interconnects," *Journal of Materials Processing Technology* 255, 500–506 (2018). doi: 10.1016/j.jmatprotec.2018.01.001.

Silver Platings and Sintered-Silver Interconnects

Large-value (>55 MPa) characteristic shear failure stresses of ambient air–processed sintered-Ag interconnects were achieved with the use of electrolytic, sputter-coated, and electroless Ag platings. The weakest failure stress in any of the sets exceeded 40 MPa. The characteristic maximum shear failure stress of all these Ag-plating sintered-Ag interconnect systems was larger than the investigated gold-plated sintered-Ag interconnects.

The logic of the use of noble metal plating in ambient air–processed sintered-Ag interconnect systems was well illustrated by their interconnect systems having shear failure stresses larger than those in an interconnect system employing no plating. The Ag-plated and the gold-plated interconnect systems were about 2× and 1.3× stronger, respectively, than the interconnect system without plating.

Details are provided in A. A. Wereszczak, B. R. Chen, B. A. Oistad, S. B. Waters, and A. T. Mayville, "Failure Stress Comparison of Different Pairings of Ag-Plating and Reflow-Oven-Processed Pressurelessly-Sintered-Ag Interconnects," in press, *Journal of Materials Science: Materials in Electronics* (2018).

Double-Sided Silver-Sintering

Strengths greater than 40 MPa can be achieved with double-sided pressureless-sintered-silver interconnects fabricated with reflow oven processing. Those high strengths are a consequence of careful processing that includes contact-drying followed by reflow oven processing methods developed at ORNL during the last few years.

Details are provided in A. A. Wereszczak, B. R. Chen, O. M. Jadaan, and B. A. Oistad, *Double-Sided Pressureless-Sintered Silver Interconnects Fabricated by Reflow-Oven-Processing*, in internal review, ORNL/TM-2018/1048, November 2018.

Cantilever Testing of Sintered-Silver Interconnects

Uniaxial cantilever loading of a pillar subjects its interconnect, metallization layer, and bonded joint to a superimposition of flexure and shear stresses. The magnitudes of the flexure-induced tensile or compressive stresses and the shear stresses are functions of the interconnect depth and thickness, the test height of the pillar

at which the cantilever force is applied (or the distance from the interconnect plane), and the Poisson's ratio, in the case of the shear stress.

The magnitude of the axial tensile stress in the interconnect was greater than the in-plane shear stress for cantilever loading. For any applied cantilever force, the applied maximum shear stress on the interconnect was independent of test height, L, whereas tensile stress increased with it; therefore, the ratio of the maximum tensile stress to maximum shear stress increased with test height L.

Details are provided in A. A. Wereszczak, B. R. Chen, O. M. Jadaan, B. A. Oistad, M. C. Modugno, J. W. Sharp, and J. R. Salvador, "Cantilever Testing of Sintered-Silver Interconnects," *Journal of Materials Science: Materials in Electronics* 29, 1530–1541 (2018). doi: 10.1007/s10854-017-8063-3.

Fracture Toughness of Sintered-Silver Interconnects

Pressureless sintered-Ag interconnects had an average apparent fracture toughness of about 1.5 ± 0.2 MPa√m at 25°C. Failure appears to have occurred at the interface between the sintered-Ag and the Ag plating on the direct-bonded carbon substrates. Automated and more optimized processing and the use of a different plating strategy (to promote better adherence to sintered-Ag), would likely increase the measured apparent fracture toughness.

The test method employed enabled valid estimation of the apparent fracture toughness of a sintered-Ag interconnect system. The claimed validity was based on demonstrated (100%) achievement of the prerequisite stable crack growth needed for fracture toughness testing as described in standardized testing of monolithic materials (i.e., ASTM C1421, E304, and E399 test standards). The analysis using work-of-fracture represented a simple approach, and the printing of sinterable Ag directly onto relevant plated substrates enabled the study of crack growth resistance in a representative and entire interconnect system. Three-point-bending of chevron-shaped interconnects desirably minimized the introduction of machine and fixture compliance and maximized the likelihood that cracking was stably initiated and propagated. Because of this test robustness, changes or trends in apparent fracture toughness from processing imperfections, non-automation, or dissimilarity in plating technologies were interpretable without complications or false positives introduced by testing-induced parasitics.

The described method offers a simple, defendable means of interpreting the resistance to crack growth and delamination for sintered-Ag interconnects, resulting in the ability to monitor the effects of processing conditions and ultimately optimize them.

Details are provided in A. A. Wereszczak, M. C. Modugno, B. R. Chen, and B. A. Oistad, *Apparent Mode I Fracture Toughness of Pressureless Sintered-Silver Interconnects*, ORNL/TM-2018/1, June 2018.

Conclusions

- Strong interconnects result from sintered-Ag interconnects processed using open-face contact drying.
- High shear strengths of pressureless sintered-Ag interconnects were produced using conventional reflow oven technologies in ambient air.
- High shear strengths of ambient air–processed sintered-Ag interconnects were achieved with the use of electrolytic, sputter-coated, and electroless Ag platings.
- Double-sided sintered-silver interconnects were processed and exhibited strength.
- A cantilever test method was developed to quantify the superimposed shear strength and tensile strength of sintered-Ag interconnects.
- A fracture toughness method was developed that offers a simple, defendable means of interpreting the resistance to crack growth and delamination for sintered-Ag interconnects, resulting in the ability to monitor the effects of processing conditions and ultimately optimize them.

Key Publications

1. A. A. Wereszczak, M. C. Modugno, B. R. Chen, and W. M. Carty, "Contact Drying of Printed Sinterable-Silver Paste," *IEEE Transactions on Components, Packaging and Manufacturing Technology* 7, 2079–86 (2017). doi: 10.1109/TCPMT.2017.2752140.
2. A. A. Wereszczak, B. R. Chen, and B. A. Oistad, "Reflow-Oven-Processing of Pressureless Sintered-Silver Interconnects," *Journal of Materials Processing Technology* 255, 500–506 (2018). doi: 10.1016/j.jmatprotec.2018.01.001.
3. A. A. Wereszczak, B. R. Chen, B. A. Oistad, S. B. Waters, and A. T. Mayville, "Failure Stress Comparison of Different Pairings of Ag-Plating and Reflow-Oven-Processed Pressurelessly-Sintered-Ag Interconnects," in press, *Journal of Materials Science: Materials in Electronics* (2018).
4. A. A. Wereszczak, B. R. Chen, O. M. Jadaan, and B. A. Oistad, *Double-Sided Pressureless-Sintered Silver Interconnects Fabricated by Reflow-Oven-Processing*, in internal review, ORNL/TM-2018/1048, November 2018.
5. A. A. Wereszczak, B. R. Chen, O. M. Jadaan, B. A. Oistad, M. C. Modugno, J. W. Sharp, and J. R. Salvador, "Cantilever Testing of Sintered-Silver Interconnects," *Journal of Materials Science: Materials in Electronics* 29, 1530–1541 (2018). doi: 10.1007/s10854-017-8063-3.
6. A. A. Wereszczak, M. C. Modugno, B. R. Chen, and B. A. Oistad, *Apparent Mode I Fracture Toughness of Pressureless Sintered-Silver Interconnects*, ORNL/TM-2018/1, June 2018.

Acknowledgements

This work is supported by the DOE Office of Energy Efficiency and Renewable Energy, Vehicle Technologies Office, under contract number DE-AC05-00OR22725. The author wishes to thank project team members: M. Chinthavali, B. Chen, B. Oistad, S. Waters, A. Mayville, M. Modugno, O. Jadaan, J. Sharp, J. Salvador, and W. Carty. Finally, the following are thanked for their various contributions: ORNL's A. Malin, R. Wiles, K. Jones, S. Campbell, R. Parten, and M. Lance.

I.7 Non-Rare-Earth Electric Motors (ORNL)

Tsarafidy Raminosoa, Principal Investigator
Oak Ridge National Laboratory
1 Bethel Valley Road
Oak Ridge, Tennessee 37831
E-mail: raminosoat@ornl.gov

Susan Rogers, DOE Technology Development Manager
U.S. Department of Energy
E-mail: susan.rogers@ee.doe.gov

Start Date: October 1, 2017 End Date: September 30, 2018
Project Funding (FY18): $650,000 DOE share: $650,000 Non-DOE share: $0

Project Introduction

The objective of this project is to enable the use of non-rare-earth traction motors and analyze the impact of new advanced materials on non-rare-earth electric motors. First, a novel rotary-transformer-based, contact-less rotor excitation system for wound rotor synchronous motors (WRSM) is presented. The proposed transformer topology significantly reduces leakage inductances, provides a better coupling factor, and significantly improves power transfer capability compared with traditional topologies as a result of its interleaved windings and resonant compensation circuits. The proposed transformer also features a non-ferrite rotating part made of lightweight, strong, nonconductive, and nonmagnetic composite material and a large air gap, allowing safe operation at high rotational speeds. Hence, this rotary transformer can enable the adoption of WRSMs for electric or hybrid vehicle traction. The performance of the proposed topology was evaluated and compared with that of a conventional rotary transformer topology. Significant performance improvement was confirmed. Second, the impact of ultra-conductive copper (UCC) winding on the power density and efficiency of traction motors is investigated. Finally, a novel demagnetization-resistant rotor design using Aluminum Nickel Cobalt (AlNiCo) permanent magnet material is proposed.

Objectives

- Evaluate a rotary transformer for contact-less power transfer to rotor excitation of WRSMs.
- Investigate the impact of UCC windings on the power density and efficiency of traction motors.
- Design an electric motor that takes advantage of the best properties of AlNiCo permanent magnets developed by Ames Laboratory

Approach

This project considers two non-rare-earth electric motors for traction: WRSM and AlNiCo PM motor. The WRSM is a non-permanent magnet option, hence it is very cost-effective and can help achieve the 30% cost reduction DOE ELT target for 2025. The project solves the reliability issue of the rotor excitation by proposing a contact-less rotor excitation system based on a novel rotary transformer technology. The high reliability of the rotary transformer and the WRSM will contribute to the achievement of the DOE ELT 2025 life expectancy target of 300,000 miles. Besides, PM motors using AlNiCo magnets are another cost-effective non-rare earth option. AlNiCo is a low-cost permanent magnet alternative that can help achieve the DOE ELT 2025 $3.30/kW cost target. Moreover, AlNiCo has the best high-temperature resistance among permanent magnet materials, which can help improve the reliability of traction electric motors and achieve the DOE ELT 2025 300,000 mile lifetime target. However, AlNiCo magnets have low coercivity, thus, they are prone to demagnetization. The main design challenge for AlNiCo PM motors is resistance to demagnetization. The project solves this challenge by proposing a novel demagnetization-resistant AlNiCo rotor design. Finally, the project analyzes the impact of using newly developed UCC as winding conductor on the power density and performance of non-rare-earth traction electric motors. This high-electrical-conductivity composite conductor

based on carbon nanotubes (CNTs) and copper can help reduce the winding losses, improve the motor efficiency, and increase the power density to meet the DOE ELT target of 50kW/L.

Results

Rotary-transformer-based, Contact-less Excitation System to Enable Wound Rotor Synchronous Motor for Traction Applications

The wound rotor synchronous motor (WRSM) is a very attractive non-permanent magnet (non-rare-earth) electric motor option that has one of the best torque/power densities compared with other machine topologies [1]. The major barrier to the adoption of WRSMs for electric vehicle traction is the rotor excitation, which has traditionally required a slip-ring and brush system. Slip-rings and brushes constitute a major reliability issue because they wear due to mechanical friction and produce dust that contaminates the transmission oil used for cooling the motor as well as the motor insulation. These issues are aggravated by the high-speed operation (up to 16,000 rpm) of traction motors. Hence, slip-rings and brushes have a limited lifetime and require frequent maintenance. They also pose a safety risk due to possible sparking.

Rotary transformers allow contact-less power transfer to rotating parts of a system [2], [3], including the rotor windings of electric machines [4], [5], [6]. This technology has the potential to enable very cost-effective non-permanent-magnet electric machines like WRSMs to be used in traction applications. This is done by replacing the slip-ring and brush system traditionally used to power the rotor winding with a rotary transformer and a rotating rectifier. A conceptual design of a rotary transformer and rotating rectifier inside a WRSM is presented in Figure I.7.1.

This project proposes a novel rotary transformer topology to solve the rotor excitation problem of WRSM traction motors (Figure I.7.2). The proposed rotary transformer technology has significantly better power transfer capability and imposes significantly less centrifugal mechanical stress on the rotating part compared with conventional and current state-of-the-art counterparts. As shown in Figure I.7.2, it features:

- Interleaved windings, which allow a significant (4×) reduction in leakage inductances and an improved coupling factor
- Composite nonmagnetic and nonconductive structural support for rotor winding, which leads to a lightweight rotor and low rotor centrifugal stress
- A large mechanical air gap, which eliminates the manufacturing tolerance limitation and allows safe high-speed operation

The increase in air gap length is offset by the reduced leakage inductances and improved coupling factor, as well as the resonant compensation circuit. A resonant compensation circuit can be used to significantly increase the power transfer capability of the proposed rotary transformer, enabling a more compact rotary transformer design for ease of integration into the WRSM. The physical size of the resonant capacitors and the associated potential integration challenges are offset by the 2× reduction in volume of the rotary transformer (Figure I.7.3).

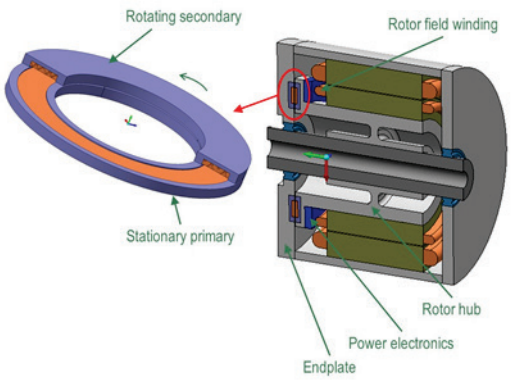

Figure I.7.1 Integration concept of a rotary transformer inside a wound rotor synchronous motor.

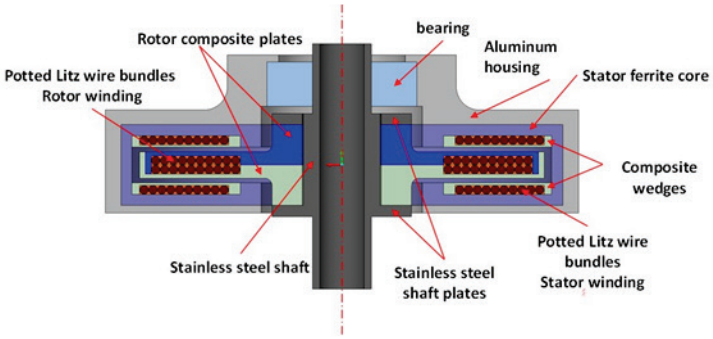

Figure I.7.2 Proposed rotary transformer topology.

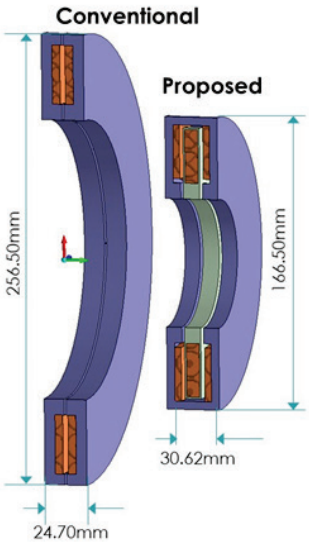

10kW designs	Conventional	Proposed
Airgap	• Small (1 mm) • Requires tight control of airgap tolerance (precision manufacturing)	• Large (1.5 mm) • Eliminates airgap tolerance constraints and allow high speed operation
Rotor material	• Ferrite • Heavy and brittle. • High centrifugal stress and retention issue at high speed • Core loss in rotor	• Composite • Lightweight and mechanically strong • Low centrifugal stress at high speed • Non-conductive, thus no core loss in rotor
Volume (dm^3)	**1.28**	**0.67**

- **1.9X lower volume.**
- **Non-conductive and non-magnetic composite rotor support to avoid core loss and minimize centrifugal stress.**

Figure I.7.3 Attributes and size of the proposed vs. conventional rotary transformers for 10 kW output power.

To better explore the design space, a computational program code that models the rotary transformer system for any combination of geometry parameters and any operating conditions is essential. The program uses a coupled transient electromagnetic finite-element model and an electrical circuit model, including resonant compensation circuits and a rectifier. The inputs to the program are the rotary transformer's geometry parameters and operating conditions, and the outputs are mutual, self, and leakage inductances, coupling factor, compensation capacitors, output power, loss, and efficiency.

With a given outer diameter and a rotor field winding resistance of 25 Ω, the dimensions of the winding windows and the thickness and inner diameter of the ferrite core were optimized to reach an output power of 10 kW while minimizing the axial length, maximizing the rotary transformer efficiency, and keeping the magnetic loading in the ferrite core at reasonable saturation level (below 0.38T for the ferrite material used). Also, given the high top speed for traction applications (up to 16,000 rpm), several iterations were conducted between the electromagnetic design and mechanical design until a mechanically viable design with satisfactory electromagnetic performance was reached.

The final optimized design is presented in Figure I.7.4. Electrical parameters are needed to calculate the primary and secondary resonant compensation capacitors and were taken from open-circuit and short-circuit finite-element simulations. Figure I.7.4 also presents the electrical parameters, the resonant capacitors, and the rotary transformer's performance. The design is capable of transferring 11.3 kW with an electromagnetic

efficiency of 97%. The final design uses 5X3/28/38 Litz wire based on AWG38 strands to minimize AC loss at the operating frequency of 20 kHz. The layout of Litz wire bundles is also shown in Figure I.7.4. Both the rotor and stator windings have two parallel circuits. The magnetic loading of the final design is also presented in Figure I.7.4. The highest flux density in the ferrite core is 0.37T.

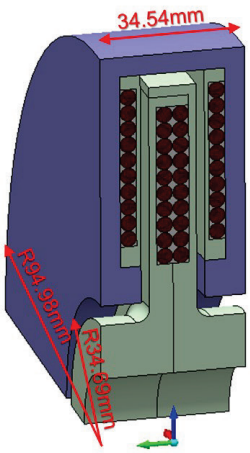

Parameters	
Primary self inductance (mH)	0.066
Primary compensation capacitor (μF)	0.963
Secondary self inductance (mH)	0.055
Secondary compensation capacitor (μF)	1.143
Coupling factor	0.956
Mutual inductance (mH)	0.058
Total leakage inductance (μH)	5.804
Performance	
Frequency (Hz)	20000
Source voltage (Vrms)	162.07
Source current (Arms)	74.29
Input power factor	0.97
Average output power (W)	11363.39
RMS load voltage (V)	533.00
RMS load current (A)	21.32
Eff%	96.97

Copper Loss (W)	**75.50**
Iron Loss (W)	**18.59**
Eddy Current Loss (W)	**260.71**
Total Loss (W)	**354.80**

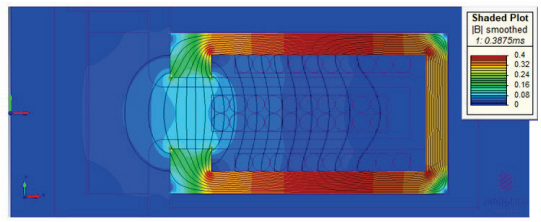

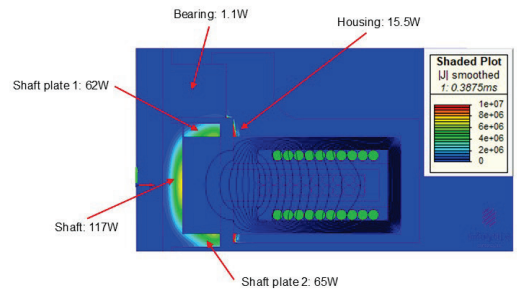

Figure I.7.4 Final optimized design: geometry, dimensions, and performance.

The fringing high-frequency magnetic field in the inner area of the rotary transformer induces eddy currents in the surrounding metallic parts of the assembly, including the housing, bearing, shaft plates, and shaft, as shown in Figure I.7.4. These eddy current losses were considered during the design process and were key in determining the inner radius of the ferrite core. The losses in the bearing and housing are very low and are not likely to produce any overheating. The losses in the shaft and shaft plates are more important and may require active cooling. Figure I.7.4 also summarizes the loss breakdown.

Because traction motors can operate at speeds up to 16,000 rpm, mechanical stress analysis is a critical part of the design process to ensure that:

- The composite rotor support material does not break due to centrifugal stress at high speed
- Any deformation of the composite rotor support material does not present any risk of rubbing between the rotor and stator
- The shaft does not break under the centrifugal stress applied by the rotor weight at high rotational speed

The rotor assembly and shaft were designed for safe operation at 16,000rpm. Several iterations of mechanical stress analyses are conducted at 20,000 rpm to accommodate a 25% overspeed margin. The mechanical stress in the rotor composite plates and the shaft of the final assembly design was evaluated at 20,000 rpm, as shown in Figure I.7.5. The stresses in the shaft and in the composite materials are below 86 Mpa and are much lower than the tensile strength of the composite material (255 MPa) and stainless steel.

The displacement was also evaluated and is presented in Figure I.7.5. A maximum displacement of 0.26 mm is shown on the outermost surfaces of the rotor composite plates and is very small compared with the mechanical air gap of 2 mm chosen in the final design; hence, there is no risk of rubbing between rotor and stator at top speed.

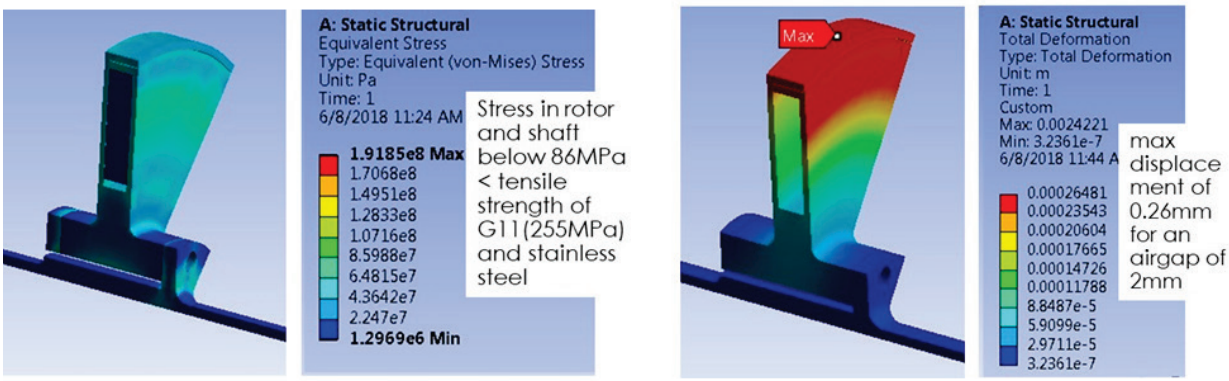

Figure I.7.5 Mechanical stress and total displacement in rotor at 20,000 rpm (25% margin from top speed of 16,000 rpm).

Rotary transformer prototypes and a test bench were designed to serve as a proof of concept for the proposed novel rotary transformer and to confirm that it is capable of transferring power to the field winding of a WRSM when the rotor is spinning at speeds up to 16,000 rpm. The field winding is emulated with a resistive-inductive load. Because the field winding inductance is high (estimated to be over 1 H), its size and weight are significant. Hence, physically spinning the load at very high speed would involve significant mechanical challenges and complicate the design of the test bench. For this reason, it was decided to mount two identical rotary transformers on the same shaft and connect their rotor windings through rotating connections inside the shaft, making it possible to use a stationary resistive-inductive load. A diagram of a test setup design is shown in Figure I.7.6.

The rotary transformer prototypes and the test bench were built and tested. Figure I.7.7 shows the assembled rotary transformer prototypes. The inductances of the stator and rotor windings of the two rotary transformer prototypes were measured and found to be in good agreement with the calculated values, as shown in Figure I.7.8. The slightly higher measured stator self-inductances are due to the leakage inductances of the leads. Also, the parameters measured on the two rotary transformers are consistent.

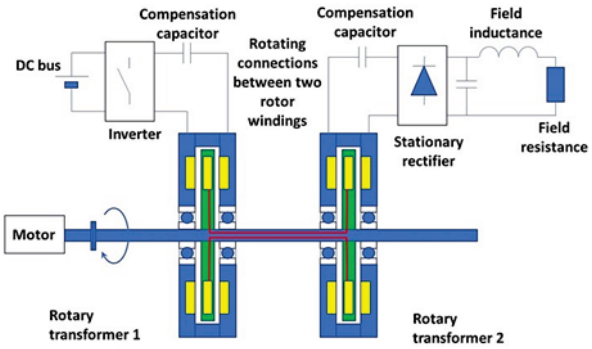

Figure I.7.6 Proof-of-concept prototype test bench design.

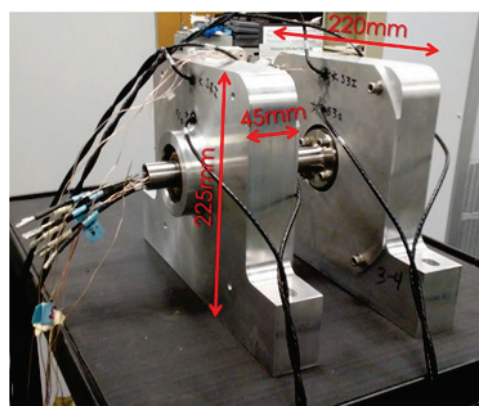

Figure I.7.7 Assembled rotary transformer prototypes.

	Calculation	Measured on Rotary Transformer 1	Measured on Rotary Transformer 2
Stator Self Inductance (uH)	66	70.5	70.4
Rotor Self Inductance (uH)	55	55.5	55.6

- Inductances are in good agreement with calculation;
- Slightly higher measured stator self inductances are due to the leads;
- Parameters measured on the two rotary transformers are consistent.

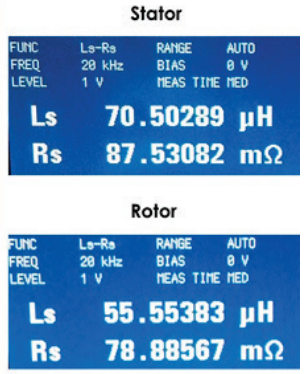

Figure I.7.8 Inductances of rotary transformer prototypes.

Finally, Figure I.7.9 shows the power transfer test results: 10.7 kW was transferred through the two rotary transformers with an efficiency of 95.9% and an input power factor of 0.91. This confirmed that the rotary transformers were able to transfer the 10 kW power they were designed for.

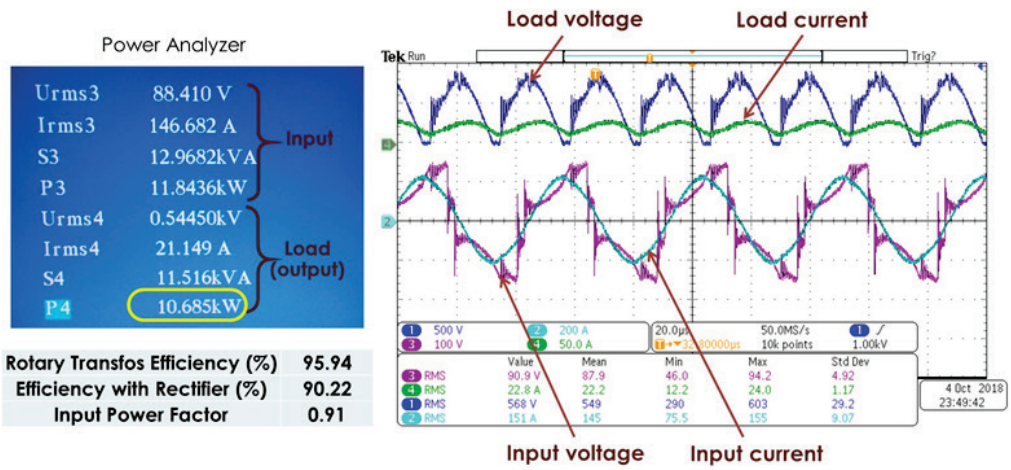

Figure I.7.9 The 10.7 kW power transfer test results.

Impact of Ultra-conductive Copper on Traction Motor Power Density and Efficiency

The aim of this study is to investigate the impact of using UCC as a winding conductor on the power density and efficiency of traction motors. UCC is a composite conductor based on copper with a CNT coating to enhance electrical conductivity, compared with conventional copper [7]. A comparison of measured electrical conductivities on UCC and conventional copper foil samples is given in Figure I.7.10. Using UCC as the conductor for the electric motor winding can help reduce the winding loss, improve the motor efficiency, and increase the power density to meet the DOE ELT target of 50 kW/L.

Two WRSMs with foil windings in both rotor and stator were designed. The first design uses conventional copper foil and served as a baseline; the second design uses CNT-coated copper foil. The motors were designed to produce a continuous power of 100 kW (i.e., torque of 201 Nm at base speed of 4750 rpm). Both motors have 72 slots and 12 poles and have the same outer diameter of 242 mm and cross section. The motors were designed to have the same efficiency, and their mass and volume were compared. The performance of the designed motors with UCC and conventional copper are shown in Figure I.7.11. For the same power and same efficiency, the current UCC samples gave a 6% reduction in mass and 7% reduction in volume.

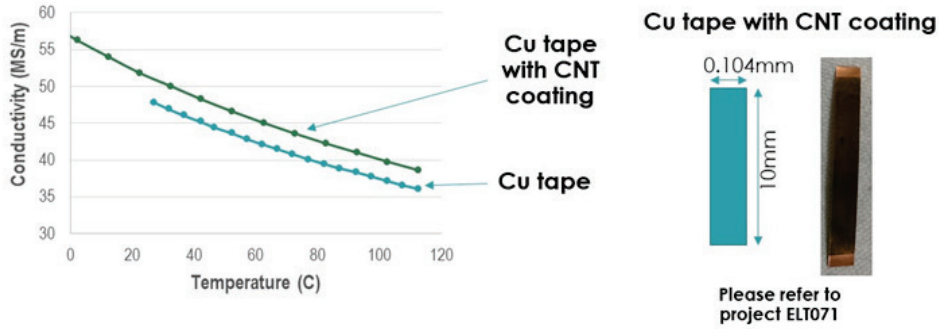

Temperature (°C)	Reference Copper Conductivity (MS/m)	CNT/Cu Conductivity (MS/m)
150	32.60	34.89

Figure I.7.10 Conductivity of ultra-conductive copper vs. reference copper.

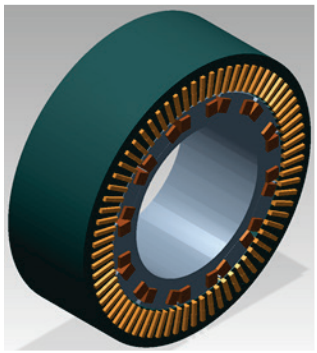

	Reference Copper	CNT/Cu
Outer diameter (mm)	242.00	242.00
Stack length (mm)	85.62	79.67
Total mass (kg)	22.07	20.71
Windings		
Stator slot fill factor (%)	56.00	56.00
Rotor slot fill factor (%)	66.93	66.93
Performance under continuous rated power		
Torque (N·m)	201.04	201.04
Output power (kW)	100.00	100.00
Efficiency (%)	92.97	92.99

Figure I.7.11 Size and weight comparison for ultra-conductive copper vs. copper winding 100 kW traction motor designs.

Novel Demagnetization-resistant AlNiCo Permanent Magnet Rotor Design for Traction Applications

AlNiCo is a low-cost and low-coercivity permanent magnet. Because of its low coercivity, it is extremely prone to demagnetization. Hence resistance to demagnetization is the major design challenge for AlNiCo traction motors. A demagnetization-resistant rotor design would enable this non-rare-earth low-cost magnet to be used in traction motors.

In this work, a novel AlNiCo permanent magnet rotor design resistant to demagnetization is proposed. The shape and dimensions of the permanent magnet blocks allow them to operate at the "approximately linear portion" of the recoil line (i.e., at a very high permeance coefficient) (Figure I.7.12). To assess the performance of the AlNiCo motor design, the BMW i3 traction motor was used as a baseline. An AlNiCo rotor that uses the stator of the BMW i3 was optimized to maximize torque and minimize torque loss by demagnetization. The design uses magnetic properties from measurements performed by Ames Laboratory on one of their AlNiCo samples. A parameterized computational code was used for the optimization of the rotor geometry.

Figure I.7.12 compares the back–electromotive force (EMF) and torque waveforms of the proposed demagnetization-resistant AlNiCo motor with the BMW i3 motor. The proposed AlNiCo motor has higher and much smoother back-EMF. It also has a much smoother torque. Hence, the AlNiCo motor does not need any skewing to reduce the slotting ripple. The BMW i3 motor has a higher torque because of an additional reluctance torque from the saliency of its rotor. However, without skewing, the torque ripple of the BMW i3 motor is high. Skewing is needed and used in the actual BMW i3 motor, and this will reduce the average torque of the actual motor.

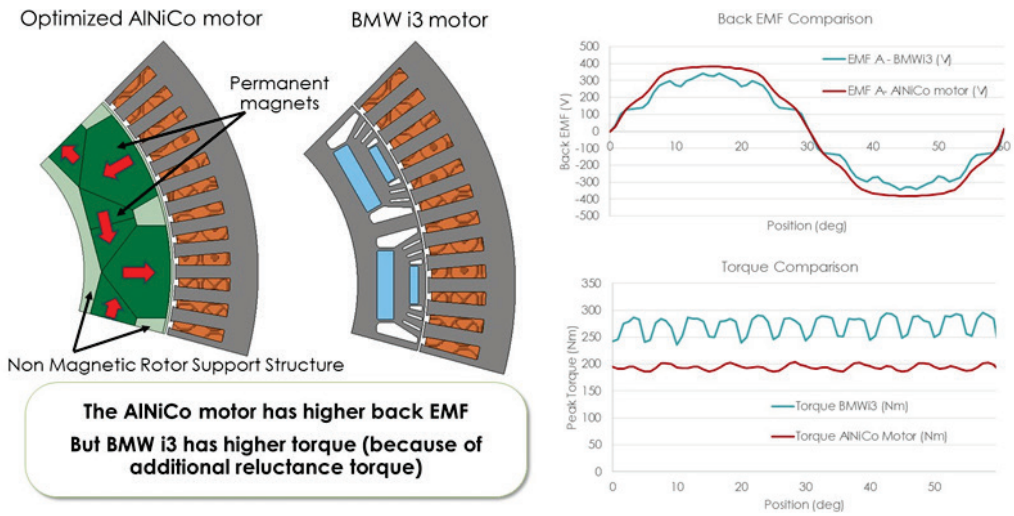

Figure I.7.12 Comparison of AlNiCo motor and BMW i3 motor.

To confirm the ability of the proposed AlNiCo rotor design to resist demagnetization, the design was subjected to the worst demagnetization scenario—a three-phase short circuit at the top speed of 16,000 rpm. The short-circuit fault was applied repetitively to determine if a demagnetized rotor would keep demagnetizing every time the fault was applied. The result is shown in Figure I.7.13: the AlNiCo rotor retained 75% of its magnetization and reached a stable magnetization state. No further reduction in back-EMF following the repeated faults was observed. This result confirms the viability of the proposed AlNiCo rotor design. It should be noted that a three-phase short circuit is an extreme fault, and its probability of happening is very low.

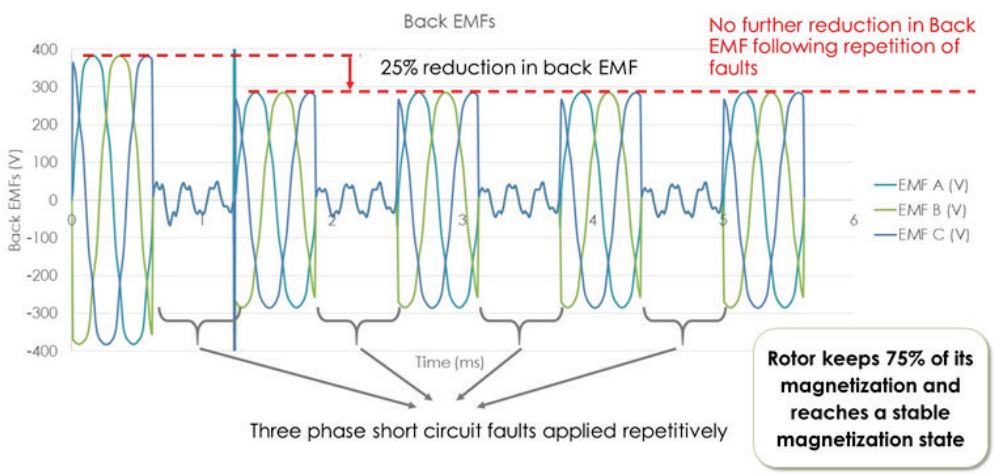

Figure I.7.13 Feasibility of the AlNiCo design under worst demagnetization scenario.

Then, the torque capability and demagnetization resistance of the proposed AlNiCo motor design as function of the overcurrent was compared with that of the BMW i3 motor. The overcurrent was applied as a purely negative Id (fully counteracting the PM excitation). The torque was calculated before and after the overcurrent was applied. The results are shown in Figure I.7.14. The torque losses by demagnetization were just slightly higher for the proposed AlNiCo rotor.

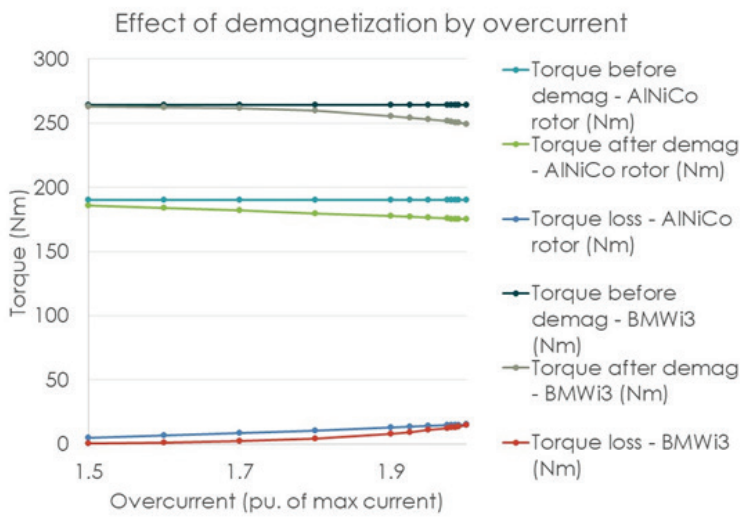

Figure I.7.14 Torque and demagnetization resistance comparison with BMW i3.

Conclusions

The proposed novel rotary transformer topology has one-fourth the leakage inductance of the baseline conventional design, as well as a better coupling factor despite the increase in magnetic air gap length. In addition, the power transfer capability of the innovative design is 2× higher compared with the conventional design because of a resonant compensation circuit. High-speed operation within a traction powertrain is enabled because of a large mechanical air gap and a strong, lightweight composite material used for the rotating part. This high-temperature material has the advantage of being nonmagnetic and nonconductive and was selected to avoid eddy current losses from the high-frequency magnetic field. Testing of a proof-of-concept prototype has confirmed a power transfer capability of 10.7 kW at 95.9% efficiency.

The impact of using UCC in the windings of wound rotor synchronous traction motors was investigated. For the same power and efficiency, the current UCC samples provide a 6% reduction in mass and 7% reduction in volume.

Finally, a novel demagnetization-resistant AlNiCo permanent magnet rotor design for a traction motor was proposed. The proposed design can enable low-cost and low-coercivity permanent magnet material such AlNiCo to be used in traction motors and remain competitive with rare-earth permanent magnet motors regarding torque density and resistance to demagnetization. The proposed design has the potential to significantly reduce traction motor cost while maintaining a power density similar to that of rare-earth permanent magnet motors.

Key Publications

1. Tsarafidy Raminosoa and Randy Wiles, “Contactless Rotor Excitation for Traction Motors,” presented at the *2018 IEEE Energy Conversion Congress and Exposition (ECCE 2018)*, Portland, Oregon, September 23–27, 2018.
2. Tsarafidy Raminosoa, “Non-Rare Earth Electric Motors,” presented at the *2018 VTO Annual Merit Review* (PUB ID 110363). Project ID: elt074.
3. Tsarafidy Raminosoa, “Contactless Rotor Excitation System,” invention disclosure. ID: 201704035; DOE S-NUMBER: S-138,700.
4. Tsarafidy Raminosoa, “Demagnetization Resistant Rotor for Low Coercivity Permanent Magnets,” invention disclosure. ID: 201804226; DOE S-NUMBER: S-138,897.

5. Tsarafidy Raminosoa, "Contactless Rotor Excitation System," provisional patent application filed, disclosure ID: 201704035; Application No.: 602/671037; date filed: 5/14/2018.
6. Tsarafidy Raminosoa, "Demagnetization Resistant Rotor for Low Coercivity Permanent Magnets," provisional patent application filed, disclosure ID: 201804226; Application No.: 62/748560; date filed: 10/22/2018.

References

1. Ayman El-Refaie, Tsarafidy Raminosoa, Patel Reddy, Steven Galioto, Di Pan, Kevin Grace, James Alexander, and Kum-Kang Huh, "Comparison of Traction Motors that Reduce or Eliminate Rare-earth Materials," *IET Electrical Systems in Transportation* 7(3), 207–214 (2017).
2. Ali Abdolkhani and Aiguo Patrick Hu, "A Novel Detached Magnetic Coupling Structure for Contactless Power Transfer," *IECON 2011—37th Annual Conference of the IEEE Industrial Electronics Society*, pp. 1103–1108.
3. Dominik Bortis, Lukas Fässler, Andreas Looser, and Johann W. Kolar, "Analysis of Rotary Transformer Concepts for High-speed Applications," *2013 Twenty-Eighth Annual IEEE Applied Power Electronics Conference and Exposition (APEC)*, pp. 3262–3269.
4. Constantin Stancu, Terence Ward, Khwaja M. Rahman, Robert Dawsey, and Peter Savagian, "Separately Excited Synchronous Motor with Rotary Transformer for Hybrid Vehicle Application," *IEEE Transactions on Industry Applications* 54(1), 223–232 (January–February 2018).
5. Enzo Michele Illiano, "Design of a Highly Efficient Brushless Current Excited Synchronous Motor for Automotive Purposes," PhD thesis, ETH Zurich. Available at https://doi.org/10.3929/ethz-a-010433793.
6. H. Krupp and A. Mertens, "Rotary Transformer Design for Brushless Electrically Excited Synchronous Machines," *2015 IEEE Vehicle Power and Propulsion Conference (VPPC)*, pp.1–6.
7. Tolga Aytug, "Ultra-Conducting Copper (UCC)," ELT071*, 2018 U.S. DOE Vehicle Technologies Office Annual Merit Review*, June 19, 2018.

Acknowledgments

This work is supported by the DOE Office of Energy Efficiency and Renewable Energy, Vehicle Technologies Office, under contract number DE-AC05-00OR22725. The author wishes to thank project team members: Randy Wiles and Jonathan Wilkins for the mechanical design and the fabrication of the proof-of-concept prototype and Omer Onar and Josiah Haruna for their help with the testing.

I.8 Ultra-Conducting Copper (ORNL)

Tolga Aytug, Principal Investigator
Oak Ridge National Laboratory
1 Bethel Valley Road
Oak Ridge, Tennessee 37831
E-mail: aytugt@ornl.gov

Susan A. Rogers, DOE Technology Development Manager
U.S. Department of Energy
E-mail: susan.rogers@ee.doe.gov

Start Date: October 1, 2017 End Date: September 30, 2018
Project Funding (FY18): $350,000 DOE share: $350,000 Non-DOE share: $0

Project Introduction

This project focuses on the design, study, and evaluation of scalable and high-throughput synthesis approaches and material technologies for the fabrication of a new class of high-performance copper (Cu) tape conductors (i.e., ultra-conductive copper [UCC] composites) that will have higher electrical (and possibly thermal) conductivity than pure Cu to increase the power density and higher-temperature operational reliability of electric motors while improving their overall efficiency. The new concepts and methods developed under this project are expected to help meet the DOE 2025 cost and performance targets for electric motors. After a decade of global research and development (R&D) efforts, the most promising UCC composites are composed of 1-dimnensional carbon nanotubes (CNTs) and Cu, but their room-temperature performance is inconsistent, and the synthetic methods are not scalable or reproducible. This project, by using scalable, cost-effective, and commercially viable processing methods, aims to demonstrate a novel technological platform to produce UCC conductors not only for electric motors but also for a broad range of components used in and for electric vehicles (e.g., bus bars, wireless charging platforms, charging cables).

The power losses associated with the electrical resistance of Cu adversely affect the efficiency and performance of all electric devices. Ballistic electrical transport in CNTs (i.e., the capability of charge carriers to travel over approximately 500 nm in nanotubes without scattering) is expected to improve the conductivity of the Cu matrix with additional CNT-enabled benefits, including low weight, flexibility, and better thermal management (Table I.8.1).

Table I.8.1 Comparison of the Properties of Single-Wall Cu vs. those of CNTs

	Cu	CNT
Electrical conductivity (MS/m)	59.6	100
Thermal conductivity (W/m-K)	400	4000
Current density (A/cm^2)	10^6	10^8

A few promising Cu-CNT composites with conductivities increased by 30% compared with the International Annealed Cu Standard have been demonstrated, but only on micrometer-long sample pieces [1], [2], [3], [4], [5]. Further improvements have been hampered by a poor fundamental understanding of the interactions between Cu and CNTs that affect bulk electrical and thermal transport properties. In addition, most of the present UCC processing strategies are unstable (leading to inconsistent results) and are limited to laboratory-scale operations, rendering them unsuitable for large-scale commercial development and production. The current approaches to making Cu-CNT composites include:

- Electrolytic processes, either to deposit a composite containing Cu ion and CNTs on a cathode or to form powders that may be consolidated later into usable wire forms;
- Die-casting, to metal forming, by mixing molten Cu with CNTs;
- Acoustically assisted coating, by which CNTs that are suspended in a fluid and agitated to deposit onto a central Cu wire;
- High-pressure laser chemical deposition with simultaneous laser-induced cladding with Cu; and
- A powder metallurgical approach using spark plasma sintering to form a Cu composite.

The main problems associated with these methods are: (1) the lack of controlled alignment of CNTs along the direction of the current flow, (2) the phase segregation of CNTs from the Cu during wire processing, and (3) the lack of fundamental understanding of how nanotube properties and CNT-Cu interfaces and interactions affect macroscale properties. Based on a theory-aided experimental approach, this project addresses these fundamental challenges so that UCCs with electrical conductivities exceeding that of pure Cu can be manufactured on a commercial scale.

Objectives

Cost and size are the key barriers to achieving the DOE ELT 2025 electric traction drive systems technical R&D targets. In the case of electric motors, reductions in volume and improvements in efficiency are limited in part by the electrical conductivity limitations of Cu windings. In addition, a stator with a Cu winding constitutes nearly 40% of the total motor cost. Therefore, the current R&D strategy to reduce cost involves the application of new materials with improved capabilities and performance in innovative motor designs [6].

The overall objective of this project is to design and develop a new class of high-performance conductors made from Cu wires and CNTs (i.e., conductors with high electrical and thermal conductivity) to increase the power density of electric motors while improving their overall efficiency. Specific R&D efforts in FY 2018 included (1) identification, development, and implementation of scalable approaches and material technologies for prototyping carbon nanomaterial–enabled UCC conductors; (2) theoretical modeling to understand metal-nanocarbon interface properties for optimized electronic/thermal transport characteristics; and (3) determination of how UCCs can improve the performance and power density of electric motors.

Approach

Our overall approach is to couple theoretical and experimental efforts to enable the design and scalable, reproducible fabrication of advanced composites that have electrical and thermal conductivity exceeding that of pure Cu and current Cu-CNT composites. To achieve this, two interrelated and equally important tasks are being pursued: (1) development of controllable processing techniques to enable scalable assembly of Cu-CNT multilayer composites and (2) theory-guided optimization for high-performance Cu-CNT multilayer composites. Figure I.8.1 schematically describes the process flow for producing UCC tapes, starting with formulation of stable CNT dispersions, deposition of aligned and uniform CNT coatings using solution-based commercially viable practices, homogeneous deposition of thin films of Cu overlayers onto CNT-coated tapes, and post-deposition thermal treatment to produce a multilayer Cu-CNT-Cu composite architectures.

The degree of nanotube alignment was analyzed by both scanning electron microscopy (SEM) and polarized confocal Raman spectroscopy, where the changes in the intensity of G and D bands are highest when nanotubes are parallel to the laser polarization direction. Cross-sectional microstructures of several samples were studied by Z-contrast scanning transmission electron microscopy (STEM). Specimen preparation was carried out by focused ion beam methods, and STEM images were recorded using a Nion UltraSTEM operating at 200 kV. The electrical conductivity of the new composites was characterized in a temperature range from 4 to 400 K using a physical property measurement system (PPMS) and at room temperature using a four-probe transport setup capable of measuring 7 cm long tapes.

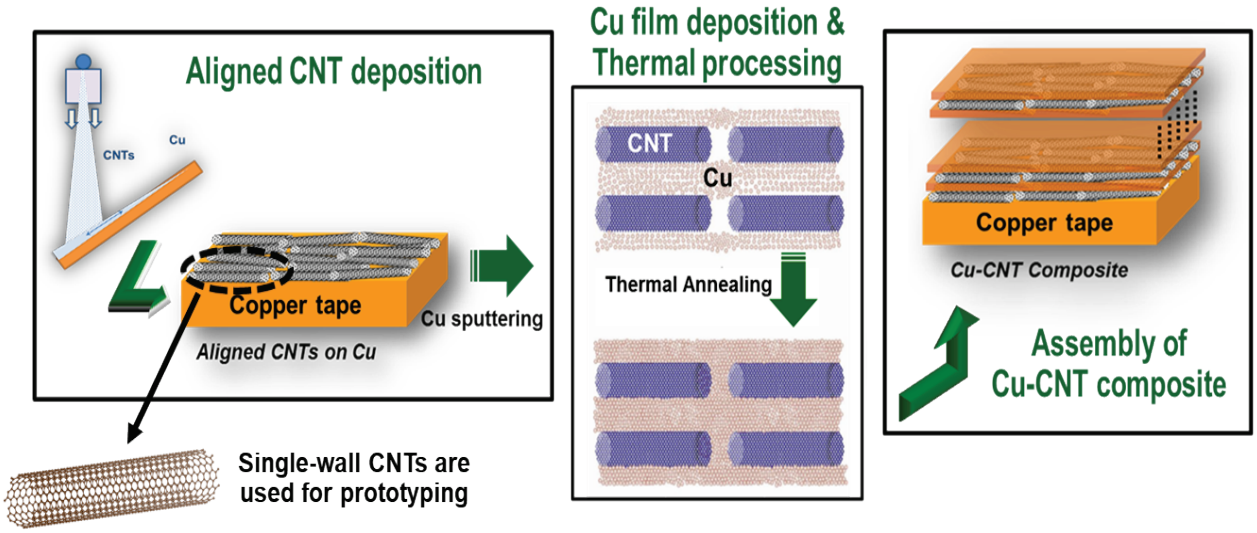

Figure I.8.1 Schematic illustration of the process flow for producing Cu-CNT-Cu multilayer composite tapes.

Results

Selection of Solvent, Surfactant, and CNT Type for the In-house Production of Stable CNT Dispersions

Understanding the dispersion behavior of CNTs in solvents is essential for the creation of stable dispersions; for the application of uniform, well-adhered CNT coatings on Cu tapes; and, more importantly, for the alignment of CNTs onto Cu tapes. A critical part of creating stable dispersions of CNTs is the selection of appropriate solvents and surfactants. After many trials of CNT dispersion formulations in various aqueous and organic surfactant-solvent systems, we identified the three best stable dispersion formulations for effective CNT deposition as mixtures of N, N-dimethylformamide (DMF) and a specially formulated commercial surfactant (AC); N-methyl-2-pyrrolidone (NMP) and AC; and methylethylketone (MEK) and AC, all of which have different boiling points and vapor pressures. Those two parameters are important because they dictate the time needed for effective shearing to occur for the alignment of the CNTs along the flow field direction. In fact, results from sonospray and air-blade–processed samples demonstrated that solvents having a higher boiling point and lower vapor pressure (e.g., NMP and DMF) yield uniform CNT coverage and alignment on

Cu, whereas a solvent having a lower boiling point and high vapor pressure (e.g., MEK) showed nonuniform coverage and no particular CNT alignment. This behavior was expected because quick solvent evaporation minimizes the extent of the shearing duration against the Cu substrate (Figure I.8.2).

The techniques identified in this study are expected to result in alignment of nanotubes with their axes parallel to the shear or flow-field direction induced between the droplets and the Cu substrate. In the case of sonospray, shear-induced alignment originated from shearing of the droplets containing CNTs against the inclined Cu surface. For the air-blade method, shearing was associated with the compressed air flow/jet from a beveled knife edge providing the maximum shear force to uniformly spread and align the CNTs along the horizontally positioned Cu tape. For the electrospinning approach, it was expected that droplet elongation during extrusion under the high voltage applied between the syringe and the rotating collector would result in alignment of the CNTs on the Cu collector.

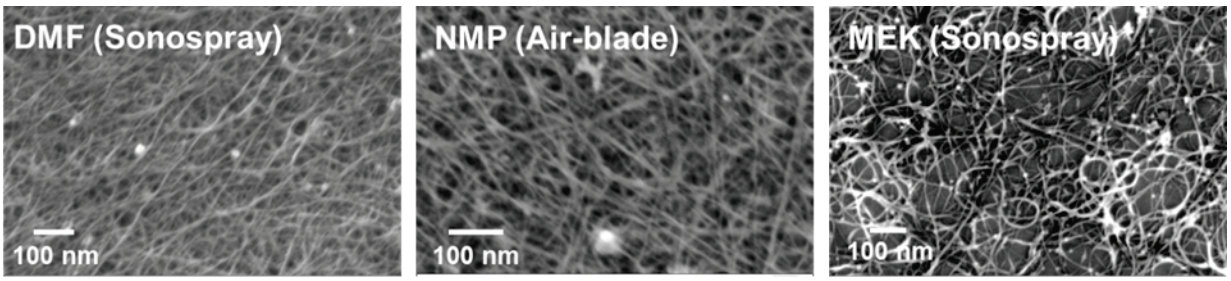

Figure I.8.2 Scanning electron microscopy images displaying the surface microstructure of CNT-coated Cu tapes using dispersions incorporating DMF, NMP, and MEK.

To create stable CNT dispersion in any solvent, appropriate surfactants must be used. In addition, to produce UCC conductors with the highest possible performance characteristics, both the organic solvent and the surfactant need to be removed (evaporated) from the CNT matrix. Hence, we used thermogravimetric analysis (TGA) to investigate the decomposition temperature and the time required for complete removal of the surfactant chemistry used to create stable dispersions in aqueous and organic solvents. Optimization of these two parameters (i.e., decomposition temperature and time) is crucial to remove both the unwanted organic solvent and polymer-based surfactant from the CNTs; otherwise, they may significantly degrade the electrical properties of the samples. TGA is a method of thermal analysis in which the mass of a sample is measured over time either as a function of increasing temperature, or isothermally as a function of time, which often allows quantitative composition analysis. Figure I.8.3 shows the weight loss as a function of time of the two commercial surfactants used in this study—AC (for organic dispersion) and AQ (for aqueous dispersion). Data for the AQ system reveal that a significant mass loss of approximately 55.6 weight (wt) % occurred during the initial isothermal stage below 100°C and a second minor weight loss occurred around 200°C, with a catastrophic weight loss accounting for roughly 38 wt % of the sample at 350°C. An inorganic residue of approximately 2.4 wt % remained after the temperature ramp. On the other hand (similar to data obtained for AQ), the AC sample showed a precipitous drop early on, attributable to the evaporation of the solvent, again below 100ºC. It accounted for more than 81% of the sample mass. After drying below 100ºC, the only subsequent weight loss was the catastrophic decomposition around 350°C, accounting for the remainder of the sample mass of approximately 18 wt %. No minor weight loss occurred at 200°C, in contrast to the AQ sample. An inorganic residue of only 0.11 wt % remained at the end of the temperature ramp.

More straightforward information is conveyed when one excludes the weight loss due to the solvent. A plot comparing the two samples is shown in the inset of Figure I.8.3, where the data are normalized to 100°C under the assumption that all mass loss below this temperature can be attributed to solvent evaporation. In our experiments, only single-wall CNTs (SWCNT) were used because of their high quality and purity compared with the multi-wall (MWCNT) counterparts. This is verified by conducting Raman and SEM analyses on both SWCNT- and MWCNT-coated Cu tapes (Figure I.8.4). Compared with the SWCNTs, the MWCNTs show a

high intensity D-band along with the G-band. The former is often referred to as the "disorder band" or the "defect band," and its intensity relative to that of the G-band is often used as a measure of nanotube quality. This result corroborates well with the SEM observations obtained for both samples (see inset). While the SWCNT-covered Cu tape was homogenously coated, with the CNTs demonstrating orientational harmony, the tape coated with MWCNT showed irregular and non-tubular flake-shapes, along with some unwanted particles on the Cu surface (inset SEM images).

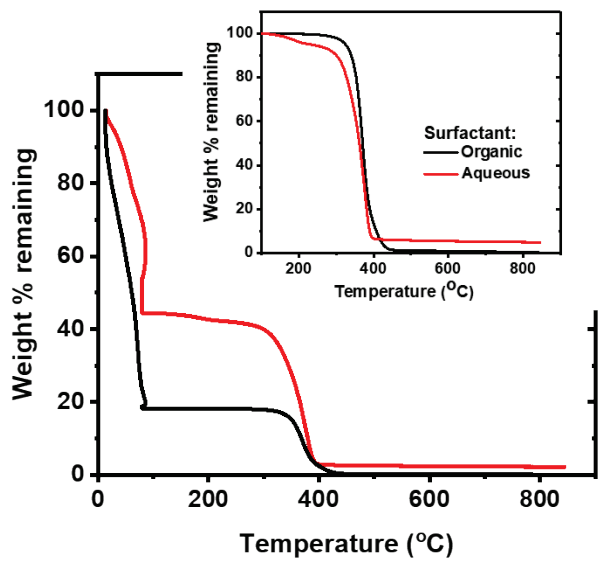

Figure I.8.3 Comparison of TGA results for mass loss versus temperature for AC and AQ. The inset shows the normalized data to 100°C.

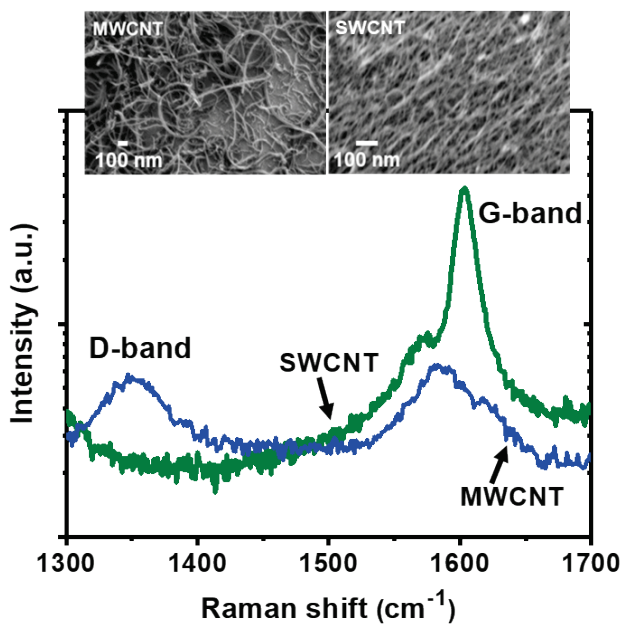

Figure I.8.4 Typical Raman spectra and scanning electron microscopy images of SWCNT and MWCNT coated Cu tapes.

Prototyping of Carbon Nanomaterial–enabled UCC Conductors

Because a large parameter space is needed for process optimization, we incorporated detailed theoretical modeling to support and speed up the experimental work. Since producing UCC multilayer composites involves depositing Cu overlayers on CNTs, followed by a heat treatment step, understanding the energetics and kinetics of Cu coatings on CNTs at the relevant experimental temperatures was imperative both to achieve a homogenous Cu coating on the CNT layers and to eliminate any current rendering defects in the Cu-CNT matrix. Classical molecular dynamics simulations determined that the coating thickness (controlled by the experimental deposition rate and flux) and the processing temperature are the two parameters key to achieving conformal Cu coverage over CNTs. Simulations also indicated the range of critical temperature (525°C<T< 875°C) above which Cu clustering is favorable independent of thickness. Figure I.8.5 shows snapshots of the simulation results for different thicknesses of Cu overlayers at 575°C and 850°C. The model assumed that CNTs were sandwiched between the Cu overlayers and the thick Cu substrate (left panels). Specifically, at relatively low temperatures around 500°C, very thin Cu coatings tend to ball up and form nanoclusters on top of the CNTs, whereas thick Cu coatings form large Cu crystals. If the coating thickness is adjusted to be somewhere in between, homogeneous Cu coverage is obtained. On the other hand, at temperatures exceeding 800°C, Cu clustering becomes inevitable for all thickness levels, and eventually the Cu evaporates from the CNT layers.

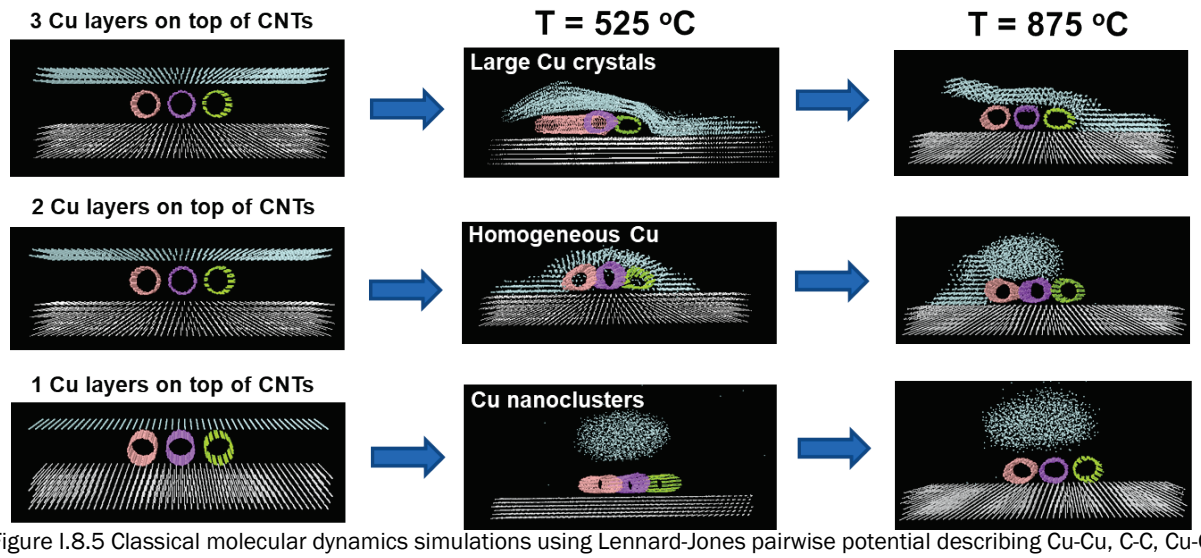

Figure I.8.5 Classical molecular dynamics simulations using Lennard-Jones pairwise potential describing Cu-Cu, C-C, Cu-C atomic interactions.

To validate this theory-guided approach with an experimental feedback loop, we conducted studies at relevant experimental conditions. We specifically investigated the influence of the Cu thin film overlayer thickness and post-deposition heat treatment conditions on the quality of the Cu coverage. As predicted by theoretical modeling, microstructural characterizations of Cu/CNT/Cu samples revealed also that the thickness of the metal overlayer and the post-annealing temperature both had a significant effect on the quality of the composite architecture. That is, if the metal overlayer was too thin (50 nm), it coalesced and formed a nonuniform discontinuous coating on the CNT surface. If it was much thicker (450 nm), it formed large grains with porous coverage after the heat treatment step at 400°C (Figure I.8.6, top left panel). Note that thicker films (bottom panels) tend to form larger grains than do thinner Cu films, resulting in coalescence into larger-grained structures with open pores between them after annealing. In probing the cross-sectional microstructure of such a porous film, it is noteworthy that the porosity was detrimental to the electrical properties of the UCC composites. The pores not only reduced the effective cross-sectional area for current transport but also acted as scattering centers for charge carriers (Figure I.8.7). On the other hand, thinner Cu films (150 nm) having smaller grain sizes yielded a more uniform, dense, homogeneous surface coverage over the CNTs (Figure I.8.6, middle panels). In contrast—supporting theoretical predictions—irrespective of the Cu film thickness,

we verified that relatively high processing temperatures (900°C) in a vacuum ambient triggered evaporation of the metal layer from the CNT surfaces (which was associated with the high vapor pressure of Cu at elevated temperatures). These results underscore the importance of theory-guided optimization of processing protocols and provisions to enable the design and reproducible performance of UCCs.

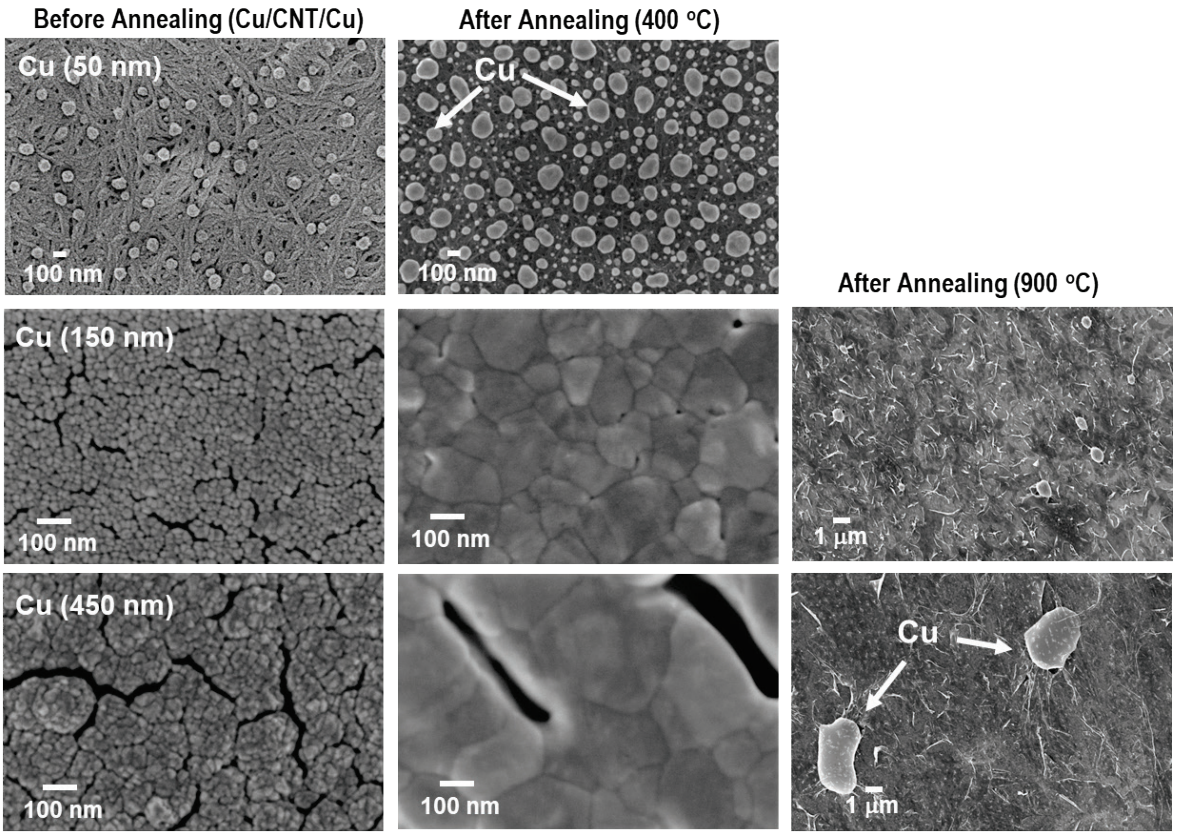

Figure I.8.6 Scanning electron microscopy images displaying the evolution of the surface microstructures of Cu/CNT/Cu tapes. Surface morphology of 50 nm (top panels), 150 nm (middle panels), and 450 nm (bottom panels) thick Cu-coated CNT/Cu tapes before and after heat treatments at 400 and 900°C. High-temperature annealing data for the 50 nm coating are not shown because the sample did not show uniform coverage at lower processing temperatures.

Using PPMS, the temperature-dependent electrical properties of single layer Cu/CNT/Cu samples processed at relatively optimized parameters are shown in Figure I.8.8. The data also include two hot-pressed Cu/CNT/Cu composites, for which the samples were pressed at 850°C and 5,000 pounds per square inch, under millitorr vacuum to enable improved electrical coupling between the Cu and CNT layers. The results showed that although the electrical resistivity for the Cu/CNT/Cu samples decreased by 5-8% compared with the reference pure Cu sample, the performance was degraded for the hot-pressed counterparts. The cause of the latter was most likely either contamination of the samples from ambient condition in the hot-pressing chamber, or damage to the CNT layers caused by the relatively high temperatures, or both.

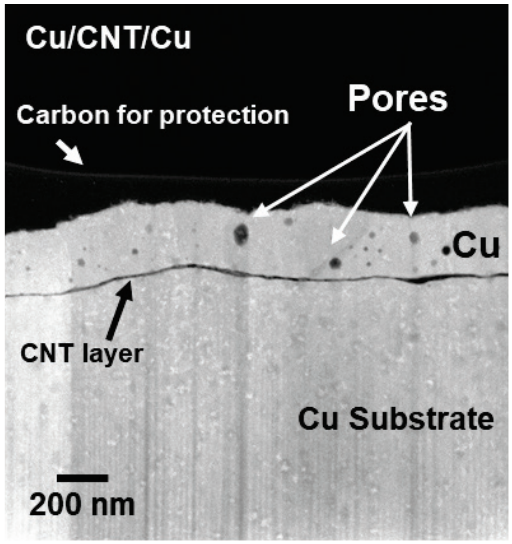

Figure I.8.7 Z-contrast transmission electron microscopy images of a Cu/CNT/Cu sample, where the Cu overlayer thickness is ~ 300 nm, illustrating the porous nature of the Cu film throughout its thickness.

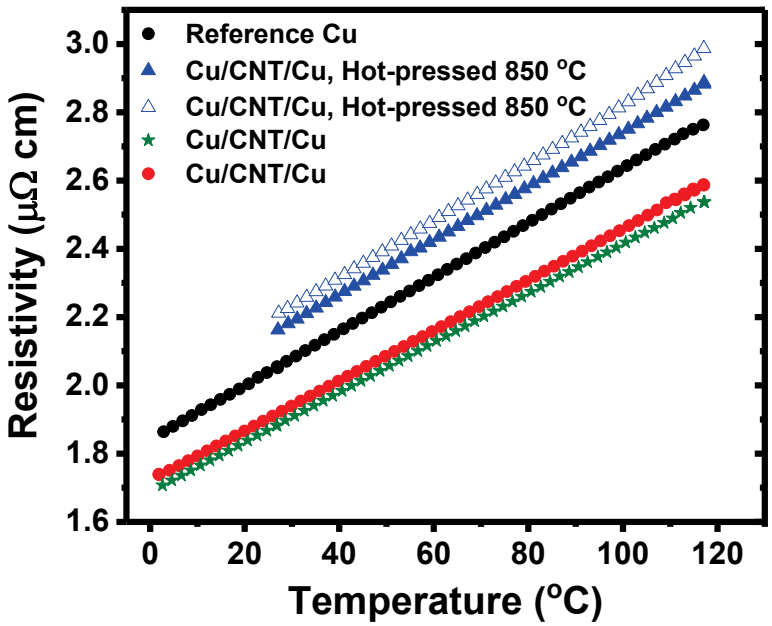

Figure I.8.8 Electrical performance of several Cu/CNT/Cu tapes as a function of temperature ranging from 0 to 120°C. Data for the reference uncoated Cu tape are also included for comparison.

Nevertheless, the improved conductivity of the pressed samples is particularly important for reliable and efficient operation of electric motors. Hence, we investigated the feasibility of using UCC composite tapes in wound rotor synchronous motors (WRSM). Two WRSMs with foil windings in both rotor and stator were designed [7]. The first design used a conventional Cu foil as a baseline reference; the second design included a UCC foil. The motors were designed to produce continuous power of 100 kW (i.e., torque of 201 Nm at a base speed of 4750 rpm). Both motors were designed to have the same efficiency, with 72 slots and 12 poles, the same outer diameter of 242 mm, and the same cross section. To obtain the most realistic fill factor, the

insulating wire coating thicknesses on the bars were included. The thickness of the coating was measured by the same method currently used for a round wire diameter of the same size as the bar thickness (0.0114 mm coating thickness for a bar thickness of 0.1 mm). A realistic slot liner thickness (0.51 mm) was also introduced, and the space taken by the insulation was accounted for in the fill factor that was used. Assuming a conductivity increase of 6% in the UCC, Table I.8.2 shows that the rectangular tape winding design enabled an ~6% reduction in the mass and an ~7% reduction in the volume of the motors incorporating UCC. These improvements were essential to reduce the winding loss, improve the motor efficiency, and increase the power density to meet the DOE ELT target of 50 kW/L by 2025.

Table I.8.2 Performance Comparison of WRSM Traction Motors with UCC against Baseline Conventional Copper. Inset: WRSM with Tape Windings in both Stator and Rotor

	Reference Cu	UCC
Outer diameter (mm)	242.00	242.00
Stack length (mm)	85.62	79.67
Mass		
Rotor core mass (kg)	5.90	5.49
Rotor coils mass (kg)	1.96	1.87
Stator core mass (kg)	9.93	9.24
Stator winding mass (kg)	4.28	4.12
Total	**22.07**	**20.71**
Stator slot fill factor (%)	56.00	56.00
Rotor slot fill factor (%)	66.93	66.93
Performance		
Torque (N·m)	201.04	201.04
Input power (kW)	107.57	107.54
Output power (kW)	**100.00**	**100.00**
Efficiency (%)	**92.97**	**92.99**
RMS phase voltage (V)	262.94	249.22
RMS phase current (A)	229.56	243.17
RMS current density (A/mm²)	17.92	18.98
Loss - Total (kW)	7.57	7.54

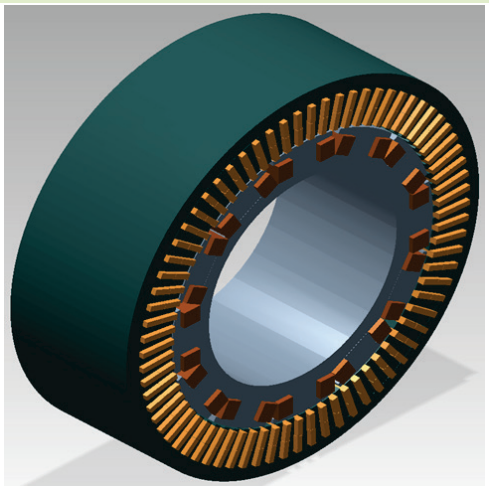

Conclusions

Advanced materials with higher electrical conductivity are needed to increase the power density and reduce costs while improving the performance and reliability of electric motors. Under this multiyear project, using scalable, cost-effective, and commercially viable processing methods, we demonstrated the feasibility of a novel materials/computational modeling platform that can facilitate the design and fabrication of advanced UCC materials for a broad range of industrial applications. The benefits that will be gained from this research can lead to high-efficiency, high-density, reduced-volume/-weight electric motors beyond the limits of what is achievable today. Specific accomplishments include: (1) identifying three scalable processing techniques for CNT deposition, as well as the types of solvent, surfactant, and CNTs needed to produce stable dispersions; (2) achieving CNT alignment using sonospray and air-blade techniques; (3) demonstrating that theoretical modeling can support experimental efforts; (4) establishing single-layer UCC prototypes and demonstrating their improved conductivity compared with reference pure Cu; and (5) evaluating the impact of UCC on the power density of a WRSM. Because of multistep processing and the associated parameter space for producing UCC tapes, future work will involve optimization of processing protocols and provisions to attain reproducible

results along with the highest possible performance characteristics. Future efforts will also include cost analysis and computational feasibility studies to support integration of UCCs in electric drive components.

Key Publications

1. Tolga Aytug, "Electric drive inverter," presented at the 2018 DOE Vehicle Technologies Office Annual Merit Review, Washington, DC, June 2017.

References

1. H. Stillman and M. Burwell, "Ultraconductive Copper Wire: Overview of Worldwide Research and Development," International Copper Association, presented at Copper 2013, Santiago Chile, December 2013.
2. C. Subramaniam, T. Yamada, K. Kobashi, A, Sekiguchi, D. N. Futaba, M. Yumura, and K. Hata, "One Hundredfold Increase in Current Carrying Capacity in a Carbon Nanotube–Copper Composite," *Nat. Commun*. 4, 2202 (2013).
3. T. Holesinger, R. DePaula, J. Rowley, K. Sperling, and J. M. Pappas, *Development of Carbon Nanotube Composite Cables for Ultra-Deepwater Oil and Gas Fiel*ds, OTC-25370-MS, Research Partnership to Secure Energy for America Phase II Final Report, 2013.
4. D. F. Lee, M. Burwell, and H. Stillman, *Priority Research Areas to Accelerate the Development of Practical Ultra-conductive Copper Conductors*, ORNL/TM-2015/403, 2015.
5. C. Subramaniam, A, Sekiguchi, T. Yamada, D. N. Futaba, and K. Hata, "Nano-scale, Planar and Multi-tiered Current Pathways from a Carbon Nanotube–copper Composite with High Conductivity, Ampacity and Stability" *Nanoscale* 8, 3888, (2016)
6. Department of Energy Electrical and Electronics Technical Team Roadmap, 2017.
7. Raminosoa, T. "Non-rare Earth Electric Motors," ELT074, 2018 U.S. DOE Vehicle Technologies Office Annual Merit Review, June 19, 2018.

I.9 Development of Radically Enhanced alnico Magnets (DREaM) for Traction Drive Motors (Ames Laboratory)

Iver Anderson, Principle Investigator
Ames Laboratory (USDOE), Iowa State University
222 Metals Development, Iowa State University
Ames, IA 50011
E-mail: andersoni@ameslab.gov

Susan Rogers, DOE Technology Development Manager
U.S. Department of Energy
E-mail: susan.rogers@ee.doe.gov

Start Date: October 1, 2013 End Date: September 30, 2018
Total Project Cost: $6,600,000 DOE share: $6,600,000 Non-DOE share: $0

Project Introduction

This project utilizes a DOE National Lab-lead effort and a demonstrated science-based process to design and synthesize a high-energy-product permanent magnet of the alnico type in bulk final shapes without rare earth (RE) elements. The magnets will be competitive with existing commercial RE-based magnets on a cost per MGOe per kg basis and will have a more sustainable long-term supply and cost outlook. This work utilizes a combination of capabilities centered in Ames Lab and collaborations with NREL, ORNL, and with a commercial magnet manufacturer, Arnold Magnetic Technologies, to leverage critical capabilities for permanent magnet development. Through a separate project to extend these results toward commercialization, Ames Lab and ORNL are also working in concert with motor performance testing partners at Ford. The DREaM project harnesses the power of fundamental science, modern instrumentation for detailed characterization, and the most advanced processing methods that respond to concerns expressed by industry partners for scale up to full-scale manufacturing capability. These new alnico magnets that are being developed do not contain RE elements; instead the main alloy components are Al, Ni, Co, and Fe, which are all abundant and readily available around the world from multiple sources (including recycling) and can be obtained in a sustainable manner. As an existing advantage, alnico magnets have superior temperature stability for their magnetic flux compared to RE-based magnet alloys, without any significant loss through the planned operating range of -55˚C to 180-200˚C. Of key importance for PM drive motors, improved alnico magnets should have superior coercivity (up to 2X) compared to current alnico magnets and retain high levels of magnetization and remanence to enable high-performance operation of advanced PM motors, even at high operating temperatures. Improved magnets also will exhibit a high level of texture and magnetic anisotropy to satisfy motor load line design, making full use of the enhanced coercivity. The improved alnico magnets should also display increased mechanical strength and toughness to permit simplified motor design/assembly and operation at higher RPM. Improved alnico magnet alloys and innovative processing methods should enable production of bulk magnets with reduced cost, compared to current RE-based magnets. Generally, the powder processing method that is being developed will permit mass production of final-shaped magnets in quantities of millions with far less machining and scrap material in a cost-efficient manner.

Objectives

Test of Co-lean alnico compatibility with magnet performance goals: Co facilitates better coercivity and thermal stability in many permanent magnets. In commercial alnico alloys, the total Co content can be as high as ~34-35 at.% in high coercivity grades such as alnico 8 and 9. Unfortunately, Co is also a strategic element that is subject to price instabilities. Reduction of Co without degrading magnetic and thermodynamic properties of alnico systems is a significant challenge in the development of advanced alnico magnets. Our previous work on the chemical ordering of alnico during spinodal transformation has enabled precise guidelines (Rigid Band Approximation approach) to devise substitution of the Co content by Fe and Ni in a

systematic way, i.e., that does not significantly change the total electron concentration of a new alloy, abiding by the *Hume-Rothery Rule*. This new knowledge of chemistry and phase relationships enabled design and testing in cast and powder form of several experimental alnico alloys with lower Co content (as much as 40 at.% less) and with gains in coercivity (of 50-60%), compared to commercial counterparts. However, a key part of our innovative powder processing approach relies on the propensity for abnormal grain growth (AGG) to achieve a highly textured microstructure for maximum magnetic anisotropy. Some indications of grain growth advantages for full-Co alnico during powder processing (see results), along with similar gains in coercivity from alternative alloying, may push the final alloy selection away from Co-lean compositions to facilitate highest magnetic properties.

Optimized processing and chemistry to enhance coercivity: Essentially, all of the past alnico studies and the exploratory portion of our work on improved alnico magnet alloys utilized cast samples. However, we are working to develop pre-alloyed gas atomized powder processing to permit rapid adoption for mass production of final-shape full-scale magnets with a grain-aligned microstructure by a solid state (controlled AGG) approach. The various commercial classes of cast alnico underwent extensive optimization by magnetic annealing and subsequent heat treatments over 40-50 years. Our modern theory and instrumentation advantages has been able to predict and observe critical magnetic nano-structure features induced by these heat treatments. Very careful control of times and temperatures were found to be necessary to achieve the best magnetic performance, as predicted by our modelling. Quantifying the sensitive relationship of processing to performance was enabled by connection of the modelling efforts to the observed chemical and nano-structural evolution. Using a prototypical alnico 8 alloy, we quenched samples at various points along complex annealing schedules and, very recently, during high temperature XRD observation (see results). Extensive characterization of the microstructures, their chemistries and magnetic properties revealed enlightening insight into the enhancement of coercivity due to processing routes.

Theory-guided optimization: The phase evolution and the chemistry of the alnico is quite complex, affecting both the intrinsic and extrinsic properties so that changes in the alloy chemistry affect the Curie temperature, which in turn alters the optimal temperature for the magnetic annealing and subsequent draw cycles. Unfortunately, a funding reduction diminished our multi-scale modeling efforts. Thus, optimization of recent alloy designs and magneto-thermal processing was based on our previous understanding level.

Approach

The team's efforts during FY2018 are broken down into two highly synergistic efforts; synthesis of samples and their characterization (which includes chemistry, microstructure, nano-structure and magnetic properties). Each of these major tasks is comprised of subtasks.

Synthesis Task: The efforts are directed to completion of work on two alnico alloy designs (both based on alnico 8H), one with full Co content and one Co-lean alloy, and, primarily, on the development of advanced processing routes to maximize coercivity, microstructural anisotropy, and magnetic energy product. These experiments will utilize a series of processing methods that appear promising from correlations between theory and experiment that we have developed, as well as from observations of industrial processing procedures. The direction of these experiments is designed along a path that can be implemented practically to accelerate major up scaling if sufficient enhancement of magnetic properties is achieved. Thus, this major task is broken into sub-tasks that move along the ladder of magnet sample synthesis.

A) Prepare sufficient quantities of high quality pre-alloyed alnico alloy powders by gas atomization experiments and utilize the resulting powders to prepare well-controlled bulk magnet samples, concentrating on powder processing studies as our ultimate intended approach.

B) Utilize alnico bulk magnet samples from sub-task A with suitable grain alignment and MA processing to pursue promising modifications of alnico (draw) annealing cycles to maximize the full development of coercivity, remanence, and energy product.

C) Prepare scaled-up Co-lean and full Co versions of modified alnico 8 alloy bulk magnets from which to extract samples for testing of mechanical and thermal properties, providing additional results for comparison to similar commercial magnets (Arnold provided alnico 8HE, and 9 for baseline).

Characterization Task: The general focus is to perform detailed magnetic and microstructural characterization of modified alnico 8 (full Co) and alnico Co-lean (alnico-8_{AMES}) alloy system samples, concentrating on these two most promising alloys, to verify effects on nano-scale and micron-scale microstructure of samples from tailored processing and compositional variations and to investigate correlations between magnetic properties and the observed microstructural and compositional changes. It is a natural outcome of the characterization efforts that extremely large data files must be analyzed efficiently to derive meaningful results, which makes it natural that this effort should also include a data management component. The sub-tasks that are listed below contribute to this overall effort:

A) Develop capability to store refined data rapidly from advanced structural characterization (e.g., XRD, XRF) and magnetic measurements in a form readily assessable by advanced data-mining methods in a form that eventually will be accessible by outside groups.

B) Perform detailed magnetic and microstructural characterization of extensive series of modified alnico 8 (full Co) and Co-lean alnico (alnico-8_{AMES}) samples to verify effects on nano-scale and micron-scale microstructure of samples from experiments with processing and compositional variations and to investigate correlations between magnetic properties and the observed microstructural and compositional changes.

C) New temperature and frequency dependent measurements on experimental alnico magnets (including full-size) will be performed to verify magnetic properties and to determine other parameters that are relevant to motor applications.

D) New effort in the characterization of the thermal and mechanical properties will provide useful data for magnet synthesis studies and can benefit motor designers with data to compare to requirements for new motor designs.

Theory Task: The work during FY2018 did not include any new theory studies.

Results

Composition Design and Magnetic Property Development:

Key factors for increasing coercivity is a combination of alloy chemistry and thermal/magnetic processing. Minor elements such as Ti, Cu and Nb were shown to be very critical in controlling microstructure and improved magnetic properties. An alloy series with compositions of $Co_{34}Al_{14.25}Ni_{12.5}Cu_yFe_{36.75-x-y-z}Ti_x\ Nb_z$ (x = 0~10, y = 0-4.2, and z = 0- 1.8 in at.%) were obtained by arc-melting in Ar atmosphere and heat treated with varying schedules with and without magnetic fields. The studies of magnetic properties of samples show that with increasing Ti, Cu and Nb contents, H_{cj} first increases, reaches a peak value, and then decreases, while M_{sat} and B_r consistently decrease for increasing Ti, Cu, and Nb. These behaviors were attributed to the volume changes of L_{21} phase, which was verified by analysis of TEM microstructures and XRD results. A peak value of H_{cj} was obtained when the volume fraction of L_{21} phase approached ~50%. On the other hand, M_{sat} and B_r decrease due to the reduction of Fe-Co phase vol.%. A recorded H_{cj} of 2715 Oe was achieved (Figure I.9.1) at one alloying "sweet spot." In addition, an M_{sat} of 10.4 kGs and a Br of 7.1 kGs, along with an H_{cj} of 2530 Oe were obtained by appropriately adjusting the contents of Ti, Cu and Nb to achieve an excellent balance. These values have met the project milestones.

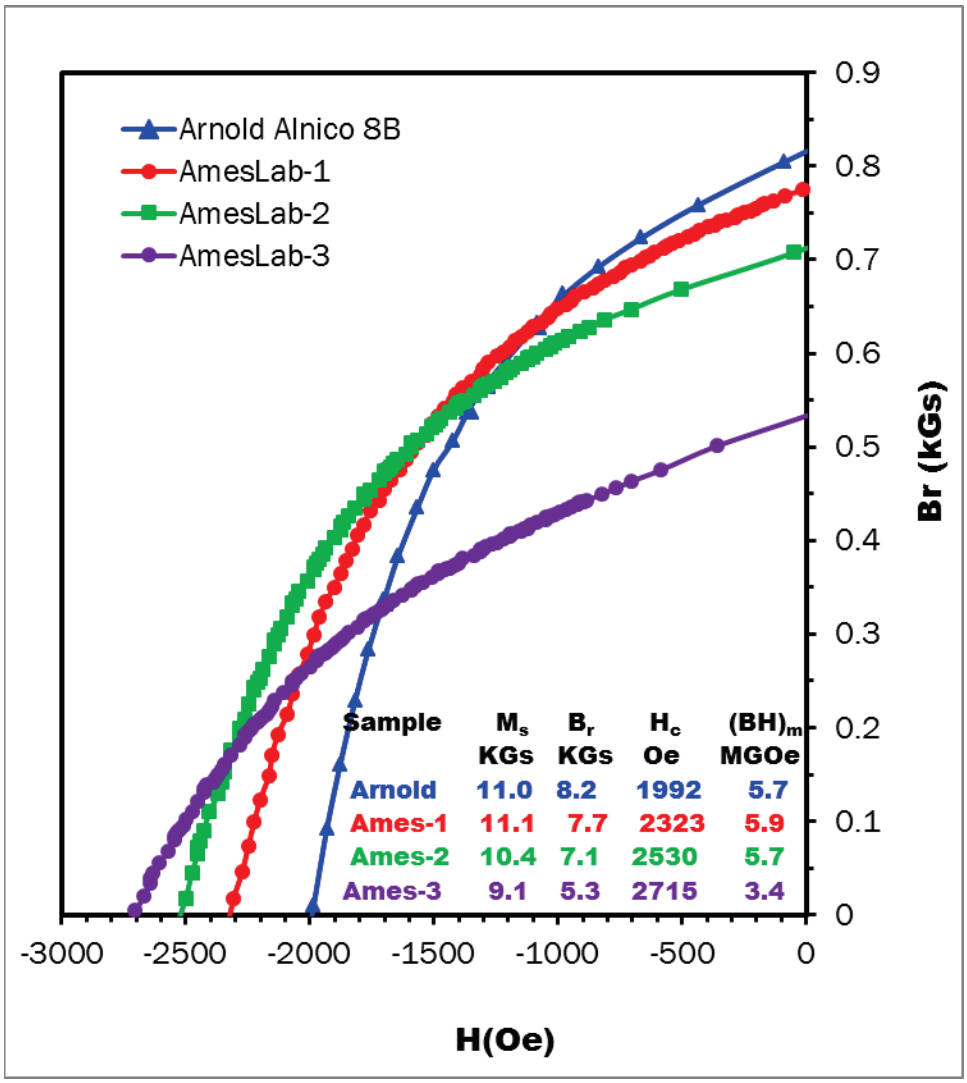

Figure I.9.1 Demagnetization Curves of Ames Processed Samples and Arnold Magnetics alnico 8B.

Effect of magnetic solutionizing and annealing on magnetic properties was also studied. Solutionizing with a 1 T magnetic field coupled with magnetic annealing for less than 3 min. increased coercivity by ~ 10%. The average diameter of spinodal Fe-Co rods is ~20-30 nm. This elevated coercivity agrees with our early modeling results that predicts higher coercivity with smaller Fe-Co rods. It also was known from our previous results that when a sample was solutionized by a conventional process (without a magnetic field) and was magnetically annealed for 1.5 min., the Fe-Co particles of the sample were very fine but linked/bridged to each other, apparently lacking the magnetic field to promote rod independence. With increased magnetic annealing time from 1.5 to 8 min., the Fe-Co particles were completely developed and isolated from each other, but grew and coarsened to 35-45 nm, as well. Therefore, the desired high H_{ci} was not achieved by rod isolation, but was diminished as predicted by the coarsened Fe-Co rods. The magnetic solutionizing process appears to help form finely-spaced arrays of initial Fe-Co precipitates and to help grow and maintain isolated Fe-Co rods during short time magnetic annealing, leading to a higher coercivity

Co content remains a concern with these alloys. Near-final shape Co-lean magnets and full-Co/Ti-enhanced alnico magnets were synthesized via solid-state sintering from 3 batches of high pressure gas atomized (HPGA) powder with a diameter of <25 µm from Ames Laboratory (both alloys) and Carpenter Technology (Co-lean only). Although cast samples of the Co-lean alloy had promising magnetic properties (as stated in our

previous FY2017 report), the suppressed abnormal grain growth (AGG) of sintered powder samples limited the ability to form large, textured grains, in turn limiting the remanence that can be achieved in this alloy. Fortunately, the full-Co/Ti-enhanced alnico alloy powder samples demonstrated the opposite, showing radically enhanced AGG after just 4 hours of sintering, yielding grains >1mm. This alloy, with its AGG characteristics is very attractive for technology transfer for powder producers and magnet manufacturers. Powder producers can readily achieve a fine powder size of <25 µm dia. and magnet manufactures can take advantage of the rapid kinetics to decrease processing time, making the full-Co/Ti-enhanced alloy an economic alnico alloy to fabricate into millions of near final bulk sized magnets.

Characterization

Mechanical Properties of alnico

In collaboration with NREL, Ames Lab provided alnico magnet samples for mechanical property evaluation (compression strength and transverse rupture strength (TRS]), and the thermal conductivity testing. Two series of Ames Lab alnico magnets were evaluated. One series was vacuum sintered alnico from HPGA powder (Ames I) and the other series (Ames II) was subjected to primary and secondary sintering with deadweight. Mechanical testing was completed at 150, 25, and -40 C to simulate the conditions that a PM motor will likely see in service. Figure I.9.2 shows that the TRS of both Ames magnet types was superior, compared to other PM materials. TRS results revealed that our secondary heat treatment process further increased mechanical properties. This is likely due to the reduction of pores from the applied weight during secondary sintering. It should be noted that Ames II alnico magnets were only tested for TRS at 25 °C due to resources available at the time.

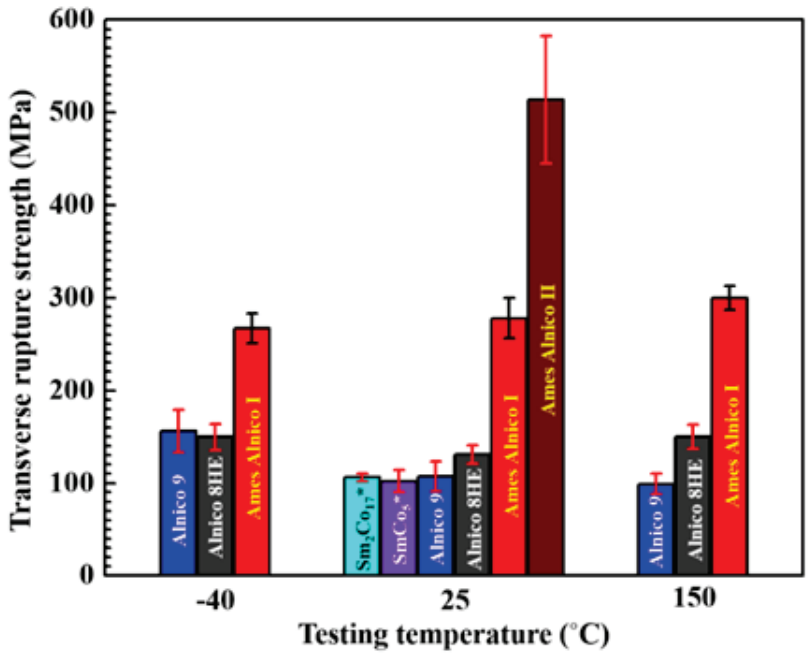

Figure I.9.2 TRS testing for Ames Laboratory Alnico at 150 °C, 25 C, and -40 °C to simulate the temperatures that a PM motor could experience while in service.

Microstructure

High resolution chemical spectroscopy and microstructural imaging (2D and 3D) have been employed to ascertain the effects of alloy composition and processing modifications. Previous micro-magnetic modeling showed that the size, shape and degree of interconnectedness of the Fe-Co rods (α_1) was crucial to controlling the coercivity. We have reconstructed a series of these magnet samples via serial sectioning and imaging with

a FIB-SEM (Focused Ion Beam – Scanning Electron Microscope). The reconstructed α_1 phase is shown in Figure I.9.3. The result not only confirms the 3D rod or prism morphology of the α_1 phase observed in SEM and TEM 2D images of the cross-section and longitudinal sections of the microstructure, but also reveals compositional inhomogeneity inside the materials. The Fe-Co-rich phase of tens of nanometers in area and several nanometers thickness is observed inside the materials and interconnects the rods. The influence of the apparent compositional inhomogeneity is expected to be small because only a small volume fraction of material has these inhomogeneities.

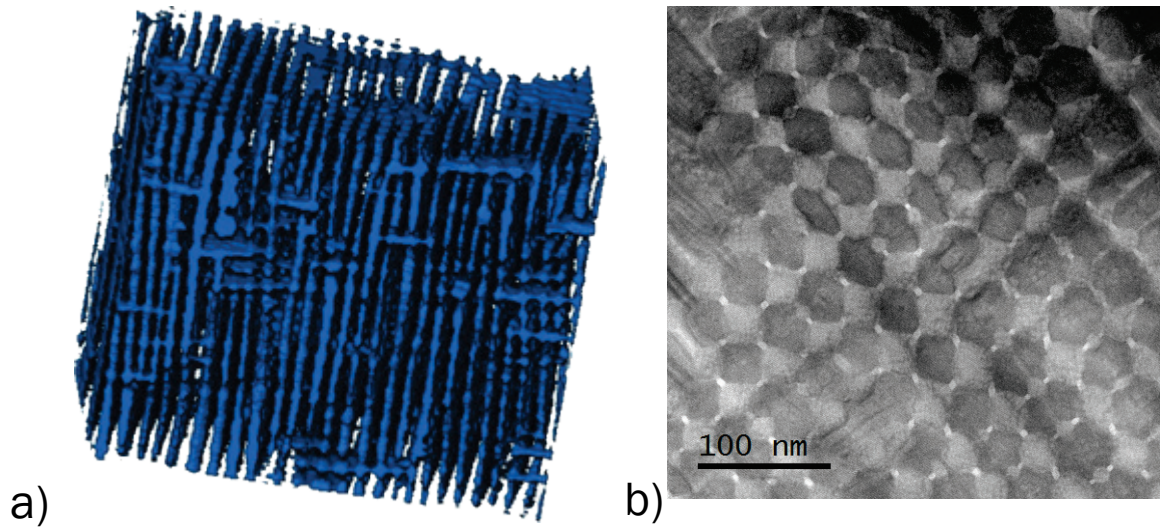

Figure I.9.3 The 3D reconstruction (volume of 1176 nm x 985 nm x 706 nm) showing that interconnected (α1)Fe-Co-rich phase is rare but does occur in this section of a grain that was well aligned to the magnetic field during magnetic annealing. b) TEM image of a similar region, but representative of a 2D transverse section of a grain that was well-aligned to the magnetic field.

Conclusions

The project has met all of our milestones, with the exception of the highest level of up-scaling, we have produced a bulk anisotropic alnico magnet with B_r in excess of 0.8 T and H_{ci} in excess of 2500 Oe. Properties of these magnets were provided to ORNL for use in a detailed motor design that is compatible with the Ford test facility. Well-controlled bulk magnet samples were fabricated with enhanced grain alignment and energy product (MGOe) and superior H_{ci} compared to commercial alnico 8HE. Bulk alnico magnet samples with further improved magnetic properties over similar commercial magnets were produced and additional thermophysical properties were evaluated at NREL.

Key Publications

1. L. Zhou, W. Guo, J.D. Poplawsky, L. Ke, W. Tang, I.E. Anderson, and M.J. Kramer, "On spinodal decomposition in alnico—a transmission electron microscopy and atom probe tomography study," *Acta Materialia,* 153 (2018) pp. 15-22.
2. E.A. Rinko, L. Hu, I.E. Anderson, A.G. Kassen, E.M.H. White, W. Tang, L. Zhou, M.J. Kramer, "Exploring Powder Processing of Cobalt-Lean Alnico Alloy as a Preferred Approach to Produce Full-Scale High-Performance Alnico Magnets with Near-Final Shape," in *Advances in Powder Metallurgy & Particulate Materials—2018*, Compiled by Animesh Bose, FAPMI, and Scott Davis (Metal Powder Industries Federation, 105 College Road East Princeton, NJ) ISBN No. 978-1-943694-18-1, pp. 385-397 (2018).
3. W.Y. Zhang, S. Valloppilly, X.Z. Li, L.P. Yue, R. Skomski, I.E. Anderson, M.J. Kramer, W. Tang, J.E. Shield, and D.J. Sellmyer, "Texture development and coercivity enhancement in cast alnico 9 magnets," AIP Advances (2018) 8(5).

4. A.G. Kassen, E.M.H. White, L. Hu, W. Tang, L. Zhou, M.J. Kramer, and I.E. Anderson, "Novel mechanisms for solid-state processing and grain growth with microstructure alignment in alnico-8 based permanent magnets," AIP Advances (2018) 8(5).
5. M.C. Nguyen, L. Zhou, W. Tang, M.J. Kramer, I.E. Anderson, C-Z. Wang, and K-M. Ho, "Cluster Expansion Model for Complex Quinary Alloy: Application to alnico Permanent Magnets," Phys. Rev. Applied 8, issue 5, (2017) p. 054016.
6. L. Hu, I.E. Anderson, A.G. Kassen, E.M.H. White, W. Tang, L. Zhou, and M.J. Kramer, "Approaching Full-Scale High-Performance Alnico Magnets with Near-Final Shape," in *Advances in Powder Metallurgy and Particulate Materials-2017*, compiled by Ryuichiro Goto and Joseph T. Strauss, (Metal Powder Industries Federation, Princeton, NJ), ISBN No. 978-1-943694-15-0, pp. 256-265 (2017).
7. A.G. Kassen, L. Hu, E.M.H. White, W. Tang, A. Palasyuk, L. Zhou, M.J. Kramer, and I.E. Anderson, "Solid-State Texture Development in Sintered Alnico-Based Permanent Magnets from High-Pressure Gas Atomized Powders for Traction Drive Technology," in *Advances in Powder Metallurgy and Particulate Materials-2017*, compiled by Ryuichiro Goto and Joseph T. Strauss, (Metal Powder Industries Federation, Princeton, NJ), ISBN No. 978-1-943694-15-0, pp. 778-790 (2017).
8. L. Ke, R. Skomski, T.D. Hoffmann, L. Zhou, D.D. Johnson, M.J. Kramer, I.E. Anderson, and C-Z. Wang, "Simulation of alnico coercivity," App. Physics Lett., 111, Issue 2 (2017), p. 022403, http://scitation.aip.org/content/aip/journal/apl/111/2/10.1063/1.4992787
9. A.G. Kassen, E.M.H. White, W. Tang, L. Hu, A. Palasyuk, L. Zhou, and I.E. Anderson, "Compression Molding and Novel Sintering Treatments for Alnico Type-8 Permanent Magnets in Near-Final Shape with Preferred Orientation," JOM, 69, no. 9, (2017), pp. 1706-1711, https://doi.org/10.1007/s11837-017-2453-0.
10. I.E. Anderson, A.G. Kassen, E.M.H. White, A. Palasyuk, L. Zhou, W. Tang, and M.J. Kramer, "Development of controlled solid-state alignment for alnico permanent magnets in near-final shape," AIP Advances, 7, issue 5, (2017) 056209, https://doi.org/10.1063/1.4973843.
11. E.M.H. White, A.G. Kassen, E. Simsek, W. Tang, R.T. Ott, and I.E. Anderson, "Net Shape Processing of Alnico Magnets by Additive Manufacturing. IEEE Transactions on Magnetics," (2017) 53(11).
12. L. Zhou, W. Tang, L.Q. Ke, W. Guo, J.D. Poplawsky, I.E. Anderson, and M.J. Kramer, "Microstructural and magnetic property evolution with different heat-treatment conditions in an alnico alloy," Acta Materialia," (2017) 133: p. 73-80.

Patent

I.E. Anderson, A. Kassen, and E.M.H. White, "Solid State Grain Alignment Of Heat Treatable Permanent Magnets In Near-Final Shape," US (utility) Patent Application filed.

I.10 Performance and Reliability of Bonded Interfaces for High-Temperature Packaging Insert Section Heading (NREL)

Paul Paret
National Renewable Energy Laboratory
15013 Denver West Parkway
Golden, CO 80401
Phone: 303-275-4376
Email: paul.paret@nrel.gov

Susan Rogers, DOE Technology Development Manager
U.S. Department of Energy
E-mail: susan.rogers@ee.doe.gov

Start Date: September 30, 2018 End Date: October 1, 2016
Project Funding (FY18): $350,000 DOE share: $350,000 Non-DOE share: $0

Project Introduction

Power electronics packaging in the rapidly growing power industry is becoming more critical than ever before. To improve performance, reduce volume and weight, and get higher efficiency out of electronics packages, wide-bandgap devices such as silicon carbide and gallium nitride are being proposed as replacements for widely used silicon (Si) devices. A redesign of the traditional packaging for power modules, both in materials and design, is necessary to exploit the faster switching speed and to enable high-temperature operation of the wide-bandgap devices. For high-temperature operation (>200°C), materials that can withstand severe thermo-mechanical stresses and function without any failure for long periods of time need to be considered. In particular, for bonded interfaces, i.e., die-attach and substrate-attach, reliable operation at elevated temperatures is a major challenge as a failure would eventually result in a thermal runaway of the entire power electronics package.

Traditionally, solders have predominantly been used as interface materials in power electronics packages in the automotive industry. With the push towards replacing Si with wide-bandgap devices, high-temperature-compatible materials have gained significant interest. Among these materials, sintered silver, along with transient liquid-phase bonding, is a leading candidate for replacing solders in novel power electronics packaging designs. In the past, sintered silver made from micron-sized silver particles demonstrated excellent reliability under accelerated thermal cycling conditions. However, the drawback of the high bonding pressure (30 – 40 MPa) requirement resulted in its limited applications and necessitated research and development of novel and simple bonding techniques of sintered silver. To this end, sintered silver paste comprising nano-silver particles were developed (Bai et al. 2006) and more recently, hybrid sintered silver paste, involving a mixture of nano- and micron-sized silver particles/flakes, are gaining traction among various researchers and the industry. With these formulations, sintering can be achieved through a purely temperature-driven diffusion of the silver particles without applying any pressure. While micron-sized sintered silver paste has made inroads into commercial power electronics packages (Göbl and Faltenbacher 2010), more work is required to establish the mechanical properties and thermomechanical reliability of large-area pressureless sintered silver pastes before adopting them for commercial applications. A comprehensive review of the different types of sintered silver pastes available in the industry is provided by Siow (2014). In this study, the merits and demerits of different types of sintered silver pastes available in the industry are compared, and the author predicts that these pastes will become mainstream in the power electronics and microelectronics packaging industry over the next few years.

In the past, research at the National Renewable Energy Laboratory (NREL) was focused on characterizing the reliability of sintered silver joints synthesized from micron-sized silver particles. Accelerated thermal cycling from -40°C to 150°C was conducted on 50.8-mm x 50.8-mm-footprint test samples, in which Si_3N_4 substrates

were bonded to copper baseplates with sintered silver material. The sample synthesis was done at Semikron. A bonding pressure of 30 – 40 MPa was applied that resulted in good quality bonding with minimal voiding. Under thermal cycling, samples survived without failure for 2,300 cycles. A 20% increase in crack area was considered as the failure criterion. More recently, research focus at NREL has shifted to characterizing novel formulations of sintered silver pastes. In collaboration with an industrial partner and Virginia Tech (VT), mechanical characterization of nano and hybrid sintered silver pastes, in which micron- and nano-sized silver particles are embedded, was completed. Reliability evaluation of these materials under accelerated thermal cycle loads is ongoing. Furthermore, thermomechanical models of sintered silver to obtain parameters such as strain energy density and J-integral were developed. Once thermal cycling is completed, the experimental data will be combined with modeling output parameters to formulate a lifetime prediction model of sintered silver.

Objectives

The major objectives in this project are:

- Conduct mechanical characterization on sintered silver under multiple strain rates and different temperatures. The output of this characterization will be an array of stress-strain curves from which constitutive model parameters can be obtained through curve fitting. These constitutive model parameters will be used as an input in finite element method simulations.
- Evaluate the reliability of sintered silver by subjecting coefficient of thermal expansion-mismatched coupons - with sintered silver as the bonded interface material - to accelerated thermal cycling tests. Crack propagation or any other failure mechanisms that originate and evolve under thermal cycling will be periodically monitored through scanning acoustic microscopy images. Thermal cycling will be continued until the samples completely delaminate or the cracks grow to a certain pre-defined percentage area.
- Develop thermomechanical models to obtain theoretical parameters such as strain energy density and J-integral, and formulate a lifetime prediction model based on these modeling outputs and experimental data.

Approach

- Mechanical Characterization
    - Sample Description

A modified double-lap sample configuration, as shown in Figure I.10.1, was selected to measure the mechanical strength of sintered silver pastes. The sample consists of a 5-mm-thick copper coupon in the middle that is bonded to thinner copper coupons (2 mm thick) on either end using sintered silver. The simple layout of this sample configuration enables an effective characterization of the joint material without the occurrence of any unintended peel stress at the interfaces. By applying a compressive force on the top of the middle coupon, as shown in Figure I.10.1, shear forces are developed in the sintered silver joints. The copper coupons were fabricated in the laboratory machine shop with a prescribed surface finish of RMS 16. After fabrication, the coupons were plated with a 4-µm-thick silver layer. The footprint of the samples was 12.7 mm x 12.7 mm.

Two types of sintered silver pastes were included in this study. In one set of double-lap samples, the copper coupons were bonded at NREL using a sintered silver paste (nano silver) that was purchased from an industrial partner, while the other set of samples was synthesized at VT using a sintered silver paste (hybrid silver) purchased from NBE Tech. The sintering profiles of each of these sintered silver paste to fabricate the double-lap sample is shown in Figure I.10.2. Once the double-lap samples were synthesized, the material bonding quality was assessed using images taken with C-mode scanning acoustic microscopy (C-SAM) at NREL. Figure I.10.3 shows select C-SAM images of double-lap samples made at NREL and VT.

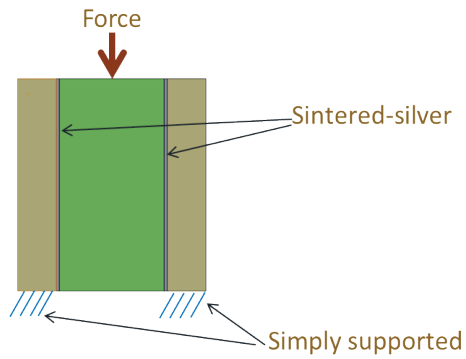

Figure I.10.1 Double-lap sample configuration for mechanical characterization

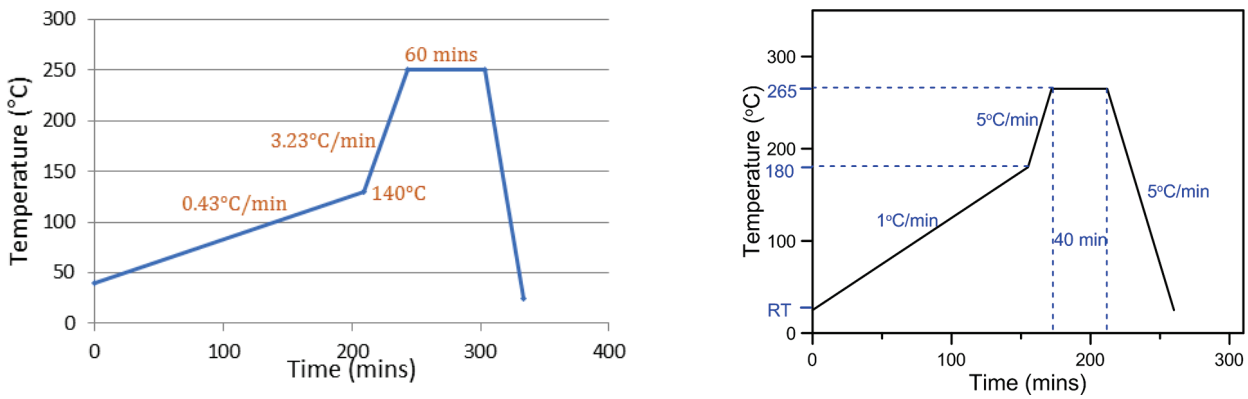

Figure I.10.2 Sintering profile of nano silver (left) and hybrid silver (right)

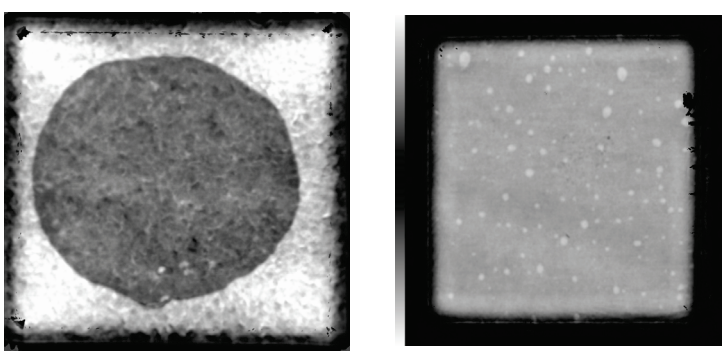

Figure I.10.3 C-SAM images of double-lap samples synthesized at NREL with nano silver (left) and at VT with hybrid silver (right). Dark/grey regions indicate a bonded interface whereas white spots/patches denote voids or other discontinuities

- Experimental Test Plan

The double-lap samples were characterized using an Instron 5966 dual column testing system at three different displacement rates: 10^{-2} mm/s, 10^{-4} mm/s, and 10^{-5} mm/s, and at three different ambient temperatures: -40°C, 30°C or room temperature (RT), and 200°C. The intent behind choosing these rates was to simulate quasi-static loading conditions at the joint interfaces, thereby qualifying the results obtained from these tests to be applicable in scenarios such as thermal cycling. In this study, the testing rates were controlled at the Instron crosshead, and it was assumed that the actual effective displacement rates at the sample interfaces were the same. For each instance of a displacement rate and temperature, a total of four samples were tested, and the average shear stress values are reported.

- Reliability Evaluation
  - Sample Description and Test Setup

Round samples of 25.4-mm diameter (1-inch diameter) were fabricated at VT with sintered silver bonded between copper and Invar coupons and subjected to accelerated thermal cycling. The thickness of the copper and Invar coupons was 2 mm and, similar to the double-lap samples, both sets of coupons were plated with a 4-µm-thick silver layer. For the pressureless samples, the sintered bond pad thickness varied between 55 µm to 75 µm whereas for the pressure-assisted samples, it varied between 110 µm and 140 µm. Also, in both cases, samples with different bond pad diameters—22 mm, 16 mm, and 10 mm—were made to study the impact of geometrical variations on the loading scenario and thus the crack initiation and propagation behavior in the sintered silver layer. Overall, pressure-assisted sintering techniques resulted in good bond quality; however, a majority of the pressureless samples exhibited large void fractions. It is to be noted that in the process of improving the bond quality of round coupons, the sintering profiles were varied from that of the double-lap samples and are shown in Figure I.10.4.

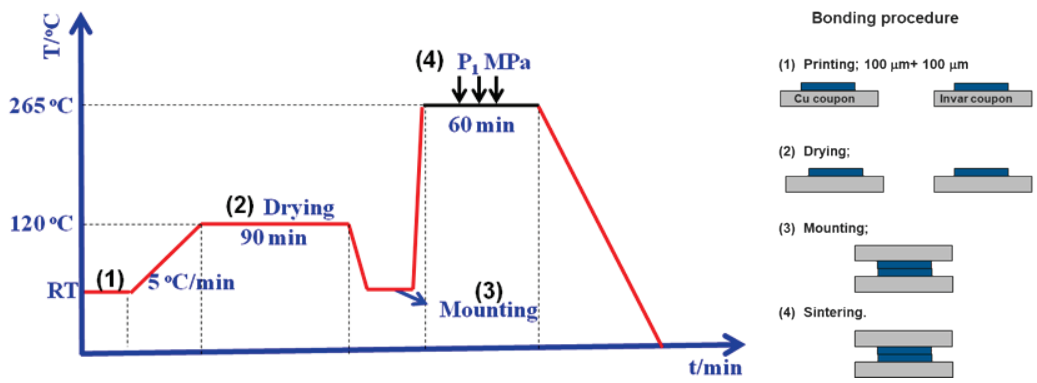

Figure I.10.4 Sintering profile of pressure-assisted round samples with hybrid silver

A thermal cycle of -40°C to 200°C was selected for conducting accelerated tests on the round samples. A cryogenically cooled thermal test platform with internal heaters was configured to achieve the required temperature targets. Prior to cycling the round samples, test coupons were placed on the thermal platform and, under thermal cycling, temperatures were monitored at multiple locations using Resistance Temperature Detector probes. Based on the temperature data, slight modifications such as attaching a copper plate on the platform, were made to ensure uniform heating and cooling of the samples.

- Thermomechanical Modeling

In addition to mechanical characterization and reliability evaluation, thermomechanical modeling of sintered silver based on a non-linear finite element method was developed. Round coupon geometries were created, meshed, and subjected to a cyclic loading environment of -40°C to 200°C. The major output of interest was strain energy density per cycle. In addition to continuum models, a fracture mechanics-based approach was adopted in which a crack was manually inserted in the model and after solution, J-integral/cycle values were extracted from the crack feature. These output parameters offer an insight into the reliability of the sintered silver material and combining them with the cycles-to-failure experimental results would result in the formulation of lifetime prediction models.

Results

- Mechanical Characterization

The direct output of shear testing on a double-lap sample using an Instron test equipment is the load-displacement curve, shown in Figure I.10.5. The two peaks in the figure denote the failure points of the two interfaces in the sample, and only the results obtained up to the first failure point are considered for further analysis. In the case of a few samples, the load-displacement graph exhibited only a single peak, which could

lead to the misconception that only one interface failed. However, both interfaces were observed to shear off for these samples during the test.

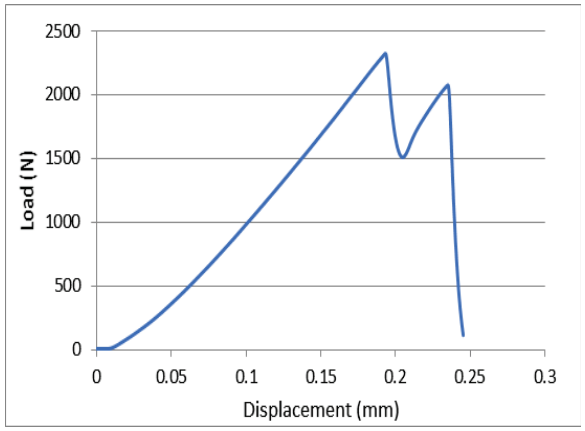

Figure I.10.5 Load – displacement graph

- Nano – silver

Double-lap samples with the nano-silver paste were synthesized at NREL using the profile shown in Figure I.10.2. The C-SAM images of these samples showed very minimal voiding at the interface regions. The average values of the peak shear stress of these samples are plotted in Figure I.10.6. The error bars represent the standard deviation of the shear stress results. At each displacement rate, there is more than a 50% drop in the shear stress value as ambient temperature is increased from RT to 200°C. Also, at a given temperature, a decrease in the applied displacement rate leads to a 40% – 50% drop in the shear stress of the sintered silver joint. The wide variation in the individual results averaged to obtain the plotted values, particularly at RT, could be likely due to small differences in the bond shape between the samples. Although the paste was printed in a circular shape, it spread out and, in a few instances, did not conform to a circular shape.

- Hybrid silver
  - Pressureless samples

Similar to the samples synthesized at NREL, mechanical characterization was conducted on double-lap samples fabricated at VT using the sintered silver paste from NBE Tech. For a given displacement rate and temperature, multiple samples were characterized, and the shear stress results were computed from the resulting load-displacement graphs. Figure I.10.7 shows a plot of the impact of displacement rate and ambient temperature on the shear stress values of these samples. As seen in the figure, there is not much difference in the shear stress values between the samples tested at -40°C and RT. However, a considerable drop occurs when the ambient temperature is raised to 200°C, a trend that was observed in the samples synthesized at NREL. For both nano and hybrid silver, the fall in shear stress values with increasing temperature could be attributed to creep deformation becoming predominant at higher temperatures, which diminishes the material resistance to failure. Also, the applied displacement rate did not have a significant impact on the shear stress values at -40°C and RT. Only when the ambient temperature was increased to 200°C did the silver paste exhibit a strong rate dependence. The decrease in shear stress at a lower displacement rate is possibly due to the higher strain hardening that occurs in the sintered silver layer and with the rise in temperature, the strain hardening rate is, in general, expected to increase.

- Pressure-assisted samples

These samples were made using the same synthesis profile as the pressureless ones except for the application of a sintering pressure at the sintering temperature. The impact of two sintering pressures, 3 MPa and 10 MPa, on the shear stress values of hybrid silver at multiple strain rates and temperatures was studied and is plotted in

Figure I.10.7. Pressure-assisted samples exhibited a significant increase (more than 100%) in the shear stress values when compared with the pressureless samples, but negligible variation was observed between the 3 MPa and 10 MPa samples. Under pressure, the sintered silver particles may have coalesced to form a compact, dense bond pad that required higher values of force to cause a shear failure. Also, a sintering pressure of 3 MPa was found to be sufficient in this case where the sample footprint was 12.7 mm x 12.7 mm, but larger pressure may be required as the bond area increases.

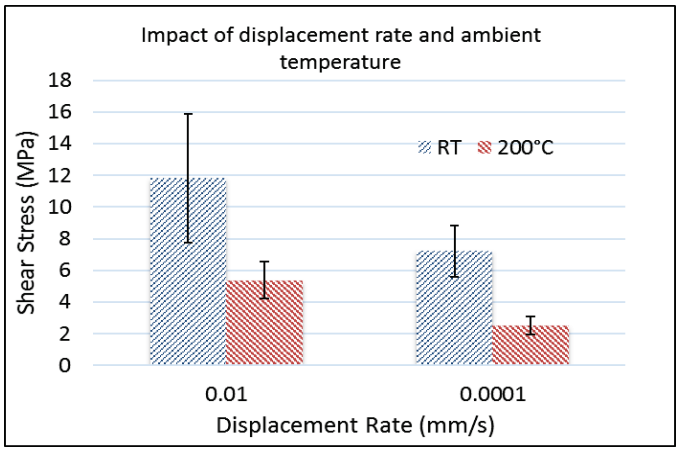

Figure I.10.6 Shear stress values of nano-silver. These samples were synthesized at NREL using pressureless sintering

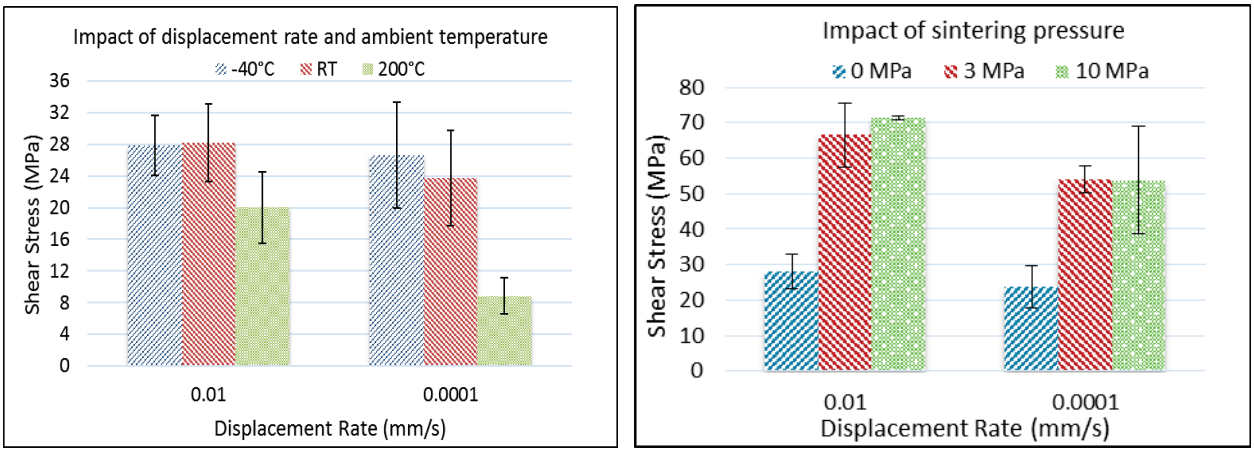

Figure I.10.7 Shear stress values of hybrid silver made using pressureless sintering (left); impact of sintering pressure on the shear stress values (right)

- Reliability Evaluation
  - Hybrid silver

Thermal cycling was performed on pressureless samples bonded with hybrid silver at VT, up to a total of 500 cycles to date. As mentioned in the Approach section, most of these samples had a large void fraction, likely due to sub-optimal synthesis procedures, and were expected to fail quickly. To monitor the bond quality and to inspect the occurrences of any failures, these samples were removed from the thermal platform at regular intervals and scanned using C-SAM. At any interval, C-SAM images were taken from both ends, i.e., the copper side and the Invar side. Figure I.10.8 shows the C-SAM images of a select few samples prior to cycling and at 500 cycles.

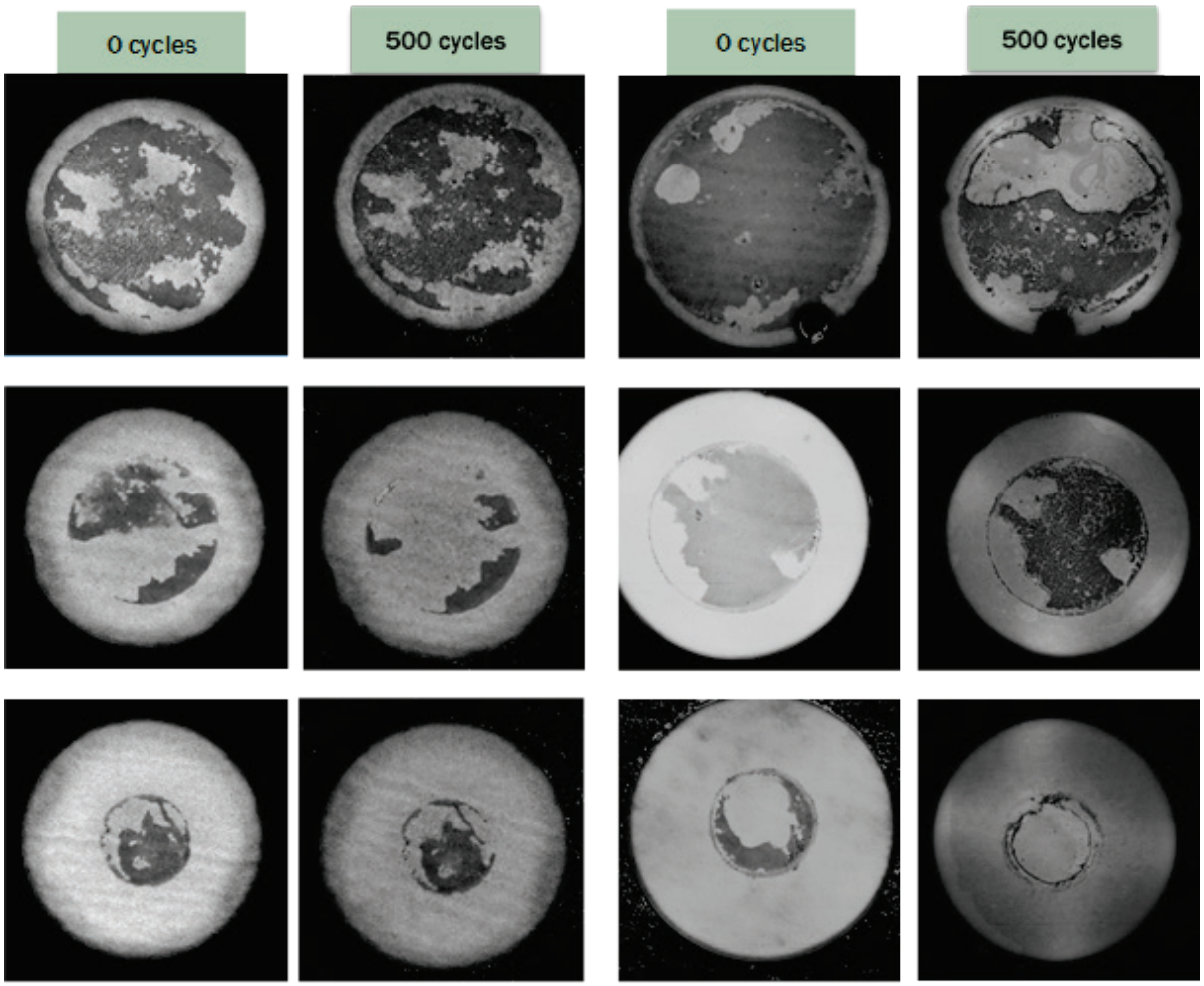

Figure I.10.8 C-SAM images of pressureless samples from copper side (left) and Invar side (right); 22 mm (top), 16 mm (center), and 10 mm (bottom).

The different layout of the bonded and failed (indicated by white patches) regions in the C-SAM images taken from either end of any given sample points to the occurrence of multiple failure mechanisms in the sintered silver layer. For the 22-mm-diameter samples, no additional failures were found to occur on the copper side under cycling whereas on the Invar side, multiple failure mechanisms initiated as indicated by the different shades of white patches in the C-SAM images. This trend was also exhibited by the 10-mm-diameter samples. For the 16-mm-diameter samples, images from the Invar side reveal the initiation of minor cracks at various random locations after 200 cycles and thereafter their gradual propagation throughout the bond. To ascertain the exact types of failure, these samples will be cross-sectioned and imaged using a digital microscope.

- Thermomechanical Modeling

Simulations were performed in the ANSYS Workbench platform to model the thermomechanical fatigue behavior of the sintered silver in the round sample configuration. Linear elastic material properties were used to define the deformation nature of the coupons, and additionally, Anand model parameters obtained from the literature were used to capture the viscoplastic characteristic of sintered silver. A thermal cycle load of -40°C to 200°C was applied on the model four times in succession based on a convergence study. In addition to the three different bond pad diameters (22 mm, 16 mm, and 10 mm) in the experimental category, more diameter variations were included in the simulations. After solution, the volume-averaged strain energy density of the entire bond pad regions was computed for the different diameter cases. In addition to strain energy density, J-

integral values were computed through ANSYS simulations as these values could possibly offer a more accurate lifetime prediction model. To obtain J-integral, a crack feature was manually embedded in the model in the region of maximum values of strain energy density (where cracks are likely to initiate). Figure I.10.9 shows the variation in strain energy density and J-integral values with the bond pad diameter. In this figure, the X-axis represent the percentage ratio of the bond pad diameter to that of the outer coupons (1-inch or 25.4 mm). The dashed lines represent the case where the bond pad thickness was 0.05 mm and the solid lines represent 0.1 mm.

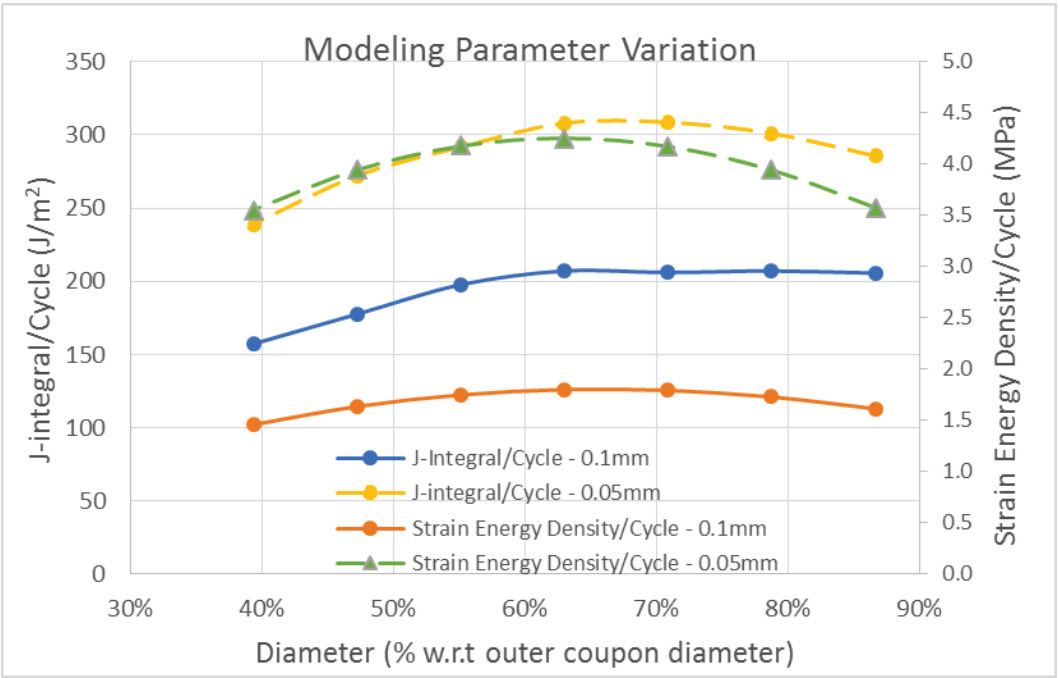

Figure I.10.9 Strain energy density results of round coupons

It is interesting to note that as the bond pad diameter or area decreases with respect to the outer coupons (right to left), strain energy density per cycle values initially increase and below a certain threshold at 60 – 70%, begin to drop. In general, for a given coefficient of thermal expansion mismatch across a bond pad, strain energy density is expected to increase for lower bond pad diameters as the mechanical load imposed by the outer coupons under thermal cycling is constrained to a smaller area. In Figure I.10.9, this is the case until the bond pad diameter is around 60 – 70 % of the outer coupon diameter. However, at even smaller diameters, it is likely that the mechanical constraint on the bond pad is caused by only the inner regions of the outer coupons, resulting in a lower load on the bond pad. This behavior is clearly observed for the 0.05 mm case, but relatively less apparent when the thickness is 0.1 mm. A possible explanation is that a thicker bond pad has a much higher stiffness and thus, becomes less susceptible to the impact of thermomechanical load. On the experimental side, these results imply that the 16-mm-diameter samples (~ 63 % on the X-axis in Figure I.10.9) are likely to fail sooner than the 10-mm samples, assuming a uniform area that is free of voids at the bond pad prior to thermal cycling. However, the variation of J-integral values is smaller until the 60 – 70 % threshold as compared to strain energy density, but then begin to drop. The difference in the behavior of these parameters with bond pad area could be attributed to their derivation process. While strain energy density is volume averaged over the entire bond pad area, J-integral – which can be seen as a crack driving force – is calculated only around the crack region. Future steps in the modeling include performing simulations with larger sized cracks to find out whether the variation of the J-integral with bond pad diameters remain the same as in Figure I.10.9 or a new trend can be observed.

Conclusions

Sintered silver is a promising interface material that can enable reliable operation of wide-bandgap power electronics components. This project focused on the mechanical and reliability characteristics of sintered silver. The conclusions provide important material and design guidelines for the automotive industry with respect to their power electronics packages.

Mechanical characterization of two different sintered silver formulations—nano silver and hybrid silver—was done at multiple temperatures and applied displacement rates. The maximum values of shear stress obtained in each case are reported. In general, shear stress of the silver pastes in this study decreased with increasing temperature and decreasing displacement rates. Applying as little as 3 MPa of sintering pressure during samples synthesis proved to be immensely beneficial for increasing the shear strength of the material.

Accelerated thermal cycling was conducted on pressureless round samples bonded with hybrid silver. Most of the samples had a large void fraction even prior to cycling due to sub-optimal synthesis procedure, which led to their failure in as few as 100 cycles. Strain energy density and J-integral results were computed for the sintered silver material in round sample configurations through thermomechanical modeling.

Key Publications

1. Paret, P., D. DeVoto, and S. Narumanchi. "Thermomechanical Modeling of Sintered Silver – A Fracture Mechanics Based Approach." IMAPS Device Packaging Conference, Fountain Hills, AZ, March 2017.
2. Paret, P., J. Major, D. DeVoto, S. Narumanchi, Y. Tang, and G. Q. Lu. "Mechanical Characterization of Sintered Silver Pastes Bonded in a Double-Lap Configuration." IPACK2018-8276, 2018 ASME InterPACK, San Francisco, CA.
3. Paret, P., D. DeVoto, and S. Narumanchi. "Thermomechanical Modeling of High-Temperature Bonded Interface Materials." Chapter accepted for publication in *High Temperature Die Attach Materials for Microelectronics: Materials, Processes, Equipment, Modelling and Reliability,* Springer Nature.

References

1. Göbl, C., and J. Faltenbacher. 2010. "Low Temperature Sinter Technology Die Attachment for Power Electronic Applications." In *2010 6th International Conference on Integrated Power Electronics Systems*, 1–5.
2. Bai, J. G., Z. Z. Zhang, J. N. Calata, and G.-Q. Lu. 2006. "Low-Temperature Sintered Nanoscale Silver as a Novel Semiconductor Device-Metallized Substrate Interconnect Material." *IEEE Transactions on Components and Packaging Technologies* 29 (3): 589–93. https://doi.org/10.1109/TCAPT.2005.853167.
3. Siow, Kim S. 2014. "Are Sintered Silver Joints Ready for Use as Interconnect Material in Microelectronic Packaging?" *Journal of Electronic Materials* 43 (4): 947–61. https://doi.org/10.1007/s11664-013-2967-3.

Acknowledgments

The contributions of Joshua Major and Douglas DeVoto in conducting the several characterization experiments are acknowledged. The author also would like to thank Yansong Tan and G-Q. Lu at VT for their valuable technical inputs and help with sample synthesis.

I.11 Power Electronics Thermal Management (NREL)

Gilbert Moreno, Principal Investigator
National Renewable Energy Laboratory
15013 Denver W Pkwy
Golden, Co 80233
E-mail: gilbert.moreno@nrel.gov

Susan Rogers, DOE Technology Development Manager
U.S. Department of Energy
E-mail: susan.rogers@*ee*.doe.*gov*

Start Date: October 1, 2016 End Date: September 30, 2018
Project Funding (FY18): $550,000 DOE share: $550,000 Non-DOE share: $0

Project Introduction

The Electrical and Electronics Technical Team (EETT) Roadmap [1] proposes aggressive research and development targets aimed at improving power electronics technology to enable the mass market penetration of electric-drive vehicles. Achieving these aggressive targets will require a decrease in cost (year 2025 cost target: $2.70/kW) and an increase in power density (year 2025 power density target: 100 kW/L) as compared with current, on-road technology. Replacing traditional silicon device-based components with more efficient and higher temperature wide-bandgap (WBG) semiconductor device-based components will enable increasing the power density. However, meeting the power density target will also require innovative thermal management solutions to increase the heat fluxes dissipated, reduce component temperatures, and allow for compact electronics packaging.

This project conducts research to develop new power electronics thermal management technologies to increase power density, enable high WBG temperature operation, and decrease cost. One of the main challenges to achieving high power densities is associated with packaging of high-temperature (250°C) WBG devices near lower-temperature-rated components (e.g., electrical boards and capacitors). Additionally, WBG device's high junction temperatures will result in large temperature gradients through the power module layers that will present reliability challenges and require higher-temperature substrates and bonding materials.

This project also supports a collaborative research effort between NREL and John Deere to research and develop advanced cooling technologies (two-phase cooling) for power electronics in heavy-duty vehicles. The work with John Deere is part of a collaborative research and development agreement (CRADA) and, due to the proprietary nature of the work, the results of this task are not provided in this report.

Objectives

The primary project objective is to develop thermal management technologies to enable achieving 100-kW/L power density target. Additional project objectives are listed below.

- Develop cooling solutions that enable high-temperature (250°C) WBG operation and low-temperature, low-cost capacitors.
- Decrease cost by proposing low-cost cooling technologies that enable decreasing the number of semiconductor devices and use automotive-qualified fluids.
- Collaborate with John Deere to develop a power-dense two-phase-cooled inverter.

Approach

We first computed a thermal target that can enable achieving a power density of 100 kW/L. The thermal target was defined in terms of a volumetric thermal resistance metric where the junction-to-coolant thermal resistance was scaled by the cold plate and power module volume requirements. Modeling analyses was then conducted

to evaluate different cooling technologies and identify the best-performing cooling strategy. The selected cooling configuration was then designed/optimized to meet the thermal target using detailed computational fluid dynamics (CFD) simulations. Future work will be conducted to complete the design of the cooling system and to conduct an experimental validation. Work will also be conducted to evaluate the use of automatic transmission fluid (ATF) as a dielectric coolant for power electronics cooling.

John Deere CRADA Task: We collaborated with John Deere to develop a two-phase-cooled inverter. John Deere designed the electrical aspects and selected components, and NREL provided thermal management support via modeling and experimental work.

Results

Defining a Thermal Metric/Target

We computed a thermal metric that is predicted to enable reaching the 100-kW/L power density target (for a 100-kW peak power inverter). The thermal metric was computed assuming a maximum junction temperature of 250°C (high-temperature WBG operation) and a coolant temperature of 65°C. Heat dissipation for a 100-kW inverter was estimated to be 2,150 W assuming 95% and 98% electric motor and WBG inverter efficiencies, respectively. The junction and coolant temperatures combined with the heat dissipation requirements were used to compute a thermal resistance that was scaled by the volume available for the power module and cooling system. The power module and cooling system volume requirements were computed by estimating the volume of the electrical boards (gate drive and control) and DC-link capacitors for a 100-kW inverter and then subtracting their volumes from 1 liter to obtain an estimate of the volume available for the power module and cooling system. The electrical board and capacitor volumes were measured from the 2012 Nissan LEAF (80-kW system) and 2015 BMW i3 (125-kW system). Table I.11.1 lists the measured component sizes and assumptions along with the estimated volume requirements for the power module and cooling system (0.24 L). The volumetric thermal resistance target was estimated to be 21 cm^3-K/W. The volume requirement value is an estimate based on existing technology (using measurements from on-road vehicles) and assumptions on capacitor size reduction and does not include all the inverter components (e.g., sensors, bus bars, enclosure). However, it provides a simplified thermal metric that can be used to guide the thermal design.

Table I.11.1 Estimated Volume for Components in a 100-kW Inverter

Component	Volume used for 100-kW/L inverter estimate [L]	Source
Gate driver (includes current sensors)	0.28	2015 BMWi3 (125-kW system)
Control board	0.23	2012 Nissan LEAF (80-kW system)
Capacitor	0.25	2015 BMWi3 (125-kW system): Assumption: BMW capacitor volume was decreased by 50% to account for a decrease in capacitor requirements for WBG devices
Remaining volume for power module and cooling system	0.24	

Selecting the Cooling Technology

Finite element (FE) thermal modeling was conducted to compare the performance of three cooling technologies and select the optimal cooling strategy for the 100-kW/L inverter. The 2015 BMWi3 power module was used for this thermal analysis. Through modeling we simulated cooling the module using either a baseplate-cooled, direct-bond-copper (DBC)-cooled, or a device-cooled configuration. For the baseplate-cooled case, cooling was provided on the lower surface of the baseplate. For the DBC-cooled case, the baseplate was removed, and cooling was provided on the DBC surface. For the device-cooled case, cooling was provided on top of the device and on the exposed surfaces of the top metallization layer. The device-cooled configuration would require the use of a dielectric coolant because the fluid is in contact with

electrically active surfaces. In the FE models, cooling was imposed by applying heat transfer coefficient (HTC) boundary conditions on the cooled surfaces. A range of HTCs was applied to evaluate the effect of the convective cooling performance on the thermal resistance.

Figure I.11.1 plots the junction-to-coolant resistance versus the heat transfer coefficient for the three cases. The results show that at higher HTCs (≥10,000 W/m^2-K), the device-cooled case provides the lowest thermal resistance. Moreover, the device-cooling configuration (with dielectric fluid) allows for directly cooling the electrical leads/bus bars, which has the benefit of reducing the capacitor and gate driver temperatures. Decreasing capacitor and electrical board temperatures is critical considering the desire to operate at higher junction temperatures and the need to increase power density (e.g., place capacitors next to high-temperature WBG devices). Based on these findings, we decided to pursue the device-cooling (with dielectric fluid) approach for the thermal management strategy.

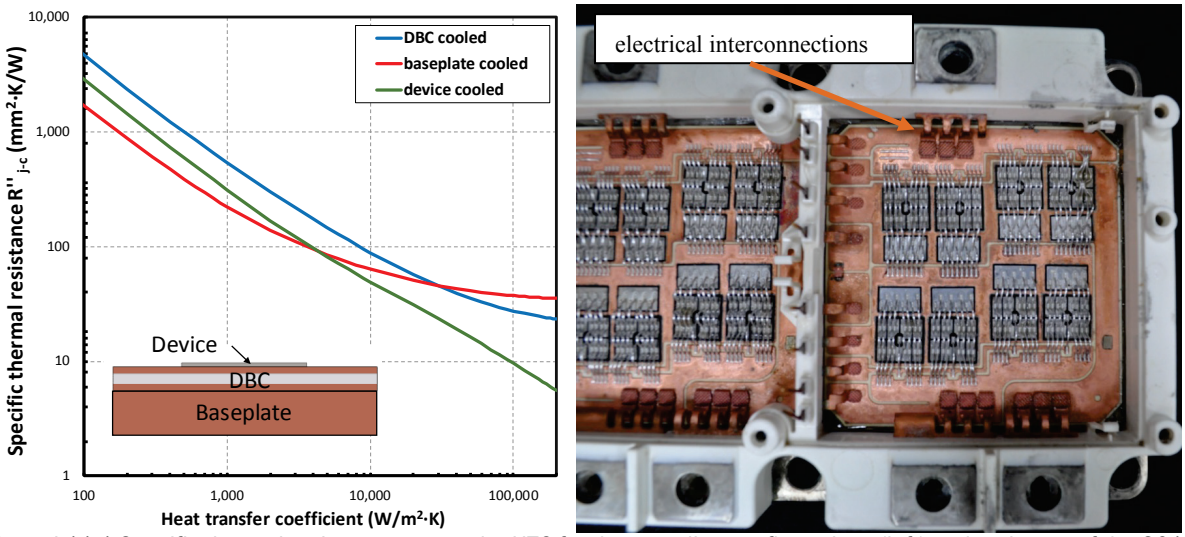

Figure I.11.1 Specific thermal resistance versus the HTC for three cooling configurations (left) and an image of the 2015 BMWi3 power module used for the thermal analysis (right).

Image credit: Xuhui Feng, NREL

In application, it may be difficult to directly cool the devices (fluid in direct contact with the device) using a dielectric fluid due to reliability concerns and the fact that the top of the devices requires electrical connections for device functionality. A more feasible variation of this cooling strategy involves using the planar package design shown in Figure I.11.2. In this configuration, the top metal (likely copper) plate has dual functionality as an electrical conductor and a heat spreader. In this configuration, the dielectric fluid cools the top surface of the top copper plate and thus eliminates direct contact between the fluid and the devices. This cooling concept also eliminates the need for thermally conductive (and expensive) ceramics (e.g., alumina, silicon nitride) since the heat flows upward through the module to the fluid.

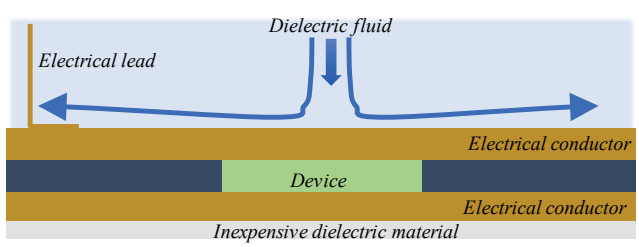

Figure I.11.2 Planar package, dielectric cooling concept

Designing the Cooling System

Several dielectric fluids are commercially available for electronics cooling applications and were considered for the planar package dielectric cooling strategy. The primary criteria in selecting dielectric fluids are the fluid's dielectric properties, viscosity, flash point, safety (non-toxic and environmentally friendly), material compatibility, and cost. EC-140 and Alpha 6 synthetic fluids were evaluated due to their relatively high flash points (flash point: EC-140 = 280°C [2], Alpha 6 = 240°C [3]) and good material compatibility. Table I.11.2 provides the properties for EC-140 at 100°C and compares them to those of water-ethylene glycol (WEG). The properties of Alpha 6 are similar to those of EC-140 but its viscosity is lower [3]. Both dielectric fluids evaluated are designed for single-phase cooling applications. Future work is planned to evaluate the use of ATF as a dielectric coolant for power electronics cooling applications.

Table I.11.2 Properties for EC-140 and WEG. All Properties Taken at 100°C except where Noted.

	Thermal conductivity [W/m-K]	Specific heat [J/kg-K]	Density [kg/m3]	Viscosity [cP]
EC-140 [2]	0.16	2,409	830 (at 16°C)	7.42
WEG [4]	0.43	3,625	1,012	0.7

CFD analysis was used to model a dielectric-fluid jet impinging on the top-side of a planar package (Figure I.11.3). These cases were representative of a submerged jet dissipating heat through single-phase heat transfer. The planar package consisted of a 5×5×0.18 mm silicon carbide (SiC) semiconductor device (e.g., metal–oxide–semiconductor field-effect transistor [MOSFET]) placed between two 0.3-mm-thick copper plates. Circular and slot jets were modeled at various jet velocities, and their performance was compared on an equivalent pumping power (pressure drop × volumetric flow rate) basis. The maximum jet velocity was intentionally kept relatively low (1 m/s maximum) to minimize both pressure drop and corrosion-erosion effects. The slot jet minor dimension (*w*) and circular jet diameter (*d*) were varied from 1 – 3 mm to evaluate the effect of these parameters on performance. The long dimension of the slot jet was maintained at 5 mm for all cases to be equal to the size of the SiC device. The spreader width (*s*) was also varied from 5.1 mm to 15 mm to evaluate the effect of heat spreading on thermal performance. EC-140 fluid, at an inlet temperature and fluid properties evaluated at 70°C, was the fluid used for the CFD simulations. The CFD simulations were conducted using laminar flow due to the relatively low fluid velocities and Reynolds numbers (< 500).

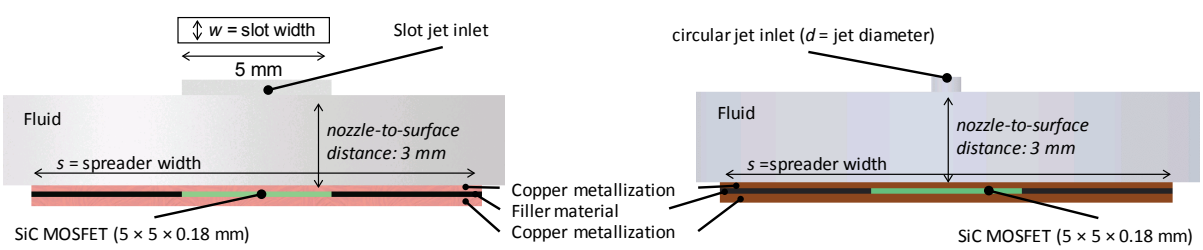

Figure I.11.3 Cross-sectional views of the three-dimensional slot (left) and circular (right) jet models used for the CFD simulations.

Figure I.11.4 plots the junction-to-coolant thermal resistance versus the pumping power for the slot and circular jet cases. The thermal resistance is computed per the equation below.

$$R_{th,j-c} = \left(T_{j,max} - T_{c,inlet}\right) / \, Heat_{device}$$

where $T_{j,max}$ is the maximum junction temperature, $T_{c,\,inlet}$ is the fluid inlet temperature, and $Heat_{\,device}$ is the total heat dissipated by the SiC device. The results for characteristic jet dimensions (*w, d*) of 1 and 3 mm are provided in Figure I.11.4. The slot jet configuration is predicted to provide lower thermal resistance as compared with the circular jet case when the characteristic jet dimension is 1 mm. However, the thermal resistance for the slot and circular jet cases are nearly identical when the characteristic jet dimension is 3 mm. Increasing the characteristic jet dimension beyond 3 mm may be unrealistic, especially for the slot jet case, due

to the higher flow rate requirements considering multiple devices (e.g., 24) will need to be cooled (assuming the flow through the devices is in the parallel configuration) and the desire to operate below 10 Lpm (typical WEG system flow rate).

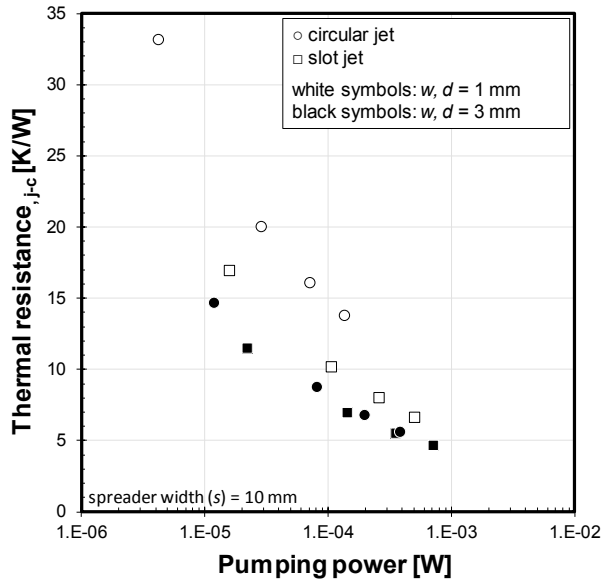

Figure I.11.4 Junction-to-coolant thermal resistance versus pumping power for the circular and slot jet configurations. Results for the 1- and 3-mm characteristic jet dimension are shown.

The thermal resistance is predicted to be relatively high (~4.7 K/W) for the highest parasitic power case considered (corresponding to 1 m/s jet velocity). This thermal performance is relatively poor compared to current/on-road automotive WEG cooling systems and thus the need to improve performance via area enhancement (e.g., fins).

CFD modeling was then conducted to evaluate the effect of fabricating fins on the top copper plate to increase surface area and thus improve thermal performance. Two finned cases were modeled—1 and 2.5 mm tall finned cases (Figure I.11.5). In both cases, the fins were part of the top copper plate and were centered directly over the SiC device. The finned area was 7×7 mm and extended 1 mm beyond the SiC footprint in an effort to increase surface area. The fin thickness and channel width were 0.2 mm for all cases. Skiving and potentially 3D printing are potential techniques to fabricate these fin structures. Due to the linear structure (i.e., not radial) of the fins, the finned cases were only modeled for the slot jet cases with a slot width of w = 1 mm. The effect of jet velocity (1 m/s maximum) and spreader width (s = 5.1 mm to 15 mm) on performance was evaluated using CFD for the two finned cases.

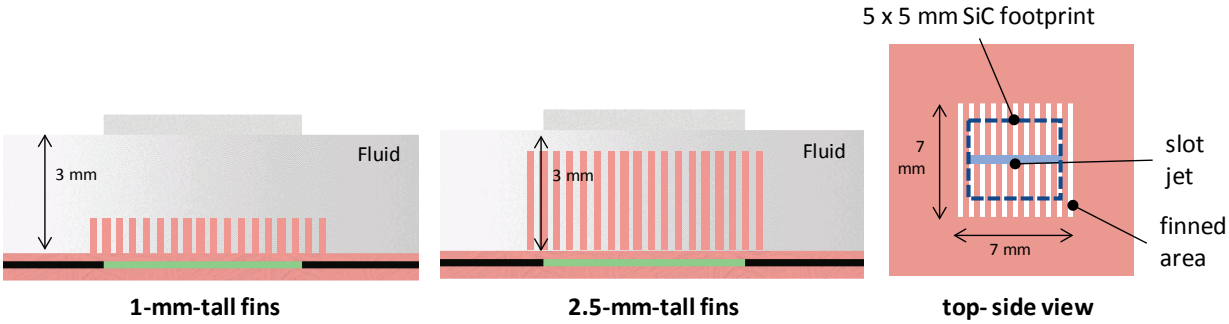

Figure I.11.5 Sectional views of the 1- (left) and 3- (middle) mm finned cases. The top view schematic is shown on the right.

Figure I.11.6 plots the junction-to-coolant thermal resistance versus the velocity for the 1- and 2.5-mm-tall fin and the baseline (no fin) configurations. The area enhancement of the fins increases heat transfer and thus reduces the thermal resistance compared with the baseline case. However, these finned-surface thermal enhancements come at the expense of higher pressure drop. The heat transfer enhancements for the 1-mm fins increases as the velocity is increased—a result of more fluid penetrating/flowing through the fins. The 2.5-mm-tall fins provide the largest enhancement of (~80% lower thermal resistance compared with baseline) due to their larger surface area. At 1 m/s jet velocity, the junction-to-coolant thermal resistance for the 2.5-mm-tall fin configuration is predicted to be ~50% lower than the thermal resistance for the 2014 Honda Accord Hybrid (Accord thermal performance obtained from [5]). This thermal performance is significant considering the relatively poor thermal properties of the dielectric fluids as compared with WEG (see Table I.11.2). Better performance (compared with the 2014 Accord) is achieved with the dielectric, planar package configuration due to the decrease of the conduction thermal resistance (i.e., removal of package material) and enhancements to the convective cooling performance (use of jets combined with highly-dense finned structures). The thermal resistance of the 2.5-mm-tall fins configuration decreases with increasing velocity at velocities lower than ~0.5 m/s. However, increasing the velocity beyond 0.5 m/s has minimal effect on the thermal resistance. The insensitivity of the thermal resistance to the fluid velocity is likely due to the characteristics of laminar flow heat transfer which is influenced by channel size and not fluid velocity (i.e., Nusselt number is a constant for laminar flow through channels).

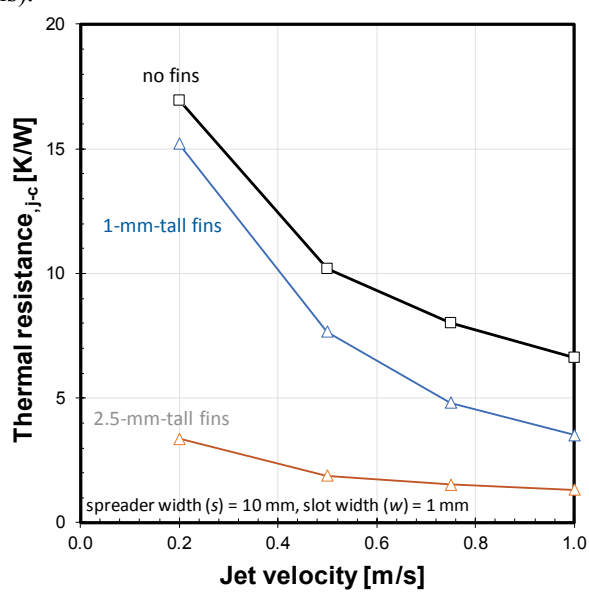

Figure I.11.6 Junction-to-coolant thermal resistance versus the jet velocity for the two-finned cases and the baseline (no fin) case.

Figure I.11.7 shows the CFD-computed temperature contours for the 2.5-mm-tall configuration at a jet velocity of 0.5 m/s, slot width of w = 1 mm, and a spreader width of w = 10 mm. A total of 90 W of heat was dissipated in the device shown in Figure I.11.7, resulting in a maximum junction temperature of 234°C. Under these conditions, 24 devices would be required to dissipate the estimated heat load (90 W × 24 = 2,160 W) for a 100-kW inverter. Figure I.11.7 also shows a conceptual three-phase inverter consisting of 24 devices. In this configuration, a manifold structure (likely made from plastic) would be required to route the dielectric fluid to impinge directly over the 24 devices. The conceptual inverter would have an approximated footprint of 60×40 mm. Assuming a total inverter and cooling system height of 25.4 mm for fluid volume, fluid manifold, fins, planar package, electrical interconnects, and enclosure, then the total volume of the inverter with cooling system is about 0.06 L, which is about one-quarter of the volume available for these components (see Defining a Thermal Metric/Target Section). The estimated volumetric thermal resistance for this inverter with cooling system is ~5 cm^3-K/W, which is considerably better than the thermal target of 21 cm^3-K/W. Work is currently being conducted to further optimize the fin structures for the dielectric fluids (EC-140 and Alpha 6) to improve

thermal performance, reduce the pumping power, and design the fluid manifold structure. Work is also being conducted to evaluate the effect of high fluid viscosity at low temperature conditions (-40°C winter temperatures).

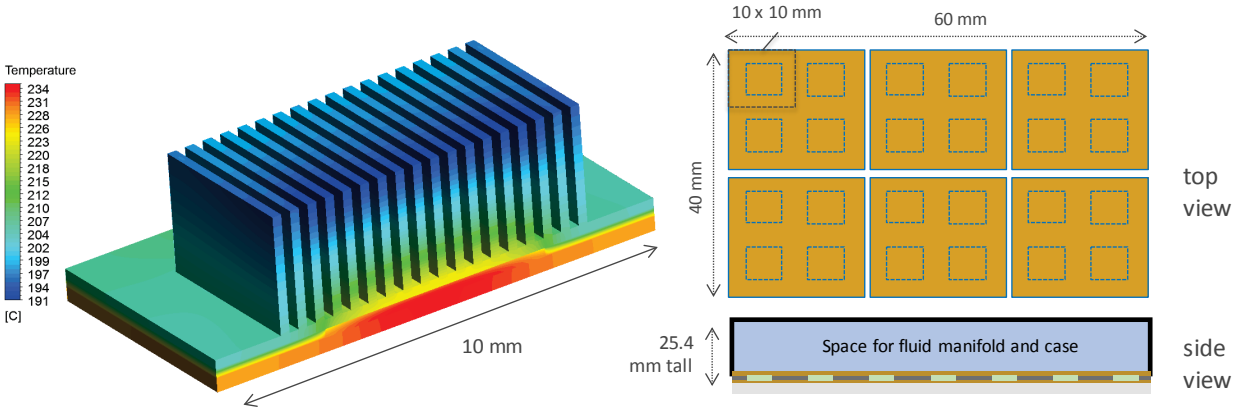

Figure I.11.7 CFD-computed temperatures for the 2.5-mm-tall fins configuration and jet velocity of 0.5 m/s (left). The fluid streamlines are shown as black lines. A schematic of a conceptual inverter with cooling system consisting of 24 devices predicted to enable reaching the 100-kW/L power density target (right).

As previously mentioned, directly cooling the electrical interconnections is a benefit of the dielectric cooling strategy. Due to the higher WBG junction temperatures, it is necessary to cool the electrical connections to mitigate heat flow and maintain capacitors and gate driver board temperatures below 100°C (assuming polypropylene film capacitors) and 125°C, respectively. Therefore, thermal analyses were conducted to estimate the cooling requirements for the electrical interconnects. The electrical interconnections were assumed to be similar in size to the electrical interconnects found in the 2015 BMWi3 power module (see Figure I.11.1). FE thermal modeling was first conducted to determine the HTC values required to keep the electrical interconnects below 100°C. CFD modeling was then used to determine the dielectric fluid velocity required to achieve the target HTCs (from FE).

A simplified model of a planar package and electrical interconnect was used for the FE analysis. The FE model is shown in Figure I.11.8 and consists of one SiC device between two copper plates (planar package) and one electrical interconnect attached to the top copper plate and extending vertically upward. In application, multiple electrical interconnects would be required, but only one was modeled here to simplify the model. The FE modeled a SiC device dissipating 90 W and applied an HTC boundary condition (13,000 W/m^2-K) on the top surface of the top copper plate to simulate cooling from a dielectric jet impinging on finned surfaces that resulted in a maximum junction temperature of 250°C. Under these conditions, HTC boundary conditions were also applied to the four sides of the interconnect (excluding the top surface) to simulate a dielectric fluid flowing across and cooling the interconnect. The HTC on the interconnect was varied to identify the HTC value that is required to keep the surface temperature at the top of the interconnect below 100°C. Cooling of the interconnect removes heat from the package, resulting in a decrease in junction temperatures as the interconnect HTC is increased (T_j drops below 250°C as shown in Figure I.11.8). Because the interconnects are the electrical and heat flow paths between the devices and the capacitors and boards, the temperature at the top of the interconnect represents the approximate temperature near the gate driver and the capacitors. All other model surfaces were assumed to be adiabatic. FE analyses were conducted to evaluate the effect of interconnect height (5 mm, 7.5 mm, and 10 mm), distance from SiC device (5 mm and 10 mm, measured from

the edge of the SiC to the leading edge of the interconnect), and aspect ratio (width × thickness: 1.5 mm × 1 mm, 2 mm × 0.5 mm, 3 mm × 0.5 mm) on interconnect top-surface maximum temperature.

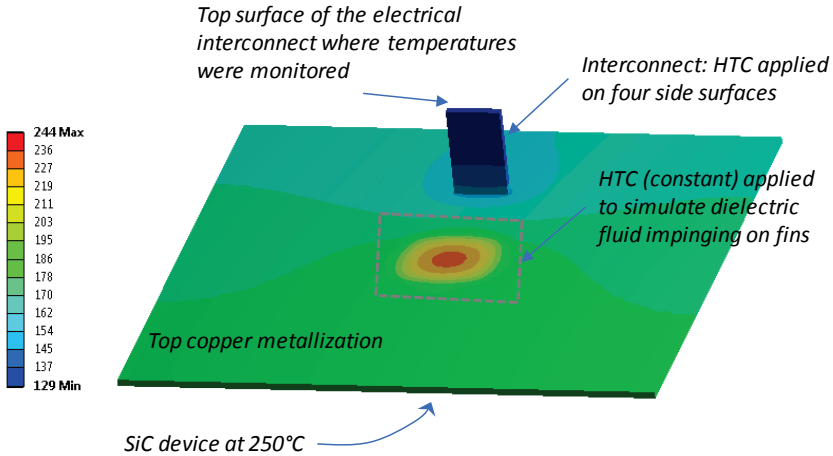

Figure I.11.8 FE model used to determine the HTC cooling requirements for cooling the electrical interconnect.

Approximately 235 FE design points were modeled to find the HTC values that are required to achieve interconnect temperatures < 100°C. Figure I.11.9 shows the FE-computed maximum top-surface interconnect temperatures for the case when the interconnect aspect ratio is 3 mm × 0.5 mm. The x-axis labels from top to bottom are the applied interconnect HTC, interconnect distance from the MOSFET, and the interconnect height. As shown, increasing the HTC and the interconnect height have the biggest effect on reducing the interconnect temperatures. HTC values ≥ 2,000 W/m^2-K are required to achieve interconnect temperatures <100°C. Higher HTC values (~5,000 W/m^2-K) are required for shorter interconnects and a closer distance between the interconnect and the MOSFET.

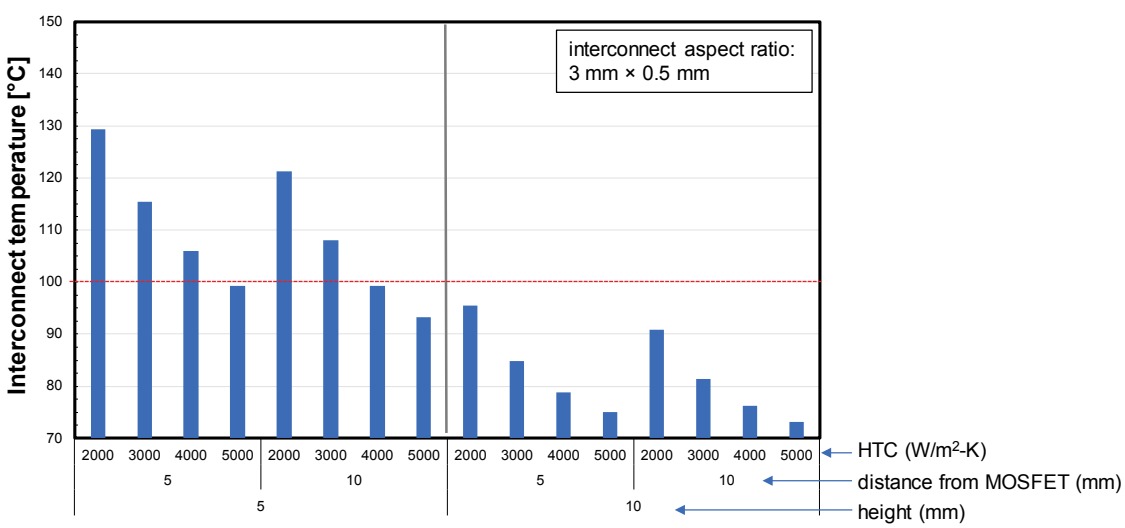

Figure I.11.9 FE-computed interconnect maximum top-surface temperatures versus the applied interconnect HTCs, interconnect distance from MOSFET, and interconnect height.

CFD simulations were then conducted to estimate the dielectric fluid velocities that would be required to achieve HTC of ≥ 2,000 W/m^2-K. The CFD modeled EC-140 dielectric fluid (inlet temperature and fluid properties evaluated at 70°C) flowing across the electrical interconnect with the fluid flow aligned with the long interconnect dimension (see Figure I.11.10). The interconnect was located within a 5 mm × 10 mm channel and was placed 20 mm downstream from the inlet. The interconnect height was fixed at 5 mm and a

250°C temperature boundary conditions was applied to the base of the interconnect. Uniform velocity and pressure outlet boundary conditions were applied at the inlet and outlet surfaces, respectively. Fluid inlet velocity was varied from 0.25 m/s to 2 m/s to evaluate its effect on the average HTC defined per the equation below.

$$\overline{HTC} = Heat/[Area_{total}\,(\overline{T_w} - T_{inlet})]$$

where *Heat* is the total heat dissipated, and T_{inlet} is the fluid inlet temperature. $Area_{total}$ is the total area and $\overline{T_w}$ is the average surface temperature for the four sides of the interconnect. Thus $\overline{HTC}$ provides the surface averaged HTC for the four sides of the electrical interconnect. The flow was modeled assuming laminar flow due to the low Reynolds numbers (625 maximum).

Figure I.11.10 plots the average HTC versus the fluid velocity for three interconnect aspect ratios. Results indicate that low fluid velocities (0.25 m/s to 0.5 m/s) can provide HTC of about 2,000 W/m^2-K. HTC values of 4,000 W/m^2-K can be achieved with fluid velocities of 1.25 m/s to 2 m/s—the exact velocity is dependent on the aspect ratio. Adding more interconnects to the model should aid in further decreasing the electrical interconnect temperatures since the interconnects are essentially fins and increasing the interconnect/fin count will improve heat dissipation.

Future work will be conducted to design a module cooling system that uses a lightweight manifold to guide the fluid first across the electrical interconnects and then to impinge over the semiconductor devices. These modeling results will be used to guide the manifold dimension to achieve the required velocities (and HTCs). Once the design work is completed, we will fabricate the cooling system and conduct an experimental demonstration of the cooling concept.

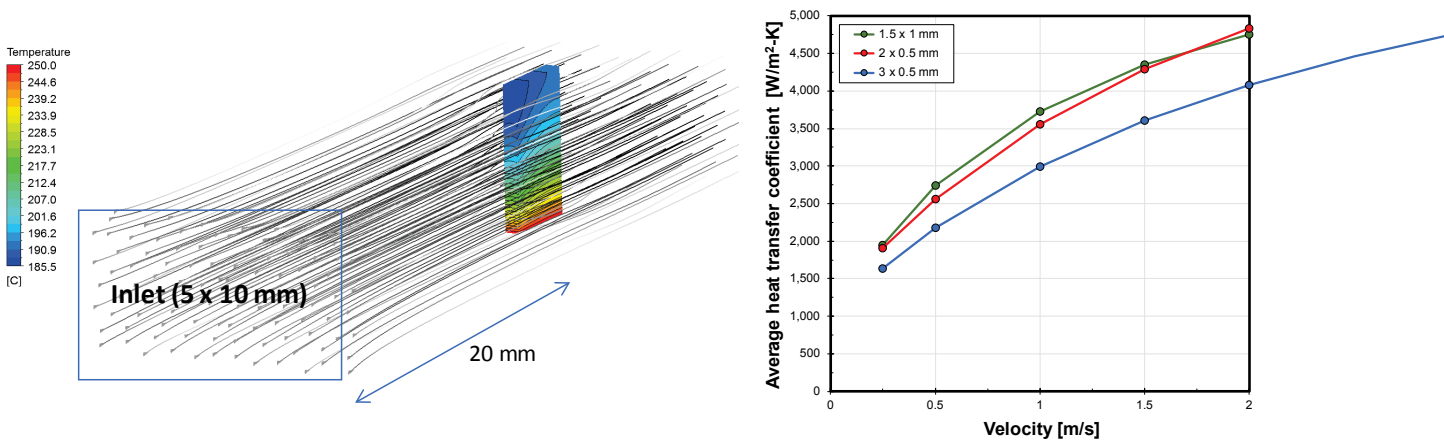

Figure I.11.10 CFD-computed electrical interconnect temperatures and relevant model dimensions (left). Interconnect average heat transfer coefficient versus the dielectric fluid velocity (right).

Conclusions

The major conclusions are summarized below.

- A volumetric thermal target/metric that would enable reaching 100-kW/L power density was defined. The thermal metric was computed assuming a maximum junction temperature of 250°C, a coolant temperature of 65°C, a heat dissipation of 2,150 W (estimated heat load of a 100-kW WBG inverter), and an estimate of the volume available for the power module and cold plate. The thermal metric was computed to be 21 cm^3-K/W and was used to guide the design of the inverter thermal management system.
- The performance of three power module cooling strategies were modeled and the results were compared to identify the best cooling strategy. Directly cooling the devices with the use of a dielectric fluid was

found to provide the lowest junction-to-coolant thermal resistance and enable cooling of the electrical interconnections and was the cooling strategy pursued in this project. Two dielectric fluids (EC-140 and Alpha 6) were used in the analyses, but work is underway to evaluate the use of ATF as the dielectric fluid because this would decrease cost, allow for the use of an automotive-qualified fluid, and enable integrating the inverter with the motor.

- A dielectric fluid-based, planar package cooling strategy was developed and is predicted to enable achieving the 100-kW/L power density target. The cooling strategy uses submerged jets impinging on highly-dense finned structures to dissipate heat via single-phase heat transfer. CFD was used to compare the performance of slot and circular submerged jets under various jet velocity and nozzle-size conditions. Work was also conducted to design the cooling system for the electrical interconnections.
- We are collaborating with John Deere to develop a two-phase cooling strategy for its inverter. We completed design of the cooling system and have fabricated prototypes for experimental validation.

Key Publications and Presentations

1. Moreno, G, "Thermal Management and Packaging of High Temperature Automotive Power Electronics." 3D Power Electronics Integration and Manufacturing Conference, College Park, MD, June 2018.
2. Moreno, G. "Power Electronics Thermal Management Research." 2018 DOE VTO Annual Merit Review, Washington, DC, June 2018.
3. Moreno, G. "Power Electronics Thermal Management Research." 2018 presentation to the DOE VTO Electrical and Electronics Technical Team, July 2018.
4. Moreno, G. "Power Electronics Thermal Management Research." 2017 DOE VTO Annual Report, 2017.

References

1. U.S. DRIVE, "Electrical and Electronics Technical Team Roadmap," U.S. DRIVE, Oct. 2017.
2. "Engineered Fluids | ElectroCool Dielectric Coolant," Dielectric Coolants | United States | Engineered Fluids. [Online]. Available: https://www.engineeredfluids.com/electrocool. [Accessed: 11-Sep-2018].
3. "Alpha-6 FluidTM," DSI Ventures, Inc., 03-Feb-2013. [Online]. Available: https://dsiventures.com/specialty-cooling/alpha-6-fluid/. [Accessed: 11-Sep-2018].
4. Alshamani, K. "Equations for Physical Properties of Automotive Coolants." SAE Technical Paper, 2003.
5. Moreno, G., Bennion K., King C., and Narumanchi S. "Evaluation of Performance and Opportunities for Improvements in Automotive Power Electronics Systems." 15th IEEE Intersociety Conference on Thermal and Thermomechanical Phenomena in Electronic Systems (ITherm) Las Vegas, NV, 2016, pp. 185–192.

Acknowledgments

The author would like to acknowledge the support provided by Susan Rogers, Technology Manager for the Electric Drive Technologies Program, Vehicle Technologies Office, U.S. Department of Energy Office of Energy Efficiency and Renewable Energy. The significant contributions of Kevin Bennion, Xuhui Feng, and Bidzina Kekelia are acknowledged.

I.12 Electric Motor Thermal Management Research (NREL)

Kevin Bennion, Principal Investigator
National Renewable Energy Laboratory
15013 Denver West Parkway
Golden, CO 80401
E-mail: kevin.bennion@nrel.gov

Susan A. Rogers, DOE Technology Development Manager
U.S. Department of Energy
E-mail: susan.rogers@ee.doe.gov

Start Date: FY2017 End Date: FY2018
Project Funding (FY18): $650,000 DOE share: $650,000 Non-DOE share: $0

Project Introduction

Thermal management for electric motors is important as the automotive industry continues to transition to more electrically dominant vehicle propulsion systems. With the push to reduce component size, lower costs, and reduce weight without sacrificing performance or reliability, the challenges associated with thermal management for power electronics and electric motors increase. The transition to more electrically dominant propulsion systems leads to higher-power duty cycles for electric drive systems. Thermal constraints place significant limitations on how electric motors ultimately perform. As summarized by Thomas Lipo, "an optimized thermal design can help increase machine rated power substantially, almost without any increase of its manufacturing costs" (Lipo 2007). The performance limitations caused by motor heating are highlighted in Figure I.12.1. The motor's ability to increase running time at higher power levels within electrical operating limits is directly related to the ability to remove heat from critical components. As thermal management improves, there will be a direct tradeoff among motor performance, efficiency, cost, and the sizing of electric motors to operate within the thermal constraints.

Thermal management of electric motors is a complex challenge because of the multiple heat transfer paths within the motor and the multiple materials and thermal interfaces through which the heat must pass to be removed. The technical challenges to motor thermal management are summarized by Hendershot and Miller as follows: "Heat transfer is as important as electromagnetic and mechanical design. The analysis of heat transfer and fluid flow in motors is actually more complex, more nonlinear, and more difficult than the electromagnetic behavior" (Hendershot and Miller 1994). Figure I.12.1 provides a cut cross-section view illustrating heat transfer and cooling paths for automotive traction drive applications. The heat generated by the electric motor is distributed throughout multiple components within the electric motor. For example, heat is generated due to losses within the stator slot-windings, stator end-windings, stator laminations, rotor laminations, and rotor magnets or conductors. The distribution of the generated heat within the components is dependent on the motor type and the operating condition (torque/speed) of the motor. The selected cooling approach for the motor impacts the path of heat flow through the motor and the temperature distribution of components. For example, as shown in Figure I.12.1, a motor cooled with a stator cooling jacket will require heat generated within the slot windings to pass through multiple material layers and material interfaces before the heat is extracted through the cooling jacket. The thermal properties of the materials and the thermal contact resistances due to the material interfaces impact the temperature distribution inside the motor as heat flows into the cooling jacket. Alternatively, direct cooling of the windings with oil or automatic transmission fluid (ATF) reduces the heat transfer path from the motor windings to the coolant. However, heat from the stator must pass through several interfaces. The resulting changes in the temperature distribution within the motor lead to hot spots within the motor that could be difficult to measure.

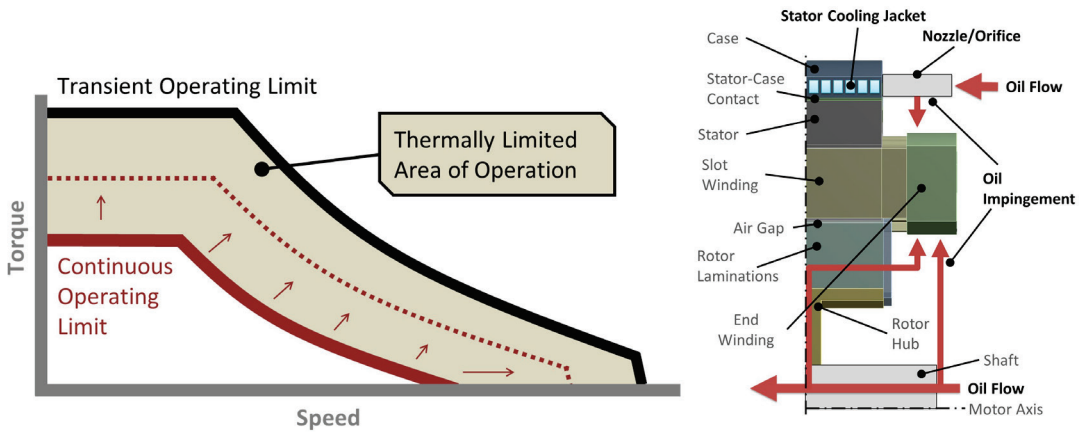

Figure I.12.1 Illustration of thermal management impact on motor operation to increase continuous power operating limits (left). Heat must pass through several layers within the motor to be extracted through active cooling such as through a cooling jacket or jet impingement cooling with oil such as ATF (right).

Objectives

The overall project objective is to provide motor researchers, developers, and suppliers with the data and analysis of motor heat transfer technologies to enable motor innovations and accelerate the use of novel materials and designs for the adoption of vehicle electrification technologies. The work combines unique capabilities, facilities, and expertise in addition to the data, analysis methods, and experimental techniques to improve and better understand heat transfer within rare-earth and reduced rare-earth motors to meet the demands of electric drive vehicles. The National Renewable Energy Laboratory's (NREL's) capabilities enable development, demonstration, and confirmation of active and passive heat transfer technologies and innovations.

Approach

The ability to remove heat from an electric motor depends on the passive stack heat transfer within the motor and the convective cooling heat transfer of the selected cooling technology. In addition, as new materials are developed, it is important to characterize temperature-dependent material properties and thermal interface properties. Characterization of new materials enables motor designers to evaluate the potential performance tradeoffs of new materials for motor applications. For this reason, the approach for the research project splits the efforts between active and passive heat transfer. Passive heat transfer refers to the geometrical layout, material selection, and thermal interfaces that affect the heat-spreading capabilities within the motor. The ability for heat to spread through the motor affects the thermal temperature gradients within the motor. The active heat transfer's convective cooling technology is the cooling mechanism that ultimately removes the heat from the motor and transfers the heat to another location to reject the heat to the ambient environment.

Active Heat Transfer

The two common approaches highlighted in Figure I.12.1 for active cooling include: 1) directly cooling the motor with oil or driveline fluids such as ATF, and 2) cooling the motor with a cooling jacket surrounding the stator. The advantages of either cooling approach depend on the application's coolant availability, the motor geometry, the motor winding configuration, and the motor loss distribution. The advantage of cooling using ATF is that it is possible to directly cool the motor windings or rotor. Past work focused on measurement of average convection coefficients of ATF jets passing through a circular orifice directly impinging on target surfaces representative of motor end windings (Bennion and Moreno 2015). This year, the focus emphasized a parametric study to quantify factors influencing the convective heat transfer coefficients. A drawing of the experimental setup highlighting the experimental factors is shown in Figure I.12.2. The experimental matrix is shown in Table I.12.1, while Figure I.12.3 shows an example running experiments that show the two jet position experiments.

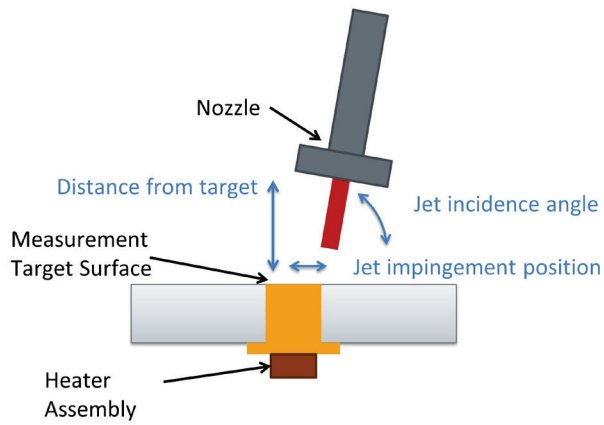

Figure I.12.2 Jet impingement experimental setup and experimental factors.

Table I.12.1 Experimental Factors and Levels

Experimental Factor	
Jet incidence angle [degrees]	90, 60, 45
Jet distance from target [mm]	5, 10, 15
Jet position on target [mm]	0 (center), 6.3
Fluid nozzle inlet temperature [°C]	50, 70, 90
Surface temperature [°C]	90, 100, 110, 120

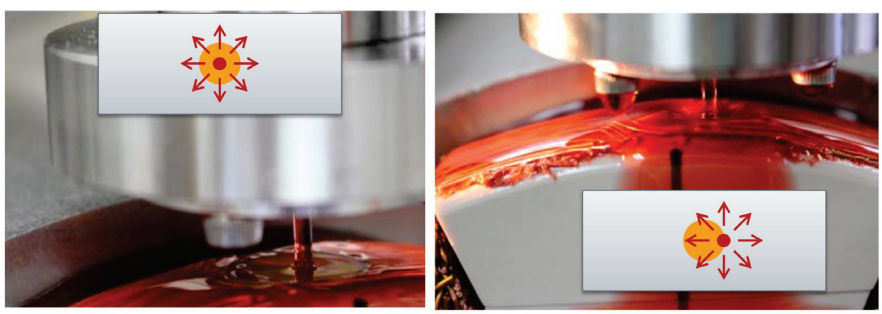

Figure I.12.3 Orifice jet center impingement (left). Orifice jet edge impingement (right)

Photo Credit: Bidzina Kekelia, NREL

Passive Heat Transfer

The passive heat transfer through the motor materials and material interfaces is critical to designing effective thermal management systems for electric motors. The work supports improved thermal models for motor design, but it also enables analysis to compare the potential impacts of new materials, fabrication methods, or material processing on motor heat transfer. During FY18 two papers were published describing efforts to develop models to predict thermal resistances within electric motors, which were validated with experimental data. The first paper was a collaboration with UQM Technologies describing the thermal contact resistance between a motor stator and aluminum press-fit housing (Cousineau et al. 2018). The second paper, accepted by the *International Journal of Heat and*

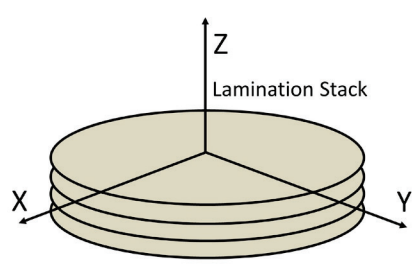

Figure I.12.4 Orthotropic thermal property orientation for machine laminations. Through-stack conductivity is along the z-axis, and in-plane thermal conductivity is along the x-y plane.

Mass Transfer in September of 2018, describes models to predict the thermal resistance of stacked steel laminations and the contact resistance between laminations (Cousineau et al. 2019). It is available online and will be available in print in 2019. The most recent paper focusing on the lamination materials is the focus of this report. The objective of the paper is to quantify the effective thermal conductivity through a stack of laminations as shown in Figure I.12.4 in the z-direction. A critical unknown that impacts the effective thermal conductivity is the interlamination thermal contact resistance. The paper outlines the experimental approach to measure the contact resistance and demonstrates how to calculate the thermal contact resistance for a known set of materials.

Figure I.12.5 shows the experimental setup for measuring the effective through-stack thermal conductivity and thermal contact resistance. The test apparatus was built in accordance with the ASTM Standard D5470-12 steady-state technique (Narumanchi et al. 2008; D09 Committee 2012). The advantage of this setup for this application is it sets up a one-dimensional heat flux to enable measurement of thermal properties in one specific direction independently of the other directions. The setup uses resistance temperature detectors (RTDs) inserted into the copper metering blocks that are located on the top and bottom of the test sample. Heat is provided to one side of the sample through electrical heaters inserted into an aluminum heater block. The cold plate is cooled with a bath circulator using silicone oil as the coolant.

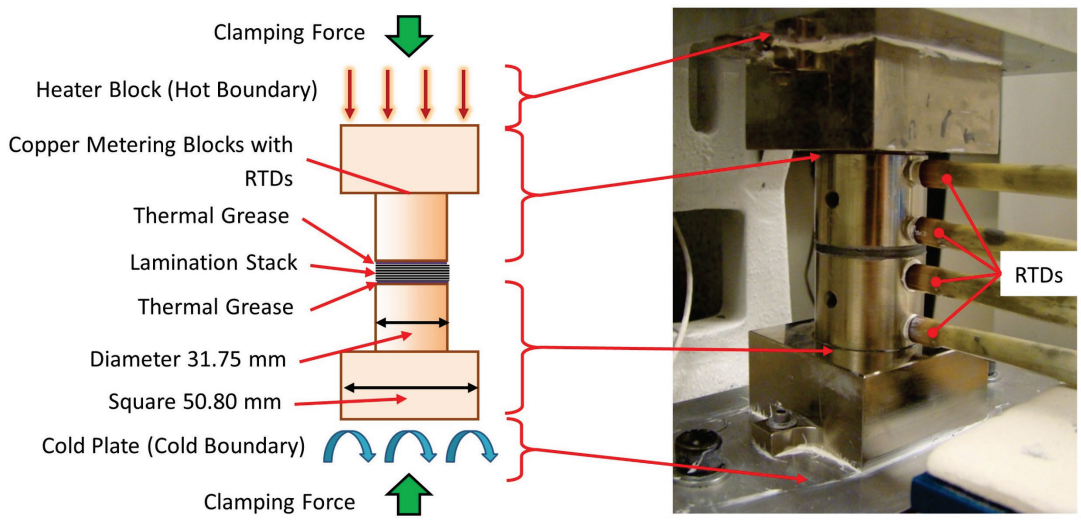

Figure I.12.5 Schematic (left) and photo (right) of the steady-state setup for measuring orthotropic thermal conductivity values

Photo Credit: Emily Cousineau, NREL

Results

The discussion included below is separated into the two focus areas described above, highlighted in the project approach. The first section summarizes progress on active heat transfer with emphasis on using ATF for cooling electric motors. The second section focuses on passive heat transfer of the electric motor, with a focus on highlighted recently published results.

Active Heat Transfer

Work on active convective cooling during FY18 focused on using ATF for cooling electric motors. Past work measured the average convective heat transfer coefficients of circular orifice ATF jets directly impinging on stationary target surfaces with surface features representative of motor end-winding (Bennion and Moreno 2015). A schematic of the orifice jet test is shown in Figure I.12.2. A parametric sensitivity study was performed to quantify their effect on cooling performance. Parameters include the fluid temperature, jet velocity, surface temperature, and relative distance of the measurement surface from the orifice jet. The heat

transfer coefficient is determined using the same approach as described previously (Bennion and Moreno 2015).

Figure I.12.6 compares the heat transfer coefficients at fluid temperatures of 50°C and 70°C, jet distance of 10 mm, and jet incidence angle of 90 degrees. The data compare the sensitivity of the heat transfer as a function of jet velocity, target surface temperature, and jet impingement location. The surface temperature of the target surface was controlled at 10°C increments between 90°C and 120°C. The impact of the jet impingement location is also highlighted with results for the jet impinging on the center of the target surface and at the edge of the target surface (6.3 mm from center). At the highest tested flow rate and 50°C fluid temperature, the impingement on the edge of the target surface resulted in about a 43% reduction in the heat transfer coefficient. The variation in the target surface temperature resulted in a 14%–15% variation in the measured heat transfer coefficient. For a 70°C fluid temperature, the impact of the jet impingement location on the target edge also shows a greater than 40% decrease in the heat transfer coefficient as compared to the condition when the jet impinges at the center of the target surface. The variation in heat transfer coefficient due to the surface temperature is also between 14%–15%.

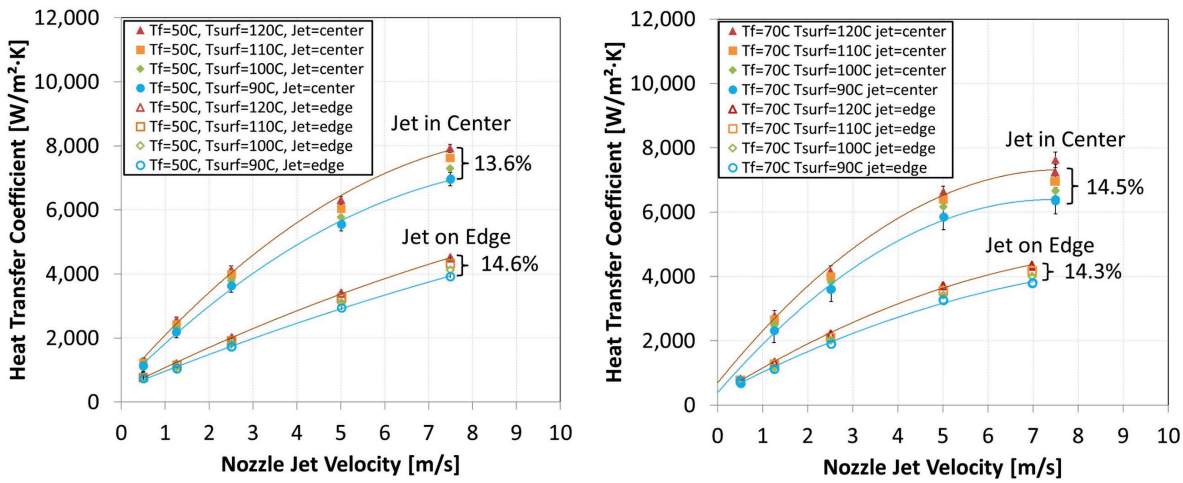

Figure I.12.6 ATF impingement heat transfer coefficient as function of jet velocity, target surface temperature, and impingement location for 50°C fluid temperature (left) and 70°C fluid temperature (right)

In addition to the experimental data described above, preliminary modeling efforts also looked at methods to simulate the computational fluid dynamics (CFD) and heat transfer of the free impinging jet. For the initial model validation work, efforts focused on the smaller scale experiment and data previously published (Bennion and Moreno 2015). To replicate the experimental approach applied in Bennion and Moreno (2015), a fluid jet of ATF ejects into a volume of air and impinges on the target surface. Figure I.12.7 shows two plots from a symmetric slice of the three-dimensional CFD model. The figure on the left shows the temperature profile of the elements within the model. The heat source and copper target surface are shown in the model and represent the hottest components. The ATF is heated as it impinges onto the copper target and then exits in the fluid exit region as highlighted in the figure. The figure on the right compares the volumetric ratios of ATF and air with black representing 100% ATF by volume. Figure I.12.8 compares the errors between the experimental data and the CFD modeling results, which are shown to be within ±10%. The development of accurate CFD models will enable studying alternative motor cooling approaches that are either too time consuming or difficult to measure through experiments.

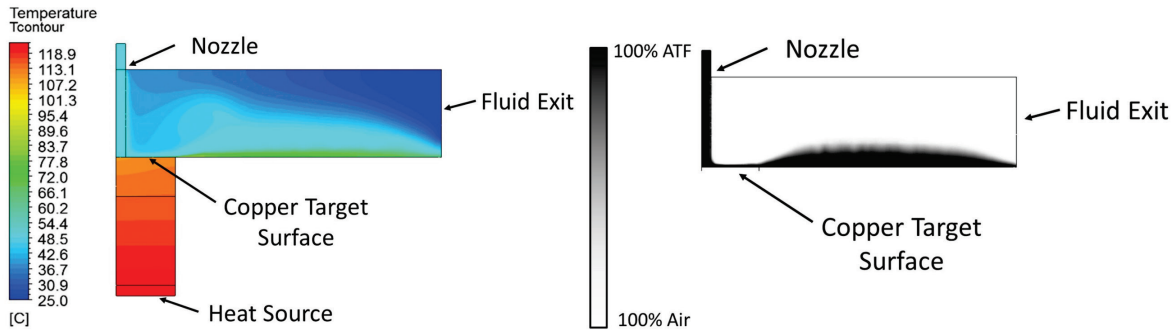

Figure I.12.7 Sample jet impingement CFD results showing temperature profile (left) and fluid volume fractions (right).

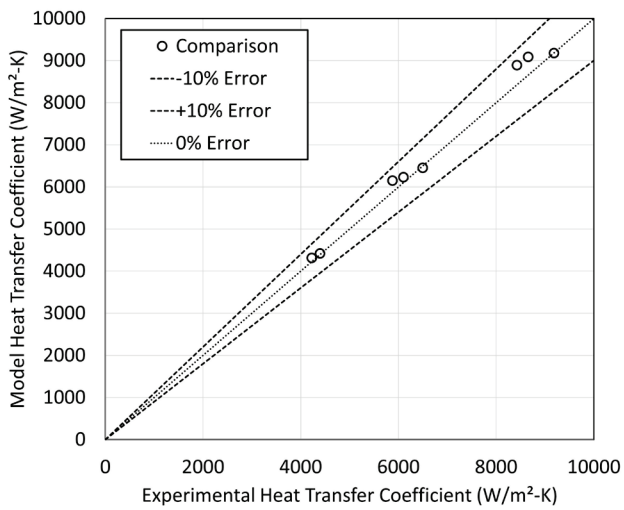

Figure I.12.8 Sample comparison of the heat transfer coefficients predicted by the model and the experimental results.

Passive Heat Transfer

The work on the passive heat transfer for motor applications focused on developing models validated against experimental data to support the simulation, design, and analysis of electric motors. The work is contained in published journal articles that describe the experimental methods, and the models used to predict the thermal characteristics of key thermal interfaces within the motor (Cousineau et al. 2018, 2019). This summary report focuses on work during FY18 describing the experimental measurements and models to predict the effective through-stack lamination thermal conductivity and interlamination thermal contact resistance results that were published. Prior work performed at NREL developed an experimental method for measuring thermal properties of stacked materials and the interface thermal resistances, but a model was not developed(Cousineau et al. 2015). During FY18, work was published in the *International Journal of Heat and Mass Transfer* describing models to predict the thermal contact resistance and effective thermal conductivity of stacked silicon steel materials commonly used within electric motors. In addition to electric motors, the results have also been used to support thermal analysis of inductors. The full details of the experiment and modeling approach are included in the recently published journal article (Cousineau et al. 2019) that is available online and will be available in hardcopy during 2019. The results are summarized below.

A critical parameter for calculating the effective through-stack thermal conductivity of a layered structure is the thermal contact resistance between each layer. For this reason, the experimental data captures the effect of lamination surface properties as shown in Figure I.12.9. The data include laminations with a smooth surface and a ridged surface as shown in Figure I.12.9. An example of the measurement results comparing the two surface topologies is shown in Figure I.12.10. When the interlamination contact resistance is plotted comparing the average data grouped by ridged and smooth surface topologies, it is clear that the different

surfaces follow two distinct trends. Depending on the clamping pressure, the ridges decrease interlamination contact resistance by 13% to 24% with respect to the smooth contacts. The general decrease in pressure dependence for the ridged surface is due to the ridges fixing the number of microscopic contact points between laminations. For the smooth surfaces, the number of microscopic contact points varies more with changes in pressure. The lower overall thermal resistance for the ridged surface is due to each contact point in the ridged pattern being at higher pressure. As the pressure increases, the advantage of the ridged surface over the smooth surface is reduced as the number of microscopic contacts becomes equal for the two surface types.

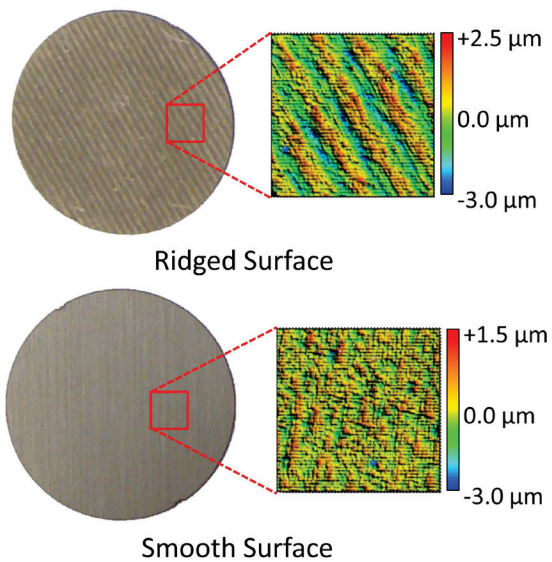

Figure I.12.9 Photo and height map of ridged and smooth surfaces

Image Source: Emily Cousineau, NREL

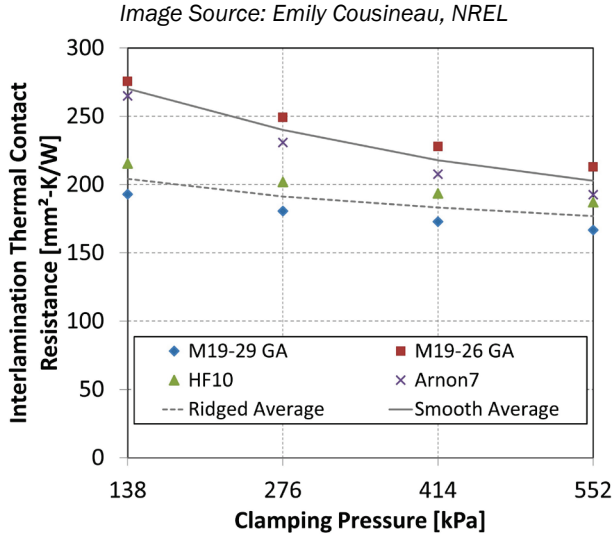

Figure I.12.10 Interlamination thermal contact resistances shown with averages of smooth samples and samples with a ridged pattern on one side.

Given the importance of the interlamination thermal contact resistance (TCR) on the total effective through-stack thermal conductivity, a key objective was to develop a model for the interlamination thermal contact resistance useful to electric motor designers. The total thermal conductance across a contact is the sum of the solid spot conductance and gas-fluid thermal conductance (Madhusudana 2014). The solid spot conductance is controlled by the ratio of the actual contact area to apparent contact area. For perfectly smooth surfaces, the

actual contact area equals the apparent contact area. In reality, surfaces are rough and have microscopic peaks and valleys that reduce the actual contact area to a fraction of the apparent contact area (the area that is apparently in contact to the naked eye). Decreasing the surface roughness or increasing contact pressure increases the actual contact area, and hence increases the solid spot conductance contribution. In this case, the loading to hardness ratio on the laminations is relatively low (<0.7 x10^{-3}), and due to the low thermal conductivity of the bulk material and the presence of the C5 coating the solid spot conductance can be neglected (Jeevanashankara et al. 1990). Neglecting the solid spot conductance, the thermal resistance of the contact is the thermal resistance of the air gap (Madhusudana and Fletcher 1981).

The C5 coating on the laminations makes a significant contribution to the interlamination thermal contact resistance. Unfortunately, the actual thermal resistance of the C5 coating is difficult to measure or estimate due to the fact that it is not a specific material, but a treatment given to the surface to obtain a desired set of electrical and machinability characteristics (A06.02 Subcommittee 2013). Removing the C5 coating by sanding alters the surface characteristics such that a comparison of the measured thermal contact resistance with and without the C5 coating was not meaningful. The coating was also found to be too thin to make a significant contribution to the bulk material thermal resistance. To incorporate the impact of the C5 coating it is assumed that the C5 coating contributes to the thickness of the mean surface separation, δ, such that the inter-lamination contact resistance takes the form of Equation 1 with t_{C5} representing the C5 coating thickness and k_{air} equal to the thermal conductivity of air.

$$R_C = (\delta + t_{C5})/k_{air} \tag{1}$$

The assumption provides good agreement with the experimental data shown in Figure I.12.11. The most prominent error source is the camber, or overall curvature to the samples, which was up to 10 µm with no loading. The experimental pressures did not fully eliminate the camber in the thicker 26-gauge samples, resulting in thermal contact resistances that are higher than the values predicted by the model, as indicated in Figure I.12.11(a).

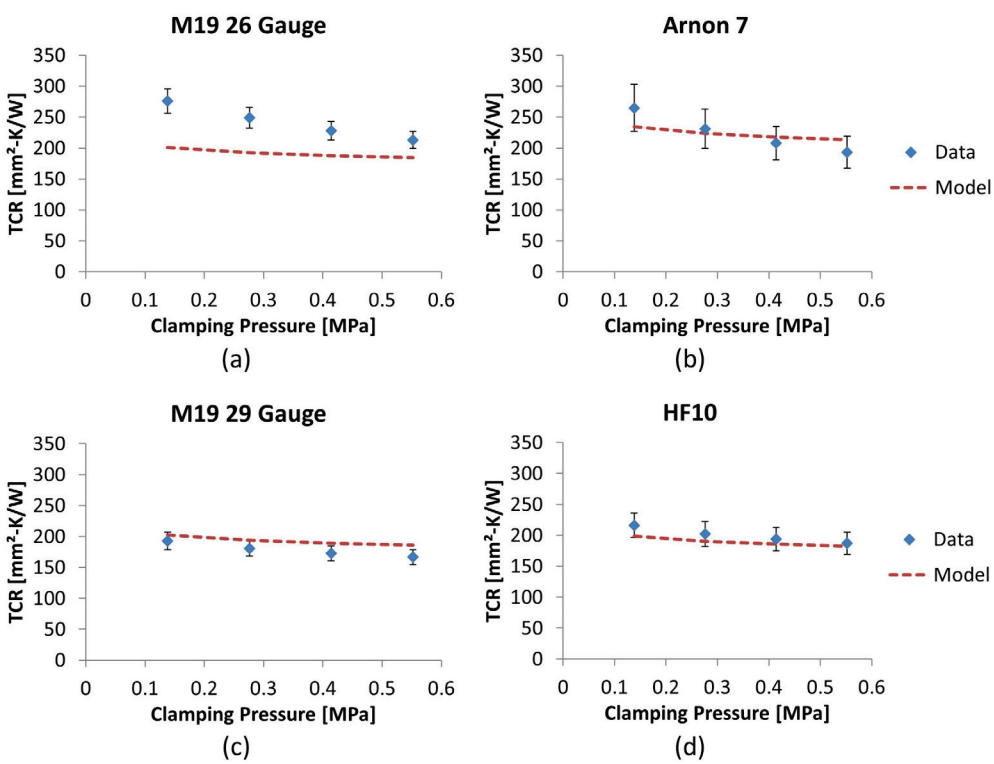

Figure I.12.11 Results predicted by the model compared to experimental data for contact resistance.

The ability to predict the interlamination thermal contact resistance and the associated through-stack thermal conductivity will support the ability to evaluate the impact of new motor materials and motor lamination assembly processes. Having data on the performance impact of new materials will enable motor designers to evaluate the impact for particular motor designs.

Conclusions

During FY18, research was performed to improve the physical understanding of motor materials, material interfaces, heat transfer, and fluid dynamics through experiments and simulation. To aid motor developers and researchers in the analysis of new motor materials, models were developed to provide estimates for material and interface properties applied to motor assemblies. This included the publication of experimental methods and models related to lamination stack thermal properties, and stator-to-cooling jacket thermal contact resistances. In addition, research was performed on automatic transmission fluid orifice jets illustrating the variation in heat transfer coefficient of ATF jets impinging on motor end windings. The experimental and modeling results support the project objective to provide motor researchers, developers, and suppliers with the data and analysis of motor heat transfer technologies to enable motor innovations and accelerate the use of novel materials and designs for the adoption of vehicle electrification technologies.

Key Publications

1. Cousineau, J.E., K. Bennion, V. Chieduko, R. Lall, and A. Gilbert. 2018. "Experimental Characterization and Modeling of Thermal Contact Resistance of Electric Machine Stator-to-Cooling Jacket Interface Under Interference Fit Loading." *J. Thermal Sci. Eng. Appl.,* 10, no. 4: 041016–7, May 2018.
2. Bennion, K. "Electric Motor Thermal Management R&D." 2018 DOE VTO Annual Merit Review, Washington D.C., June 2018.
3. Cousineau, J.E., K. Bennion, D. DeVoto, and S. Narumanchi. 2019. "Experimental Characterization and Modeling of Thermal Resistance of Electric Machine Lamination Stacks." *International Journal of Heat and Mass Transfer* 129: 152–159.

References

1. A06.02 Subcommittee. 2013. "ASTM A976-13, Standard Classification of Insulating Coatings for Electrical Steels by Composition, Relative Insulating Ability and Application." West Conshohocken, PA: ASTM International. https://www.astm.org/Standards/A976.htm.
2. Bennion, Kevin, and Gilberto Moreno. 2015. "Convective Heat Transfer Coefficients of Automatic Transmission Fluid Jets with Implications for Electric Machine Thermal Management." In *ASME 2015 International Technical Conference and Exhibition on Packaging and Integration of Electronic and Photonic Microsystems and ASME 2015 12th International Conference on Nanochannels, Microchannels, and Minichannels*. San Francisco, CA, United States: ASME.
3. Cousineau, Emily, Kevin Bennion, Douglas DeVoto, Mark Mihalic, and Sreekant Narumanchi. 2015. *Characterization of Contact and Bulk Thermal Resistance of Laminations for Electric Machines.* Golden, CO: National Renewable Energy Laboratory. NREL Technical Report NREL/TP-5400-63887.
4. Cousineau, J. Emily, Kevin Bennion, Victor Chieduko, Rajiv Lall, and Alan Gilbert. 2018. "Experimental Characterization and Modeling of Thermal Contact Resistance of Electric Machine Stator-to-Cooling Jacket Interface Under Interference Fit Loading." *Journal of Thermal Science and Engineering Applications* 10, no. 4: 041016-041016–7. https://doi.org/10.1115/1.4039459.
5. Cousineau, J. Emily, Kevin Bennion, Douglas DeVoto, and Sreekant Narumanchi. 2019. "Experimental Characterization and Modeling of Thermal Resistance of Electric Machine Lamination Stacks." *International Journal of Heat and Mass Transfer* 129 (February): 152–59. https://doi.org/10.1016/j.ijheatmasstransfer.2018.09.051.

6. D09 Committee. 2012. "Test Method for Thermal Transmission Properties of Thermally Conductive Electrical Insulation Materials." West Conshohocken, PA: ASTM International. http://www.astm.org/Standards/D5470.htm.
7. Hendershot, J.R., and Timothy John Eastham Miller. 1994. *Design of Brushless Permanent-Magnet Motors*. Oxford, UK: Magna Physics Publishing.
8. Jeevanashankara, C.V. Madhusudana, and M.B. Kulkarni. 1990. "Thermal Contact Conductances of Metallic Contacts at Low Loads." *Applied Energy* 35, no. 2: 151–64.
9. Lipo, Thomas A. 2007. *Introduction to AC Machine Design*. 3rd ed. Wisconsin Power Electronics Research Center, University of Wisconsin.
10. Madhusudana, C.V., and L.S. Fletcher. 1981. "Gas Conductance Contribution to Contact Heat Transfer." In *AIAA, 16th Thermophysics Conference*.
11. Madhusudana, Chakravarti V. 2014. *Thermal Contact Conductance*. 2nd ed. Mechanical Engineering Series. Cham: Springer.
12. Narumanchi, S., M. Mihalic, K. Kelly, and G. Eesley. 2008. "Thermal Interface Materials for Power Electronics Applications." In *11th Intersociety Conference on Thermal and Thermomechanical Phenomena in Electronic Systems (ITherm)*, 395–404. Orlando, FL: IEEE. https://doi.org/10.1109/ITHERM.2008.4544297.

Acknowledgments

The significant contributions from Emily Cousineau, Doug DeVoto, Xuhui Feng, Bidzina Kekelia, Joshua Major, Gilbert Moreno, and Jeff Tomerlin (NREL) to the project are acknowledged. The support, collaboration, and sample motor materials provided by Andrew Wereszczak (Oak Ridge National Laboratory) are also acknowledged.

II. Electric Drive Technologies Development

II.1 Dual Phase Soft Magnetic Laminates for Low-cost, Non/Reduced-Rare-Earth Containing Electrical Machines (GE)

PR Subramanian, Principal Investigator
GE Global Research Center
One Research Circle
Niskayuna, NY 12309
E-mail: subrampr@ge.com

Steven Boyd, DOE Program Manager
U.S. Department of Energy
E-mail: steven.boyd@ee.doe.gov

Start Date: October 1, 2016 End Date: September 30, 2019
Project Funding: $6,148,355 DOE share: $4,299,285 Non-DOE share: $1,849,050

Project Introduction

In this project, GE is scaling-up the processing of an innovative dual phase soft magnetic material which will enable electric traction drive manufacturers to achieve the cost target of $4.7/kW peak power. Cost reduction is driven by enabling non-rare earth materials containing machine designs with over 40% reduction in active material cost due to the elimination of rare earth magnets. A full-scale prototype motor with 55 kW peak power, 30 kW continuous power capability will be manufactured with the dual phase material to prove both performance and manufacturability.

The dual phase magnetic material is a uniquely programmable material with the capability of having its magnetic permeability being locally controlled at the millimeter scale. The magnetization can be programmed to have values between zero and full saturation to meet the machine design requirements without having to remove the material in these regions to reduce the flux leakage. This capability enables rotor and/or stator poles to be magnetically decoupled, while maintaining mechanical integrity of the laminations. As shown in Figure II.1.1, bridges and centerposts used to define flux barriers in SynRel and IPM machines may be made non-magnetic, improving the effectiveness of the barrier. The left image shows where the non-magnetic (orange) regions are patterned into the magnetic (green) laminate. The middle image shows an actual laminate in which a ceramic mask has been applied. The exposed regions will become non-magnetic after nitrogenation. The right image shows a laminate after nitrogenation, placed underneath a magnetic indicator film. The stripe domains shine through the regions which have been made non-magnetic. The magnetic decoupling of the poles reduces the flux leakage from pole to pole on the rotor, meanwhile improves the flux linkage between the rotor and stator. Maintaining the mechanical integrity enhances the mechanical strength for high speed operation, thus enhancing the machine power capacity, power factor, power density, and efficiency. The ability of the non-magnetic regions to act as retaining elements shows the greatest advantage in machines with high tip speeds. Thus, dual phase materials are particularly well suited to the high power density, high efficiency designs used in the transportation market sector.

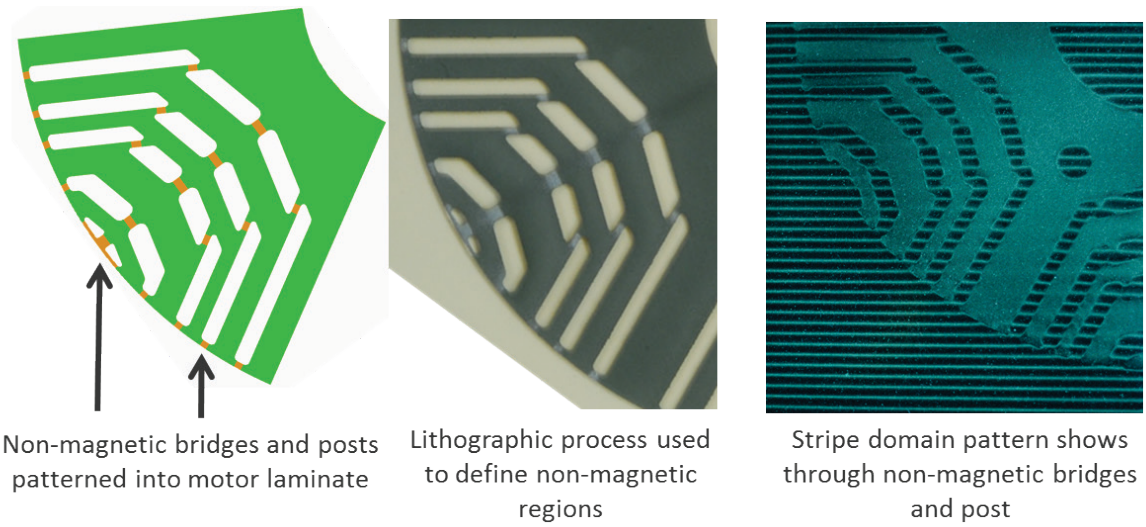

Figure II.1.1 Illustration of the dual phase structure in a laminate used to manufacture a SynRel machine.

Objectives

GE Global Research leads a team comprised of Carpenter Technology Corp. and Oak Ridge National Lab to advance unique and innovative dual phase soft magnetic material technology to Technology Readiness Level (TRL) 7 and demonstrate the material in a 30 kW electric motor for electric vehicles. Dual phase laminate materials will revolutionize the design of electric machines by opening the design space for new cost-effective and sustainable topologies. Dual phase laminates have the potential to be the first, completely new class of soft magnetic materials to be introduced in over a quarter of a century. Their introduction will lead to a step change in system performance and could dramatically accelerate the penetration of electric vehicles into the global automotive market. Dual phase magnetic materials offer the electric motor designer the ability to locally control the magnetic saturation level in a motor laminate at the millimeter scale, while at the same time enhancing the mechanical strength of the laminate material, resulting in an enhancement in motor performance and efficiency.

The project goal is to demonstrate scaled-up manufacturing of the dual phase magnetic materials, and demonstrate a full-scale traction motor manufactured with this material. Two motor proto-types are fabricated using the dual phase material: 1) A subscale prototype with a continuous power rating of ≈3.7 kW (5 hp) has been fabricated in the second year to demonstrate dual phase alloy process improvement; and 2) a full-scale prototype with a continuous power rating of ≈30 kW (40 hp) will be fabricated in the third year of the effort to demonstrate a manufacturable machine that can be tested in an operational environment, thus achieving TRL 7.

Approach

The team is comprised of GE Global Research, Carpenter Technology Corporation, and Oak Ridge National Lab. GE is responsible for selecting the motor topology, writing performance specifications, and performing detailed design activities for the two prototypes. GE performs in depth testing of each prototype on test facilities located in the Electric Machines Laboratory. Existing motor drive electronics are used to validate performance over the envelope of speed, power and torque conditions defined for electric vehicle motors.

Figure II.1.2 shows the manufacturing method for the prototypes with dual phase magnetic laminate rotors. Carpenter has responsibility for producing the 0.010” rolled sheet of the dual phase magnetic material needed for the prototypes. This requires developing the melt practice, heat treatment sequences, and rolling schedules customized for this alloy. This amount of material is sufficient for producing both prototypes. The rotor design for each prototype is laser cut from the rolled sheet. GE applies the ceramic mask needed to modulate the uptake of nitrogen into the laminates and create the specified pattern of magnetic and non-magnetic regions. The coated laminates are nitrogenated at high temperature, which austenitizes the regions to be made non-

magnetic. GE then removes the ceramic mask prior to assembly of the rotor stack. A prototype manufacturer, Applinetics Engineering LLC, shrink fits the rotor stack onto a shaft prior to integration into the prototypes.

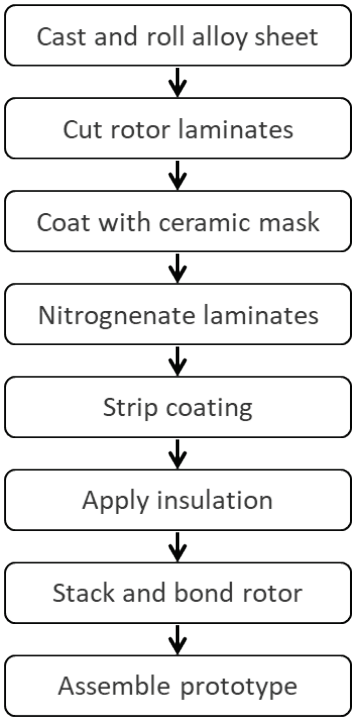

Figure II.1.2 Manufacturing sequence for prototypes containing dual phase magnetic laminates.

In parallel, GE and ORNL perform an in-depth study of the nitrogenation kinetics of the dual phase alloy material. The studies are performed on coated coupons and laminates prepared by GE. ORNL explores the effect of nitrogenating conditions on the austenitization of the alloy. Residual stress analysis is performed to verify finite element calculations of the stress states caused by differential thermal expansion between the magnetic and non-magnetic regions. The results of the coupon tests are used to optimize gas nitrogenation furnace parameters to minimize total cycle time and cost. Further, the residual stress analysis is used to set design rules that will avoid warpage and minimize distortion in the nitrogenation processing of the rotor laminates.

The first annual performance period focused on 1) scale-up of alloy production at Carpenter, 2) optimization of nitriding furnace parameters at ORNL, and 3) detailed subscale prototype design at GE. The first annual Go/NoGo condition is the creation of a subscale motor design that shows a calculated level of performance in excess of a best in class design using conventional materials. The second annual performance periods focused on 1) scaled-up processing of the subscale dual phase rotor laminates, 2) assembly and test of the subscale prototype, and 3) detailed design of the full-scale prototype. The second annual Go/NoGo condition is a demonstration of the subscale prototype and measured power output of 3.7 kW. The third annual performance period will focus on 1) scaled processing of the full-scale dual phase rotor laminates for the full-scale prototype, 2) and assembly and test of the full-scale prototype.

Results

A subscale synchronous reluctance prototype motor has been fabricated using a dual phase laminate rotor manufactured by the sequence shown in Figure II.1.2. The motor installed onto a dynameter test stand at GE Global Research Electric Machines Laboratory is shown in Figure II.1.3.

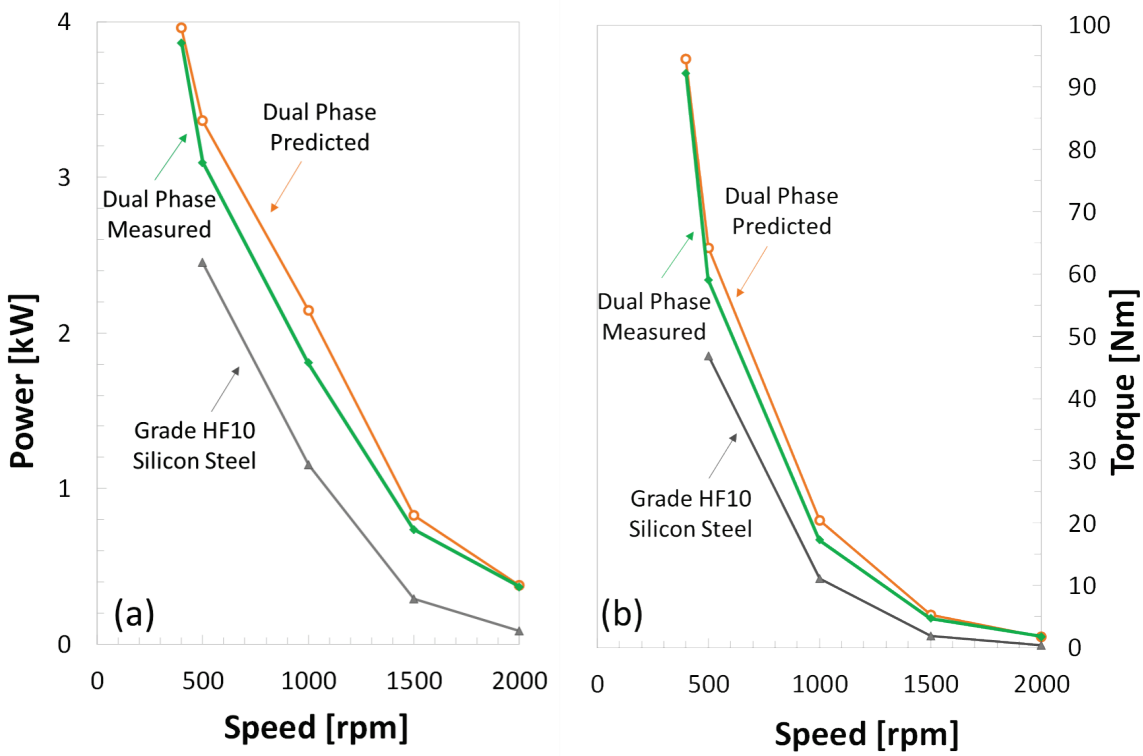

Figure II.1.3 Measured performance of a sub-scale dual phase synchronous reluctance prototype compared with predicted performance by design. The prototype with a rotor manufactured from 0.010" thick Dual Phase sheet is measured to have at least 30% higher power and torque output than a synchronous reluctance motor with its rotor made of grade HF10 Silicon Steel by the same design.

The prototype was then tested in a speed range between 400 and 2000 rpm and three current levels between 10 and 30 A (peak). The measured maximum steady state power output reaches 3.9 kW. With this result, we have passed the Budget Period 2 Go/NoGo decision point.

Figure II.1.4 Subscale prototype motor on a dynameter test stand.

Figure II.1.4 presents a comparison of predicted and measured performance of the sub-scale prototype motors. The data show that the prototype with a rotor manufactured from 0.010" thick dual phase alloy sheet has higher power and torque output than a similarly sized prototype with a rotor manufactured from 0.010" thick Silicon Steel (the HF10 grade). These performance gains persist over a wide speed range. At low speed, the

dual phase machine is measured to have 30% greater power and torque output than a silicon steel machine, exceeding the 20% performance increase target. The predicted and measured performance agrees very well with each other in the low and high-speed ranges, showing less than 10% deviation. The deviation might have originated from the difference between the material properties used for calculation and in the prototype rotor. The magnetic properties used for calculation were measured using a bonded ring laminate core. Although the ring laminate core was fabricated using the same processing procedures as used for the prototype rotor laminates, different geometry and bonding stress may cause different magnetic performance.

Significant development work has been completed on retiring the risks in scaled-up dual phase laminates manufacturing. A supply chain is being developed from starting material production to dual phase laminates processing with industrial partners. The fact that the measured subscale prototype performance meets the predicted performance proves both the performance and manufacturability of the dual phase laminates. Market development is ongoing with the GE Ventures organization to find potential licensing partners for the technology.

Detailed electromagnetic, mechanical, and thermal design of the full-scale synchronous reluctance prototype has been completed. The calculated performance of the full-scale design compared to the targeted values is shown in Table II.1.1. All technical performance meets the VTO 2020 advanced traction motor targets [1]. The production of the full-scale dual phase rotor laminates and the motor assembly process have been started.

Table II.1.1 Target vs. Calculated Performance of the Full-scale 55 kW Dual Phase Prototype

Parameter	Target	Calculated
Peak Power (kW)	≥55	56.2
Continuous Power (kW)	≥30	34
Specific Power (kW/kg)	≥1.6	1.93
Power Density (kW/l)	≥5.7	5.86
Maximum Speed (rpm)	14,000	14,000
Maximum Efficiency (%)	≥95	95.3
Cost ($/kW)	≤4.7	TBD

The analysis work that had been conducted at Oak Ridge National Laboratory has provided valuable data on the processing conditions needed to properly nitrogenate the dual phase alloy in a production scale. A kinetics model has been established based on experimental data. A contour map of magnetization vs time and temperature has been plotted, which can be used for quick determination of processing parameters in particular conditions. The ORNL team developed the residual stress analysis method using an XRD Portable Residual Stress Measurement System. The experimental results on a successfully nitrogenated laminate indicate that there are significant residual surface stresses in the radial direction. The data from different locations on the laminate indicate that the residual stresses after nitrogenation heat treatment may not be uniformly distributed, which agrees with the calculated stress distribution conducted by GE mechanical engineers. The measured residual stress data will help with the design of the laminates to reduce warpage and maintain mechanical integrity under load.

Conclusions

The second Go/NoGo decision point has been passed with a sub-scale SynRel motor made of dual phase material measured with increased performance relative to a similar design made of conventional silicon steel by 30%. The full-scale synchronous reluctance prototype design has been completed. The calculated performance of the full-scale design meets the DOE 2020 advanced traction motor targets. The production of the full-scale prototype has been started. Work performed at Oak Ridge National Laboratory has resulted in valuable data on the nitrogenation kinetics and residual stress in subscale prototype laminates of the dual phase

material. A supply chain is being established for dual phase material manufacturing with industrial partners. Market development with the GE Ventures organization to find potential licensing partners for the technology continues.

Key Publications

1. Lawrence Bernard Kool, Min Zou, Wanming Zhang, Susan Corah, Christopher Klapper, Francis Johnson, Steve Buresh, "Method for forming a nitrogenation barrier and machine formed using a body having the nitrogenation barrier", US Patent Application Publication 20180183279A1, published June 28, 2018.

References

1. Patel B. Reddy, Ayman M. EL-Refaie, Steven Galioto, and James P. Alexander, "Design of Synchronous Reluctance Motor Utilizing Dual-Phase Material for Traction Applications", *IEEE Transactions on Industry Applications*, vol. 53, No.3, pp. 1948-1957, May/June 2017

Acknowledgements

The project team would like to acknowledge all the research members who performed different portions of the material development, motor design, motor fabrication & testing tasks. In particular, we would like to thank Karthik Bodla, Steve Buresh, Sue Corah, Shenyan Huang, Anoop Jassal, Christopher Klapper, Lawrence Kool, Di Pan, Changjie Sun, Wanming Zhang, Joseph Zierer, Min Zou (from GE-GRC), and Frank Johnson (formerly of GE-GRC). We would also like to thank our external partners from Oak Ridge National Laboratory - Michael Brady, Craig Bridges, Hunter Henderson, and Orlando Rios.

II.2 Cost Effective 6.5% Silicon Steel Laminate for Electric Machines (Iowa State University)

Jun Cui, Principal Investigator
Iowa State University
2220 Hoover Hall
Materials Science and Engineering Department
Ames, IA, 50011
E-mail: cuijun@iastate.edu

Steven Boyd, DOE Program Manager
U.S. Department of Energy
E-mail: steven.boyd@ee.doe.gov

Start Date: October 1, 2016 End Date: September 30, 2019
Project Funding: $4,268,002 DOE share: $3,835,152 Non-DOE share: $432,850

Project Introduction

Rare Earth magnet is the most expensive component in permanent magnet motor. Since 2000, the price of the rare earth NdFeB-Dy magnet has gone through a series of volatile rises and falls. The price of Nd oxide increased from ~$10/kg in 2000 to ~$80/kg in 2010, then jumped to an historical high of $244/kg in 2011. It fell sharply to $37/kg in 2016, then back up again, to $51/kg in 2017, and back down to $46/kg in 2018. As Europe and China are aggressively pursuing electric vehicle with higher efficiency, the demand for rare earth magnet is expected to be doubled by 2025. The rising demand and manufacturing cost make it difficult to meet the DOE 2025 cost target of $6/kW for the 100 kW electric drive system.

MnBi permanent magnet is the only non-rare earth magnet holds a viable potential to meet the DOE cost target. The cost is expected be ~$26/kg when mass produced. This cost estimation is based on the same methodology used by IMARC group (ID: 2818708, 2014) to study the economic feasibility of a rare earth magnets manufacturing plant. The price of MnBi magnet is expected to be stable over the next few decades due to the world-wide availability of the elements Mn and Bi. It is important to understand that criticality is defined by availability, not by abundance. Rare earth elements Nd and Dy are critical elements not because they are rare, but because the major reserves are concentrated in a few countries. These elements may not be available to the rest of the world due to the political and economic conflict of interests. According to 2016 US Geological Survey, there are 181 producers of Bi in 22 countries around the world.

Unfortunately, non-rare earth permanent magnets are not as powerful as the rare earth magnets. The highest energy product that the MnBi permanent magnet can achieve using the current technology is about 8 MGOe at room temperature, albeit 20 MGOe is the theoretical limit and evidences shown 10 MGOe is possible. The current energy product of 8 MGOe is about 20% of that of the NdFeB magnet. In order to meet the DOE 2022 power density targets of 1.6 kW/kg and 5.7 kW/L, the motor has to be operated at much higher excitation frequency, which in turn, demands advanced soft magnetic materials to make up the efficiency loss due to the rising eddy current.

Electrical steel with 3.2% Si is the most common soft magnetic material used by motor and power electronics industries. While the excellent performance/cost ratio justifies the popularity of the 3.2 wt.% Si steel, its limited physical properties are hindering the further improvement of motor efficiency, power density and cost. The current trend in the motor and power electronics industry is to increase the excitation frequency because it leads to higher power density with lower $/kW. However, higher excitation frequency also results in higher eddy current and lower efficiency. For example, a 100 kW motor at 50 Hz with 90% efficiency would deliver 200 kW when running at 100 Hz, but efficiency would decrease to 80%.

Thinner laminate reduces eddy current loss, but very thin laminate has a poor stacking factor and increases assembly cost. With lamination thickness at its practical limit, mitigating increased eddy current requires increasing electrical resistivity. Advanced soft magnetic materials, such as nanocrystalline and amorphous soft magnetic materials, possess higher electric resistivity but the cost is high and the thickness is limited to <0.03 mm. With such thin thickness, the stacking factor can only reach 0.687, about 28% less active magnetic volume than that of the 0.4 mm laminate. High Si electrical steel has the potential to be both efficient and cost effective. Increasing Si content improves magnetic and electrical properties, with ~6.5 wt.% being optimum. Compared to the 3.2 wt.% Si steel, saturation magnetization decreases by 10% (to 1.7 T) but permeability improves by 27% (to 19,000 at 1 kHz), while electric resistivity improves by 44% (to 82 μΩ-cm) and magnetostriction reduces from 7.8 ppm to 0.1 ppm. However, with increasing Si content, Si atoms start to pair and form ordered phases. The emerging B2 and $D0_3$ phases embrittle the A2 matrix. At 6.5 wt.% Si, the steel is too brittle to be cold rolled or stamped. The current manufacturing method diffuses Si into the thin gauge 3.2 wt.% Si steel after chemical deposition. It is an elegant engineering solution. Unfortunately, the method has notable shortcomings. Manufacturing cost is high (~5X of the price of 3.2 wt.% Si steel), productivity is limited, sheet thickness (0.1 mm) is thinner than the one for common motor lamination, the final product is brittle and difficult to stamp. Even with these shortcomings, the 6.5 wt.% Si steel 0.1 mm sheet made by JFE is still steadily gaining market share.

This project develops a near net shape molding process that could enable the application of 6.5 wt.% Si steel for electric motors at a cost competitive with the cost effective 3.2 wt.% Si steel. The anticipated breakthrough material could reduce motor cost by enabling higher excitation frequency and higher power density without sacrificing efficiency; or for a given power density, it could lead to 35% reduction in core loss and 3% increase in motor efficiency. In addition to the materials effort, the project designs, constructs and evaluates a non-rare earth motor that integrates the novel MnBi magnet for rotor and the advanced Fe-6.5%Si steel laminate for stator.

Objectives

The objective is to demonstrate a cost effective non-rare earth PM motor. The new motor uses MnBi magnet as the permanent magnet in rotor and Fe-6.5%Si as the stator laminate material. It operates at 400 Hz and has 5~10 kW power. The target cost is 2/3 of the rare earth motor with same power.

Approach

Our approach for lowering PM motor cost is three folds: 1) use non-rare earth magnet to control magnet cost, 2) increase motor excitation frequency to improve motor power density, and 3) use advanced soft magnetic materials to improve motor efficiency at high frequency. The project team comprises two universities (Iowa State University and Delaware University) specialized in magnetic materials and alloy development; one national lab (Ames Lab) specialized in predictive materials science, mid-scale (10 kg) alloy casting and processing, and magnetic materials development; and one company (United Technologies Research Center) specialized in motor design, construction and testing.

- For MnBi magnet, the demonstrated energy density of a bulk MnBi magnet (9 gram) is about 8.5 MGOe at room temperature. It was fabricated using a lab-scale warm compaction process that was developed by a previous DOE supported project. Unfortunately, large warm press is not commonly used by the magnet industry. Our approach is to study and understand the thermodynamics of the demonstrated warm compaction process and apply the understanding to develop a robust process without using any special equipment.
- High excitation frequency (400 Hz) is used to make up the loss in power density caused by weaker magnet. Our approach to improve the torque/power density of the motor is to use advanced flux switching topologies that would enable focused flux and improve average airgap flux density.
- Fe-6.5%Si steel is used for stator lamination to mitigate the efficiency loss at high frequency. The challenge is how to cost-effectively fabricate the brittle 6.5%Si steel laminate. Our approach is based

on the observation that rapid solidified Fe-6.5%Si flakes is ductile. This unique property is possible because the heterogeneous formation of α2-FeSi (B2) and α1-FeSi (D03) ordered phases are suppressed. These ductile flakes can be pressed to near-net-shape in high green density, then sintered for full density and desired magnetic properties. The approach is simpler than the cold roll, stamping and lamination process.

Results

MnBi Permanent Magnet

MnBi bulk magnet has been fabricated using the following procedure: a) Align the loose powder in magnetic field to obtain high degree of texture; b) Press the loose powder into a green compact in the magnetic field. The force is moderate (<12 MPa) and the compact is <70% dense; c) Warm-compact the green compact at 240~250 °C with 100 MPa compressive stress. The obtained bulk magnet is >95% dense. The problem with this procedure is that the ratio of the remanence magnetization (Mr) and the saturation magnetization (Ms) is low (<70%). In order to achieve the milestone energy product (8 MGOe), the Mr/Ms ratio needs to be >80%. A comparison of the feedstock powder and the fabricated bulk magnet shows that the Mr/Ms ratio starts at 93%, but drops to 79% after warm compression. Apparently, the fabrication process disturbed the powder alignment, reduced the Mr/Ms ratio, which in turn resulted in lower energy product.

A new process involving an intermediate cold isostatic pressing (CIP) was developed in 2017 and optimized in 2018. The new process replaced the uniaxial compression with isostatic pressure, allowing majority of the powder to be densified without rotational movement, thereby kept high degree of alignment. Details of the fabrication process is summarized in Table II.2.1.

Table II.2.1 Processing Steps for Powder Fabrication and Consolidation

Process name	Conditions
Arc melting	10 g sample, re-melted 5 times
Melt spinning	wheel speed 8-12 m/s
Ribbon annealing	290°C for 5-6 days
Ball milling ribbon powder	8-10 hrs, powder particle size<5um
2nd annealing for fine powder	290°C for 5-6 days
Fine powder coating	Mixed with bakelite solution
Aligned and pre-press	Magnetic field: 1.5 T
Cold isostatic press (CIP)	CIP pressure: 345 MPa
Warm sintering	230°C for 1 hr
Bulk magnet coating	Silver spray for corrosion protection

The fabricated magnets consistently exhibit the desired physical properties, meeting or exceeding the target energy production of 8 MGOe. Figure II.2.1 depicts the magnetization vs field data of a typical MnBi magnet fabricated using the newly developed process. The significance of this achievement is that there will be no need of the expensive large-scale warm compaction system, and the CIP system commonly used by the magnet manufacturers can be used to densify the aligned powder and to produce bulk magnet with superior performance. This achievement lays the foundation for economic manufacturing of non-rare earth magnet. In FY18, the new process was standardized and tested by several non-expert undergraduate lab assistants. In FY19, 300 magnets (10 gram/each) will be manufactured using this process and installed in the prototype motor designed by UTRC team.

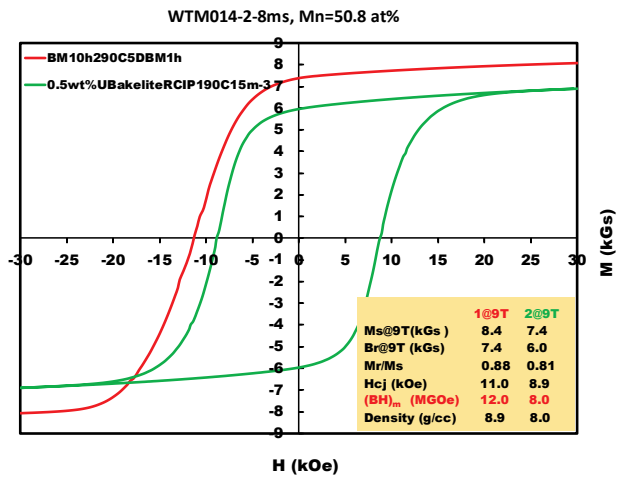

Figure II.2.1 Magnetization vs. applied field hysteresis loops of the feedstock powder (red) and the bulk magnet fabricated using the newly developed CIP process (green). The energy products of the feedstock powder and the bulk magnet are 12 MGOe and 8 MGOe, respectively.

Note that the high energy product of the feedstock powder is measured using MnBi powder mixed with alignment wax. The weight of the wax is removed from the equation when calculating the magnetization.

Near net shape molding of Fe-6.5%Si laminate

The team was able to reliably produce Fe-6.5%Si flakes for physical properties characterizations and for near-net-shape molding. Figure II.2.2 shows the picture of the flakes produced in one run.

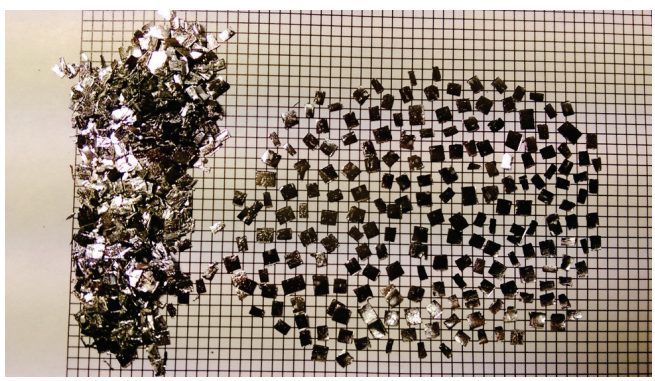

Figure II.2.2 Flakes of Fe-6.5wt%Si prepared by melt spun method. The flakes on the right are spread out to show their dimensions. Flake dimensions are uniform in length (2 mm), but the width varies due to an undulating melt pool.

Flakes produced at different wheel speeds were examined for its physical properties (saturation magnetization, coercivity, electrical resistivity, and hardness). Saturation magnetization decreases with increasing wheel speed because higher cooling rate may lead to more disordered phase with less magnetization; coercivity increases with wheel speed because higher cooling rate leads to finer grains with higher coercivity; electrical resistivity decreases with increasing wheel speed likely due to the increase of grain boundaries; and finally, hardness sharply decreases once wheel speed exceeds 10 m/s. The ribbons prepared at different wheel speed were examined with SEM and TEM. The missing $D0_3$ spots and fading B2 spots for the ribbon prepared at 30 m/s validate our hypothesis that high cooling rate will suppress $D0_3$ phase formation and reduce B2 phase formation, which results in improved ductility.

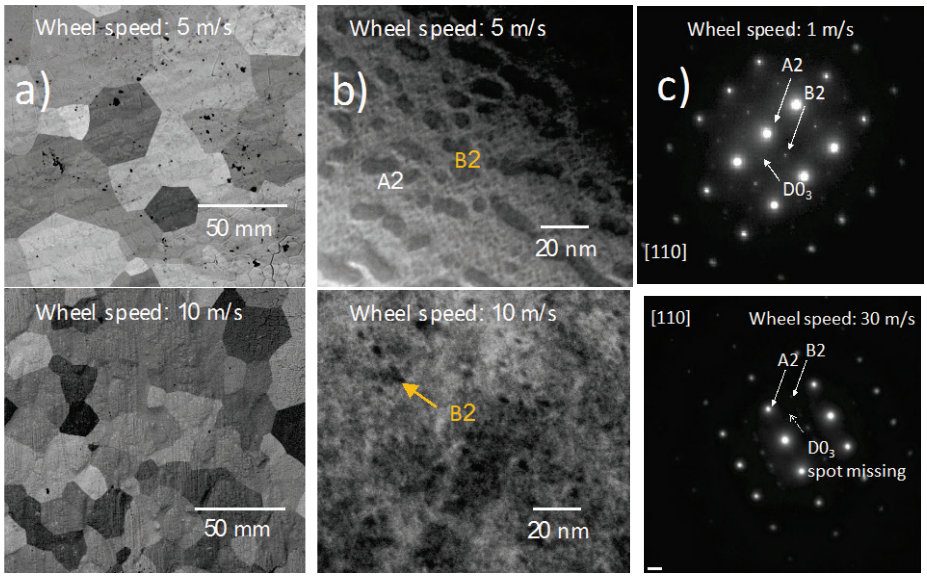

Figure II.2.3 SEM images of the ribbons prepared at 5 m/s and 10 m/s; and TEM images of the ribbons prepared at 1 m/s and 30 m/s.

Over one kilogram of ductile flakes has been produced in FY18. They are used to fabricate rings with 0.4, 2, and 5 mm thickness and 50 mm OD. The rings come with various levels of inter flake coatings for electrical insulation, varying from 0-100 nm, to several microns with wheel speed set at 10 m/s. Figure II.2.4 depicts a ring with 50 mm OD, 37 mm ID, and 4.76 mm thickness. The densification of the ring reached 98%. The sample was evaluated for its closed loop DC magnetic properties. The measured properties are coercivity 29.5 A/m, maximum permeability 13.1k, flux density at 800 A/m, i.e., B8, 1.32 Tesla, and B25 1.42 Tesla. Table II.2.2 compares the core loss of the bulk sample fabricated using melt-spun flakes (ISU-185-2) to the thin sheet produced by the steel company JFE in Japan using the diffusion method. It shows the flake approach can produce 50% thicker sample with similar core loss. This achievement proves that using melt-spun flake as feedstock for near-net-shape molding is feasible.

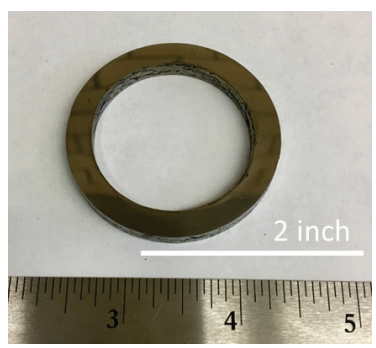

Figure II.2.4 A 50 mm OD ring sample consolidated from melt-spun 6.5% Si steel flakes.

Table II.2.2 Comparison of Core Loss (400 Hz, 10 kOe) of the Ring Sample Consolidated using Melt-Spun Flake and the Thin Sheet Commercially Produced by JFE

	ISU185-2	JNEX-core	JNHF-core
Thickness (mm)	0.33	0.1	0.2
W 10/400 (W/kg)	15.1	5.7	14.5

It has been determined that the application of coating effectively reduced the eddy current losses, resulting in lower losses of the coated, thick samples compared to uncoated ones. However, the iron loss is still significant for the thick samples, mainly due to insufficient lamination. Our future work will focus on improving coating quality. Three directions will be investigated: (1) evaluate a thin application of polymer binder as a uniform coating (2) apply a coating via chemical vapor deposition technique (3) prepare and evaluate inter-laminated bulk samples by loading the coating and flakes alternatively prior hot pressing.

Motor design

UTRC has completed the detailed design and optimization for a Fractional Slot Concentrated Winding (FSCW) Surface Permanent Magnet (SPM) machine with a 10-poles and 12-slots combination using the physical properties reported for MnBi magnets and the 6.5% Si steel from JFE.

Figure II.2.5 shows target performance metrics for torque and power as function of speed. These motor specifications are developed for a peak power of 10 kW at 2000 RPM and a rated power of 6 kW from speed ranging from 2000 RPM to 8000 RPM.

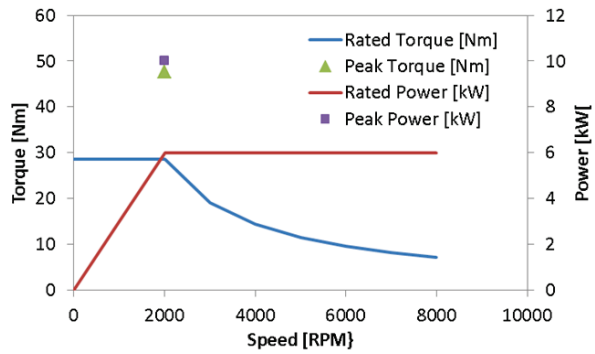

Figure II.2.5 Target performance metrics for torque and power as function of speed

Table II.2.3 summarizes detailed performance specifications for above defined target metrics of specific power density, power density and target active material cost. Applying the selected power and power density together, estimated target weight of the machines is 7.69 kg with in a volume of 2.2 liters and target active material cost of $47. In-addition to the power density and cost metrics, team also aims to achieve an efficiency of 95% at ½ rated speed and ½ rated torque. Peak torque and rated torque at based speed (2000 RPM) are 47.75 Nm and 28.65 Nm respectively, while rated torque at maximum speed (8000 RPM) is 7.16 Nm in order to deliver rated power of 6 kW.

Table II.2.3 Detailed Performance Specifications

Specifications	Units	Values
Peak Power	kW	10
Continuous Power	kW	6
Max Speed	RPM	8000
Min Frequency	Hz	300
Voltage	V	325
Max per Phase Current	A rms	35
Characteristics Current	A rms	< 35
Weight	Kg	7.69

Volume	L	2.2
Unit Material Cost	$	47
Max Efficiency @1/2 Rated Speed and ½ Rated Torque	%	95%
Based Speed	RPM	2000
Peak Torque @ Rated Speed	Nm	47.75
Rated Torque @ Rated Speed	Nm	28.65
Max Speed	RPM	8000
Torque @ Max Speed	Nm	7.16

Lepper-Nutmeg, Inc. was contracted to build the designed motor. To avoid the potential delay by the materials team, the first prototype uses dummy magnetic materials. For the permanent magnet, rare-earth SmCo magnet was engineered to mimic the performance of the MnBi magnet; while for the 6.5% Si steel, the steel sheet was directly purchased from JFE and laser-cut by Lepper-Nutmeg. Figure II.2.6 shows the prototype stator and rotor being constructed. In FY19, the second prototype motor will be built using the actual MnBi magnet and the consolidated 6.5% Si flake.

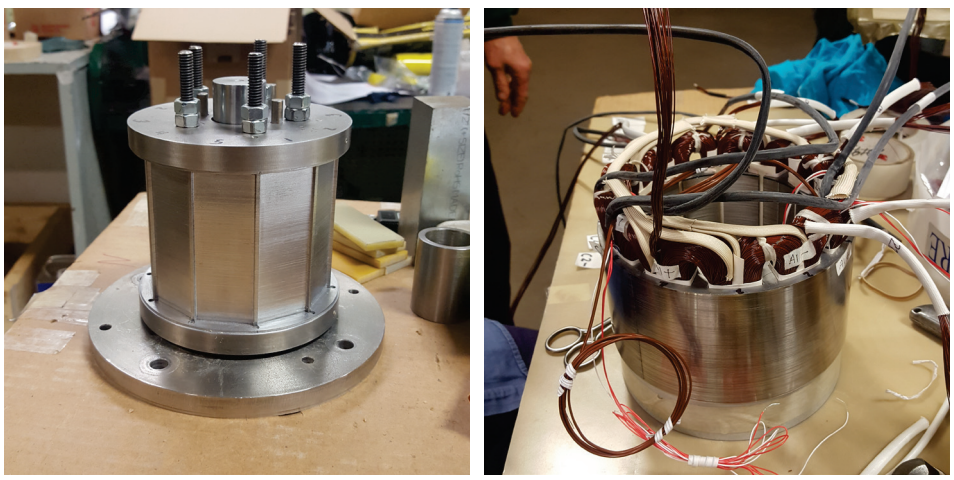

Figure II.2.6 Picture of the prototype rotor (left) and stator (right), both using 0.1 mm 6.5%Si steel purchased from JFE.

Conclusions

A robust and cost-effective process was developed to fabricate bulk MnBi permanent magnet. The process uses the common cold-iso-press process to densify the magnet while keeping the powder aligned. The newly developed process not only improves the squareness of the demagnetization curve, but also reduce the capital cost of the large-scale warm compression system. A significant progress was made toward near-net shape molding of thick 6.5%Si steel laminate. Ductile flakes with desired size and shape can be routinely produced; the obtained flakes can be consolidated into rings with excellent mechanical and magnetic properties. While our recent results proved the concept of near-net shape molding of 6.5%Si steel, they also showed that high quality flake coating and lamination are critical for overall iron loss and motor efficiency. Lastly, the design of our first 400 Hz prototype motor (1.3 kW/kg and 4.5 kW/L) has been complete. The prototype is being constructed. The expected delivery date is March 30, 2019.

Key Publications

1. Cui, Senlin, Gaoyuan Ouyang, Tao Ma, Chad R. Macziewski, Valery I. Levitas, Lin Zhou, Matthew J. Kramer, and Jun Cui. "Thermodynamic and kinetic analysis of the melt spinning process of Fe-6.5 wt.% Si alloy." *Journal of Alloys and Compounds* 771 (2019): 643-648.
2. Tangudu, Jagadeesh, Gaoyuan Ouyang, and Jun Cui. "Trade Studies for a Manganese Bismuth based Surface Permanent Magnet Machine." In *2018 IEEE Transportation Electrification Conference and Expo (ITEC)*, pp. 600-605. IEEE, 2018.
3. Ouyang, Gaoyuan, Brandt Jensen, Wei Tang, Kevin Dennis, Chad Macziewski, Srinivasa Thimmaiah, Yongfeng Liang, and Jun Cui. "Effect of wheel speed on magnetic and mechanical properties of melt spun Fe-6.5 wt.% Si high silicon steel." *AIP Advances* 8, no. 5 (2018): 056111.
4. Gabay, A. M., G. C. Hadjipanayis, and J. Cui. "Preparation of highly pure α-MnBi phase via melt-spinning." *AIP Advances* 8, no. 5 (2018): 056702.
5. Cui, Jun, Matt Kramer, Lin Zhou, Fei Liu, Alexander Gabay, George Hadjipanayis, Balamurugan Balasubramanian, and David Sellmyer. "Current progress and future challenges in rare-earth-free permanent magnets." Acta Materialia (2018).
6. Ouyang, Gaoyuan, Dennis, Kevin, Jensen, Brendt and Cui, Jun. “Near net shape BULK laminated silicon iron electric steel for improved electric resistance and low high frequency loss”, Provisional patent filed (2018)

II.3 Highly Integrated Wide Bandgap Power Module for Next Generation Plug-In Vehicles (General Motors)

Brian Peaslee, Principle Investigator
General Motors Global Propulsion Systems
777 Josyln Ave
Pontiac, MI 48340
Phone: (248) 917-2341
Email: brian.peaslee@gm.com

Steven Boyd, DOE Program Manager
U.S. Department of Energy
E-mail: steven.boyd@ee.doe.gov

Start Date: January 1, 2016 End Date: September 30, 2019
Project Funding: $5,673,086 DOE share: $3,793,697 Non-DOE share: $1,879,389

Project Introduction

The purpose of the project is to research, develop, and demonstrate a Highly Integrated Wide Bandgap (WBG) Power Module targeting Next Generation Plug-In Vehicles. Developed power module will be functionally and mechanically optimized for the next generation powertrain in electric vehicles. Main target is to design and develop a three-phase voltage source inverter with the new WBG power module that will achieve or exceed specified power, power density and cost targets, while operating at increased efficiencies. Operation at increased efficiencies will enable range improvements in electric vehicles.

Objectives

WBG power modules developed under this project targets to achieve a Specific Power greater than 14.1 kW/kg, Power Density greater than 13.4 kW/L at a cost of less than 3.3 USD/kW.

Approach

Critical to implementing fast switching WBG devices, is reduction of power module electrical parasitics such as power loop and control loop inductances. Although the power module package is designed to enable faster switching of SiC devices, with a gate drive board specifically designed to provide more effective control and protection of the SiC MOSFET switches.

GM, along with its subrecipient Virginia Polytechnic Institute and State University, is exploring improvement of the following components and features: gate drive circuitry, high bandwidth phase leg current measurement, fast over current protection, gate drive IC's with high common-mode transient immunity (CMTI), low DC loop inductance and low inductance gate control interface.

To improve the WBG power module power density GM, with its subrecipient Monolith Semiconductor, is exploring new SiC devices which are expected to operate at higher junction temperatures. Given the higher temperature operation, power module packaging needs to be improved to enable robust and reliable operation at these increased temperatures. GM, and its subrecipient Oak Ridge National Lab, will evaluate bonding, joining and thermal management technologies that can further reduce overall thermal impedance and improve high temperature reliability.

- To achieve the aggressive power density target for the module level with high reliability requires:
- Selection of minimal number of SiC die, currently 4 die are paralleled per single switch
- Eliminating the free-wheeling SiC by using the SiC MOSFET body diode
- Double-sided sintering of the die to substrate and power connections

- Total thermal resistance reduction from die to coolant channel
- Evaluate die performance and characteristics at high junction temperatures

The project targets to reduce power module size and weight compared to the state of art automotive power modules, that are primarily manufactured using insulate gate bipolar transistor (IGBT) die.

GM will verify the performance of the power module prototype using a selected set of GM production validation tests. The tests include performance reliability, power stage, and inverter level active load testing.

Results

The project is currently in its third year. The GM team, its subrecipients and suppliers have developed a functional power module. Work this past year included power module design, prototyping and detailed module characterization. Verification testing demonstrated the prototype power module performance is close to specified requirements and targets. Requirements and targets of the power module were shared in the previous year's annual report. More detailed performance results are provided in this section. Power module development work focused on assembling power module which included sintering and multi-layer Al-AlN substrate, together with the utilization of low resistance CREE SiC 900V, 10mΩ switches. Below is a summary of the accomplishments for each area.

Power Module Design and Static Characteristic

A three-phase power module, utilizing CREE devices, was designed for dc bus voltage operation at 600Vdc, 425A peak current, and 300Arms phase current. Given the bidirectional die characteristic, the switch conducts in both directions, effectively reducing conduction losses. Figure II.3.1 shows the power module prototype and its corresponding electrical schematic. The power module is designed to have ultra-low conduction and switching losses. The module's low inductance design demonstrates low drain to source voltage overshoot during fast switching transients (Figure II.3.7). High power density package is achieved by removing the anti-parallel diodes and utilizing the SiC MOSFET internal body diode during 3rd quadrant operation. The power module has a very symmetrical layout which is critical for high speed switching operations. While targeted to traction inverter applications, the power module is well suited for use in boost converter applications.

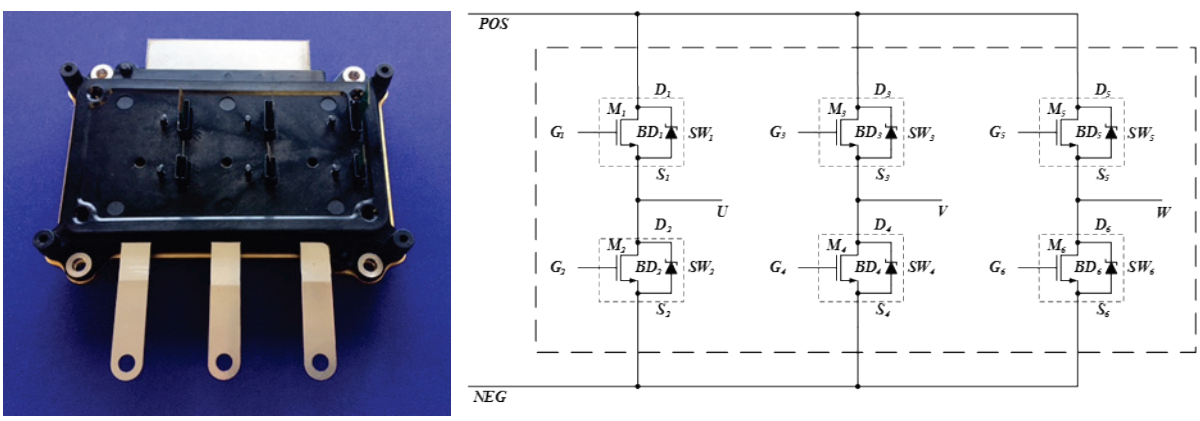

(a) module (b) electrical schematic

Figure II.3.1 Manufactured prototype of the power module: (a) module picture (b) electrical schematic. Work performed by General Motors Subrecipient, Virginia Polytechnic Institute and State University, CPES

The prototype power module was fully characterized using a curve tracer. Measured results are presented in this section. Power module output characteristics have very low resistance, which means lower conduction losses. Measured device characteristic at Vgs=15V and at room temperature are shown in Figure II.3.2. Additionally, switch output characteristics were measured for different Vgs voltages as shown in Figure II.3.3.

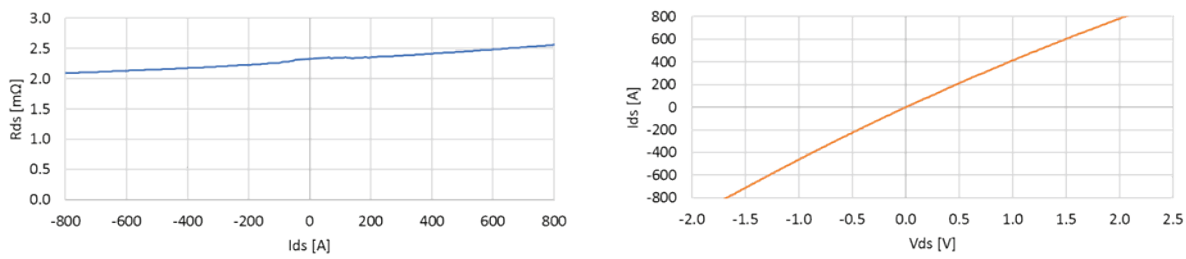

(a) Switch resistance (b) Switch output characteristic

Figure II.3.2 Static characteristic of designed power module: (a) switch resistance (b) output characteristic

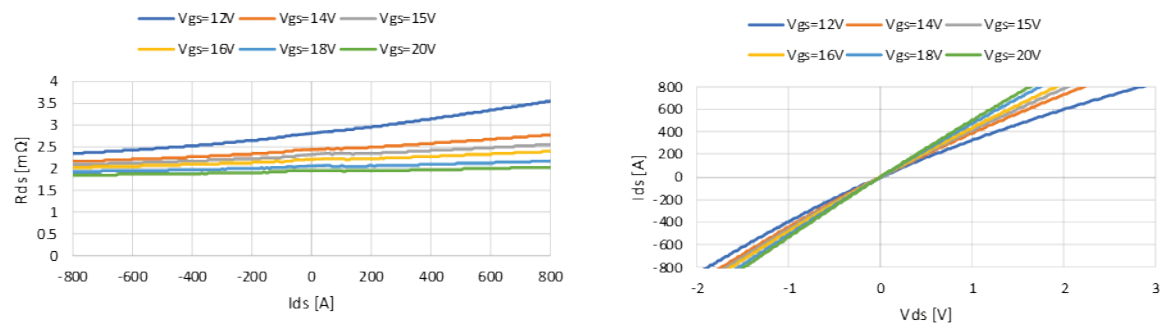

(a) Switch resistance (b) Switch output characteristic

Figure II.3.3 Static characteristic of designed power module for different Vgs voltages: (a) switch resistance (b) output characteristic

Although lower resistance is possible at higher gate voltages, device lifetime is reduced when continuously switched using elevated control voltages. An optimized gate voltage of 16V is used. At this drive level, the module has lower resistance, and enough margin for robust and reliable operation. A flex circuit was integrated into a power module, to reduce gate inductance, and to low gate voltage overshoots during switching transients. The low inductance gate loop enabled controlling the MOSFET with an increased gate voltage, without voltage overshoot which would compromise lifetime.

Figure II.3.4 details the increased switch resistance of approximately 37.5% at high temperatures.

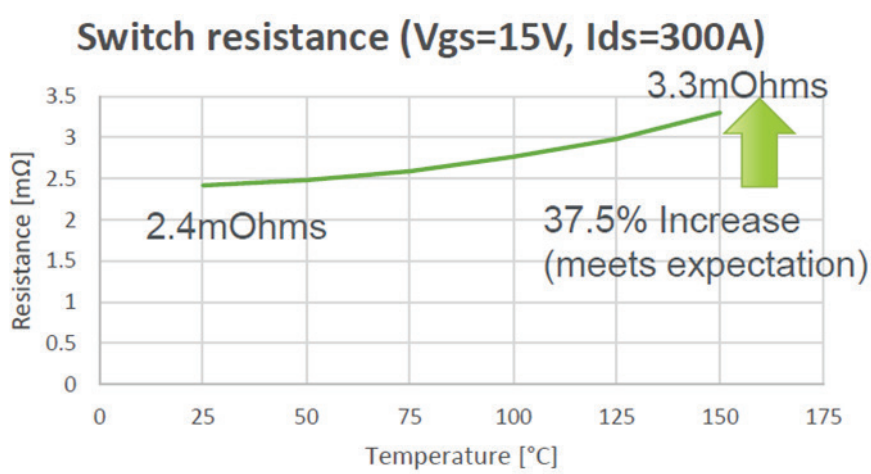

Figure II.3.4 Switch on state resistance for different temperatures

Figure II.3.5 shows internal body diode during 3rd quadrant operation. While these losses appear high, the body diode only conducts during the dead-time when the gate is off. This is very short period of time and does not significantly affect die temperature. Dead-time typically is at the order of a few microseconds for IGBT power modules and it is expected that in an SiC MOSFET the dead time can be reduced by a factor of 5 to 10. To keep the die temperatures low, dead time will need to be at a minimum with enough margin to prevent shoot-through. Reliable device operation requires accurate gate voltage control and regulation. A study was performed to estimate the deadtime delays and subsequent control variation that can be expected in a typical automotive environment. Losses during body diode conduction had minimal impact to power losses and no impact to the thermal design. The additional body diode losses are within the thermal margin design shown to keep the junction temperature below 175°C.

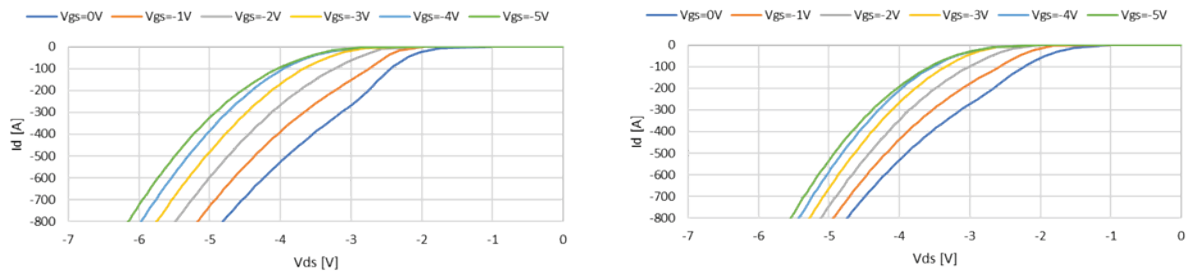

(a) Room temperature (b) Hot temperatures

Figure II.3.5 Output characteristic of internal body diode: (a) room temperature (b) hot temperatures

Dynamic Characteristic of Power Module

Double pulse testing was used for power module dynamic characterization. Double pulse test set-up is shown in Figure II.3.6. It includes power module bus bars laser welded to a DC bulk capacitor. Laser welding provides low resistance and low inductance connection significantly reducing power stage total stray inductance. The gate drive board is designed with a well regulated gate drive power supply with a low inductance connection to the power module gates. A novel combination of flex PCB and careful design of gate driver board circuit layout yielded very low ringing at the MOSFET gate.

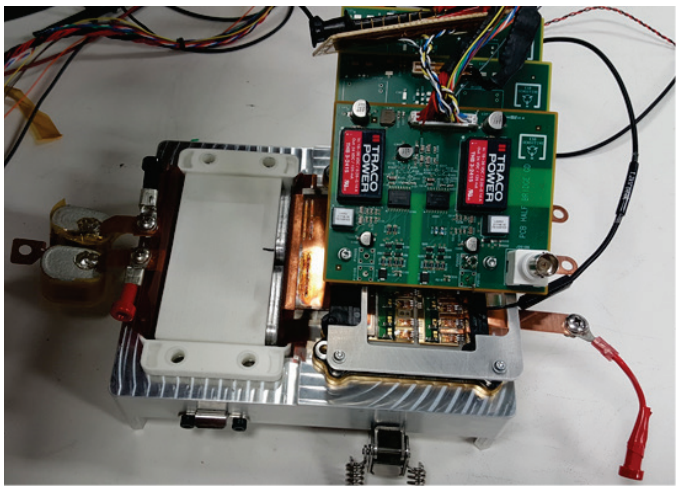

Figure II.3.6 Hardware set-up for double pulse testing

Typical turn-on and turn-off waveforms are shown in Figure II.3.7. Representative switching waveforms at 600V, 500A were chosen to represent maximum DC voltage at highest current. Turn-on loss is measured 13.37mJ, while the turn-off losses is measured 10.08mJ. In both switching events di/dt slew rate is above

15A/ns, while dv/dt slew rates are above 23V/ns. In this case total switching loss at 600V, 500A is measured to be 23.45mJ, which is 3-5 times lower compared to standard automotive silicon IGBT modules.

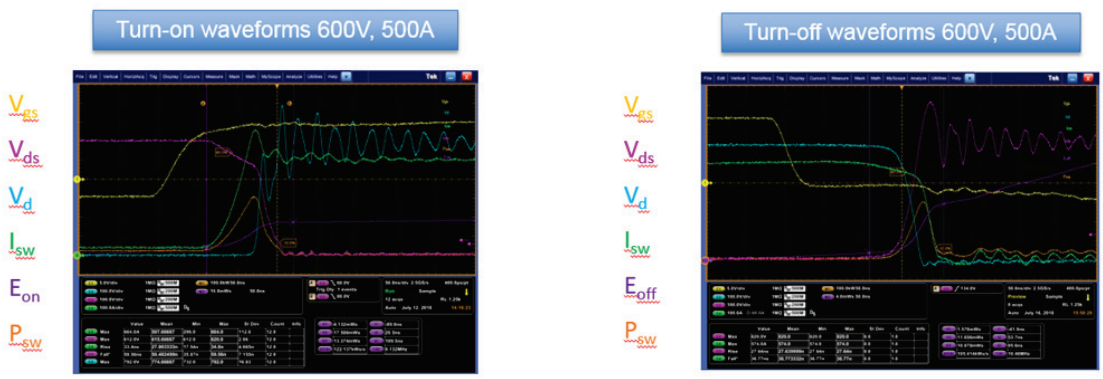

(a) Turn on switching transient (b) Turn off switching transient

Figure II.3.7 Representative switching waveform during switching transients: (a) turn-on (b) turn-off

Turn-on process occurs in two steps, which can be clearly seen by observing drain source voltage. During the first phase, body diode of the upper switch is preparing to block full voltage. In this phase drain source voltage decreases slowly, with a moderately low slew rate. When the body diode is ready to block the full bus voltage rapid switching occurs and drain source voltage sharply drops down to zero volts, correspondingly body diode sharply increases to the dc bus voltage. Commutation process is inherent for the power module and cannot be eliminated. The primary design freedom is changing the gate drive resistance. Furthermore, during turn-on process, the body diode is turning off and a large overshoot is generated. Selected gate resistance values ensure that overshoot on the body diode stays below device voltage limit (900V).

Turn-off also needs to be fast to ensure minimal losses while minimizing voltage overshoot. Due to the low inductance design, it is possible to turn-off devices using fast di/dt slew rates, while corresponding voltage overshoot stays below 900V. Power loop inductance of the module was measured experimentally to be approximately 7.5nH, which is very close to values predicted by simulation.

Figure II.3.8 shows power module switching losses measured at 600 V DC bus. Turn on switching waveforms reveal low switching losses. Switching losses increase linearly as current is increased. If large inductance is present on the kelvin source pin, the turn-on process would slow down and plateau level would exist in the drain source voltage. Plateau voltage level would have relatively high value and would substantially increase turn-on losses. If power module package has significant kelvin source inductance in the control loop, turn-on losses would increase exponentially as current is increased. The power module was designed to decouple control and power loops. The measured switching losses validated our design approach.

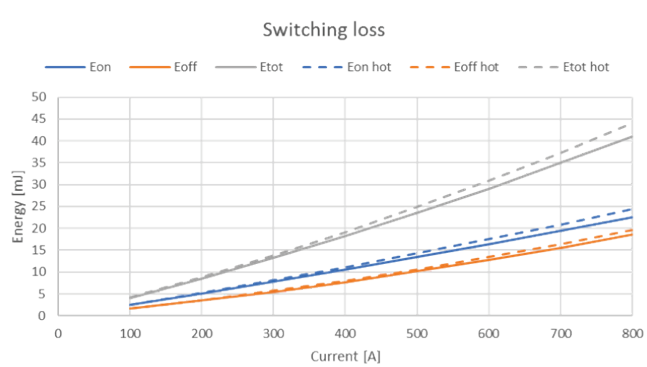

Figure II.3.8 Power module switching losses: (a) turn on losses (blue) (b) turn off losses (orange) (c) total switching losses (gray)

System loss and inverter efficiency

The effects of lower conduction and switching losses of power modules were studied at the vehicle level and traction inverter losses are estimated for several representative operating points. Table II.3.1 shows most important inverters parameters during operation. Results show that the inverter operates with high efficiency, above 99.05%. Although hot temperatures losses were used as the worst-case loss indicator, overall inverter losses remain relatively low when compared to Si IGBT based inverters. Even for the highest output power of the inverter, power module dissipates only 2.67kW, while corresponding temperature rise is only 62°C. Further improvements in power module are possible with larger wire bonds or a better conductor material.

Table II.3.1 Inverter Loss Breakdown for Different Operating Points

	Operating Point 1	Operating Point 2	Operating Point 3	Operating Point 4
Bus Voltage	600V	600V	600V	600V
Phase Current	300Arms	350Arms	400Arms	500Arms
Conduction Loss	135W	184W	241W	380W
Switching Loss	63W	75W	87.5W	114W
Thermal Impedance	0.14°C/W	0.14°C/W	0.14°C/W	0.14°C/W
Total Inverter Loss	1.14kW	1.37kW	1.75kW	2.67kW
Inverter Power	168kW	196kW	225kW	281kW
Efficiency	99.32%	99.30%	99.22%	99.05%
Temperature Rise	27°C	32°C	41°C	62°C

The inverter use cycles are being studied under critical conditions needed to increase vehicle range and efficiency. Two configurations are studied:

1. Today's standard DC bus voltage ranges common to this generation of EVs
2. Higher DC bus voltages being investigated in a future generation of EVs

This power module's higher efficiency over a broad range of voltages will provide lower cycle average losses versus the present generation of Silicon IBGT based traction inverters.

Gate Driver Progress

In an effort to improve monitoring of the switch and bandwidth of current sensing under fault conditions, a gate drive board utilizing a Rogowski coil current sensing technique was implemented. The intent of the circuity is to measure R_{dson} of SiC switch and dynamically monitor the switch during operation. To gauge the accuracy of online V_{ds} measurements, $R_{DS_{on}}$ will be monitored through multi pulse tests and compared with static results obtained with curve tracer. Switches being measured heat up during multi pulse testing, given the increased test time. The resulting temperature increase should not be significant, but was investigated.

Very good accuracy, under 1%, for currents above 40 A was observed. Circuitry was able to measure from 35 mV (10 A) ÷ 700 mV (160 A) and -38 mV(-10 A) ÷ -611 mV (-160 A) as shown in Figure II.3.9. Both measurements on low and high temperature behave in the same manner and no distinguishable difference is noticed, indicating good thermal coupling between two diodes and lot to lot variation. Further investigation of the accuracy and precision of the developed measurement technique will be performed in the future.

Performance of the measurement method are given below:

- Rogowski coil current voltage monitoring sensors are found to be satisfactory and comparable to conventional current and voltage measurement solutions.
- Estimation errors are maximum at low currents, but below 4.5%.
- In addition for switch currents above 40A, switch Rdson value is estimate with very high accuracy, below 1.5%.
- Switch resistance estimation does not show significant difference in precision for ambient and high temperatures.

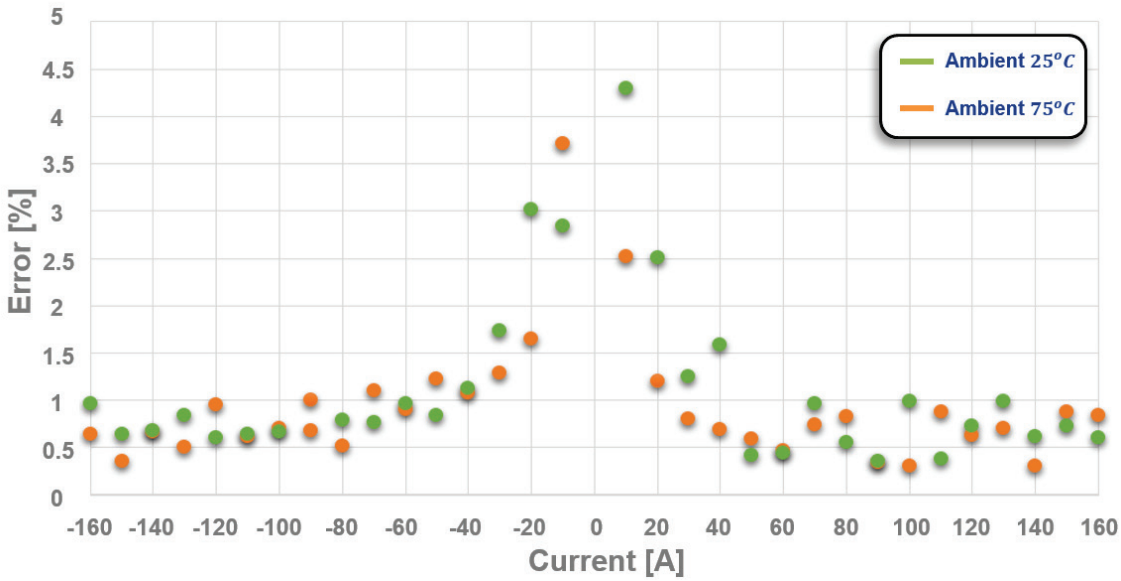

Figure II.3.9 DC measurement error of R_{dson} estimation

Work performed by General Motors Subrecipient, Virginia Polytechnic Institute and State University, CPES

Conclusions

- A low loss high speed SiC MOSFET based power module was built and tested, providing significant loss reduction, to enable inverter operating efficiencies higher than 99.00%
- Total SiC power module losses are estimated at a third of standard industrial IGBT power modules
- A complete power stage design concept including power module and dc bulk capacitor is about half the size of industry leading silicon IGBT power stage designs
- Power stage inductance was reduced 4-5 times when compared to standard automotive solutions measuring 7.5nH which correlated well to modeling

Key Publications

1. S. Mocevic *et al*., "Comparison between desaturation sensing and Rogowski coil current sensing for shortcircuit protection of 1.2 kV, 300 A SiC MOSFET module," *2018 IEEE Applied Power Electronics Conference and Exposition (APEC)*, San Antonio, TX, 2018, pp. 2666-2672.
2. S. Mocevic *et al*., "Phase Current Sensor and Short-Circuit Design Detection Based on Rogowski Coil Integrated on Gate Driver for 1.2kV SiC MOSFET Half-Bridge Module," *2018 IEEE Energy Conversion and Congress Expo (ECCE)*, Portland, OR, 2018, pp. 393-400.

3. A. Romero *et al*., "Non-destructive and Destructive Shortcircuit Characteriztion of a High-Current SiC MOSFET," *2018 IEEE Energy Conversion and Congress Expo (ECCE)*, Portland, OR, 2018, pp. 862-867.
4. "WBG Application Opportunities in Automotive Power Conversion", APEC 2018
5. DOE Annual Merit Review Vehicle Technologies Program, June 2018
6. Power America WBG Summer Workshop, August 2018

Patents

The two previously reported Records of Invention have been approved to go forward in the patent application process

1. "Low Cost Dual Insulated Layer Substrate Power Module with Low Electrical Inductance" (P036622)
2. "Power Module Assembly With Reduced Inductance" (P036694)

Three new patents have been submitted this year

1. "High frequency dc bulk capacitor design with interleaved busbar structure", (P044918)
2. "Low inductance power module for traction inverters", (P045682)
3. "Rogowski Coil Current Sensor for Inverter Module Switches Protection and Phase Current Reconstruction", (P047964 and filed provisionally with VTIP)

II.4 High Speed Hybrid Reluctance Motor Utilizing Anisotropic Materials (General Motors)

Edwin Chang, Principal Investigator
General Motors Global Propulsion Systems
777 Joslyn Avenue
Pontiac, Michigan, 48360
E-mail: edwin.chang@gm.com

Steven Boyd, DOE Program Manager
U.S. Department of Energy
E-mail: steven.boyd@ee.doe.gov

Start Date: October 2016 End Date: September 2019
Project Funding: $7,081,060 DOE share: $4,637,060 Non-DOE share: $2,444,000

Project Introduction

The objective of this project is to design and verify motor concepts with without heavy rare earth (HRE) content capable of achieving DoE Motor Year 2020 performance and cost targets. These three motor variants are Variant 1: Heavy Rare Earth-free Permanent Magnet Motor (HRE-free PM motor), Variant 2: Synchronous Reluctance Motor (SyRM) with Small HRE-free Magnet Assist, and Variant 3: Hybrid Induction Motor with Insert Copper Bars and Cast Aluminum End-rings.

Objectives

This project will research, develop, and demonstrate 3 new motor types for traction applications. Each design should be capable of achieving or exceeding the following technical targets, set by the DoE to be achieved by 2020:

- Cost ($/kW) less than $4.7
- Specific Power (kW/kg) greater than 1.6
- Power density (kW/L) greater than 5.7

These motors are enabled by the following technologies, which are evaluated through the course of this project:

- HRE-free magnets must be developed to meet stringent coercivity and remanence performance criteria
- Copper – aluminum interfaces must be developed to be robust in a traction motor environment
- Motor electromagnetic and mechanical design techniques must be developed to ensure that these enabling technologies can be incorporated to meet motor performance requirements.

Each design should demonstrate advantages over conventional baseline designs in one or more of the following categories: cost, efficiency, and power density. Each design is also expected to have proven manufacturability and to undergo typical durability and performance testing by GM to ensure they meet market requirements.

Approach

Three motor design types will be studied to determine the feasibility of each approach. These three motor variants will be selected based on their expected ability to meet the technical targets. The design approaches will take advantage of material advancements which will allow these motors to meet the performance requirements without heavy rare earth elements or rare earth elements altogether.

The project will concentrate on four major tasks:

1. Material Evaluation and Selection
2. Electromagnetic and Mechanical Machine Design
3. Electric Motor Prototype Manufacturing
4. Verification Testing and Performance Evaluation

Task 1: Material Evaluation and Selection

- Development of the requirements for Grain Oriented Electrical Steel (GOES)
- Survey of available grades of GOES
- Industry survey of GOES available grades and Selection for Electromagnetic Design Studies
- Execution of FEA-based design studies for Synchronous Reluctance Motor using GOES, and Hybrid Synchronous Reluctance Motor using Anisotropic HRE-free magnets and GOES
- Development of, working with suppliers, HRE-free anisotropic magnet material
- Evaluation of the developed anisotropic HRE-free magnets and Non-Oriented Electrical Steel (NOES) for use in the motor laminations.

Task 2: Electromagnetic and Mechanical Design of 3 Machines

- Detailed structural, thermal, and electromagnetic analysis of the machine concepts to ensure that the motors meet both the performance and reliability objectives required for use in General Motor's electrified vehicle portfolio
- Generation of an Indentured Bill of Materials (BoM)

Task 3: Electric Motor Prototype Manufacturing

- Prototype motors will be built to ensure that those meet all GM Production Bill of Process (BoP) requirements
- Production Manufacturing Equipment will be identified and its associated costs will be documented
- Comprehensive test plan for machine verification will be defined and durability test plan for demonstration will be developed

Task 4: Verification Testing and Performance Evaluation

- All three motor designs will be calibrated for peak torque and efficiency
- Machines will be tested for performance and efficiency verification
- Torque and power vs. speed curves will be generated
- Complete efficiency maps for both motoring and generating will be generated for operations at different voltage levels
- Measured performance maps will be compared to the predicted results for data correlation purposes
- Rotor durability testing will be executed on two variants (Synchronous Reluctance motor with HRE-free Magnet Assist and High Performance Hybrid Induction Motor using Inserted Copper Bars and Aluminum Die Cast End-rings) and will include rotor speed cycling at various RPM to induce fatigue failures in the rotor laminations
- HRE-free PM motor variant will be excluded from rotor durability testing due to its similarity to other production designs that have previously demonstrated superior reliability

Oak Ridge National Laboratory, ORNL, a co-recipient of this project, is responsible for aspects of materials testing. The objectives are to characterize material properties of electrical steels and cast Al to Cu bar interfaces.

Results

Motor Design

Table II.4.1 Summarizes the Motor Designs. The Designs Exceed the DoE Motor Year 2020 Power Density and Specific Power Targets.

	HRE-free PM Motor	Synchronous Reluctance Motor with HRE-free PM Assist	Hybrid Induction Motor with Insert Cu Bars and Cast Al End-rings
Stator Outer Diameter (mm)	208	190	190
Rotor Outer Diameter (mm)	139.5	69.525	69.525
Stator Core Length (mm)	200	100	100
Power (kW)	148	89	84
Torque (N-m)	372	249	310
Max RPM	12000	16650	14000

The Variant 1 motor was a two layer V permanent magnet design using HRE-free neodymium-iron-boron (NdFeB) magnets. Figure II.4.1 shows the lamination 2D design and the power-speed and torque-speed curves of the motor. Despite the lower magnet coercivity due to the HRE-free composition, the resistance to demagnetization was shown to be acceptable. Cost evaluation of the HRE-free PM machine is shown to beat the cost target of $4.7/kW.

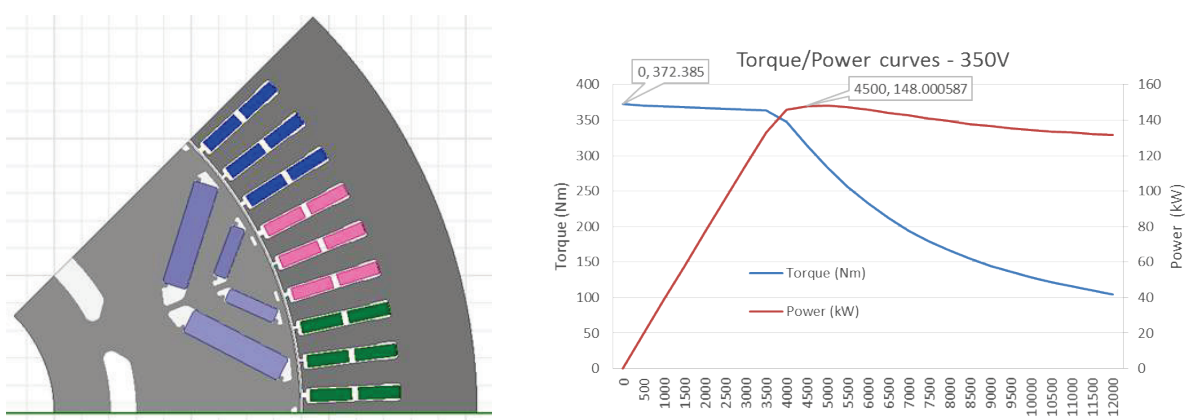

Figure II.4.1 Variant 1 2D lamination design, left. Torque-speed and power-speed curves, right.

Variant 2 was achieved using a four barrier design and stress relief features in the rotor webs to enable mechanical strength at higher speeds. Small HRE-free magnets provide magnetic saturation of the webs. The 2D lamination design, torque-speed curve, and power-speed curve are shown in Figure II.4.2.

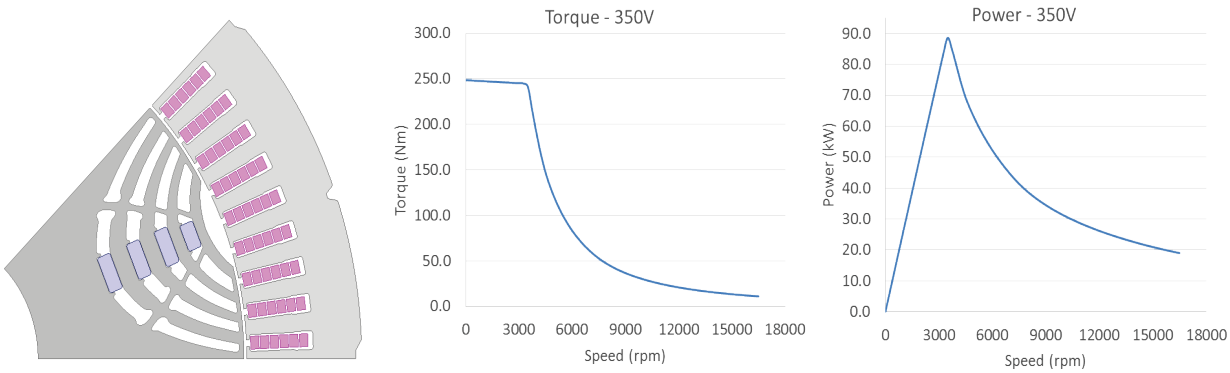

Figure II.4.2 Variant 2 2D lamination design, left. Torque-speed curve, middle. Power-speed curve, right.

Variant 3 implemented inserted copper bars and aluminum end-rings. The aluminum end-rings enable lower cost while the copper bars enable lower losses in the slots, resulting in higher continuous torque. The 2D structure is shown in Figure II.4.3, along with the continuous torque comparison.

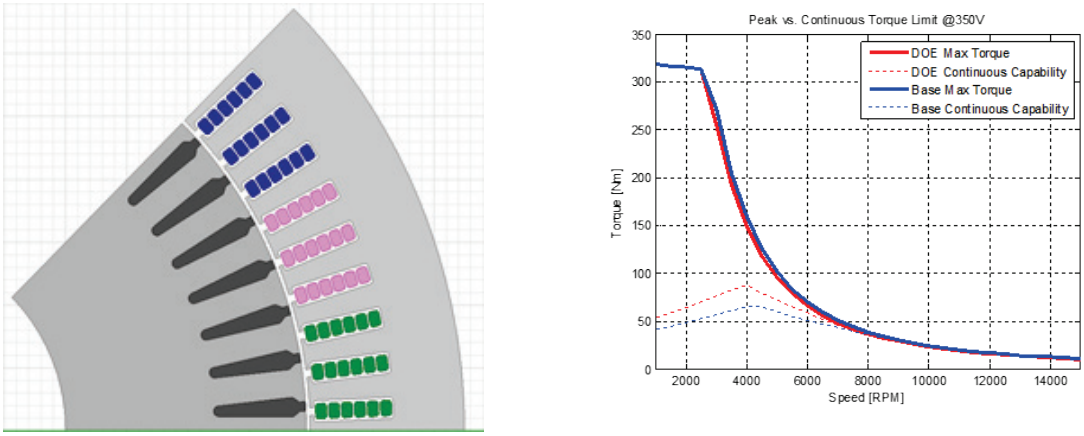

Figure II.4.3 Variant 2, 2D lamination design, left. Torque-speed and power-speed curves with comparison to baseline AI design, right.

Motor Manufacturing

General Motors identified and worked with key suppliers to source and produce the subcomponents required. Stators for the HRE-free PM motor and Cu-Al hybrid induction motor were manufactured by GM Global Propulsion Systems in Pontiac, and are shown in Figure II.4.4. The stamping of the HRE-free PM rotor cores and SyRM with small HRE-free PM assist rotors are ongoing, along with the aluminum casting of the hybrid Cu-Al induction motors. The prototype HRE-free PM rotors and SyRM with small HRE-free PM assist rotors will be stamped on a progressive die and interlocked to be most comparable in mechanical performance to production baseline designs. A horizontal press and mold were selected for the hybrid Cu-Al induction motor. The mold was designed using casting flow simulations.

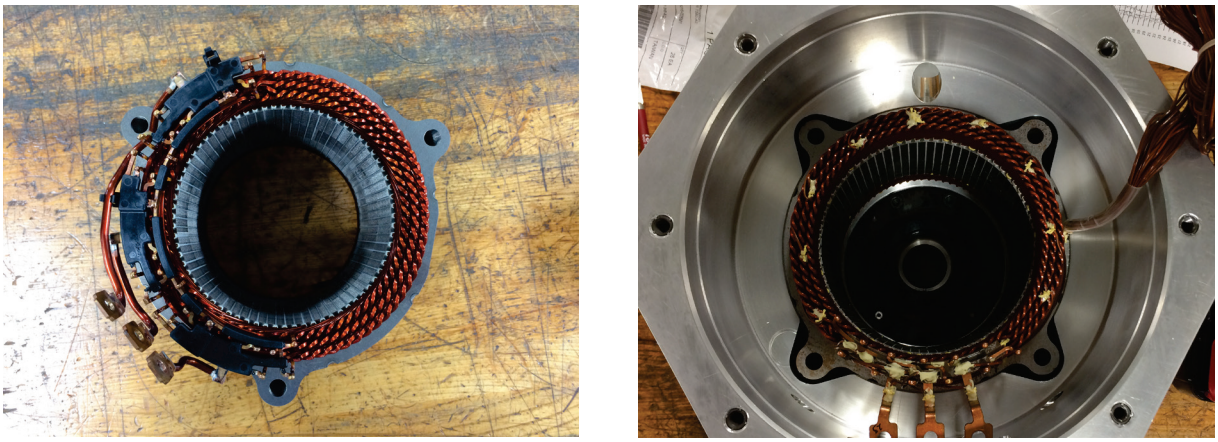

Figure II.4.4 Variant 1, stator, left. Variant 3 stator in fixture, right.

Although concerns were present for the magnetization of the HRE-free PM machine due to the position and microstructure of the HRE-free magnets, finite element analysis results showed that the rotor would be able to be magnetized using standard magnetization equipment without necessary upgrades.

Due to manufacturing restrictions related to the slot fill of the stators, the stator for Variant 2 and Variant 3 had to be modified from the original design by decreasing the slot tooth size. This led to a small reduction in torque at low speeds, but resulting in no change in the peak power or the motor ability to meet the DoE power targets. The results of this design change is shown below in Figure II.4.5.

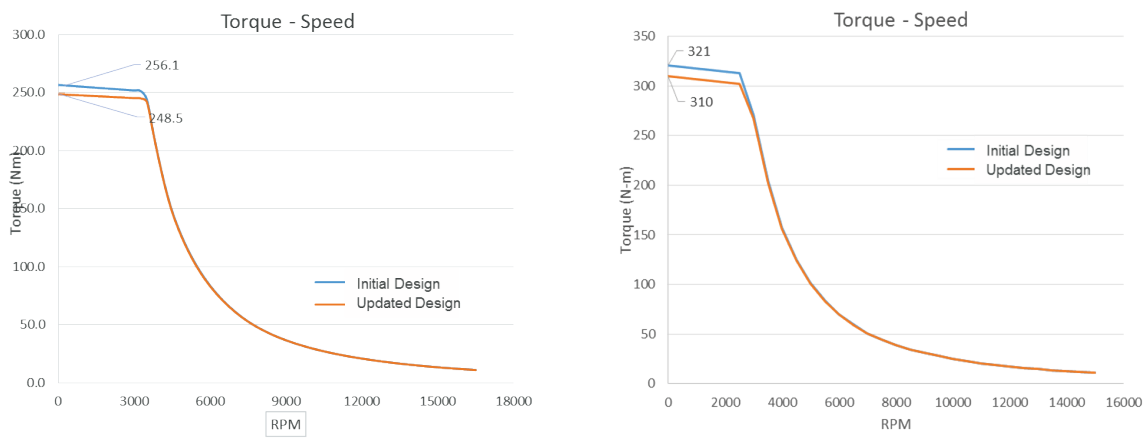

Figure II.4.5 Variant 2, left, and Variant 3, right, power loss due to slot tooth width decrease

Motor Testing

Demagnetization testing of rotors was performed to better set the requirements for demagnetization. The testing was completed for rotors containing three different levels of coercivity, each showing three steps of demagnetization of the rotor. The demagnetization was then correlated with the test results, which will lead to better demagnetization prediction and more accurate motor protection.

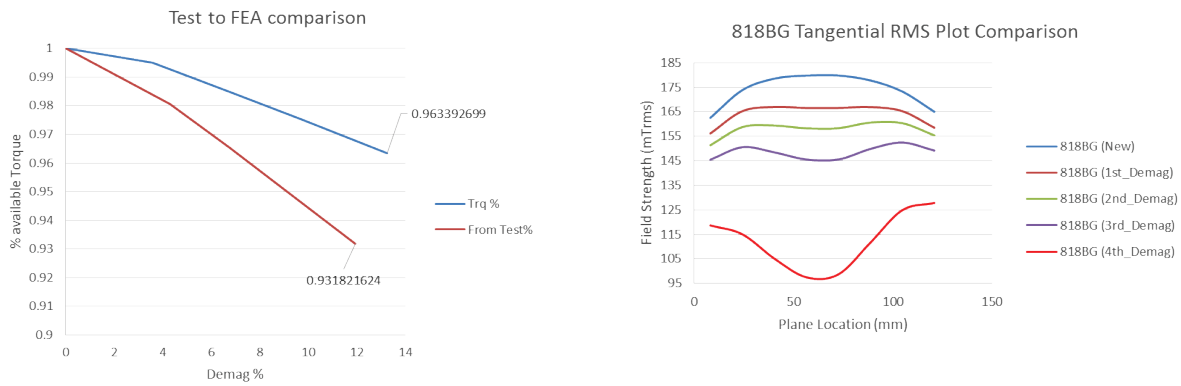

Figure II.4.6 Predicted demagnetization compared to experimental results, left. Field measurement of sequential demagnetization tests along the motor axis, right.

Oakridge National Lab Materials (ORNL) Testing

ORNL is working with steel samples and copper/aluminum bars that were provided by GM for materials analysis. There are various sample sizes and shapes for three steel products that are being used for metallography such as compositional analysis, texture analysis, and other items that will be observed with various types of microscopy. Electromagnetic properties are being measured in an Epstein test frame and a single sheet test fixture. Effects from residual stresses are also being observed during single sheet testing. Comprehensive testing of electromagnetic properties is underway and results will be processed and analyzed in the first quarter next fiscal year.

ORNL and GM have held detailed discussions and requirements associated with the following analyses:

- Edge analysis – optical analysis of sheared edge from stamping operation
- Microhardness – harness in various locations in cross-section
- Compositional analysis – to determine composition of material
- Coating thickness – important for stacking factor and resistance between laminations
- Coating composition – same as above.
- Density
- Electromagnetic properties – baseline frequencies and flux densities have been established
- Tensile and fatigue requirements.

A series of tensile tests were conducted with three candidate materials on the most readily available equipment shown in Figure II.4.7. Processed stress-strain curves are shown in Figure II.4.8, and the correlating mechanical properties from the tensile tests are shown in Table II.4.2, Figure II.4.9, and Figure II.4.10. The material 46185-2 has a much higher ultimate tensile strength (UTS) of 604 MPa when compared to a UTS of 486 MPa and 427 for materials 54424-2 and 55006-2, respectively. It is important to note that this test setup in typically used with larger samples with higher force requirements, and therefore, raw data from the tests indicates considerable variation in the stress-strain as a result of the sensor, actuator, and feedback system being intended for larger loading. A smaller tensile test frame is now available, and more extensive testing including multiple samples for repeatability is currently underway.

Figure II.4.7 First Tensile Test Setup.

Burress, ORNL

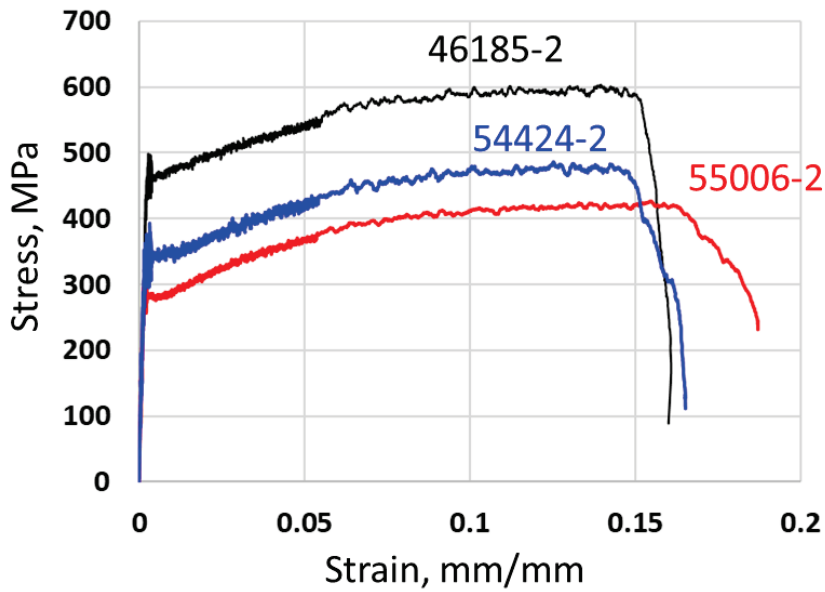

Figure II.4.8 Comparison of stress-strain curves of three candidate materials.

Burress, ORNL

Table II.4.2 Comparison of Properties from First Tensile Tests.

Parameter	46185-2	55006-2	54424-2	Notes
0.2% Yield, MPa	463	281	338	
UTS, MPa	604	427	486	
Total Elongation	0.161	0.187	0.165	
Uniform Plastic Strain	0.143	0.153	0.124	End of linear part to max uniform strain
E, GPa*	190	190	190	*The elastic modulus from first tests was not accurate due to large noise, it is 190GPa with about 10% variation

Burress, ORNL

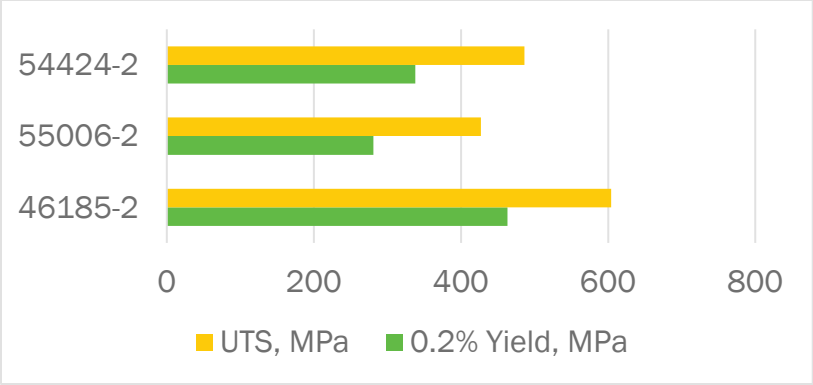

Figure II.4.9 Comparison of ultimate tensile strength and 0.2% yield for three candidate materials.

Burress, ORNL

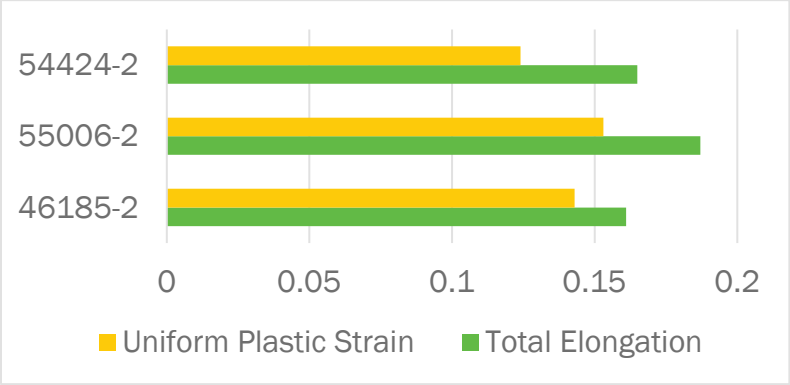

Figure II.4.10 Comparison of uniform plastic strain and total elongation for three candidate materials.

Burress, ORNL

Conclusions

Design of the three motor variants were completed, with predictions of performance, mechanical strength, and thermal performance completed. The motor designs showed promise in exceeding the DoE 2020 motor targets for power density and specific power, with strategies to exceed the DoE cost targets. All motor sub-components were sourced, with the majority of components delivered to GM Global Propulsion Systems in Pontiac for prototype manufacturing. The motor builds are ongoing, which will allow GM to identify cost and manufacturing opportunities and risks. Motor validation and testing is planned to move forward to verify the predicted performance.

Key Publications

Patent Applications

1. "Rotor for an Electric Machine" (P045263)

Acknowledgements

ORNL testing managed by Tim Burress, who also contributed the text for the ORNL Materials Testing portion for this report. Motor designs were completed by Jorge Cintron-Rivera, Jihyun Kim, and Jingchuan Li. GM electric drive engineering, research and development, motor manufacturing, and development/validation contributed design, manufacturing, and testing expertise to this project. GM contract management performed by Sean Campbell. NETL project management performed by John Tabacchi.

II.5 Assessing Class 3-8 HEV and EV Vehicles Operating on North American Roads and Their Supply Chain for Drive-Train Motors, Inverters, Converters and Batteries (Synthesis Partners, LLC)

Christopher L. Whaling, Principal Investigator
Synthesis Partners, LLC
11250 Roger Bacon Drive, Suite 2
Reston, VA 20190
E-mail: cwhaling@synthesispartners.com

Steven Boyd, DOE Program Manager
U.S. Department of Energy
E-mail: Steven.Boyd@ee.doe.gov

Start Date: October 1, 2017 End Date: September 30, 2018
Project Funding: $229,959 DOE share: 100% Non-DOE share: 0%

Project Introduction

This work covered original research on the number and type of Class 3-8 (medium- and heavy-duty) HEV and EVs on North American (NA) roads, including information on the suppliers of traction drive inverters, converters, motors and batteries for Class 3-8 HEV and EV vehicles operating on NA roads. Synthesis Partners ("Synthesis") employed an integrated primary and secondary source data-driven approach focused on NA. In addition to quantifying the Class 3-8 HEV and EV supply chain, Synthesis identified and characterized potential research and development (R&D) gap areas that are relevant to VTO's mission of energy affordability, efficiency and resiliency in the Class 3-8 HEV and EV market. This chapter is a brief summary and additional information will be available in a forthcoming public report by Synthesis.

Objectives

The objective of this work is to provide EERE with quantitative and qualitative information on markets, trends and technologies relevant to the mission of increasing energy affordability, efficiency and resiliency – an in particular with regard to Class 3-8 HEV and EVs operating on NA roads. This work also identified and characterized R&D gaps and capabilities that can (if left unaddressed) impede the transition of R&D work into high-quality US-based jobs. By collecting, analyzing and reporting vetted, multi-sourced data regarding the user-base of Class 3-8 HEV and EVs operating on NA roads, this project provides EERE with actionable intelligence to support prioritizing and transitioning VTO R&D work into high-quality US-based jobs.

Approach

This research is based on a calendar year 2018 assessment of thousands of secondary sources alongside hundreds of anonymized, primary industry sources that exchanged information with Synthesis directly. The secondary sources are interpreted according to guidance provided by confidential information secured from primary sources. Each primary source is hereby acknowledged by Synthesis and thanked for their time and contributions to this effort. All errors and omissions remain the sole responsibility of Synthesis.

Synthesis collected and analyzed quantitative and qualitative data on the following elements:

- Number, make, model, manufacturer of Class 3-8 HEV and EV commercial vehicles on the road in North America (NA: U.S., Canada, Mexico) for the most recent full year public data is available;
- For the population of vehicles identified, for the same year, identify the suppliers of drive-train inverters, converters, motors, and batteries (which can include cells); and
- Rank suppliers identified by revenue and numbers of units shipped (as publicly available, or reasonably inferred).

- Synthesis employed the information and insights from mainly primary sources to identify gaps, constraints and bottlenecks in the NA supply chain for traction drive components for Class 3-8 HEV and EVs.

Note that this work builds on prior years of in-depth primary source development by Synthesis, executed on behalf of EERE. For example, during FY16-FY17 Synthesis assessed US export sectors relevant to electrical engineering in the autonomous vehicle industry, in terms of relative size by sales, and growth rates, in order to identify high strength or competitive US sectors. The top-ranked sectors identified are home to some of the most highly competitive and innovative US-based firms. These sectors were then reviewed to identify and assess potential new R&D areas, defined as technical areas in which the EERE has not previously engaged and where R&D investments could address a gap. That context was employed in identifying critical gaps and opportunities to fill gaps in the Class 3-8 HEV and EV vehicle sectors.

Results

Figure II.5.1 provides a summary review of the sources accessed in FY18 and the level of effort executed to match the task requirements.

Sources Accessed	Selected Outcomes
Secondary sources accessed February 2018 – July 2018. Approximately 1,600 websites, news articles, press releases and research papers were reviewed for original data and to identify the most appropriate primary, 3rd party market research and other organizational sources.	From this initial search, along with a review of Synthesis' internal proprietary database of nearly 1,000 primary sources, approximately 400 highly relevant companies, associations, laboratories or individuals were identified for close examination. Nine (9) 3rd party market research reports were assessed in-depth and 17 organizations were identified as having valuable data for follow-up by VTO going forward.
High-Relevance Contacts Approximately 400 executive and other contacts were identified as highly relevant, including: Sr. Execs = 165 Mid-Level Execs = 165 Other (Researchers, State, Federal or Non-Profit) = 70	Approximately 900 unique, custom contacts made via telephone and email to the 400 high-relevance contacts. From the telephone and email primary source contacts, 35 in-depth interviews were completed. In addition, approximately 50 additional in-person conversations were executed during APEC 2018 in San Antonio.

Distribution of High-Relevance Contacts

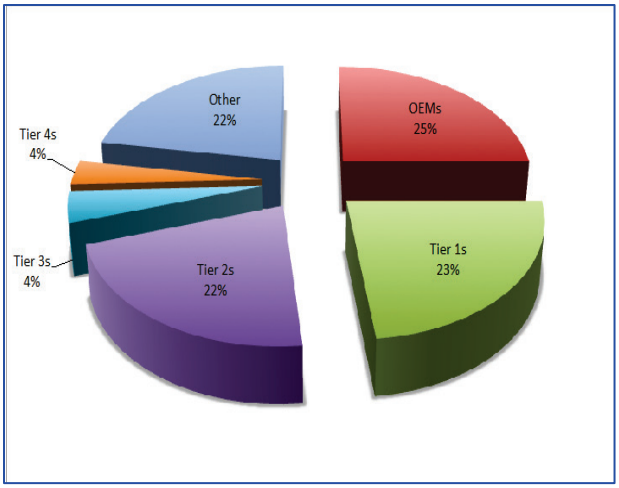

Distribution of high-relevance contacts:

OEMs = 25%

Tier 1 = 23%

Tier 2 = 22%

Tier 3 = 4%

Tier 4 = 4%

RD&E = 7%

Other* = 22%

*Other includes: Academic, Associations, Consultants, Dealers, Distributors, Federal Government, Fleet Operators, Integrators, Investors, State and Local Government, Market Research Firms, Publications, RD&E Entities, Repair/Service Orgs. and Software Firms.

Figure II.5.1 Sources Accessed and Selected Outcomes

Figure II.5.2 depicts the relevant Class 3-8 vehicle classifications, determined by the gross vehicle weight rating (GVWR) of the vehicle.

Light Duty Trucks

- Class 1 – This class of truck has a GVWR of 0 to 6,000 pounds (0 to 2,722kg).
- Class 2 – This class of truck has a GVWR of 6,001 to 10,000 pounds (2,722 to 4,536 kg).
- Class 3 – This class of truck has a GVWR of 10,001 to 14,000 pounds (4,536 to 6,350 kg).

Medium Duty Trucks

- Class 4 – This class of truck has a GVWR of 14,001 to 16,000 pounds (6,351 to 7,257 kg).
- Class 5 – This class of truck has a GVWR of 16,001 to 19,500 pounds (7,258 to 8,845 kg).
- Class 6 – This class of truck has a GVWR of 19,501 to 26,000 pounds (8,846 to 11,793 kg).

Heavy Duty Trucks

- Class 7 – This class of truck has a GVWR of 26,001 to 33,000 pounds (11,794 to 14,969 kg).
- Class 8 – This class of truck has a GVWR of greater than 33,001 pounds (14,969 kg), and includes all tractor-trailers.

Figure II.5.2 Relevant Class 3-8 vehicle classifications, determined by the gross vehicle weight rating (GVWR) of the vehicle

Source: "Commercial Motor Vehicle Classification", Martin Murray, 11-18-16, https://www.thebalance.com/commercial-motor-vehicle-classification-2221025; Accessed 10-11-17.

Table II.5.1 depicts selected quantitative data from the new Class 3-8 HEV and EV NA database. This database represents the first integration of market study information, primary source insight and other secondary sources including the Federal Transit Agency's (FTA) Revenue Vehicle Inventory database regarding Class 3-8 HEV and EVs on the road in NA. All vehicles covered in the new Class 3-8 HEV and EV

NA database include information on each model of vehicle, including classes based on reported or inferred gross vehicle weight rating (GVWR).

Table II.5.1 Estimated Number of Class 3-8 HEV and EVs on the Road in North America in 2018

Type of HEV and EV	Estimated Number in Operation in North America in 2018
Class 3-8 Trucks on the Road in NA	11,909
Class 3-8 Buses in Transit Fleets on the Road in NA	13,826
Class 3-8 Converted/Up-Fitted Trucks or Vans on the Road in NA	3,187
Estimated Total Number of Class 3-8 HEV and EVs Operating on the Road In North America in 2018.	**28,922**

Source: Synthesis Partners, LLC 2018

While suppliers of motors, batteries, inverters and converters to Class 3-8 HEV and EVs in NA did not provide information on the exact number of vehicles supplied that are operating in NA only, they did supply information on numbers of Class 3-8 HEV and EVs supplied that are in operation globally. That data is summarized below, in Table II.5.2.

Table II.5.2 Estimated Number of Class 3-8 HEV and EVs Supplied Globally, Based on Information from Suppliers of Class 3-8 HEV and EV Drive Train Components, as of 2018.

Category of Class 3-8 HEV and EV Drive Train Component Supplier	Estimated Number of Class 3-8 HEV and EV Supplied Globally, Based on Viewpoints of Component Suppliers, As of 2018
Motor System Suppliers	Approximately 47,400 Class 3-8 HEV and EVs Supplied Globally
Inverters and Converters Suppliers	Approximately 10,300 Class 3-8 HEV and EVs Supplied Globally
Battery Suppliers	Approximately 32,300 Class 3-8 HEV and EVs Supplied Globally

Source: Synthesis Partners, LLC 2018

Table II.5.2 provides a range of estimates for the global scale of Class 3-8 markets for the motor, inverter, converter and battery participants, of which NA is a large part. This is not a final answer and represents just the output of primary source research among sources focusing solely on the NA market. Of course, not every vehicle that is supplied by a motor, inverter or battery supplier is confirmed operating on the road, nor is a unique vehicle; nonetheless, Chart 4 provides an estimate of the size of the global Class 3-8 HEV and EV market from component suppliers' point of view.

Figure II.5.3 through Figure II.5.5 provide summary data on the number of HEV and EVs *in operation in NA*, by type of vehicle (e.g., Truck, Bus or Fleet Vehicle, or Up-fitted Truck or Van) and by main component supplier (e.g., Motor, Inverter and Converter, or Battery supplier).

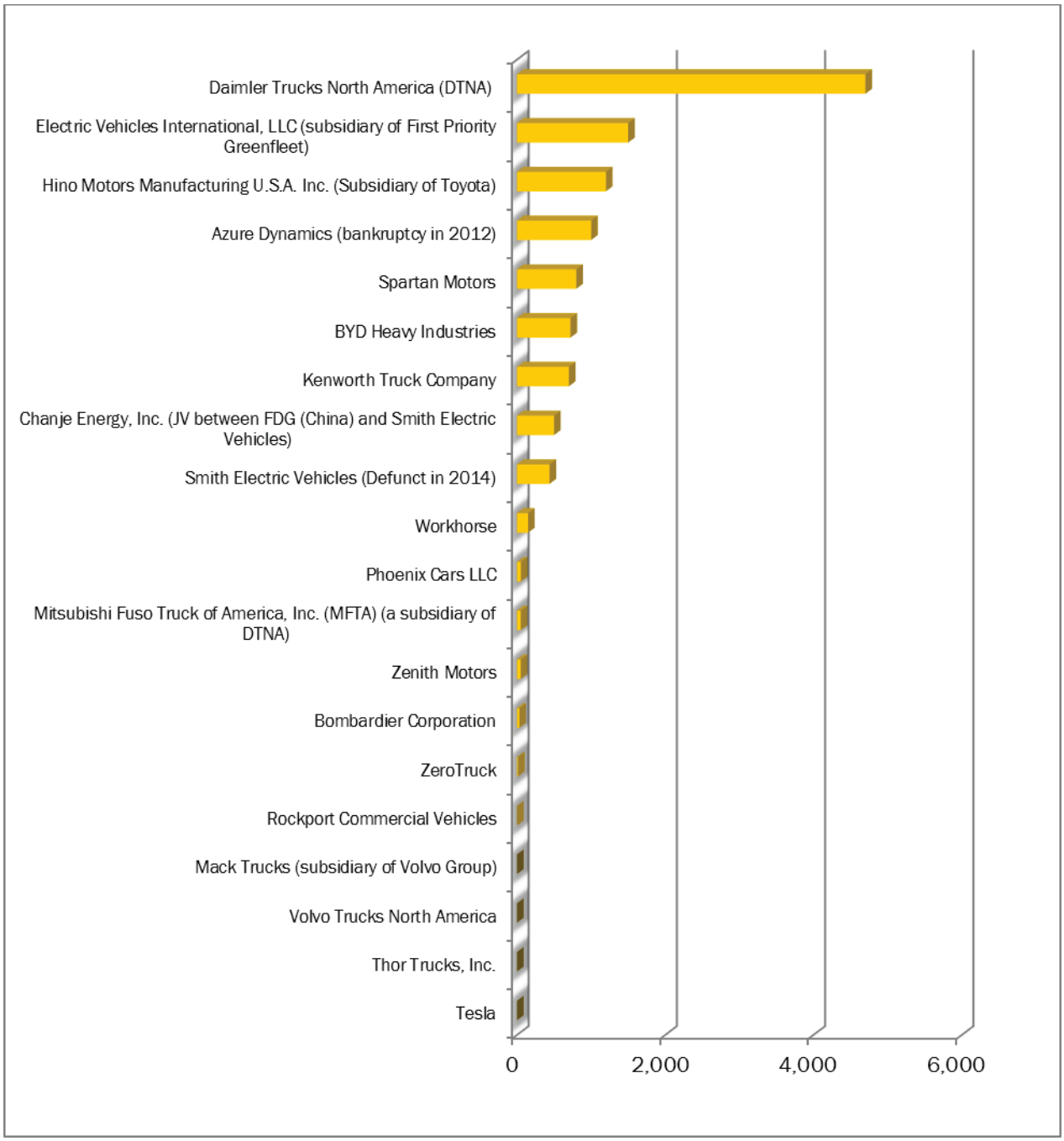

Figure II.5.3 Estimated Number of Class 3-8 HEV and EV Trucks, By Supplier, In Operation in NA in 2018.

Source: Synthesis Partners LLC, 2018

The total number of Class 3-8 HEV or EV trucks in operation in NA in 2018 is estimated to be 11,909.

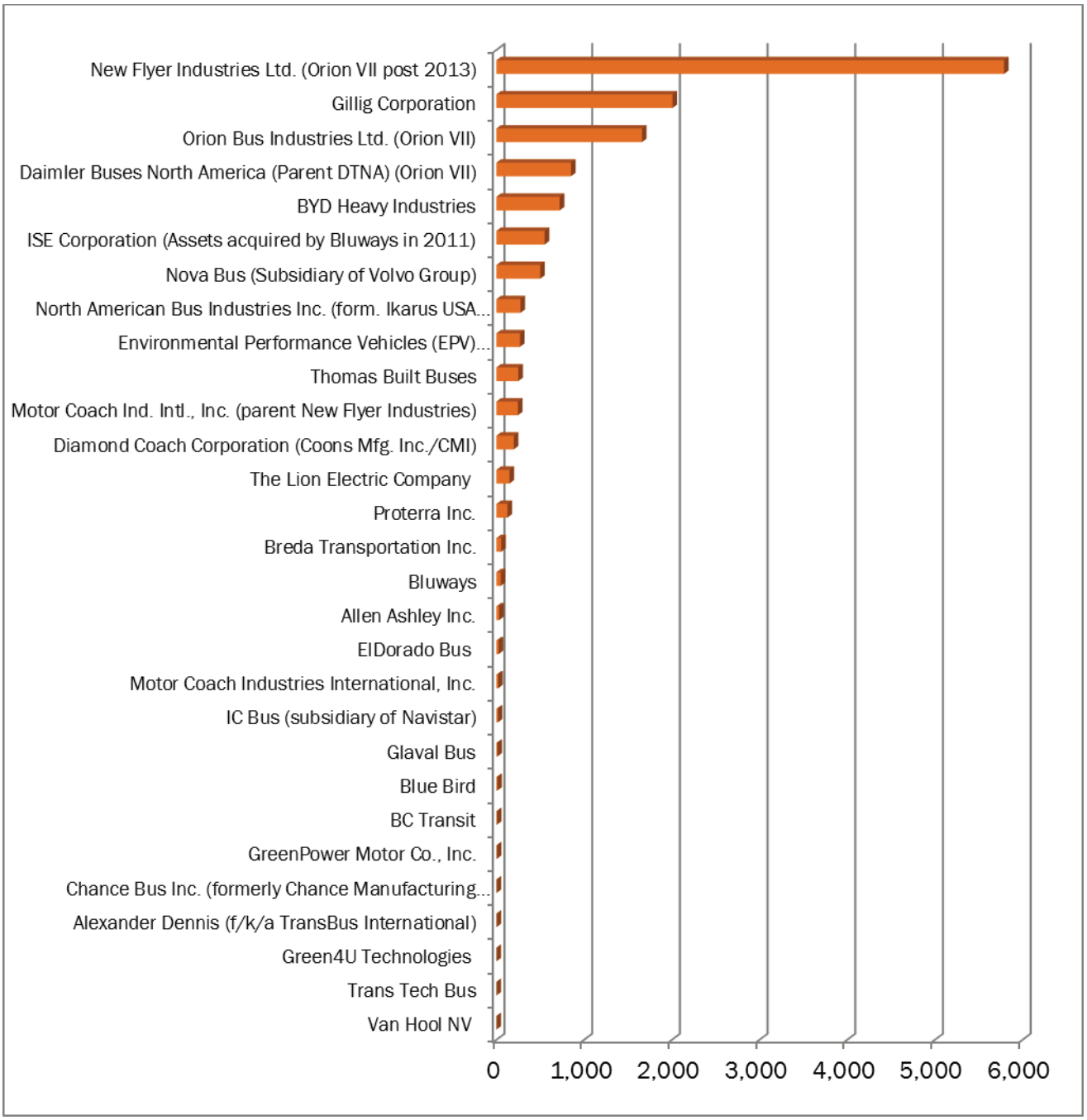

Figure II.5.4 Estimated Number of Class 3-8 HEV or EV Buses, By Supplier, in Operation in NA in 2018.

Source: Synthesis Partners LLC, 2018

The total number of Class 3-8 HEV or EV buses in operation in NA in 2018 is estimated to be 13,826.

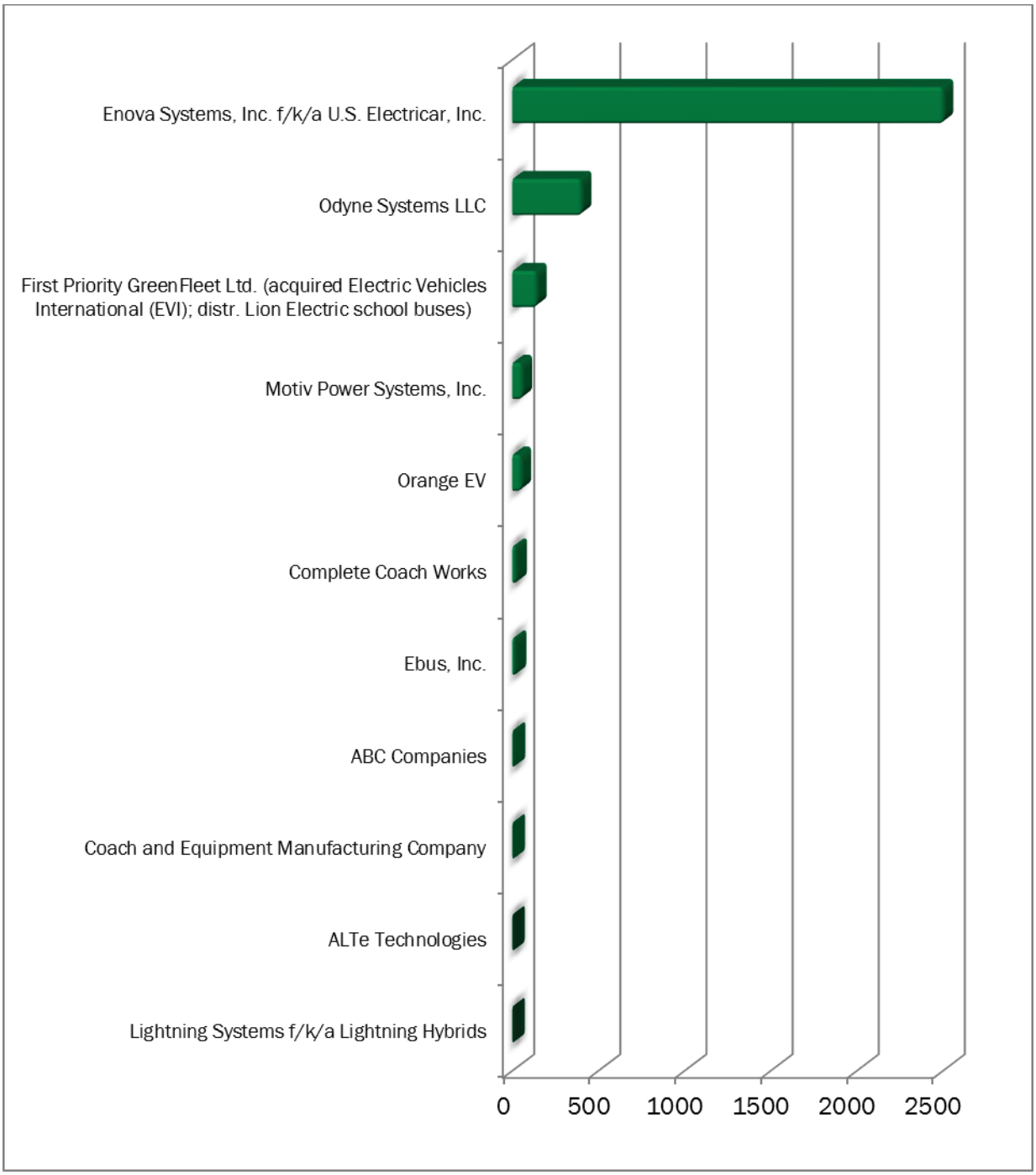

Figure II.5.5 Estimated Number of Class 3-8 Up-fitted HEV or EVs, By Supplier, In Operation in NA in 2018.

Source: Synthesis Partners LLC, 2018

The total number of Class 3-8 HEV or EV converted vehicles in operation in NA in 2018 is estimated to be 3,187.

Conclusions

This project on the Class 3-8 HEV and EV NA supply chain has been able to show through vetted, multi-sourced data that:

- The total number of Class 3-8 HEV or EV trucks in operation in NA in 2018 is estimated to be 11,909.
- The total number of Class 3-8 HEV or EV buses in operation in NA in 2018 is estimated to be 13,826.
- The total number of Class 3-8 HEV or EV converted vehicles in operation in NA in 2018 is estimated to be 3,187.

In addition, this project can draw the following conclusions about R&D gaps in the Class 3-8 HEV and EV NA supply chain.

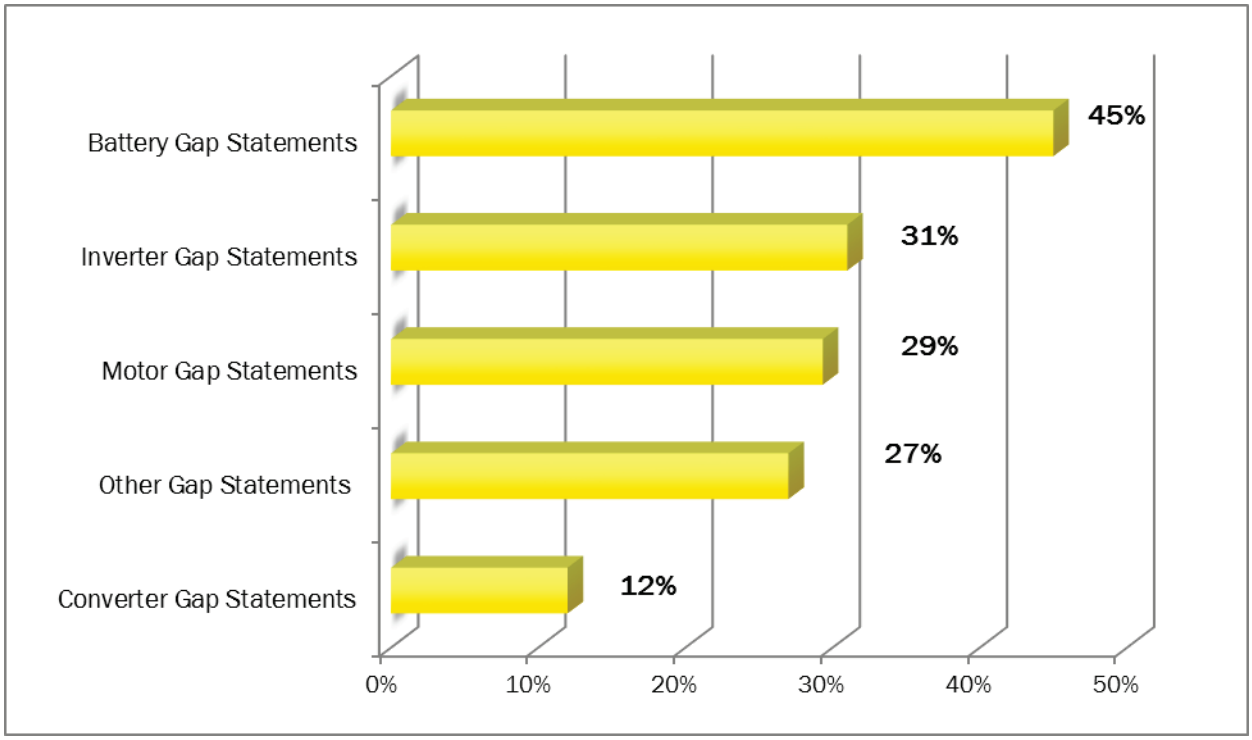

Figure II.5.6 Frequency of expert source statements about gaps in the NA Class 3-8 HEV and EV supply chain, by main topic: 2013 to present

Source: Synthesis Partners LLC, 2018

A gap is defined as a constraint or bottleneck that limits the growth of Class 3-8 HEV and EV growth in NA – and which is based on factors that are largely under the control of R&D organizations ("internal factor"). For example, an internal factor may be a technology performance limitation or an engineering design issue that prevents needed technology from being available in a certain size, weight, cost and form factor required for Class 3-8 HEV or EV use. By contrast, an external factor (which this research does not cover) may be the willingness of consumers to buy HEV or EVs, or the relative cost-competitiveness of HEV or EVs as compared to internal combustion engine vehicles based on the price of fuel. The distribution of the supply chain gap statements was analyzed by examining 100s of expert source statements made directly to Synthesis from 2013 through 2018.

Please note that statements by sources may cover more than a single category and the percentages add up to more than 100% because gap statements can cover more than a single category. More details regarding the in-depth interviews and corresponding gap analysis results are available from Synthesis.

Based on frequency of occurrence, the following specific statements can be made about plausible gaps in the NA Class 3-8 HEV and EV supply chain. [Note: The following analysis assumes that significance of gaps can be valued based on frequency of source statements about such gaps; this does not mean that any individual gap statements are not worthy of special consideration, or that any one gap statement may not exceed – in certain contexts and time-frames – the significance of all other gap statements combined.]:

1. Batteries appear to be the most important field of gaps in the Class 3-8 HEV and EV NA supply chain.
2. After Batteries, the next priority category of gaps includes Inverter, Motor and Other Gap statements. These three fields of gap statements appear to be similar in significance based on frequency.
3. The “Other” category addresses gap statements about manufacturability, public incentives and subsidies, regulation, standards, costs, materials and software (among other topics). More drill-down into each gap statement is feasible, to show how within each main gap category several sub-topics are raised by sources, all with varying frequency.
4. Converter gap statements emerge as the least significant in terms of frequency of occurrence.
5. Drilling down within the Battery gap category, one finds that the majority of concerns or gap statements relate to “Other.” To help clarify “Other” gap statements include statements such as:
6. “Lithium-ion manufacturing continues to be based on the same equipment used originally for the manufacture of cassette tapes”;
7. "Battery plants are of much greater scale, depressing prices ever further”; and
8. "Engineering and infrastructure firms need to be given significant roles in innovating solutions."
9. Across all major components – Batteries, Motors, Inverters and Converters – the existence of many “Other” gap statements reflects the diffuse and deep range of gap topics and suggests the need for more attention on such “Other” statements to help define, develop and execute a proactive and strategic response.
10. Materials represent an important category of gaps inside of the Battery category and reflect the ongoing need for fundamental materials science for better catalysts and electrolytes.
11. Across Batteries, Motors, and Inverters, the core question of how to engineer solutions that maximize performance at competitive costs remains the topic of most general concern. This is reflected in the data that shows across all main topic areas except Converters, the Engineering and Cost gap topics are represented with highest or near-highest frequency.
12. In Motors, Inverters and Converters, the least important topics based on frequency of occurrence are Standards, Software and Materials. This suggests that with regard to HEV and EV Class 3-8 suppliers of Motors, Inverters and Converters, the first priority gaps they are addressing relate to Engineering, Costs and/or Other topics.

13. Finally, in Batteries the role of Standards is considered a worthy area of attention as a gap, though certainly not as significant as Engineering, Costs, Materials and Other areas in the battery development domain.

Finally, this project showed that there are many sources with a keen interest in the Class 3-8 HEV and EV supply chain in NA, eager to engage with EERE on finding solutions to key R&D gaps and constraints. Synthesis acknowledges all sources again for their valuable contributions to this report.

Key Publications

Selected publications by Synthesis based on EERE sponsored work:

1. Synthesis Partners, LLC. Autonomous and Connected Vehicle Research and Development Gap Analysis, November 2017.
2. Synthesis Partners, LLC. North American Motors Supply Chain Analysis, March 2016.
3. Synthesis Partners, LLC. Review of Public Data on Costs of WBG Substrate Manufacturing, February 2015.

Acknowledgements

Special thanks to Mr. Steven Boyd for his technical guidance and management of this effort, and to Ms. Adrienne Riggi, Contracting Officer at the National Energy Technology Laboratory (NETL) for her ongoing oversight of this effort. Also Synthesis acknowledges the entire EERE-VTO team for active interest and support of this work. Synthesis team members are:

- Richard Holcomb, Managing Partner.
- Steve Johnson, Senior Researcher.
- Ryan Bunch, Researcher.
- Michael Willis, Senior Analyst and AMR 2018 Presenter.

II.6 Wound Field and Hybrid Synchronous Machines for EV Traction with Brushless Capacitive Rotor Field Excitation (Illinois Institute of Technology)

Ian P. Brown, Principal Investigator
Illinois Institute of Technology
3301 S Dearborn St. #103
Chicago, IL 60616
E-mail: ibrown1@iit.edu

Daniel C. Ludois, Principal Investigator
University of Wisconsin-Madison
1415 Engineering Dr.
Madison, WI 53706
E-mail: ludois@wisc.edu

Steven Boyd, DOE Program Manager
U.S. Department of Energy
E-mail: steven.boyd@ee.doe.gov

Start Date: October 1, 2017 End Date: March 31, 2019
Project Funding: $999,752 DOE share: $999,752 Non-DOE share: $112,955

Project Introduction

For mass adoption of pure and hybrid electric vehicles (EVs) there is concern regarding the cost and materials supply chain for the vehicle's main traction motor. While DOE programs have been successful at lowering the cost of traction inverters and wide bandgap power electronics, the cost of traction electric motors has been resistant to change. Today interior permanent magnet synchronous machines (IPMSMs) and induction machines (IMs) are the commercially dominant traction motors. The rare-earth permanent magnets (PMs) used in IPMSMs have been subject to market volatility and are largely single sourced from a foreign power. They are also a significant fraction of the cost of IPMSMs and impose temperature limits.

Additionally, the PMs provide a fixed flux level which is always, "on", leading to safety concerns during inverter faults and requiring additional current to be injected into the machine during field weakening to buck the magnetic flux. This additional current lowers the power factor of the machine, requiring that the traction inverter be oversized to supply the reactive current, leading to increased ohmic losses in the stator and inverter. Induction machines (IMs) must also draw reactive current from the traction inverter to magnetize the machine leading to lower power factor.

Would field synchronous machines (WFSMs) and hybrid excitation synchronous machines (HESMs) are potentially advantageous alternatives to the commercially dominant IPMSMs and IMs. WFSMs are PM free, and because the DC field magnetization is from the rotor side the power factor of the machine is high if not unity over most of the operating space. The complete control of the field excitation provides the potential for optimal field weakening and large constant power speed ranges with loss minimization. HESMs use a combination of PM and wound field excitation to combine the high efficiency of IPMSMs with the easy field weakening and high power factor of WFSMs while using considerably less PM. They also reduce the field power requirements.

EV traction applications require extremely high reliability and power density inhibiting the use of brushes and other classical field power transfer technologies such as brushless exciters. Brushless capacitive power transfer offer an attractive means of providing power transfer to the rotor field windings of WFSMs and HESMs.

Objectives

The objective of this project is to design, develop, and demonstrate wound field and hybrid excitation (permanent magnet and wound field) synchronous machines, with brushless power transfer to the rotor field winding, capable of achieving the performance metrics in Table II.6.1. A focus of this project is the cost target of 4.7 $/kW. The brushless field power transfer will be accomplished using capacitive coupling or combined capacitive magnetic coupling.

Table II.6.1 Prototype Wound Field and Hybrid Excitation Synchronous Machine Target Metrics

Parameter	Budget Period 2 Prototype	Budget Period 3 Prototype
Peak Power (kW)	≥55	≥55
Continuous Power (kW)	≥ 30	≥ 30
Specific Power Density (kW/kg)	1.5	1.6
Volumetric Power Density (kW/l)	5.0	5.7
Cost ($/kW)	-	4.7

Approach

To meet the cost and power conversion targets a number of approaches are being developed simultaneously in the context of wound field and hybrid excitation synchronous machines though many of the technologies will also apply to other electric machine types and applications.

- Die compressed windings to increase the slot fill of the stator and rotor windings for increased power density and efficiency.
  - Target slot fill of ~75% to 80% compared to 40 to 45% for random/mush distributed windings.
  - Single thermal mass with no air voids and improved heat transfer at the spray/end turn interface.
  - Possible to utilize aluminum wire for significant cost and weight savings with similar performance random/mush copper distributed windings.
- Brushless power transfer to the rotor field winding using electric fields in a capacitive power coupler (CPC) excited by high frequency power electronics.
  - Reduce the mechanical complexity of the rotating capacitors. Three simpler rotating capacitor designs have been investigated: journal bearings, integrated LC coupler, and printed circuit board (PCB) capacitive plates with a tank circuit.
  - Increase the frequency of excitation to the Megahertz regime to allow the use of a smaller capacitance, e.g., PCB based capacitors with a relatively large airgap.
  - Develop a wide bandgap (GaN or SiC) power converter with high efficiency which minimizes losses by operating in resonant soft switching.
- Reduce the punching scrap from the construction of the lamination stack. Typically 40% of the steel is scrapped when punching IPMSM laminations.
  - Leverage cut core and roll-up stator and rotor designs.
  - Segmented lamination structures allow for higher fill factors with needle or bobbin winding both rotor and stator windings and even higher slot fills with die compressed windings with added benefit of reduced end turn length.
  - Develop low space harmonic content fractional slot concentrated windings able to operate at high speeds compatible with needle or die compressed windings.

- Hybrid excitation synchronous machines to lower the field power requirements.
  - Bias the field flux for the most common operating point in a drive cycle with PMs.
  - Ideally utilize non-rare earth permanent magnets.
  - Extend the constant power speed range compared to pure permanent magnet machines.
- Develop high performance controls for WFSMs and HESMs.

The overall concept model of the WFSMs and HESMs system incorporating some of the above approaches is shown in Figure II.6.1.

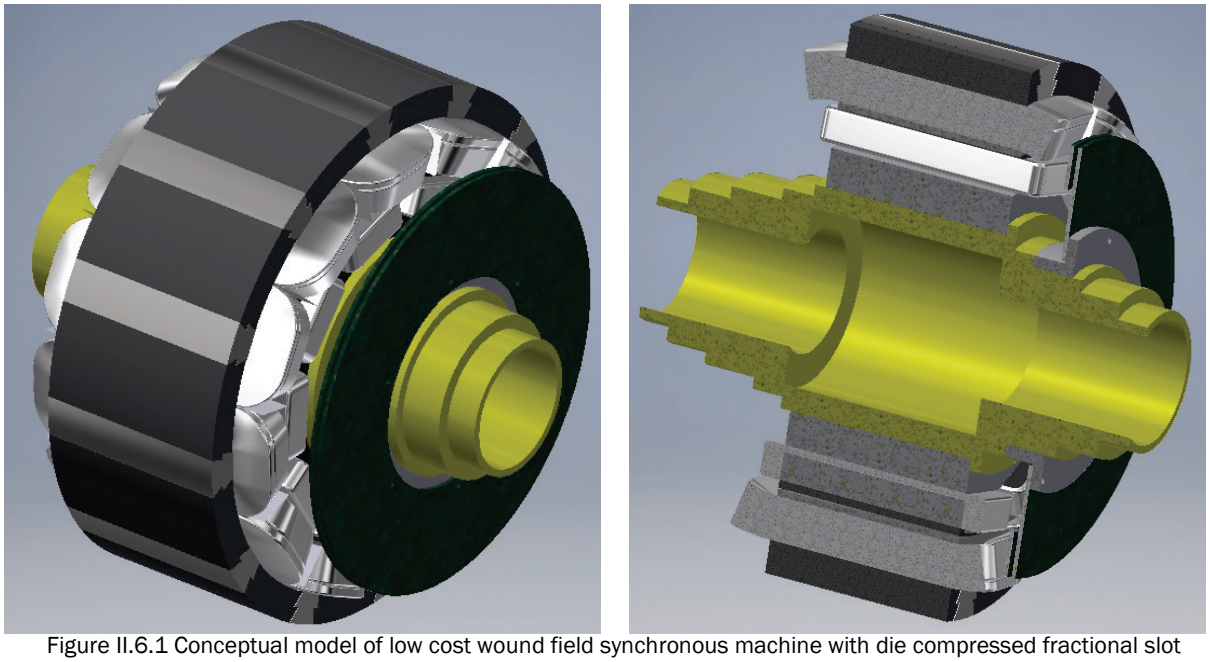

Figure II.6.1 Conceptual model of low cost wound field synchronous machine with die compressed fractional slot concentrated stator windings and rotor windings with low scrap segmented structure. Field power is transmitted using a brushless capacitive coupler manufactured from printed circuit boards.

Results

Major outcomes from this second budget period include the following items:

Construction of a WFSM prototype rotor with a die compressed field winding

The construction of the WFSM prototype rotor with a die compressed field winding was completed. A compression die for the field winding was manufactured from hardened A2 steel. Coil compression was completed with two hydraulic presses. The first press to ensure proper alignment of the all the die components under relatively low forces, ~300,000 lbs and a second press to ~780,000 lbs held for greater than 1 minute to compress and densify the coil. The die components and a compressed coil are shown in Figure II.6.2. The compressed coils insulated with Nomex 410 were fitted around salient laminated poles with epoxied on PEEK endcaps. The entire salient pole structure including the compressed coil was then slid into a laminated rotor yoke hub, Figure II.6.3. The salient poles are retained axially using two PEEK rings with negative dovetails that are held in place with a nut and washer on an aluminum hub.

(a) (b)

Figure II.6.2 Die for compression of rotor field winding coil (a), and representative compressed coil (b).

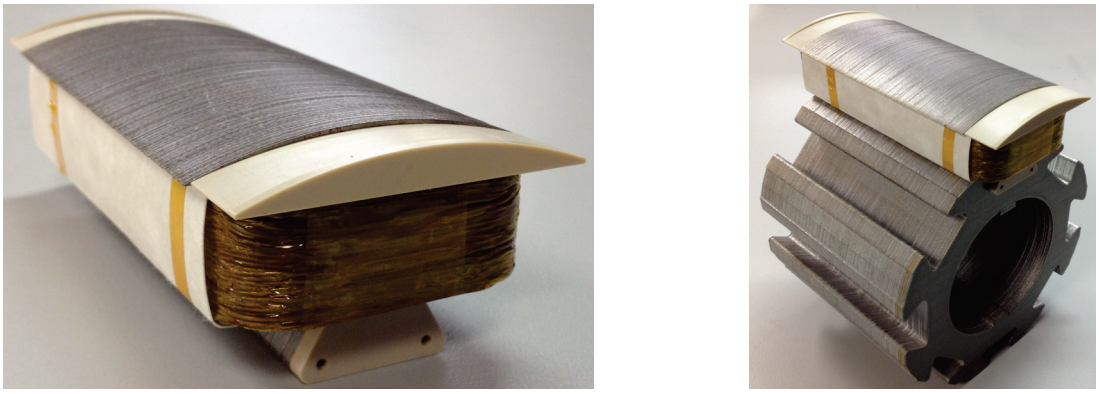

(a) (b)

Figure II.6.3 Salient pole with die compressed field winding (a), and pole assembly slid into rotor yoke dovetail slot.

Development of Printed Circuit Board Capacitive Power Couplers for Rotor Field Excitation

During budget period one a three phase capacitive power coupler and GaN inverter was designed, prototyped, and preliminary tested. During this past budget period more extensive testing of the three phase capacitive power coupler was carried out. The three phase CPC demonstrated the necessary operation, but throughput power and efficiency were limited by the equivalent series resistance (ESR) of the coupler and circulating current/tuning issues associated with imbalance among the three phases. Since the bottle neck was the CPC and not the GaN inverter, the decision was made to go to a single phase CPC. Although from power transfer first principles perspective 3 phases should deliver more power, the implementation issues associated with leakage and imbalance (in the current CPC form factor) are a drawback. Additionally, the switches of the GaN inverter are underutilized and the elimination of a phase leg will save cost without degrading the capability of the inverter for the intended application. Tradeoffs between the single phase and three phase CPC coupling structures are detailed in Table II.6.2. The prototyped single phase CPC coupling structure is pictured beside its three phase counterpart in Figure II.6.4 and the single phase GaN inverter. The single phase CPC was measured to have 3x lower ESR and less leakage per unit coupling capacitance than its three phase counterpart as plotted in Figure II.6.5.

Table II.6.2 Capacitive Coupler Qualitative Comparison

	Capacitance Utilization	Drive Electronics & Passive Components	Leakage Capacitance & Dielectric Loss	Tuning Difficulty & Circulating Current Issues
Single Phase	Worse	Simpler	Better	Simpler
Three Phase	Better	More Complex	Worse	More Complex

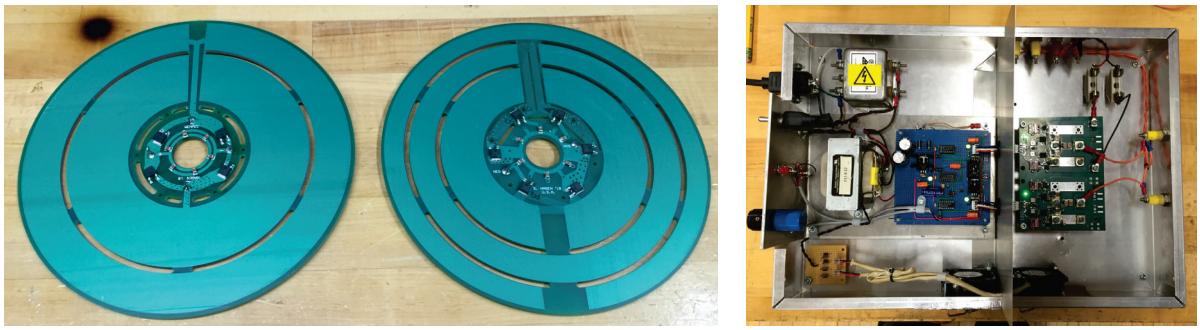

(a) (b)

Figure II.6.4 Single Phase (left-a) and three phase (right-a) rotating capacitive PCBs (a), and single phase GaN inverter.

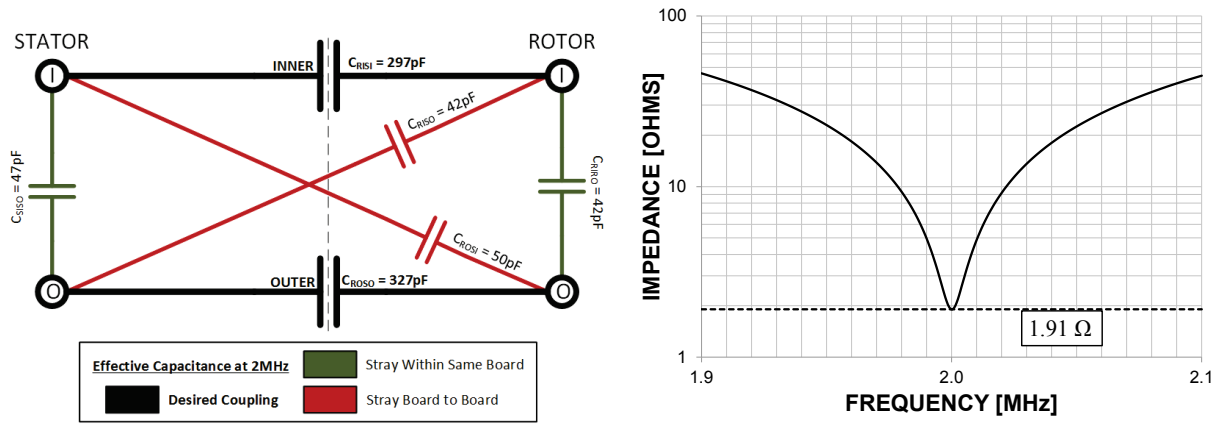

(a) (b)

Figure II.6.5 Coupling and stray capacitances (a) and measured ESR (b) of single phase PCB CPC.

The inverter to drive the system was reduced from three phase legs to two, making it a single phase inverter and compatible with the new CPC. The inverter design itself is largely the same as before, except the control board has become analog, rather than digital. The primary reason for this is to provide a development platform for easy self-sensing or resolver capability of the CPC. The MHz switching frequency of the inverter is generated by a voltage controlled oscillator (VCO) which will form the backbone of a Phase Lock Loop (PLL) to track the resonance of the rotor in future capacitively salient CPC designs. This will potentially enable the CPC to have resolver functionality. Going forward, the air core inductors of the resonant tank circuit will be replaced by those with ferrite cores for better shielding. Future work will include design and optimization of an inductor structure which: 1) minimizes core loss, 2) minimizes conduction loss, 3) is significantly more compact than current air core devices, 4) can withstand kV peak voltages within the resonant tank circuit. Preliminary designs are based on inductors used for DC-DC converters [5].

The bench testing of the single phase CPC is summarized in the two tables below. Input DC power to the inverter and output DC power to the field winding were recorded. The CPC tank was driven at 2 MHz. The bottle neck for throughput power is the CPC ESR, and with lower rotor field resistance, the 600 W metric is difficult to meet. Initial tests with a rotor field resistance of 38.5 Ω generated excessive loss in the CPC, given the increased current required, Table II.6.3. During testing with the lower field resistance, efficiency was limited to 83%. To meet the necessary power requirement efficiently, the rotor resistance was increased to 92 Ω, thereby reducing the ESR losses of the CPC via reduced current and increased voltage, Table II.6.4. With the higher resistance, the Go/No-Go point of > 600 W was satisfied with a DC-DC efficiency of up to 94%. Future revisions of the rotor rectifier board will include "buck" converter capability to maintain low rotor resistance but appear as a higher impedance to the CPC.

Table II.6.3 Single Phase CPC Bench Testing at 2 MHz

Field Resistance 38.5 Ω						
I_{IN} (A)	V_{IN} (V)	I_{OUT} (A)	V_{OUT} (V)	P_{IN} (W)	P_{OUT} (W)	Eff (%)
0.681	18.60	0.50	20.74	12.65	10.37	81.98
1.35	36.37	1.00	40.26	49.10	40.26	82.00
1.96	57.20	1.49	61.49	112.11	91.62	81.72
2.59	77.62	2.00	81.21	201.04	162.42	80.79
3.17	95.00	2.51	100.58	301.15	252.46	83.83

Table II.6.4 Single Phase CPC Bench Testing at 2 MHz and High Field Winding Resistance

Field Resistance 92 Ω						
I_{IN} (A)	V_{IN} (V)	I_{OUT} (A)	V_{OUT} (V)	P_{IN} (W)	P_{OUT} (W)	Eff (%)
1.30	85.54	1.05	96.19	111.20	101.00	90.83
1.83	121.77	1.47	136.51	222.84	200.67	90.05
2.25	151.72	1.82	169.54	341.37	308.56	90.39
2.66	185.19	2.25	206.36	492.61	464.31	94.26
3.06	216.43	2.58	238.94	662.28	616.47	93.08

Development of a low switching frequency deadbeat-direct torque and flux control approach for WFSM

In the previous budget period a deadbeat-direct torque and flux control (DB-DTFC) approach for WFSMs was developed [6]. The discrete time observers and torque line were derived using a z-transform approach. This approach will be referred to as a high switching frequency WFSM DB-DTFC. Using a z-transform approach makes the implicit assumption that cross-coupled states are latched between sample instants. WFSMs have two sets of state cross-couplings, d-q axes and d-f axes where the d-q axes cross-coupling is also speed dependent. At high sampling to fundamental frequency (S2F) ratios this assumption has relatively little impact on the control performance. However, as the S2F ratio decreases the control performance and stability of the system is compromised. One approach for proper discrete time modeling and DB-DTFC taken in interior permanent magnet synchronous machines and inductions machines is to use a sampled Laplace approach for discretization. Unfortunately because of the extra field state and cross-coupling in WFSMs closed form sampled Laplace derivations become computationally unfeasible.

A Taylor series approximation of the sampled Laplace discretization was developed as an alternative approximate approach to a full closed form sampled Laplace discretization. The approximation error and stability of the system is a function of the number of terms, k, in the Taylor series. With k = 4 terms less than 1% approximation error at very low switching frequencies (<1 kHz) and stability can be guaranteed for all speeds. Solution for the Volt.-sec. for the inverter to apply to the WFSM is found using a Newton-Raphson approach. Typically the convergence to the Volt.-sec. solution is very rapid; only one iteration if there is no change to the torque or flux linkage commands. The Taylor series sampled Laplace discretization approximation and Newton-Raphson iterative Volt-sec solution are termed the low switching frequency WFSM DB-DTFC. A publication describing this control approach was published in the IEEE Energy Conversion Congress and Exposition (ECCE) conference proceedings [1].

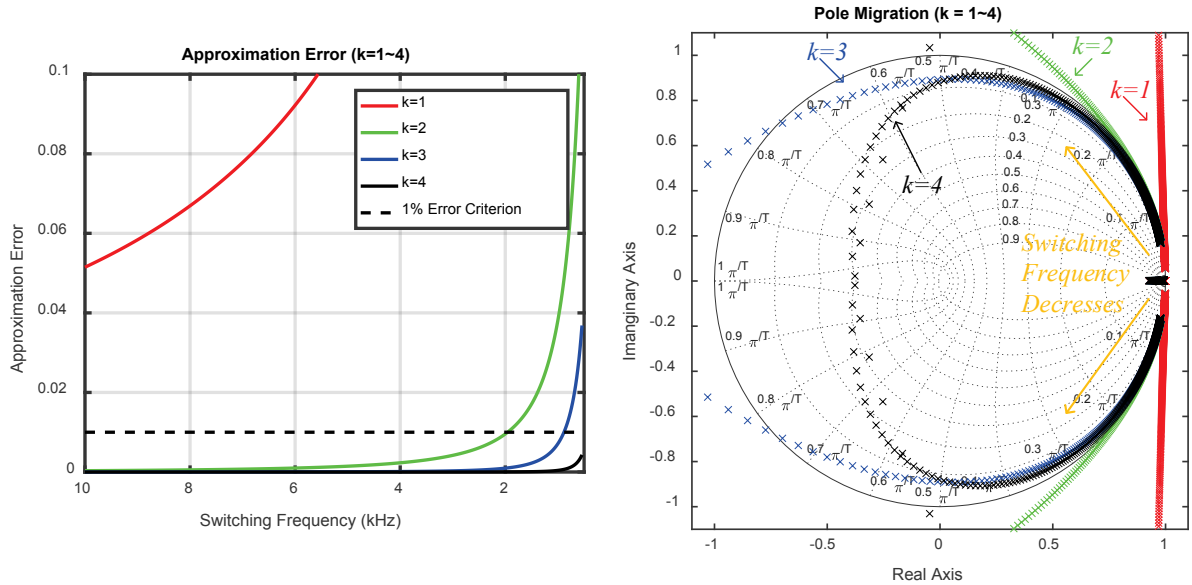

(a) (b)

Figure II.6.6 Open loop approximation error for different number of Taylor series terms as a function of switching frequency (a), and the discrete pole migration as a function of switching frequency for different number of Taylor series terms (b).

The experimentally measured performance of the high and low switching frequency WFSM DB-DTFC approaches has also been compared at a number of operating points [1]. A representative comparison is shown in Figure II.6.7 for operation at 4000 RPM, 5 kHz switching frequency, and single update of the Volt-sec. command per switching period during voltage limited operation. The low switching frequency DB-DTFC has an unacceptable transient in the torque and current and flux linkage observer estimates. The high switching frequency WFSM DB-DTFC shows excellent control performance with a short finite settling step response in the torque and accurate observer predictions.

Design of WFSM with die compressed stator and rotor windings and reduced scrap

The electromagnetic design of a WFSM with die compressed windings on both the stator and rotor has been completed. Segmentation is used on both the stator and the rotor for reduced scrap during punching. The die compressed coil must be inserted as a single unit unlike classical distributed windings where turns maybe inserted one by one. In most cases on the stator this necessitates the use of a fractional slot concentrated winding (FSCW) layout. Normally, FSCWs are used in low speed machines because their large space harmonic content. Electric vehicle traction motors are trending towards higher speeds to increase their power density. To reduce the space harmonic content of the FSCW used in the new WFSM prototype with a for the targeted maximum speed of 12,000 RPM a 12 slot 10 pole configuration with two winding subsets was adopted. The two winding subsets are displayed spatially and also wound in a combined star-delta configuration to achieve a 30 degree phase shift in the excitation between windings. This winding configuration emulates a six phase machine and eliminates a number of harmonic orders. Electromagnetic optimization was carried out at 4,000 RPM for two different stator to rotor current density ratios: 24 A/mm^2 to 20 A/mm^2 and 33 A/mm^2 to 30 A/mm^2. The Pareto fronts of the optimized designs are shown in Figure II.6.8. Designs indicated by a solid circle were then down-selected for re-simulation at the opposite current density. The re-simulated designs at the opposite current density are indicated by the diamond mark. The design selected for prototyping is the largest solid red-dot and solid red diamond which correspond to the same design at two different current density ratios.

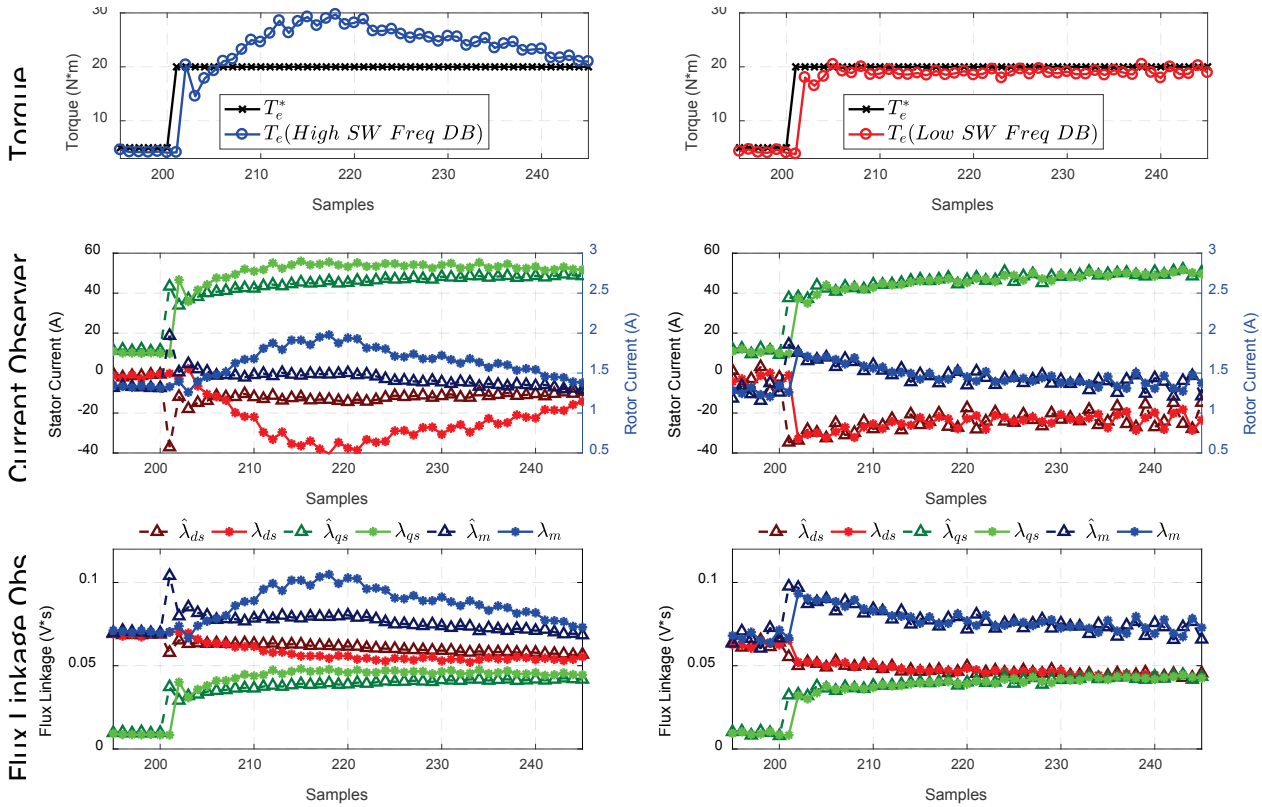

(a) High switching frequency WFSM DB-DTFC (b) Low switching frequency WFSM DB-DTFC

Figure II.6.7 Performance comparison of high and low switching frequency WFSM DB-DTFC at 4,000 RPM and 5 kHZ switching frequency.

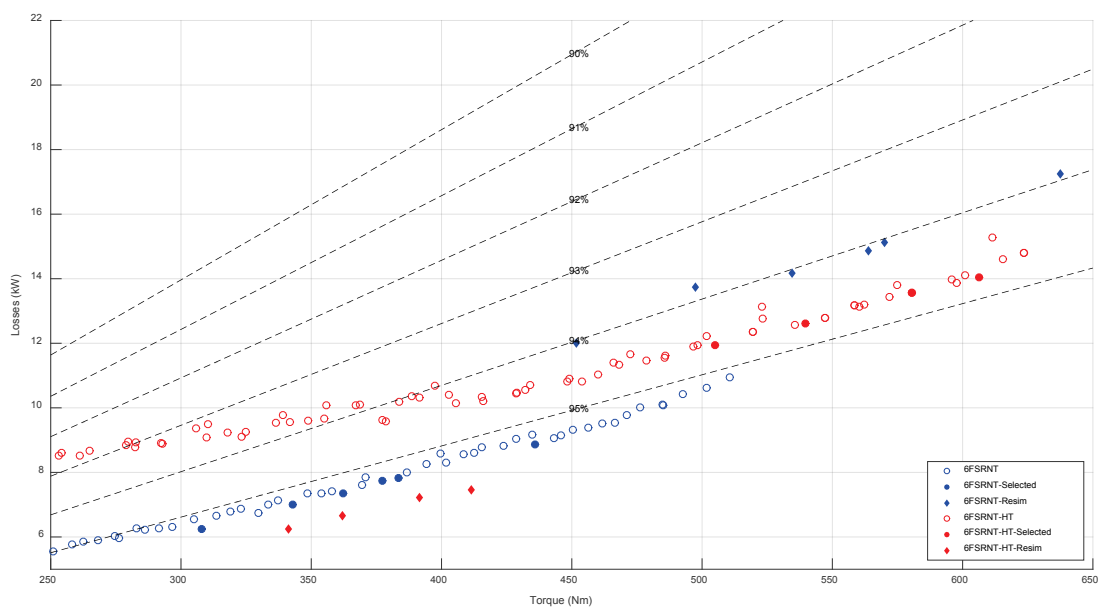

Figure II.6.8 Electromagnetic optimization Pareto fronts of 12 slot 10 pole star-delta designs for two different current density ratios at 4,000 RPM. Down-selected designs from original simulations are solid dots. Corresponding designs re-simulated at the opposite current density are indicated by a diamond mark.

Design of HESM with multiple field weakening modes

A new parallel flux dual rotor HESM concept has been developed. The wound field rotor section can boost or buck the d-axis flux or counteract the armature reaction in the q-axis with dynamic changes between operating modes possible. This great flexibility in the field excitation allows for the machine to be designed for electromagnetic infinite constant power speed range (CPSR) with unity power factor using either stator-rotor flux weakening or rotor flux weakening. A provisional patent has been filed for this HESM concept [4]. A prototype HESM rotor has been designed and is being constructed for experimental verification of the new multiple field weakening modes.

Conclusions

WFSMs and HESMs with brushless capacitive rotor field power transfer are being developed as a high performance low cost EV traction motor option. In the coming budget period the previously constructed prototype WFSMs and HESMs will be dynamometer tested at higher power levels. Additional HESMs and WFSMs will be constructed and dynamometer tested including an HESM with adjustable field excitation axis and WFSM with stator and rotor die compressed windings with reduced punching scrap. Cost evaluation of the best in class WFSM or HESM will also be carried out.

Key Publications

1. Y. Nie, I.P. Brown, "Low Switching Frequency Deadbeat-Direct Torque and Flux Control of Wound Field Synchronous Machines," in Proceedings of the 2018 Energy Conversion Congress and Exposition (ECCE), Portland, OR, Sept. 23-27, 2018.
2. A. Di Gioia, I.P. Brown, F. Giulii Capponi, "Design and Characterization of a Radial Flux Wound Field and Permanent Magnet Hybrid Excitation Synchronous Machine," in Proceedings of the 2018 Energy Conversion Congress and Exposition (ECCE), Portland, OR, Sept. 23-27, 2018.
3. A. Di Gioia, I.P. Brown, F. Giulii Capponi, "Analytical Sizing of Radial Flux Hybrid Excitation Synchronous Machines," in Proceedings of the 2018 Energy Conversion Congress and Exposition (ECCE), Portland, OR, Sept. 23-27, 2018.
4. Provisional patent application, 62630346, "AC Synchronous Machine with Three Phase Excitation and Permanent Magnet Excitation.

References

1. R.S. Yang, A.J. Hanson, D.J. Perreault, and C.R. Sullivan, "A Low-Loss Inductor Structure and Design Guidelines for High Frequency Applications," in Proceedings of the 2018 IEEE Applied Power Electronics Conference and Exposition (APEC), San Antonio, TX, 2018, pp. 579-586.
2. Y. Nie, I.P. Brown, D.C. Ludois, "Deadbeat-Direct Torque and Flux Control for Wound Field Synchronous Machines," IEEE Transactions on Industrial Electronics, Vol. 65, No. 3, 2018 DOI: 10.1109/TIE.2017.2739696.

II.7 Development and Demonstration of Medium-Heavy Duty PHEV Work Trucks (Odyne Systems LLC)

John R. Petras, Principal Investigator
Odyne Systems LLC
W237 N2878 Woodgate Road, Suite 2
Pewaukee, WI 53072
Phone: (262) 544-8405; Fax: (262) 544-8421
E-mail: John.Petras@Odyne.com

Ken Kelly, Principal Investigator
National Renewable Energy Laboratory (NREL)
15013 Denver West Parkway
Golden, CO 80401
E-mail: Kennith.Kelly@nrel.gov

David Smith, Principal Investigator
Oak Ridge National Laboratory (ORNL)
2370 Cherahala Blvd
Knoxville, TN 37932
E-mail: Smithde@ornl.gov

Steven Boyd, DOE Program Manager
U.S. Department of Energy
E-mail: Steven.Boyd@ee.doe.gov

Start Date: January 19, 2017 End Date: January 31, 2021
Project Funding: $6,172,732 DOE share: $2,149,644 Non-DOE share: $4,023,088

Project Introduction

The heavy-duty vehicle market (Class 6-8) has been a difficult segment for the introduction of plug-in vehicles due to the large energy storage requirement (with corresponding cost), challenging duty cycles, and the diversity of vehicle configurations. The Work Truck market represents a significant opportunity for Heavy-Duty PHEV adoption. Odyne proposes development of a new class of PHEV Work Truck which will be modularized and customized to provide optimal ROI across multiple customers and applications. The proposed project will first demonstrate this technology as a Utility Work Truck variant:

- The usage cycle includes driving and stationary/worksite power requirements, ensuring full daily usage of the grid-charged battery (battery size: 25-40kWhr). Though daily driving can often be short (an average of 26 miles per day), worksite power includes substantial demand (hydraulics, exportable 110/220V power, 12V support, HVAC).
- Worksite power demands for conventional vehicles require continuous loaded engine operation, resulting in significant emissions, fuel consumption and noise impacts.
- These trucks serve an industry that is strongly incentivized to promote vehicle electrification, and which has publically committed to spending a portion of their annual vehicle purchase budget on electrified vehicles (EEI press release of 11/18/14).

This project will develop and demonstrate a medium/heavy duty plug-in hybrid solution capable of meeting the needs of the work truck market while delivering fuel and emissions reductions of 50% when evaluated against the full-day work truck duty cycle.

Objectives

The project goal is to design, develop, and demonstrate a new generation of medium/heavy-duty plug-in hybrid electric work truck that achieves a 50% reduction in fuel consumption versus a conventional vehicle baseline when evaluated across a full day work cycle representative of the vocational work truck. The primary objectives are:

- To simulate, design and develop unique and innovative integrated powertrain, software, and calibrations which will optimize the complete diesel/transmission/hybrid powertrain and demonstrate the potential for driving fuel efficiency improvements greater than 40% with commensurate reductions in GHG emissions.
- To develop and validate a modular Lithium Ion battery system based on high volume lower cost cells and modules that are utilized in the light-duty sector which will meet the power, energy, and duty cycle requirements of the MD-HD vocational truck market at a cost approaching half that of currently available low volume solutions.
- To integrate fully electrified worksite functions and a daily duty cycle optimization function with the powertrain and battery solutions on an OEM class 6-7 chassis and demonstrate the capability of 50% reduction in total fuel used when measured against a full day duty cycle's and real world performance.
- To demonstrate ten optimized PHEV work trucks and validate the vehicle's operating performance, emissions and full work cycle fuel reduction in excess of 50%.

Approach

The proposed solution incorporates a simple, parallel hybrid system that allows the torque of the electric motor to augment the torque output of the diesel engine, thus saving fuel. The motor speed is synchronized with the engine speed through the existing power take-off (PTO) unit. The traction motor drives the PTO, adding torque to the rear axle, or converts torque from the PTO into power to charge the PHEV batteries (see Figure II.7.1). Six patents have been granted, and other patents are pending prior to initiation of this project.

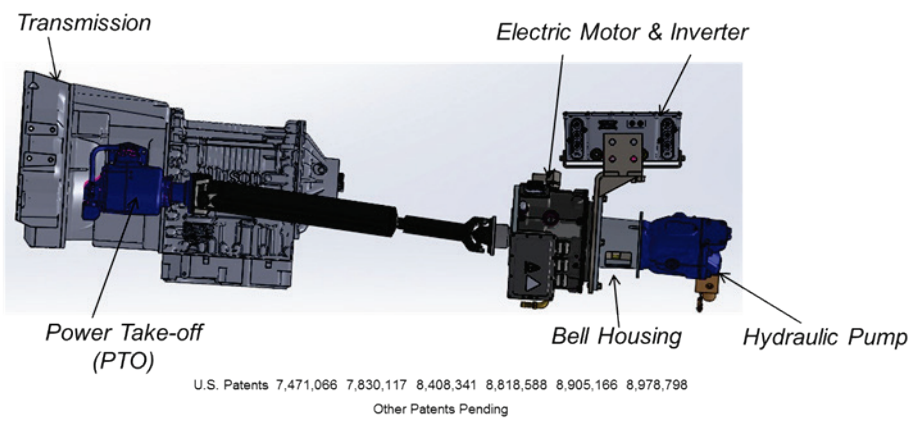

Figure II.7.1 Odyne Powertrain Configuration

The system is also designed to provide full jobsite engine off electrification utilizing power from the lithium ion battery system to provide 120/240 V exportable power, 12V chassis systems support, high efficiency electric heating and air conditioning along with the power to drive the primary work equipment (Figure II.7.2).

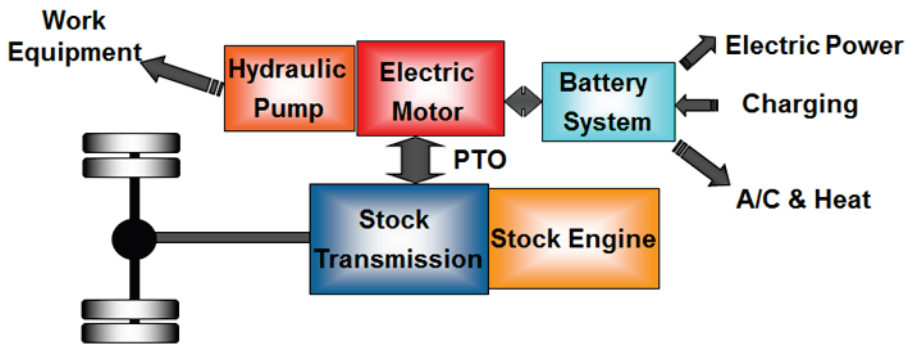

Figure II.7.2 Odyne Hybrid Architecture

The project will be conducted in three periods:

Period 1: System Design and Analysis: Analysis of existing fleet data will be performed and will be used for the establishment of baseline driving and full day usages cycles and current vehicle performance for system simulation, development and test. The project will create designs and systems which, when integrated, will produce a Medium-Heavy duty work truck capable of achieving requirements under real world conditions. The period will conclude with an analytical simulation verifying this performance improvement.

Period 2: System and Vehicle Verification: The subsystems will be verified and refined using prototype hardware and the full vehicle will undergo final development, functional and performance test. The prototype phase will conclude with test results confirming that the final design will provide a ≥50% reduction in fuel use under real world conditions. Approximately ten vehicles will be built to support field test and evaluation.

Period 3: Prototype Vehicle Demonstration: Ten vehicles will be put in regular service with telematics to measure performance. The Recipient will analyze the data along with customer feedback and will report the real-world reduction in fuel use and customer acceptance of the technology.

The three-year period of the project will integrate three development streams into a final Prototype vehicle solution and 10 vehicle field demonstrations:

Powertrain Development and Optimization

- Odyne - Lead, Hybrid Powertrain development and design, Hybrid optimization and control strategies
- NREL – Duty cycle analysis, Dynamometer test, Full-year fuel use simulation and analysis
- Oak Ridge National Lab – Powertrain simulation and optimization, HIL Test
- Allison Transmission – Transmission control and optimization strategies

Battery Development

- Odyne – System Specifications and integration requirements, system integration test
- AVL Engineering, Ricardo Strategic Consulting – Battery System supply chain evaluation
- Supplier TBD – Lithium Ion Module and BMS Supplier, Component System integration requirements

Chassis Development & Integration

- Odyne – System design, control, cost, and integration lead, Systems Efficiency & Sizing, System build
- Freightliner – OEM Chassis Integration improvements, Prototype and demonstration chassis supplier

Results

In FY18, the project completed the period 1 design and analysis tasks in June 2018 and began initial period 2 system and vehicle verification activities which will span FY 19 and be concluded in the first quarter of FY20.

Powertrain Development and Optimization

Baseline Dynamometer Testing – NREL completed baseline dynamometer testing 2017 Freightliner M2 vehicle equipped with a current generation Odyne hybrid system. As was expected, the mild hybrid driving strategy utilized in the current system yielded small improvements in fuel use for the driving only cycles (Table II.7.1) and large improvements in fuel use and emissions in the stationary work cycles (Table II.7.2)

Table II.7.1 Baseline Dynamometer Drive Cycle Results

Odyne-NREL Baseline Drive Cycle Testing		Fuel economy MPG	Hybrid Improvement %	Battery Use kWh/mi
UDDS	Conventional	6.19		
	Hybrid	6.31	1.99%	0.02
ODYNE High	Conventional	7.53		
	Hybrid	7.53	0.05%	-0.02
ODYNE Medium	Conventional	6.04		
	Hybrid	6.30	4.26%	0.16
ODYNE Low	Conventional	4.22		
	Hybrid	4.58	8.47%	0.47
HHDDT Transient	Conventional	5.86		
	Hybrid	6.24	6.57%	0.21

Table II.7.2 Baseline Dynamometer Work Cycle Results

PTO shaft work specific results comparison			
	NOx	CO2	Fuel Use
	g/kW-hr	g/kW-hr	g/kW-hr
Calculated equivalent electrical PTO	**3.34**	**1815.21**	**549.59**
Tested conventional PTO	**32.61**	**8483.42**	**2827.03**

NREL then created a model combining the dynamometer results with telematics analysis reported in FY17 to predict the full year fuel savings of the current hybrid fleet of 119 utility vehicles. The analysis created 3 clusters of vehicles with common usage traits and predicted average fuels savings of the clusters ranging from 40 to 47% (Figure II.7.3)

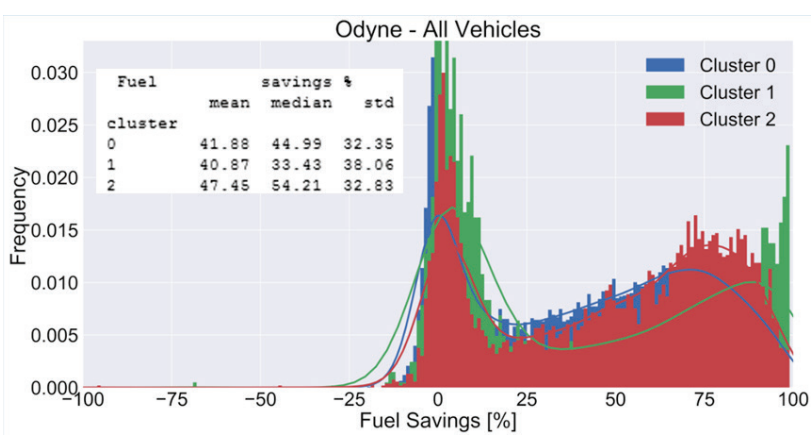

Figure II.7.3 NREL fuel savings model

Powertrain Simulation - Odyne worked with Oak Ridge National Laboratory (ORNL) to correlate a baseline Simulink model representing the current Hybrid system based on the dynamometer data provided by NREL. Alternative hybrid driving strategies were then evaluated on the model resulting in a predicated 35-52% improvement in driving fuel economy depending on drive cycle (Figure II.7.4)

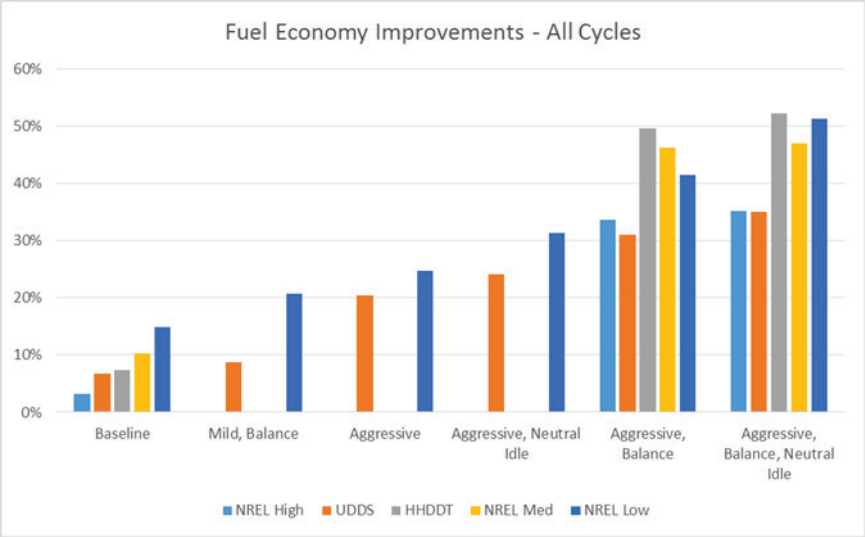

Figure II.7.4 Predicted fuel economy improvements

Battery Development

Odyne worked with Ricardo Strategic Consulting to perform a global supply chain search for a low cost modular battery system which will meet the power and energy needs of the PHEV work truck at a cost below $400 per kilowatt-hour. Over 50 potential suppliers were contacted, over 50% of those returned no-quotes due to the lower volumes of the truck market. Of those returning quotes, most were above $800 per kilowatt-hour, 2 were between $600-$700 and one provided a quote of $352 per kilowatt-hour. Odyne exited FY18 in project and design negotiations with the low cost supplier.

Chassis Development & Integration

In FY18, Odyne purchased the Freightliner M2 Chassis that will become the prototype PHEV work truck, completed the design of the PHEV system incorporated into the Freightliner Chassis and began preparations to build up the prototype test chassis (Figure II.7.5, Figure II.7.6, Figure II.7.7)

Figure II.7.5 Freightliner M2 test truck chassis

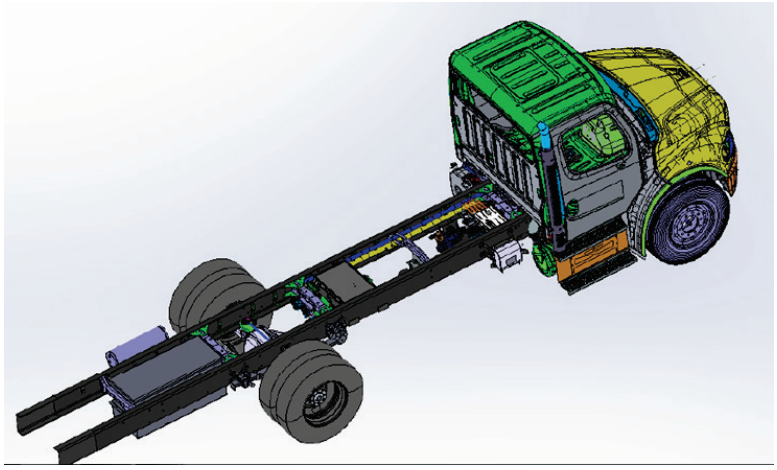

Figure II.7.6 Isometric view - Freightliner M2 model with hybrid components

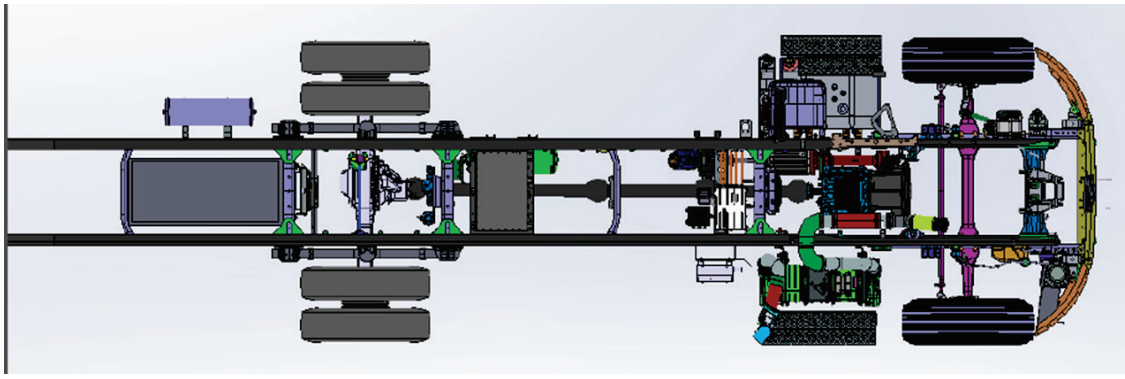

Figure II.7.7 Plan view - Freightliner M2 model with hybrid components

Conclusions

In FY18, the project team competed the Period 1 tasks of testing a baseline vehicle on the NREL ReFuel Dynamometer based of driving and jobsite cycles created from existing vocational vehicle telematics data, developing and correlating a Simulink hybrid truck model, developing algorithms which show the potential to provide 35-50% driving fuel economy, and creating a hybrid chassis design based on a Freightliner M2 Medium-Heavy duty chassis which is predicted to deliver a 50% improvement in full-cycle fuel economy in the typical work truck environment. Odyne exited FY18 preparing to build the Freightliner PHEV chassis for development, refinement and test.

Key Publications

There were no publications produced in FY2018

Acknowledgements

Odyne wishes to acknowledge the substantial contributions of John (Jason) Conley (NETL), Eric Miller, Peter Sindler, Jonathan Burton, Matt Thornton, Len Strand, Kevin Walkowicz (NREL), Adian Cook, Dean Deter (Oak Ridge National Laboratory), Greg Mann (Allison Transmission), Dan Purdy (Freightliner Trucks), and Mark Kuhn, Alan Munday (Ricardo Strategic Consulting)

II.8 V2G Electric School Bus Commercialization Project (Blue Bird Corporation)

Andy Moore, Principal Investigator
Blue Bird Corporation
402 Blue Bird Boulevard
Fort Valley, GA 31030
E-mail: andy.moore@blue-bird.com

Steven Boyd, DOE Program Manager
U.S. Department of Energy
E-mail: steven.boyd@ee.doe.gov

Start Date: February 1, 2017 End Date: December 31, 2020
Project Funding: $1,931,434 DOE share: $957,036 Non-DOE share: $974,108

Project Introduction

Two key contributors to the sustainable energy economy of the future are now in view. One is the exploitation for electricity generation of intermittent resources such as solar photovoltaics and wind. The other is the transportation sector's transition from direct use of fossil fuels to electricity. The potential exists to integrate these two elements in a strongly synergistic relationship. The batteries in electric vehicles can store energy and stabilize grid conditions in a way that offsets the intermittency of renewable generation resources. The income generated through this dual use of vehicle batteries can reduce the total cost of ownership of electric vehicles and hasten their displacement of fossil-powered incumbents.

The problem addressed by the V2G Electric School Bus Commercialization Project is that no guidebook exists for this process of mutually beneficial integration. While all of the technological elements are in place and have been demonstrated in various settings, the challenges on commercial and regulatory dimensions remain substantially unaddressed. Heavy-duty vehicles lend themselves most readily to V2G use cases in that they have large batteries, are often grouped in fleets, and often have predictable and limited working hours. Yet as of today, purchasers of trucks or buses can not readily deploy a V2G fleet and reap the benefits of grid integration for themselves or the electricity system.

Objectives

At the highest level, the goal of the V2G Electric School Bus Commercialization Project is to help blaze a trail for the V2G concept through pertinent commercialization and regulatory landscapes via the development and real-world deployment of a fleet of grid-integrated school buses. If successful, the Project will be a catalyst for the creation of policies and precedents that will allow subsequent V2G fleets to interconnect and operate as distributed energy resources in their selected service territories.

At a practical level, Project objectives include development of a V2G electric school bus model that has a short path to total-cost-ownership parity with fossil-powered buses; a replicable template for both financing school-district uptake of V2G buses; and the physical and commercial arrangements for deploying the buses as distributed energy resources. Specifications targeted by the Project that will support these objectives are an energy efficiency of 1.1 kWh per mile or better, and a standards-compliant bidirectional charge/discharge power capacity of 200 kW. The objectives will be tangibly realized via a fleet of eight type-C original-equipment V2G electric school buses that will be transferred to and operated by the Rialto Unified School District (Rialto USD) in California.

Approach

The Project is structured into three Budget Periods, the first two of which culminate in go/no-go decision points. In each Budget Period, vehicle-oriented and charging-system-oriented activities run in parallel.

The vehicle-oriented focus of BP1 is technology advancement and prototype vehicle development. The scope in this area includes on-board design elements that significantly influence energy efficiency, including thermal management of batteries and other assemblies; drivetrain gearing; and the adjustment of energy management parameters based on real-time conditions and inputs. The scope also includes development of an inverter with bidirectional power capacity of 200 kW and grid-forming capability.

The charging system focus of BP1 is design of the charging system at Rialto USD's pupil transportation facility and initiation of the interconnection application process with host utility Southern California Edison (SCE). The scope at this stage also includes the design of the charging interface immediately up- and downstream of the charging port on the bus.

The go/no-go point at the end of BP1 calls for energy efficiency testing of one of the prototype vehicles on the REFUEL dynamometer of Project team member National Renewable Energy Laboratory (NREL) to verify that a prototype bus has achieved a stipulated intermediate point of energy efficiency.

The vehicle-oriented focus of BP2 is prototype vehicle refinement, and construction of the production buses for the Rialto USD. One of the four prototype vehicles will be used for safety and durability testing to ensure compliance with Blue Bird's corporate standards and all applicable Federal Motor Vehicle Safety Standards. Another prototype will be equipped with the full suite of energy efficiency measures developed during BP1. A third will serve as the model for the production buses that will be deployed at Rialto USD. In parallel, the inverter will be tested by a nationally recognized testing laboratory (NRTL) to certify that it is in compliance with applicable standards for electrical devices and electric vehicles, including IEEE 1741 and SAE J3072.

One focus of BP2's charging system work will be installation of the relevant equipment at Rialto USD's pupil transportation facility. Another will be completion of the interconnection application process with SCE. Once this step is completed, it will be possible to develop terms and conditions for the Rialto USD fleet to participate in California's wholesale power market. This will involve negotiation with SCE and the California Independent System Operator (CAISO).

The go/no-go point at the end of BP2 calls for another round of energy efficiency testing by NREL. The goal at this point will be achievement of the 1.1 kWh per mile target. The bus that will be used for this purpose is not intended to be a prototype for a commercial vehicle. Rather, it will be a reference point that incorporates a very robust suite of efficiency-oriented improvements that can be drawn upon as Blue Bird seeks the optimal tradeoff between bus purchase price and operating cost profile in subsequent generations of commercial EV school buses.

The parallel vehicle and charging system tracks of BP1 and BP2 will converge with the deployment of the buses in BP3. Key phases of the Rialto USD fleet's performance will be tracked and documented, including the buses' real-world energy efficiency and their generation of revenues in CAISO's wholesale power markets. Another focus of BP3 will be development of a Market Transformation Plan through which Blue Bird will develop measures to overcome commercial hurdles to EV school bus adoption. An important aspect of this work will be exploration of financing expedients, such as leasing of batteries, to bring the up-front price of the vehicles to parity with conventional school buses, and to achieve total-cost-of-ownership parity via offset of lease payments with V2G revenues and savings on fuel and maintenance expenses.

Results

The Project is currently in the second half of BP1. Results have so far been achieved in the domains of drivetrain architecture, thermal management, prototype vehicle development and profiling, and charging system design.

Drivetrain Architecture

In the drivetrain architecture domain, modeling exercises were completed by electric drivetrain subcontractor Efficient Drivetrains, Inc. (EDI) and NREL. EDI's modeling was done on its proprietary simulation platform, NREL's on its FASTSim platform. As a first step, NREL created a representative school bus drive cycle – named the NREL School Bus Cycle – using data from its FleetDNA database and data collected specially from Rialto USD's school bus routes. Then, for each entity's modeling exercise, paired values for motor speed and torque associated with operation within the NREL School Bus Cycle were graphed onto a map showing how motor efficiency varies with these same two variables. (See Figure II.8.1)

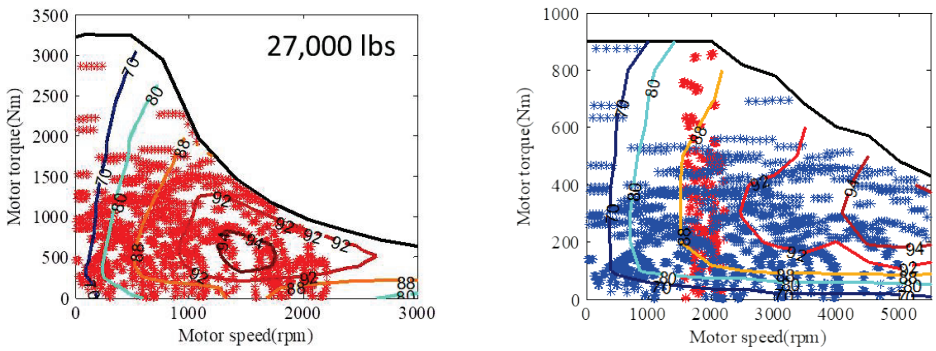

Figure II.8.1 Left: Efficiency map of TM4 3000 motor + single gear ratio on the NREL School Bus Drive Cycle. * = motor operating point. Right: Efficiency map of UQMHD 250 + Eaton 2-speed transmission. * = 1st gear motor operating point. * = 2nd gear motor operating point. Both cases: loaded vehicle weight of 27,000 lbs. Per EDI's proprietary simulation platform.

In EDI's version of the modeling, the consistent indication is that direct-drive architecture produces better energy efficiency than a geared, two-speed configuration. In NREL's, the indication is the opposite. (See Table II.8.1) However, in NREL's case, the advantage for the geared configuration is modest. Hence, NREL concluded that "adding a transmission to the School Bus does improve motor efficiency, but the impact is not significant to the extent that the current design should be revised."

Table II.8.1 Motor Efficiency Modeling Results for the NREL Drive Cycle

		EDI Proprietary Simulation Platform		NREL FASTSim Platform	
	Weight (lbs.)	Average Motor Efficiency	KWh per Mile	Average Motor Efficiency	KWh per Mile
TM4 motor + single speed	33,000	86%	1.84	84%	1.95
	27,000	87%	1.67	86%	1.55
	22,000	87%	1.44	87%	1.31
UQM motor + Eaton 2 speed gearbox	33,000	85%	2.10	90%	1.76
	27,000	85%	1.80	90%	1.49
	22,000	84%	1.56	91%	1.27

Thermal Management

In the thermal management domain, the original concept tagged for exploration was a system that would integrate selected vehicle functions in a series of interconnected thermal loops. Control algorithms embedded within EDI's PowerSuite control module would read and respond to data from an array of distributed sensors. In addition to the battery pack, the system would cover auxiliary systems such as steering and brakes whose energy consumption is influenced by the temperature of hydraulic motors and air compressors. The possibility of including the climate control function in the scheme was considered as well.

A first iteration of this system was developed and installed on an early version of prototype bus P1. EDI described the results in a monthly report:

> A lesson learned was that it was very difficult to develop controls that were efficient and kept all elements at their ideal temperatures. For example, there were times when the batteries needed to be cooled but the passenger area needed to be heated. Also, the amount of heat lost just passing fluid through the radiator, even without the fans on, was larger than expected and suggests [the need for] bypass capability. In addition, since buses made for different areas of the country have varying heater configurations and air conditioning capacities, this would have required varying sets of software to try and optimize the system for each potential configuration. So, for the P1 bus, it was decided to completely separate the bus passenger compartment HVAC system and the battery/drive system HVAC system.
>
> -- *"Progress Report, DOE/Blue Bird/Adomani V2G School Bus Program, Reporting Period December 2017." Efficient Drivetrains, Inc. January 19, 2018.*

In subsequent modeling, EDI concluded that the goal of maximizing energy efficiency can be best served by managing temperature via a series of heating-and-cooling loops dedicated to discrete functions. The company developed new sets of specifications for major components and, among other outcomes, selected a new compressor-inverter unit whose performance specification allow a reduction in weight and volume to about half those of units used in previous vehicles. The new components were then set up in a bench-testing unit to identify optimal settings under various operating conditions.

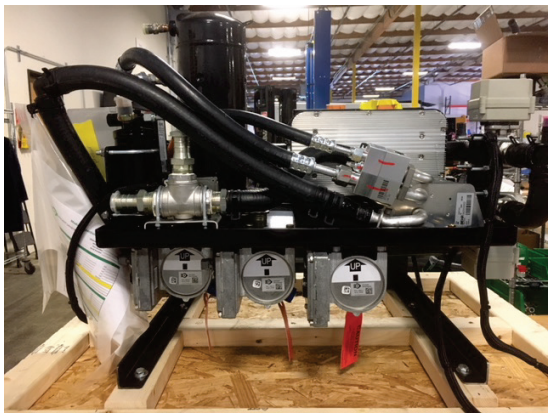

Figure II.8.2 EDI's thermal management bench test unit. Note the three water pumps at the bottom of the unit. One will support battery heating/cooling and the other two will support drive system and bus heating/cooling.

Prototype Vehicle Development and Profiling

P1, the Project's first formal prototype vehicle, was constructed using components from EDI's standard drivetrain with a view to carrying out three missions: 1) accomplishing a first- pass at marriage of the EDI system with the Blue Bird chassis and body; 2) identifying opportunities for technical improvements in vehicle systems that can be implemented on subsequent prototypes; and 3) creating a "business as usual" baseline for electric school bus energy efficiency. The baseline energy efficiency reading will be used in the calculation of the first go/no-go energy efficiency benchmark: [("business as usual" energy efficiency – 1.10 kWh/mile) / 2] + 1.10 kWh/mile = G/N-G benchmark.

P1's construction was followed by a commissioning phase. The key focus at this stage was programming the vehicle control module to achieve safe and efficient operation of on-board systems, including braking, steering, and throttle function. With commissioning complete, P1 was sent to NREL's REFUEL facility for energy efficiency profiling. The bus was placed on the dynamometer and run through the NREL School Bus Cycle as

well as a cycle based on actual readings from data loggers placed on incumbent Rialto USD school buses; a standard industry heavy-duty vehicle cycle (the California Air Resources Board's Heavy Heavy-Duty Diesel Truck Cycle); and a cycle based on a test course around Blue Bird's factory in Fort Valley, Georgia. The team agreed that the benchmark value from the exercise should be based on a run of the NREL School Bus Cycle with the bus loaded to the halfway point between its empty weight of 22,000 lbs. and its GVWR of 33,000 lbs.

Table II.8.2 Energy Efficiency Results for P1 from NREL's REFUEL Dynamometer (arithmetic deviations due to rounding)

Cycle	Traction Energy (kWh)	Regenerated Energy (kWh)	Net Energy (kWh)	Distance (miles)	Energy Efficiency (kWh/mile)
NREL School Bus Cycle (27,000 lbs.)	-11.2	2.1	-9.0	5.9	1.53
NREL School Bus Cycle (22,000 lbs.)	-10.0	1.9	-8.1	5.9	1.37
Rialto Cycle	-17.2	3.7	-13.5	7.6	1.80
CARB HHDDTNC	-36.5	1.5	-35.0	25.7	1.36
Fort Valley Cycle (27,000 lbs.)	-25.1	3.2	-21.9	20.6	1.06
Fort Valley Cycle (22,000 lbs.)	-22.7	3.1	-19.6	20.6	0.95

The energy efficiency value from the NREL School Bus Cycle with the bus loaded at 27,000 lbs. was 1.53 kWh/mile. This was adopted as the benchmark value. This value is reflective of the current state of electric bus technology as exemplified by a 2017 demonstration of type C Lion electric school buses in Massachusetts. (In November 2017, a value of 1.38 kWh/mile was reported for one bus; a value of 1.63 kWh/mile was reported for a another [1]) Based on the benchmark value, the target energy efficiency for go/no-go point #1 will be 1.32 kWh per mile.

In the time since the profiling of P1, work has started on the second prototype bus. This has been the occasion for detailed execution of Blue Bird's new-vehicle engineering process. In parallel, EDI has continued to adapt its assemblies and systems to the specific demands of a commercial type C school bus. Modules receiving attention included the vehicle controller hardware; the high-voltage power distribution unit; and both the low-voltage and high-voltage electrical harnesses.

Charging System Design

The Project's buses will be domiciled at a new pupil transportation facility that is being built by the Rialto USD. With Project team support, Rialto USD has engaged extensively with SCE in the design of the electric service for the transportation facility. Rialto USD, the Project team, and Nuvve, the Project's designated V2G platform provider, have collaborated on the design of charging system elements downstream from the utility meter.

In parallel, the Project team has initiated the interconnection application process with SCE. Both SCE and CAISO prefer to wait until the interconnection contracting process has reached an advanced stage before negotiating terms and conditions of electricity supply and participation in wholesale markets.

Conclusions

The Vehicle-to-Grid Electric School Bus Commercialization Project team has so far laid the foundation for accomplishment of the Project's objectives. Key design decisions have been made, an energy efficiency baseline and intermediate benchmark have been established, and opportunities for technical improvements

have been identified across a variety of vehicle systems and functions. Work to build on the foundation is on-going in the new fiscal year.

Key Publications

1. Boggess, M., Blue Bird V2G Electric School Bus Commercialization Project. U.S. Department of Energy Vehicle Technologies Office 2018 Annual Merit Review, June 20, 2018, Washington, D.C. Project ID: EE0007995.

References

1. Vermont Energy Investment Corporation. Electric School Bus Pilot Project Evaluation. April 2018. Note: This report comprehensively describes the Massachusetts project. The specific data cited was conveyed by Vermont Energy Investment Corporation in an unpublished presentation in February 2018.

III. Grid and Infrastructure: Industry Awards

III.1 Zero Emission Drayage Trucks Demonstration - ZECT I (SCAQMD)

Matt Miyasato, Principal Investigator
South Coast Air Quality Management District
21865 Copley Dr.
Diamond Bar, CA 91765
E-mail: mmiyasato@aqmd.gov

Phil Barroca, Co-Principal Investigator
South Coast Air Quality Management District
E-mail: pbarroca@aqmd.gov

Lee Slekak, DOE Program Manager
U.S. Department of Energy
E-mail: lee.slezak@ee.doe.gov

Start Date: October 1, 2012 End Date: December 31, 2019
Project Funding: $9,374,641 DOE share: $4,169,000 Non-DOE share: $5,205,641

Project Introduction

On-road heavy-duty diesel trucks are one of the largest sources of diesel particulate matter and NOx emissions in the South Coast Air Basin. The large number and extensive operation of conventionally powered higher emitting mobile sources continue to have an adverse impact on air quality and public health in this region, particularly on communities adjacent or in proximity to the various transportation corridors that facilitate the significant volume of goods movements from the San Pedro Bay Ports - Ports of Los Angeles and Long Beach. As a measure to reduce the impact and to meet federal ambient air quality standards, South Coast Air Quality Management District (SCAQMD) has been working with regional stakeholders, including the Ports of Los Angeles and Long Beach, to promote and support the development and deployment of advanced zero emission cargo transport technologies. In 2012, SCAQMD applied for and received a $4.17 million grant from the DOE under the Zero Emission Cargo Transport Demonstration Program to develop and demonstrate Class 8 electric drayage trucks with zero emission operation capability in real world drayage service.

Objectives

This project is to develop and demonstrate zero emission capable electric truck technologies in real world drayage operations to assess its technical feasibility to support demanding drayage duty cycles. The project is also to promote and accelerate market adoption of electric truck technologies in cargo transport operations, by engaging trucking fleets, the end users, in demonstrations to experience the technologies first hand.

Approach

SCAQMD, as the award recipient, will provide overall project management in this project. TransPower and US Hybrid, locally based EV system developers and vehicle integrators in Southern California, are to develop a total of eleven Class 8 zero emission capable drayage trucks for demonstration, based on four different architectures, consisting of two types of battery electric vehicles (BEVs) and two types of plug-in hybrid electric vehicles (PHEVs) with all-electric range capability as summarized in Table III.1.1. Initial portfolio of demonstration technologies included a fuel cell truck by Vision Motors and another battery electric truck from Balqon. However, with these two technology providers dropping out due to financial hardship, the portfolio was amended to the current mix by adding two PHEV technologies in 2015.

Upon completion, demonstration vehicles are deployed in real world drayage service for up to two years of demonstration with fleet partners at the San Pedro Bay Ports. During the demonstration, vehicle performance and O&M data will be collected and analyzed by National Renewable Energy Laboratory (NREL) to assess technical feasibility and market viability of the technologies in drayage truck applications. In addition, at least one truck from each technology is tested on chassis dynamometer at the University of California, Riverside (UCR) for performance validation and optimization.

Table III.1.1 2012 Zero Emission Cargo Transport Demonstration Portfolio

	Battery Electric Trucks		Plug-In Hybrid Electric Trucks	
Developer	TransPower	US Hybrid	TransPower	US Hybrid
No. of Trucks	4	2	2	3
Hybrid Architecture	N/A	N/A	Series	Parallel
Chassis	International Prostar	International Prostar	International Prostar	Peterbilt 384
Traction Motor	Dual PM Motor 300 kW	Induction Motor 320 KW	Dual PM Motor 300 kW	223 kW PM Motor (403 kW combined)
Transmission	Automated Manual	Direct Drive	Automated Manual	Automatic
Auxiliary Power Unit	N/A	N/A	3.7L CNG	8.9L LNG
Battery/Storage Capacity	215 kWh-311 kWh	240 kWh	138 kWh/60 DGE	80 kWh/72 DGE
Charger	On-Board ICU 70 kW	On-Board 60 kW	On-Board ICU 70 kW	On-Board 20 kW
Refuel Time	2.5–4 hrs	3-4 hrs	2 hrs/15 min	3-4 hrs/15 min
Drayage Range	75-150 miles	70-100 miles	200 miles/ 30-40 AER miles	250+ miles/ 30 AER miles

Results

Battery Electric Trucks (BETs)

TransPower

TransPower completed the development and demonstration of all four BETs funded under this project. Three of the four BETs, EDD2, 3 and 4, continued operation in drayage service through 2017, with EDD3 and EDD4 being deployed in service for almost two years, and EDD2 in service for nearly three years since January 2015. As of this report, the four EDD trucks, including EDD1, which has been out of service due to a series of problems relating to its batteries, have accumulated approximately 26,000 drayage miles as recorded by NREL and 38,000 miles overall. Table III.1.2 summarizes daily average use and performance characteristics for EDD trucks 2-4, in comparison to baseline diesel trucks in comparable duty cycles running short-haul drayage operations. As shown in the table, EDD trucks averaged 5.08 hours and 43.69 miles of operation per day, similar to the baseline diesel trucks that operated 6 hours per day, averaging 52.26 miles in drayage service. What is notable is that both EDD trucks and diesel trucks spent well over 50% of their operating hours idling, mostly while waiting in queues to load and unload cargo containers at the port terminals. This is typical for short-haul drayage trucks operating at the Ports and such duty cycles are an ideal match for electric trucks which, unlike conventional diesel trucks that keep its engine running for A/C and other amenities during such operations, can use battery power for hoteling loads with zero tailpipe emissions, thus providing significant fuel savings as well as considerable benefits in air quality and public health. Also noted is that the EDD trucks demonstrated much higher fuel efficiency, averaging 2.13 kWh/mi or 17.68 MPG_{de}, which is three times better than the 5.67 MPG for the baseline diesel trucks, providing significant savings in fuel costs.

Table III.1.2 Average Daily Use – TransPower BETs

	EDDs (EDD2 – EDD4)	Baseline Diesel Filtered[1]
Operational Time (hr)	5.08	6.02
Idle/Stationary Time (hr)	2.86	3.67
Daily Distance (mile)	43.69	52.26
Average Driving Speed (mph)	19.79	22.45
Regen Energy (%)	17.20	N/A
A/C Energy Use (kWh)	3.07	N/A
Remaining SOC (%)	54.74	N/A
Energy Efficiecy (kWh/mi)	2.13	6.64[2]
Fuel Economy (MPG_{de})	17.68[2]	5.67

1. Filtered out days with distance >100 mi and Ave. driving speed >40 mph

2. kWh/mi and MPGde calculated using 37.656 kWh/gallon of diesel fuel

EDD truck demonstration started with two fleets, namely TTSI and SA Recycling in January 2015, and expanded to include Cal Cartage, National Retail Transportation, Knight Transportation, PASHA, and 3 Rivers Trucking. Feedback from fleet operators and drivers was generally positive, describing the trucks as quiet, clean and easy to drive, especially in the stop-and-go traffic at the Ports. However, range limitation continues to be the main challenge to overcome for the fleets to readily adopt and deploy the trucks in drayage service without any limitations. In order to address this challenge, TransPower explored several high density battery chemistries, including the Nissan Leaf nickel manganese cobalt (NMC) batteries that have greater energy capacity compared to lithium iron phosphate (LFP) batteries deployed in the EDD trucks demonstrated. Also, as battery technology is expected to improve in energy density, TransPower expects the operating range of EDD trucks to increase from the current fully-loaded range of 70 miles to perhaps 200 miles, considered by many fleets as the minimum range for drayage trucks. EDD trucks 1, 3, and 4 are in the process of being retrofitted with the NMC battery technology as well as being up-fitted with Fuel Cell range extender technology under CARB's Fast Track Fuel Cell Program.

Figure III.1.1 TransPower EDD trucks on display

US Hybrid

US Hybrid completed and delivered the first of their two BETs to TTSI in late 2016, however, due to unexpected delays in permitting and installation of EVSEs at the TTSI's new location in San Pedro, the truck was not deployed in drayage service until July 2017. Since its deployment, this truck has completed 61 days of service, and has logged 1,798 drayage miles. Preliminary data, as reported by NREL, shows that the truck has a median daily use of 7.32 hours and 21.7 miles of operation, and a daily average efficiency of 2.17 kWh/mi in electrical energy. US Hybrid has also conducted additional testing for validation and optimization. The testing included medium and long distance excursions on surface streets and highways, as well as pulling a fully loaded trailer over the Vincent Thomas Bridge, a suspension bridge located in the San Pedro Bay Port complex with a 7% grade. The truck demonstrated sufficient power to manage the bridge with a full load while maintaining posted speed limits.

US Hybrid is completing its second BET and has changed its lithium-ion battery technology to nickel manganese cobalt (NMC). After having experienced more than usual share of glitches and reliability issues with the batteries in the first BET, US Hybrid switched its battery supplier to A123 and also opted to use the higher energy density NMC battery technology, which has 30% higher energy density than the lithium iron phosphate batteries (LFP) used in the first truck. US Hybrid received the NMC batteries in early Q3 2018 and expects to commence demonstration in Q1 2019. The unexpected delays in battery delivery and subsequent integration and testing of these cells in the demonstration truck have resulted in the project being extended through at least Q3 2019 to allow US Hybrid time to conduct meaningful demonstration ad data collection efforts.

Figure III.1.2 US hybrid battery electric truck

Plug-In Hybrid Electric Trucks (PHETs)

TransPower

TransPower continues its work to demonstrate its small APU, series battery electric hybrid truck. The first of two contracted PHETs was completed in 2017. The truck completed a series of testing for validation and optimization, including local and highway driving, in-field operation of the auxiliary power unit (APU) for extended range, and initial load pulling exercises. TransPower also concluded research to characterize variable valve control signals for higher RPM and power on its test dyno cell, which has been constructed using all of the parts and features of the production article generator sets to run calibration testing of custom engine control software. Efforts to convert the APU from the power limited stationary-trim mode to the full power potential automotive-trim mode has not proved successful due to an inability to obtain the engine codes necessary to operate the engine at higher power levels and output. As a result the APU is restricted to a stationary-trim power output level which is approximately 55% of full design performance (automotive-trim) capability. This limited power output will limit range extension and on-highway performance under load, meaning its deployment will be more near-dock and near domicile. The vehicle was designed as an electric truck with on-board series hybrid electric generation. The limited electrical power output of the APU means the vehicle is now more battery dominant than originally designed. TransPower is nearing completion of its second PHET which will be identical to PHET-1 but will utilize the higher energy density NMC batteries used in the Nissan

Leaf. With both PHETs transitioning to being more battery dependent, but still utilizing an on-board APU generator, their side-by-side demonstration is expected to provide additional information on battery technology and the effects of limited supplemental on-board electric generation. This project is also being extended through at least Q3 2019 to allow TransPower time to complete meaningful demonstration and data collection effort.

Figure III.1.3 TransPower PHET pulling its first trailer

US Hybrid

US Hybrid is demonstrating a hybrid system that converts an existing 8.9L ISL-G engine, which is considered underpowered for heavy-duty drayage operations, to a plug-in parallel hybrid truck capable of providing sufficient power and torque, comparable to a larger 12L engine, that can support a full range of demanding drayage duty cycles. Although this PHET technology was added in midstream in late 2015, US Hybrid made considerable progress, having completed and delivered two of the three contracted PHETs to TTSI in 2017. After completing necessary paperwork and vehicle inspections, the trucks were deployed in drayage service in July 2017. Based on preliminary data, as provided by NREL, the two trucks have collectively operated 269 days and logged more than 13,840 miles in drayage service, with each vehicle contributing nearly equal miles. The two trucks have produced a daily mean average of 3.83 hours of daily usage and 40.43 travel miles. Individually, US Hybrid's PHET-1 and 2 experienced different operation. PHET-1 saw 51 fewer days of operation, experienced longer median operating times and distances per event, significantly longer idle time, twice as much regeneration energy and lower energy efficiency than PHET-2. The net average fuel economy for each vehicle as calculated by NREL is: 9.1 mpg_{deq} (PHET-1) and 12.8 mpg_{deq} (PHET-2).

Figure III.1.4 US Hybrid PHET pulling a container for TTSI

The third PHET was delivered to UCR for chassis dyno testing to improve engine control and SOC control strategies to further reduce NOx emissions and enhance fuel economy.

Conclusions

Despite many challenges, including withdrawal of two technology providers in 2015, this project has been largely successful. As of September 2018, eight of the eleven electric trucks funded under this project have been completed with the remaining three scheduled for completion in 2019. NREL has received various data from these trucks including more than 34,000 miles of collective reported activity with drayage operators. Additional miles have been accrued on these trucks that have not been included in the NREL report that include transportation to and from the technology integrator, or for vehicle trials and testing. Overall, the trucks that have completed demonstration have proven successful in demonstrating their feasibility in various drayage operations and handling daily loads and many routine schedules. The trucks have generated significant interest from trucking companies, which helps to promote and to accelerate market adoption of electric truck technologies in cargo transport operations.

Based on available data collected from demonstration vehicles and feedback from fleet operators and drivers, these electric trucks have demonstrated sufficient power and torque to support real world drayage operations, while providing superior fuel economy over conventional diesel trucks in short-haul drayage duty cycles. The feedback from drivers was generally positive, with comments on its quiet and easy operations as well as smooth accelerations during take offs. These trucks also demonstrated sufficient capability to manage steep grades, even with a full load, including the Vincent Thomas Bridge, a suspension bridge located in the San Pedro Bay Port complex with sections reaching a 7% grade. As expected, fleets expressed concerns over limited operating range for battery electric trucks. Fleets cited the range limitation as a significant barrier for them to fully adopt and deploy these trucks in regular drayage service.

In order to address this barrier, TransPower has been looking into several high density battery chemistries, including nickel manganese cobalt which has greater energy capacity relative to lithium iron phosphate used in the EDD trucks. Furthermore, as the next generation of batteries is introduced with even higher energy density, TransPower expects to increase the operating range of EDD trucks from the current 70 miles to over 200 miles, even with a full load, supporting a wider range of drayage operations.

US Hybrid has successfully demonstrated the feasibility and superior performance of converting an existing conventionally-powered Class 8 truck to a parallel electric hybrid truck, specifically an existing Cummins 8.9L ISLG-powered LNG-fueled truck. The parallel hybrid system provided seamless and sufficient power and torque in routine drayage operations, that many operators compared to trucks equipped with larger Cummins ISX12 engines. The combined power systems also produced a fuel economy benefit of better than 60% relative to the conventionally fueled baseline trucks. Two of the three PHETs have been deployed in drayage service since July 2017 and received positive feedback from drivers and operators alike, especially on its exceptional power and torque. Upon successful demonstration in this project, US Hybrid aims to market the system to drayage fleets as a viable technology to convert the somewhat underpowered 8.9L natural gas-powered drayage truck into a higher power and torque plug-in hybrid electric truck.

III.2 Zero-Emission Delivery Vehicles Deployment Project (Houston-Galveston Area Council)

Andrew J. DeCandis, Principal Investigator
Houston-Galveston Area Council
3555 Timmons Lane, Suite 120
Houston, TX 77027
E-mail: Andrew.DeCandis@h-gac.com

Lee Slezak, DOE Technology Development Manager
U.S. Department of Energy
E-mail: Lee.Slezak@ee.doe.gov

Start Date: October 1, 2012 End Date: January 30, 2019
Project Funding: $3,990,170 DOE share: $1,230,177 Non-DOE share: $2,760,000

Project Introduction

The Houston-Galveston Area Council (H-GAC) and the Center for Transportation & the Environment (CTE) have partnered to establish the Houston Zero Emission Delivery Vehicle Demonstration Project. The primary objective of the project is to demonstrate the effectiveness of all-electric delivery vehicles in the Houston-region and to show that these vehicles can perform at the same level of operation as similarly sized diesel delivery vehicles, while reducing vehicle emissions and petroleum consumption. To meet this objective, this project has supported the deployment of 18 all-electric delivery trucks that have been deployed in the Houston-Galveston-Brazoria NAAQS 8-hour ozone nonattainment area.

Vehicles and the demonstration fleet were selected through a Call for Projects process. This Call was open to national, regional, and/or local fleets with the stipulation that the vehicle deployment and operation would occur within the Houston-Galveston region. In addition to funding the deployment of delivery vehicles and charging infrastructure for the winning fleet, the project demonstrates vehicle operations, collects data, and reports on project results for a period of two years after deployment.

Objectives

The primary objective of this project is to deploy eighteen (18) zero-emission all electric trucks and demonstrate the effectiveness of the all-electric delivery vehicles to at the same level of operation as similarly sized diesel delivery vehicles while reducing vehicle emission and petroleum consumption.

The project vehicles are deployed and selected through a Call for Projects process and deployed on delivery routes in the Houston-Galveston area. Large national fleets and progressive regional fleets that operate diesel and gasoline delivery vehicles in the region were initial targets for fleet deployment and testing. The process for integration of all-electric vehicles into fleets will result in both emission and noise reductions over diesel and gasoline counterparts. Fleets will also be able to reduce their reliance on petroleum-based fuels and realize significant cost savings over conventional counterparts.

As a result of the Call for Projects process, United Parcel Service (UPS) and Workhorse were selected as the fleet/vehicle team for this project. UPS has accepted and deployed 18 project vehicles that were manufactured by project OEM Workhorse. Additionally, CTE has worked with UPS and Workhorse to plan, select, and model the routes on which the project vehicles have been deployed. The project team procured, installed, and tested vehicle charging stations in preparation for vehicle deployment. With the demonstration period in progress, the project is now conducting a series of tests to validate vehicle performance against the model and is currently collecting operational data for all 18 project vehicles.

Approach

System Description

Workhorse has developed a new chassis for this project and for the commercial market. The W88 chassis is designed to meet the needs of a wide range of customers. At the same time, it is a universal chassis from an operations perspective and closely matches the existing UPS package truck specifications.

The Workhorse E-100 electric vehicle is 100% electric powered by a 120kWh battery pack giving it a useful range of 80 miles in a typical 120-150 stop per 8-hour package delivery shift. The range of the Workhorse truck should be more than adequate to cover the average 50 to 65 mile per day routes in Houston. The vehicle has no transmission — it is a direct drive to the differential making it very efficient. The electric motive drive is a 2200NM regenerative drive capable of powering a 23,000-pound vehicle from a dead stop up a 23% incline.

Top speed of the vehicle is limited to 65 mph. Typical differential ratios are 4.78 to 1 and 5.1 to 1 for the direct drive. The vehicle has a supervisory controller that interfaces with the Battery Management System, the Body Control Module, and the Brake Module, and the charging system to control the vehicle. There is an onboard level two J1772 charger, either 7KW or 18KW depending on the customer preference. The vehicle can also be fitted with inductive charging if needed, however this configuration is not used in the current project.

Testing

UPS, in partnership with CTE and Workhorse, is reporting vehicle and charger specifications as well as operational and maintenance data for all project vehicles. Data collected also includes powertrain and battery operational data. Additionally, average data from the UPS non-electric fleet vehicles is taken into consideration as may be required for comparative analysis. All information collected by Workhorse and UPS shall be provided to CTE. CTE will analyze the data and, with H-GAC, will summarize for submittal to DOE.

Testing Variables

- Vehicle Operations
  - Daily Mileage
  - Operating Time
  - Payloads
  - Speed
  - State of Charge
  - Auxiliary Loading
  - Maintenance Logs
- Charging Operations
  - Daily Charge Times
  - State of Charge
  - Energy Consumption
  - Utility Costs

  - Maintenance Logs
- Data Collected will be used to calculate a number of analytical factors, including, but not limited to:
  - Fuel Efficiency (i.e., $/mile, kWh/mile, etc.)
  - Cargo Ton-Miles/Vehicle
  - Cargo Ton-Miles/Fleet
  - Reduction in Petroleum Consumption
  - Reduction of Green House Gas Emissions (Million Metric Tons of Carbon Equivalent (MMTCE)/year)
  - Reduction of Criteria Pollutant and Toxic Emissions
  - Expected Life Cycle Benefit Analysis

Demonstration Period

The project includes a two-year demonstration of each project-procured all-electric truck under real world conditions.

Data Collection Strategy

The 18 Workhorse vehicles were tested for durability and are equipped with data collection and monitoring systems to tract variables from the battery management, drive system, cooling systems, etc. Coast-down testing was used to determine projected energy usage per mile; use case testing was accomplished to verify that vehicle energy usage is consistent with projected usage. Limits of charge and discharge were set as to ensure that the main battery will operate to its projected life without overstressing it.

Real time data is sent to a server for storage and analysis and parameters are modified as necessary to insure the vehicle performs to its design parameters.

Vehicles prototypes are tested on steep hills and anticipated normal driving conditions locally to get baseline data before TRC testing. Data is collected to determine energy usage per mile under various driving conditions and compared to predicted models to determine battery life, range, acceleration etc. Major vehicle maintenance for production vehicles can be performed at Workhorse dealers across the country.

Infrastructure Requirements

Each vehicle comes with a water-cooled J1772 level 2 charger on-board. The charger is typically 12kWh, 220 Vac. Vehicles may be optionally equipped with 25KW induction charging.

Commercialization

It is believed that the vehicles used in this project will result in a positive business case on a total cost of ownership basis for UPS and other selected fleets. This is due to the lower cost of electricity and lower maintenance costs as compared to fuel and maintenance of diesel medium- and heavy-duty vehicles.

Results

The project team has contracted with United Parcel Service (UPS) for the purchase of eighteen (18) all-electric delivery vehicles. These vehicles were manufactured by and purchased from Workhorse (formerly known as AMP Electric). The resultant vehicle is the Workhorse E-100 Electric Delivery Van. All 18 of these vehicles

have been fully manufactured and delivered by Workhorse to the Houston region and subsequently deployed by UPS to deliver packages within the Houston region.

Basic information about the project vehicles:

Table III.2.1 Project Vehicle Information

Vehicle Range	80 to 90 miles
Top Speed	65 mph
Battery Capacity	120 kWh
Motor	180 kW
Motor Torque	1,106 ft-lbs

Figure III.2.1 The Workhorse E-100 electric delivery van

Courtesy Workhorse/UPS

From the beginning of the demonstration period until September 30, 2018, the 18 project vehicles have traveled a total of 170,648 miles (84,833 in FY18) within the Houston region for an average of 9,480 miles per vehicle. On a per trip basis, these vehicles travel approximately 50 miles per which is well within the stated maximum range for this model of 80 to 90 miles per trip. For these 18 vehicles, trip lengths range from 38 miles per trip to 65 miles per trip.

Project vehicles have resulted in significant fuel savings at UPS over the course of the project to date. Project vehicles have used approximately 152,453 kWh of electricity for operations through September 2018. The same number of diesel-powered package cars would have used 23,319 gallons of fuel to accomplish the same distance of travel. Additionally, the average cost of operation of these electric vehicles in the Houston-based UPS fleet is approximately $0.06 per mile compared to the equivalent diesel vehicle which would cost approximately $0.30 per mile. As a result, the project vehicles have resulted in an estimated cost saving of $30,269 to date. Finally, as a result of this project, UPS has reduced fleet NOx emissions (an ozone precursor) by 177 pounds and reduced CO2 emissions by 521,882 pounds.

Significant Issues

The Workhorse E-100 Electric Vehicles have been in service since May/June of 2016. Throughout this time, the vehicles have been tracked by the Workhorse monitoring system, Metron. Since the beginning of the demonstration period in November 2017, project vehicles have seen various amounts of downtime resulting in a project-wide 39% utilization rate. The issues that have resulted in these utilization rates can be separated into a couple of different areas: software issues with the Battery Management System, third-party hardware issues, and manpower issues.

The Battery Management System (BMS) has multiple functions including helping to load balance the cells while charging and to also monitor the electrical system. When a cell appears to be out of balance then the BMS unit shows a fault. Workhorse found the software algorithm in the unit to be more sensitive than necessary for the application. Workhorse has potentially fixed this issue by working with the vendor to decrease the voltage monitoring sensitivity and adjusting the mounting of the BMS.

There have also been additional issues with third-party vehicle components that have reduced utilization rates among project vehicles. Major components with issues include: DC/DC converters that showed significant failure rates; vehicle chargers from small manufacturers with slow project turnaround; and a small number of trucks that could experience “Limited Power” conditions due to multiple potential issues. Additionally, long lead times from many of these component suppliers has resulted in longer vehicle downtimes that would otherwise have been expected.

Conclusions

This project is producing a record of on-road experience and operational data which will serve to accelerate the introduction and penetration of electric transportation technologies. To accomplish these goals, 18 zero-emission all-electric trucks manufactured by Workhorse have been deployed at UPS distribution facilities across the Houston region and are currently delivering packages as part of an ongoing a two-year demonstration period.

Through the ongoing demonstration period, the project vehicles have been able to adequately meet the needs of UPS for delivery of packages within the region. Despite this success, utilization of project vehicles continues to be lower than expected. This has largely been due to issues regarding vehicle software, faulty vehicle components sourced by Workhorse from external suppliers. These issues were largely the result of non-standard components and the difficulties of deploying early stage vehicle technology. Vehicle utilization has been increasing over the latter months of this project, however full utilization has not yet reached full usage. Despite these issues, this vehicle demonstration has resulted in the purchase of additional vehicles of the existing model by UPS and the joint development of an all new electric delivery vehicle line by Workhorse and UPS.

H-GAC will continue to monitor, analyze and report the demonstration data for 18 existing all-electric vehicles for the remainder of the demonstration period.

III.3 San Pedro Bay Ports Hybrid & Fuel Cell Electric Vehicle Project –ZECT 2 (SCAQMD)

Joseph Impullitti Program Supervisor
South Coast Air Quality Management District
21865 Copley Drive
Diamond Bar CA 91765
Email: jimpullitti@aqmd.gov

Lee Slezak, DOE Technology Development Manager
U.S. Department of Energy
E-mail: Lee.Slezak@ee.doe.gov

Start Date: October 1, 2014 End Date: September 30, 2019
Project Funding: $20,410,075 DOE share: $9,725,000 Non-DOE share: $10,685,075

Project Introduction

The proposed project area is known as the Los Angeles Goods Movement and Industrial Corridor. This area is adjacent to the Ports of Long Beach and Los Angeles, the busiest port complex in North America. The area is in an industrial setting with diesel truck activity mingled with a variety of uses including residences, schools, daycares and senior centers. The area is also a known Environmental Justice Community made up of predominantly low-income and minority populations that are adversely impacted by vehicle emissions.

The proposed technologies, fuel cell range extenders and hybrid electric trucks, face many challenges in the process of commercialization: proper sizing of the fuel cell stack, battery and fueling system; system integration and packaging of power train components and systems for safe, efficient and economical deployment of the technologies are just a few of the challenges. Many options exist in sizing the energy systems for these type of vehicle architectures – making the battery, engine or fuel cell dominate in size; plug in charging versus operation in charge sustaining mode and sizing of the energy storage system. Considerations for the power requirements of vehicle under load and providing enough onboard energy to attain the range requirements for the drayage operation and duty cycles all come into play in the design of the energy storage and power systems. Another challenge is to design the energy and power train systems described above and then integrate them into a vehicle for safe and efficient operation that can be made economical in volume and series production.

Objectives

- Reduce criteria pollutants and GHG's in South Coast Air Basin by reducing diesel emissions from transportation and movement of goods
- Accelerate introduction and penetration of zero and near-zero emission fuel cell and hybrid technologies in cargo transport sector
- Execute a joint project with the Port of Los Angeles and Long Beach consisting of demonstration, data collection and analysis of seven fuel cell and hybrid trucks on five different vehicle architectures.

Approach

Our approach to implementing the proposed technology is to address some of the challenges of developing the fuel cell range extended and hybrid truck platforms with the cost and time constraints of this FOA. By bringing together small to medium sized vehicle integrator contractors along with global manufactures and developers our strategy is to obtain the best partners with innovation and experience for this project. Vehicle integrators Transportation Power, Hydrogenics and U.S. Hybrid, are extremely cost effective in demonstrating proof of concept and exploring design variants in a timely fashion; OEM's BAE Systems a global defense and security company, Kenworth Trucks a major truck OEM and Ballard Power Systems an international fuel cell

manufacturer have engineering and manufacturing capabilities and experience; both BAE and Ballard have experience in developing fuel cell transit buses. Together our project contractors offer the opportunity to explore design variations concurrently and address many of the challenges developing new technologies in a timely and cost effective manner. Some of the metrics that will be used to evaluate the design variants of the five fuel cell range extended and hybrid architectures are: operational capabilities (range), energy usage and efficiency, fueling/charging requirements and costs compared to diesel powered trucks.

ZECT 2 Projects:

CTE/BAE Systems and Kenworth are developing a battery electric truck with a hydrogen fuel cell range extender. The vehicle will operate in electric mode at all times and all speeds until the battery energy system reaches a lower operating state of charge level, at which point the hydrogen range extender would be activated to supplement power.

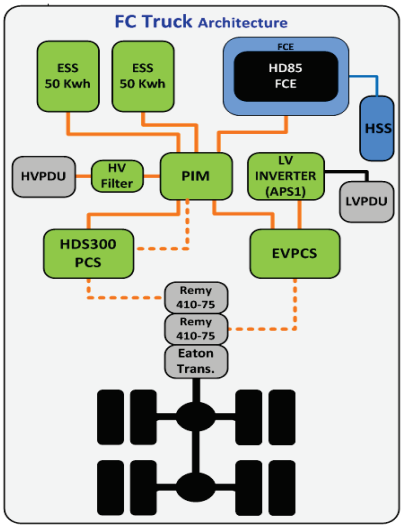

Figure III.3.1 BAE/Kenworth vehicle system

TransPower is developing two battery electric trucks with hydrogen fuel cell range extenders. These trucks will employ a small fuel cell and stored hydrogen. One truck will be equipped with a 30 kW fuel cell and one with a 60 kW fuel cell, enabling a direct comparison of both variants.

Figure III.3.2 TransPower fuel cell truck in foreground & CNG truck in background

U.S. Hybrid is developing two equivalent battery electric trucks with an on-board hydrogen fuel cell generator. Each truck is estimated to have 20 kg of hydrogen storage at 350 BAR with an estimated fueling time under 10 minutes.

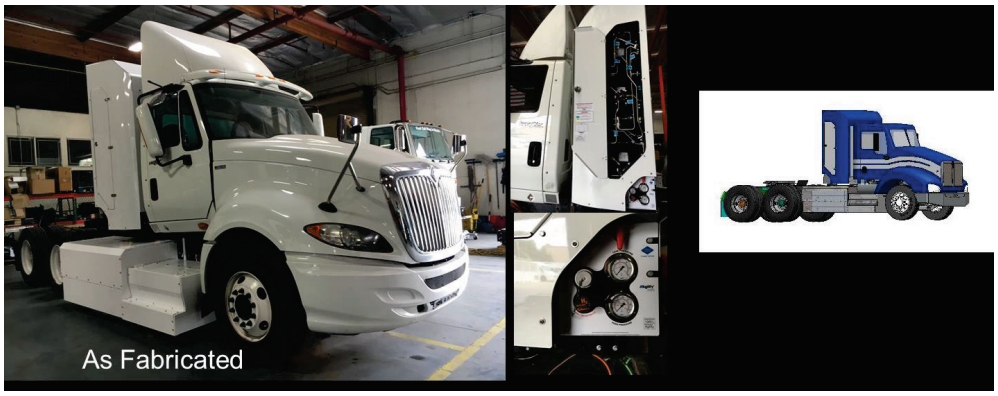

Figure III.3.3 U.S. hybrid truck: design to fabrication

GTI/BAE Systems and Kenworth are developing one hybrid battery electric truck with CNG range extender. The proposed technical concept provides an all-electric mode, and in a conventional hybrid mode using CNG. The truck will have an on-board battery charger to fully charge the batteries in daily use.

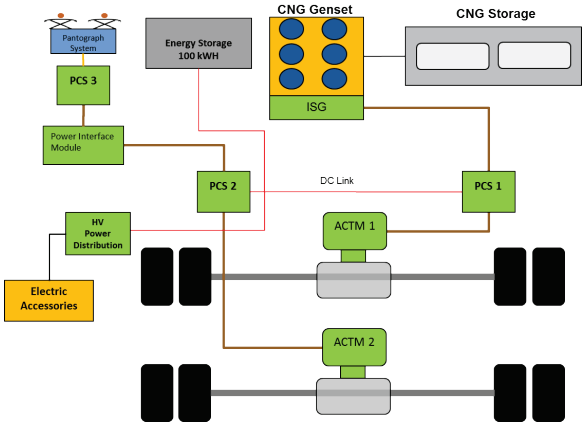

Figure III.3.4 BAE - CNG hybrid system architecture

Hydrogenics is replacing International Rectifier in the ZECT 2 San Pedro Bay project and they will be developing and demonstrating a fuel cell range extended Class 8 truck. Hydrogenics working with Daimler's VVG dealership group developing a fuel cell range extended truck under a California Energy Commission (CEC) project.

Table III.3.1 Hydrogenics Vehicle Systems Specifications

Item	Target Specification
Chassis	Daimler Freightliner Cascadia Day Cab
GVWR	80000 lbs
Fuel Cell Power System	Hydrogenics Celerity Plus
Electric Drive	Siemens ELFA PM Motor
Battery	ACTIA 100 kWh
System Voltage	650 V
Hydrogen Storage	30 kg @ 350 bar
Refuel Time	10-15 minutes
Expected Range	150-200 mi

Results

TransPower

Fourth Quarter 2017: The first fuel cell truck has accumulated over 1,000 miles, including trips from San Diego County to the Los Angeles/Long Beach area for AQMD related demonstrations on July 25 and September 7, 2017. Other travels included from Escondido to Riverside, taking the hilly route along Interstate 15, and excursions into the Poway and San Diego regions. The first truck was also showcased at the Fuel Cell Seminar and Exhibition in Long Beach in early November 2017, shortly after its frame was extended. Refueling has been done at the Del Mar fueling facility, and at other more northerly locations including Long Beach and Riverside.

First Quarter 2018: Earlier reports provided detailed descriptions of the failure of an YHKAM cell in a battery-electric test truck funded under a separate project. As mentioned in our second quarter report for 2017, we resumed test driving of a small number of trucks with YHKAM cells, including the first fuel cell truck built under this project, without any recurrences of this problem. Thus far, this failure has turned out to be an isolated incident, so we have gained confidence that we can carry out the full demonstration project with the first fuel cell truck using the YHKAM cells already installed into the vehicle. However, during the third quarter of 2017, we elected to switch to Nissan's "Gen-4" batteries, developed for the Nissan Leaf, for the second truck. This has further delayed deployment of the second truck, as a new battery pack design had to be developed and implemented. At present, we an advanced Nissan battery subsystem ready to install onto the second fuel cell truck and this truck is expected to be completed by May 2018.

Second Quarter 2018: The first truck was commissioned in 2017 and has been stationed at TTSI starting late 2017. During the present period the second truck subsystems were systematically connected and commissioned such that the first the truck could be driven as an electric truck. The E-truck commissioning of the second truck, driving as an electric vehicle using battery power with the new more energetic battery packs, is complete. The truck now has hydrogen fuel and fuel cell systems installed and at end of quarter is in the fuel cell commissioning phase. During this phase the fuel cell subsystems are systematically brought up under CAN control, coolant, air handling and isolation control are evaluated, the hydrogen tankage is purged such that it can contain pure pressurized hydrogen as needed for power generation. As the stationary commissioning is completed the test drive phase of commissioning can begin (in July).
Other activities during Q2 2018:

- Continued test and implementation of the first prototype truck, including a training session for first responders
- The prototype FCT was a key exhibit at the Long Beach Convention Center for the ACT Expo

- Assembly of the second truck has been completed and the vehicle is in commissioning phase
- After delays due to some technical glitches and initiation issues such as training of drivers, Truck #1 has entered commercial use
- Deployment of Truck #2 is planned for the middle of the third quarter.

Third Quarter 2018: Accomplishments of the quarter include:

- The first truck, FC1, has been in service at TTSI with limited use. As of the first of the month the odometer reported 3048 km, but the truck was held from service due to a leakage from one of the hydrogen tank valves. This valve was replaced in July, to be followed almost immediately with leakage observed in the identical (dump valve) location. Hence the remaining 3 valves were replaced (after a delay in receiving the new design replacement valves) in mid-August.
- As the truck was to re-enter service a failed hydrogen sensor was noted, the sensor was replaced the third week of August. End of August odometer 3074 km
- Noting the truck was not being used, likely due to extended period out of service. Also, came to light that if drivers get stuck due to a truck failure, they do not get paid. This was addressed with staff at TTSI, in which they indicated that in a recent breakdown (a drivetrain fault that could not be reproduced) TTSI did see that the driver was paid. We discussed mechanisms for seeing that if a failure occurs the driver can count on getting paid.
- As of end of month there have been two faults which have interrupted operation in the last two weeks of operation, one reported as a drive train fault and one as a fuel cell overheating fault, neither have recurred. Currently a TransPower technician is riding right seat to be immediately available to the TTSI driver making the deliveries such that if there is a fault it can be immediately addressed, and hopefully the cause ascertained. Mileage at last reading (Fleet Karma data logging) was 3731 km (657 km usage during September).

US Hybrid

Fourth Quarter 2017: In this quarter, The FCe™80 underwent more performance and duty cycle testing. The data shows that the FCe™80, fuel cell engine running on ambient pressure and using the high efficiency isolated dc-dc converter, is the best in its class. We are still expecting further optimization of the fuel cell engine. Also, in this quarter performance on truck assembly was slow due to US Hybrid relocating its vehicle integration facility from Torrance, CA to Carson, CA, a bigger facility with better integration and yard for customer demonstration, service, and maintenance.

First Quarter 2018: For this period we have finalized and finished the assembly of H2 Truck #1. We have also started the road testing for truck #1. Also during Quarter 1, we have taken it to TTSI for demonstration.

In this quarter, The FCe™80 underwent more performance and duty cycle testing. The data shows that the FCe™80, fuel cell engine running on ambient pressure and using the high efficiency isolated dc-dc converter, has the best/highest efficiency in its class globally for mobile applications, while we are still expecting further optimization of the fuel cell engine.

This quarter performance on truck assembly was slow due to US Hybrid relocating its vehicle integration facility from Torrance, CA to Carson, CA, a bigger facility with better integration and yard for customer demonstration, service, and maintenance.

Delivered the truck to TTSI/Customer for initial drive and testing and validated the fueling interface with customer station by doing a fueling from TTSI/Customer fueling station.

Second Quarter 2018: Accomplishments for Q2 2018:

- H2Truck #1 has been deployed and operating at TTSI.
- Fuel use of 0.17kg/mile (Loaded, 80,000 lbs. GVWR) and 0.1 kg/mile unloaded (19,000 lbs. Curb).
- In late June, there was a problem with the truck body computer, not allowing the A/C operation. The truck was taken to Westrux (dealer) and by the date of this report the truck is fixed and back on service. Figure III.3.1 & Figure III.3.2 display various plots for H_2Truck #1 with and without the trailer.
- H2Truck #1 was operated with 54,000 lbs and 80,000 lbs load and confirm that we can sustain battery charge for operation around the port and constant speed of 55 mph, with 80kW FCe80 fuel cell engine.
- Energy efficiency and fuel consumption was quantified for the operation and is continued to determine a correct range estimation and reporting to driver.
- Various critical operation temperature and water balance was confirmed.
- H2Truck #2, Assembly status;
- Hydrogen tank assembly integrated and tested.
- Fueling interface integrated.
- Electric Powertrain (Motor and controller) installed, needing some completion of wiring harness and commissioning.
- Auxiliary systems (compressor, eHydrulic and dc-dc converter) integrated and tested.

Third Quarter 2018: US Hybrid deployed vehicle H2Truck #1 and began operation at TTSI. Along with deployment, the vehicle's Operator's Manual and Service Maintenance Manual were provided. Following deployment of the first vehicle, a problem was encountered. During our in-house life testing, US Hybrid detected that the vehicle's manifolds showed evidence of corrosion that penetrated the coating, which was due to the supplier's Q/A. In order to solve this issue as quickly as possible, the FCe80 power plant was sent to our South Windsor, Connecticut facility, where it is currently going through manifold upgrades. This caused our high value of conductivity. Also, during the FC engine removal, we noticed that the WEG cooling system has evidence of rust and debris particulates. These debris may be due to not fully flushing or aging of the old radiator (this is a repowered 2012 truck). We are changing the cooling lines and re-flushing the system to ensure that there are no debris/containment in WEG.

CTE/BAE and Kenworth Fuel Cell Truck

Fourth Quarter 2017: During this reporting period, South Coast Air Quality Management District (SCAQMD) directed the team to open Budget Period 3 in order to reallocate funds between tasks.

California Air Resources Board (CARB) denied CTE's experimental use permit stating that it needed to come from Kenworth. Kenworth resubmitted the application and the team is waiting for CARB's approval. The CARB experimental use permit is necessary to operate the truck on public roads in California.

CTE Work Completed in Q4 2018:

- Maintained an integrated project schedule and continued working with BAE and Kenworth to ensure their own schedules are compatible with each other and the overall project schedule.
- Administered weekly team meetings and posted meeting minutes.
- Administered action items for the project.

- Continued tracking design requirements and goals based on the prime contract, CTE proposal, and requirements of project team members.
- Compiled monthly and quarterly progress reports with input from team members.

First Quarter 2018: The Kenworth truck returned from the CES exhibition in Las Vegas but the team was unable to power up the truck when it arrived. There was a week's worth of effort needed to investigate the power drain and restore the vehicle to working order. Systems were run through several wake-up and run tests and driven to confirm the chassis was not damaged or defective.

The cooling systems are in place and perform above their requirements. The team also installed all shore power circuitry in the truck and resolved a fault in the anti-lock braking system (ABS). The truck was taken out of fixed-gear transmission operation and the team tuned the transmission for smoother shifting, primarily under full load conditions above 45mph. Control changes for regenerative braking were finished and tested. After a routine hydrogen fill, the fuel cell stopped functioning and fault code data could not be transferred wirelessly or retrieved manually. Ballard was able to arrive on site quickly to resolve the issue; the fuel cell was re-tuned and re-calibrated to deliver expected performance, and the team implemented a new fault code communication protocol. During an early road test, the vehicle accelerated unintentionally due to a miscommunication between two Kenworth systems. The transmission splitter, a pneumatic piston on the arm that shifts between three different states, was not set fully in neutral position before the transmission system thought it was, resulting in acceleration.

Kenworth implemented a 3-level fix that includes a tightened neutral zone, a tightened propulsion when the vehicle is shifting between gears, and a torque limit was set in speed control mode where the torque can't exceed 5% or else propulsion is suspended.

The team noticed that the charging system was shutting down before all batteries reached full state of charge. A hardware-software-combination solution was implemented. This solution turns off the auxiliary components (sans fuel cell system heating elements) when the main batteries reach full state of charge so that the 24V batteries can be charged.

Second Quarter 2018: Kenworth began conducting track testing, road trials, and system tuning during this reporting period. Initial vehicle data packets have been created and are under review before being sent to NREL. Extended range testing is underway, and testing indicates that the vehicle meets or exceeds all contractually required performance.

The emphasis of track testing is rapid mileage accumulation testing to accumulate as many miles as possible and under multiple loads, full range of vehicle speeds and varying operational characteristics that replicate real world applications. The vehicle, to date, has accumulated more than 12,000 miles of track testing and some operations on the open road.

The team has also begun planning for post-testing, pre-delivery activities such as training for vehicle operators, maintenance teams, and local First Responders. Kenworth visited the demonstration site to review and update vehicle manuals to best serve the end user, TTSI. An escalation plan is currently under development for if the vehicle goes out of service during the demonstration period.

Third Quarter 2018: The emphasis of track testing is rapid mileage accumulation testing to accumulate as many miles as possible and under multiple loads, full range of vehicle speeds and varying operational characteristics that replicate real world applications. The Kenworth hydrogen fuel cell electric truck, to date, has accumulated more than 12,000 miles of track testing and some operations on the open road.

During the reporting period, the vehicle experienced faults related to power steering, the transmission, and the fuel cell engine that caused significant downtime. The vehicle was shipped to Kenworth's engineering center

for diagnosis and repair, and Ballard was on-site for all fuel cell diagnostic and repair activity. Several software upgrades were implemented into the vehicle to continue optimizing performance. At the close of the reporting period, the vehicle was being repackaged to be sent back to Paccar Technical Center (PTC) with the goal of achieving 40 fault-free hours of continuous operation before being shipped to the demonstration site.

GTI/BAE and Kenworth CNG Hybrid Truck

Fourth Quarter 2017: Specific project administrative tasks that were addressed this period include continuation of all reporting, contractual, and invoicing efforts. The Team has continued to hold weekly meetings to discuss accomplishments and issues.

Technically, the Kenworth team progressed as scheduled. The chassis was stripped of the original equipment that needed to be replaced by hybrid and custom components. The new component designs were either fabricated in house or at local shops. All parts are in house and were held in waiting until the hybrid drive system could be installed. The hybrid drive system for this chassis is a matched set to a parallel project. The drive system for this chassis was installed in an engine test laboratory at BAE. Lessons learned from the other system were tested at BAE to speed up the drive system commissioning process. Each issue found during the first drive system commissioning tests were first tried and tested at BAE. This phase of testing was completed and the drive system was disassembled and shipped to Kenworth. An oil leak was found at BAE and the transmission manufacturer was brought in to resolve, modify, and test the resolution at Kenworth. The last piece received for this project was the transmission and this repair has to be completed before installing on the chassis. This modification is pending but will not impact build schedule.

First Quarter 2018: Specific project administrative tasks that were addressed this period include continuation of all reporting, contractual, and invoicing efforts. The Team has continued to hold weekly meetings to discuss accomplishments and issues.

Technically, the team progressed very well during this period. The full truck integration is now complete and operational testing has begun.

Several challenges were addressed during this project period. Weighing of the truck disclosed that the weight on the front axle marginally exceeded the rating for the front axle. To correct this, a higher rated axle has been ordered and will be installed and tested on HECT before the truck is released for use on public roads. This higher weight also caused us to boost the power of our power steering pump in order to facilitate turning of the wheels while stationary. Another issue identified in preliminary testing was an apparent pressurized air leak into the transmission. This leak manifested itself in spitting transmission oil out of the vent stack when gears were changed. Root cause was traced down to a pinhole created during fabrication of one of the transmission actuators. This was corrected and the system is shifting correctly without losing any transmission fluid. There were also an unexpected number of minor electrical issues (i.e., bad contacts in connectors, harnesses mis-wired). This points to a desire to have more sophisticated test harnesses that will be able to exercise and test entire truck systems which becomes more practical when multiple units of the same truck are to be fabricated. Field testing on the ZECT truck uncovered that our shore power connections and charging system needed to be upgraded. A more advanced “smart” shore power charging port was designed built, tested, and installed on the HECT truck. The new shore power system ensures that power is sent to the areas of the truck that need power and that fully charged or unused sections of the truck systems (e.g., battery heating on warm nights) do not draw power. The new system also makes it easy to charge the High Voltage batteries to full power overnight. This means the truck starts the work day with a full battery charge, which maximizes zero-emission miles and extends its range for a single CNG fill.

Second Quarter 2018: The Kenworth CNG Hybrid truck has been in extensive testing at PACCAR Technical Center (PTC). This includes performance testing to verify that the truck will meet or exceed all contractual requirements; and rapid mileage accumulation driving to verify reliability. HECT has accumulated more than

300 miles of track testing replicating most field test scenarios. Many issues have been identified and resolved with priority in order to continue accumulating mileage and identify further unforeseen issues.

A troubling issue has been uncovered - an error in the #2 ACTM motor's resolver's offset. Each ACTM is made up of two motors, each with their own resolver. Specific component testing has yet to disclose the root cause of the issue. Software and firmware workarounds were attempted, worked for a period and long enough to promote efforts to the next level of analysis. However, the offset has yet to be fully resolved and has temporarily halted track testing. The team will update SCAQMD when the issue has been resolved.

The delivery of the truck to TTSI has been delayed due to the issue with the ACTM resolver. The team is hopeful that track testing will resume in late July and updates on progress will be sent to SCAMD as soon as they are available. It is typical that issues are found during the Rapid Mile Accumulation phase of testing and the project team will continue to address any issues as they arise.

Third Quarter 2018: Track testing of the CNG Hybrid truck continues at the PACCAR Technical Center. The tests have shown themselves to be invaluable in finding operational and performance issues prior to releasing the vehicle to TTSI fleet. The Kenworth team completed modifications to the Hybrid Electric Cargo Transport (HECT) transmission shifting algorithms and feedback from the test engineers suggests the latest changes were a success. The key determination for success will be the vehicles ability to repeat the shifts for duration of a reliability test.

The following issues appeared during the last quarter, and unfortunately occurred in succession, which therefore kept the vehicle out of test for a significant amount of time. It appears that we have resolved simple issues and have now moved to issues that require significant effort. BAE and Kenworth controls teams struggled to manage a phase shift issue within the motor resolver. Two conflicting theories, software versus hardware issues were vetted to determine the root cause of a motor fault that shut down operations. PTC conducted tests based on requests from the motor supplier, none of which could identify a solution. At this point, the vehicle was too unreliable to continue testing. Testing was stopped; the vehicle was pulled from the track and returned to Kenworth R&D for a vehicle tear down and inspection. The electric motor supplier completed the tear down, component and assembly analysis, and determined that the rotor assembly had not been properly torqued and was moving when introduced to extreme loads and operating conditions. The motors were reassembled with high strength fasteners, properly torqued, and returned to Kenworth for continued testing.

Hydrogenics

Fourth Quarter 2017: Hydrogenics accomplishments for the quarter include the following:

- Fuel Cell System & Cradle: Continued to build up Celerity cradle with hoses from cooling package, coolant pump, and 3 way valve, overflow reservoir and have confirmed fit. Installed fully built up Celerity cradle into the truck for additional fit check and made required modifications to chassis. Released brackets for mounting Celerity to the truck frame
- Battery System: Supporting ACTIA's thermal modeling activities. ACTIA confirmed they will utilize a 23 Ah cell instead of a 20 Ahr cell that will be used which amounts to a 15% increase of the stored energy in the battery pack up from 76 kWh to approximately 90 kWhr. Finalized chiller solution with ACTIA, Technotrans will supply the chiller. The chiller has been placed on order by ACTIA. ACTIA initiated build of the cell modules. Mid of quarter, ACTIA informed Hydrogenics that the vendor they selected to supply the battery enclosure housings had backed out of the project. ACTIA solicited and received quotations from three machine shop vendors with onsite visits. Continue weekly calls with ACTIA to ensure successful delivery of the high voltage battery system and compatibility of the selected chiller system and to optimize and finalize battery distribution box details.

First Quarter 2018: The Celerity cradle with Celerity fuel cell and power steering motor assembly is ready for cooling priming and test validation with test validation taking place early in the next reporting period. Truck chassis modifications following test fits of Celerity cradle into Chassis have been completed including finalizing brackets for mounting Celerity to the truck frame.

Early in this quarter, battery supplier ACTIA released purchase order to new housing supplier following holiday shutdown. As at January 25, 2018, ACTIA worked towards battery pack delivery at Hydrogenics by late Feb 2018 but experienced delays at powder-coating. Cooling plates for cell attachment have been received at ACTIA's facility on January 17, 2018. Cooling plates have been machined but needed to be modified to ACTIA specification; modifications where completed on January 30, 2018 with plan to finish attaching coolant plates to cells by early February and complete final assembly of pack by end of February and commence EOL pack testing. Module build up with cooling plate attachment continued and ACTIA planned to mount modules in the internal cell frame once the internal cell frame arrives at ACTIA facility. ACTIA experienced some further delays in receiving frame materials. In particular inner frame slave plates on February 8, 2018, received housing and brackets February 12, 2018. ACTIA test fit housing with brackets February 13, 2018 but due to packaging issues with the battery module and inner frame, delayed the final assembly of the first pack and second battery pack. Second battery pack assembly initiated in March 2018. Full EOL testing is delayed pending completion of first and second battery pack assembly and finalization of EOL test plan.

Second Quarter 2018: Celerity fuel cell system has completed the factory acceptance testing and passed. The system has been installed into the Celerity cradle. Load testing of the Celerity system has started with a coolant flow test of the Celerity system plumbed to the Grayson radiator, Iwaki pump, and the complete cooling system for the fuel cell. Load testing and cooling system flow testing of the Celerity system and the integrated cooling system functionality has been confirmed by running the Celerity system as it will be run in the truck with its own cooling system and air delivery system.

Third Quarter 2018: Status as of End of Quarter:

<u>Fuel Cell System & Cradle</u>

Completed the load and coolant flow testing of the Celerity system and the integrated cooling system. A revised air intake manifold system designed to boost performance for high duty cycle truck applications was designed, built and test validated and performance confirmed.

Celerity system was reinstalled in truck with successful fit check of all components with hood closed.

<u>Battery System</u>

- Multiple software updates were received and installed by ACTIA USA from ACTIA Germany, testing and verification of the software updates continued.
- ACTIA delivered the battery packs, PSM box, and chiller to Hydrogenics on August 30, 2018. Hydrogenics received and inspected all ACTIA components and performed fit-check of ACTIA components. Battery chiller has been mounted to the truck. Hydrogenics engineering reviewed final end of line ("EOL") test data and test report before accepting delivery of the ACTIA battery packs
- ACTIA sent engineer to Hydrogenics Mississauga to perform post-delivery power on check of the battery pack communications and proved out all systems checked out ok.
- ACTIA will support integration of battery packs and chiller into the vehicle as needed

III.4 Medium-Duty Urban Range Extended Connected Powertrain (MURECP), (Robert Bosch LLC)

Alexander Freitag, Principal Investigator
Robert Bosch LLC
38000 Hills Tech Drive
Farmington Hills, MI 48331
E-mail: Alexander.Freitag@us.bosch.com

Lee Slezak, DOE Technology Development Manager
U.S. Department of Energy
E-mail: Lee.Slezak@ee.doe.gov

Start Date: August 18, 2016 End Date: November 30, 2019
Project Funding: $6,716,791.00 DOE share: $4,731,884.00 Non-DOE share: $1,984,907.00

Project Introduction

The purpose of this project is to develop and demonstrate a commercially viable PHEV powertrain for MD vehicles that reduces fuel consumption by 50% on a real-world drive cycle by utilizing an advanced dual-planetary gear transmission with multiple clutches, coupled with cost-optimized electric machines. Such an improved powertrain efficiency will translate to a reduced fuel consumption of approximately 26 million diesel gallons per year, based on an average use of 22,000 miles per year at 8.3 mpg and a 30% market penetration for Class 4 delivery trucks.

The proposed design approach optimizes all powertrain components, particularly the internal combustion engine [ICE], the electric powertrain, and the battery pack to result in an incremental price and economic payback required for widespread commercial fleets' purchase without requiring financial incentives. Future developments are planned to explore the suitability of the MURECP powertrain for Class 2b – 8a delivery trucks.

Objectives

Key objectives:

- Dual Planetary Gear Transmission with multiple clutches, enabling the use of cost-optimized electric motors (PC/LD separated motor generators, high speed/ power dense design).
- Development of a multi-mode control strategy that ensures system optimal efficiency under a wide range of operating conditions, especially with the flexibility of powersplit operation.
- Efficient downsizing of the ICE for further reductions in fuel consumption.
- Electronic Horizon forward-looking input to HEV and EV driving modes, maximizing real-world fuel consumption reduction.
- Provide a ~35 mile all-electric range, achievable with existing battery packs on the CSHVC cycle.

Approach

The project will be conducted in 3 budget periods:

Budget Period 1 (Aug '16 – Nov '17): Powertrain Development: Hybrid-electric vehicle topologies will be investigated through simulation and evaluation of each configuration on a real-world drive cycle to define the technical requirements and most promising architecture for the powertrain system.

Budget Period 2 (Dec '17 – Feb '19): Powertrain Integration: The supervisory control algorithms, battery management system, thermal energy management, and vehicle control strategy will be integrated with the

conventional powertrain controller and further refined. The mechanical design and assembly of the hybrid drive system will also be completed along with the manufacturing of the prototype transmission. All PHEV solution components and a downsized diesel engine will be integrated onto the prototype vehicle.

Budget Period 3 (Mar ’19 – Dec ’19): Powertrain Demonstration: The prototype vehicle will be tested and deployed, including chassis dynamometer testing and demonstrations on closed courses or while shadowing an in-use delivery truck to quantify the achievable benefits and help finalize the control algorithms. In-use fleet operation with the prototype vehicle will be conducted.

Results

Subtask 3.1 – Develop Physics-Based Battery Model

Software development and battery modeling for enabling two packs in parallel has been started, building upon the work completed in a previous internal project. In order to allow two series production battery packs to operate in parallel, a gateway device / functionality is required, so that 1) the VCU sees only 1 battery pack and 2) the contactor closing and additional safety features of each pack do not inhibit the functionality of the other pack. The Multi Pack Coordinator (MPC) has been designed based on the existing systems and components. The BCM (Body Control Module) toolchain and development environment is understood and setup.

Task 4 – Hybrid Drive System Definition, Hardware Procurement

The target PHEV system architecture has been defined and consists of two SMG180/120 electric motors (200 Nm/ 80 kW peak performance) with two AC/DC inverters. A model and picture of the first prototype build transmission is shown in.

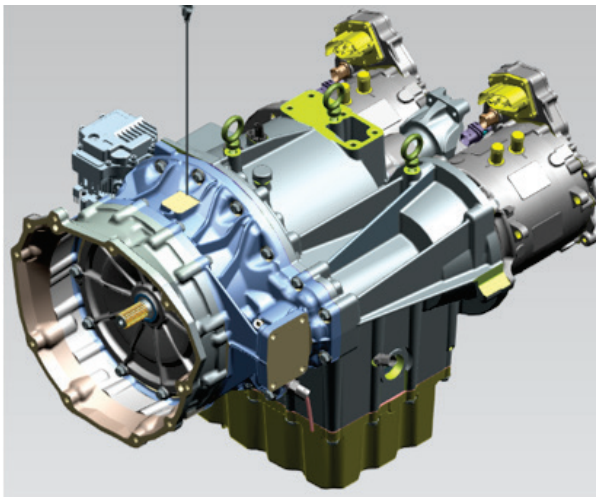

Figure III.4.1 Target PHEV transmission design

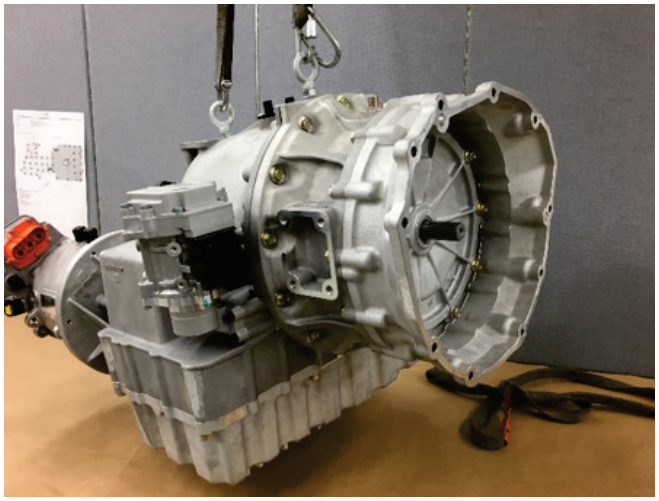

Figure III.4.2 PHEV transmission model / first prototype

Task 5 – ECU / VCU HW & SW Development

The embedded controller hardware setup has been finalized. The PHEV controls are split between a VCU (Vehicle Control Unit), an ECU (Engine Control Unit), and a TDG1 (Transmission Controller). The PHEV energy management strategy was developed using a physics-based simulation environment, and were then transferred to the VCU embedded controller. Transmission clutch controls are being run on the TDG1 transmission controller, which allows us to use a single controller for all required actuators, instead of using separate modules to control transmission solenoids.

Model-based controllers for the power-split and electric-only torque paths run on the vehicle controller. The functionalities implements by these controllers include optimal powertrain operating mode determination, component torque limit calculation, and dynamic component torque determination. Driver inputs from the

pedal and gear lever are converted to desired torque requests for each of the powertrain components. These functionalities were tested on the powertrain dynamometer.

Interfaces for torque filtering and interventions were added to the torque path. These filter functions can be enabled if necessary on the vehicle to improve drivability. The differing dynamic responses of the electric motors and the ICE require careful coordination and calibration of the driver torque demand. Some of the torque interventions are not needed in Class 4 truck applications, but are included to enable applicability for other vehicle applications.

Subtask 7.1 – Develop Power Prediction Algorithm

An improved predictive Equivalent Consumption Minimization Strategy (ECMS) was compared in simulation to the current rule-based PHEV operating strategy. ECMS showed favorable results for both charge sustaining and for linear SOC ramp decline conditions. Future work includes further validation using more complex simulation environments, and potential implementation in the vehicle.

Task 8 – Hybrid Drive System Design

Layout and assembly on chassis of powertrain completed. Layout and assembly of subsystems on chassis ongoing. A dual 24V power pack system will be integrated from Dare Auto (FZB) to support electro-hydraulic power steering and braking with the ICE off. Components and engineering support have been ordered. Packaging model shown in Figure III.4.2

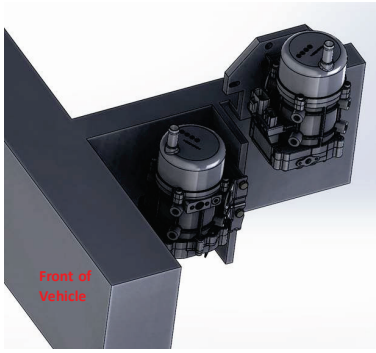

Figure III.4.3 Electro-hydraulic Power Steering (EHPS) Packaging and Bracket Design

Thermal management system layout defined. System evaluation, especially for the refrigerant and HVAC ongoing. Detailed thermal system model in GT-suite being constructed. A system schematic is shown in Figure III.4.4, including new thermally controlled valves developed by VOSS. Cooling package upgrade from

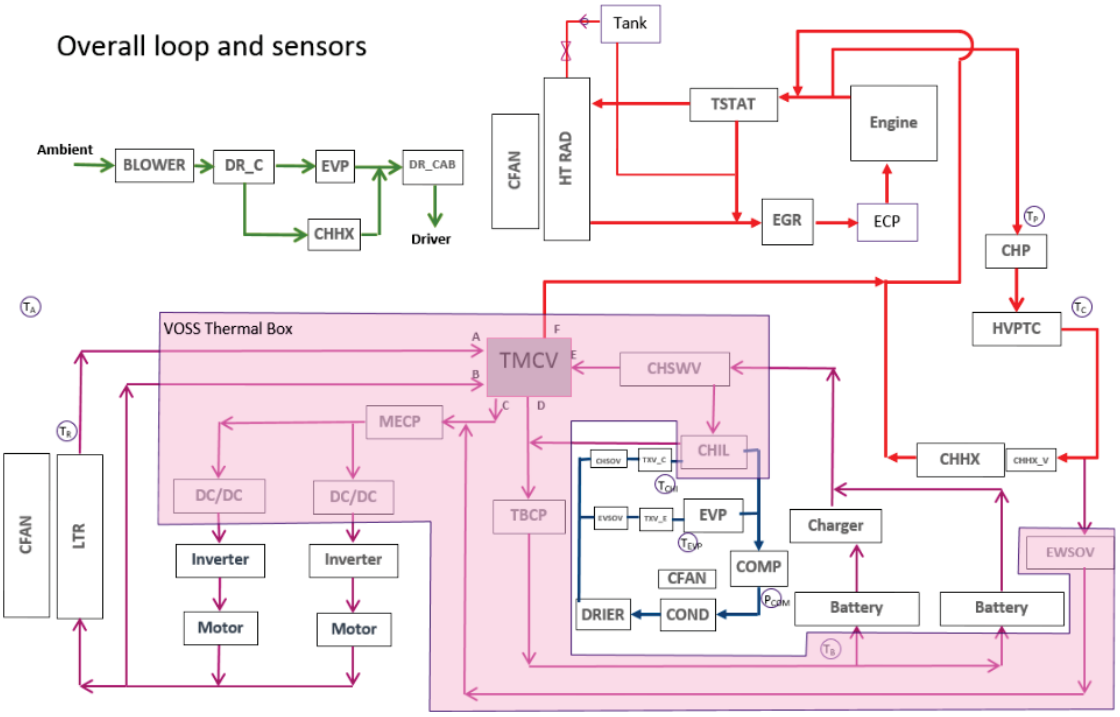

Figure III.4.4 Thermal system design with VOSS thermally actuated control valve and five modes

Modine ordered. VOSS integrated the majority of the thermal system into a 'Fluids Box' which will ease integration onto the chassis.

Electrical/ Electronic Architecture system designs have been frozen. The EE Architecture layout is provided in Figure III.4.5. Final pin-to-pin reviews for all sub-systems is on-going.

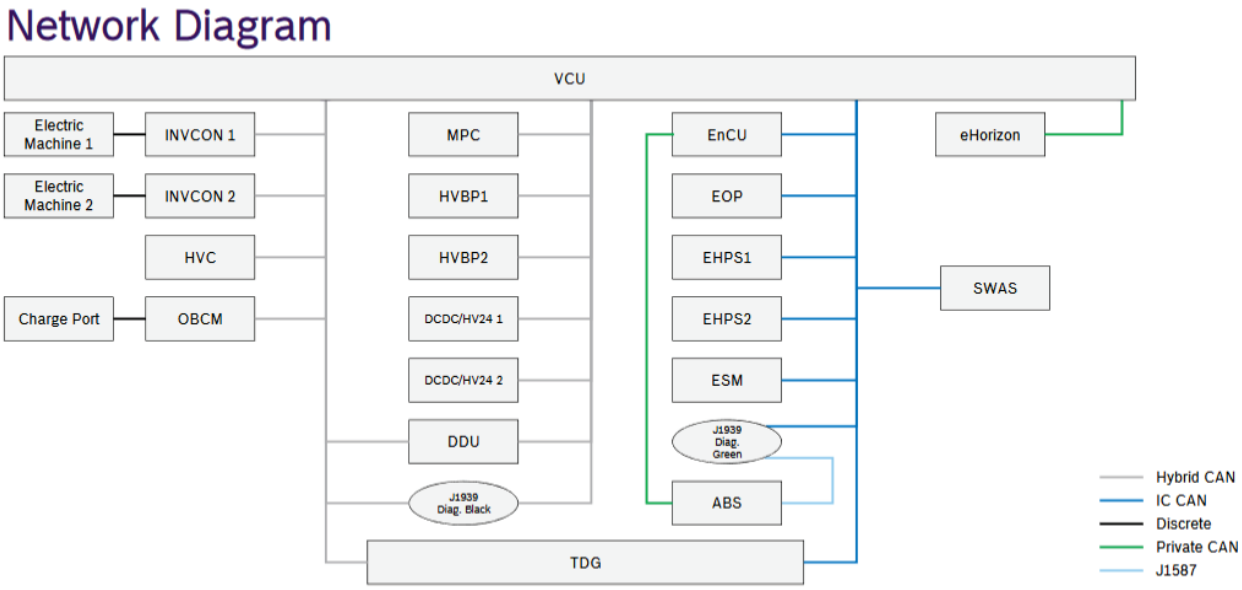

Figure III.4.5 Complete Vehicle Network Diagram

Subtask 9.2 – Electronic Horizon Controls Integration Interface/Interaction

Evaluated predictive control utilizing State of Charge (SOC) strategy (trajectory) without observing a significant improvement using a detailed SOC reference over a simplified SOC reference ramp over distance. Commenced predictive engine start/stop evaluation.

Subtask 10.1 – Downsized Engine Calibration

Completed baseline testing with conventional eight speed automatic transmission completed on powertrain dyno. Results are displayed in Figure III.4.6.

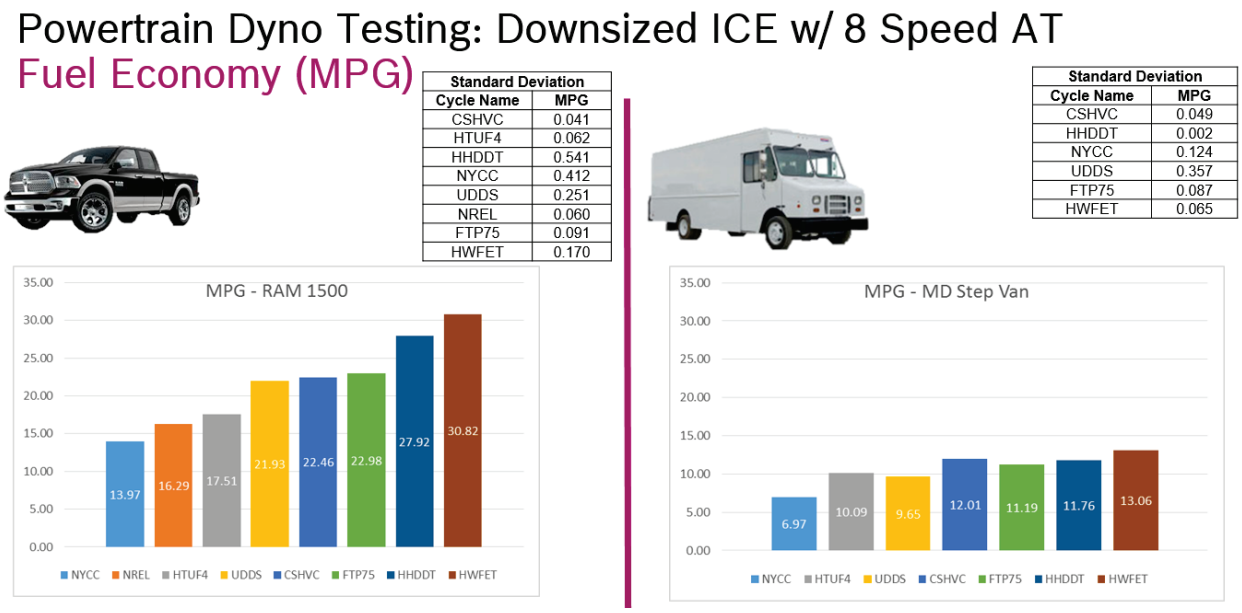

Figure III.4.6 Powertrain dyno testing summary.

Subtask 10.3 – VCU & ECU Software Implementation

Vehicle and powertrain controls will be run on three hardware controllers: Vehicle Control Unit (VCU), Engine Control Unit (ECU), and Transmission Control Unit (TDG1). The VCU is responsible for torque path calculations, electric drive component interfaces and drivers, operation strategy and mode switch handling. The TDG1 will be responsible for actuating transmission solenoids. It will further get feedback from sensors in the transmission and communicate them to the VCU. The ECU is responsible for ICE control.

Mode switch functionality is currently being implemented in the VCU software. A mode switch command is determined based on factors such as powertrain efficiency, component limits, and driver demand. Based on the current and target modes, the system will actuate transmission solenoids and powertrain components to reach the target mode and speed / torque setpoint.

Initial versions of the transmission actuation control strategy and calibrations have been implemented in the TDG1. The interfaces for actuating hardware components and communication adapters have been set up. High voltage battery and e-drive components interfaces have been completed, while the high voltage charger communication interface and functionality is still being defined.

Subtask 10.4 – Integrated Powertrain Calibration Optimization

A complete powertrain calibration on the engine dynamometer will be performed, enabling additional fuel consumption reduction when integrating the downsized engine with the 2PG transmission. ICE shifting strategies identified in task 2 above will be validated with measurements. PHEV transmission clutch calibration completed on the engine dyno. One motor and two motor EV mode along with Powersplit testing and calibration ongoing.

Subtask 11.1 – Powertrain Integration Packaging Study

A packaging study was conducted individually on each subsystem first, then for all components (e.g., down-sized engine, 2PG transmission, electric motors, battery pack, additional cooling system). The components were brought together, paying close attention to the various interfaces, to develop the complete vehicle integration solution. Final packaging report provided by Morgan Olson as shown in Figure III.4.7.

Subtask 11.2 – Sub-System Integration

The truck body was separated from the chassis according to work instructions supplied by Morgan Olson. The conventional powertrain and sub-systems were removed from the chassis. Based on the 3D CAD model, the down-sized engine coupled with "set-up" transmission housing installed on chassis. Exhaust system installed on chassis. Various sub-systems being installed on chassis while truck body is raised up.

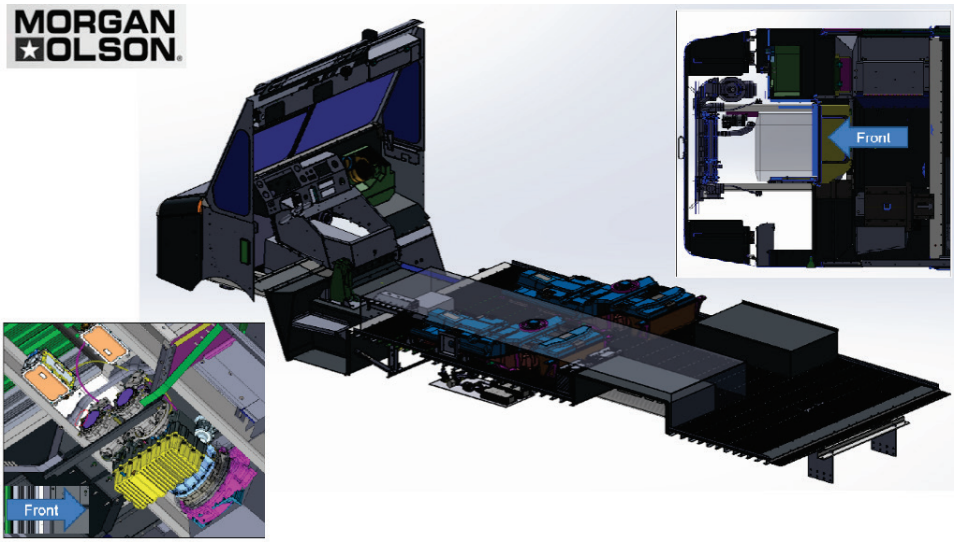

Figure III.4.7 Vehicle Packaging Study Report–completed by Morgan Olson

Conclusions

Utilizing the selected design for the target architecture from 2017 activities, the integration phase of the PHEV powertrain commenced. Supervisory control algorithms, battery management system, thermal energy management, and vehicle control strategy were integrated with the conventional powertrain controller and are now being further refined. The mechanical design and assembly of the hybrid drive system were completed along with the manufacturing and delivery of two prototype transmissions. All PHEV solution components and a downsized diesel engine are being integrated onto the prototype vehicle. In parallel, engine dyno test results with a downsized diesel engine assembled to a hybrid transmission show positive initial results.

Key Publications

1. Patent Applications: U.S. Application No.: 16/140,645; Title: MULTI-MODE POWER SPLIT HYBRID TRANSMISSION WITH TWO PLANETARY GEAR MECHA-NISMS; Filing Date: September 25, 2018, Inventor: Ziheng Pan et al.; U of M Ref. 7471-02; HDP Ref.: 2115-007471-US
2. Publications: AMR 2018 presentation given on June 20. Oral-only presentation given at the SAE World Congress in April.
3. Media Reports: Press release and media articles were initiated during the Bosch Mobility Experience Event in May. Trucks.com article published by Alan Adler on May 24, 2018.

III.5 Cummins Electric Truck with Range-Extending Engine (ETREE) (Cummins, Inc.)

John Kresse, Principal Investigator
Cummins, Inc.
1900 McKinley Ave.
Columbus, Indiana 47201
E-mail: john.kresse@cummins.com

John Jason Conley, DOE Program Manager
U.S. Department of Energy
E-mail: john.conley@netl.doe.gov

Start Date: July 1, 2016 End Date: February 28, 2020
Project Funding: $6,295,281 DOE share: $4,126,570 Non-DOE share: $2,168,711

Project Introduction

Many medium duty commercial vehicles (classes 5 - 7) have daily duty cycles with energy requirements that may lend themselves to the use of a plug-in electrified powertrain. However, often the duty cycle energy requirements are near, or over, the limits that can be served by a pure battery electric vehicle (BEV). A range extending electric vehicle (REEV) architecture may enable the fleet operator's needs to be met using a substantial amount of grid energy, while also allowing the vehicle to complete any number of more challenging duty cycles typically completed by conventionally powered vehicles.

The Cummins Electric Truck with Range Extending Engine (ETREE) project makes use of grid energy to offset fuel consumption used by medium duty commercial vehicles and, specifically, those that are used for class 6 urban/suburban pickup and delivery.

The ETREE project aims to develop a class 6 (GVW 26k lb.) box truck, with equivalent performance to conventional diesel-powered trucks. That goal of the project is to reduce fuel consumption by at least 50% over a wide range of urban/suburban pickup and delivery applications.

Objectives

In the target vehicle (a Kenworth K270 equipped with a 24' van body), the electrified powertrain will achieve at least a 50% fuel consumption reduction for a wide range of pickup and delivery work day drive cycles compared to the baseline powertrain (a Cummins 6.7L ISB diesel engine and automatic transmission).

The Kenworth K270 with the ETREE powertrain will be demonstrated in simulation, in a powertrain test cell, on a test track (SAE J1526 testing), and in fleet operation.

Approach

ETREE is a Cummins-led project with assistance from the following partners:

- PACCAR, Inc.,
- Argonne National Laboratory (ANL),
- National Renewable Energy Laboratory (NREL), and
- The Ohio State University (OSU)

The project will:

- Develop target entire work day duty cycles by employing NREL's FleetDNA and DRIVE Analysis Tools.
- Rely on simulation (by ANL, Cummins and OSU) to determine component requirements for a plug-in series hybrid.
- Build test vehicles which include:
  - The use of applicable electrified vehicle accessories,
  - Appropriate thermal management systems, and
  - An electric braking system (EBS) to promote kinetic energy recovery while maintaining conventional vehicle drivability.
- Employ a "test heavy" project schedule (simulation, powertrain test cell located at Cummins Technical Center, test tracks, and fleet operators) to confirm predicted results.
- Identify & deploy test vehicle(s) to fleet operators that would likely use these vehicles in production.

Results

Previously, the ETREE project developed the target work day duty cycles which are used to measure the project against its objectives. These work day duty cycles, denoted NREL 80 and NREL 100, are 80 and 100-mile duty cycles, respectively, applicable for use for class 6 pickup and delivery. Their required duty cycle energies are in the 80th and 95th percentile of all measured duty cycles available in NREL's FleetDNA database. In the past year, these work day duty cycles were shared with the industry by Adam Duran at the 2018 SAE World Congress.[6]

In FY2017, simulation against the work day duty cycles, and against typical class 6 performance metrics, ANL, Cummins and OSU identified the components as summarized in Table III.5.1. This component selection assured the fuel consumption reduction targets will be met on the work day duty cycles. Also in FY2017, the simulation results were validated in a powertrain test cell, equipped with a battery emulator at the Cummins Technical Center as shown in Figure III.5.1.

Table III.5.1 Summary of ETREE Powertrain Components

Component	Description
Traction Motor	160 kW permanent magnet traction motor
Transmission	Allison 3000 ETREE transmission with transmission input stop-start system
Nominal DC bus voltage	700 VDC
Energy Storage	112 kW-h NMC Li-ion battery
Range Extender – Generator	130 kW permanent magnet generator
Range Extender – Engine	155 kW ISB4.5 w/ full complement of aftertreatment components (diesel particular filter, selective catalytic reduction, diesel oxidation catalyst)
Final Drive Ratio	5.29

[6] Duran, A., Le, K., Kresse, J. and Kelly, K. entitled "Development of 80- and 100- Mile Work Day Cycles Representative of Commercial Pickup and Delivery Operation," SAE Technical Paper 2018-01-1192.

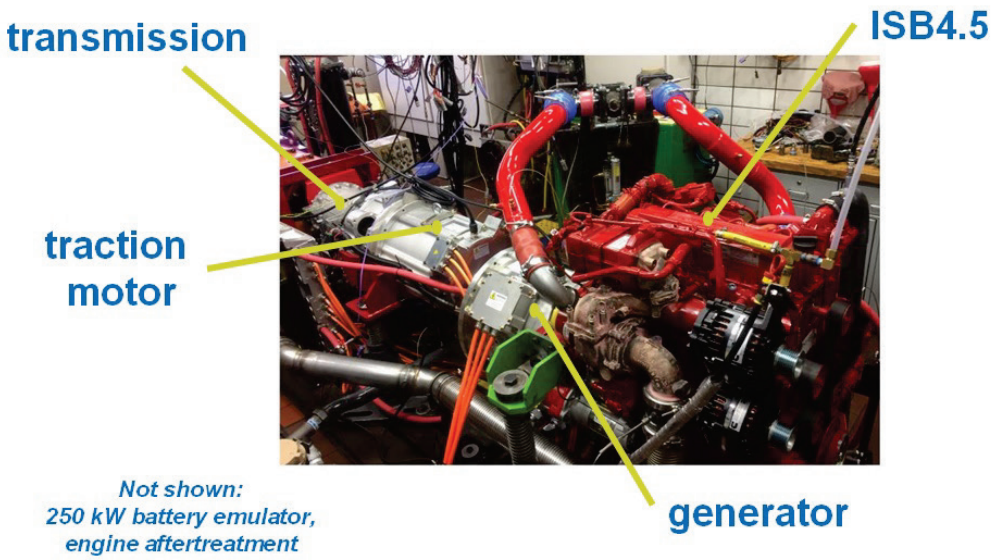

Figure III.5.1. ETREE powertrain test cell located at Cummins Technical Center, Columbus, Indiana

In FY2018, two test trucks were built based on the Kenworth K270 / Peterbilt Model 220 chassis. These trucks underwent validation testing where it was found that the original 112 kw-h NMC li-ion batteries did not exhibit the desired robustness for a demonstration project to be used at a customer location. Due to this reliability concern, the decision was made to create alternate batteries.

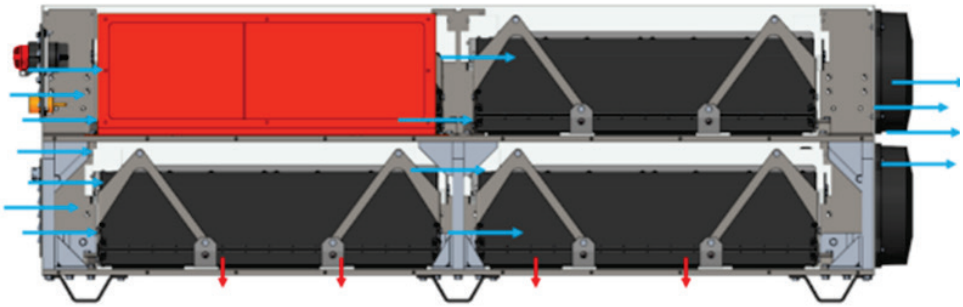

Figure III.5.2. ETREE alternate battery—drivers side enclosure (shown without cover)

An alternate battery (drivers side enclosure shown in Figure III.5.2), consisting of a nominal total energy capacity of 123 kw-h, was designed to fit the space-claim of the original batteries. This battery, consisting of 14 44V/200A-h production Li-ion battery modules – or 7 on each vehicle side – connected in series, was developed in less than four months. After construction, the battery underwent extensive testing at the Battery Innovation Center (BIC) in Newberry, Indiana. The full suite of tests was completed as scheduled, and the batteries are currently being integrated onto the test trucks. As the new batteries exceed the electrical energy capacity of the original batteries, the fuel consumption reduction potential of the updated ETREE system should exceed the original predictions.

Also in FY2018, working with WABCO (a supplier of commercial vehicle braking systems), controls software was developed to integrate an electronic braking system (EBS) with the traction motor's negative torque capability (typically used to recover vehicle kinetic energy during vehicle deceleration events). The objective of this "brake blending feature" is to enable a commercial electric vehicle to drive similarly to a conventional diesel truck under all driving conditions and battery state-of-charge. The next step in this task is to validate the functionality of this system on the test truck.

A key technical objective of the project is to demonstrate on a test track, during a J1526 test (employing a baseline and ETREE truck), the project fuel consumption targets are met. Planning with Southwest Research Center, who will administer the testing at a test track in Uvalde, Texas, has begun to define the test and procedures. This includes the modification of the target NREL 80 drive cycle, by NREL and Cummins, so that is more appropriate to operation on a test track while still containing similar energy requirements and drive cycle metrics.

A summary of key technical results is shown in Table III.5.2.

Table III.5.2 Summary of Technical Results for FY2018

Key Technical Result	Objective	Status
Build ETREE demonstration vehicle	Create two target work day duty cycles applicable to class 6 urban/suburban pickup and delivery	complete
Build alternate battery pack	Successfully built two 123 kw-h battery packs	complete
Test alternate battery pack	Tested in test cell at Battery Innovation Center in Newberry, Indiana; awaiting vehicle test	50% (test cell complete, awaiting vehicle test)
Install electronic brake system (EBS) brake blending system	For the first time in a North America commercial truck application, integrate a braking system which integrates foundation brakes and traction motor negative torque to enable a consistent driving experience across battery state-of-charge	60%; software & controls integration complete. Awaiting hardware install and vehicle validation
Measure fuel consumption reduction on test track-adjusted NREL 80 target cycle via J1526 test	Measure fuel consumption reduction on test track via J1526 testing administered by Southwest Research Institute at Uvalde, TX test track	Delayed until Feb 2019

Conclusions

The ETREE program team has developed an EV powertrain and related systems to meet the project goals. The team has validated the powertrain in a powertrain test cell. While validating the test truck, the high voltage battery did not exhibit the required robustness for a system that will ultimately be delivered to a customer. Therefore, the decision was made to develop a robust battery, based on existing production battery components; this decision delayed the project by roughly four months.

The alternate batteries, which have a slightly greater energy capacity and therefore promise to exceed the initial fuel reduction goals, have been successfully tested, off-vehicle. The team is working to complete the updated vehicle validation test plan which will culminate in a J1526 fuel consumption test operated by Southwest Research Institute at a test track located in Uvalde, Texas.

Key Publications

1. The following technical paper, based on ETREE project work, was presented at the 2018 SAE World Congress:
   Title: Development of 80 and 100 Mile Work Day Cycles Representative of Commercial Pickup and Delivery Operation
   Primary Author: Adam Duran of NREL
   Additional Authors: Ke Li and John Kresse of Cummins, Ram Vijayagopal of ANL
2. The following technical paper, also based on ETREE project work, was presented at the 2018 ASME Dynamic Systems and Controls conference:
   Title: Battery Discharge Strategies for Energy Management in Electrified Truck for Pick-up and Delivery Application
   Primary Author: Mukilan Arasu
   Additional Authors: Qadeer Ahmed and Giorgio Rizzoni

III.6 Medium Duty Vehicle Powertrain Electrification and Demonstration (McLaren Engineering)

Mr. Wiley McCoy, Principal Investigator
McLaren Engineering div of Linamar
32233 W Eight Mile Road
Livonia, MI 48152
E-mail: Wiley.Mccoy@Linamar.com

Lee Slezak, DOE Technology Development Manager
U.S. Department of Energy
E-mail: lee.slezak@ee.doe.gov

Start Date: June 1, 2016 End Date: March 20, 2020
Project Funding: $3,650,000 DOE share: $2,640,000 Non-DOE share: $1,010,000

Project Introduction

This project is intended to address a number of technical barriers regarding use of electric / hybrid drive systems in the medium duty marketplace as described in the Vehicle Technologies Multi-Year Program Plan. Specifically, the technical barriers are:

- Acceptance of electric drive as Medium Duty vehicle choice.
- Reduce the carbon footprint of transportation (FE Improvement)
- Cost of hybridization (medium duty TCO)

A team consisting of industry leading engineering, production and user companies was formed to specify, design, build and test a commercially viable medium duty drive system that would reduce fossil fuel use by a minimum of 50% in real world drive cycles. McLaren Linamar, AVL, & UPS are partnered to achieve the program objectives.

Objectives

Project Objective / Expected Outcome - to attain a 100% improvement in Fuel Economy over real world drive cycles for medium duty package delivery vehicles & achieve a system at project conclusion that can be commercialized at a reasonable Total Cost of Ownership.

Approach

Project Approach - Team has developed the hybrid system specifications in simulation and completed the first milestone by showing a 100% fuel economy improvement over real world drive cycles measured over UPS delivery routes. This completed the first phase of the program. The second phase, which is still in progress, is to design and develop a plug-in hybrid powertrain, incorporating a novel medium duty electric drive axle. The team is in the process of building and commissioning 4 demonstration vehicles and will conduct a demonstration of performance, cost and reliability for a period of up to 12 months.

Future work will include a third phase of system demonstration. This demonstration will commence in Q1 of the 2019 CY. At present, the team is in the process of final build and commissioning of the demonstration vehicles. McLaren / Linamar is responsible for design and build of the eAxle; AVL has simulated the system & design, built and installed in one vehicle the energy storage and range extender systems. In a change to program responsibilities, McLaren will take over the final build and commissioning responsibilities and will use other suppliers of build services to complete the vehicles for the demonstration. UPS will conduct the demonstration on real world package delivery routes and transmit data back to the McLaren team for ongoing analysis of performance, durability and reliability. This project is intended to support commercialization of the

system. An analysis of the system cost and complexity, as well as a calculation of total cost of ownership will also be completed with the support of UPS. At the end of or during the demonstration phase a decision will be made regarding commercialization of the systems on a broader group of package delivery vehicles.

Results

In the 2018 FY, the entire time was used to source components, build initial units, test both sub-systems and the full axle system, build energy storage systems, source and build range extender systems, and complete the physical build of one vehicle for calibration work. The other 3 units are in various states of completion. Large challenges arose during this FY. The first and most critical was the slow delivery of key components from contracted suppliers. The extremely late deliveries pushed back sub system build and the assembly of the vehicles. The second major challenge was that testing of the subsystems revealed the need for updates to create a reliable and durable system for the demonstration. It was agreed by all stakeholders that delays should be minimized but not at the expense of achieving a highly reliable product. These delays also necessitated a shift in work share among the participants for completing and commissioning the vehicles and for support during the demonstration phase. This plan was developed and enacted by McLaren.

The technical results achieved in this FY were to complete phase 2 (April 30, 2018). The technical deliverable was to demonstrate that the 100% Fuel Economy improvement was attained. This occurred through the running of Veh 1 systems as a Hardware-in-the-loop setup on the AVL dyno in CA using the UPS drive cycle that would be a simulation of the routes being used in the demonstration. The results were favorable and showed compliance with the phase exit criteria.

Phase 2 Technical Milestones Completed

- The Designs Were Completed, Released And Sourced.
- The Procurement, Assembly And Test Of Sub-Systems Have Been Completed.
- Vehicle 1 Powertrain Has Been Assembled And Tested For FE Improvement

Below are a final layout drawing of the hybrid system as shown for the Ford chassis builds and a series of photos showing some of the sub-systems in built or/or test conditions.

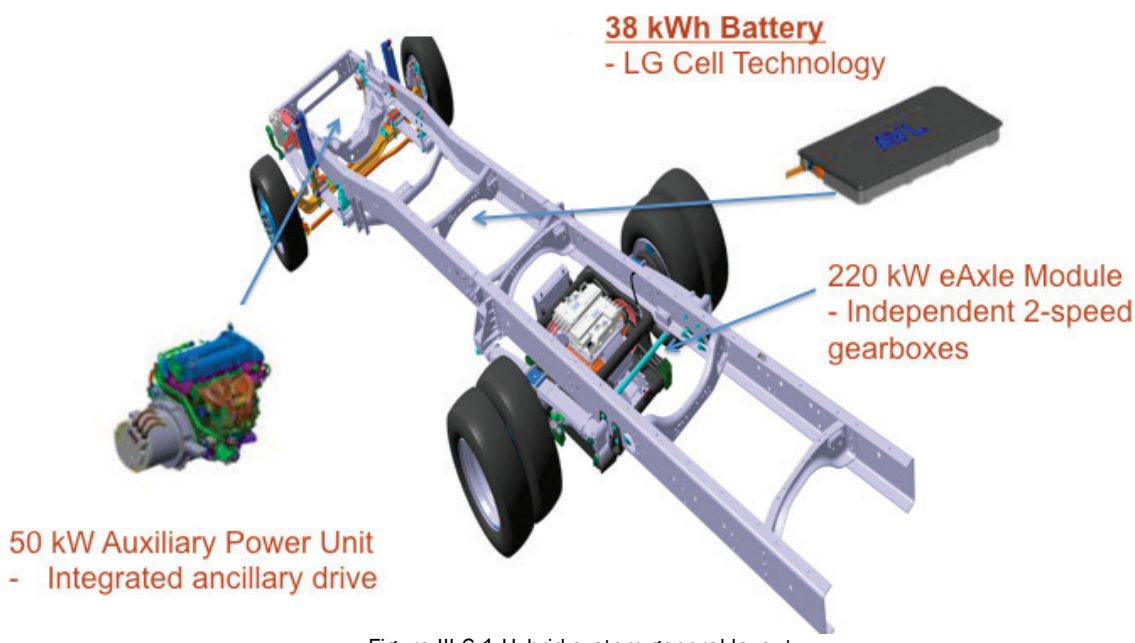

Figure III.6.1 Hybrid system general layout

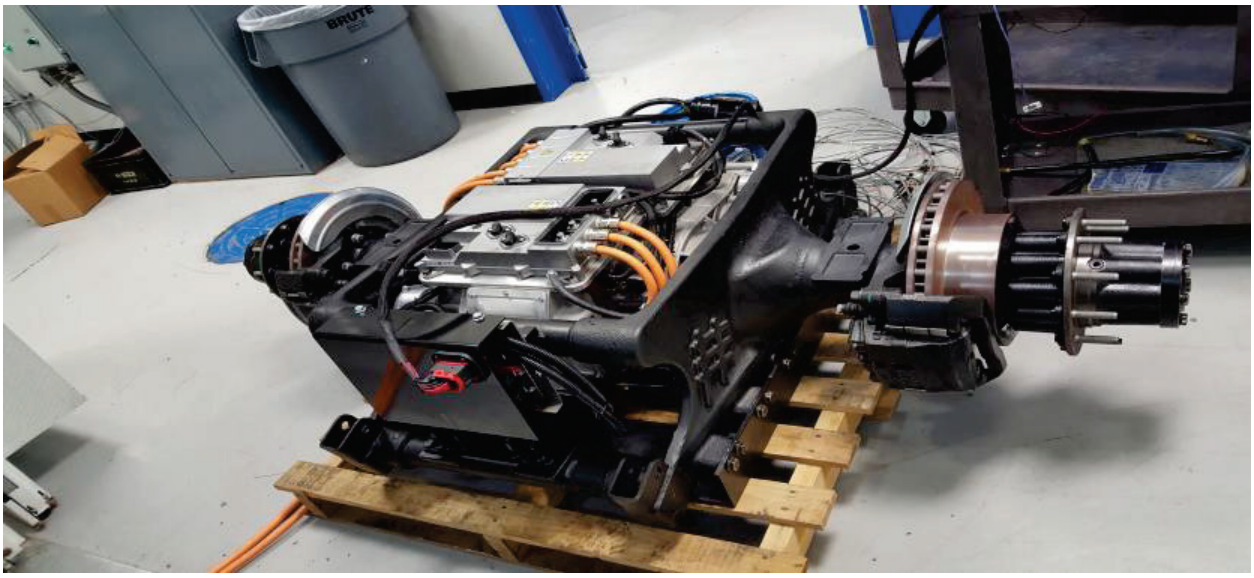

Figure III.6.2 Complete eAxle system

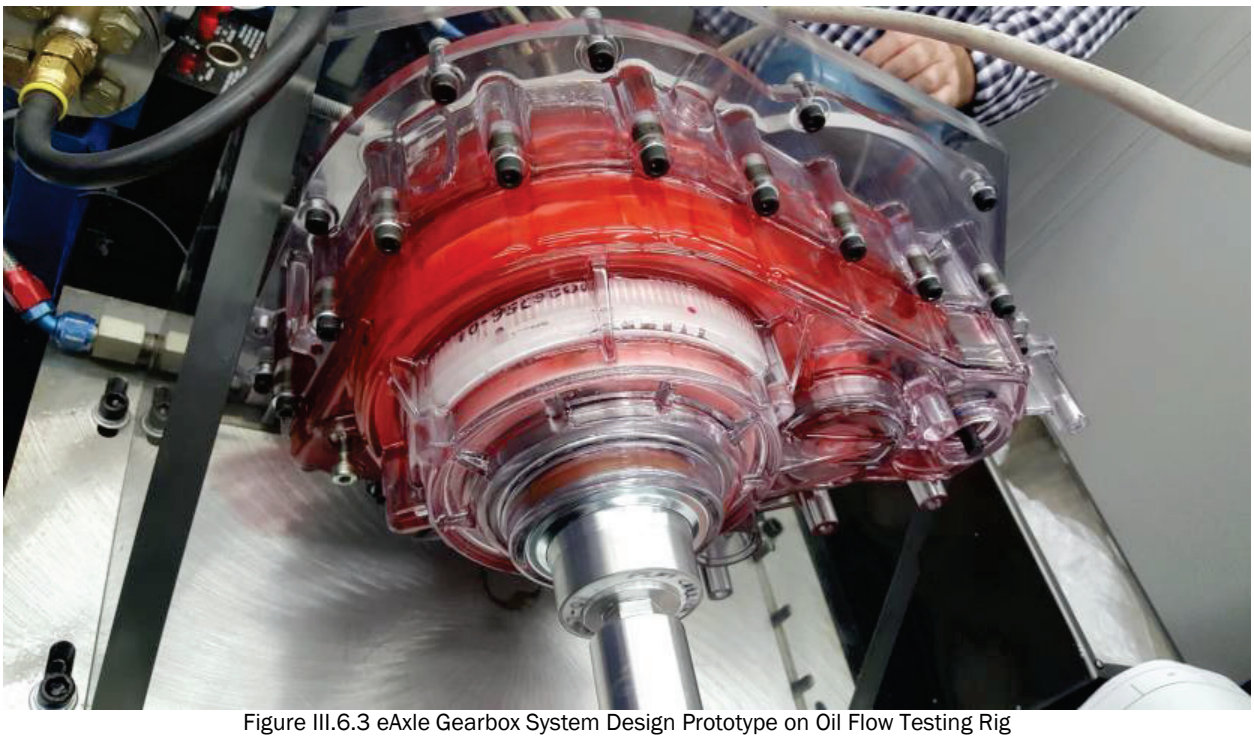

Figure III.6.3 eAxle Gearbox System Design Prototype on Oil Flow Testing Rig

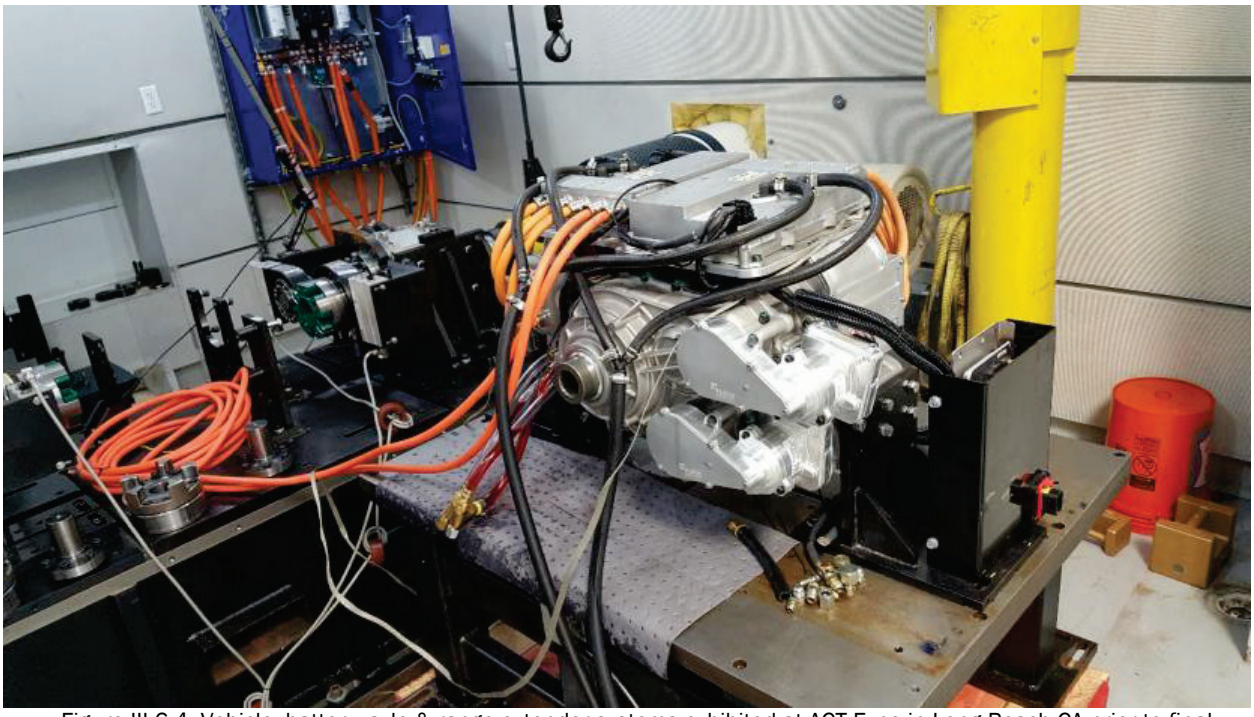

Figure III.6.4 Vehicle, battery, axle & range extender systems exhibited at ACT Expo in Long Beach CA prior to final assembly of demonstrator. These are actual demonstrator subsystems.

Figure III.6.5 Oil lube flow testing of completed eAxle system

Conclusions

As of the end of FY18, the conclusions of this program to date are:

1. A system can be designed and built using advanced modeling and simulation tools that will demonstrate an electrified vehicle powertrain system that will achieve the overall program objectives.
2. A novel eAxle system, energy storage & range extender systems have been built and tested for installation and final calibration in 4 demonstration vehicles. Vehicle 1 is the primary system development vehicle.
3. The timing of a 4-vehicle demonstration on real world package delivery routes has taken more time that originally anticipated primarily due to supplier delays and subsystem development issues. The demonstration can commence in Q1 of CY 2019.
4. Commercial interest has been confirmed. The results of the demonstration will determine the magnitude of full volume production that could be attained through by providing data for an accurate TCO. (Total Cost of Ownership)

III.7 Bidirectional Wireless Power Flow for Medium-Duty Vehicle-to-Grid Connectivity (CALSTART)

Omer C. Onar, Technical Principal Investigator
Oak Ridge National Laboratory, Power Electronics and Electric Machinery Group
National Transportation Research Center, 2360 Cherahala Boulevard
Knoxville, TN 37932
E-mail: onaroc@ornl.gov

Steven Sokolsky, Project Principal Investigator
CALSTART
1509 Wendy Ln.
Madison, WI 53716
E-mail: ssokolsky@calstart.org

Lee Slezak, DOE Technology Development Manager
U.S. Department of Energy
E-mail: Lee.Slezak@ee.doe.gov

Start Date: October 1, 2016 End Date: December 30, 2019
Project Funding: $2,631,321 DOE share: $1,949,007 Non-DOE share: $712,314

Project Introduction

Wireless power transfer (WPT) is a paradigm shift in electric-vehicle (EV) charging that offers the consumer an autonomous, safe, and convenient option to conductive charging and its attendant need for cables. With WPT, charging process can be fully automated due to the vehicle and grid side radio communication systems, and is non-contacting; therefore, issues with leakage currents, ground faults, and touch potentials do not exist. It also eliminates the need for touching the heavy, bulky, dirty cables and plugs. It eliminates the fear of forgetting to plug-in and running out of charge the following day and eliminates the tripping hazards in public parking lots and in highly populated areas such as shopping malls, warehouse loading areas, recreational areas, parking buildings, etc. Furthermore, the high-frequency magnetic fields employed in power transfer across a large air gap are focused and shielded, so that fringe fields (i.e., magnetic leakage/stray fields) attenuate rapidly over a transition region to levels well below limits set by international guidelines for the public zone.

With the bidirectional wireless power transfer, not only vehicles can be wirelessly charged, but also the vehicles can wirelessly provide power back to the grid or the facility. With bidirectional power flow, vehicles can be enabled to provide microgrid or grid support or ancillary services. Grid support may include peak shaving, renewable energy firming/integration, time of use energy management, power quality improvement, voltage regulation, reactive power compensation, etc. Grid ancillary services to be provided might include spinning and non-spinning reserves, area/frequency regulation, load following, scheduling and dispatch, etc. In the case of an outage, vehicle batteries can also serve as an emergency backup power for a period of time.

In this project, CALSTART, ORNL, UPS, Workhorse Group, Cisco Systems, and the University of Tennessee, Knoxville proposed to model, research, analyze, design, develop, integrate, and demonstrate a bi-directional wireless power transfer system (BWPT) suitable for Class 5 and Class 6 medium-duty PHEV delivery trucks. The project team will design, develop, integrate, and test a bi-directional wireless charging system capable of meeting the 11-inch ground clearance needed for UPS delivery trucks. After integrating to a Workhorse manufactured plug-in hybrid electric vehicle (PHEV), the system performance will be demonstrated at the deployment site. Within the first budget period of the project (May 2017-May 2018), team has completed the modeling, simulations, design, and analysis of the system power conversion stages including the 3-phase active front-end rectifier with power factor correction (also grid interface inverter), primary-side high-frequency inverter (also primary-side rectifier), primary and secondary-side resonant tuning components,

primary and secondary-side electromagnetic coupling coils, vehicle-side high-frequency rectifier (also the vehicle-side high-frequency inverter). As of submission time of this report, we are 6 months into the second budget period in which we develop, test, and integrate the hardware for the power conversion stages. Once all the power conversion stages are tested individually and as a whole system, vehicle integrations will be completed. In the last budget period, system will be deployed with full vehicle integrations for the testing, demonstrations, and data collection purposes.

Objectives

The overall project objectives can be summarized as follows:

1. Provide an automated, high power, interoperable, high-efficiency wireless charging of plug-in electric medium duty delivery trucks with a nominal ground clearance of approximately eleven (11) inches.

2. Optimize the add-on vehicle-side wireless charging components through integration and utilization of already existing vehicle-side components while implementing grid-side controls and regulations to reduce the vehicle-side cost, size, volume, and complexity.

3. Utilize bi-directional wireless charging systems when trucks are parked in the yard for staging to provide grid support applications or ancillary or grid support services such as frequency regulation, load leveling/peak shaving/load factor improvement/reactive power support/demand charge management, and spinning/non-spinning reserves.

4. Provide an integrated > 20kW wireless charging system (grid to vehicle) with high efficiency (85%) while meeting the international guidelines on electromagnetic and electric field emissions during charging and include all other appropriate safety features.

5. In vehicle-to-grid mode, achieve 6.6kW wireless power transfer to building or grid loads.

6. Provide modeling and analysis of the benefits of wireless charging technology with respect to operational efficiency improvements and overall vehicle and building energy efficiency.

Approach

Starting from the AC grid to the vehicle battery terminals, the system power converters must be well designed and operated in order to achieve high efficiency. In addition, power flow control to the pick-up system should be resolved where the control parameters (DC link voltage, frequency, duty cycle, phase-shift, etc.) are actively controlled to improve efficiency while meeting the vehicle-side target voltage, current, and/or power. Simultaneously, vehicle-side DC link or battery voltage, current, temperature, and the state-of-charge (SOC) should be carefully monitored and fed-back to the primary side for controls. Moreover, the battery management system (BMS) or other vehicle-side converters (onboard chargers or DC/DC converters) should be monitored for safety. The bidirectional wireless charging system that will be used in this project is shown in Figure III.7.1. This is the overall system architecture that is determined and agreed upon by the technical team. For this architecture, the baseline performance metrics have been defined and system specifications are currently being worked on as the proper sizing of the power electronic devices and passive components are important to meet the vehicle charging demands. Since the overall system architecture is now defined, the team is cascading down the system design to the subsystems, including both the grid and vehicle sides, and then to the components for hardware fabrication. As shown in Figure III.7.1, system utilizes a three-phase rectifier/inverter system that interfaces the system to the grid. During charging, an active-front end rectifier with power factor correction (PFC), delivers power from the grid with high power factor to the high frequency power inverter's input. The input (grid) current is controlled in order to regulate the inverter input voltage, depending on the amount of power to be transferred to the battery. The high-frequency power inverter generates the high-frequency current for the primary coupling coil. The high-frequency transformer between the inverter and the primary coil provides galvanic isolation for safety and protection of the equipment. The transformer also provides voltage matching for the system and provides control flexibility for the voltage. On

the vehicle side, there is a receive coil with a tuning capacitor, a rectifier/inverter, and a filter capacitor. During discharging or vehicle battery powering the AC grid/building loads, the vehicle-side converter is operated in an inverter mode and delivers high-frequency current to the vehicle coil. The vehicle-side coil generates a magnetic field that is linked to the ground coil. The ground coil induces a high frequency voltage that is rectified and inverted to 60Hz to power the building loads or to provide power to the AC grid.

Figure III.7.1 System level diagram of the proposed architecture for the bidirectional wireless charging system.

The first step in the design process was to determine the architecture of the active front-end rectifier/inverter which is a bidirectional grid interface converter. Technical team performed a very comprehensive literature review on three-phase bidirectional grid-connected power electronics interfaces. Among other candidate interface topologies, team determined to use the two-level voltage source converter (VSC) due to the

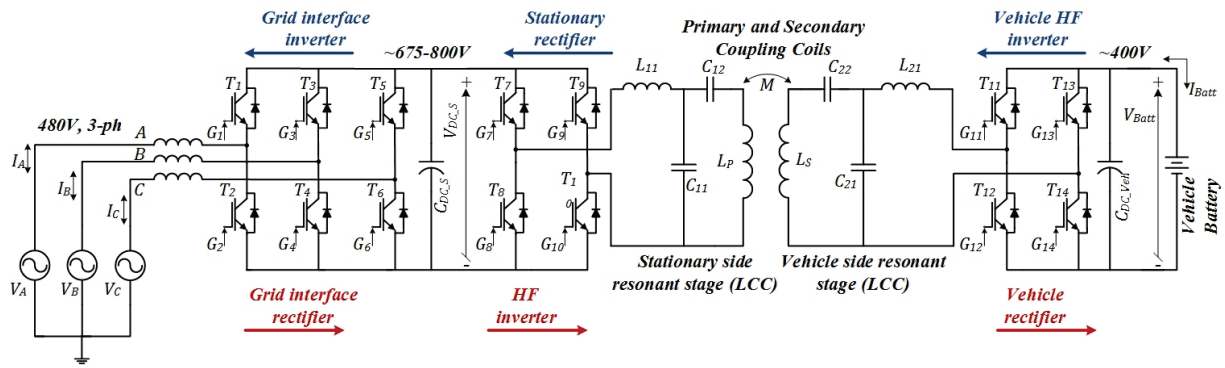

advantages among the other topologies. For the primary-side high-frequency inverter/rectifier as well as the vehicle-side high-frequency rectifier/inverter, the converter topology is designed to be a full-bridge converter with two phase-leg modules per converter. The active front-end grid interface converter design parameters are summarized in Table III.7.1.

Table III.7.1 Grid Interface Converter Design Parameters

Parameter	Description	Value
$R_a=R_b=R_c=R$	Three-phase AC line resistance	5 mΩ
$L_a=L_b=L_c=L$	Three-phase AC line indcutance	~750 μH
$V_{an}=V_{bn}=V_{cn}$	Three-phase phase-to-neutral RMS voltage	277V (480 phase-to-phase)
f	Nominal grid frequency	60 Hz
V_{DC}	Nominal DC bus voltage	800 V
P_N	Nominal power	> 20 kW
C_{DC}	DC bus capacitor	1 mF
S for pf=0.6	Apperant power rating	40 kVA

Next, team has designed the resonant stage of the system along with all the resonant tuning components which is optimized to deliver the rated power from the 800V dc bus to vehicle battery with 650V nominal voltage. The specifications of the coupling coils are provided in Table III.7.2 while Figure III.7.2 shows the resonant tuning and coupling coil component parameters. Figure III.7.3 represents the three-dimensional CAD model of the coupling coils.

Table III.7.2 Grid Interface Converter Design Parameters

Parameter	Inductance	Dimensions	Turns	Ferrite mass	Wire mass	Plate mass	Total mass
Primary	133 μH	34×28.5×1.5"	7	59.8 lbs.	15.2 lbs.	109 lbs./in	102 lbs.
Secondary	123 μH	34×28.5×1.5"	6.5	59.8 lbs.	14.3 lbs.	109 lbs./in	102 lbs.

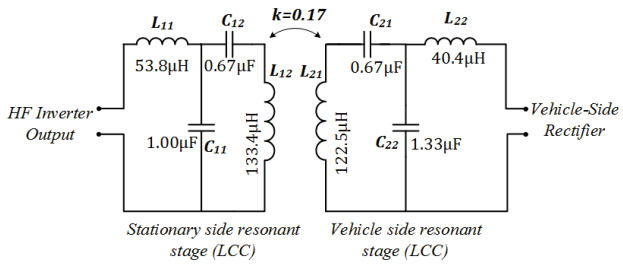

Figure III.7.2 System resonant stage parameters.

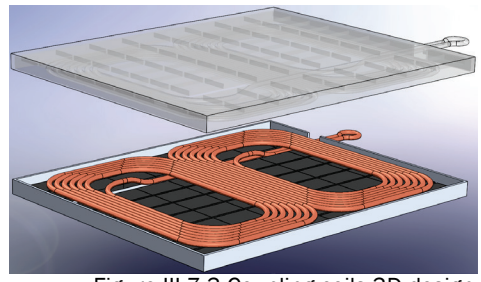

Figure III.7.3 Coupling coils 3D design.

The physical coils built at ORNL is shown in Figure III.7.4 while Figure III.7.5 shows the electromagnetic field distribution analysis of the couplers.

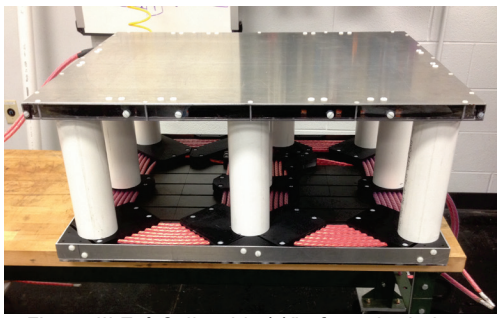

Figure III.7.4 Coils with 11" of nominal airgap.

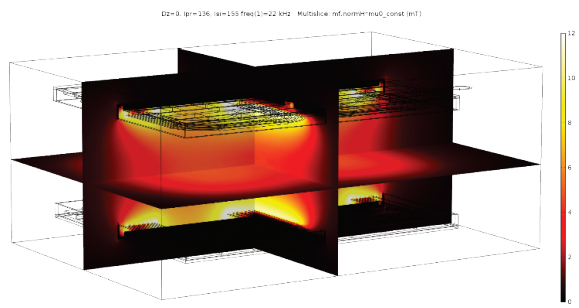

Figure III.7.5 EM field distribution analysis of the coils.

Along with the coupling coils, team also has completed the design and hardware development of the resonant tuning inductors for both primary and secondary-sides as well as the 3-phase grid-side inductors. Design details of the grid-side inductor and the primary and secondary-side inductors are summarized in Table III.7.3. Figure III.7.6 shows the physical inductors built for the project.

Table III.7.3 Design Parameters of the Grid-Side and Primary and Secondary-Side Resonant Inductors

Parameter	Grid-side inductor	Primary-side inductor	Secondary-side inductor
L	0.75 mH	52.6 μH	39.5 μH
I_{rms}	53.03 A	45 A	55 A
Core	AMCC500	0R49928EC	0R49928EC
Al	0.38 μH/trn	6.227 μH	6.227 μH
# of turns	50	23	20
Airgap	4 mm	9.33	9.39
B_{max}	1.1781	0.197	0.208
Volume	481.25 cm³	202	202
Core loss	0.4268 W	11	12.64
f	60 Hz	22 kHz	22 kHz

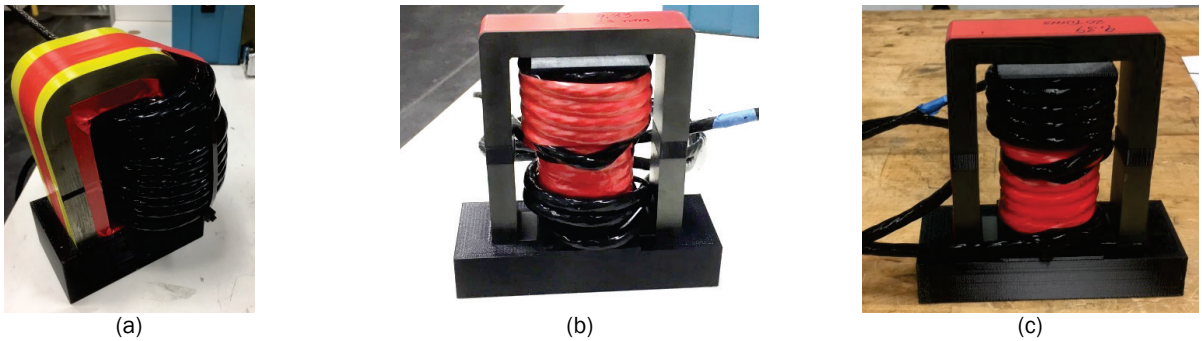

(a) (b) (c)

Figure III.7.6 Grid interface inductor (1 of the 3) (a), primary-side (b), and secondary-side (c) resonant tuning inductors.

For all the components built, the design target values and the actual (physical) component values are represented in Table III.7.4. As shown in this table, all of the component parameters are closely matching the design target values.

Table III.7.4 Design Parameters of the Grid-Side and Primary and Secondary-Side Resonant Inductors

Component	Design Target	Physical Value	% Error
Grid interface inductors	$L_A=L_B=L_C \geq 0.75$ mH	$L_A=L_B=0.910$ mH, $L_C=0.905$ mH	NA, 0.9 mH is better
Primary tuning inductor L_{11}	$L_{11}=53.8$ µH	$L_{11}=54$ µH	0.37%
Primary tuning capacitor C_{11}	$C_{11}=1$ µF	$C_{11}=1.02$ µF	2%
Primary tuning capacitor C_{12}	$C_{12}=0.67$ µF	$C_{12}=0.669$ µF	0.15%
Primary coil L_{12}	$L_{12}=133.4$ µH	$L_{12}=128.5$ µH	3.6%
Secondary tuning inductor L_{22}	$L_{22}=40.4$ µH	$L_{22}=41.18$ µH	1.93%
Secondary tuning capacitor C_{22}	$C_{22}=1.33$ µF	$C_{22}=1.336$ µF	0.45%
Secondary tuning capacitor C_{21}	$C_{21}=0.67$ µF	$C_{22}=0.668$ µF	0.30%
Secondary coil L_{22}	$L_{22}=122.5$ µH	$L_{12}=123.2$ µH	1.83%

Results

Simulation results include the grid interface converter 3-phase voltage and current waveforms in charge and discharge mode of operations which is transitioned at t=0.25 second as shown in Figure III.7.7. As seen from this figure, harmonic distortions on the grid current is minimal. During the charging, grid voltage and current sinusoidal waveforms are in phase while in discharge mode, they have 180° phase-shift between the voltage and current.

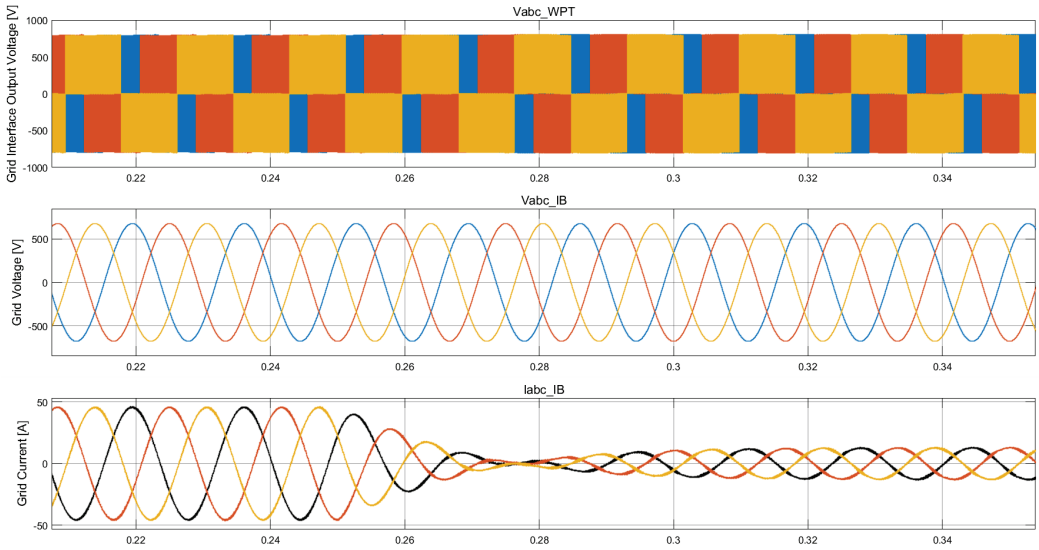

Figure III.7.7 Simulation results of the grid interface converter with charge mode (t<0.25s) and discharge mode (t>0.25s).

Simulations also include the resonant stage characterization and sensitivity analysis to the coupling factor and the load variations under various conditions as a function of the operating switching frequency. As shown in Figure III.7.8, inverter output current automatically gets adjusted to the coupling factor variations which simplifies the control system. System also exhibits coupling factor independent constant current source at the primary coil at the resonant frequency. The phase angle between the inverter output and current is also constant and equals to 0° at resonant frequency. In Figure III.7.9, system response under load variations is presented. While the inverter output current is adjusted to the load level, primary coil current is still constant regardless of the load. Primary coil operates as a load-independent current source in all operating conditions. Inverter also operates with unity power factor regardless of the load and coupling factor. In Figure III.7.10, the dc-to-dc and high-frequency resonant side voltage and current waveforms are presented for both charging and discharging modes of operation. From top, waveforms show the inverter input voltage and current, inverter output voltage and current, primary coil voltage and current, secondary coil voltage and current, and the load voltage and current.

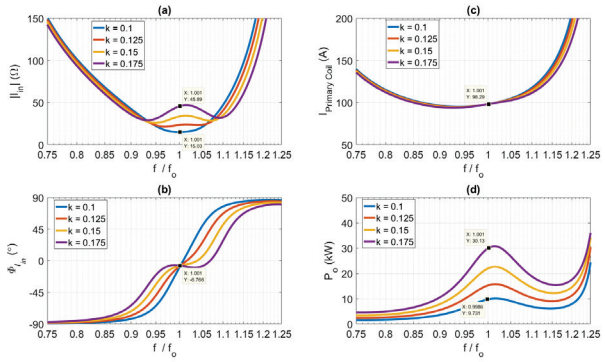

Figure III.7.8 Coupling factor sensitivity analysis.

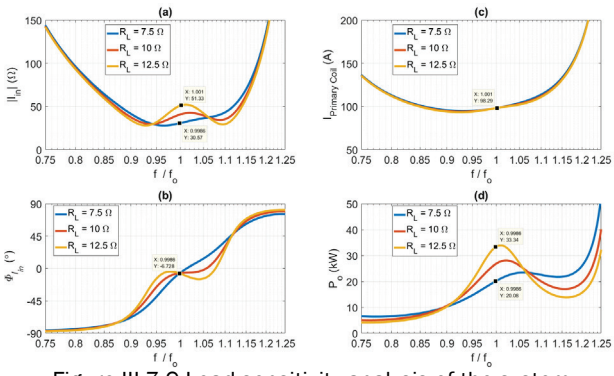

Figure III.7.9 Load sensitivity analysis of the system.

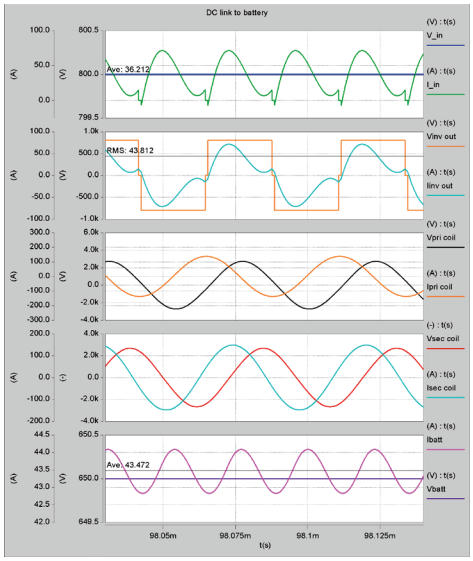

Figure III.7.10 Charge-mode simulation waveforms.

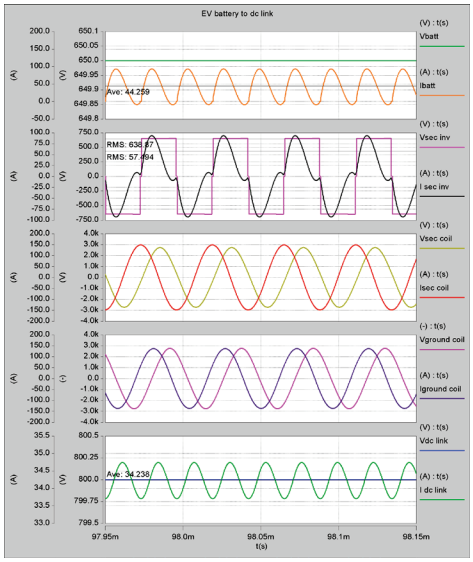

Figure III.7.11 Discharge-mode simulation waveforms.

Conclusions

From the start of this project in May 2017, the team has been working on modeling, simulations, analysis, and design of the system power conversion stages. Upon the successful design review meeting in May 2018 which concluded the first budget period of the project, team started building the hardware of all the system power conversion stages along with the control systems. This report focuses on the progress made on the component and subsystem design of the system along with the component value tests and verifications. During the rest of the budget period, the hardware will be completed which will be followed by performing the functionality testing of all the power conversion stages. Then, the system will be bench top tested as a whole system prior to the vehicle integrations.

Key Publications

1. Conference paper: "*Secondary Active Rectifier Control Scheme for a Wireless Power Transfer System with Double-Sided LCC Compensation Topology*," to be included in the Proceedings of the 44th Annual Conference of the IEEE Industrial Electronics Society (IECON), October 21-23 2018, Washington, D.C.

Acknowledgements

Project team would like to thank Mr. John Jason Conley of the National Energy Technology Laboratory (NETL) for his continuous guidance and support on this project.

III.8 Comprehensive Assessment of On-and Off-Board Vehicle-to-Grid Technology Performance and Impacts on Battery and the Grid (Electric Power Research Institute (EPRI)) [DE-EE0007792]

Sunil Chhaya PhD, Principal Investigator
Electric Power Research Institute (EPRI)
3420 Hillview Ave, Palo Alto, CA 943041338
E-mail: schhaya@epri.com

John J. Conley, DOE Program Manager
U.S. Department of Energy/NETL
E-mail: john.conley@netldoe.gov

Start Date: October 1, 2016 End Date: December 30, 2019
Project Funding: $2,786,278.00 DOE share: $1,547,678.00 Non-DOE share: $1,238,600.00

Project Introduction

There is heightened interest in the value for Vehicle-to-Grid (V2G) applications to provide energy management services to support grid reliability and resiliency. The research community is seeking to maximize the total value of a vehicle by exploring other services beyond transportation, but the automotive manufacturing and transportation battery communities remain reluctant to embrace V2G applications because of uncertainties associated with the exposure to grid applications and concerns about potential degradation of the transportation battery. Also, there are the challenges for enabling V2G technology development of bidirectional power electronics with the functionality, communications, and controls that are compliant with applicable regulatory and safety requirements, and standards. This proposal is to address the automotive industry concerns and the regulatory challenges to V2G technology.

The requirements for grid interconnected bidirectional inverters impose significant challenges to the automakers for on-vehicle inverter V2G functionality Automakers self-certify their vehicles to Society of Automotive Engineers (SAE) and Federal Motor Vehicle Safety Standards (FMVSS) requirements, and do not submit vehicles to National Recognized Test Laboratories (NRTL) such as UL. SAE is addressing this by developing SAE J3072 "Interconnection Requirements for On Board Utility Interactive Inverter Systems" providing communications and process requirements for validating the on-vehicle inverter certification. It incorporates the test certifications required by UL 1741 and requirements of IEEE1547. Acceptance by utilities of a J3072 compliant vehicle inverter certification is an open issue. As a part of a collaborative California Energy Commission program the team evaluated and verified these requirements for on-vehicle bidirectional inverters.

In contrast, off-vehicle inverter enabled V2G using DC charging avoids the issues and challenges relative to on-vehicle V2G inverters. DC chargers contain the charge control electronics and are a location fixed asset that is hard wire connected to the grid. Because DC chargers are a fixed standalone product they can easily be UL tested, certified, and site permitted. No vehicle UL certification would be required. The vehicle is only required to be DC charge capable with embedded J2847/2 communications software and J2931/1 power line communications (PLC) compliant connectivity with the DC charger which is standard with all DC charge capable Electric Vehicles.

The DC charger integrated off-vehicle bidirectional inverter is the most viable strategy and less challenging method for automakers to engage in commercialization of V2G as a distributed resource. However, there are still the automaker concerns with battery capacity degradation from V2G cycling and impacts on warranty services. This DOE project is to address the development, implementation, and verification of DC charging

integrated off-vehicle bidirectional inverter enabled V2G; and to assess the impact of V2G cycling on battery durability. Also, will be working with the SAE J2847/2 task force in the development and testing of the control messaging requirements and protocol for V2G communications that is presently ongoing.

Objectives

The objective of the program is to test and evaluate grid DER management / integration use cases using V2G bidirectional power flow (charging and discharging) integrated with solar and stationary energy distributed resources in the AC (on-vehicle) and DC (off-vehicle) domains. The outcome is data to be analyzed and evaluated for performance, durability, and usage characteristics of the V2G technology, and impacts on battery life and vehicle components. As such, the proposal involves evaluation of Vehicle to Grid (V2G) technologies for on-vehicle (AC) and off vehicle (DC) bi-directional inverters thereby providing the best research value for the DOE.

The project goals are:

- Provide experimental and analytical basis to V2G technology as a key enabler in improving the value of owning a Plug-in Electric Vehicle.
- Demonstrate the usefulness of off-vehicle Smart Power Integrated Node (SPIN) system to further enhance the value of V2G by enabling increased renewable generation on the grid and providing Vehicle to Home type services in conjunction with on-vehicle and off-vehicle storage.
- Provide experimental and analytical basis for assessing effect on EV batteries from their application to grid services
- Provide key metrics for evaluation of performance and value of an off-vehicle V2G system in comparison to an on-vehicle V2G system
- Assess the effect of transformer constraints on grid service implementation
- Provide analytical framework and research results on the valuation of V2G services for high-impact (high-stress) regions of the distribution grid

Approach

The project is the comprehensive development, testing, and evaluation of Vehicle to Grid (V2G) and energy management technologies for on-vehicle bidirectional inverters, through a companion cost share project and for off-vehicle bidirectional inverters, through this DOE funding request. Figure III.8.1 provides a representative overview of the two V2G projects. The cost share funded project focuses on the effects of V2G energy management on the distribution system using on-vehicle inverter enabled bi-directional power flow to balance solar output for improved grid reliability and stability, including an economic evaluation of V2G services.

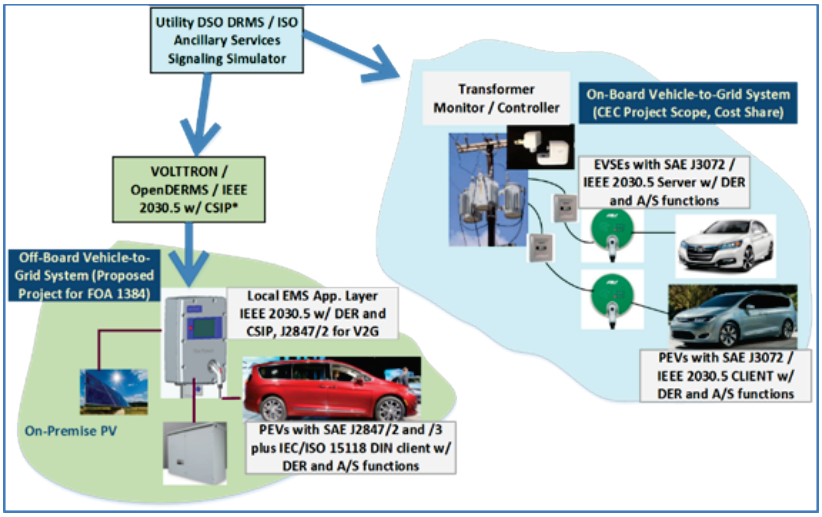

Figure III.8.1 Project Structural Overview of On-Vehicle AC and Off- Vehicle DC V2G

The focus of this DOE project is to develop, test, and demonstrate off-vehicle inverter enabled bidirectional power flow (V2G) utilizing a DC charging bi-directional converter integrated into a Smart Power Integrated Node (SPIN) system. The communications, control, and interface functionality for the SPIN system will be based on SAE standards (SAE

J2847/2, J2931/1, J2931/4). The intent is to demonstrate a fully functional, grid-compatible DC charging based V2G end-to-end system that provides secure, interoperable communications and information processing.

The uniqueness is the SPIN system capability to control and process power flow between PEVs (charging/discharging), the grid, local solar and backup energy storage with a single multifunctional modular unit. The SPIN system will synchronize these energy sources to act as dispatchable DER. Innovation lies within the development of V2G with DC bi-directional charging, and support of local Distributed Energy Resource (DER) integration use cases that will accelerate the deployment of V2G as a part of an integrated DER ecosystem.

The project is to achieve the objectives through accomplishment of the following activities:

- Development/fabrication of the Smart Power Integrated Node System hardware integrating a bidirectional dual active bridge converter using Wide Band Gap SiC power module technology with DC charging functionality (6.7kW to 10kW).
- Development/integration of the system control and communications software utilizing standards based protocols with interoperability between the SPIN system, utility or Energy Service Provider, and the PEV. This includes the development/integration of Energy Management System (EMS) control algorithms and functionality in the SPIN hardware for integrating V2G with solar and back up energy storage as coordinated distributed energy resources. Expectation is to extrapolate data on customer value and utility benefits for V2G DER integration.
- Develop/test determined cycle plan based on selected grid service use cases in both a lab environment and subsequently in a vehicle field demonstration. Evaluate battery life and conduct battery durability impact testing and analyses
- Conduct a field or in-lab demonstration of the V2G grid service use cases utilizing 3 to 5 Fiat Chrysler Pacifica PHEVs fully developed SPIN systems. The systems will be connected to a single transformer to allow evaluation of the grid impact from clustered EV charging and discharging.

The design, component technical specification, and simulation of the SPIN bidirectional converter has been completed by Flex Power Control (FPC) under a Technology Innovation contract from EPRI. ORNL has had specific experience in the development and integration of Wide Band Gap Silicon Carbide (SiC) power module devices in inverter systems for electric drive propulsion systems, and will provide engineering expertise to evaluate, test and verify the SPIN system design. Hardware fabricator Current Ways has established expertise and knowledge in power electronics manufacturing engineering and in UL certification processes. FPC, ORNL, and Current Ways have an established interaction on the design for the SPIN system and are collaborating on the design and fabrication of the FPC-designed SPIN technology.

The SAE J2847/2 and J2847/3 standards incorporating the required PEV/charger communications for PEV reverse power flow are in progress. EPRI is a working member of the SAE Task Force and is engaged in the development of these standards. This project will correlate with the development of the standards and provide a basis for verification of the determined communications requirements.

Kitu Systems is presently developing the IEEE 2030.5 software into the AeroVironment EVSE for the CEC V2G project, which will be leveraged to successfully implement the software for the SPIN system. Additionally, EPRI will work with Fiat Chrysler to implement the required J2847/2 communications for V2G, which are based on the DIN 70121 protocol, into the Pacifica Mini Van PHEVs for the field demonstration.

EPRI has been working to develop and deploy DER management control algorithms in another project in Southern California around a community of Zero Net Energy homes, and these control algorithms will utilize the underlying stack developed by Kitu Systems that creates open standards-based communications. This experience integrating DER as well as the code-base will be leveraged to develop and implement the SPIN

EMS control algorithms for coordinated DER management of V2G, solar, and back up energy storage, establishing the capability for micro grid operations at the local facility or residential level. EPRI's ongoing work with NREL on the INTEGRATE projects will inform the open DERMS and DRMS integration. In addition, EPRI will develop the grid models and provide the simulated utility DR and ISO regulation command/request signals for activating V2G during the lab testing and field demonstration phases.

LG Chem are the world leaders in electric mobility and grid-scale Lithium-ion batteries and will be an active participant in this project to lend both battery application, testing and data interpretation expertise, with battery hardware and test services to create data sets that can be analyzed.

Fiat Chrysler Group is making available Model Year 2017 Pacifica PHEVs for this pilot which will be modified to add V2G services related hardware and control algorithms. The on-vehicle V2G communications module utilizing J2847/3 standard application based on IEEE2030.5 protocol will be developed by EPRI and Kitu Systems. EPRI is developing the IEEE2030.5 translation to the vehicle CAN to ensure interoperability of the protocols for V2G functionality and control.

Special facilities access and planned utilization:

ORNL: Characterization and system integration testing of the Spin System will be accomplished at the ORNL *Power Electronics and Electric Machinery Laboratory* is in the National Transportation Research Center (NTRC), which has more than 9,000 square feet of space for developing, fabricating, and testing the next-generation power electronics and electric machine technologies. Lab testing of the complete V2G system with the SPIN system and LG battery packs will be accomplished at the *Distributed Energy Communications and Control (DECC) Laboratory* at ORNL which focuses on distribution system control and operation, grid interconnection and control of distributed energy resources including energy storage and electric vehicles, as well as smart grid, and communication applications.

The University of California, San Diego, also known as UCSD, is a public research university located in the La Jolla neighborhood of San Diego California in the United States. The university occupies 2,141 acres near the coast of the Pacific Ocean with the main campus resting on approximately 1,152 acres. UC San Diego is the seventh oldest of the 10 University of California campuses. UCSD is the host and testing site for multiple California Energy Commission funded EV Infrastructure projects with a comprehensive installation of DC Fast Chargers and AC Level 2 EVSEs from multiple manufacturers and EV service providers.

Fiat Chrysler Group: Fiat Chrysler group's Auburn Hills engineering center has world-class facilities and engineering staff that will be leveraged to do vehicle software and CAN bus integration of the grid communications hardware and software, as well as system commissioning and integration with SPIN module available for functional testing and performance assessment. One Pacifica PHEV will remain with Chrysler to validate any software or hardware changes in the lab before making them in the field.

Results

Completed the implementation and site demonstration of the AC On-Vehicle V2G end to end communications and control technology. Four vehicles (1 Honda Accord PHEV / 3 Chrysler Pacifica Van PHEVs) were upgraded with on-vehicle bi-directional charging inverters (Figure III.8.2) and EV Communications Controllers (EVCC) (Figure III.8.3) incorporating J3072 and IEEE 2030.5 Distributed Energy Resource (DER) and Demand Response Level Control (DRLC) function sets and communications protocols, and J2931/4 Power Line Communications (PLC) utilizing the HomePlug GreenPhy chipset. Included interoperability for CAN communications to the vehicle control module. The Honda Accord PHEV EVCC was developed separately from the Chrysler Pacifica Van EVCC by the University of Delaware. The Electric Vehicle Supply Equipment (EVSE) utilized was the

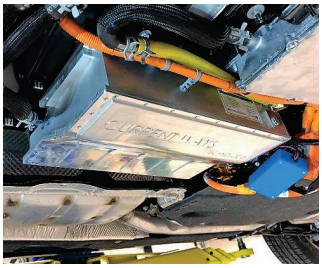

Figure III.8.2 Bi-directional Charging Inverter Installed into Chrysler Pacifica Van PHEVs

AeroVironment Level 2 AC Charger modified with an IoTecha MEVSE communications module incorporating the HomePlug GreenPhy PLC chipset and the IEEE 2030.5 bridge communications to the EVCC incorporated into the PHEVs. Four of the AV modified EVSEs were installed at the University California San Diego (UCSD) parking lot demonstration site (Figure III.8.4).

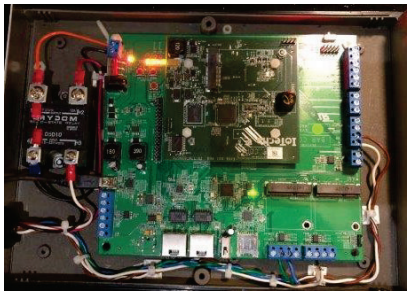

Figure III.8.3 EV Communications Controller (EVCC) Chrysler Pacifica Van PHEV

Figure III.8.4 UCSD Parking Lot Demonstration Site and Chrysler Pacifica Van PHEV and Honda Accord PHEV

The site was modified (

Figure III.8.5) to provide four modified EVSEs, 75KVA transformer, 400A panel, and 12kW solar conductor

from co-located solar panel structure. The primary site controller was the Transformer Management and Monitoring System (TMS) () developed by the Electric Power Research Institute.

Figure III.8.5 Demonstration site charging island (4 EVSEs, 75KVA transformer, 400A panel, transformer management system

Figure III.8.6 Transformer Management and Monitoring System (TMS)

The TMS contains the V2G control algorithms, metering/measurement devices, and provided the network interface communications for processing of the DSO/ISO simulated commands / requests. The basis for the control algorithms is the capability to manage the V2G cycles within the constraints provided by the EV driver for minimum SOC, max SOC, and time charge in needed. The TMS controls are incorporated using the IEEE 2030.5 server protocol for the Distributed Energy Resource (DER) and Demand Response Level Control (DRLC functions with communications to the PHEVs through the EVSE PLC bridge. The site demonstration and testing was conducted over a four week period during the months of May and June 2018. The TMS managed and operated the PHEV charging and discharging controls associated to an aggregated residential transformer application. The residential load and solar profiles utilized for defining solar generation and residential load constraints/conditions were extrapolated from US Energy Information Administration data sources. The control schemes and algorithm validation use cases addressed four areas: Peak Shaving, Over-generation Mitigation, Ramping Power support, and Ancillary Services.

The TMS contains the V2G control algorithms, metering/measurement devices, and provided the network interface communications for processing of the DSO/ISO simulated commands / requests. The basis for the control algorithms is the capability to manage the V2G cycles within the constraints provided by the EV driver for minimum SOC, max SOC, and time charge in needed. The TMS controls are incorporated using the IEEE 2030.5 server protocol for the Distributed Energy Resource (DER) and Demand Response Level Control (DRLC functions with communications to the PHEVs through the EVSE PLC bridge. The site demonstration and testing was conducted over a four week period during the months of May and June 2018. The TMS managed and operated the PHEV charging and discharging controls associated to an aggregated residential transformer application. The residential load and solar profiles utilized for defining solar generation and residential load constraints/conditions were extrapolated from US Energy Information Administration data sources. The control schemes and algorithm validation use cases addressed four areas: Peak Shaving, Over-generation Mitigation, Ramping Power support, and Ancillary Services.

The DC V2G off-vehicle inverter technology application is being addressed through the development of the Smart Power Integrated Node (SPIN). The SPIN integrates power electronics mode control functions for bi directional power flow management between DER assets (including PEV DC Charging), the grid, and facility loads. Includes the implementation of the IEEE 2030.5 server /client software (DER and Demand Response Load Control (DRLC) function sets) for utility DSO interface and communications, meter telemetry for energy consumption and power flow data monitoring, and data analytics processing algorithms for energy utilization and cost optimization.

The SPIN proof of concept rack system (Figure III.8.7) consists of two 5kW bidirectional converters (OBCMs), DC Switching, DC Charging Communications Control Module (CCM), and metering/measurement telemetry that is centrally integrated and controlled through the SPIN Unit Master Controller. The SPIN Unit Master Controller integrates the power electronics controls software, multi operational power configuration controls, and algorithmic functionality for DER/V2G energy management. The SPIN System includes a cloud server providing data analytics and DER optimized utilization strategies based on real time data from the SPIN Unit Master Controller about the local node load (residence/facility) conditions and status of the DER devices, including the EV SOC status and customer charging preferences or constraints. The server merges external data such as weather conditions affecting solar generation, electricity pricing tariffs, etc., and calculates an optimization strategy to maximize energy efficiency or mitigate cost. The primary objective is the functional verification of the SPIN capability to provide DC Charging hardware connectivity to the EV, to integrate the communications and control software requirements for DC charging and discharging, and to manage DC V2G as a local DER asset to support grid reliability.

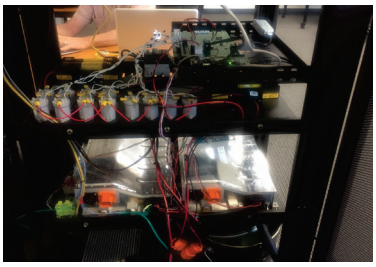

Figure III.8.7 SPIN rack mounted unit for power controls and analytics algorithmic S/W integration and testing

Software architecture is developed specifying the development and implementation requirements for the Utility DSO interface communications (OpenADR and IEEE2030.5), SPIN DC charging/discharging communications (J1772, DIN70121, J2847/2, J2847/3), SPIN to EV V2G communications (IEEE2030.5), and application of Rule 21 Common Smart Inverter Profile (CSIP) communications protocol. Developed board specifications for the Supply Equipment Communications Controller (SECC) and the Electric Vehicle Communications Controller (EVCC) which include the Power Line Communications (J2931/1) functionality.

Fiat Chrysler Automobile (FCA) initiated the modifications of a Chrysler Pacifica Van PHEV to incorporate DC bi-directional charging functionality, DC control protocols, and V2G EVCC module adaptable for DC off-vehicle inverter application.

Developing emulator for simulation and verification testing of the SPIN Unit Master Controller software controls for integrating and managing the utilization of solar, battery energy storage, and EV DC

charging/discharging. Determined use case scenario for testing and data modeling are peak shaving for locational and wide area demand response, renewables over/under generation ramping mitigation/offset in response to day ahead forecasts and real-time response to latent grid conditions due to intermittent weather; ancillary services such as reg up/down; and cost optimization.

Conclusions

Preliminary conclusions based on the resulting evaluations of the AC On-Vehicle V2G implementation and demonstration are:

Requirement for utility adoption of J3072

A significant barrier to the commercialization of the electric vehicle onboard V2G technology is the adoption of the SAE J3072 standard to enable automaker self-certification of onboard inverters to be CPUC Rule 21 compliant per IEEE 1547. Recommendation is that compliance can be achieved through electric vehicle compatibility certification with UL marked bi-directional AC EVSEs. The site permit for grid interconnection will be based on the UL listing of the EVSE to be certified for bi-directional power flow. J3072 authenticates the electric vehicle inverter model has been certified to be compatible with the UL listed EVSE. Note that DC V2G does not require utilization of the J3072 protocol. The inverter is located off-vehicle in the DC Charger which would be permitted as a fixed site grid interconnected electronic device.

Effective for residential transformer and community aggregation application

The Transformer Management System monitoring and control strategy enables improved situational awareness for the utility to manage distribution reliability, and the ability to integrate electric vehicle managed charging for aggregation at the residential transformer and community sub feeder levels. The SPIN System would support residential transformer and community aggregation through utilization of the cloud analytics and optimization functionality. SPIN units will be enables to interface with aggregation control entities or systems either directly or through the cloud server.

Local site electrical integration evaluation required to identify transients affects

During the UCSD site demonstration experienced circuit voltage and frequency anomalies that affected the continuity of communications between the TMS and the electric vehicles. The electric vehicle onboard charge modules were recording error faults and going to sleep due to frequency and voltage spikes. Preliminary voltage and frequency measurements could not provide any conclusive information to the fault investigation.

Table III.8.1 Summary of Objectives, Accomplishments, Learnings and Future Scope for On-Vehicle V2G Development

Objectives	Accomplishments	Learnings	Gaps to Scale Implementation
Develop and implement end to end open standards-based V2G communications system	Validated end to end interoperability and application of V2G SAE and IEEE 2030.5 standards	J3072 requirement for utility adoption – compatibility certification with UL marked bi directional AC EVSE	Defined SAE J3072 Interoperability Certification body requirements and harmonized UL/SAE labeling
Implement dynamic V2G management use cases	TMS automated energy management capability implemented – supports interaction with DSO / ISO grid service requests	Effective for residential Transformer energy monitoring for constraints due to load and stress conditions – community aggregation application	Transformer Management System software can be integrated at any edge of the grid node – transformer, DMS, DERMS or Facility EMS
Data collection and performance analysis	Simulated data verifies algorithmic functionality – Demo data collection ongoing	Local site electrical integration evaluation required to identify transients affects – further research required	Implement more powerful 'edge of the grid' computing tech
Assess cost/benefit – customer, utility, and societal perspectives	Positive value proposition for EV owners (5X V1G)	The preliminary assessment makes for a strong case for creating incentive structures for V2G	Define, verify and validate through customer participation incentive mechanisms that are viable and acceptable to customers to maximize participation, along with cost analysis for additional hardware on vehicles
Define and implement on-vehicle V2G converter and integrate with grid power and communication systems	Integrated grid-tied bidirectional charger and J3072 client control module with on-vehicle battery and controller	System integration revealed grid interaction both in terms of compatibility, interconnection requirements and a need to define clearer electrical integration standards	Define electrical grid integration and compatibility requirements for on-vehicle inverters (or align them with the smart inverter requirements), including testing and interoperability protocols.

The preliminary value assessment provides strong case for creating incentive structures for V2G

The value and cost benefit assessment and modeling analysis show a cumulative maximum benefit of V2G to the grid (net of cost increment) to be between $450/year per vehicle to $1850/year/vehicle. This effectively is approximately 5 times the value of V1G for similar grid service applications

The adjoining table summarizes the on-board V2G task accomplishments and learnings succinctly.

Key Publications

The publications are in the form of reports and presentations. A list is provided, and copies can be provided upon request.

1. DOE DE-EE0007792 Review 7-27-2017-final.ppt
2. DE-EE_0007792_Q2-2017_Report V1
3. V2G Cost Benefit Assessment Framework Document
4. V2G Vehicle Requirements and Algorithm Implementation Document V_1.0
5. System Requirements V3 Approved
6. Transformer Management System Algorithms – Graphs.ppt
7. California Energy Commission Report - Distribution System Constrained Vehicle to Grid Services for Improved Grid Stability and Reliability

IV. Grid and Infrastructure: Grid Modernization

IV.1 Vehicle to Grid Integration Pathway (ANL, INL, LBNL, NREL, PNNL)

Rick Pratt, Principal Investigator
PNNL
P.O. Box 999, K5-17
Richland, WA 99354
E-mail: rmpratt@pnl.gov

Lee Slezak, DOE Technology Development Manager
U.S. Department of Energy
E-mail: Lee.Slezak@ee.doe.gov

Start Date: April 1, 2016 End Date: March 30, 2019
Project Funding (FY18): $1,000,000 DOE share: $1,000,000 Non-DOE share: $0

Project Introduction

The Vehicle to Building Integration Pathway project (GM0062) will develop and demonstrate pre-normative methods needed to develop a standardized and interoperable communication pathway and control system architecture between Plug-in Electric Vehicles (PEVs), Electric Vehicle Support Equipment (EVSE) and Building/Campus Energy Management Systems (BEMSs) to enable the integration of clean variable renewable sources with workplace PEV charging infrastructure to promote greater PEV adoption. This communications and control platform will provide access to real-time system monitoring information, establish an infrastructure to coordinate intelligent assets, manage energy consumption behind the meter, reduce peak demand charges resulting from vehicle charging, and potentially participate in energy and/or ancillary services markets.

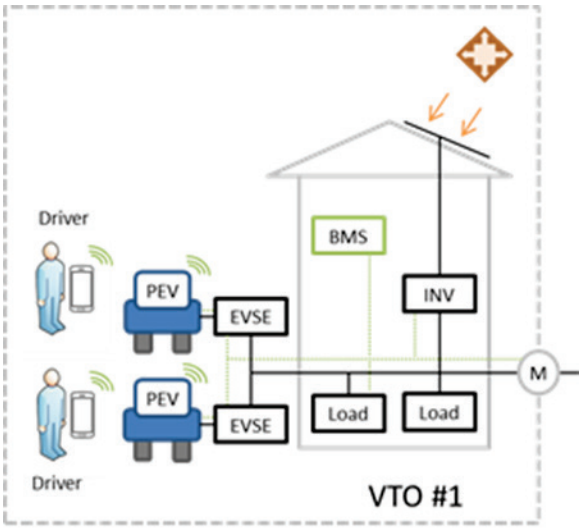

Figure IV.1.1 GM0062 workplace charging project scope

Objectives

A successful project includes developing use cases for scalable systems and demonstrating at multiple laboratories affordable, communications and control platforms controlling multiple PEVs charging. The demonstrations will use transactive control constructs showing demand charge reductions, providing value to PEV owner and grid, and integrating rooftop solar and building controls. Use cases and testing plans that leverage ongoing work will be developed in FY 2016. Annual demonstrations will show increasing capability, control algorithm advancement, and leverage existing test beds at ANL, NREL, and PNNL. An FY 2018 task includes integrating an INL-developed cyber communications monitoring capability.

Approach

ANL, INL, LBNL, NREL and PNNL jointly developed the workplace vehicle charging demonstration use cases, communication requirements and control requirements needed to demonstrate coordinated PEV charging under time varying commercial building load conditions that minimize demand charges. These use

cases have been reviewed by an Industry Advisory Board (IAB) and integrated with the communication and control requirements to form the basis for performing four electric vehicle charging demonstrations.

7. The demand response (DR) demonstration showed that the integration platform enabled aggregated PEVs to each provide their maximum power variation (e.g., 3.3kW or 6.6kW) in response to the DR signal using the developed communication and control requirements.

8. The second demonstration included aggregated building loads, multi-vehicle charging loads, and the dynamic workplace PEV charging use cases and showed that the integration platform mitigates peak demand charges from vehicle charging, maximizes available charging power delivered to the PEVs, and prioritizes energy delivery to PEVs with highest energy needs (e.g., low state of charge / short charging time available).

9. The third demonstration integrated variable renewable resources into the workplace charging demonstration with aggregated building loads, multi-vehicle charging loads, and dynamic workplace PEV charging use cases developed. The demonstration verified that the integration platform mitigates peak demand charges from vehicle charging and prioritizes renewable energy delivery using state of charge, charging time available, and the customer's desire for "greenest", "cheapest", or "fastest" charge. These inputs enabled the platform's control algorithms to optimize charging based on the building's priorities and the PEV driver's preferences.

10. The fourth demonstration is planned for CY2019 and will implement Transactive Control methods into the PEV charging control system. A successful demonstration will verify the control system's capability to use Transactive Control methods; maximize available charging power delivered to the PEVs; and prioritize energy delivery to PEVs with highest energy needs (e.g., low state of charge / short charging time available).

Results

NREL led the multi-lab GM0062 Use Case development task and the process was guided through feedback from the Industry Advisory Board. Feedback was received from seventeen of fifty vehicle manufacturers (OEMs), utility, and regulatory entities. Follow-up was provided via conference calls, a February Grid Integration Tech Team meeting, and at the Grid Modernization Lab Consortium (GMLC) annual review poster session in April. Several entities were very excited about the work and eager to receive updates.

Figure IV.1.2 provides a graphical representation of the feedback received and emphasized the Advisory Board need for emphasis in load control areas (e.g., demand response, capacity deferral, and price-based controls) as well as demand charge mitigation. This industry feedback provided valuable guidance toward maximizing the value of demonstrations performed.

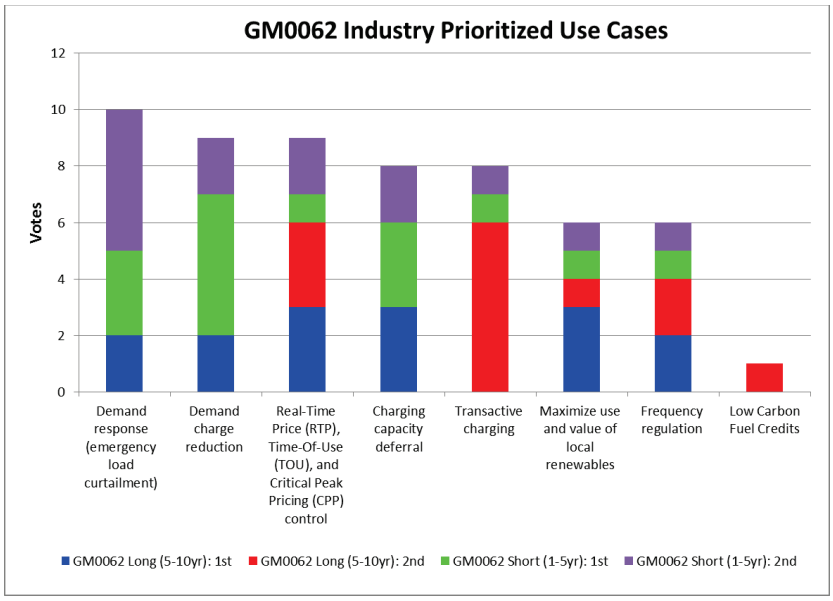

Figure IV.1.2 GM0062 industry advisory board prioritized use cases

The first demonstration was a standards-compliant (OpenADR), multi-vehicle, workplace charging demand response (DR) use case was demonstrated at ANL, NREL and PNNL. The red ellipse in Figure IV.1.3 shows the DR system response using ANL's CIP.io platform developed to coordinate scheduled charge control variations (charge power, load shedding, timing, etc.). The demonstrations at NREL and PNNL also showed that their platform design enabled the aggregated PEVs at each location to provide their maximum power variation in response to the DR signal generated by an OpenADR VTN hosted by ANL.

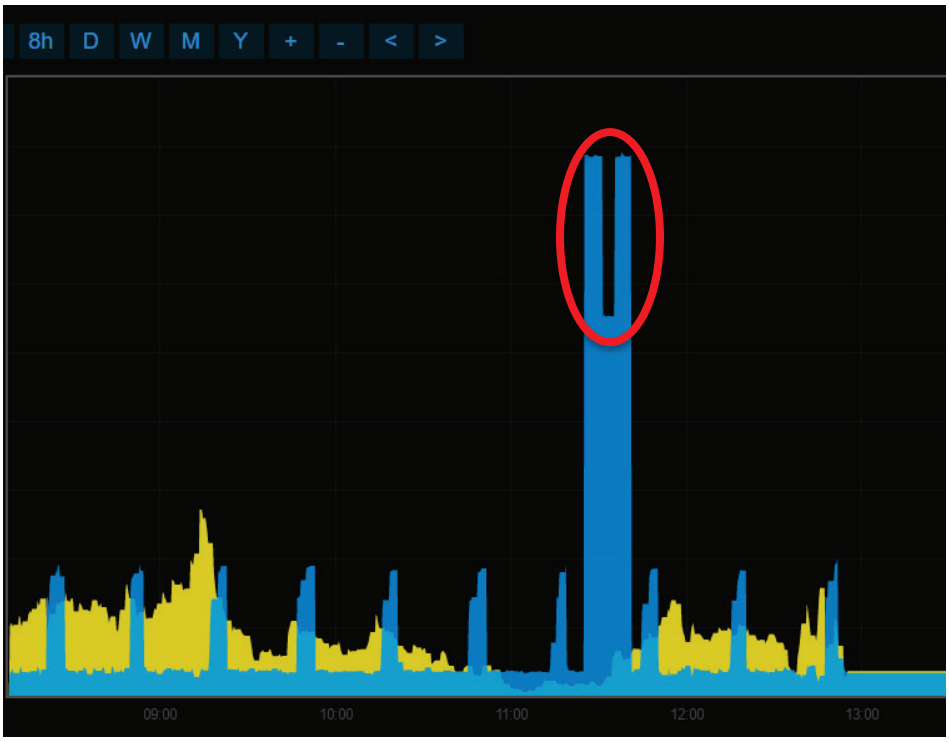

Figure IV.1.3 ANL demand response

The second demonstration, Demand Charge mitigation, was also demonstrated at ANL, NREL and PNNL. The objective of Demand Charge mitigation is to limit aggregated PEV charging load if the total building load exceeds the monthly peak power. Additional charges must be paid (~$7-10/kW) if the 15-min average building load exceeds the monthly peak power. Implementing PEV charging controls to prevent PEV charging from causing payment of demand charges was the focus of this demonstration. Figure IV.1.4 shows the implementation of PNNL's VOLTTRON-based control system used to limit PEV charging load when building demand increased above the 16kW Demand Charge mitigation threshold. Exceeding the peak power threshold could cause up to a $40/month additional utility charge for the building owner.

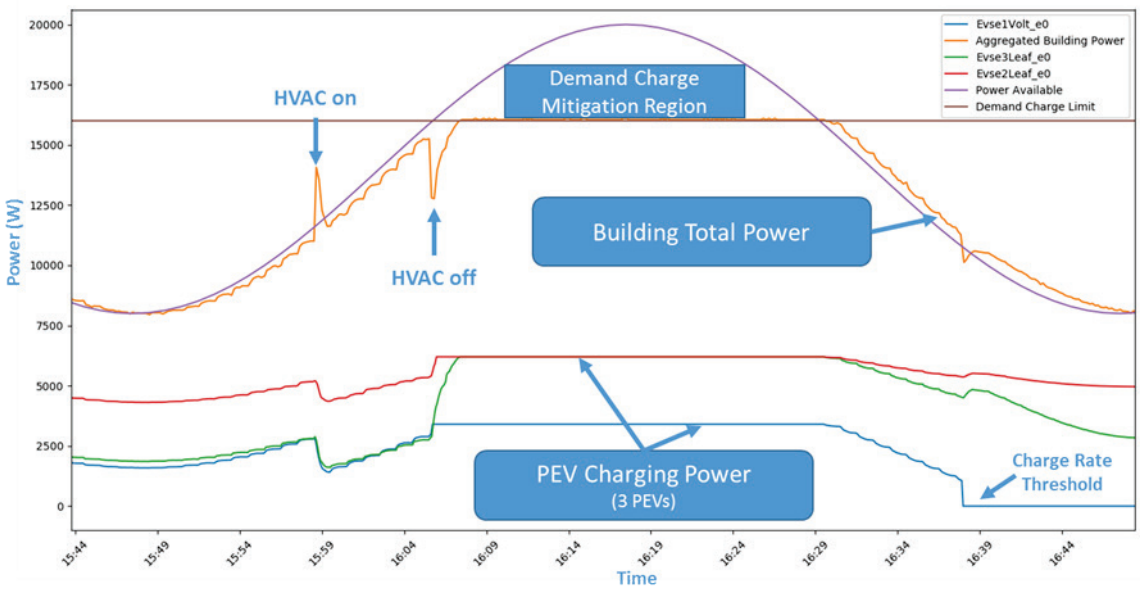

Figure IV.1.4 PNNL demand charge mitigation EVSE / PEV control response

Figure IV.1.4 shows two Nissan LEAFs and one Chevy VOLT charging using the PNNL charging control. Each PEV's charging power differs based on the state of charge, maximum charging rate, charging time and the current Available Power.

The ANL PEV-Owner Preference-based charging demonstration was performed on six EVSE at the Smart Energy Plaza. The ANL smart charge adapter was utilized on these six EVSE for metering, monitoring and control. The demonstration was deployed during the afternoon of September 20, 2018 from 2:30 pm to 5:00 pm CDT. Figure IV.1.5 is a plot of the entire demonstration including the plaza power, solar generation, aggregated PEV charging, Plaza Power Limit (setpoint), and DC fast charging power (AC kW). The setpoint was changed throughout the demonstration to test the reactiveness of the algorithm. The plaza power (green) rarely exceeded the power limit (red), only during transients and then corrected itself.

Figure IV.1.5. ANL preferential-based PEV charging demonstration with six PEVs

NREL maintained operation of the charging management system and has continued collecting daily data on the energy request, energy delivered, planned departure, and actual departure of NREL users of the EVSE system. The continued operation of the charging system through Q3 resulted in a particularly interesting event on June 19, 2018 around 12pm. During this event the campus net load went from 1.6 MW to 4 MW in 6 minutes due to cloud coverage of the onsite PV as a large thunderstorm moved into the area. The curtailed EVSE power during the management is about 28 kW, which resulted in about $470 savings based on NREL's demand charge rage ($16.79/kW). If we had turned off all the EVSE's during that period, we would have curtailed 49 kW and saved $823. This event highlights the need for better prediction of the EV driver's charging need and a mechanism to pass on the marginal cost of such an event.

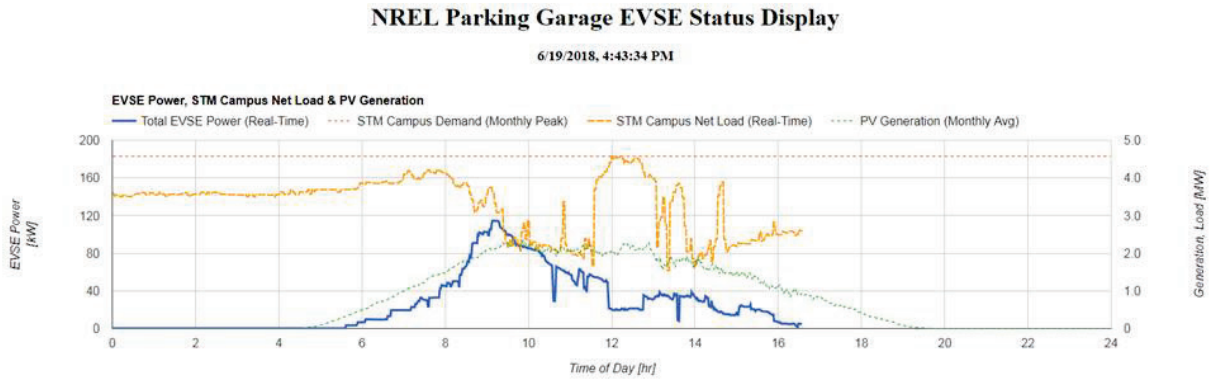

Monthly Peak	Campus Net Load	Total EVSE Power	Curtailed EVSE Load
4.576 [MW]	2.585 [MW]	0.063 [kW]	No load management

Figure IV.1.6. NREL control system campus net load during June 19th event

LBNL has performed PEV charging economic analyses in three regions in the U.S. – Minneapolis, Miami, and San Francisco for a medium office building over an entire year. The office building has a solar array sized to deliver 25% of the building's annual energy. The local electrical energy / price / demand charges were applied to the building owner assuming 50% of the workers drove a PEV and there were enough EVSEs to simultaneously charge all. The key simulation outcomes to date are:

A. The cost difference between uncontrolled and controlled EVs is defined by demand charges in all three cases.

B. In the presence of demand charges, uncontrolled EVs lead to an unstable demand charge cost mostly dependent on the building load and solar irradiance daily conditions.

C. Controlled EV charging leads to a stable electricity cost as EVs do not further increase the demand charges.

D. In the absence of demand charges, the additional cost induced by EVs is the same for uncontrolled and controlled scenarios.

E. Additional economic analysis work is planned including developing an annualized demand charge cost that will be used to estimate the payback period associated with implementing PEV charging control technology.

A summary of the developed control system capabilities is shown in Table IV.1.1.

Table IV.1.1 Test Bed / Control System Capabilities

Test Bed / Control System Capabilities	ANL System	NREL System	PNNL System
Control Approach	Central Control	Central Control	Distributed Control
EVSEs	6	36	7
Components	Smart Energy Plaza, CIP.io & Smart Charge Adapters	NREL Parking Garage & Raspberry Pi controllers	PNNL Lab Homes, Bldg. 3820 & VOLTTRON & Raspberry Pi controllers
Control Goal	Maintain total load below configurable peak		
Functional Approach	Building EMS controls each charging PEV to meet buildings goal (demand charge mitigation, frequency reg., etc). Control based on PEV's needs.	System controller optimizes each PEV charge schedule to not exceed Demand Charge Limit	System controller sets control system goals and each PEV controller optimizes its PEV charge schedule to not exceed system goal
Operation	• PEV's ranked by Instantaneous missing DC Ah; control adjustments based upon available power and PEV's use of available power • Minimum charge rate maintained	• PEV amp-hours needed updated each second • Minimum charge rate maintained PEV's ranked by energy required, highest deficit increased to limit; then next PEV	• Available power = Bldg Goal – Current Power • PEV priority = kWh needed / (time remain * charge rate) updated each second • PEV power change = Available Power * priority / total priority

Table-IV.1.2 Standards and Equipment Gaps Identified

Gaps Identified	Standards
Standards	• The SAE J1772 requirement for a charging PEV to respond within 5 seconds of a change in charge limit could restrict system use in grid services that require faster response times, such as frequency regulation.
Current EVSEs	• OCPP 1.6 (Building to EVSE Communication) is the first standardized attempt at smart charging control for EVSE. Limited implementation. • EVSE OEM specific API access into EVSE controls / data is limited with varying degrees of latency.
Current PEVs	• Current SOC, final SOC and Time Charge is Needed (TCIN) is only available through 3rd party solutions or vehicle owner input into control system. The ISO-15118 standard could provide this information.
Current EVSE/PEV	• Currently, only one EVSE and one PEV vendor have implemented the communications (ISO-15118) between the EVSE and PEV that would enable digital communication to be shared between the PEV and EVSE.

Conclusions

The Demand Response, Demand Charge mitigation, and PEV owner specified charging preferences demonstrations have been successfully implemented into commercially available PEVs and EVSEs using the existing Society of Automotive Engineering (SAE) standards. The following conclusions have been developed:

- No PEV or PEV control modifications are needed to adjust the PEV charging rate. All charging rate control can be implemented by adjusting the EVSE / PEV signal that sets the maximum charging rate the EVSE can support (EVSE Control Pilot Duty Cycle).
- The charging rate control was implemented by implementing external control of the EVSE Control Pilot signal to overcome the limited API and external charging rate control capabilities of commercially available EVSEs.
- The existing standards (SAE-J1772 and ISO-15118) need to be updated to enable PEV charging rate control that will support all developed use cases.

Key Publications

1. GM0062 poster presentation on 9/5/2018 at the GMLC Peer Review in Washington, DC.
2. GM0062 project presentation on 6/21/2018, “Vehicle to Grid Integration Pathway”
3. R. Pratt and L. Bernal, “Distribution System V1G PEV Charging Impacts Report”, January 2018.
4. M. Jun and A. Meintz, “Workplace Charge Management with Aggregated Building Loads”, 2018 IEEE Transportation Electrification Conference and Expo (ITEC), June 2018.
5. GM0062 poster presentation on 4/18/2017 at the GMLC Peer Review in Washington, DC.
6. GM0062 prioritized use cases were presented on 2/22/2017 to the GITT Meeting in Denver, CO.

IV.2 GM0085 Systems Research for Standards and Interoperability

Don Scoffield, Principal Investigator
Idaho National Laboratory
P.O. Box 1625
Idaho Falls, ID, 83415-2209
E-mail: don.scoffield@inl.gov

Lee Slezak, DOE Technology Development Manager
U.S. Department of Energy
E-mail: lee.slezak@ee.doe.gov

Start Date: May 1, 2016 End Date: April 30, 2019
Project Funding (FY18): $3,480,000 DOE share: $3,480,000 Non-DOE share: $0

Project Introduction

As plug-in electric vehicles (PEVs) increasingly penetrate the marketplace, the integration of electric vehicles into the grid is essential to ensure the continued reliability and security of the grid. To accomplish this, the project has developed a hardware-in-the-loop platform to study integration of numerous electric vehicles on a residential distribution feeder. This testbed will be used to develop and test charging control strategies for PEVs and then to quantify the benefit of controlling PEV charging. In general, there are two categories of approaches for PEV charging coordination: centralized and decentralized. Decentralized approaches provide a low computational complexity, but may not achieve optimal outcomes [1]. Centralized approaches will achieve optimal outcomes but usually have a high computational complexity [2]. The control approach developed in this project was designed to provide a low computational complexity but also achieve near optimal outcomes.

Objectives

- Develop control strategies to manage PEV charging
- Quantify the benefits of controlling PEV charging
- Investigate the feasibility of PEVs providing grid services
- Determine if uncontrolled PEV charging can cause concerns for the grid.

Approach

It is likely that PEVs will be charged at many different venues in the future like at home locations, work locations, the shopping mall, etc. The best approach for controlling PEV charging in many cases depends on the charge location. For example, when PEVs are charged at buildings there is benefit in integrating the PEV charging into the building load. On the other hand when PEVs charge at home locations there may be benefit in controlling and coordinating the PEV charging of many PEVs across a distribution feeder. In this project, PEV charging control strategies were developed to control PEV charging at residences as well as at commercial buildings. After the PEV charging control strategies have been developed, the benefit of controlling PEV charging can be quantified by comparing controlled scenarios with uncontrolled charging scenarios. The benefits of controlling PEV charging will be quantified using the following metrics:

- Cost savings of avoided distribution feeder upgrades
- New generation capacity avoided

Results

The PEV charging control strategy to control PEV charging at residences has been developed and tested on the hardware-in-the-loop platform. The control strategy was tested on the IEEE 34 node distribution feeder that was scaled up to represent a residential feeder with 75,000 homes. In these tests, 50% of the homes owned a PEV and the residential load came from PG&E's typical residential load data. Using this setup, the ability of PEVs to provide both capacity deferral and voltage support was studied. Results from each of these cases are described below.

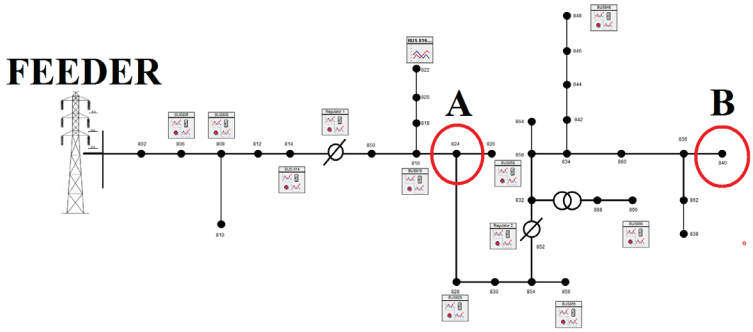

Figure IV.2.1 IEEE 34 node feeder. Bus A and bus B are marked in red.

Capacity Deferral

Controlling PEV charging shifts the PEV charging to off-peak hours, which flattens the load curve and mitigates the need for capacity upgrades. When PEV charging is not controlled, the PEV charging occurs at the same time as the non-PEV load peak, which drastically increases the peak feeder load. In the test scenario, the peak load is reduced by 65 MW when the PEV charging is controlled. Stated another way, uncontrolled PEV charging would cause a 55% increase in peak load, but when the PEV charging is controlled, the peak load only increases by 4%.

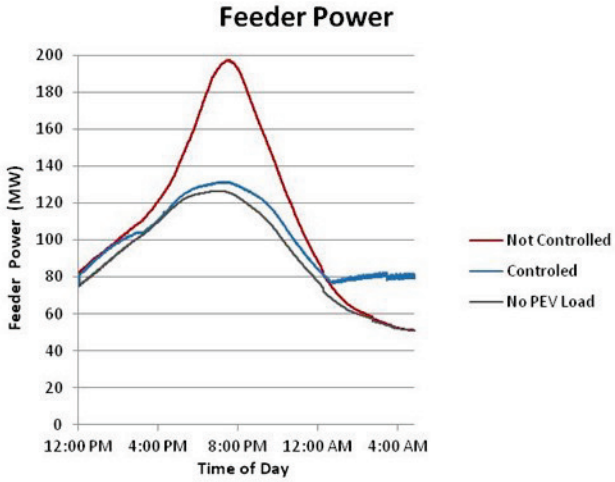

Figure IV.2.2 Feeder Power when PEV charging is controlled and not controlled.

Voltage Support

Controlling the PEV charging also provides voltage support to the distribution system feeder by flattening the voltage profile. Figure IV.2.3 shows the voltage profiles for two nodes on the IEEE 34 node feeder when the PEV charging is controlled and when the PEV charging is not controlled. When the PEV charging is controlled, it is much flatter and the voltage is always within ±5% of nominal. When the PEV charging is not controlled, utility upgrades will be needed to ensure the voltage does not deviate outside ±5% of nominal voltage.

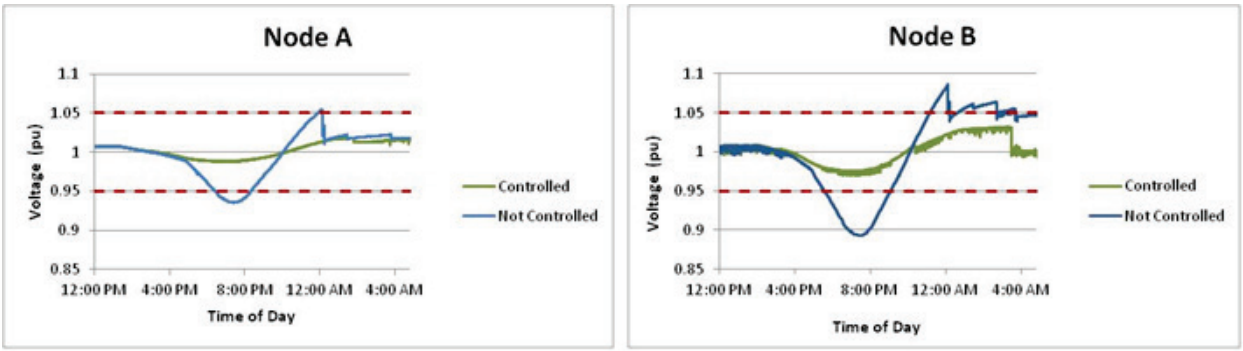

Figure IV.2.3 Voltage when PEV charging is controlled and not controlled for two nodes on the IEEE 34 node feeder.

Conclusions

Widespread PEV charging may cause concerns for the grid if the charging is not controlled. In this project, several charging control strategies have been developed to control PEV charging directly and to coordinate PEV charging across many commercial buildings. It has been demonstrated that the charging control strategy that controls the PEV charging directly enables PEVs to provide capacity deferral as well as voltage support. This charging control strategy is both scalable and computationally efficient, which allows it to manage the charging of hundreds of thousands of PEVs when deployed on an ordinary pc.

Key Publications

1. Yi, Z., and D. Scoffield, “A Data-Driven Framework for Residential Electric Vehicle Charging Load Profile Generation,” in 2018 IEEE Transportation Electrification Conference and Expo (ITEC), IEEE, June 2018, pp. 519-524.
2. Dias, F. G., D. Scoffield, M. Mohanpurkar, R. Hovsapian, and A. Medam, “Impact of controlled and uncontrolled charging of electrical vehicles on a residential distribution grid,” in 2018 IEEE International Conference on Probabilistic Methods Applied to Power Systems (PMAPS), IEEE, June 2018, pp. 1-5.
3. Markel, T., A. Meintz, K. Hardy, B. Chen, T. Bohn, J. Smart, D. Scoffield, R. Hovsapian, S. Saxena, J. MacDonald, S Kiliccote, K. Kahl, and R. Pratt, "Multi-Lab EV Smart Grid Integration Requirements Study," NREL/TP-5400-63963, National Renewable Energy Laboratory, May 2015.
4. Dias, F. G., Y. Luo, M. Mohanpurkar, R. Hovsapian, and D. Scoffield, “Potential for plug-in electric vehicles to provide grid support services, in Transportation Electrification Conference and Expo (ITEC), IEEE, June 2017, pp. 294-299.

References

1. Bessa, R. J., and M. Matos, "Global against divided optimization for the participation of an EV aggregator in the day-ahead electricity market. Part I: Theory," *Electric Power Systems Research*, Vol. 95, February 2013, pp. 309-318.
2. Jian, L., Y. Zheng, and Z. Shao, "High efficient valley-filling strategy for centralized coordinated charging of large-scale electric vehicles," *Applied Energy*, Vol. 186, January 2017, pp. 46-55.

IV.3 Diagnostic Security Modules for Electric Vehicle to Building Integration (GMLC) [Category 2 GMLC 0163]

Kenneth Rohde, Principal Investigator
Idaho National Laboratory
2525 N Fremont Ave, Idaho Falls, ID 83415
E-mail: kenneth.rohde@inl.gov

John Smart, Co-Principal Investigator
Idaho National Laboratory
2525 N Fremont Ave, Idaho Falls, ID 83415
E-mail: john.smart@inl.gov

Lee Slezak, DOE Technology Development Manager
U.S. Department of Energy
E-mail: lee.slezak@ee.doe.gov

Start Date: May 1, 2016 End Date: June 30, 2019
Project Funding (FY18): $1,650,000 DOE share: $1,650,000 Non-DOE share: $0

Project Introduction

America faces several important challenges in the next 10 to 15 years in terms of modernizing the electric grid to ensure it is safe, secure, resilient and efficient, so that the grid is able to withstand and recover from unexpected outages, maintain high quality of service, and conserve energy. Vehicle-to-Grid (V2G) technologies have been receiving increased attention as a network service that would be integrated into the Building Energy Management Systems (BEMS) to more efficiently operate their resources. However, the lack of established communication standards between devices, vehicles, and supervisory systems makes the BEMS extremely vulnerable to cyber attacks.

Objectives

The overall goal of this project is to develop a Diagnostic Security Module (DSM) Framework for creating an end-to-end security architecture for the integration of modern Plug-in Electric Vehicles (PEV) with Electric Vehicle Supply Equipment (EVSE) and a Building Energy Management System (BEMS). The DSM Framework will create a secure communications channel to coordinate PEV charging activities with a BEMS operator while notifying the BEMS operator of any cyber security problems associated with the PEV or EVSE. The DSMs will integrate with a wide range of device types (EVSE, PEVs, etc.) and vendors, and provide enhanced awareness of the security state when implementing an integrated building and PEV environment.

Major activities in this project includes (1) the investigation of potential security vulnerabilities, (2) development of the DSMs modules, (3) development of the prototype environment, and (4) implementation of a security protocol that can be used to further design and implement future standards and protocols. The later years include the integration of the DSM prototype into the building-level PEV charging environment created by the Multi-lab EV Smart Grid Working Group partners as proposed by GM0062 Vehicle to Building Integration Pathways.

Approach

The Idaho National Laboratory and the University of Louisiana at Lafayette are performing the following research and development activities to create a Diagnostic Security Module Framework.

Assessment of security vulnerabilities: The integration of smart grid enabled devices, such as EVSE units and PEVs with enhanced communication capabilities poses new risks to the electric grid. The vulnerabilities of the devices and implications of these risks are still not well understood. Given that these new electric vehicles

and their chargers are now available to the general public, these devices can be exploited by the cyber security community at large (i.e., hackers) to find potential vulnerabilities. A theory currently posed by the cyber security community is that a compromised PEV can be used as a mechanism to infect the smart charging stations available to the public. Thus the infected PEV becomes a transport mechanism for malware that specifically targets EVSE stations.

DSM Modules for end-to-end monitoring and integrated security monitoring: The DSMs will be designed to provide an additional layer of security by monitoring the devices to which they are connected and reporting any suspicious behavior or abnormal conditions. A safety and security framework will be developed to address the need for a distributed and collaborative intelligent system to monitor and protect a modern automated building. This framework will be distributed as a component of the DSMs located throughout the connected building environment. This will allow for the monitoring and detection of physical and cyber problems that might affect the overall health of the integrated building environment. The development of the DSM modules and communications framework addresses the need of the Vehicle Technologies Office to provide a security framework for the integration of Electric Vehicles and charging equipment into a central monitoring and management station (e.g., BEMS).

Prototype implementation & demonstration: The work performed during this project will integrate DSMs with multiple PEVs, a variety of EVSEs (Level 1, Level 2, and DC Fast), and a single BEMS. A new ChargePoint EVSE will be added to the existing equipment located at INL. This additional EVSE, along with other Smart Grid enabled EVSEs located at INL, will provide a variety of equipment for which to test and develop the DSM Framework. The ChargePoint EVSE is a new system yet to be evaluated for cyber security issues, so a portion of the first year of development will include an assessment of this device. The other EVSEs at INL have already been assessed as part of a previous DOE project. This prototype environment will allow research and testing of a subset of an integrated building environment with a deep understanding of the potential cyber security issues present in the systems.

Security protocols and standards for seamless and secure integration of PEV's charging equipment and BEMS: The DSM Framework will implement a security based protocol for sharing physical and cyber security information of the components to which they are connected. This protocol will be used to further develop standards that are currently being implemented throughout the electric vehicle industry, such as Smart Energy Profile (SEP) 2.0 and SAE J2931/7.

Results

The following list summarizes the project milestones completed during the FY 2018 fiscal year (October 2017 – September 2018):

11. Completed the implementation of the "generic" vehicle DSM algorithms for monitoring an EV. This includes basic vehicle fingerprinting and monitoring, and the reporting of generated alerts to the BEMS operator interface (Figure IV.3.1). Specific DSM algorithms for the Nissan Leaf and Chevrolet Volt are still in development.

12. A DSM "alpha" system was delivered to PNNL for integration in their electrification research laboratory. PNNL is testing the DSM system and analyzing the performance and benefits of DSM and will generate a paper documenting the test result in FY19.

13. Performed initial cyber security testing of the DC Fast Charger (DCFC) at INL to determine potential impacts to the energy grid. The test results showed measureable events on the local power distribution system as a result of cyber intrusion (Figure IV.3.2). These tests also provided further insight into how DSM should monitor the DCFC.

14. The project team attended the SAE CyberAUTO 2018 Challenge (July) in Detroit, MI and confirmed with the SAE organizers that the DSM project will participate in CyberAUTO 2019. This will include

the deployment of the DSM framework with a ChargePoint Level 2 EVSE, an ABB DCFC, and two TBD electric vehicles.

15. An analysis of various communication protocols used for "smart charging" was completed, and the Dedicated Short Range Communications (DSRC) protocol was selected for use in the DSM framework. Although DSRC does not provide any native methods for directly managing EVSE, it provides the functionality and flexibility for coordinating the many different devices that are used in the Electric Vehicle to Building Integration use-case of this project.

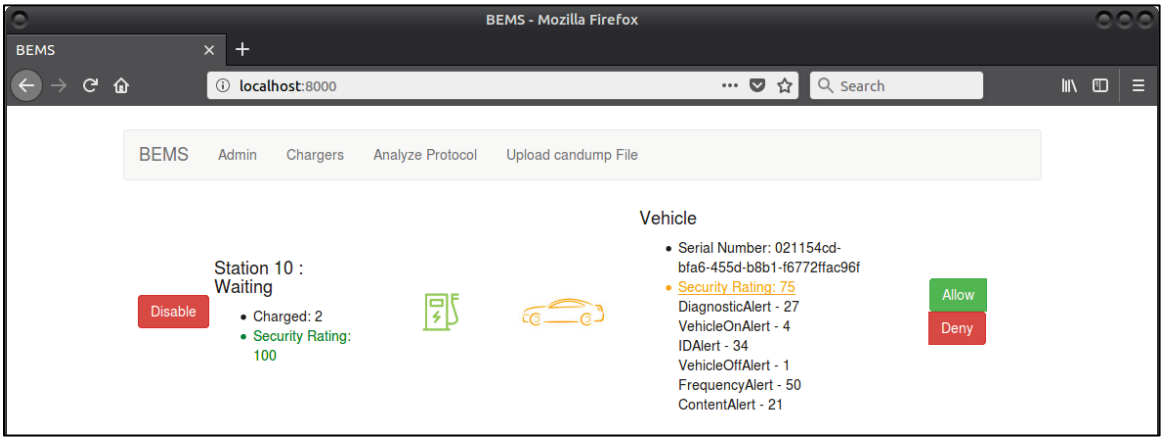

Figure IV.3.1 DSM operator status in BEMS (Alpha System)

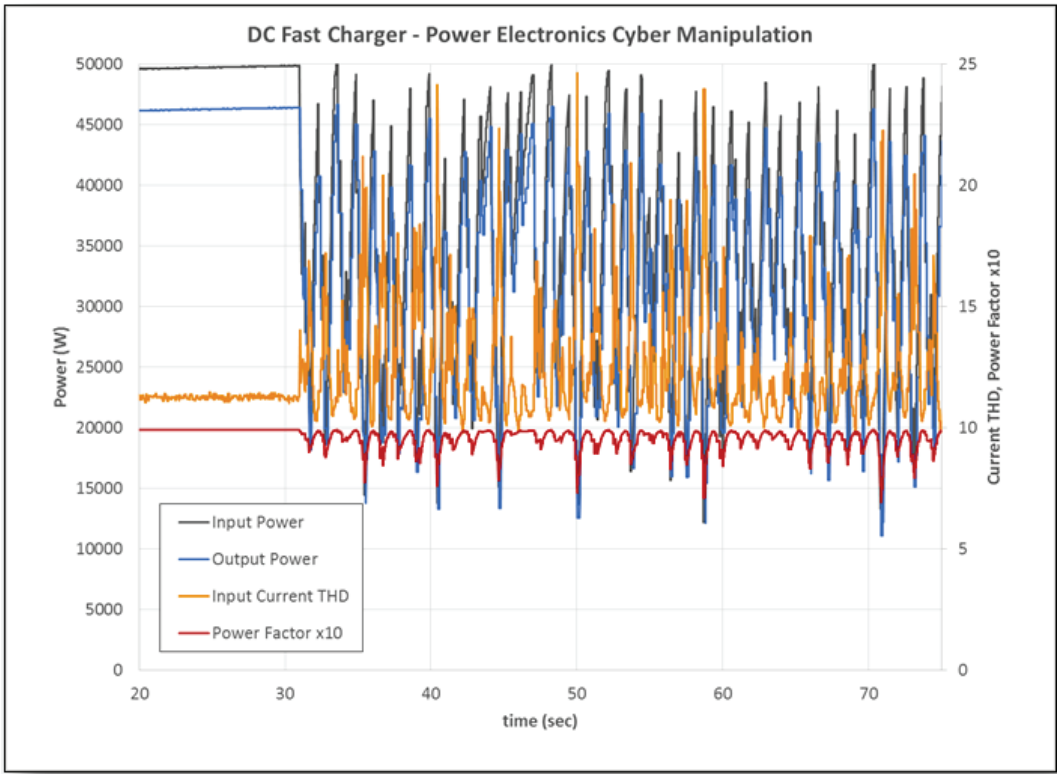

Figure IV.3.2 DCFC cyber manipulation results

Conclusions

At the conclusion of this project, a functional DSM Framework will be demonstrated at the SAE CyberAUTO 2019 challenge in Detroit, MI (July 2019). A report detailing the methods used and the success of DSM will also be published in a journal such as the SAE International Journal of Transportation Cybersecurity and Privacy. This report will also include the DSRC message dictionary created to support DSM communications.

During the third and final year of this project, the following activities are planned:

1. Testing and tuning the monitoring algorithms for the Volt and Leaf test vehicles.
2. Completion of the algorithms to monitor the ChargePoint Level 2 EVSE using DSM.
3. Development of a DSM device for the ABB DCFC to include DC fast charging as part of the DSM framework capabilities.
4. Analysis of the DSM framework performed by teams at NREL and PNNL after the DSM is integrated into their electrification laboratories.
5. A technical presentation of the DSM framework and the potential cyber impacts of the charging infrastructure will be presented during the technical track of the S4x19 conference in January 2019. This presentation was accepted as a peer-reviewed call for presentations.
6. Deployment of a DSM enabled charging environment at the SAE CyberAUTO 2019 challenge. DSM enabled EVSE and EV will be included as assessment targets in the challenge.
7. Generation of the final DSM report and publication for a journal, such as SAE, and will include the DSRC message dictionary used in DSM.

Key Publications

1. Diagnostic Security Modules for Electric Vehicle to Building Integration, VTO Annual Merit Review Meeting (Presentation), June 2018
2. Electric Vehicle Cyber Security and the Diagnostic Security Module Project, SAE CyberAUTO 2018, Detroit, MI, July 2018
3. Diagnostic Security Modules for Securing Electric Vehicles, GMI Peer Reivew Meeting (Poster Session), September 2018

IV.4 Testing Network and Open Library

Matthew Lave, Principal Investigator
Sandia National Laboratories
P.O. Box 969
Livermore, CA 94551-0969
E-mail: mlave@sandia.gov

Rob Hovsapian, Co-Principal Investigator
Idaho National Laboratory
1955 N. Fremont Avenue
Idaho Falls, ID 83415
E-mail: rob.hovsapian@inl.gov

Lee Slezak, DOE Technology Development Manager
U.S. Department of Energy
E-mail: Lee.Slezak@ee.doe.gov

Start Date: April 15, 2016 End Date: April 15, 2019
Project Funding (FY18): $2,600,000 DOE share: $2,600,000 Non-DOE share: $0

Project Introduction

This Grid Modernization Laboratory Consortium (GMLC) Testing Network and Open Library project (GMLC 1.2.3) accelerates grid modernization by (a) providing comprehensive information about testing infrastructure available at DOE National Labs and beyond, and (b) creating a repository of models and testing resources such as testing protocols. These goals are critical to accelerate development, validation, standardization, adoption and deployment of new grid technologies. A related goal is to enable national laboratories to drive innovation more effectively and synergistically, including by combining testing and modeling capabilities across multiple facilities to create integrated, advanced capabilities.

The electric power grid is a complex system comprised of devices connected electrically which are affected by controls, communications, and markets. There are a wide variety of rapidly evolving technologies and performance characteristics that are increasing system complexity and demanding new requirements. The DOE National Labs have extensive capabilities that can help test and model these evolving technologies to understand their impact to grid operations. To achieve a truly modernized electric power grid, industry and other organizations need access to these testing resources across a wide range of technology readiness levels to accelerate commercialization of new technologies and improve grid planning.

However, national lab testing and modeling capabilities can be difficult to identify due to a historical lack of consistency regarding how information on capabilities is communicated to the public. The level of detail available and the location of such information can even vary greatly across the different laboratories, or across programs within a single organization. For example, a national lab may have detailed information regarding its PV systems testing capabilities available publicly online, but no available information regarding its energy storage testing capabilities. Further, there has been no overarching coordination framework, making it difficult to integrate capabilities into more effective multi-institutional test beds that can handle systems-level testing and validation with live data—as opposed to isolated device testing at a single facility. This lack of coordination has resulted in inefficient utilization and the potential for duplication of efforts at different national labs.

Objectives

This project has two major objectives:

- Objective 1 – Establish a Grid Modernization Laboratory Consortium Testing Network (GMLC-TN) that will function as an agreement-based association to maintain and disseminate information related to testing capabilities, information about models and testing-related resources.
- Objective 2 – Develop and establish a Grid Modernization Laboratory Consortium – Open Library (GMLC-OL) that serves as a public repository for component models tools and testing resources. The GMLC-OL will be designed in a manner such that it is self-maintained through user inputs and feedback.

Approach

The three-year approach to meet the project objectives is:

Establish Foundations: *PY1 (April 2016 to April 2017)*

- Hosted a stakeholder workshop to understand user needs
- Cataloged and published testing capabilities at the DOE National Labs.
- Studied existing consortia with similar goals to understand organization, funding, sustainability, etc.
- Developed a framework for the open library

Deploy Testing Network and Open Library: *PY 2 (April 2017 to April 2018)*

- Formed gridPULSE (Public User Library for Systems Evaluation of grid-related devices) as a membership-based consortium covering testing network and open library
- Website (gridPULSE.org) with interactive listing of test capabilities, open library implementation, and ability to contact gridPULSE for more information
- Expanded testing capability catalog to include differentiating capabilities of test facilities
- Populated the open library with models from National Labs, especially GMLC projects

Ensure Future Sustainability: *PY 2 (April 2018 to April 2019)*

- Developing a sustainability plan, including ongoing operating costs, membership, roles, potential funding
- Outreach including technical sessions at conferences, participation in other GMLC project meetings, and wide-audience webinars
- Expanding the open library to increase the number of tools, models, and test procedures included and to improve usability

Results

Major achievements to date include:

Establishment of the gridPULSE consortium

As seen in Figure IV.4.1, gridPULSE consortium was formed to achieve the GMLC 1.2.3 project goals of: (a) enacting a testing network of electric grid-related testing resources at the national laboratories and (b) implementing an open library of electric grid-related, validated models and simulation tools. While the GMLC 1.2.3 project has a finite timeline and distinct goals, gridPULSE is the sustaining, unified implementation of these testing network and open library. In this way, gridPULSE will support grid innovation and help identify and bridge gaps in testing and modeling resources.

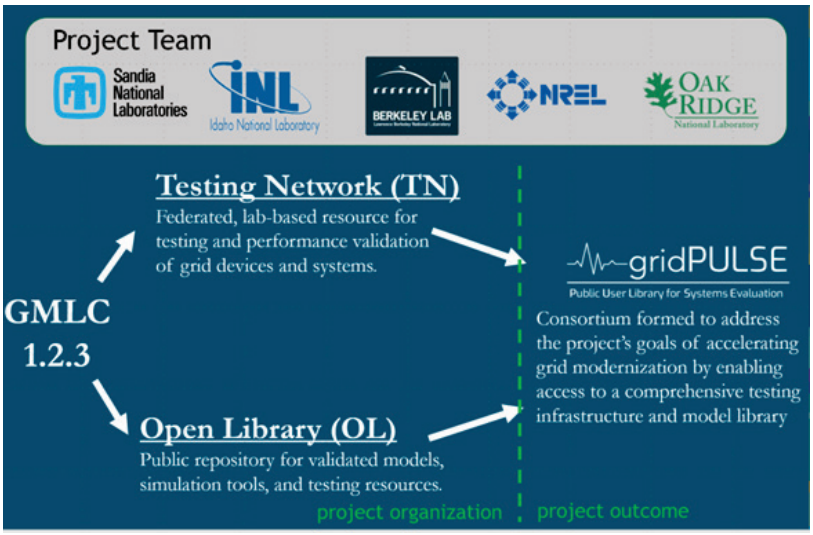

Figure IV.4.1 GMLC 1.2.3 project organization and relation to gridPULSE.

"Members" of gridPULSE will be those with testing capabilities and/or models to contribute. This initially consists of the five national laboratory team members for the GMLC 1.2.3 project, entities that have testing capabilities and/or modeling tools to deploy. As the consortium advances, membership will expand to include additional national laboratories' resources and capabilities and to include facilities beyond national laboratories (e.g., universities).

"Users" of gridPULSE will be those interested in testing or modeling related to grid modernization, including industry, university, and national laboratory employees. Users do not require special authorization, as information presented through gridPULSE will be available publicly.

Testing Capabilities and Facilities Catalog

Through an extensive self-assessment of grid-related test capabilities and facilities, the project team assembled the Catalog of National Laboratory Testing Resources, as seen in Figure IV.4.2. The catalog contains information about testing facilities and capabilities across 12 Department of Energy (DOE) National Laboratories. It has information on both unique test facilities (49 facilities) as well as the test capability and applicable technology area for each (100s of test capability / technology area pairs). This robust information allows the end-user to make decisions about which facility or facilities are best suited for testing his or her device. For example, a user could quickly identify which facilities conduct testing in the PV technology area, and could then read details on the specific capabilities of each of those facilities.

The information contained in the catalog focuses on testing and characterization of devices and systems that are connected to, or interface with, the electric grid. Isolated generation systems were considered beyond the scope of this project, but information regarding how generation assets interact with the grid was accepted. The catalog only includes resources where a national laboratory has established capabilities and infrastructure that are actively being used to conduct testing, or that have previously been used to conduct significant testing for a particular technology area and continue to be maintained for such work. The catalog is available publicly through the gridPULSE website (see website section below).

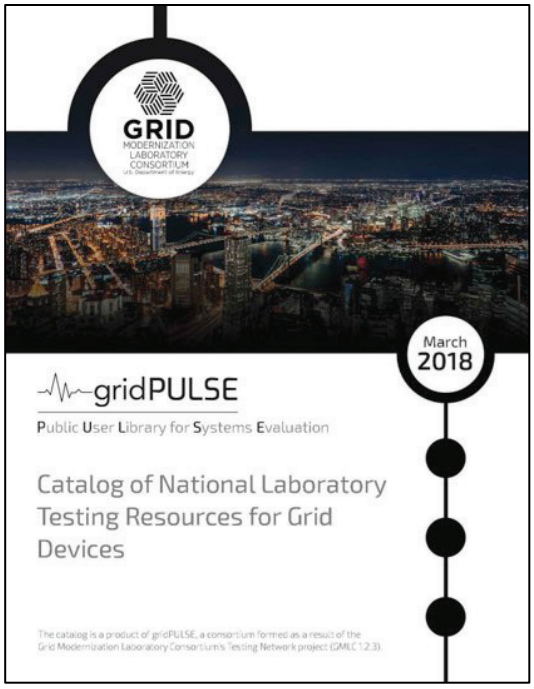

Figure IV.4.2 Cover page for the gridPULSE Catalog of National Laboratory Testing Resources.

Open Library Implementation

The open library is a collection of open models related to grid modernization. Models are organized into four broad categories: Generation, Transmission, Distribution, and Smart Home. In each category are sub-categories (e.g., within both Transmission and Distribution are sub-categories for PV). Each model entry in the open library has a link to download high-level information such as the ownership, version, contacts, and detailed information such as theoretical basis, specifications, interface opportunities, and validation.

The team has been engaging university, industry, and other GMLC projects to provide models to the open library and to suggest improvements to the user interface. Specifically, industry partners including hardware-in-the-loop companies are advising on how models and tools obtained from the open library can interface with their products to increase the capabilities for grid-related testing.

Participating partners have started actively entering models, tools, and datasets. During this phase, we have requested them to report their user experience and point out any eventual concerns or errors that they have identified. We received extensive feedback that we have leveraged to improve user experience with the objective to optimize the platform design to entering a model into the open library within 5 to 10 minutes. To achieve this, we considered the minimum number of required entry fields and information for model submission, the clarity on the field requirements as well as additional explanations for each field, the design layout, and the simplicity and effectiveness of the available options and account management. The objectives have been fulfilled and we will keep improving the design towards an optimal solution.

The open library is implemented on the gridPULSE website (see website section below), as seen in Figure IV.4.3. The project team has added over 35 entries and at least 40 more have been identified and will be added in the near future.

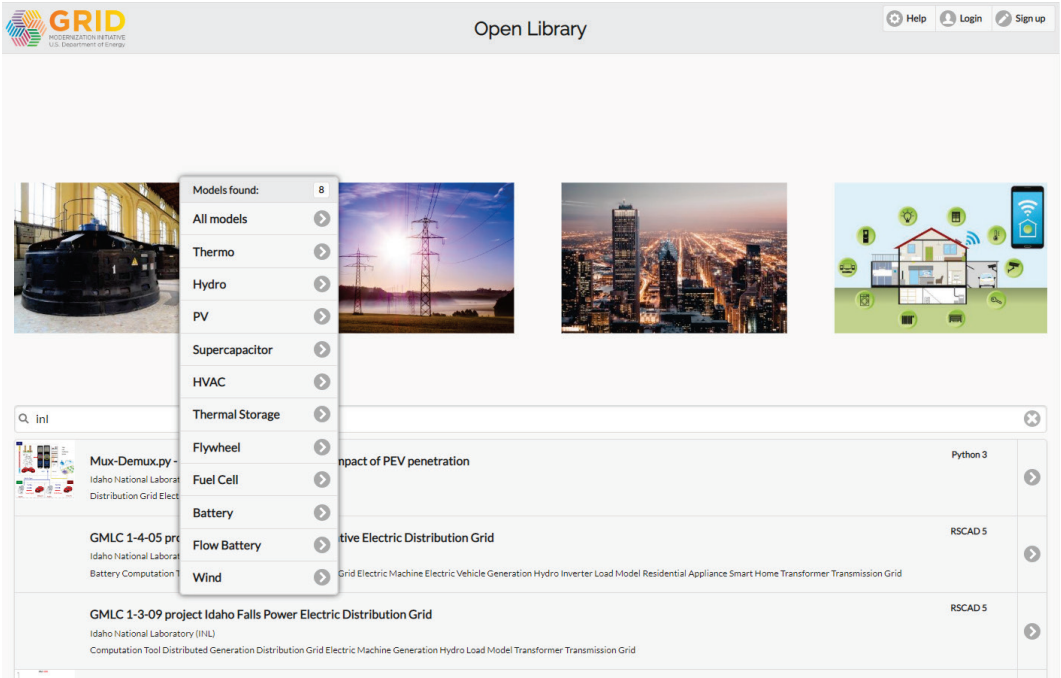

Figure IV.4.3 Open Library implementation, showing model categories (images at top) and entries (table at bottom).

gridPULSE website (gridPULSE.org)

The primary tool for both members and users of gridPULSE is the web interface: gridPULSE.org (see Figure IV.4.4). Members will use the website to submit and update information on testing capabilities, provide models to the open library, and list contact details to begin partnerships discussions. Based on this information, users will be able to access detailed information on national test facilities, download useful models, and efficiently establish partnerships in a way that is more streamlined and provides more detailed and useful information than accessing each member's website individually.

Website taxonomy reflects the major project accomplishments:

- About gridPULSE – describes the gridPULSE consortium, how to use the resources, and has details on partnering with the DOE National Labs
- Testing Resources – ability to download the testing capabilities catalog or to browse through an interactive version that can be sorted and filtered
- Open Library – implementation of the open library allowing the user to search or sort the models and tools, view significant details on each entry, and has links to download the models or tools
- Contact Us – form to get in touch with the gridPULSE team for testing requests, additional information on open library models, or general questions

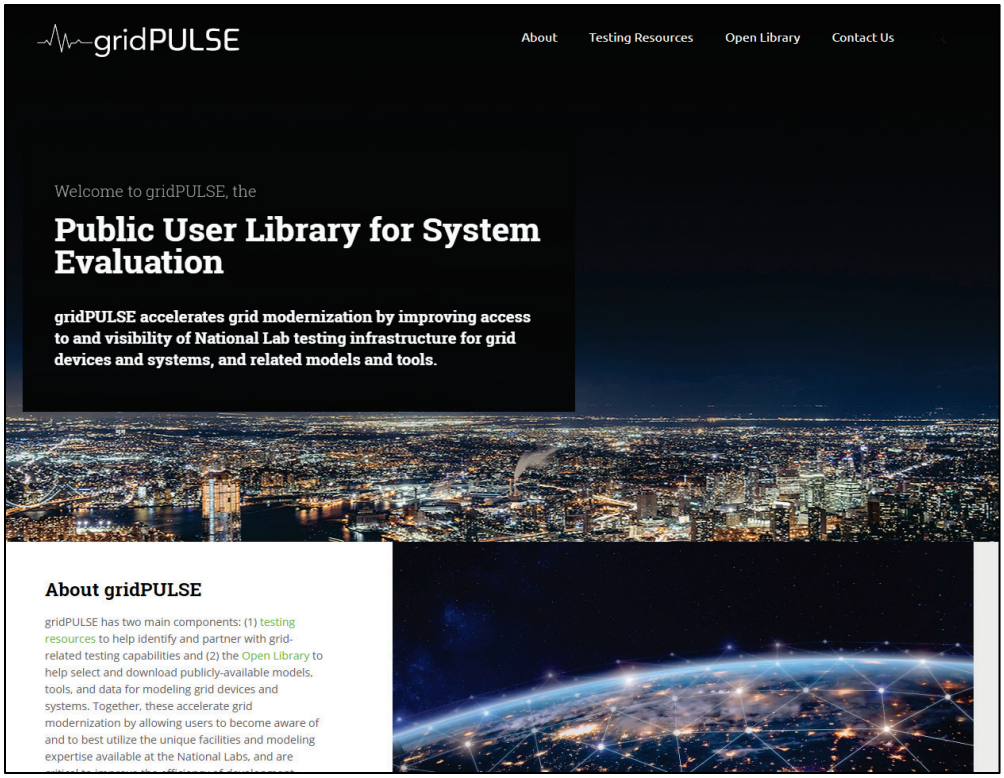

Figure IV.4.4 gridPULSE.org website, showing links (top right) to About, Testing Resources, Open Library, and Contact Us.

Conclusions

Through our outreach and information collecting activities so far, we have both validated the need for, and significantly populated the Testing Network and Open Library. Industry stakeholders have emphasized the need for an easier path to understanding and partnering with DOE National Lab facilities and models. The gridPULSE consortium addresses this, mainly through the gridPULSE.org website by serving as the vehicle for disseminating information on testing and modeling capabilities, and additionally enables enhanced interaction such as facilitating testing requests and allowing users to contribute models to the Open Library.

Ongoing efforts are focused on continued population and updating of the Testing Network and Open Library to ensure maximum value. We are focused on sustainability and outreach to ensure this work has maximum impact. We are publicizing and soliciting feedback through conference presentations, webinars, and additional project socialization such as participating in other GMLC project team meetings. We are drafting a sustainability plan to propose how gridPULSE will continue beyond the end of this project. That plan is taking into consideration the value proposition to users as well as possible future funding sources.

Key Publications

1. M. Lave, “gridPULSE: Public User Library for Systems Evaluation to Accelerate Grid Modernization”: in proceedings of the 2018 IEEE 45th Photovoltaic Specialist Conference (PVSC), SAND 2018-6192C.
2. D. Grubbs, “Catalog of National Laboratory Testing Resources for Grid Devices,” published March 2018, available at: https://gridmodtools.org/testing-catalog/. SAND 2018-4170R.

IV.5 GMLC 1.4.2 – Definitions, Standards and Test Procedures for Grid Services from Devices (PNNL, with ANL, INL, LBNL, LANL, NREL, ORNL, SNL)

Robert Pratt, Principal Investigator
Pacific Northwest National Laboratory
P.O. Box 999
Richland, WA 99354
E-mail: robert.pratt@pnnl.gov

Teja Kuruganti, Principal Investigator (2nd)
Oak Ridge National Laboratory
P.O. Box 2008
Oak Ridge, TN 37831
E-mail: kurugantipv@ornl.gov

Lee Slezak, DOE Technology Development Manager
U.S. Department of Energy
E-mail: Lee.Slezak@ee.doe.gov

Start Date: October 1, 2017 End Date: Project continuation evaluated annually
Project Funding (FY18): $2,031,000 DOE share: $2,031,000 Non-DOE share: $0

Project Introduction

This project's (GMLC Foundational Topic 1.4.2's) overarching goal is to enable and spur the deployment of a broad range of distributed energy resource (DER) devices with the ability to provide much of the flexibility required for operating a clean and reliable power grid at reasonable cost. The required flexibility, expressed in the form of a growing number of increasingly valuable services at the bulk system and local distribution levels, is largely embodied in grid services that are provided by power plants and substations today. However, it is also increasingly reflected in wholesale market products or utility programs in which DERs participate. The project's objectives address the primary barriers that limit the ability of grid operational and planning tools to assess the ability of such devices to provide these services, at scale, in the future power grid.

The project addresses the most important device classes expected to play critical roles in a modernized grid: responsive equipment and appliances in buildings, batteries, electric vehicle chargers, hydrogen infrastructure (fuel cells and electrolyzers), and smart inverters for PV solar and batteries.

Existing grid services include ancillary services (regulation, reserves, ramping) that keep the grid in supply-demand balance, in addition to managing peak loads to reduce infrastructure capacity requirements, and managing wholesale purchase and production costs. Industry has also envisioned new reliability services from DERs such as artificial inertia and participation in remedial action schemes that enhance the reliability and stability of the bulk grid, and new distribution-level services such as mitigating rapid voltage changes and reverse power flows from high solar PV penetrations.

As its primary technical goal, ***the project will provide a general, standard device model with a battery-equivalent interface applicable to each device class.*** This will be in the form of an equivalent battery model, useful for comparing and aggregating the capabilities of devices from different classes and extrapolating their ability to perform grid services. This interface is designed to be modular and readily incorporated in grid planning and operational tools. It will be simple and generic to use, representing all device types together with allowing for only a single, common dispatch algorithm for each grid service, rather than a custom algorithm for each device class. Such a common model is highly desireable for the tools used to plan and design new and

modernized grid infrastructure, and to operate transmission- and distribution-level grid management/control systems and markets, to properly take into account the roles and functions of DER devices in the future grid.

Developing a unified modeling approach for evaluating the performance of grid services from DER devices is the basis for achieving the project's **overall strategic outcomes:**

- Enable utilities and grid operating entities to accurately assess the contribution of DER devices, at the planning and operational time scales, by using models of their performance that can be incorporated into the tools used to plan and operate the grid.
- Encourage device manufacturers to add the capabilities needed to supply existing and new grid services by clearly articulating the performance characteristics required and a means for evaluating their engineering and economic potential in various regions of the nation.

Objectives

The project will help improve the capability of devices to provide an increasingly valuable and broader range of grid services by completely articulating the device performance needed to supply grid services, many of which are not well understood by device manufacturers. It will also identify and quantify the effects of performing grid services on devices' efficiency, and tabulate impacts that may affect equipment lifetimes or that reduce their ability to provide other services to the user, so that any such negative impacts can be mitigated by improved device designs or grid operational strategies.

Finally, by highlighting the potential of their devices to provide grid services, the project encourages manufacturers to build the required capabilities into their devices at the factory, where it is far less expensive than adding them later in field retrofits by utilities or customers. This ultimately lowers the costs for devices that must ultimately be borne by the power grid, whether through purchase or incentives, and hence increases their penetration at scale.

The project's objectives address the need to construct the capability for planning and operational tools to estimate how well the devices can provide a wide range of services, at scale, in the future power grid. Building upon the accomplishments of the project's first year, which was oriented toward an overlapping but somewhat different set of objectives, the project will:

1. Develop and publish a standard set of device models describing the operational and engineering constraints (including human factors) for each of a wide variety of device classes so that fleet performance in providing grid services can be readily estimated with high-fidelity.

2. Develop and publish a battery-equivalent model interface for each of the device classes to provide a simple, standard, and common (across device classes) "virtual battery" interface so that high-level grid planning and operation tools can readily evaluate grid services from device fleets.

3. Define prototypical "drive cycles" representing the time-series injection or withdrawal of real and reactive power that each of a wide variety of grid services require from device fleets, and conduct a trial analysis summarizing the performance of devices against those drive cycles in engineering and economic terms.

4. In collaboration with industry, develop characterization test protocols for three device classes (water heaters, commercial refrigeration systems, and electric vehicles), and conduct actual tests on a typical such devices and validate that the protocols, and the device and battery-equivalent models produce valid results.

5. Conduct a study of existing DOE appliance and equipment efficiency testing protocols to identify existing results and suggest additional test elements or analyses of data already being collected that could characterize important parameters describing the response capabilities of relevant device classes.

Approach

Before DER devices can penetrate the marketplace for grid services at scale, grid planners and operators need to be able to accurately and conveniently assess and value services that DERs can provide, in order to design appropriate markets and incentives for them and to properly account for their capabilities in the planning process. Similarly, manufacturers need a means of evaluating the degree to which their equipment could potentially provide various services, and how much potential value would be derived by the grid from doing so. The presumption is that a large share of that value would accrue to the purchaser of the device, but that must exceed the marginal cost of providing those capabilities in the equipment.

So, ***the project will develop and validate a model-based procedure to asses a device fleet's ability to provide any grid service.*** This will consist of a device model encapsulating the physical and human factors constraints pertinent to each class of DER device. The device models account for limitations on input and output power, the duration that the device can sustain (i.e., the energy it has available), and the energy efficiency of operating the device in the pattern required to supply a service. The device model is used to update these parameters, which interact in complex, non-linear ways, on a time-series basis as the device is dispatched to provide a grid service. One model will be developed to represent each device class in the project. Others may be added at a future date.

Further, the analyses conducted in the course of operations and planning must be able to readily access the information in these device models. Embedded in operational and planning tools are algorithms that dispatch DER device fleets to accomplish grid services. The complexity of doing this for each of a wide variety of device classes is a key barrier that must be overcome. So, ***the project will develop a single, common, battery interface from the device models to these high level models, so they can use a single algorithm to dispatch DER fleets of any type.*** This will greatly facilitate use of the latest device models, and allow new device classes to be readily added as new device models with battery-equivalent interfaces are developed.

It is important to be able to link the device models to actual, measured physical performance characteristics of devices. So, ***in collaboration with industry, the project will develop device characterization test protocols for three device classes (water heaters, commercial refrigeration systems, and electric vehicles)*** for use by manufacturers, utilities, and other organizations to measure the relevant performance parameters. ***The project will conduct validation tests for these devices, comparing modeled to actual performance,*** using segments of the prototypical annual drive cycles for each grid service.

Finally, an important opportunity for DOE is the potential to leverage existing appliance and equipment efficacy standards tests to obtain measured values for device characteristics that define device's ability to perform grid services. So, ***the project will review the efficiency testing procedures to determine a) characteristics and parameters that are already measured, b) characteristics and parameters that can be derived from data collected during the tests with further analysis, and c) marginal additions to the tests that could obtain additional parameters at low additional cost.***

PNNL leads the project. Table IV.5.1 lists the roles and responsibilities of all the national laboratories in the project. The work will be divided among various device classes, with a track for each of them managed by a national laboratory with the expertise to develop and test the device models. On a parallel track, several laboratories lead also lead a task on grid services, as indicated in the table.

Table IV.5.1 Device Class and Grid Services Responsibilities by Laboratory

Laboratory	Device Class Lead	Grid Services Lead
PNNL		Peak load management Artificial inertia/frequency response
NREL	Water heaters PV/inverters	Distribution voltage management/PV impact mitigation

SNL	Batteries/inverters	
ANL	Electric vehicles	
ORNL	Heating/cooling equipment Commercial refrigeration systems	
LBNL		Regulation, Spinning reserve Ramping Capacity market dispatch
INL	Fuel cells Electrolyzers	
LLNL	(Liaison to other modeling projects)	Wholesale energy market/production cost dispatch

PNNL and ORNL share responsibility for producing a report on opportunities to leverage and extend existing DOE appliance and equipment efficiency testing protocols to characterize devices subject to such testing. This includes residential air conditioners, water heaters, refrigerators; commercial rooftop units and refrigeration.

Results

During Project Year 2, the project team developed a common structure for all the device models and grid services, all of which are open-source and programmed in Python (also open source). One of the primary foci was defining a general architecture for the relationship and information exchange between high-level grid models (e.g., production cost, markets, transmission operations, distribution operations, etc.), device fleet models, and individual devices or sub-fleets.

This generic architecture is shown in Figure IV.5.1, described here. The green box at the top represents a high-level grid model conducting an analysis that includes the contributions of devices in supplying grid services it models. In Step 1 (red circle), the high level model makes a request of a device fleet via the battery-equivalent interface (or API – application program interface). This request includes the time-step being undertaken and a request for real-or reactive power delivered for the grid service (average) during the time step (from seconds up to one hour), and/or the current price and price forecast. The high-level model makes this request with knowledge of the device fleet's power, energy, and other constraints from the previous time step (Step 4, see below).

The device fleet model (pink box) undertakes the next step of coordinating the response of each device or sub-fleet. A sub-fleet differs from an individual device only in that it has a weighting factor greater than 1.0, i.e., that it represents a segment of the device population with identical characteristics. Sub-fleets are defined by the analyst to represent the diversity of characteristics and states in the entire population needed to conduct a meaningful analysis. That is, they are within the purview of the high-level modeler to define. For the project's trial analysis, default sub-fleet populations of devices will be defined that represent the range of device characteristics found in a typical population.

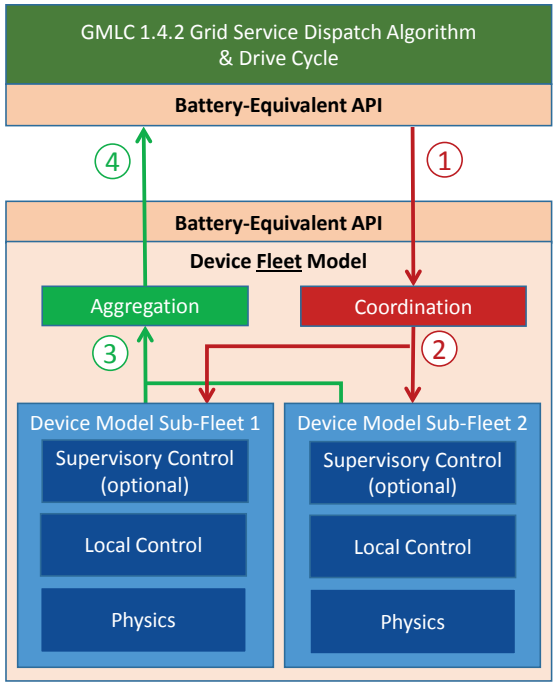

Figure IV.5.1 Software architecture of services and device models

The device fleet model developed is the most general, common case of a benevolent aggregator dispatching the fleet to deliver the exact service requested while minimizing any negative impacts on the devices and device owners. The aggregator is assumed to be omniscient in that it has full access to information specific to each *instance* of a device in the fleet that is being modeled to represent a segment of the device population, i.e., all relevant variables regarding states, modes, owner limitations on use, etc. with which to understand how to allocate the request for service to individual device/sub-fleets, based on whether a given device/sub-fleet can and will respond to the request for service. It may do this by distributing the request evenly to all devices able to respond, for example, or to equalize some utility or "pain" function. The allocation algorithm is specific to each device class. It is also subject to modification or change in the future to reflect other allocation mechanisms devised by high-level modelers. The coordination algorithm then passes on the grid service request and time step to each device/sub-fleet model to implement the time step (Step 2).

The device model has three basic elements, in the general case. At the root is a physical model of the device itself, based on the characteristics supplied by the high-level analyst. Examples of the physical modeling processes include electrical and thermal power and energy flows in a battery, or a hot water tank, etc. Above that lies a control model that includes processes like the basic thermostat operation of a water heater's heating elements, or a battery charge controller. In the general case, above the basic control lies another layer of supervisory control, which can modify the control's setpoints, within acceptable ranges defined by the analyst, to adjust the power input to or withdrawn from the grid by the device. For example, a water heater's supervisory control may raise the hot water setpoint to turn a water heater "off", or keep it "off". At any point during the time step, a device may balk at continuing to supply the service if its limits (specified by the high-level modeler) are exceeded.

The difference between the device's power injection (output to the grid, or the negative of its consumption) when providing the service, compared to when it is not providing a service, defines the power provided to the grid service. While trivial in the case of a battery, in many device classes (particularly loads) the base case involves a level of consumption that must be modeled and tracked separately so the difference can be calculated.

Not shown in the diagram, each device model has access to a data bus containing boundary condition information for the geographical location of the device (weather) and topological location of the device (voltage). The analyst responsible for the high-level model, or that model itself, updates this information at each time step as required.

Upon completion of the time-step, the device model reports its average power injection and power supplied for the service to the device fleet model in Step 3. It also reports how much energy it contains at the end of the time step, and the maximum and minimum limits on power and energy it can supply in the upcoming time step. It also provides details about its throughput efficiency and constant energy losses when discharging or charging energy from its source or storage, limits on ramp rates, etc.

In Step 4, the fleet model simply aggregates the actual power supplied for the service, and the limits and other variables applicable to the next time step, translates these into battery-equivalent interface terms, and passes them up to the high-level model.

In an additional, parallel effort, PNNL and ORNL developed recommendations for extensions or modest additions to appliance standards testing that would be useful for estimating how well devices can provide grid services. The project reviewed the test procedures for residential electric water heaters, residential refrigerators, residential HVAC, commercial HVAC and commercial refrigeration, and developed some initial recommendations for additional tests that could be added or results that could be obtained from exiting tests. This report is designed to assist internal DOE-BTO strategies, and will be at DOE discretion whether to publish it. It is also intended to serve as timely notice for the DOE-BTO Standards program, per their request, about any proposed testing activities for appliances that are subject to efficiency standards.

In a second parallel effort, ANL, NREL, and ORNL developed written specifications of proposed device characterization tests for water heaters, commercial refrigeration systems, and electric vehicles that will be conducted in the third year of the project. The team developed a draft report detailing the models, test equipment, parameters collected/estimated, and model validation procedures that will be used. This report is designed to be a foundation for discussions of the test plans with industry during Project Year 3.

Conclusions

The project has completed the specification of the general battery-equivalent interface for eight device models and is preparing to publish the models in the form of an open-source Python-based software library. The project is in the final stages of completing the grid services software that will be used for exercising the models and provide insights into devices' abilities to respond to a range of prototypical grid services. The project has analyzed how existing appliance standards test procedures could be leveraged to provide equipment parameters useful for characterizing how well devices can supply grid services, and has developed plans for testing example devices from three device classes—electric vehicles, commercial refrigeration, and water heaters—to validate their device models.

Key Publications

1. Recommended Practice for Characterizing Devices' Ability to Provide Grid Services – Working Draft for Comment Only. Pratt, R.G. and Z.T. Taylor. March, 2017. Pacific Northwest National Laboratory, Richland, Washington. PNNL-26253. On line at: https://gridmod.labworks.org/resources/recommended-practice-characterizing-devices%E2%80%99-ability-provide-grid-services.
2. Options for Additional Tests or Results from Appliance Standards Test Procedures. Butzbaugh, J.B., E.M. Johnson, and J.D. Munk. (Draft Internal Report to DOE). July 2018. Pacific Northwest National Laboratory, Richland, Washington. Unpublished.

3. GMLC 1.4.2 - Device Characterization Test Plan. Kuruganti, T., M. Duoba, and C. Booten. July 2018. (Draft Internal Report to DOE). Pacific Northwest National Laboratory, Richland, Washington. Unpublished.

Acknowledgements

The project has a large number of contributors from eight national laboratories. The principal investigators Rob Pratt (PNNL) and Teja Kuruganti (ORNL) would like to thank these key contributors, including:

PNNL:	Taylor, Todd	Liu, Yuan	Winiarski, Dave	Ngo, Hung	Butzbaugh, Josh
ANL:	Duoba, Mike	Fernandez Canosa, Alejandro			
INL:	Mohanpurkar, Manish	Kadavil, Rahul			
LBNL:	Schwartz, Peter	Liu, Jingjing			
LLNL:	Edmunds, Tom	Donde, Vaibhav			
NREL:	Booten, Chuck	Ding, Fei	Maguire, Jeff	Jin, Xin	Mahmud, Rasel
ORNL:	Munk, Jeff	Xue, Sonny	Dong, Jin	Bhandari, Mahabir	
SNL:	Rosewater, David				

V. Grid and Infrastructure: Fast Charging Enabling Technologies

V.1 Demand Charge Mitigation Technologies

Andrew Meintz, Principal Investigator
National Renewable Energy Laboratory
15013 Denver West Parkway
Golden, CO, 80401
E-mail: Andrew.Meintz@nrel.gov

Lee Slezak, DOE Technology Development Manager
U.S. Department of Energy
E-mail: Lee.Slezak@ee.doe.gov

Start Date: October 1, 2017 End Date: September 30, 2019
Project Funding (FY18): $600,000 DOE share: $600,000 Non-DOE share: $0

Project Introduction

Most commercial buildings or facility pay for their electricity bills with two types of charges --- energy charge and demand charge. Energy charge is the cost for the total energy use for the month and demand charge is the charge for the peak power demand of the month. The peak power demand of the month for billing is usually calculated as an average demand in 15-minute time frames. For example, NREL has a contract with the utility at $0.04/kWh for energy charge and at $16.79/kW for demand charge as of 2017. Therefore, electricity cost can be lowered not only by using energy efficient products but also reducing peak demand by distributing power demand throughout the day for flexible devices and specifically plug-in electric vehicles (PEV).

NREL conducted experiments for demand charge mitigation by controlling power of electric vehicle supply equipment (EVSE). Initially work at NREL has been focused on level-2 charging — typically 3.3kW to 7.2 kW — of PEVs where there is flexibility in the time in which vehicles can be charged during a workday. This approach however is not possible when considering DC fast charging — typically 50 kW but expected to reach 350 kW— where there no flexibility in time. This effort explores the charge/discharge control of an energy storage system (ESS) to mitigate demand charges.

Objectives

One of main issues with demand charge mitigation and load control is scalability as the number of devices with controllable load increases. Distributed control without information on the other devices, e.g., controllable water heater, HVAC, etc. may cause the system to become unstable. Suppose that load control of individual devices is dependent on the total load and are completely distributed (each control system does not have information on other control systems). Then, if a controller of a device reduces its load during the peak, it will lower the total load. Then, a controller of another device may try to increase its load because total load has reduced, which increases total load again and makes the system unstable. Centralized control algorithms [1] can solve this problem by coordinating the controllers together but it is not efficient if the size of the system becomes large and its scalability limits the addition of new resources.

Many algorithms are proposed for demand side management using game theory approach [2], [3]. They use real-time pricing information in solving the problem, which is not available in every territory and the conditions for the Nash equilibrium are not always satisfied in real-world situation. Different from the abovementioned techniques, this project aims to develop a centralized control algorithm with the hierarchical control structure. The developed controller manages the different controllable loads at NREL campus (e.g., EVSEs, buildings, ESSs, etc.), so that peak shaving is realized.

Approach

One method to resolve the issue described in the previous section is distributed control with hierarchical structure and utilization of an energy constraints approach as described in [4]. A similar approach is used in the GM0085 project to develop a PEV charging aggregator [5]. In the case of a PEV, it has a required energy amount that is needed by departure time. The energy delivered to the PEV along the time will lie somewhere in the gray area in Figure V.1.1 (a). The upper bound of the plot implies that the PEV is charged at the maximum rate as soon as it is plugged-in. The lower bound means the PEV starts charging as late as possible so that the requested energy amount can be delivered by the departure time. In other words, the upper bound means it uses the maximum available energy at its earliest time and the lower bound means that the energy is used at its latest time. Energy constraints for stationary ESS are a little different from the ones for PEV because the ESS not only consumes but also provides energy. Further there is no fixed departure time for the ESS and thus an arbitrary time horizon must be chosen. Examples of energy constraints for stationary ESS and a controllable building load (e.g., HVAC) are illustrated in Figure V.1.1 (b) and (c), respectively. ESS energy constraints can go below zero because it can provide energy to a building. Energy constraints for the controllable building load have multiple slopes because the power demand by the load depends on its constraints such as air temperature boundaries and air circulation requirements in the case of an HVAC. If we have multiple devices, the aggregate energy constraints are represented as the plot in Figure V.1.1 (d). The goal is to find an optimal energy use first at each time step given total energy forecast and second to then allocate the obtained energy amount to each device depending on its priority of energy need.

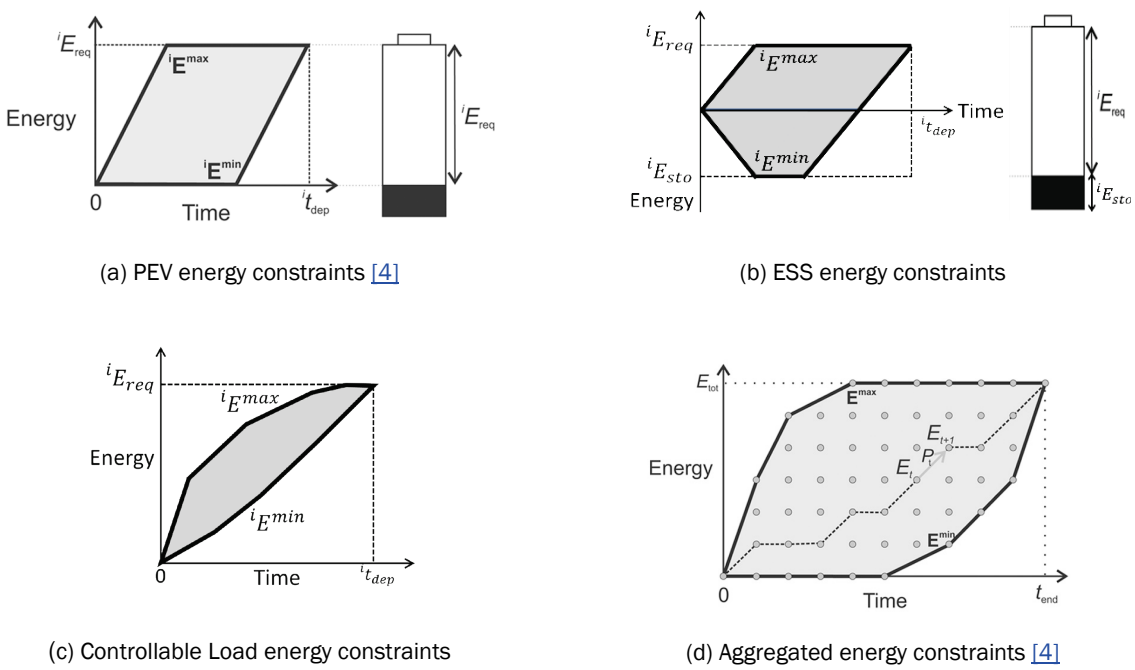

(a) PEV energy constraints [4]

(b) ESS energy constraints

(c) Controllable Load energy constraints

(d) Aggregated energy constraints [4]

Figure V.1.1 Energy envelop of each device and aggregated energy envelop

This two-step energy allocation algorithm can be extended to a distributed system that is arranged in hierarchal structure. A diagram of a system with hierarchical control structure is illustrated in Figure V.1.2. The local controllers control each device connected to them. The local controllers have energy constraints of each device connected to them and send aggregate energy constraints to the controller in the above level. The local controllers receive energy assignments from the controller above them and allocate the assigned energy to each device connected to them as previously described. The same thing is repeated in the controllers in the section level. The controllers in the section level will receive each aggregated energy constraint from the local controllers, aggregate the lower aggregated energy constraints, and send it to the level above. In this way, the system can be easily scaled and as a result the complexity of the system is linearly proportional to the size of

the system. In this architecture, each local controller has a different interface depending on the type of device it controls. For example, a local controller for an EVSE with Open Charge Point Protocol (OCPP) should have OCPP interface or a local controller for a smart thermostat with Smart Energy Profile (SEP) 2.0 needs to have SEP 2.0 interface. However, controllers in the section level have a common structure and only communicate in-terms of time and energy allowing for the system to easily scale based on the fundamental requirement of each device.

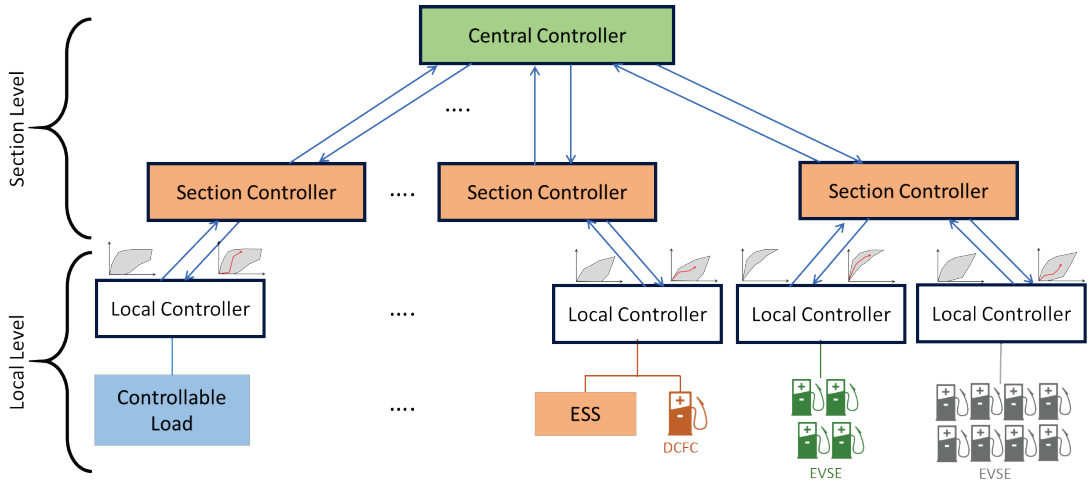

Figure V.1.2 Structure of distributed control with hierarchy

Results

The main advantage of DC fast chargers is their capability to charge PEV's in short time. From this perspective, it does not make much sense to reduce charge power during the peak in the similar way as with AC level-2 EVSE's because it disregards the main purpose of DC fast chargers. Deployment of energy storage systems (ESS) might be a way to fully utilize the advantage of DC fast chargers and alleviate loads to grid. NREL installed a 50 kW DC fast charger by Tritium along with a 40-kWh stationary battery system by Sharp, as depicted in Figure V.1.3. The Tritium DC fast charger has one CHAdeMO connector and one combined charging system (CCS) connector.

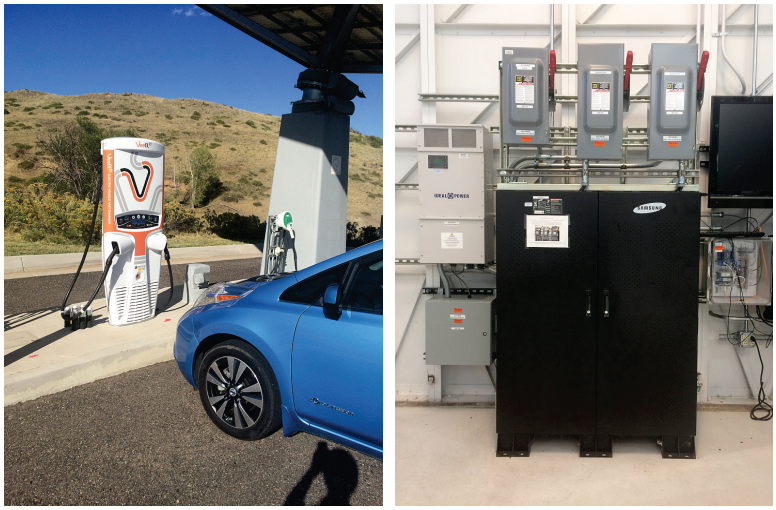

Figure V.1.3 Tritium 50 kWh DC fast charger (left) and 40 kWh stationary ESS by Sharp (right)

The battery system is tied with the building meter and controls the battery so that the building load does not exceed a certain value called clipping level. The value of clipping level can be changed by using the API developed by Sharp. The battery starts to discharge if the 15-minute average of the building load exceeds the clipping level value less an offset called zone discharge offset. Figure V.1.4 illustrates how the battery is controlled depending on building load and clipping level value. The negative battery power implies the battery is discharged to provide power to the building. The building load data is the real-time load recorded and

includes the charge and discharge power of the ESS. This data is provided for a day with variable solar production and a level-2 charge event in the morning hours.

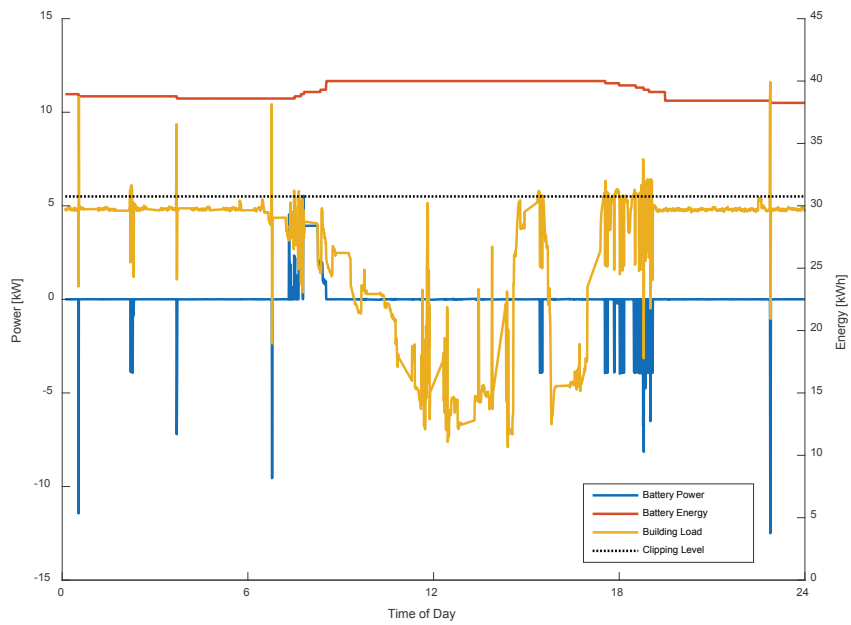

Figure V.1.4 Plots of building load, clipping level, battery power, and battery energy

Demand charge mitigation tests of a DC fast charger in conjunction with a stationary batter have been performed. A Nissan LEAF with CHAdeMO inlet was used. Results of the tests are shown in Figure V.1.5. The clipping level was set to 20 kW (gray dotted line in the plot). Without a stational battery for demand charge mitigation of a DC fast charger, the instantaneous building load would have risen above 40 kW (brown dashed line) once the DC fast charger is used. The stationary ESS alleviates load by the DC fast charger by providing energy to grid and demonstrates it performs well for demand charge mitigation.

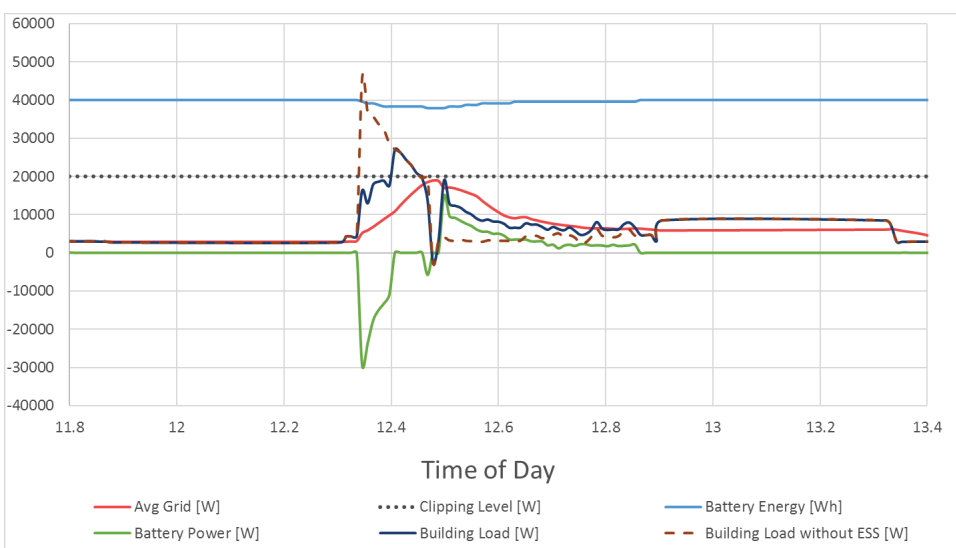

Figure V.1.5 DCFC demand charge mitigation with ESS

Conclusions

NREL has demonstrated independent level-2 EVSE management in the GM0062 project and independent ESS control associated with a DC fast charger for demand charge mitigation in this project. In FY19, NREL will install additional EVSE with different interface protocols (SEP 2.0, OCPP, REST, etc.), which will require an integrated control system, not individual control, for demand charge mitigation as the size of the system increases. An extended version of the energy constraint approach proposed in [4] is suggested. The system architecture of an integrated control system for EVSE and ESS for the NREL campus is illustrated in Figure V.1.6. With this structure, the system can be extended easily to accommodate additional controllable load such as smart HVAC, lighting, water heaters, etc.

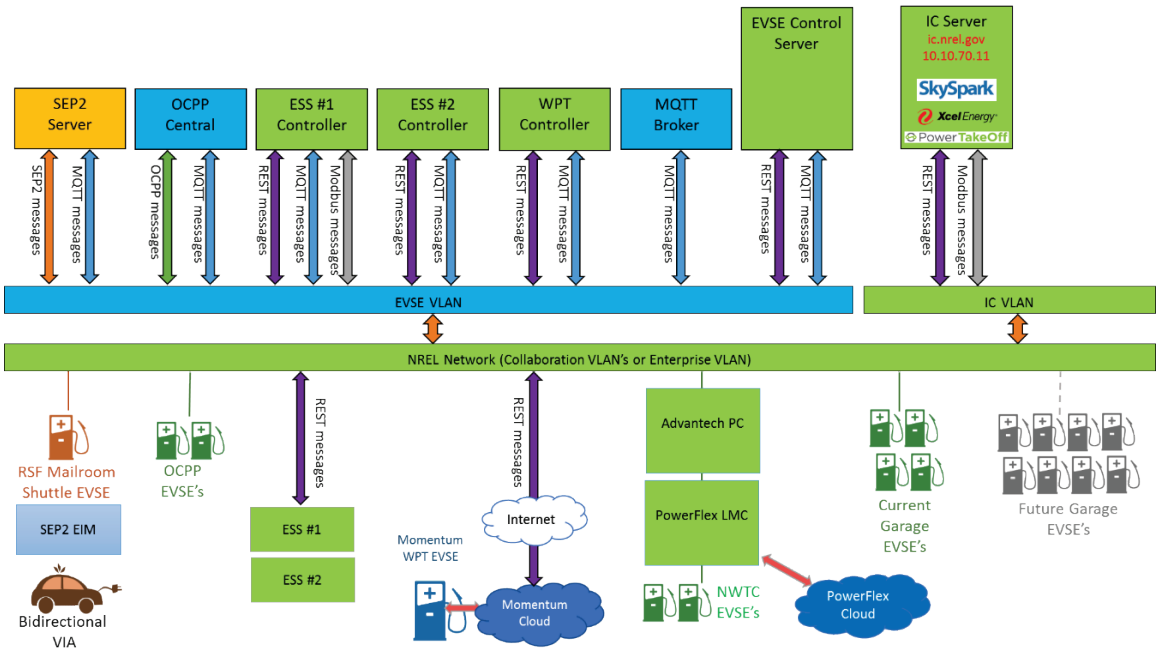

Figure V.1.6 Architecture of integrated control system for EVSE and ESS at NREL

References

1. T. Logenthiran, D. Srinivasan, and T. Z. Shun, "Demand side management in smart grid using heuristic optimization," IEEE Trans. Smart Grid, vol. 3, no. 3, pp.1244-1252, 2012
2. Z. Ma, D. S. Callaway, and I. A. Hiskens, "Decentralized charging control of large populations of plug-in electric vehicles," IEEE Trans. Control Systems Technology, vol. 21, no. 1, pp.67-78, 2013
3. M. H. K. Tushar, C. Assi, and M. Maier, "Distributed real-time electricity allocation mechanism for large residential microgrid," IEEE Trans. Smart Grid, vol. 6, no. 3, pp. 1353–1363, 2015.
4. S. Vandael, B. Claessens, M. Hommelberg, T. Holvoet, and G. Deconinck, "A scalable three-step approach for demand side management of plug-in hybrid vehicles," IEEE Trans. Smart Grid, vol. 4, no. 2, pp.720-728, 2013
5. Z. Yi, D. Scoffield, A. Meintz, M. Jun, M. Mohanpurkar, A. Medam ": A Highly Efficient Control Framework for Centralized Residential Charging Coordination of Large Electric Vehicle Populations," in preparation
6. T. Logenthiran, D. Srinivasan, and A. M. Khambadkone, "Multi-agent system for energy resource scheduling of integrated microgrids in a distributed system," Electr. Power Syst. Res., vol. 81, no. 1, pp. 138–148, 2011

V.2 Fast Charging: Grid Impacts and Cybersecurity (INL)

Richard "Barney" Carlson, Co-Principal Investigator
Idaho National Laboratory
P.O. Box 1625
Idaho Falls, ID 83415-2209
E-mail: richard.carlson@inl.gov

Kenneth Rohde, Co-Principal Investigator
Idaho National Laboratory
P.O. Box 1625
Idaho Falls, ID 83415-2209
E-mail: kenneth.rohde@inl.gov

Lee Slezak, DOE Technology Development Manager
U.S. Department of Energy
E-mail: lee.slezak@ee.doe.gov

Start Date: October 1, 2017 End Date: September 30, 2018
Project Funding(FY18): $1,000,000 DOE share: $1,000,000 Non-DOE share: $0

Project Introduction

With the increasing progression towards electrified transportation, the charging infrastructure required for an electrified fleet must be reliable, safe, and secure. Technology and engineering advancements must ensure the charging infrastructure provides benefit, or at least, does not negatively impact the electric grid. Additionally, the charging infrastructure network must be robust to cyber manipulation to ensure safe, reliable, and secure charging operation for the electrified fleet.

Objectives

The Fast Charging: Grid Impacts and Cyber Security project objectives are to investigate and assess the interaction of fast charging with the grid, specifically from the energy and power needs of electric vehicle (EV) drivers, as well as the cybersecurity vulnerabilities of fast charging with respect to the electric grid stability and robustness.

Approach

As EV charging energy requirements increase and charge power capabilities also increase, understanding the grid impacts and cybersecurity vulnerabilities of charging infrastructure are of utmost importance to develop and implement mitigation solution to ensure security and robustness. In this project, a production DC fast charger (DCFC) was investigated to assess cybersecurity vulnerabilities in relation to potential grid impacts. This 50-kW DCFC has both the SAE J1772 CCS connection as well as the CHAdeMO connection. In addition to cybersecurity vulnerability assessment and testing, initial analysis was performed to develop potential usage profiles for future high power charging sites. This will help researchers understand the demands of future EV charging on the grid and provide context for future cybersecurity.

Results

DCFC Cybersecurity and Grid Interaction

Idaho National Laboratory (INL) research staff investigated several of the vulnerabilities identified in a production 50-kW DCFC. Multiple attack vectors on the DCFC exist that enable access to the DCFC power electronics control system by an external entity or nefarious actor. When one of several of the attack vectors is manipulated, the DCFC immediately stops current flow (a.k.a. "stop charge event"). Other attack vectors also results in the DCFC to stop charging by merely invoking an error state in the DCFC. Ultimately, all of these cases result in the DCFC ended power transfer in a short duration.

During the "stop charge event," the DCFC input AC power decreases from full charge power (52.7 kW) to standby power (0.3 kW) in 0.020 seconds. This is a rate of -2.6 MW/s. Figure V.2.1 shows the three-phase AC input current and power response of the charge system. The result of one DCFC stop charge event has minimal impact to the local electric grid, but if multiple DC fast chargers are concurrently manipulated to stop charging, the impact can be quite large since the rate of change of current is very high.

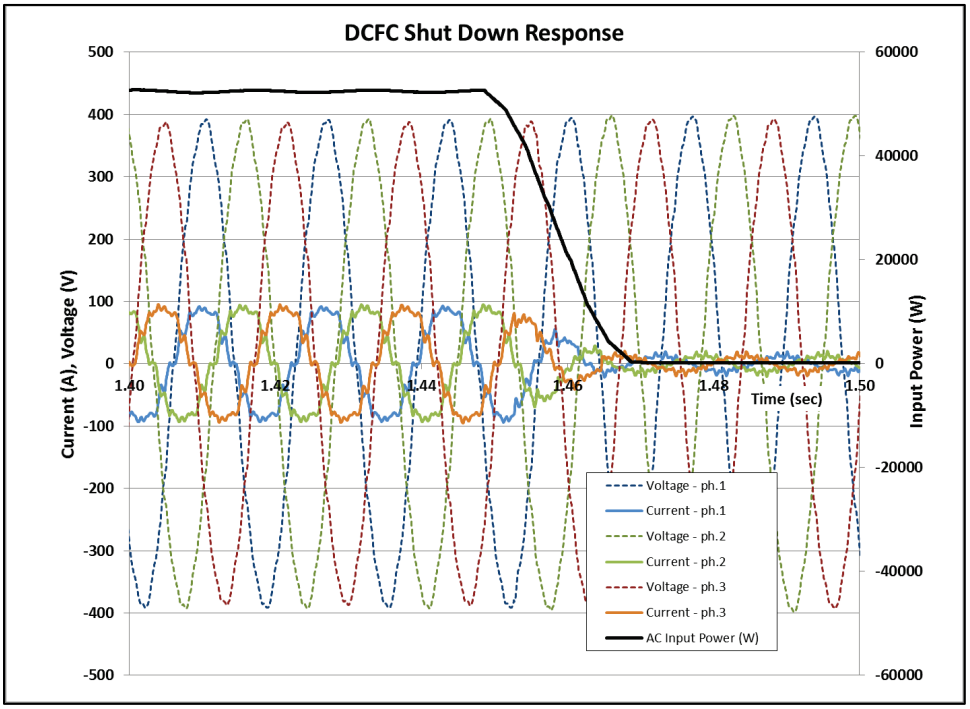

Figure V.2.1 "Stop Charge" response of DCFC during a charge event

During the stop charge event, the DC output current decreases at a high rate from 125 to 0 A DC in 0.150 seconds (-8400 DC A/s). The SAE J1772 standard specifies the minimum DC current ramp rate is -200 A/s during the shutdown sequence2 (DCFC initiated or vehicle-initiated shut down). Therefore, the rate of change in DC current is over 40 times greater than minimum requirements, which is advantageous for safety or other failure modes, but perhaps negatively impactful on grid stability due to the high rate of change of AC current. It is expected that a 350-kW XFC charger of a similar modular design of the DCFC will decrease input power at the same rate as the DCFC as shown in Figure V.2.1 (-2.6 MW/s), therefore decreasing from full to standby power in 0.140 seconds.

Additional exploitable vulnerabilities exist within DCFC that can disrupt the operational coordination between the modular power electronics. This exploitable vulnerability manipulates the internal power electronics control architecture that results in transient power fluctuations of the charger power flow. Ultimately, this causes poor power quality at the input to the DCFC, including low power factor and high input current total harmonic distortion.

With access and control of the high level controls of the DCFC internal power electronic modules, a malicious event was initiated that caused significant transient oscillation in power flow from the DCFC, which in turn resulted in a significant reduction in input power factor and increase in input current total harmonic distortion. Figure V.2.2 shows the steady-state DCFC operation followed by the results from the malicious control of internal power electronics systems causing significant fluctuations in power quality and total harmonic distortion.

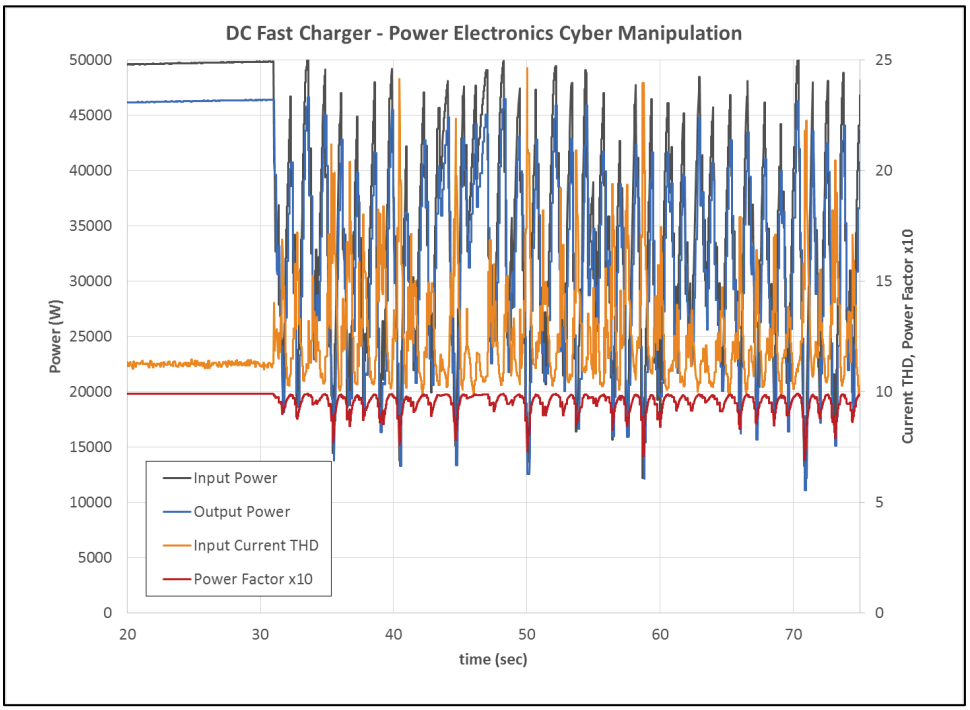

Figure V.2.2 DCFC power quality during malicious control event

The poor power quality that resulted from this cyber manipulation event is well outside of industry requirements for power quality. Significant disruption could occur to other devices connected nearby on the grid to the compromised DCFC.

The grid impacts of DCFC will depend upon the loads that the charging stations and sites add to the grid. A charging site may have multiple co-located chargers that draw power simultaneously which results in highly dynamic and variable total power required from the grid. Prior research from the industry has used the simple assumptions that fast charging occurs at constant power for nearly the entirety of the charge. Even though this is valid for Level 2 charging, this is not accurate for DC fast charging. To this end, INL research staff developed several load profiles at potential future charging sites, including the dynamic power draw of individual charging events.

One of the load profiles developed was for a charging site with four 150-kW DCFC stations. The station utilization was based upon real-world 50 kW DCFC use and charging energy needs collected from charge events of high-energy, long range EVs. Another charging site investigated was a longer-term scenario with twenty 400-kW DCFC stations, where fast charging is a 'gas station-like' experience (high power, very short charge duration). The utilization of this station was based upon the usage of modern-day gasoline stations and fuel needs of the drivers using those stations. The resulting power profiles can be seen in Figure V.2.3.

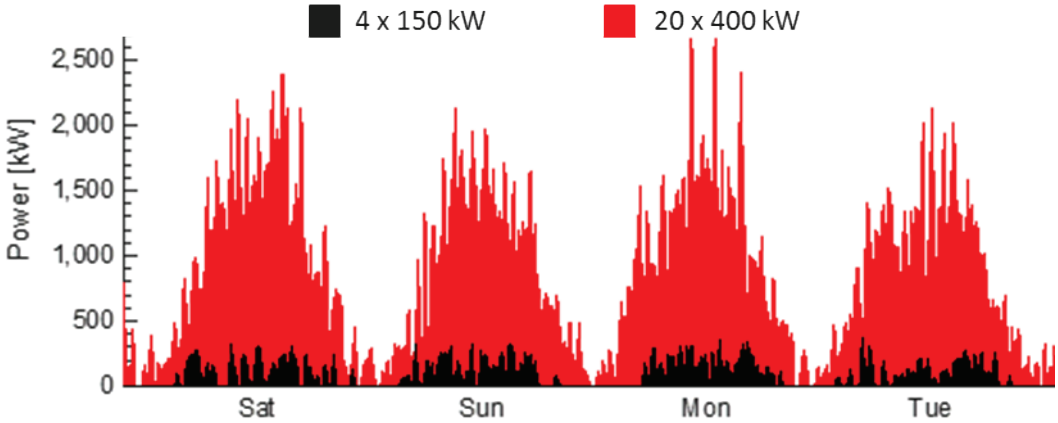

Figure V.2.3 Power draw for potential future charging sites over several sample days.

The electric grid loads required by future charging sites could be very large and highly variable throughout a day and vary from day to day. This type of load profile is rarely seen on today's electric grid, and the effects that widespread deployment of these types of high-power EV charging loads could have on the grid require further research to ensure robust and resilient operation.

Conclusions

Security and resiliency of EV charging infrastructure has shown to be very important. The research detailed here showed the interaction between charging infrastructure and the electric grid as a result of a cybersecurity manipulation events. It is expected that EV charge power will continue to increase and the power and energy needs of EV charging sites will also increase. This will only augment the effects of cybersecurity vulnerability manipulation and will have the potential to have much larger grid impacts. With proper, cyber-informed engineering solutions, EV charging infrastructure will provide the power and energy needed for electrified transportation without negative impacts to the grid.

References

1. Metcalf, M., et al., "Electric Program Investment Charge (EPIC) Final Report - EPIC 1.25: DC Fast Charging Mapping," PG&E, September 2016.
2. SAE J1772, "Electric Vehicle and Plug in Hybrid Electric Vehicle Conductive Charge Coupler," October 2017.

V.3 Extreme Fast Charging – High Power Wireless Power Transfer

Veda P. Galigekere, Principal Investigator
Oak Ridge National Laboratory, Power Electronics and Electric Machinery Group
National Transportation Research Center, 2360 Cherahala Boulevard
Knoxville, TN 37932
E-mail: galigekerevn@ornl.gov

Omer C. Onar, Principal Investigator
Oak Ridge National Laboratory, Power Electronics and Electric Machinery Group
National Transportation Research Center, 2360 Cherahala Boulevard
Knoxville, TN 37932
E-mail: onaroc@ornl.gov

Jason Pries, Principal Investigator
Oak Ridge National Laboratory, Power Electronics and Electric Machinery Group
National Transportation Research Center, 2360 Cherahala Boulevard
Knoxville, TN 37932
E-mail: priesjl@ornl.gov

Madhu Chinthavali, Principal Investigator
Oak Ridge National Laboratory, Power Electronics and Electric Machinery Group
National Transportation Research Center, 2360 Cherahala Boulevard
Knoxville, TN 37932
E-mail: chinthavalim@ornl.gov

Lee Slezak, DOE Technology Development Manager
U.S. Department of Energy
E-mail: Lee.Slezak@ee.doe.gov

Start Date: October 2017 End Date: September 2018
Project Funding(FY18): $450,000 DOE share: $450,000 Non-DOE share: $0

Project Introduction

Although the transition to electric vehicles (EVs) is beneficial in several aspects, they are yet to achieve wide acceptance. Range anxiety and long battery charging time continue to be critical challenges to mass adaptation of EVs. Range anxiety can be mitigated by having higher energy battery packs (> 100 kWh), but these higher capacity battery packs require much longer charging time. DC fast charging has enabled charging power levels around 40-50 kW in most cases and some up to 100-120 kW and reduces the charging time to less than an hour [1], [2]. As the charging power level increases, DC fast charging, which is a conductive charging technique, requires bulkier cables and very large and difficult to handle plugs and connectors which adds to the weight and makes the charging process cumbersome. It also requires active thermal management of the conducting cable and this makes the charging system susceptible to leaks and the associated hazards. In order to meet the U.S. Department of Energy's XFC (extreme-fast charging) goal of decreasing the charge time of a 300–mile range light duty electric vehicle to 15 minutes or less [2], the charging system requires power transfer levels that are well in excess of the maximum 22kVA (at the input) level considered by the SAE J2954 standard development for light duty vehicles [3]. Because power transfer capability is proportional to the cross-sectional area of the coil pair, minimizing the coil size to achieve low cost and facilitate mounting of the vehicle assembly is a difficult task at faster charging rates.

The main goal of this project to model, simulate, design, and analyze a high-power wireless power transfer (WPT) that can reach up to 100-200 kW power transfer levels in with a single line of power conversion system

without paralleling multiple inverter, coupling coils, and rectifiers. The project evaluated, modeled, and designed the high-frequency power inverter, vehicle-side power conditioning unit (rectifier and filter), and the high-frequency electromagnetic coupling coils. Activities in this fiscal year includes modeling and simulation of these system components to achieve a beyond-the-state-of-the-art technology development for these low-TRL (technology readiness level) components and systems.

Objectives

The objectives of the project include to review, analyze, model, and determine the most appropriate high-power WPT system architecture (including both the magnetics and power electronics) in terms of maximum power, power transfer efficiency, and the size and volume feasibility (compactness). This survey, benchmarking, modeling, and analysis is followed by the actual design, development, integration, and testing phases. Simulation and modeling results are used to validate the system feasibility, efficiency, and performance.

Approach

For this project, first, team completed the modeling and simulation of a ~200kW WPT system to identify optimal power electronics and electromagnetics architecture suitable for high power density and robust operation. Then, the WPT coils and the resonant tuning configuration are co-optimized using the finite element analysis (FEA) simulations to realize compact WPT coils with minimal resonant tuning component voltage and current stress. Next, the system level design of WPT system was performed including the design and assembly of the power electronics hardware, WPT coupling coils, and subsystem level evaluations. Finally, the high-power WPT system was experimentally validated and demonstrated up to 120kW power level.

When designing the system parameters, team considered around 650-700V nominal battery voltages which are already in use in some of the electric medium duty vehicles. At the front-end DC link, also using 650-700V input voltages will be very likely due to the 480V AC three-phase rectified systems. These voltage levels at the input and output allowed for the use of 1200V silicon carbide power MOSFETs with no reverse recovery losses and minimal conduction losses. Our initial investigation is focused on reaching the 100kW target to gain insight for further system level refinements. Therefore, we focus on the simplest tuning topology (series-series) with matched coils since the second order tuning networks result in more significant higher–order harmonics at the inverter output [4]. However, the coil currents are still very close to sinusoidal, and we are free to use the coil current amplitude as an extra design degree of freedom. The coil design procedure outlined here can be performed in this higher dimensional space by considering a mapping between Litz wire gauge, total diameter (including insulation), and effective cross-sectional area. The size of the coils required to achieve a given mutual inductance depends on the operating current density of the coil: A higher current density allows a larger amp–turn density, resulting in smaller coils. A higher current density also results in higher loss densities, so efficiency is a concern. Even if efficiency is constant, it would be necessary to dissipate a fixed amount of power over a smaller surface area. For the coil design optimization, the quarter-model of a DD coil optimization model was used with the symmetry and anti-symmetry boundary conditions defined to reduce the computational load.

The design of WPT coils is dependent on the power level, frequency of operation, the current carrying capacity of the conductors constituting the coil, and the power transfer height or the coil-to-coil distance. In this work, DD coil has been selected as the coil geometry owing to its higher power transfer height for a given coil diameter and current. A custom made Type 2 Litz (5x5x5/33/38) wire with an equivalent AWG 2 current carrying capacity of 130 A is used in the design. A bifilar winding scheme is used to handle the maximum coil current of 200 A. The dimensions of the designed 100 kW DD coils are 825 mm × 609 mm × 33 mm. The secondary DD coil is identical to the primary coil. The details of the optimized coil design are in Table V.3.1.

Table V.3.1 100 kW DD Coil Design Parameters

Parameters	# of primary turns	# of secondary turns	Frequency	Dimensions
Value	4	4	22 kHz	825 × 609 × 33 mm

The coils were optimized to maximize power density by adjusting the number of turns and winding window dimensions to achieve the targeted mutual inductance while minimizing the total coil area. As a tradeoff between the switching losses in the power electronics and the coil dimension, an operating frequency of 22 kHz was selected which is also consistent with the frequency bands being considered for high- power wireless charging systems by the SAE J2954/2 standards development committee. The 100 kW DD coil with design details shown in Table V.3.1 was simulated in COMSOL FEA simulation package for a nominal coil-to-coil distance of 5 inches. The simulated coil (primary and secondary coil are identical) and mutual inductances were 52.3 µH and 24.6 µH, respectively and resulted in a coupling coefficient k of 0.47. Figure V.3.1 shows the simulated flux distribution in the ferrites for the 100 kW DD coil while Figure V.3.2 shows physical primary coil built at the laboratory. The worst case losses in the DD coil pair by simulation was found to be around 2.0 kW. This is within the expected range of the thermal limits of the envisaged mechanical design of the coils and also indicates a minimum of 98% coil-to-coil power transfer efficiency.

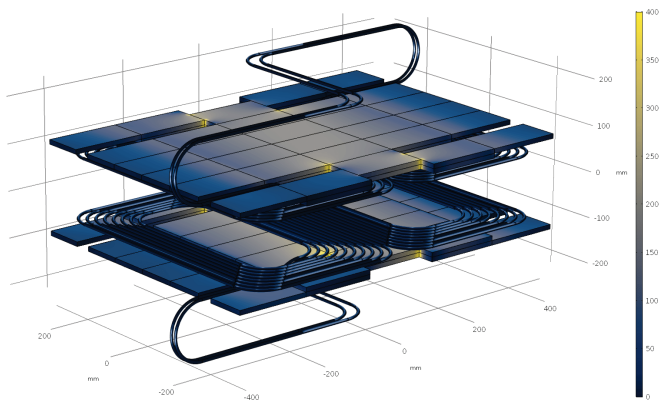

Figure V.3.1 FEA simulation result of the DD coil pair designed for 100 kW operation with nominal airgap.

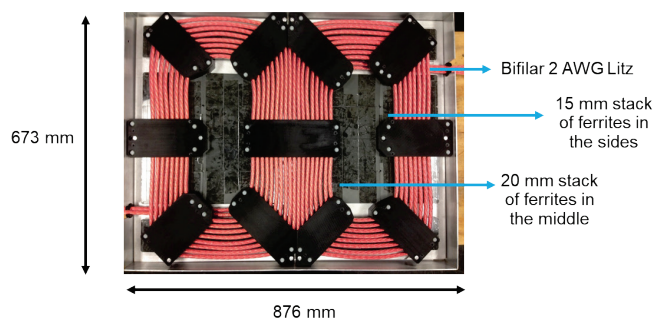

Figure V.3.2 High-power DD coil with 2 AWG Litz wire validated up to 120 kW.

The series-series tuned resonant stage circuit diagram is shown in Figure V.3.3. The equivalent circuit model of the series-series tuned WPT system based on the loosely coupler transformer model was created for the frequency domain analysis. Frequency domain analysis included deriving the system characteristics and the sensitivity to the coupling and load variations. Resonant network parameters from FEA simulation results utilized in the simulation model to analyze performance. The physical resonant stage with coupling coils and the tuning capacitors are shown in Figure V.3.4.

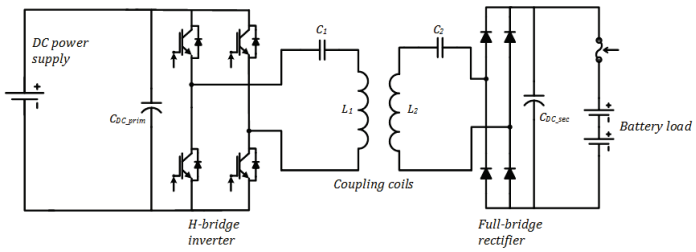

Figure V.3.3 System level circuit diagram of the series-series tuned WPT system.

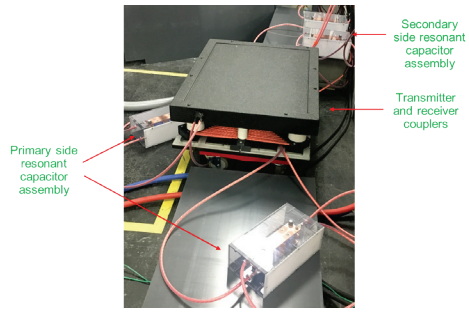

Figure V.3.4 The actual resonant stage.

For the high-frequency inverter at the primary-side and the high-frequency rectifier at the secondary-side, CAS325M12HM2 1200 V / 325 A silicon carbide phase leg module from Wolfspeed with a maximum allowable junction temperature of (175°C) is selected. The devices in the module have low on resistance R_{DS_on}=7.5 mΩ at 175°C and rated current. The preliminary worst case losses estimated for 100 kW operation was considerably lesser than the allowed power handling capability of 1500 W per phase leg as per the data sheet. Additionally, CAS325M12HM2 is an optimized low stray inductance (≤5 nH) planar package which should enable higher frequency switching. CGD15HB62LP gate driver card compatible with CAS325M12HM2 is utilized in conjunction with a Texas Instruments DSP board to implement phase-shift control for the HF inverter. The CAS325M12HM2 has discreet SiC Schottky diodes which is utilized as the secondary side rectifier. The high-frequency high-power inverter built for this project is shown in Figure V.3.5. This inverter was tested up to 120 kW and has a specific power of 26.08 kW/kg with its 4.6 kg weight.

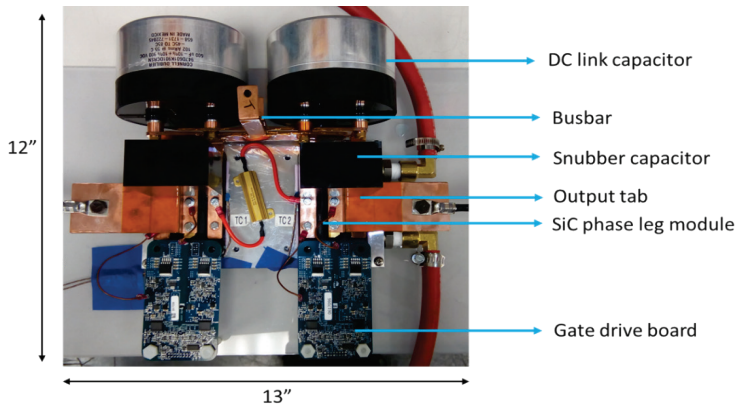

Figure V.3.5 High-power inverter/rectifier used in primary and secondary-side power stages.

Results

The designed high-power DD coils with parameters corresponding to Table V.3.1 were assembled and is shown in Figure V.3.2 and Figure V.3.4. The overall dimensions of the assembled coils are 876 mm x 673 mm. The measured primary and secondary coil inductances were 50.86 µH and 50.91 µH, respectively. The coupling coefficient was measured to be k = 0:44. Series-parallel combination of high frequency polypropylene conduction cooled capacitors were utilized to obtain the required 1 µF capacitance with the ability to withstand a voltage of 2400 V_{RMS}. Two identical inverter units were assembled with one envisaged to operate as the HF inverter and the other to be used as the secondary rectifier. The prototype of the HF inverter assembled is shown in Figure V.3.5. The laboratory setup of the experimental system is shown in Figure V.3.6. In the experiments, the DC input power to the inverter is provided by two series-connected E&M Power 450V / 100 kW DC emulators while on the secondary side, an NHR 9300 1200V / 100 kW battery emulator was employed in parallel with resistors in order to achieve 120kW load power.

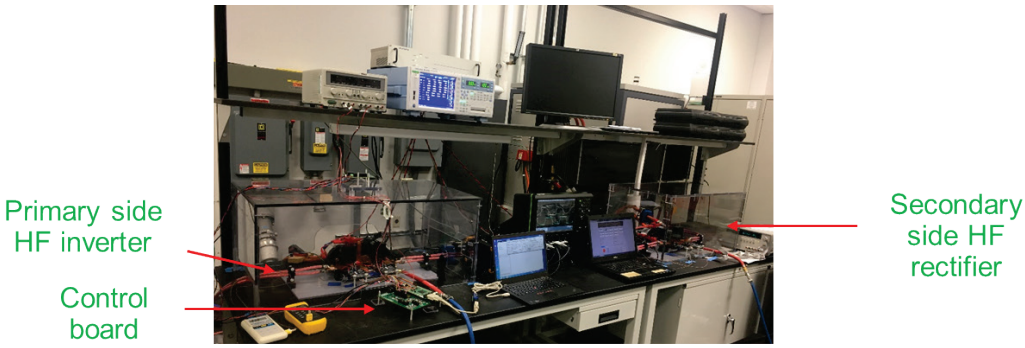

Figure V.3.6 Laboratory experimental setup of the 120 kW wireless power transfer system with the hardware integrations.

In Figure V.3.7, the Yokogawa WT1800 high-precision power analyzer test results are presented at 120 kW power transfer to the load. Test results represented in Figure V.3.7 include the voltage (U_{rms}), current (I_{rms}), active power (P), reactive power (Q), apparent power (S), power factor (λ), power angle (Φ), and the voltage (U_{C1}, U_{C2}) across the resonant tuning capacitors C_1 and C_2. In these results, Element 1 represents the primary-side inverter DC input, Element 2 represents the inverter output (applied to the primary resonant tank), Element 4 represents the secondary resonant tank (rectifier input), and Element 5 represents the rectifier output (battery). Figure V.3.8 shows the inverter, coil-to-coil, rectifier, and the overall dc-to-dc efficiency at 120 kW operation. As seen in this figure, inverter operates at 99.029% efficiency, coil-to-coil efficiency is 98.617%, and secondary-side rectifier efficiency is 99.385%. In Figure V.3.9, the system level diagram with stage-by-stage power flow and efficiencies are shown with 124.49kW input power and 120.83kW output power. In Figure V.3.10, the oscilloscope captured waveforms of the primary-side inverter output and secondary-side rectifier input are shown indicating the zero-voltage turn-on and very low current (quasi-zero) turn-off of the inverter switches which results in extremely low switching losses.

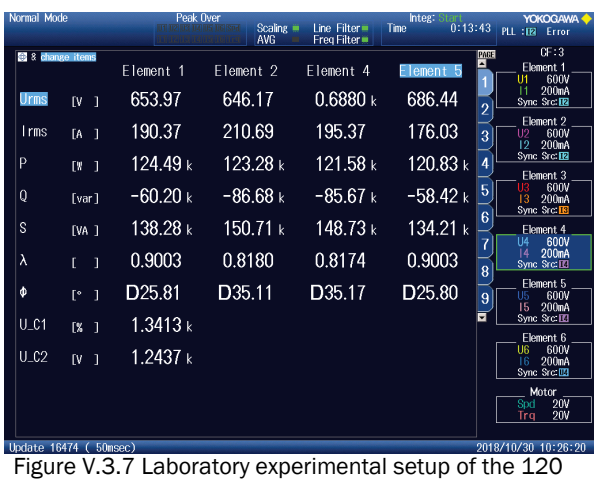

Figure V.3.7 Laboratory experimental setup of the 120 kW wireless power transfer system with the hardware integrations.

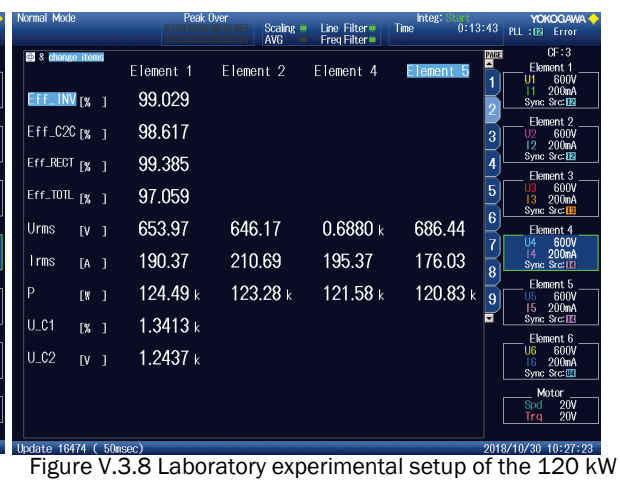

Figure V.3.8 Laboratory experimental setup of the 120 kW wireless power transfer system with the hardware integrations.

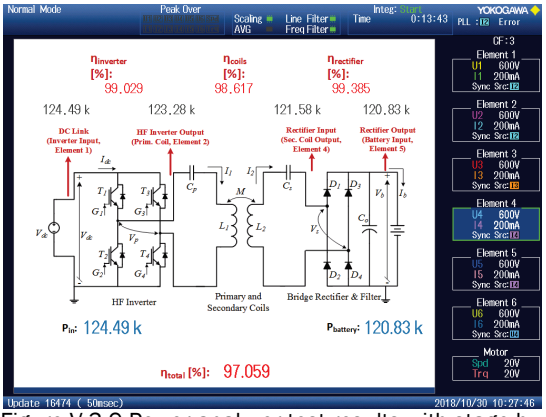

Figure V.3.9 Power analyzer test results with stage-by-stage power flow and efficiencies.

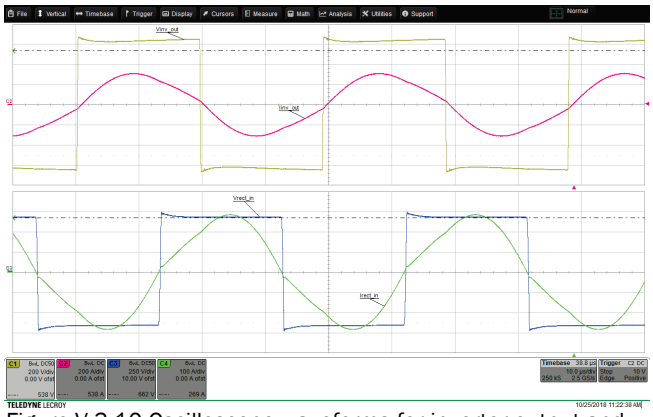

Figure V.3.10 Oscilloscope waveforms for inverter output and rectifier input on primary and secondary sides.

The cascaded efficiency of the system can also be calculated by multiplying the power stage efficiencies such that $\eta_{overall} = \eta_{inverter} \times \eta_{coil-to-coil} \times \eta_{rectifier} = 99.029\% \times 98.617\% \times 99.385\% = 97.06\%$ which confirms the power analyzer measured dc-to-dc overall efficiency of 97.059%.

Experimental test results also show the electric and electromagnetic field emissions measured using a Narda EHP-200 isotropic field measurement device that is placed 31.5 inches away from the center of the primary coupler. As seen in, the electric field is measured to be 14.06 V/m while the international limit is 83 V/m set by the ICNIRP (International Figure V.3.11 Commission on Non-Ionizing Radiation Protection) at the measurement point. As shown in Figure V.3.12, the magnetic field is measured to be 21.64 µT while the international limit is 27 µT. These electric and electromagnetic field emission test results at 31.5 inches away from the center of the primary coil are shown in Figure V.3.11 and Figure V.3.12, respectively.

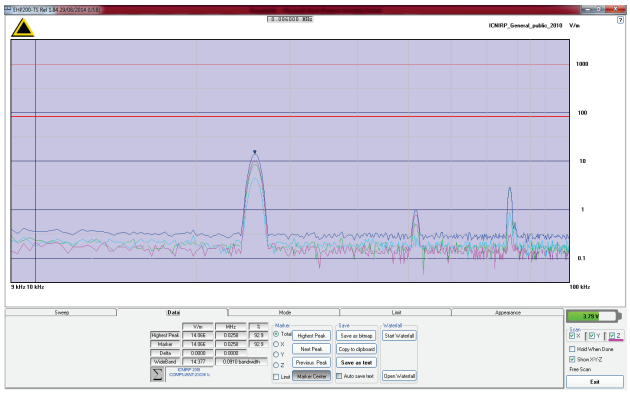

Figure V.3.11 Electric field emissions at 31.5” away from the center of the primary coil (14.06 V/m highest peak).

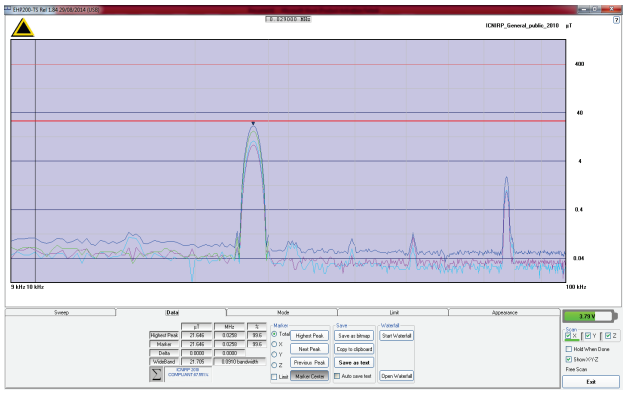

Figure V.3.12 Magnetic field emissions at 31.5” away from the center of the primary coil (21.64µT highest peak).

Conclusions

In this project, an optimized DD electromagnetic coupling coil has been designed and prototyped based on FEA simulations and system level considerations. A single phase state-of-the-art 1200 V SiC phase leg modules (CAS325M12HM2) based high efficiency inverter is designed, assembled and utilized to enable a high power stationary wireless charging system capable of transferring 120 kW. The resonant stage was analyzed based on the loosely coupled transformer model and the analyses agreed well with experimental measurements. The wireless charging system was tested at 120 kW and had a measured dc-to-dc efficiency of more than 97 % at nominal coil-to coil airgap. Future work will include high-power dynamic wireless charging system design and development for dynamic wireless charging applications as well as demonstrating 100 kW

and 300 kW system design and full vehicle integrations and demonstrations under relevant activities sponsored by DOE VTO.

Key Publications

1. M. Mohammad, J. Pries, O. C. Onar, and V. Galigekere, "Design of an EMF Suppressing Magnetic Shield for a 100kW Double-D-Coil Wireless Charging System for Electric Vehicle," *accepted for presentation, IEEE Applied Power Electronics Conference and Exposition*, conference to be held in March 2019, Anaheim, CA.
2. J. Pries, V. Galigekere, O. C. Onar, and G. –J. Su, "Coil power density optimization and trade-off study for a 100 kW electric vehicle IPT wireless charging system," in *Proc., IEEE Energy Conversion Congress and Exposition* (ECCE), September 2018, Portland, OR.
3. V. Galigekere, J. Pries, O. C. Onar, and G. –J. Su, "Design and implementation of an optimized 100 kW stationary wireless charging system for EV battery recharging," in *Proc., IEEE Energy Conversion Congress and Exposition* (ECCE), September 2018, Portland, OR.

References

1. M. Yilmaz and P. T. Krein, "Review of battery charger topologies, charging power levels, and infrastructure for plug-in electric and hybrid vehicles," IEEE Transactions on Power Electronics, vol. 28, no. 5, pp. 2151–2169, May 2013.
2. D. Howel, S. Body, B. Cunningham, S. Gillard, and L. Slezak, "Enabling Fast Charging: A Technology Gap Assessment," U.S. Department of Energy, October 2017. [Online]. Available: https://energy.gov/sites/prod/files/2017/10/f38/XFCn%20Technologyn%20Gapn%20Assessmentn%20Reportn FINALn 10202017.pdf
3. Society of Automotive Engineers, Wireless Power Transfer for Light-Duty Plug-In/Electric Vehicles and Alignment Methodology. SAE International. [Online]. Available: http://standards.sae.org/j2954n 201711/
4. S. Li, W. Li, J. Deng, T. D. Nguyen, and C. C. Mi, "A double-sided lcc compensation network and its tuning method for wireless power transfer," IEEE Transactions on Vehicular Technology, vol. 64, no. 6, pp. 2261–2273, June 2015.

V.4 Interoperability, Grid Integration and Fast Charging (ANL)

Keith Hardy, Principal Investigator
Argonne National Laboratory
9700 S. Cass Ave.
Lemont, IL 60439
Email: khardy@anl.gov

Lee Slezak, DOE Technology Development Manager
U.S. Department of Energy
E-mail: Lee.Slezak@ee.doe.gov

Start Date: October 1, 2016 End Date: September 30, 2018
Project Funding: $11,102,574 (3 yrs) DOE share: $11,102,574 Non-DOE share: $0

Project Introduction

Argonne's FY 2018 activities supporting interoperability and grid modernization were continuations of tasks initiated in the Lab Call awarded for FY 2016. High power DC charging was added in the latter part of FY 2017 and focused on infrastructure modifications to accommodate the higher power input requirements.

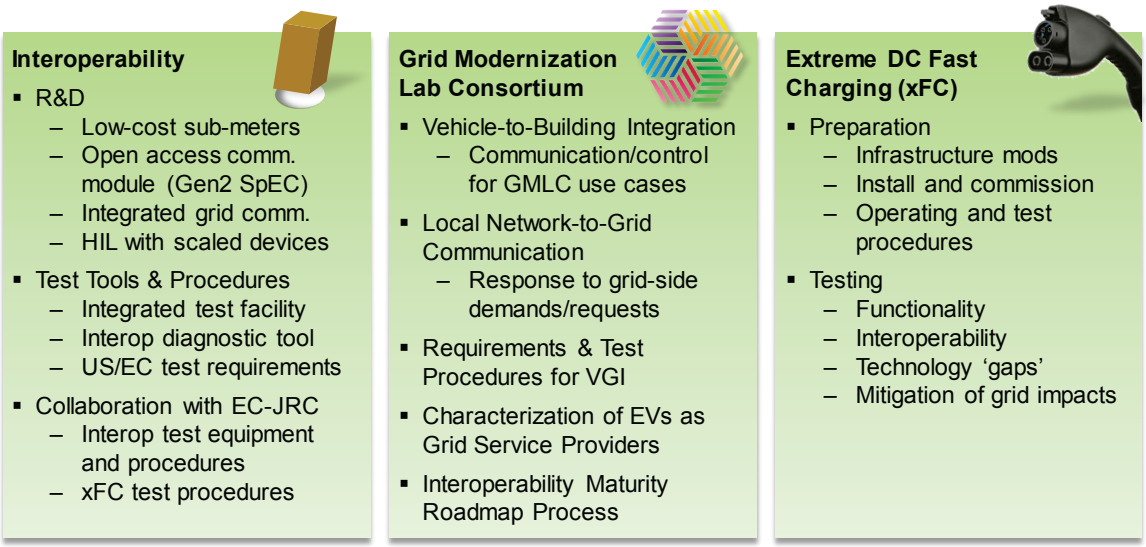

Figure V.4.1. FY 2018 DOE VTO/GMLC support activities

Interoperability activities, in cooperation with industry partners, produce enabling technologies, support standards development and promote harmonization of EV interoperability requirements and test procedures. The GMLC tasks are multi-lab efforts with joint deliverables. Integrating and testing high power DC charging (aka 'xFC' for extreme fast charging) resulted from Argonne's years of involvement in Global InterOP, which included US and European automotive OEMs as well as the EC's Joint Research Center (EC-JRC).

Objectives

The EV-Smart Grid Interoperability Center has evolved over the last six years from developing technologies and tools that support EV interoperability to those supporting vehicle-grid integration, which utilize similar connectivity and communication technologies. The premise is that networking electric vehicles, building systems, renewable energy and energy storage…and holistically managing the energy flow…offer additional benefits/value to EV customers, supports workplace energy management and minimizes negative impacts on

the local grid. Therefore, the objectives of Argonne's activities have been to develop an integrated network of devices to test the premise, identify the associated connectivity/communication requirements and develop enabling technologies that were not available commercially.

In brief, the FY 2018 objectives:

- Produce more robust designs of the enabling technologies, i.e., sub-meters, second-generation SpEC module and the Smart Charge Adaptor/Diagnostic Electric Vehicle Adaptor (SCA/DEVA), to prepare them for field-testing in FY 2019.
- Complete the installation of devices and integrated communication with the Common Integration Platform (CIP.io) at the Energy Plaza, i.e., PV inverters, AC L2 EVSE, DC xFC EVSE, second-use vehicle battery, metering and the Opal RT real-time simulator (and the Distributed Network Model); necessary to develop integrated control algorithms and demonstrate the use cases as well as to prepare for Hardware-In-the-Loop (HIL)-based grid impact studies in FY 2019.
- Demonstrate a subset of the GMLC use cases using the network of devices and CIP.io (a 'subset' because the GMLC program started in the middle of the FY; the complete set of uses cases is planned to be completed by Q3 FY 2019). The emphasis for these cases is 'controlled' versus 'smart' charging, which is not possible until EVs and EVSE are equipped with the appropriate communication protocols (assumed to be available from our industry partners in FY 2019).
- Continue international cooperation to coordinate high power DC charging (HPC in Europe; xFC for extreme fast charging in DOE terminology) test procedures, conduct the joint pilot of the Interoperability Maturity Roadmap Process (GMLC 1.2.2 – Strategic Interoperability), collaborate on the Smart Vehicle-Grid Integration Proposal (DOE VTO Lab Call for FY 2019-2021) and provide technical support at the APEC Automotive Dialog meetings (coordinated by Dept. of Commerce).

Approach

Interoperability

Research and development

- Smart Charge Adaptor/Diagnostic Electric Vehicle Adaptor (SCA/DEVA): perform gap analysis (i.e., prototype characteristics versus commercial design requirements) and preliminary design for commercialization (partner: Planet Innovation)
- Sub-meters: leverage the BTO-funded commercialization activity and apply latest developments to electric vehicle supply equipment (EVSE, aka charging equipment), e.g., DC metering (partners: 2G Engineering, Amzur Technologies)
- Open access communication module: design a second generation SpEC module to reduce cost and enhance functionality as either an EV or EVSE control module; target 60-70% cost reduction (partner: Planet Innovation)
- Develop the CIP.io interfaces for the additional devices in the Energy Plaza and integrated control algorithms to support the VTO and GMLC studies; devices include inverters for the additional PV array, AC L2 EVSE, DC xFC EVSE, second-use vehicle battery and metering (partner: CSS)
- Develop and integrate a distributed network model with Opal RT and CIP.io to enable HIL studies, i.e., the integrated network of devices is the system under test and the grid model provides the simulated test environment; or the device power consumption characteristics of the Energy Plaza network can be scaled and imposed on nodes of the distributed network model to assess grid impacts, e.g., voltage fluctuations (partner: Michigan Technological University)

Test Tools and Procedures

- Integrated Test Facility: complete installation and networking of the additional devices, listed above, in the Energy Plaza (partners: Porsche Engineering, Argonne Sustainability Program)
- Interoperability test equipment: acquire and evaluate the Comemso AC/DC interop test tool

Collaboration with the European Commission's Joint Research Center (EC-JRC)

- Extreme fast charging/high power charging (xFC/HPC) EVSE: collaborate with EC-JRC to develop common test requirements and procedures for Europe and the US; focusing on assessing functionality, performance, interoperability, safety and cybersecurity of the xFC/HPC EVSE at the Energy Plaza and EC-JRC in Italy.
- Interoperability test equipment and procedures: coordinate evaluation of the Comemso test tool

Grid Modernization Laboratory Consortium

Argonne supported GMLC tasks defined as 'program-specific', which were defined and directed by the Vehicle Technologies Office (i.e., GM 0062 and 0085), and 'foundational', i.e., those defined by the GMLC management team as having more broad application across program offices (GMLC 1.2.2, 1.4.1 and 1.4.2). The foundational tasks are summarized only briefly since they will be addressed in more detail in the GMLC annual report.

- Utilize the Energy Plaza network to demonstrate the GMLC uses cases with controlled charging
  - Demand response (DR) – Demonstrate that EVSE charging power can be controlled in response to a DR signal.
  - Demand charge mitigation – Demonstrate that charge power can be managed (individually) for multiple vehicles such that a pre-set power value is not exceeded while meeting individual charge preferences.
  - Preferential charging – Demonstrate that demand charges while maximizing the use renewable energy and the meeting customers' preferences for "greenest", "cheapest" or "fastest" charge.
  - Frequency regulation – Demonstrate the ability to meet the requirements of a frequency regulation signal using charge control of multiple vehicles.

Local Network-to-Grid Communication (GM 0085)

- The project was re-scoped in FY18 to integrate the GM0062 and GM0085 and leverage the work of GM0062 to provide forecasts to the aggregator model of GM 0085. Argonne would define the process and method of providing the forecasts.

Strategic Interoperability (GMLC 1.2.2)

Following the team's adaptation of the general Interoperability Maturity Mapping (IMM) process for GMLC, Argonne's role has been to initiate an EV roadmap trial of the methodology and interoperability roadmap model. Following unsuccessful attempts to establish a US trial, the project will focus on the rollout of charging infrastructure in Europe in cooperation with EC-JRC beginning in FY 2019.

Requirements and Test Procedures for Vehicle-Grid Integration (GMLC 1.4.1)

This project focuses on gaps in requirements and test procedures to support the development of standards for interoperability across technologies, i.e., to support integration of a variety of grid-connected devices. Argonne's focus is EV requirements and test procedures and harmonizing those with a variety of standards and

test procedures such as the IEEE2030.5/SEP EVSE test procedure draft, created with industry input and hosted by the Sunspec Alliance SDO. The effort necessitates liaison with several standards committees that were previously considered outside the scope of vehicle technologies.

Characterization of EVs as Grid Service Providers (GMLC 1.4.2)

Argonne is developing a 'grid cycle' for vehicles that combines 'real world' driving and activity schedules with actual grid service request schedules from grid operational data; vehicle testing began in FY 2018 and will continue in FY 2019.

Extreme Fast Charging (xFC)

The xFC task was added to Argonne's responsibilities by VTO in late FY 2017; the intent was to understand the implications/impacts of high power charging from technological and infrastructure perspectives. Based on Argonne's relationship with US and European automotive manufacturers developed in Global InterOP, Porsche Engineering offered to contribute 2 x 350 kW EVSE hardware for installation at Argonne's Energy Plaza to support interoperability testing. In addition Argonne would acquire a 200 kW EVSE from BTC Power (Porsches Engineering's US partner) to compare the characteristics of Porsche's dedicated design to BTC Power's modular design. Though the intent was to complete installation and initiate testing of both EVSE in FY 2018, most of the effort was spent on preparation for installation due to delays in hardware delivery and commissioning.

Preparation

- Infrastructure modifications
  - It was determined that the 200 kW EVSE would be located on the 'high power' fueling island with the 50 kW Tritium EVSE and the 2 x 350 kW EVSE would be located adjacent to the building and the parking lot in a layout that would approximate a roadside installation in the US.
- Installation and commissioning
  - 200 kW EVSE the fueling island: This effort would require additional components to comply with Argonne safety requirements, e.g., emergency power cutoffs, and connectivity to the power panel in the building.
  - 2 x 350 kW installation adjacent to the building: This would require excavation, a foundation for the transformer building, a direct connection to the 13.2 kVA supply, conduits for electrical and cooling lines to the power and cooling boxes as well as the two dispensers
- Operating and test procedures
  - An initial test plan was proposed by Porsche Engineering and additional information was expected from the initial testing of high power EVSE at the EC-JRC in Ispra. The intent is to combine these to produce a compatible plan for characterizing functionality, interoperability, safety, etc. This will include characterization with the Comemso interoperability test equipment. It is expected that we will gain access to electromagnetic characteristics evaluated at EC-JRC; their facility was constructed for the purpose of characterizing EVs and EVSE emissions as well as evaluating the results of bombardment with signals generated outside of the vehicles or EVSE.

Testing

The intent is to utilize common European and US procedures to evaluate the 200 kW and 2 x 350 kW systems. That could not be accomplished in FY 2018 due to delays in delivering and commissioning the EVSE hardware. The 200 kW system was commissioned late in the fiscal year and will be evaluated in FY 2019. The

transformer building of the 2 x 350 kW system was installed, but the balance of the system (power and cooling boxes plus two user units) will not be delivered and commissioned until Q2/Q3 FY 2019.

Results

Integrated Test Facility

Figure V.4.2. Argonne Smart Energy Plaza Facility in Lowell, Illinois

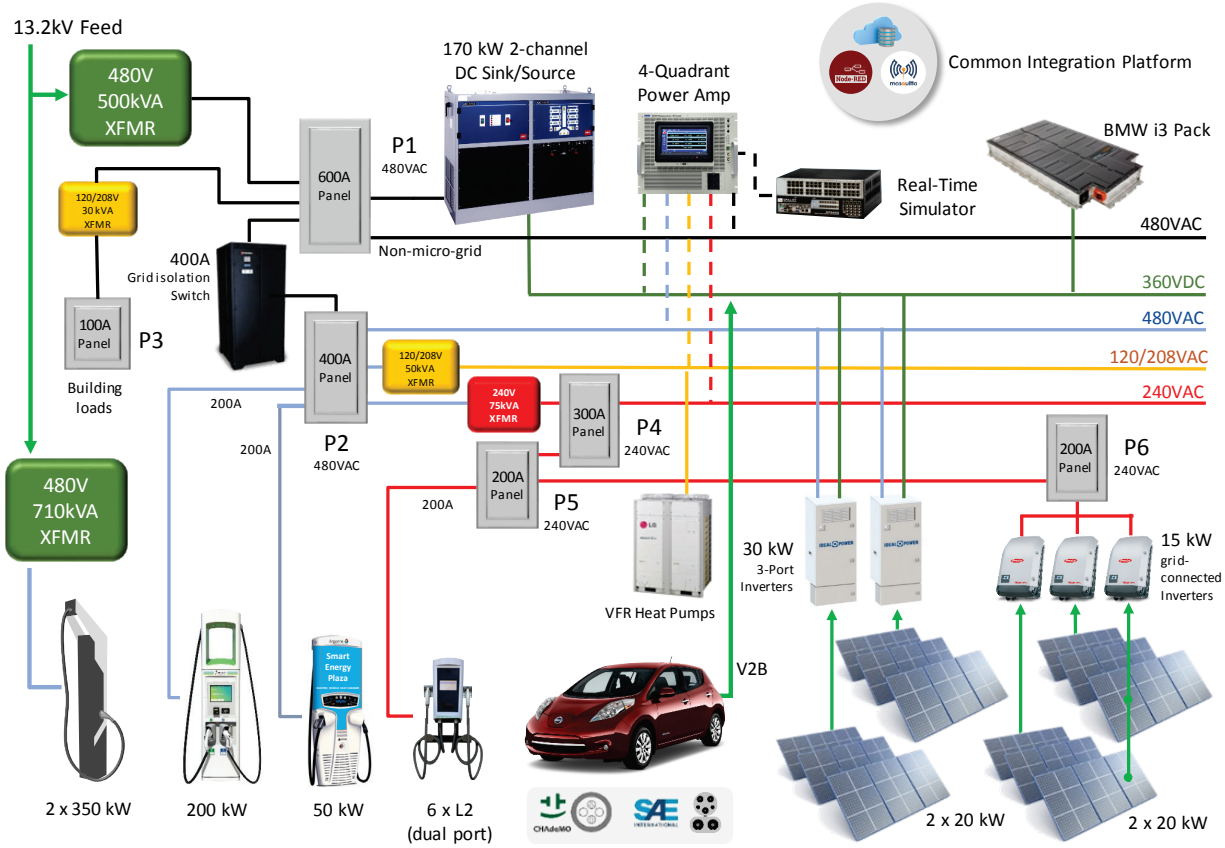

Figure V.4.3. Basic connectivity of devices at the Smart Energy Plaza

Completed installation of additional devices at the Smart Energy Plaza (40 kW solar canopy with inverters and metering, three dual port AC L2 EVSE, 200 kW DC EVSE, BMW i3 'second-use' vehicle battery and Opal RT real-time simulator), the Distributed Network (grid) Model and integration with CIP.io. The renovation of

the former gas station was funded by the Argonne Sustainability program and the research equipment was funded by DOE VTO; leading to the building and the EV charging program being recognized with a 2018 DOE Sustainability Award

Progress on Innovative Technologies under Development

- **Low-cost sub-meter for xFC DC EVSE (1000Vdc/500Adc)** – A key factor in the reduced size of the metrology circuit board, approximately 2" x 2", that can be mounted directly to the terminals of a current sensing shunt; fabrication and demonstration is planned for FY 2019.

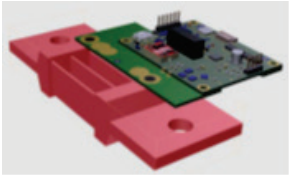

Figure V.4.4 xFC sub-meter design

- **Smart Grid PEV Communication (SpEC) Module 2.0** – The original SpEC module has been redesigned with partner Planet Innovation, targeting a BOM cost goal of under $75. SpEC2 includes an onboard AC and DC energy meter, ground fault interrupter (GFI) circuit and more general purpose input/output (GPIO). The SpEC2 module can be configured as non-networked or smart AC EVSE communication controller (SECC) or an electric vehicle communication controller (EVCC). Alpha prototypes are expected to be delivered in Q1 FY 2019.

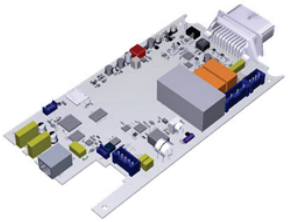

Figure V.4.5 SpEC2 module design

- **Smart Charge/Diagnostic EV Adaptor (SCA/DEVA)** – The original version of the SCA ('alpha') has been redesigned to be more robust for field testing and add diagnostic functions. An alpha gap analysis was completed with Planet Innovation to determine design requirements for the Beta version. FCA and Qmulus worked with Argonne to determine functional requirements for DEVA.

Figure V.4.6 SCA/DEVA beta design

GMLC Vehicle-to-Building Integration project (GM 0062)

Argonne developed charge control algorithms and successfully demonstrated the following GMLC-defined use cases at the Smart Energy Plaza, using real vehicles, alpha SCAs and L2 AC EVSE:

- **Demand charge mitigation** – Integrated control of multi-vehicle charging in a dynamic workplace environment can avoid peak demand charges by controlling to a power limit, while maximizing available charging power and prioritizing PEVs with the highest energy needs. Argonne's control algorithm is based on instantaneous missing capacity (DC Ah) of individual PEVs.
- **Preferential charging** – Optimal power draw of the plaza (i.e., not exceeding a pre-set power limit) can be managed with CIP.io while meeting the individual EV charging power requirements and preferences of their drivers (e.g., cheapest, greenest, fastest).

- **Control pilot Pulse Width Modulation (PWM) response** – The latency and resolution of control with an example PEV was shown to be 1-2 seconds, including two-way communication and vehicle response time, based on results from a Chevy Volt controlled by an SCA.

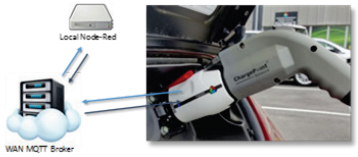

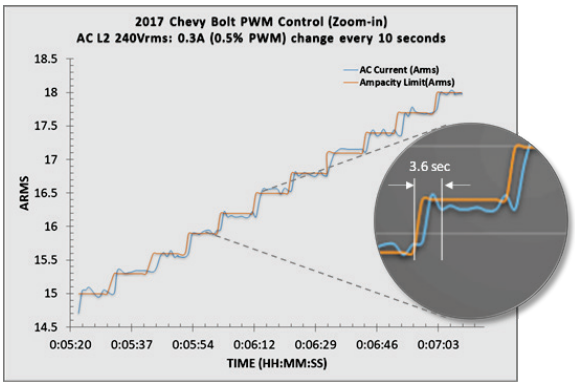

Figure V.4.7 Two-way communication latency example

- **Frequency regulation** – An ancillary service provided by Independent System Operators (ISOs) in the US, this has typically been the most lucrative grid services market. Four PEVs were aggregated on non-networked EVSE to follow the standard PJM RegD test signal and their control pilot duty cycles were modulated with SCAs. Results indicated that communication latency and PEV response times (~3 seconds) align with the requirements of this market.

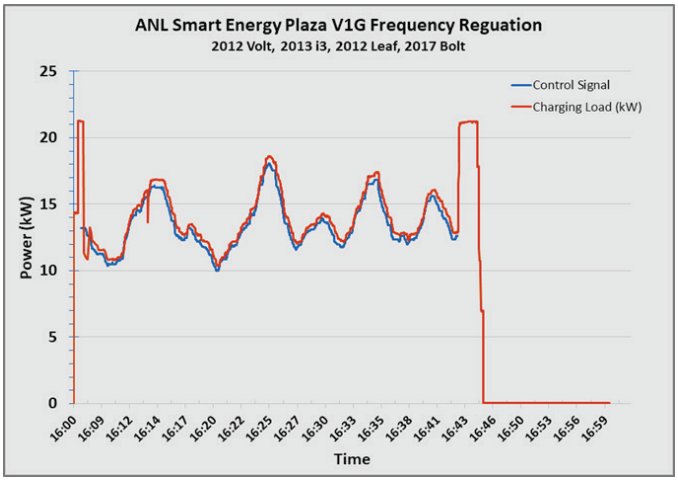

Figure V.4.8 Response time example – aggregated EVs

GMLC Local Network-to-Grid Communication (GM 0085)

The project was re-scoped in FY 2018 to utilize EVSE charging load forecasts in their EV charging aggregator model; the forecasts would be provided by GM0062. Argonne defined the process and method to provide the forecasts utilizing the CIP.io approach. Inter-lab communication over the internet was established via the ANL TLS encrypted global MQTT Broker. Argonne led the design of the communication protocol (topics/payloads), provided instructions and code for each lab to integrate their systems into CIP.io and created a method to "playback" energy forecasts to the INL aggregator to aid in testing.

International Cooperation

Argonne's EV-Smart Grid Interoperability Center and the EC-JRC are collaborating to harmonize test requirements and procedures for EV interoperability under the auspices of the DOE cooperative agreement with EC-JRC of 2016. This activity originally focused on AC charging and PEV test procedures, but has shifted to high power DC charging (up to 350 kW), associated interoperability test equipment and grid integration.

The EC-JRC Ispra, IT laboratory is working with European vehicle OEMs and EVSE manufacturers to test high power (350 kW) DC EVSE from four manufacturers, ABB, Efacec, Ionity and Tritium. The Ionity EVSE utilizes the same components as the Porsche Engineering/BTC Power EVSE being installed at Argonne. Argonne and EC-JRC are sharing lessons learned regarding test procedures and the implications for each system; valuable information as the intent is to develop a common transatlantic EVSE test procedure in FY 2019. In addition, EC-JRC has developed a smart home test lab at their Petten, NL location. Argonne and EC-JRC will be working together to implement compatible communication integration approaches to support the Smart VGI Project in FY 2019.

Argonne has continued to support the Department of Commerce at meetings of the APEC Automotive Dialog regarding EV interoperability and vehicle-grid integration. Requests from several countries to learn the technical approach to PEV-grid integration at Argonne have continued as well. The relatively small technical team in the interoperability and grid integration activities has limited Argonne's contribution to hosting visits.

Conclusions

Facilities/capabilities – Most of the essential devices to support VTO and GMLC research at the Smart Energy Plaza have been installed and connected to the common integration platform. The exceptions are the remaining components of the 350 kW EVSE system (power and cooling boxes plus the two dispensers) and a power source/sink for xFC power mitigation studies. In addition, the HIL capability has been established with the Opal RT and Distributed Network Model.

Enabling technologies – The Argonne-developed sub-meters, SpEC2 communication modules and the Smart Charge/Diagnostic EV Adaptor (SCA/DEVA) will be ready for field testing with industry partners in FY 2019.

GMLC use cases – Argonne has successfully demonstrated the controlled charging use cases on schedule and will complete the basic GMLC use cases by Q3 FY 2019. The basic uses will be repeated with smart charge control will be demonstrated in FY 2019 and FY 2020; made possible by industry partners providing vehicles and EVSE equipped with the ISO 15118 standard communication protocol.

International cooperation – The Department of Commerce is committed to maintaining technical as well as diplomatic representation at the APEC Automotive Dialog meetings due to the global interest in deploying EVs and requests to learn more about EV interoperability and grid integration activities at Argonne. Argonne's participation is perceived as a positive influence on relations between the economies and offers the opportunity to work together to develop a common understanding of the benefits of harmonized, or at least compatible, standards and regulations.

Key Publications

Publications

1. Cao, Chong, Bo Chen and Jason Harper. "Plug-in Electric Vehicle Charging Control Adapting to Limited Power Resources." Paper to be presented at the 10th Conference on Innovative Smart Grid Technologies, February 18, 2019 - February 21, 2019.

Patents/Copyrights

1. J. D. Harper, "node-red-oadr-ven", Copyright 2018, Argonne National Laboratory, Submitted.

U.S. DEPARTMENT OF
ENERGY

Office of
ENERGY EFFICIENCY &
RENEWABLE ENERGY

For more information, visit:
energy.gov/eere/vehicles

DOE/EE-1832 April 2019